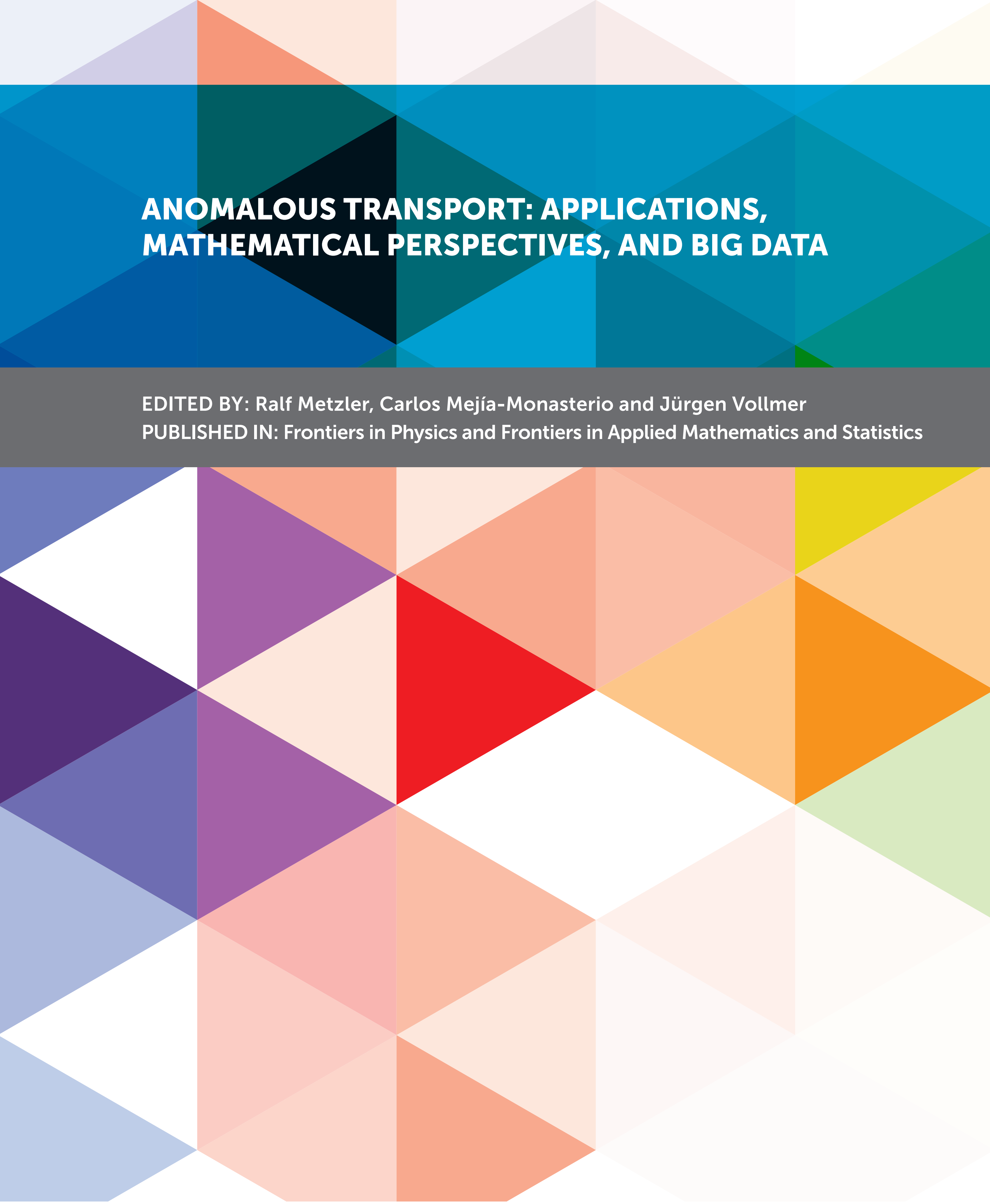

ANOMALOUS TRANSPORT: APPLICATIONS, MATHEMATICAL PERSPECTIVES, AND BIG DATA

EDITED BY: Ralf Metzler, Carlos Mejía-Monasterio and Jürgen Vollmer
PUBLISHED IN: Frontiers in Physics and Frontiers in Applied Mathematics and Statistics

frontiers Research Topics

ISSN 1664-8714
ISBN 978-2-88966-365-1
DOI 10.3389/978-2-88966-365-1

About Frontiers

Frontiers is more than just an open-access publisher of scholarly articles: it is a pioneering approach to the world of academia, radically improving the way scholarly research is managed. The grand vision of Frontiers is a world where all people have an equal opportunity to seek, share and generate knowledge. Frontiers provides immediate and permanent online open access to all its publications, but this alone is not enough to realize our grand goals.

Frontiers Journal Series

The Frontiers Journal Series is a multi-tier and interdisciplinary set of open-access, online journals, promising a paradigm shift from the current review, selection and dissemination processes in academic publishing. All Frontiers journals are driven by researchers for researchers; therefore, they constitute a service to the scholarly community. At the same time, the Frontiers Journal Series operates on a revolutionary invention, the tiered publishing system, initially addressing specific communities of scholars, and gradually climbing up to broader public understanding, thus serving the interests of the lay society, too.

Dedication to Quality

Each Frontiers article is a landmark of the highest quality, thanks to genuinely collaborative interactions between authors and review editors, who include some of the world's best academicians. Research must be certified by peers before entering a stream of knowledge that may eventually reach the public - and shape society; therefore, Frontiers only applies the most rigorous and unbiased reviews.

Frontiers revolutionizes research publishing by freely delivering the most outstanding research, evaluated with no bias from both the academic and social point of view. By applying the most advanced information technologies, Frontiers is catapulting scholarly publishing into a new generation.

What are Frontiers Research Topics?

Frontiers Research Topics are very popular trademarks of the Frontiers Journals Series: they are collections of at least ten articles, all centered on a particular subject. With their unique mix of varied contributions from Original Research to Review Articles, Frontiers Research Topics unify the most influential researchers, the latest key findings and historical advances in a hot research area! Find out more on how to host your own Frontiers Research Topic or contribute to one as an author by contacting the Frontiers Editorial Office: researchtopics@frontiersin.org

ANOMALOUS TRANSPORT: APPLICATIONS, MATHEMATICAL PERSPECTIVES, AND BIG DATA

Topic Editors:
Ralf Metzler, University of Potsdam, Germany
Carlos Mejía-Monasterio, Polytechnic University of Madrid, Spain
Jürgen Vollmer, Universität Leipzig, Germany

Citation: Metzler, R., Mejía-Monasterio, C., Vollmer, J., eds. (2021). Anomalous Transport: Applications, Mathematical Perspectives, and Big Data. Lausanne: Frontiers Media SA. doi: 10.3389/978-2-88966-365-1

Table of Contents

frontiers in Physics

EDITORIAL
published: 23 November 2020
doi: 10.3389/fphy.2020.622417

Editorial: Anomalous Transport: Applications, Mathematical Perspectives, and Big Data

Carlos Mejía-Monasterio[1]*, *Ralf Metzler*[2] *and Jürgen Vollmer*[3]

[1]Laboratory of Physical Properties, School of Agricultural, Food and Biosystems Engineering, Technical University of Madrid, Madrid, Spain, [2]Institute for Physics and Astronomy, University of Potsdam, Potsdam-Golm, Germany, [3]Institut für Theoretische Physik, Universität Leipzig, Leipzig, Germany

Keywords: anomalous (or non-Fickian) diffusion, anomalous heat conduction, stochastic dynamics, molecular overcrowding, dynamical systems

Editorial on the Research Topic

Anomalous Transport: Applications, Mathematical Perspectives, and Big Data

Diffusion is a fundamental process that addresses the stochastic motion of a test particle and the emerging broadening of its distribution function in the course of time. Diffusive-like motion was first reported in 1828 following the seminal experiments by Robert Brown a year earlier on the erratic motion of micron-sized granules contained in Clarkia *pulchella* pollen grains [1]. The theoretical foundations of Brown's observations were established almost a century later by Einstein, Sutherland, Smoluchowski, and Langevin [2–5].

Diffusion theory is a fundamental and well established area of research which continues to be very active. Concurrently, a broad range of stochastic phenomena exhibit significant deviations from normal diffusive behavior, commonly termed as anomalous diffusion. Anomalous transport is ubiquitously observed in many complex systems, ranging from the electronic transport of solid-state disordered systems [6], the motion of molecules inside living cell [7] and on their membrane [8], in the telomere motion inside the nucleus of mammalian cells [9], in soil transport [10], in heat transport in low-dimensional systems [11], and in certain classes of billiards [12], among a host of other phenomena.

From a statistical view point, all these diverse phenomena share a common description depending on how the broadening of the distribution function of the process $\xi(t)$ grows in time. This is customarily measured by the variance of the second moment, the so-called mean squared displacement (MSD) $\langle \xi^2(t) \rangle \simeq t^\gamma$. Normal diffusion corresponds to an MSD that grows linearly in time $\gamma = 1$, while anomalous diffusion is classified as subdiffusive for $\gamma < 1$ and superdiffusive $\gamma > 1$. From a dynamical view, there is a wealth of theoretical research devoted to unveil the physical mechanisms that can induce anomalous diffusion (see, e.g., Refs. 13–15 and references therein).

From an experimental point of view the past decade has vividly changed the field. Video microscopy and particle tracking are providing a rapidly increasing wealth of highly-resolved experimental observations. Moreover, numerical simulations of ensembles of trajectories are now feasible also for disordered systems where one must average over many realisations of the geometry. The resulting data sets should best be addressed from a big data perspective to extract characteristic transport properties. Firstly, this poses challenges for the automatic data processing and parameter inference. Secondly, it calls for new mathematical perspectives that underpin the data analysis from a unified point of view. In particular, data sets are big enough now to address the anomalous decay of correlations in the dynamics and to search for universality in the transport.

Edited and reviewed by:
*Alex Hansen,
Norwegian University of Science and Technology, Norway*

***Correspondence:**
*Carlos Mejía-Monasterio
carlos.mejia@upm.es*

Specialty section:
This article was submitted to Interdisciplinary Physics, a section of the journal Frontiers in Physics

Received: 28 October 2020
Accepted: 29 October 2020
Published: 23 November 2020

Citation:
Mejía-Monasterio C, Metzler R and Vollmer J (2020) Editorial: Anomalous Transport: Applications, Mathematical Perspectives, and Big Data. Front. Phys. 8:622417. doi: 10.3389/fphy.2020.622417

The aim of this Research Topic attempts to unify different visions, approaches and methodologies around the field of anomalous diffusion, to present an overview of the state of the art of the field, and insight into the main directions of current research. The research topic comprises 19 contributions discussing current issues, from experiments to theory, in anomalous transport. Here is a brief overview of these contributions.

A pathway to obtain anomalous diffusion is through molecular crowding and confinement. These two constraints prevail in living cells, where anomalous transport is often observed. With the advent of experimental techniques such as Fluorescence Spectroscopy (FS) and Single-Particle Tracking (SPT) we are able to study the dynamics in the cell and the cell kinetics that determine the essential processes of the living matter. This is the subject of the perspective article by Wringer et al. After an extensive overview Wringer et al. propose a collaborative global challenge to unify data benchmarks of biologically-relevant measures.

Memory effects have in general a strong influence on transport, leading to non-stationarity and aging. Using spectral theory Lapolla et al. discuss the non-Markovian stochastic processes that arises in the projected dynamics, like, e.g., in coarse-graining. Following this approach and using the coordinate Bethe *ansatz* Lapolla et al. are able to solve the problem of single file diffusion in a tilted box, where projection corresponds to the dynamics of the tagged particle after tracing out the dynamics of the rest of the particles.

Masó-Puigdellosas et al. also consider memory effects of resetting dynamics. They study how anomalous diffusion exhibited by otherwise diffusive random walks is determined when the walkers are subject to random relocations with memory. They show that the type of transport, from subdiffusive to superdiffusive is determined by the details of the resetting dynamics.

Over the last few decades different classes of anomalous transport have been described and observed. They include situations in which the MSD grows linearly in time as in normal diffusion, yet the statistics of the displacement is described by a strongly non-Gaussian probability distribution function. Such a situation, known as Brownian yet non-Gaussian diffusion (BnGD), is often observed in soft matter, biological and complex systems, and in general, in transport through heterogeneous environments [16]. Generalisations to non-Gaussian fluctuations include diffusing diffusivities [17], and strong anomalous diffusion in which the time scaling of the moments of the displacement is nonlinear in the moment's order [18].

Brownian yet non-Gaussian diffusion is the subject of the article of Baldovin et al. in which the authors consider a polymerization process in a closed fixed volume and with a fixed number of polymers. Following the statistics of the polymers center of mass they show that BnGD is a direct consequence of the polymerization process.

Di Tullio et al. discuss how anomalous diffusion emerges from diffusive dynamics on complex heterogeneous environments. They consider different models of anomalous diffusion such as continuous time random walks, Brownian motion with grey noise, and time-subordinated processes with a heterogeneous condition in which spatial and temporal scales are in turn random variables following a proper distribution, and show how this rescaling determines the type of anomalous transport.

Heterogeneous diffusion is characterised by an initial sampling of the local environment to a later exploration of the surrounding effective medium, yielding generically transient anomalous diffusion. Spakowitz studies the emergence of anomalous diffusion in heterogeneous environments. He models heterogeneity with a diffusivity that varies with position. By means of diagrammatic techniques, Spakowitz obtains an exact expression for the particle Green's function that captures the spatially varying diffusivity.

Active microrheology studies the response of a complex medium to the passage of a tracer particle that is driven through it, as in a colloid driven by an external force through a quiescent bath. The tracer particle reaches a stationary state in which the external force and the dragging force equilibrate. In the stationary state the tracer particle produces a nonequilibrium inhomogeneity in the density of the medium which in general leads to anomalous diffusion of the tracer [19].

Werner et al. consider the transport of asymmetrically grafted nanoparticles, often called hairy nanoparticles, that are pulled through a quiescent bath. Because of the external pulling the grafted colloids change the depletion zone around them, which in turns leads to an anisotropic effective viscosity. Werner et al. study the dependence of the friction force exerted by the bath on the profile of the local viscosity, and discuss the consequences of their results for active microrheology.

Bacteria are an example of active matter in which each bacterium transduces chemical energy into motion. Therefore, active matter is intrinsically out of equilibrium. What happens when a bacteria cell moves across complex geometries? This is the topic that Weber et al. address in their article. It is known that bacteria strongly interact with their surroundings and are often guided by confinements. Weber et al. consider a bacteria moving inside a labyrinth with square lattice geometry. The bacteria's motion is modelled as a run-and-tumble. Their analytical predictions show a transient non-Gaussian diffusion and compare well with experiments.

In the article of Um et al. active matter is further investigated. Modelling self-propelled particles as a Langevin dynamic driven by a telegraphic active noise, which essentially describes the transport of an active particle under confinement. Um et al. show that depending on the properties of the noise, different types of transport emerge, and they discuss relations with run-and-tumble and Lévy walks.

Reza Shaebani et al. consider the run-and-tumble model, characteristic of bacteria's motion and derive an expression for the MSD. They show that depending on the dynamic parameters and on the initial position of the process, the MSD exhibits a variety of transient regimes of anomalous transport. In all cases diffusion sets in asymptotically, with a diffusion coefficient that turns out to be independent of the initial starting of the process.

Territoriality is ubiquitous in the animal kingdom. Among mammals it is often associated with individuals marking their passage, to which other individuals react upon their encounter. A simple model for this situation is the so-called Territorial Random Walk (TRW) which comprises diffusion and local avoidance mechanism. Sarvaharman et al. consider a correlated TRW in which walkers are persistent and analyse the phase diagram picture that arises in this situation.

Transport in biological systems occurs in a complex "disordered" environment characterised by geometric disorder and the existence of energy barriers. For instance, inside the cell the actin cytoskeleton forms a cellular compartmentalisation for the proteins diffusing in the plasma membrane. It is believed that such constraints are responsible for the commonly observed subdiffusion. Muñoz-Gil et al. discuss the dynamics of a random walk in a compartmentalisation substrate where compartments are separated by barriers with random transmittance. They show that in their model a stochastic transmittance is essential to anomalous diffusion.

Segovia Gutierrez et al. present experimental results for the dynamics of synthetic trimer molecules in a random potential energy landscape that is realised by a random light field. Using SPT techniques they study the translational and rotational MSD showing that trimers move subdiffusively. However, such anomalous behavior is transient and converges to normal diffusion in the long time limit.

While anomalous diffusion has been well established over decades, anomalous heat transport was experimentally observed for the first time in 2008 [20]. Almost 200 years ago Joseph Fourier established from simple physical assumptions that the transport of heat must be described by a diffusion equation. Even when this is overwhelmingly observed, a first principles derivation of Fourier's law of heat conduction is still absent.

In the attempts to derive the diffusive character of heat conduction it has turned out that in low-dimensional systems Fourier's law probably does not hold. From a theoretical viewpoint, anomalous heat transport arises in general due to the strong dynamic correlations existing in low-dimensional systems, though a detailed understanding has remained elusive for decades. An overview of these issues appear in the review article of Benenti et al. They discuss anomalous heat transport in anharmonic chains of oscillators, considering magnetic fields and long-range interactions, among others. Furthermore, they discuss the important case of coupled transport which is the essence of generic thermodynamic transport. Benenti et al. close their review with an overview of open problems and future perspectives.

Concerning one-dimensional systems, the current picture that emerges is that when heat transport turns anomalous it means that the heat conductivity depends on the global state of the system rather than on its local properties. In the review article of Dhar et al. the authors discuss this non-locality, due to which Fourier's law is replaced by a non-local fractional diffusion equation. Dhar et al. review the different theoretical approaches leading to this framework and offer an exhaustive overview of recent progress.

Giberti et al. further discuss the non-locality implied by an anomalous heat conduction and how this affects the important assumption of Local Thermal Equilibrium (LTE). The non-local description of heat transport has direct fundamental consequences on the definition of local intensive thermodynamic quantities and therefore, on the LTE. To study these consequences Giberti et al. show that one-dimensional chains of oscillators interacting through a Lennard-Jones potential exhibit anomalously large distortions and fluctuations that hinder an appropriate thermodynamic treatment.

By means of parameter estimation from a finite set of trajectories and machine learning techniques Ridha Znaidi et al. provide algorithmic strategies to uncover the underlying dynamics of such trajectories. They assume the dynamics to be described by a set of fractional partial differential equations, which in the extended systems are able to describe anomalous diffusion.

Finally, the automatic data processing and parameter inference is discussed by Natole et al. For any scoring function, the **a**rea **u**nder the receiver operating characteristic **c**urve (AUC) is equivalent to the probability of a positive sample ranking higher than a negative sample. As such the AUC is a standard classification measure used in the analysis of imbalance class data and in clinical trials such as the development of vaccines to mitigate the COVID-19 pandemic. In their article Natole et al. develop a stochastic learning algorithm that maximises the AUC with respect to accuracy.

We are confident that this collection of articles provides a timely showcase for the state of the art in the field of anomalous diffusion. Moreover we look forward to see how the topics presented here will inspire further work in this rapidly developing field.

AUTHOR CONTRIBUTIONS

All authors listed have made a substantial, direct, and intellectual contribution to the work and approved it for publication.

FUNDING

CM-M acknowledges financial support from the Spanish Government grant PGC2018-099944-B-I00 (MCIU/AEI/FEDER, UE). RM acknowledges the Foundation for Polish Science (Fundacja na rzecz Nauki Polskiej, FNP) for a Humboldt Honorary Polish Research Scholarship.

REFERENCES

1. Brown R. A brief account of microscopical observations made in the months of June, July and August 1827, on the particles contained in the pollen of plants; and on the general existence of active molecules in organic and inorganic bodies. *Phil Mag* (1828) 4:161–73. doi:10.1080/14786442808674769.
2. Einstein AA. Über die von der molekularkinetischen Theorie der Wärme geforderte Bewegung von in ruhenden Flüssigkeiten suspendierten TeilchenÜber die von der molekularkinetischen Theorie der Wärme

geforderte Bewegung von in ruhenden Flüssigkeiten suspendierten Teilchen. *Ann Phys* (1905) 322:549–60. doi:10.1002/andp.19053220806.

3. Sutherland W. LXXV. a dynamical theory of diffusion for nonelectrolytes and the molecular mass of albumin. *Lond Edinb Dubl Phil Mag* (1905) 9:781–5. doi:10.1080/14786440509463331.
4. von Smoluchowski M. Zur kinetischen Theorie der Brownschen Molekularbewegung und der Suspensionen. *Ann Phys* (1906) 326:756–80. doi:10.1002/andp.19063261405.
5. Langevin P. Sur la théorie de movement brownien. *Compt. Rend. Acad. Sci* (1908) 146:530–3.
6. Bouchaud JP, Georges A. Anomalous diffusion in disordered media: statistical mechanisms, models and physical applications. *Phys Rep* (1990) 195:127–293. doi:10.1016/0370-1573(90)90099-n.
7. Saxton MJ. Anomalous subdiffusion in fluorescence photobleaching recovery: a Monte Carlo study. *Biophys J* (2001) 81:2226–40. doi:10.1016/s0006-3495(01)75870-5.
8. Nicolau DV, Hancock JF, Burrage K. Sources of anomalous diffusion on cell membranes: a Monte Carlo study. *Biophys J* (2007) 92:1975–87. doi:10.1529/biophysj.105.076869.
9. Bronstein I, Israel Y, Kepten E, Mai S, Shav-Tal Y, Barkai E, et al.. Transient anomalous diffusion of telomeres in the nucleus of mammalian cells. *Phys Rev Lett* (2009) 103:018102. doi:10.1103/physrevlett.103.018102.
10. Martin RL, Jerolmack DJ, Schumer R. The physical basis for anomalous diffusion in bed load transport. *J Geophys Res Earth Surface* (2012) 117:01018. doi:10.1029/2012jf002608.
11. Lepri S, Livi R, Politi A. Thermal conduction in classical low-dimensional lattices. *Phys Rep* (2003) 377:1–80. doi:10.1016/s0370-1573(02)00558-6.
12. Armstead DN, Hunt BR, Ott E. Anomalous diffusion in infinite horizon billiards. *Phys Rev E* (2003) 67:021110. doi:10.1103/physreve.67.021110.
13. Metzler R, Klafter J. The random walk's guide to anomalous diffusion: a fractional dynamics approach. *Phys Rep* (2000) 339:1–77. doi:10.1016/s0370-1573(00)00070-3.
14. Klages R, Radons G, Sokolov IM. *Anomalous transport: foundations and applications*. Weinheim, Germany: Wiley-VCH (2008)
15. Sokolov IM. Models of anomalous diffusion in crowded environments. *Soft Matter* (2012) 8:9043–52. doi:10.1039/c2sm25701g.
16. Wang B, Kuo J, Bae SC, Granick S. When Brownian diffusion is not Gaussian. *Nat Mater* (2012) 11:481–5. doi:10.1038/nmat3308.
17. Chechkin AV, Seno F, Metzler R, Sokolov IM. Brownian yet non-Gaussian diffusion: from superstatistics to subordination of diffusing diffusivities. *Phys Rev X* (2017) 7:021002. doi:10.1103/PhysRevX.7.021002.
18. Castiglione P, Mazzino A, Muratore-Ginanneschi P, Vulpiani A. On strong anomalous diffusion. *Phys Nonlinear Phenom* (1999) 134:75–93. doi:10.1016/s0167-2789(99)00031-7.
19. Bénichou O, Illien P, Mejía-Monasterio C, Oshanin G. A biased intruder in a dense quiescent medium: looking beyond the force-velocity relation. *J. Stat. Mech* (2013) 2013:P05008. doi:10.1088/1742-5468/2013/05/p05008.
20. Chang CW, Okawa D, Garcia H, Majumdar A, Zettl A. Breakdown of Fourier's law in nanotube thermal conductors. *Phys Rev Lett* 101 (2008) 075903. doi:10.1103/PhysRevLett.101.075903.

Conflict of Interest: The authors declare that the research was conducted in the absence of any commercial or financial relationships that could be construed as a potential conflict of interest.

frontiers in Physics

ORIGINAL RESEARCH
published: 18 March 2019
doi: 10.3389/fphy.2019.00031

Diffusion Through a Network of Compartments Separated by Partially-Transmitting Boundaries

Gorka Muñoz-Gil[1], *Miguel Angel Garcia-March*[1]*, *Carlo Manzo*[2]*, *Alessio Celi*[1,3,4] *and Maciej Lewenstein*[1,5]

[1] *ICFO - Institut de Ciències Fotòniques, The Barcelona Institute of Science and Technology, Barcelona, Spain,* [2] *Facultat de Ciències i Tecnologia, Universitat de Vic - Universitat Central de Catalunya (UVic-UCC), Vic, Spain,* [3] *Center for Quantum Physics, University of Innsbruck, and Institute for Quantum Optics and Quantum Information, Austrian Academy of Sciences, Innsbruck, Austria,* [4] *Departament de Física, Universitat Autònoma de Barcelona, Bellaterra, Spain,* [5] *ICREA, Barcelona, Spain*

Edited by:
Carlos Mejía-Monasterio,
Polytechnic University of Madrid,
Spain

Reviewed by:
Diego R. Amancio,
University of São Paulo, Brazil
Haroldo Valentin Ribeiro,
Universidade Estadual de Maringá,
Brazil

***Correspondence:**
Miguel Angel Garcia-March
miguel.garcia-march@icfo.eu
Carlo Manzo
carlo.manzo@uvic.cat

Specialty section:
This article was submitted to
Interdisciplinary Physics,
a section of the journal
Frontiers in Physics

Received: *20 November 2018*
Accepted: *21 February 2019*
Published: *18 March 2019*

Citation:
Muñoz-Gil G, Garcia-March MA,
Manzo C, Celi A and Lewenstein M
(2019) Diffusion Through a Network of
Compartments Separated by
Partially-Transmitting Boundaries.
Front. Phys. 7:31.
doi: 10.3389/fphy.2019.00031

We study the random walk of a particle in a compartmentalized environment, as realized in biological samples or solid state compounds. Each compartment is characterized by its length L and the boundaries transmittance T. We identify two relevant spatio-temporal scales that provide alternative descriptions of the dynamics: (i) the microscale, in which the particle position is monitored at constant time intervals; and (ii) the mesoscale, in which it is monitored only when the particle crosses a boundary between compartments. Both descriptions provide—by construction—the same long time behavior. The analytical description obtained at the proposed mesoscale allows for a complete characterization of the complex movement at the microscale, thus representing a fruitful approach for this kind of systems. We show that the presence of disorder in the transmittance is a necessary condition to induce anomalous diffusion, whereas the spatial heterogeneity reduces the degree of subdiffusion and, in some cases, can even compensate for the disorder induced by the stochastic transmittance.

Keywords: random walk, anomalous diffusion, stochastic processes, complex systems, barriers

1. INTRODUCTION

The characterization of the diffusive behavior in complex environments is crucial in many fields, ranging from biology [1], via physics and chemistry, to geology [2]. Recently, it has been shown that a large number of systems display anomalous diffusion associated to spatial and/or energetic disorder of the environment. Often, the motion of particles in such systems has been shown to be subdiffusive, i.e., $\langle x^2(t)\rangle \sim t^\sigma$ with anomalous exponent $0 < \sigma < 1$. The characterization of this movement provides important information on the disorder of the media and on the laws governing the system [3]. The advances in this field have been mainly driven by developments in fluorescence microscopy, which enable us to record movies of single particles diffusing in living matter, with a spatial precision of a few nanometers at the millisecond time scale [4].

The presence of barriers that prevent the particles to freely diffuse in the environments is a general mechanism used to explain subdiffusion [5]. Indeed, there exists a plethora of works treating the effect of these barriers in various forms, from local maxima in potential landscapes [6] to thin slices of poorly diffusive materials [7]. Recently, an analytical approach has been proposed for sufficiently regular geometries [8]. Recent experimental observations in cellular biology have shown that the actin cytoskeleton acts as a compartmentalization scaffold for proteins diffusing in the plasma membrane [9, 10], hence stressing the importance of studying the motion in such environments. Moreover, the evidence of the occurrence of ergodic and non-ergodic processes in the diffusion of biomolecules [11] has triggered the description of models in which geometric and energetic disorders coexist [12, 13].

In this article, we study a general barrier model, where a particle performs an unbiased random walk through a complex environment made by a mesh of compartments separated by barriers with random transmittance. A schematic of the system is shown in **Figure 1**. We show that even though the particle performs a Brownian motion within each compartment, the stochasticity of the barrier's transmittance induces anomalous diffusion for the overall movement. We also explore the effect of the stochasticity in the length of the compartments, showing that it generally increase the anomalous exponent, up to restoring normal diffusion.

In order to study the behavior of the particle, we propose a coarse-graining approach transforming the rather complex walk of the particle (mainly due to the interaction with the boundaries) into two very well known theoretical models describing anomalous diffusion: continuous time random walks and Lévy walks. The former, introduced by Montroll and Weiss [14], consists in a random walk where the time between successive steps is a stochastic value. Similarly, a Lévy Walk [15] consists in a random walk where not only the step time is a stochastic variable, but also its length. For a comprehensive introduction to both models, we refer the readers to Klafter and Sokolov [16] and Zaburdaev et al. [17].

In the most general description of our system, we show how the walk of the particle can be mapped into a Lévy walk with rests, where flight times depend on the step size. In our system, the steps and rests are not alternate but have complementary probabilities at each event. We show how the existing theory for a Lévy walk with rests can be extended to study such kind of walk. We determine the relationship between the stochasticity of the environment and the anomalous diffusion of the particle by solving different configurations of our system, characterized by fixed or random compartment sizes and boundary transmittances.

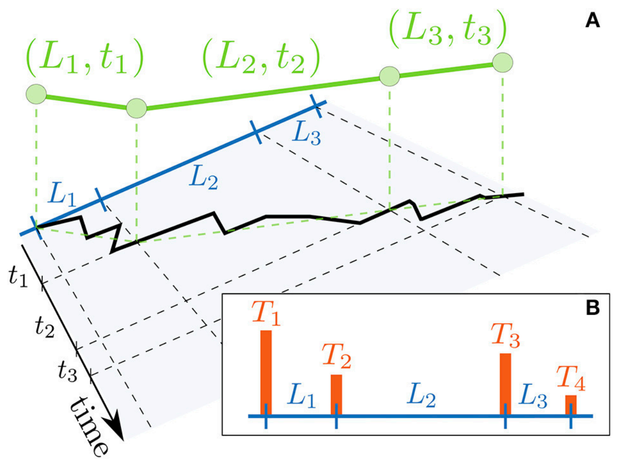

FIGURE 1 | Schematic of the system. **(A)** Example of a one dimensional compartmentalized environment, with compartment size L and boundary transmittance T. Higher boundaries represent lower transmittance. For simplicity we plot the meshwork as formed by the segments of a line. **(B)** Motion of the particle in such environment. The dark line represents the microscale description of the motion and the green one indicates its mesoscale description, in this case a Lévy walk with steps given by their length and flight time (L, t).

2. MATERIALS AND METHODS

The motion takes place on an environment characterized by a set of compartments with size $\{L_i\}_{i=1}^N$, with $N \gg 1$ and $L_i \in [1, \infty)$. We treat the size of the compartments as a stochastic variable, following the probability distribution function (PDF) $g(L)$. The compartments form a meshwork with unbounded connectivity, which we assume to be always sufficiently large such to make very unlikely that the particle returns to the same compartment after leaving it. The boundary between the compartments is partially reflective, i.e., a particle reaching a boundary has a finite probability T of moving through the boundary to the next compartment and a complementary probability $R = 1 - T$ of being reflected. The transmittance of each segment $\{T_i\}_{i=1}^N$, $T \in (0, 1]$ is a random variable drawn from the PDF $q(T)$.

For the sake of simplicity, we focus on the case where the compartments consist in one-dimensional segments (see **Figure 1A**). The extension of this theory to two- or three-dimensional supports, like circles or spheres, is conceptually straightforward but more elaborated and geometry-dependent, since it requires the determination of the stochastic time that the particle spends in each support. The particle performs an unbiased, discrete, random walk through the environment, temporarily confined between the boundaries until it is transmitted to the next compartment.

The motion of particles in disordered media has been thoroughly studied in the past [18]. The usual approach is to explicitly solve the diffusion equation for the system under study. For instance, such direct approach has been recently applied to subdiffusive particles through the barrier separating two liquids [19]. However, when considering systems like the one presented above, where both the boundary transmittance and compartment length are stochastic variables, the direct approach is complicated and does not lead to exact analytical results. Therefore, we use an alternative method to solve the motion of the particle through such a system. First, we distinguish between a microscale description, in which the position of the particle is monitored at constant times $<< L^2/D$ with D being the diffusivity, and a mesoscale description, in which the position is sampled at times subordinated to the exit from a compartment. We note here that, by definition, the asymptotic behavior of the motion of the particle coincides on both scales. Therefore, studying the movement at the mesoscale provides a correct description of the movement at long times.

In the mesoscale description, the microscopic walk of the particle (represented by the black line in the same figure) is reduced to a collection of lengths (L_i) and times (t_i) traveled to exit the compartments, as shown by the green line of **Figure 1B**. As a matter of fact, the length traveled by the particle in each step corresponds to the size of the compartment itself. The *flight time* t_i is the stochastic time the particle spent bouncing between the boundaries before being transmitted to next compartment. In our case, this time is related to the transmittance T and length L of the compartment through the conditional probability $\phi(t|T, L)$. One can then write the joint probability for the particle to be in a compartment of length L and boundary transmittance T at time t as

$$\psi(t, L, T) = \phi(t|T, L)g(L)q(T). \tag{1}$$

Once inside a compartment, the particle has two options: leaving through the same boundary through which it entered, or through the opposite one. Since our approach monitors the particle only when exiting a boundary, in the latter case, the particle has traveled a distance equal to the size of the compartment. However, in the former, the particle is not effectively moving, since it occupies the same position when entering and exiting the compartment. This translates into a rest with duration equal to the time taken to exit the compartment. Therefore, after entering each compartment, the particle has a probability of resting $\varphi_r(L, T)$ and the complementary probability of walking $\varphi_w(L, T) = 1 - \varphi_r(L, T)$.

Through this coarse-graining approach, we convert the microscale walk into a Lévy walk with rests, with flight times depending on the jump length [20]. Previous works have extensively studied such kind of walks, both with alternating walks and rests [16] or with an equal probability of resting and walking [17]. However, our system shows a substantial difference, since it displays different probabilities of resting or walking, $\varphi_r + \varphi_w = 1$, that can be used to calculate the PDFs of walk $[\psi_w(t)]$ and rest times $[\psi_r(t)]$ as

$$\psi_{w(r)}(t) = \int_1^\infty dL \int_0^1 \varphi_{w(r)}(L, T)\psi(t, L, T)dT, \tag{2}$$

and, in the spirit of Zaburdaev et al. [17], to derive the density of particles at position x and time t in the Fourier–Laplace space

$$P_\Sigma(k, s) = \int_0^1 P_{\Sigma,T}(k, s, T)dT, \tag{3}$$

where

$$P_{\Sigma,T}(k, s, T) = \frac{\Psi_r(s)P_0(k) + \left\{\varphi_w(x, T)\Psi(x, s, T)\right\}_k \psi_r(s)P_0(k)}{1 - \{\varphi_r(x, T))\psi(x, s, T)\}_k \psi_r(s)}. \tag{4}$$

Here, $P_0(x)$ corresponds to the initial distribution of particles, $\Psi(t) = \int_t^\infty \psi(t')dt'$ to the survival probability, i.e., the probability of not jumping until time t, $\Psi(x, t, T) = \int_t^\infty \psi(x, t', T)dt'$ to the PDF of the displacement of the walker during the last uncompleted step, and $\{f(x)\}_k$ to the Fourier transform of $f(x)$. For constant step/rest probabilities, e.g., $\varphi_w = \varphi_r = 1/2$, Equation (4) leads to the known result for the Lévy walk with rests [17].

However, when the previous condition is not fulfilled, solving Equation (4) requires the calculation of $\varphi_w(L, T)$. A case in which $\varphi_w(L, T)$ is easily solvable is when the boundaries are completely transmitting, i.e., $q(T) = \delta(T - 1)$. In that case, one finds

$$\varphi_w(L, T = 1) = \varphi_w(L) = 1 - \frac{L}{L + 1} \sim L^{-1}. \tag{5}$$

For $T \neq 1$, obtaining an analytical expression for $\varphi_w(L, T)$ is a challenging task [21]. A trick commonly used to avoid this difficulty consists in considering an *annealed* system [18], i.e., assuming that each time the particle exits a compartment, it reappears at the center of the next one. In this case, the particle will always travel a distance $L_i/2$ to escape the ith-segment, independently on the exit side, hence eliminating the presence of rests. In this case $\varphi_w(L, T) = 1\ \forall L, T$ and the motion of the particle is then a Lévy walk with flying times depending on the jump length [20]. This is also analogous to the case in which, once the particle enters a compartment, it cannot cross again the same edge it entered from and thus will always travel a distance L_i. For this reason, in the following we will refer to this approximation as the *osmotic* approach, in contrast with the general case that we name *non-osmotic*.

From now on we will focus on the osmotic approach, which allows for a thorough theoretical description in the different configurations considered. In the osmotic approach, Equation (4) takes the much simpler form

$$P_\Sigma^{(\mathrm{OA})} = \frac{\Psi(k, s)}{1 - \psi(k, s)}, \tag{6}$$

where $\psi(k, s) = \int_0^1 \psi(k, s, T)dT$.

To characterize the motion of the particle, we will use the mean squared displacement (MSD), defined as $\langle x^2(t)\rangle = -P''(k, s)|_{k=0}$, which can be rewritten as Massignan et al. [22]

$$\langle x^2(s)\rangle = \int_0^1 dT \left[\frac{-\psi''(k, s)|_{k=0}}{s[1 - \psi_w(s)]} + \frac{-\Psi''(k, s)|_{k=0}}{1 - \psi_w(s)}\right]. \tag{7}$$

As we will show later through numerical simulations of the microscopic walk, in spite of the simpler description, the osmotic approach displays the same long time behavior as the non-osmotic one.

3. RESULTS

In the following, we will use the method described above to solve the motion of the particle in different configurations of the system. We will first consider the case in which each boundary has a different transmittance, drawn stochastically from the PDF $q(T)$, but all the compartments have equal length. We will then briefly comment about the case in which the stochasticity is only present in the compartment length. Last, we will consider the case where both the length and boundary transmittance are random variables. For each case, we will give the analytical solutions of the mesoscopic walk and compare it to numerical simulations of the microscopic description.

The form of the conditional probability of the exit time given a compartment of size L and transmittance T is common to all the cases. A reasonable assumption based on the Brownian motion is that, independently on the expression of this conditional probability, it should give an average time for exiting a compartment $\langle t \rangle$ which depends on the length as L^2. We can further assume that the dependence on T is such that $\langle t \rangle \propto (L/T)^2$. We checked that this behavior is consistent with the numerical results for a collection of T and L, finding that the average exit time follows an exponential behavior, $\propto \exp -tL^2/T^2$, for large L and small T. For all cases numerically considered, even when the distribution did not match an exponential behavior, we found a quadratic dependence on L/T. Therefore, we assume the simplest distribution which produces the expected behavior of the average exit time, which is

$$\phi(t|T, L) \sim \delta(t - (L/T)^2). \tag{8}$$

This form of the conditional time also has the advantage of simplifying the analytical expressions and, as we discuss below, allows us to correctly model the microscopic motion in all the cases considered. The analytical calculation of this conditional probability falls beyond the scope of this work. We note that previous works have focused in the investigation on the exit time in similar structures [23, 24], but do not provide a useful expression for our particular system nor a practical way to derive it.

We will now consider the case in which the boundaries have all the same transmittance, i.e., $q(T) = \delta(T - \bar{T})$, with $\bar{T} \in (0, 1]$. We will consider that each compartment has a different length, retrieved from the PDF

$$g(L) = \beta L^{-1-\beta}. \tag{9}$$

Our first step is to calculate the distribution of flight times, which is done by convolving Equation (1) over all possible values of L

$$\psi_L(t) = \int_1^{\infty} \phi(t|L, \bar{T}) g(L) dL \propto t^{-1-\beta/2}. \tag{10}$$

Using this result and Equations (1) and (7), we find that $\langle x^2(t) \rangle \sim t \ \forall \ T$, i.e., the particle performs normal diffusion. Therefore, the stochasticity of the compartment length does not imply any effect on the MSD and, indeed, similar results are obtained when using regular compartment size. We would like to emphasize that this result holds for any finite T different from zero. In fact, as shown in Lapeyre [25], for $T = 0$ subdiffusion occurs. In the presence of transmitting boundary, there is no mechanism that confines the particle for pathologically long times, so particles diffuse normally in the asymptotic limit.

A very different result arises when considering disordered boundary transmittances $\{T_i\}_{i=1}^N$ distributed according to a power law PDF

$$q(T) = \alpha \left(\frac{1}{T}\right)^{1-\alpha}. \tag{11}$$

We first analyze the case in which the compartments have all the same size, i.e., the lengths $\{L_i\}_{i=1}^N$ are distributed according to the PDF $g(L) = \delta(L - \bar{L})$, where $\bar{L} \in [1, \infty)$. We refer to this system as the spatially ordered case. In the osmotic approach, the walk consists on a collection of steps of size $\bar{L}$ with flight times drawn from the PDF

$$\psi(t) = \int_0^1 \phi(t|\bar{L}, T) q(T) dT \propto t^{-1-\alpha/2}. \tag{12}$$

As all the steps have equal length, the walk reduces to a continuous time random walk with waiting time PDF given by Meroz et al. [12]. Thus, in the spatially ordered case the MSD is given by Charalambous et al. [26]

$$\left\langle x^2(t) \right\rangle^{(\mathrm{SO})} \xrightarrow{t \to \infty} t^{\alpha/2}, \tag{13}$$

showing that the particle undergoes subdiffusive motion for $0 < \alpha < 1$. In **Figure 2A** we show the numerical results corresponding to MSD calculated for a single value of $\alpha = 0.2$ and different values of $\bar{L}$ by using the microscale description for the spatially ordered case. The plot shows that the motion is initially Brownian and become subdiffusive at longer times. The time at which the onset of subdiffusion occurs increases as $\bar{L}$ grows, corresponding to the time needed to reach the boundary, of a compartment. The asymptotic value of the MSD for any $\bar{L}$ is given by Muñoz Gil et al. [13]. This is a first indication that anomalous diffusion can only be obtained by considering stochastic boundary transmittance with a heavy-tail PDF. In the spatially ordered case, the distribution of transmittances of the media can be directly inferred from the asymptotic behavior of the MSD of the particle.

We will now consider the case where both compartment length and boundary transmittance are stochastic variables. As stated before, this situation can be modeled at the mesoscale as a Lévy walk with flight times depending on the step size. We consider that the transmittances are distributed according to Equation (11) and the compartment lengths as described by Equation (9). Following the method used to derive Equation (12), we can calculate the PDF of flight times by convolving the conditional probability $\phi(t|T, L)$ with Equations (11) and (9), to find

$$\psi_f(t) \propto t^{-1-\gamma}, \quad \text{with } \gamma = \begin{cases} \alpha & \text{if } \beta > \alpha, \\ \beta & \text{if } \beta < \alpha. \end{cases} \tag{14}$$

By using the previous result and Equation (1) we can determine the MSD through its Laplace transform as in Equation (7). In the time domain we find

$$\left\langle x^2(t) \right\rangle^{(\mathrm{SD})} \xrightarrow{t \to \infty} t^{\frac{1}{2}(2-\beta+\gamma)}. \tag{15}$$

The values of the MSD exponent $\sigma = \frac{1}{2}(2 - \beta + \gamma)$ obtained for different values of α and β are shown in **Figure 2B**. In **Figure 2C** we further show the values of the MSD exponent calculated from numerical simulations for the microscale description of the walk (dashed lines) and the theoretical value given by Equation (15). The numerical calculation and the theoretical prediction show

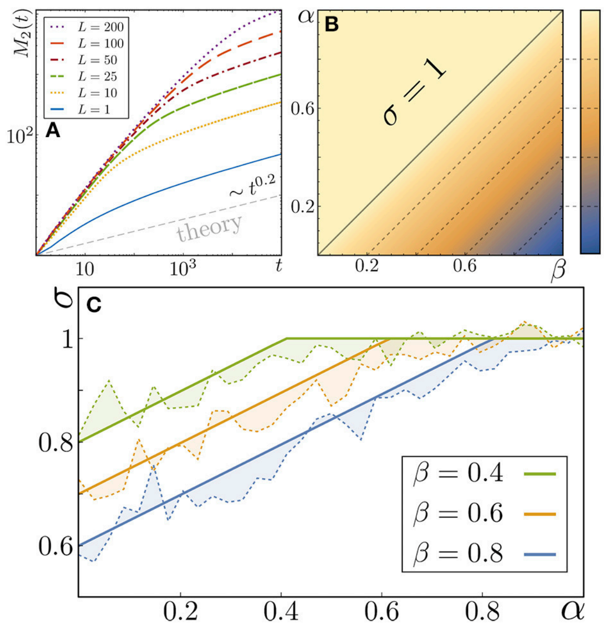

FIGURE 2 | (A) MSD of a particle moving in an system of compartments of equal length and boundary transmittances distributed following (11), with $\alpha = 0.2$. All curves are calculated for the microscale and tend to the predicted subdiffusive motion given by (13). A larger L leads to a larger time for the onset of subdiffusion to occur. The dashed bottom line corresponds to the mesoscale and coincides with the theoretical prediction. **(B)** Value of the exponent of the MSD in a system with stochastic compartment sizes and boundary transmittance, given by (15). **(C)** Comparison between the predicted results of the previous case and numerical simulations of the microscopic walk (dashed lines).

a good agreement. It can be noticed that, when $\alpha > \beta$ (and thus $\gamma = \beta$), the particle movement is normally diffusive (see Equation (15) and **Figures 2B,C**). Therefore, the stochasticity in the length of the segments is capable of compensating for the disorder that would be induced by the stochasticity in transmittance, that would generate a subdiffusive motion with anomalous exponent $\sigma = \alpha/2$ in the case the segments lengths were regular. In addition, for $\beta > \alpha$, the motion is subdiffusive, but with a higher anomalous exponent as compared to the case in which the lengths were regular. Therefore, in this case the two disorders compete, producing a weaker subdiffusion.

4. DISCUSSION

In this article, we introduce a coarse-graining method that we use to study diffusion through complex environments. This method is useful to study systems in which the microscopic behavior of the particles is too involved to be described analytically. To obtain a description of the motion in such cases, we propose a procedure that allows one to transform the microscopic walk into well-known theoretical models, such as Lévy Walks or continuous time random walks. The coarse-grained transformation maps the original walk performed at the microscale into a simplified movement at a larger scale (which we term mesoscale) that captures the relevant properties of the environment. This allows for a complete analytical characterization of the diffusion in terms its observables, such as the mean square displacement.

To illustrate the use of the proposed method, we consider the diffusion in an environment consisting of compartments with random sizes and/or transmittances. To resolve the diffusion of the system at the microscale, one needs to consider the complex interaction of the particle with the boundary of each compartment. For some simple systems, e.g., when all the compartments have the same size, it is possible to get an analytical solution of the microscale motion. In this cases, we show that a heavy-tailed distribution of boundary transmittance is a necessary requirement to induce subdiffusion. However, for more intricate spatially-disordered environments, it is often difficult to obtain an analytical solution at the microscale. This is the scenario where our method allows to get insights on the motion while neglecting microscopic details. As an example, we demonstrate that when the compartments length is a stochastic variable, geometric disorder alone cannot generate subdiffusion. However, it can affect the one generated by the heterogeneity in the boundary transmittance. Namely, increasing the geometric disorder reduces the degree of subdiffusion, as it increases the value of the anomalous exponent toward one. We thus fully characterize the mean-square displacement exponent as a function of the parameters controlling the heavy-tailed distributions of both the lengths and barrier heights.

The model presented in this article might be a useful framework to interpret diffusion in a variety of systems composed of compartment of varying size and barriers. A striking example of such kind of system is provided by eukaryotic cells, highly compartmentalized at different spatial scales to provide optimal conditions to perform specific functions [27]. The presence of compartments has been shown to affect the diffusion of transmembrane proteins in the plasma membrane, e.g., as a consequence of a self-similar actin network acting as semipermeable barrier [9].

An interesting outlook of our model could consist in the possibility of its further generalization, as to include previously proposed models for diffusion in complex environment. For example, our approach shares important features with the previously proposed comb model [28]. In fact, the comb model can be considered as a continuous-time random walk with stochastic waiting time, the latter derived from first-passage time. This system can be analyzed through our coarse-grained approach upon conversion of the waiting time distribution into a stochastic transmittance. The realization of the comb model including convective terms [29], could be further implemented in our approach, e.g., through the use of asymmetric transmittance.

AUTHOR CONTRIBUTIONS

All authors contributed conception and design of the study. GM-G, AC, and MG-M developed the theory. GM-G performed the simulations. GM-G, MG-M, and CM wrote the paper. ML supervised research. All authors contributed to manuscript revision, read and approved the submitted version.

FUNDING

This work has been funded by the Spanish Ministry MINECO (National Plan15 Grant: FISICATEAMO No. FIS2016-79508-P, SEVERO OCHOA No. SEV-2015-0522, FPI), European Social Fund, Fundació Cellex, Generalitat de Catalunya (AGAUR Grant No. 2017 SGR 1341 and CERCA/Program), ERC AdG OSYRIS, EU FETPRO QUIC, and the National Science Centre, Poland-Symfonia Grant No. 2016/20/W/ST4/00314. CM acknowledges funding from the Spanish Ministry of Economy and Competitiveness and the European Social Fund through the Ramón y Cajal program 2015 (RYC-2015-17896) and the BFU2017-85693-R, and from the Generalitat de Catalunya (AGAUR Grant No. 2017SGR940). AC acknowledges financial support from the ERC Synergy Grant UQUAM and the SFB FoQuS (FWF Project No. F4016-N23). GM acknowledges financial support from Fundació Social La Caixa. AC acknowledges support from the UAB Talent Research program and from the Spanish Ministry of Economy and Competitiveness under Contract No. FIS2017-86530-P.

ACKNOWLEDGMENTS

We acknowledge Oriol Rubies for the initial numerical exploration of the problem and John Lapeyre and Vasily Zaburdaev for inspiring and useful discussions.

REFERENCES

1. Tan P, Liang Y, Xu Q, Mamontov E, Li J, Xing X, et al. Gradual crossover from subdiffusion to normal diffusion: a many-body effect in protein surface water. *Phys Rev Lett*. (2018) **120**:248101. doi: 10.1103/PhysRevLett.120.248101
2. Berkowitz B, Cortis A, Dentz M, Scher H. Modeling non-Fickian transport in geological formations as a continuous time random walk. *Rev Geophys*. 44:RG2003. (2006) doi: 10.1029/2005RG000178
3. Metzler R, Jeon JH, Cherstvy AG, Barkai E. Anomalous diffusion models and their properties: non-stationarity, non-ergodicity, and ageing at the centenary of single particle tracking. *Phys Chem Chem Phys*. (2014) **16**:24128–164. doi: 10.1039/C4CP03465A
4. Manzo C, Garcia-Parajo MF. A review of progress in single particle tracking: from methods to biophysical insights. *Rep Prog Phys*. (2015) **78**:124601. doi: 10.1088/0034-4885/78/12/124601
5. HausK JW, Kehr W. Diffusion in regular and disordered lattices. *Phys Rep*. (1987) **150**:263–406.
6. Bernasconi J, Beyeler HU, Strässler S, Alexander S. Anomalous frequency-dependent conductivity in disordered one-dimensional systems. *Phys Rev Lett*. (1979) **42**:819. doi: 10.1103/PhysRevLett.42.819
7. Novikov DS, Fieremans E, Jensen JH, Helpern JA. Random walks with barriers. *Nat Phys*. (2011) **7**:508. doi: 10.1038/nphys1936
8. Moutal N, Grebenkov D. Diffusion across semi-permeable barriers: spectral properties, efficient computation, and applications. *arXiv preprint* arXiv:180706336 (2018).
9. Sadegh S, Higgins JL, Mannion PC, Tamkun MM, Krapf D. Plasma membrane is compartmentalized by a self-similar cortical actin meshwork. *Phys Rev X*. (2017) **7**:011031. doi: 10.1103/PhysRevX.7.011031
10. de Wit G, Albrecht D, Ewers H, Kukura P. Revealing compartmentalized diffusion in living cells with interferometric scattering microscopy. *Biophys J*. (2018) **114**:2945–50. doi: 10.1016/j.bpj.2018.05.007
11. Weigel AV, Simon B, Tamkun MM, Krapf D. Ergodic and nonergodic processes coexist in the plasma membrane as observed by single-molecule tracking. *Proc Natl Acad Sci USA*. (2011) **108**:6438–43. doi: 10.1073/pnas.1016325108
12. Meroz Y, Sokolov IM, Klafter J. Subdiffusion of mixed origins: when ergodicity and nonergodicity coexist. *Phys Rev E*. (2010) **81**:010101. doi: 10.1103/PhysRevE.81.010101
13. Muñoz Gil G, Charalambous C, García-March MA, Garcia-Parajo MF, Manzo C, Lewenstein M, et al. Transient subdiffusion from an Ising environment. *Phys Rev E*. (2017) **96**:052140. doi: 10.1103/PhysRevE.96.052140
14. Montroll E, Weiss GH. Random walks on lattices. II. *J Math Phys*. (1965) **6**:167.
15. Shlesinger M, Klafter J, Wong Y. Random walks with infinite spatial and temporal moments. *J Stat Phys*. (1982) **27**:499–512. doi: 10.1007/BF01011089
16. Klafter J, Sokolov IM. *First Steps in Random Walks: From Tools to Applications*. Oxford: Oxford University Press (2011).
17. Zaburdaev V, Denisov S, Klafter J. Lévy walks. *Rev Mod Phys*. (2015) **87**:483. doi: 10.1103/RevModPhys.87.483
18. Bouchaud JP, Georges A. Anomalous diffusion in disordered media: statistical mechanisms, models and physical applications. *Phys Rep*. (1990) **195**:127–293. doi: 10.1016/0370-1573(90)90099-N
19. Kosztołowicz T, Wasik S, Lewandowska KD. How to determine a boundary condition for diffusion at a thin membrane from experimental data. *Phys Rev E*. (2017) **96**:010101. doi: 10.1103/PhysRevE.96.010101
20. Zaburdaev VY. Random walk model with waiting times depending on the preceding jump length. *J Stat Phys*. (2006) **123**:871–81. doi: 10.1007/s10955-006-9104-0
21. Lehner G. One dimensional random walk with a partially reflecting barrier. *Ann Math Stat*. (1963) **34**:405–12. doi: 10.1214/aoms/1177704151
22. Massignan P, Manzo C, Torreno-Pina J, García-Parajo M, Lewenstein M, Lapeyre G Jr. Nonergodic subdiffusion from Brownian motion in an inhomogeneous medium. *Phys Rev Lett*. (2014) **112**:150603. doi: 10.1103/PhysRevLett.112.150603
23. Khantha M, Balakrishnan V. First passage time distributions for finite one-dimensional random walks. *Pramana*. (1983) **21**:111–22. doi: 10.1007/BF02894735
24. Dybiec B, Gudowska-Nowak E, Hänggi P. Lévy-Brownian motion on finite intervals: Mean first passage time analysis. *Phys Rev E*. (2006) **73**:046104. doi: 10.1103/PhysRevE.73.046104
25. Lapeyre GJ Jr. Anomalous diffusion from Brownian motion with random confinement. *arXiv preprint* arXiv:150407158 (2015).
26. Charalambous C, Munoz-Gil G, Celi A, Garcia-Parajo M, Lewenstein M, Manzo C, et al. Nonergodic subdiffusion from transient interactions with heterogeneous partners. *Phys Rev E*. (2017) **95**:032403. doi: 10.1103/PhysRevE.95.032403
27. Trimble WS, Grinstein S. Barriers to the free diffusion of proteins and lipids in the plasma membrane. *J Cell Biol*. (2015) **208**:259–71. doi: 10.1083/jcb.201410071
28. Weiss G, Havlin S. Some properties of a random walk on a comb structure. *Phys A*. (1986) **134**:474–82. doi: 10.1016/0378-4371(86)90060-9
29. Baskin E, Iomin A. Superdiffusion on a Comb Structure. *Phys Rev Lett*. (2004) **93**:120603. doi: 10.1103/PhysRevLett.93.120603

Conflict of Interest Statement: The authors declare that the research was conducted in the absence of any commercial or financial relationships that could be construed as a potential conflict of interest.

frontiers
in Applied Mathematics and Statistics

ORIGINAL RESEARCH
published: 19 June 2019
doi: 10.3389/fams.2019.00030

Stochastic AUC Optimization Algorithms With Linear Convergence

Michael Natole Jr.[1], *Yiming Ying*[1]* *and Siwei Lyu*[2]

[1] *Department of Mathematics and Statistics, University at Albany, State University of New York, Albany, NY, United States,*
[2] *Department of Computer Science, University at Albany, State University of New York, Albany, NY, United States*

Area under the ROC curve (AUC) is a standard metric that is used to measure classification performance for imbalanced class data. Developing stochastic learning algorithms that maximize AUC over accuracy is of practical interest. However, AUC maximization presents a challenge since the learning objective function is defined over a pair of instances of opposite classes. Existing methods circumvent this issue but with high space and time complexity. From our previous work of redefining AUC optimization as a convex-concave saddle point problem, we propose a new stochastic batch learning algorithm for AUC maximization. The key difference from our previous work is that we assume that the underlying distribution of the data is uniform, and we develop a batch learning algorithm that is a stochastic primal-dual algorithm (SPDAM) that achieves a linear convergence rate. We establish the theoretical convergence of SPDAM with high probability and demonstrate its effectiveness on standard benchmark datasets.

Keywords: AUC maximization, imbalanced data, linear convergence, stochastic optimization, ROC curve

Edited by:
Carlos Mejía-Monasterio,
Polytechnic University of Madrid,
Spain

Reviewed by:
Junhong Lin,
École Polytechnique Fédérale de
Lausanne, Switzerland
Jinshan Zeng,
Jiangxi Normal University, China

***Correspondence:**
Yiming Ying
yying@albany.edu

Specialty section:
This article was submitted to
Mathematics of Computation and
Data Science,
a section of the journal
Frontiers in Applied Mathematics and
Statistics

Received: *08 March 2019*
Accepted: *27 May 2019*
Published: *19 June 2019*

Citation:
Natole M Jr, Ying Y and Lyu S (2019)
Stochastic AUC Optimization
Algorithms With Linear Convergence.
Front. Appl. Math. Stat. 5:30.
doi: 10.3389/fams.2019.00030

1. INTRODUCTION

Quantifying machine learning performance is an important issue to consider when designing learning algorithms. Many existing algorithms maximize accuracy, however, it can be a misleading performance metric for several reasons. First, accuracy assumes that an equal misclassification cost for positive and negative labeling. This assumption is not viable for many real world examples such as medical diagnosis and fraud detection [1]. Also, optimizing accuracy is not suitable for important learning tasks such as imbalanced classification. To overcome these issues, Area Under the ROC Curve (AUC) [2, 3] is a standard metric for quantifying machine learning performance. It is used in many real world applications, such as ranking and anomaly detection. AUC concerns the overall performance of a functional family of classifiers and quantifies their ability of correctly ranking any positive instance with regards to a randomly chosen negative instance. This combined with the fact that AUC is not effected by imbalanced class data makes AUC a more robust metric than accuracy [4]. We will discuss maximizing AUC in a batch learning setting.

Learning algorithms that maximize AUC performance have been developed in both batch and online settings. Previously, most algorithms optimizing AUC for classification [5–8] were for batch learning, where we assume all training data is available making those methods not applicable to streaming data. However, online learning algorithms [9–14], have been proven to be very efficient to deal with large-scale datasets and streaming data. The issue with these studies is that they focus on optimizing the misclassification error or its surrogate loss. These works all attempt to overcome the problem that AUC is based on the sum of pairwise losses between examples from different classes, making the objective function quadratic in the number of samples. Overcoming this issue is the challenge of designing algorithms to optimize the AUC score in either setting.

In this work, we present a new stochastic batch learning algorithm for AUC maximization, SPDAM. The algorithm is based on our previous work that we can reformulate AUC maximization as a stochastic saddle point problem with the inclusion of a regularization term [15]. However, the key difference from our previous work is that SPDAM assumes that the distribution is uniform and is solved as a stochastic primal dual algorithm [16]. The proposed algorithm results in a faster convergence rate than existing state-of-the-art algorithms. When evaluating on several standard bench mark datasets, SPDAM achieves performances that are on par with other state-of-the-art AUC optimization methods with a significant improvement in running time.

The paper is organized as follows: Section 2 discusses related work. Section 3 briefly reformulates AUC optimization as a saddle point problem. Section 4 exploits section 3 with the assumption that the distribution is a uniform distribution over the data and introduces SPDAM. Section 5 details the experiments. Finally, section 6 gives some final thoughts.

2. RELATED WORK

AUC has been studied extensively because it is an appropriate performance measure for when dealing with imbalanced data distributions for learning classification. Designing such algorithms that optimize AUC is a significant challenge because of the need for samples of opposite classes. An early work first maximized the AUC score directly by performing gradient descent constrained to a hypersphere [17]. Their algorithm used a differentiable approximation to the AUC score that was accurate and computationally efficient, being of the order of $\mathcal{O}(n)$, where n is the number of data observations. Another early work optimized the AUC score using support vector machines [6].

In more recent work [18–22], significant progress has been done to design online learning algorithms for AUC maximization. Online methods are desirable for evaluating streaming data since these methods update when new data is available. However, a limitation of these methods is that the previous samples used need to be stored. For iteration t and where the dimension of the data is d, this results in a space and time complexity of $\mathcal{O}(td)$. This is an undesirable property because these algorithms will not scale well for high-dimensional data as well as will require more resources. To overcome the quadratic nature of AUC, the problem of optimizing the AUC score can be reformulated as a sum of pairwise loss functions using hinge loss [19, 22]. The use of a buffer with size s was proposed. This lessens the complexity to $\mathcal{O}(sd)$. However, if the buffer size is not set sufficiently large this will impact the performance of the method.

Again, using the idea of reformulating AUC as a sum of pairwise loss functions was further expanded upon [18]. Using the square loss function instead of hinge loss, a key observation was made in which the mean and covariance statistics of the training data could be easily updated as new data becomes available. Unlike the previous work where s samples needed to be stored, these statistics only needed to be stored. However, this algorithm still results in scaling issues for high-dimensional data because storing the covariance matrix results in a quadratic complexity of $\mathcal{O}(d^2)$. The authors did make note of this issue and proposed using low-rank Gaussian matrices to approximate the covariance matrix. The approximation is not a general solution to the original problem and depends on whether the covariance matrix can be well approximated by low-rank matrices.

Work has been also been done to maximize AUC using batch methods. In Ding et al. [23], the authors propose an algorithm that uses an adaptive gradient method that uses the knowledge of historical gradients and that is less sensitive to parameter selection. The method proposed in Gultekin et al. [24] is based on a convex relaxation of the AUC function, but instead of using stochastic gradients, the algorithm uses the first and second order U-statistics of pairwise distances. A critical feature of this approach is that it is learning rate free as training the step size is a time consuming task.

More recently, work based on Ying et al. [25] has been expanded upon. The critical idea was the primal and dual variables introduced have distinct solutions. Two different works took advantage of this observation. The first work developed a primal dual style stochastic gradient method [26] while the other develops a stochastic proximal algorithm that can have non-smooth penalty functions [27, 28]. Both algorithms achieve a $\mathcal{O}(1/T)$ convergence rate up to a logarithmic term.

3. PROBLEM STATEMENT

First, consider $\mathcal{X} \subseteq \mathbb{R}^d$ to be the input space and $\mathcal{Y} = \{-1, +1\}$ the output space. For the training data, $\mathbf{z} = \{(x_i, y_i),\ i = 1, \ldots, n\}$, we assume to be *i.i.d.* and the samples are obtained from an unknown distribution ρ on $\mathcal{Z} = \mathcal{X} \times \mathcal{Y}$. As in Ying et al. [25], we restrict this work to the family of linear functions, i.e., $f(x) = \mathbf{w}^\top x$.

3.1. AUC Optimization

The ROC curve is the plot of the true positive rate vs. the false positive rate. The area under the ROC curve (AUC) for any scoring function $f : \mathcal{X} \to \mathbb{R}$ is equivalent to the probability of a positive sample ranking higher than a negative sample [3, 29]. It is defined as

$$\text{AUC}(f) = \Pr(f(x) \geq f(x') | y = +1, y' = -1), \tag{1}$$

where (x, y) and (x', y') are independently drawn from ρ. The intent of AUC maximization is to find the optimal decision function f:

$$\begin{aligned} \arg\max_f \text{AUC}(f) &= \arg\min_f \Pr(f(x) < f(x') | y = 1, y' = -1) \\ &= \arg\min_f \mathbb{E}\Big[\mathbb{I}_{[f(x') - f(x) > 0]} \big| y = 1, y' = -1\Big], \end{aligned} \tag{2}$$

where $\mathbb{I}(\cdot)$ is the indicator function. As in Ying et al. [25], define $p = \Pr(y = 1)$. Recall that the conditional expectation of a random variable $\xi(z)$ is defined by $\mathbb{E}[\xi(z)|y = 1] = \frac{1}{p} \iint \xi(z) \mathbb{I}_{y=1} d\rho(z)$. In (2), the indicator function is not continuous, and is usually replaced by a convex surrogate such as the ℓ_2 loss $(1-(f(x)-f(x')))^2$ or the hinge loss $\big(1-(f(x)-f(x'))\big)_+$. We used the ℓ_2 loss for this work as it has been shown to be statistically consistent with AUC while the hinge loss is not [18, 30]. Letting λ be a regularization parameter, AUC maximization can be formulated by

$$\begin{aligned}&\operatorname*{argmin}_{\mathbf{w}} \mathbb{E}\Big[(1-\mathbf{w}^\top(x-x'))^2|y=1,y'=-1\Big]+\frac{\lambda}{2}\|\mathbf{w}\|^2,\\ &=\operatorname*{argmin}_{\mathbf{w}} \frac{1}{p(1-p)}\iint_{\mathcal{Z}\times\mathcal{Z}}(1-\mathbf{w}^\top(x-x'))^2\\ &\mathbb{I}_{[y=1,y'=-1]}d\rho(z)d\rho(z')+\tfrac{\lambda}{2}\|\mathbf{w}\|^2.\end{aligned} \tag{3}$$

where the samples (x,y) and (x',y') are independent. When ρ is a uniform distribution over training data $\mathbf{z}$, we obtain the empirical minimization (ERM) problem for AUC optimization studied in Gao et al. [18] and Zhao et al. [22]

$$\operatorname*{argmin}_{\mathbf{w}} \frac{1}{n^+n^-}\sum_{i=1}^{n}\sum_{j=1}^{n}(1-\mathbf{w}^\top(x_i-x_j))^2\mathbb{I}_{[y_i=1\wedge y_j=-1]}+\frac{\lambda}{2}\|\mathbf{w}\|^2, \tag{4}$$

where n^+ and n^- denote the numbers of instances in the positive and negative classes, respectively.

3.2. Equivalent Representation as a Saddle Point Problem (SPP)

As in Ying et al. [25], AUC optimization as in (3) can be represented as stochastic Saddle Point Problem (SPP) (e.g., [15]). A stochastic SPP is generally in the form of

$$\min_{u\in\Omega_1}\max_{\alpha\in\Omega_2}\Big\{f(u,\alpha):=\mathbb{E}[F(u,\alpha,\xi)]\Big\}, \tag{5}$$

where $\Omega_1\subseteq\mathbb{R}^d$ and $\Omega_2\subseteq\mathbb{R}^m$ are non-empty closed convex sets, ξ is a random vector with non-empty measurable set $\Xi\subseteq\mathbb{R}^p$, and $F:\Omega_1\times\Omega_2\times\Xi\to\mathbb{R}$. Here $\mathbb{E}[F(u,\alpha,\xi)]=\int_\Xi F(u,\alpha,\xi)d\Pr(\xi)$, and function $f(u,\alpha)$ is convex in $u\in\Omega_1$ and concave in $\alpha\in\Omega_2$. In general, u and α are referred to as the primal variable and the dual variable, respectively. In this work, we modified our formulation for AUC maximization to include a regularization term. We give a modified version of the result in Ying et al. [25] that includes the L^2 term. First, define $F:\mathbb{R}^d\times\mathbb{R}^3\times\mathcal{Z}\to\mathbb{R}$, for any $\mathbf{w}\in\mathbb{R}^d$, $a,b,\alpha\in\mathbb{R}$ and $z=(x,y)\in\mathcal{Z}$, by

$$\begin{aligned}F(\mathbf{w},a,b,\alpha;z)&=(1-p)(\mathbf{w}^\top x-a)^2\mathbb{I}_{[y=1]}+p(\mathbf{w}^\top x-b)^2\mathbb{I}_{[y=-1]}\\&\quad+2(1+\alpha)(p\mathbf{w}^\top x\mathbb{I}_{[y=-1]}-(1-p)\mathbf{w}^\top x\mathbb{I}_{[y=1]})\\&\quad-p(1-p)\alpha^2+\frac{\lambda}{2}\|\mathbf{w}\|^2.\end{aligned} \tag{6}$$

Equation (6) is similar as in our previous work [25]. The only difference is the inclusion of a regularization term. The main result still holds in a similar manner.

Theorem 3.1. *The AUC optimization (3) is equivalent to*

$$\min_{\substack{\mathbf{w}\in\mathbb{R}^d\\(a,b)\in\mathbb{R}^2}}\max_{\alpha\in\mathbb{R}}\Big\{f(\mathbf{w},a,b,\alpha):=\int_{\mathcal{Z}}F(\mathbf{w},a,b,\alpha;z)d\rho(z)\Big\}. \tag{7}$$

In addition, we can prove the following result.

Proposition 3.1. *For any saddle point* $(\mathbf{w}^*,a^*,b^*,\alpha^*)$ *of the SPP formulation (7),* $\mathbf{w}^*$ *is a minimizer of the original AUC optimization problem (3).*

Proof: Let $\bar{f}(\mathbf{w},a,b,\alpha)=1+\frac{\int_{\mathcal{Z}}F(\mathbf{w},a,b,\alpha;z)d\rho(z)}{p(1-p)}+\frac{\lambda}{2}\|\mathbf{w}\|^2$ and let $(\mathbf{w}^*,a^*,b^*,\alpha^*)$ be a saddle point of the problem

$$\min_{\substack{\mathbf{w}\in\mathbb{R}^d\\(a,b)\in\mathbb{R}^2}}\max_{\alpha\in\mathbb{R}}\bar{f}(\mathbf{w},a,b,\alpha).$$

Since the order of the two minimization [i.e., minimizing with respect to $\mathbf{w}$ and minimizing with respect to (a,b)] does not affect the result. This implies, for every fixed $\mathbf{w}$, (a^*,b^*,α^*) is a saddle point of the sub-problem

$$\min_{(a,b)\in\mathbb{R}^2}\max_{\alpha\in\mathbb{R}}\bar{f}(\mathbf{w},a,b,\alpha).$$

Notice from the proof for Theorem 3.1 that

$$\begin{aligned}&\mathbb{E}\Big[(1-\mathbf{w}^\top(x-x'))^2|y=1,y'=-1\Big]+\frac{\lambda}{2}\|\mathbf{w}\|^2=\\&\min_{(a,b)\in\mathbb{R}^2}\max_{\alpha\in\mathbb{R}}\bar{f}(\mathbf{w},a,b,\alpha).\end{aligned} \tag{8}$$

Hence,

$$\mathbb{E}\Big[(1-\mathbf{w}^\top(x-x'))^2|y=1,y'=-1\Big]+\frac{\lambda}{2}\|\mathbf{w}\|^2=\bar{f}(\mathbf{w},a^*,b^*,\alpha^*).$$

This further implies

$$\begin{aligned}&\min_{\mathbf{w}}\mathbb{E}\Big[(1-\mathbf{w}^\top(x-x'))^2|y=1,y'=-1\Big]+\frac{\lambda}{2}\|\mathbf{w}\|^2=\\&\min_{\mathbf{w}}f(\mathbf{w},a^*,b^*,\alpha^*).\end{aligned} \tag{9}$$

As $\mathbf{w}^*$ is a minimizer of the righthand side of the Equation (9), $\mathbf{w}^*$ is also a minimizer of the lefthand side of the equation.

4. STOCHASTIC PRIMAL-DUAL ALGORITHM FOR AUC MAXIMIZATION

The algorithm developed in our previous work focused on the population objective of the saddle point problem (7). It is essentially an online projected gradient descent algorithm which has an optimal convergence rate $\mathcal{O}(1/\sqrt{t})$. This convergence rate is distribution-free, i.e., it holds true for any distribution ρ.

In this section, we are concerned with the case that the distribution ρ in (7) is a uniform distribution over the given data $\mathbf{z}=\{z_1,\ldots,z_n\}$. Denote by $\mathbb{N}_n=\{1,2,\ldots,n\}$ for any $n\in\mathbb{N}$. Now, when ρ is a uniform distribution over finite data $\{(x_i,y_i):i\in\mathbb{N}_n\}$, we can reformulate (4) as a SPP as in (5):

$$\min_{\substack{\mathbf{w}\in\mathbb{R}^d\\(a,b)\in\mathbb{R}^2}}\max_{\alpha\in\mathbb{R}}\frac{1}{n}\sum_{i\in\mathbb{N}_n}F(\mathbf{w},a,b,\alpha,z_i). \tag{10}$$

In this case, the AUC optimization is equivalent to the saddle point problem (10). For this special case, we will develop in this section a stochastic primal-dual algorithm for AUC optimization (10) which is able to converge with a linear convergence rate. To this end, we now consider the following general saddle point problem for AUC maximization

$$\min_{\mathbf{w},a,b}\max_{\alpha}\Big\{\frac{1}{n_+}\sum_{i\in\mathbb{N}_n}(\mathbf{w}^\top x_i-a)^2\mathbb{I}_{y_i=1}+\frac{1}{n_-}\sum_{i\in\mathbb{N}_n}(\mathbf{w}^\top x_i-b)^2\mathbb{I}_{y_i=-1}$$

$$+2(1+\alpha)\mathbf{w}^\top\Big[\frac{1}{n_-}\sum_{i\in\mathbb{N}_n}x_i\mathbb{I}_{y_i=-1}-\frac{1}{n_+}\sum_{i\in\mathbb{N}_n}x_i\mathbb{I}_{y_i=1}\Big]-\alpha^2$$

$$+\Omega(\mathbf{w})\Big\}, \tag{11}$$

where $\Omega(\mathbf{w})$ is a penalty term. If $\Omega(\mathbf{w})=\mathbb{I}_{\|\mathbf{w}\|\leq R}(\mathbf{w})$, the above formulation is equivalent to the saddle point formulation (10).

Before describing the detailed algorithm, we introduce some notations and slightly modify the saddle formulation (11). Specifically, denote by n_+ and n_- the numbers of samples in the positive and negative classes, respectively. In this discrete case $p=\frac{n_+}{n}$. Let $\mathbf{b}=\mathbf{m}_- - \mathbf{m}_+$ where $\mathbf{m}_+$ and $\mathbf{m}_-$ are the means of the positive and negative classes, respectively, i.e., $\mathbf{m}_+=\frac{1}{n_+}\sum_{i\in\mathbb{N}_n}x_i\mathbb{I}_{y_i=1}$ and $\mathbf{m}_-=\frac{1}{n_-}\sum_{i\in\mathbb{N}_n}x_i\mathbb{I}_{y_i=-1}$. For any $i\in\mathbb{N}_n$, denote

$$\bar{x}_i=\frac{x_i-m_+}{\sqrt{2p}}\quad\text{if } y_i=1,\qquad \bar{x}_i=\frac{x_i-m_-}{\sqrt{2(1-p)}}\quad\text{if } y_i=-1. \tag{12}$$

Let $g(\mathbf{w})=\frac{|\mathbf{b}^\top\mathbf{w}|^2}{2}+\mathbf{b}^\top\mathbf{w}+\Omega(\mathbf{w})$. To satisfy the hypothesis that g is a λ strong convex function, we will let $\Omega(\mathbf{w})=\frac{\lambda}{2}\|\mathbf{w}\|^2$. Now we have the following reformulation of (11), based on which we will develop a stochastic primal-dual algorithm for AUC maximization.

Proposition 4.1. *Formulation (13) is equivalent to*

$$\min_{\mathbf{w}}\max_{\beta}\Big\{\frac{1}{n}\sum_{i\in\mathbb{N}_n}\beta_i\mathbf{w}^\top\bar{x}_i-\frac{\|\beta\|^2}{2}+g(\mathbf{w})\Big\}, \tag{13}$$

where $g:\mathbb{R}^d\to\mathbb{R}$ *is defined, for any* $\mathbf{w}\in\mathbb{R}^d$, *by* $g(\mathbf{w})=\frac{|\mathbf{b}^\top\mathbf{w}|^2}{2}+\mathbf{b}^\top\mathbf{w}+\Omega(\mathbf{w})$.

Proof: By minimizing out a, b and α, formulation (11) is equivalent to

$$\min_{\mathbf{w}}\max_{\alpha}\Big\{\frac{1}{n_+}\sum_{i\in\mathbb{N}_n}(\mathbf{w}^\top(x_i-\mathbf{m}_+))^2\mathbb{I}_{y_i=1}$$

$$+\frac{1}{n_-}\sum_{i\in\mathbb{N}_n}(\mathbf{w}^\top(x_i-\mathbf{m}_-))^2\mathbb{I}_{y_i=-1}+2\mathbf{b}^\top\mathbf{w}+|\mathbf{b}^\top\mathbf{w}|^2+\Omega(\mathbf{w})\Big\}.$$

Substituting (12) into the above equation yields the desired result.

Recall that $\kappa=\max\{\|x_i\|:i\in\mathbb{N}_n\}$. We can establish the following linear convergence rate of SPDAM.

TABLE 1 | Pseudo-code of Stochastic Primal-Dual Algorithm for AUC maximization.

```
Stochastic Primal-Dual Algorithm for AUC Maximization (SPDAM)
1. Choose parameters $\sigma > 0$ and $\tau > 0$
2. Initialize $\beta^{(0)}$ and $\mathbf{w}^{(0)}$. Let $\bar{\mathbf{w}}^{(0)} = \mathbf{w}^{(0)}$ and $u^{(0)} = \frac{1}{n}\sum_{i\in\mathbb{N}_n}\beta_i^{(0)}\bar{x}_i$.
3. For $t = 0, \ldots, T-1$ do
     Uniformly and randomly choose $I \subseteq \mathbb{N}_n$ of size $m$ and execute the following updates:
       $\beta_i^{(t+1)} = \begin{cases}\mathrm{argmax}_{\beta_i\in\mathbb{R}}\{\beta_i\langle\bar{\mathbf{w}}^{(t)}, x_i\rangle - \frac{|\beta_i|^2}{2} - \frac{|\beta_i-\beta_i^{(t)}|^2}{2\sigma}\} & \text{if } i\in I\\ \beta_i^{(t)} & \text{otherwise.}\end{cases}$
       $u^{(t+1)} = u^{(t)} + \frac{1}{n}\sum_{i\in I}(\beta_i^{(t+1)} - \beta_i^{(t)})x_i$.

       $\bar{u}^{(t+1)} = u^{(t)} + \frac{n}{m}(u^{(t+1)} - u^{(t)})$.
       $\mathbf{w}^{(t+1)} = \mathrm{argmin}_{\mathbf{w}\in\mathbb{R}^d}\{\langle\bar{u}^{(t+1)}, \mathbf{w}\rangle + g(\mathbf{w}) + \frac{\|\mathbf{w}-\mathbf{w}^{(t)}\|^2}{2\tau}\}$.

       $\bar{\mathbf{w}}^{(t+1)} = \mathbf{w}^{(t+1)} + \theta(\mathbf{w}^{(t+1)} - \mathbf{w}^{(t)})$.

4. end for
5. Output: $\mathbf{w}^{(T)}$ and $\beta^{(T)}$
```

Theorem 4.1. *Assume that g is* λ*-strongly convex. Let* $(\mathbf{w}^*,\beta^*)$ *be the saddle point of (13). If the parameter* σ,τ *and* θ *are chosen such that*

$$\sigma=\frac{(n-m)+\sqrt{(n-m)^2+4n\kappa^2m/\lambda}}{8m\kappa^2},\tau=\frac{1}{4\sigma\kappa^2}\ \textit{and}$$

$$\theta=1-\frac{\lambda}{\lambda+2\sigma\kappa^2},$$

then, for any $t\geq 1$, *the SPDAM algorithm achieves*

$$\Big(\frac{1}{m}+\frac{1}{4\sigma m}\Big)\mathbb{E}\big[\|\beta^{(t+1)}-\beta^*\|^2\big]+\Big(\lambda+\frac{1}{2\tau}\Big)$$

$$\mathbb{E}\big[\|\mathbf{w}^{(t+1)}-\mathbf{w}^*\|^2\big]+\frac{1}{4\tau}\mathbb{E}\big[\|\mathbf{w}^{(t+1)}-\mathbf{w}^{(t)}\|^2\big]$$

$$\leq\theta^t\Big[\Big(\frac{1}{m}+\frac{1}{2\sigma m}\Big)\|\beta^{(0)}-\beta^*\|+\Big(\lambda+\frac{1}{2\tau}\Big)\|\mathbf{w}^{(0)}-\mathbf{w}^*\|^2\Big]. \tag{14}$$

Before we present the proof for the above theorem. It is useful to make some comments. Firstly, the proposed algorithm in **Table 1** is inspired by the stochastic primal-dual algorithm proposed in Yu et al.[16] and Zhang and Lin [31] which focused on Support Vector Machines (SVM) and logistic regression. Secondly, the algorithm SPDAM enjoys faster convergence over the stochastic projected gradient method in our previous work. However, the incremental primal-dual algorithm here, in contrast to the algorithm in **Table 1** which can deal with streaming data, is not an online learning algorithm, since it needs to know a priori the number of the samples, the ratio of the samples of positive class, and means of the positive and negative classes. We now will prove the main theorem. The following lemma is critical for proving Theorem 4.1.

Lemma 4.1. *For the updates in SPDAM, we have*

$$\left(\frac{1}{m}+\frac{1}{2\sigma m}\right)\mathbb{E}\big[\|\beta^{(t+1)}-\beta^*\|^2\big] = \left(\frac{1}{2\sigma m}+\frac{n-m}{nm}\right) \mathbb{E}\big[\|\beta^{(t)}-\beta^*\|^2\big] - \frac{1}{2\sigma m}\mathbb{E}\big[\|\beta^{(t+1)}-\beta^{(t)}\|^2\big] + \mathbb{E}\big[\langle \bar{u}^{(t+1)}, \bar{\mathbf{w}}^{(t)}-\mathbf{w}^*\rangle\big], \tag{15}$$

and

$$\left(\lambda+\frac{1}{2\tau}\right)\mathbb{E}\big[\|\mathbf{w}^{(t+1)}-\mathbf{w}^*\|^2\big] \le \frac{1}{2\tau}\mathbb{E}\big[\|\mathbf{w}^{(t)}-\mathbf{w}^*\|^2\big] - \frac{1}{2\tau}\mathbb{E}\big[\|\mathbf{w}^{(t+1)}-\mathbf{w}^{(t)}\|^2\big] - \mathbb{E}\big[\langle \bar{u}^{(t+1)}, \mathbf{w}^{(t+1)}-\mathbf{w}^*\rangle\big]. \tag{16}$$

Proof: We first prove Equation (15). For any $i \in \mathbb{N}_n$, let $\tilde{\beta}_i$ be defined as

$$\tilde{\beta}_i = \operatorname*{argmax}_{\beta_i \in \mathbb{R}} \left\{ \beta_i \langle \bar{\mathbf{w}}^{(t)}, x_i\rangle - \frac{|\beta_i|^2}{2} - \frac{|\beta_i - \beta_i^{(t)}|^2}{2\sigma} \right\}.$$

Hence,

$$\frac{|\beta_i^{(t)}-\beta_i^*|^2}{2\sigma} + \frac{|\beta_i^*|^2}{2} - \beta_i^*\langle \bar{\mathbf{w}}^{(t)}, x_i\rangle = \frac{|\beta_i^{(t)}-\tilde{\beta}_i|^2}{2\sigma} + \frac{|\tilde{\beta}_i|^2}{2} - \tilde{\beta}_i\langle \bar{\mathbf{w}}^{(t)}, x_i\rangle + \left(\frac{1}{2}+\frac{1}{2\sigma}\right)|\tilde{\beta}_i - \beta_i^*|^2. \tag{17}$$

Observe, by the definition of the saddle point $(\mathbf{w}^*, \beta^*)$, that

$$\beta^* = \operatorname*{argmax}_{\beta_i} \left\{ \beta_i \langle \mathbf{w}^*, x_i\rangle - \frac{|\beta_i|^2}{2} \right\}.$$

Consequently, $\tilde{\beta}_i\langle \mathbf{w}^*, x_i\rangle - \frac{|\tilde{\beta}_i|^2}{2} = \beta_i^*\langle \mathbf{w}^*, x_i\rangle - \frac{|\beta_i^*|^2}{2} - \frac{1}{2}|\tilde{\beta}_i - \beta_i^*|^2$ which implies that $\frac{|\tilde{\beta}_i|^2}{2} - \frac{|\beta_i^*|^2}{2} = (\tilde{\beta}_i - \beta_i^*)\langle \mathbf{w}^*, x_i\rangle + \frac{1}{2}|\tilde{\beta}_i - \beta_i^*|^2$. Putting this back into (17), we have

$$\frac{|\beta_i^{(t)}-\beta_i^*|^2}{2\sigma} + (\tilde{\beta}_i - \beta_i^*)\langle \bar{\mathbf{w}}^{(t)} - \mathbf{w}^*, x_i\rangle = \frac{|\beta_i^{(t)}-\tilde{\beta}_i|^2}{2\sigma} + \left(1+\frac{1}{2\sigma}\right)|\tilde{\beta}_i - \beta_i^*|^2. \tag{18}$$

Let $\mathcal{F}_t$ be the sigma field generated by all random variables defined before round t. Taking expectation conditioned over $\mathcal{F}_t$ implies that

$$\begin{aligned}
&\mathbb{E}\big(|\beta_i^{(t)} - \beta_i^{(t+1)}|^2 | \mathcal{F}_t\big) = \frac{m}{n}|\tilde{\beta}_i - \beta_i^{(t)}|^2,\\
&\mathbb{E}\big(|\beta_i^{(t+1)} - \beta_i^*|^2 | \mathcal{F}_t\big) = \frac{m}{n}|\tilde{\beta}_i - \beta_i^*|^2 + \frac{n-m}{n}|\beta_i^{(t)} - \beta_i^*|^2,\\
&\mathbb{E}\big(|\beta_i^{(t+1)}|^2 | \mathcal{F}_t\big) = \frac{m}{n}|\tilde{\beta}_i|^2 + \frac{n-m}{n}|\beta_i^{(t)}|^2,\\
&\mathbb{E}\big(\beta_i^{(t+1)} | \mathcal{F}_t\big) = \frac{m}{n}\tilde{\beta}_i + \frac{n-m}{n}\beta_i^{(t)}.
\end{aligned}$$

Using the above equalities to represent terms involving $\tilde{\beta}_i$ by $\beta_i^{(t+1)}$ on the righthand side of (18), we have

$$\left(\frac{1}{m}+\frac{1}{2\sigma m}\right)\mathbb{E}\big[|\beta_i^{(t+1)}-\beta_i^*|^2|\mathcal{F}_t\big] = \left(\frac{1}{2\sigma m}+\frac{n-m}{nm}\right) |\beta_i^{(t)}-\beta_i^*|^2 - \frac{1}{2\sigma m}\mathbb{E}[\|\beta^{(t+1)}-\beta^{(t)}\|^2] + \mathbb{E}\big[\langle \bar{\mathbf{w}}^{(t)}-\mathbf{w}^*, \frac{1}{m}(\beta_i^{t+1}-\beta_i^*) + \frac{1}{n}(\beta_i^{(t)}-\beta_i^*)x_i\rangle|\mathcal{F}_t\big]$$

Taking the summation over $i \in \mathbb{N}_n$ and noticing that $\bar{u}^{(t+1)} = \frac{1}{m}\sum_{i\in\mathbb{N}_n}(\beta_i^{t+1}-\beta_i^*)x_i + \frac{1}{n}\sum_{i\in\mathbb{N}_n}(\beta^{(t)}-\beta_i^*)x_i$, we have

$$\left(\frac{1}{m}+\frac{1}{2\sigma m}\right)\mathbb{E}\big[|\beta^{(t+1)}-\beta^*|^2|\big] = \left(\frac{1}{2\sigma m}+\frac{n-m}{nm}\right) \mathbb{E}[\|\beta^{(t)}-\beta^*\|^2] - \frac{1}{2\sigma m}\mathbb{E}[\|\beta^{(t+1)}-\beta^{(t)}\|^2] + \mathbb{E}\big[\langle \bar{\mathbf{w}}^{(t)}-\mathbf{w}^*, \bar{u}^{(t+1)}\rangle\big],$$

which completes the proof of the first estimation (15).

Now we turn our attention to the proof of inequality (16). Indeed, by the definition of $\mathbf{w}^{(t+1)}$ and λ-strongly convexity of g, there holds

$$\langle \bar{u}^{(t+1)}, \mathbf{w}^*\rangle + g(\mathbf{w}^*) + \frac{\|\mathbf{w}^{(t)}-\mathbf{w}^*\|^2}{2\tau} \ge \langle \bar{u}^{(t+1)}, \mathbf{w}^{(t+1)}\rangle + g(\mathbf{w}^{(t+1)}) + \frac{\|\mathbf{w}^{(t+1)}-\mathbf{w}^{(t)}\|^2}{2\tau} + \left(\frac{\lambda}{2}+\frac{1}{2\tau}\right)\|\mathbf{w}^{(t+1)}-\mathbf{w}^*\|^2. \tag{19}$$

Let $u^* = \frac{1}{n}\sum_{i\in\mathbb{N}_n}\beta_i^* x_i$. By the definition of the saddle point $(\mathbf{w}^*, \beta^*)$, there holds

$$\langle u^*, \mathbf{w}^{(t+1)}\rangle + g(\mathbf{w}^{(t+1)}) \ge \langle u^*, \mathbf{w}^*\rangle + g(\mathbf{w}^*) + \frac{\lambda}{2}\|\mathbf{w}^{(t+1)}-\mathbf{w}^*\|^2.$$

Adding the above inequality with (19) and arranging the terms yields that

$$\left(\lambda+\frac{1}{2\tau}\right)\|\mathbf{w}^{(t+1)}-\mathbf{w}^*\|^2 \le \frac{\|\mathbf{w}^{(t)}-\mathbf{w}^*\|^2}{2\tau} - \frac{\|\mathbf{w}^{(t+1)}-\mathbf{w}^{(t)}\|^2}{2\tau} - \langle \mathbf{w}^{(t+1)}-\mathbf{w}^*, \bar{u}^{(t+1)}-u^*\rangle.$$

This completes the proof of the lemma.

Now we are ready to prove Theorem 4.1 using Lemma 4.1.

Proof: Adding (15) and (16) together, we have

$$\begin{aligned}
&\left(\frac{1}{m}+\frac{1}{2\sigma m}\right)\mathbb{E}\big[\|\beta^{(t+1)}-\beta^*\|^2\big]+\left(\lambda+\frac{1}{2\tau}\right)\\
&\mathbb{E}\big[\|\mathbf{w}^{(t+1)}-\mathbf{w}^*\|^2\big]\\
&\le\Big(\frac{1}{2\sigma m}+\frac{1}{m}-\frac{1}{n}\Big)\mathbb{E}\big[\|\beta^{(t)}-\beta^*\|\big]\\
&+\frac{1}{2\tau}\mathbb{E}\big[\|\mathbf{w}^{(t)}-\mathbf{w}^*\|^2\big]-\frac{1}{2\sigma m}\mathbb{E}\big[\|\beta^{(t+1)}-\beta^{(t)}\|^2\big]\\
&-\frac{1}{2\tau}\mathbb{E}\big[\|\mathbf{w}^{(t+1)}-\mathbf{w}^{(t)}\|^2\big]\\
&+\mathbb{E}\big[\langle u^{(t)}-u^*+\frac{n}{m}(u^{(t+1)}-u^{(t)}),\bar{\mathbf{w}}^{(t)}-\mathbf{w}^{(t+1)}\rangle\big]. \qquad (20)
\end{aligned}$$

By the definition of $u^{(t)}, u^{(t+1)}$ and $\bar{\mathbf{w}}^{(t)}$, we have

$$\begin{aligned}
\langle u^{(t)}-u^*+\frac{n}{m}(u^{(t+1)}-u^{(t)}),\bar{\mathbf{w}}^{(t)}-\mathbf{w}^{(t+1)}\rangle
&=\theta\langle u^{(t)}-u^*,\mathbf{w}^{(t)}-\mathbf{w}^{(t-1)}\rangle\\
&-\langle u^{(t+1)}-u^*,\mathbf{w}^{(t+1)}-\mathbf{w}^{(t)}\rangle\\
&+\frac{n\theta}{m}\langle u^{(t+1)}-u^{(t)},\mathbf{w}^{(t)}-\mathbf{w}^{(t-1)}\rangle\\
&+\frac{n-m}{m}\langle u^{(t+1)}-u^{(t)},\mathbf{w}^{(t)}-\mathbf{w}^{(t+1)}\rangle.
\end{aligned}$$

By the Cauchy-Schwartz inequality, letting $X=[x_1,x_2,\ldots,x_n]^\top$ and noticing that $\kappa^2\sigma=\frac{1}{4\tau}$ we have

$$\begin{aligned}
n\langle u^{(t+1)}-u^{(t)},\mathbf{w}^{(t)}-\mathbf{w}^{(t-1)}\rangle&=\left\langle\sum_{i\in K}(\beta_i^{(t+1)}-\beta_i^{(t)})x_i,\mathbf{w}^{(t)}-\mathbf{w}^{(t-1)}\right\rangle\\
&\le\frac{\|\beta^{(t+1)}-\beta^{(t)}\|\kappa^2 m}{4\sigma\kappa^2 m}+\frac{\|\mathbf{w}^{(t)}-\mathbf{w}^{(t-1)}\|^2 m}{4\tau}\\
&=\frac{\|\beta^{(t+1)}-\beta^{(t)}\|}{4\sigma}+\frac{\|\mathbf{w}^{(t)}-\mathbf{w}^{(t-1)}\|^2 m}{4\tau}. \qquad (21)
\end{aligned}$$

Likewise,

$$\begin{aligned}
n\langle u^{(t+1)}\quad -u^{(t)},\mathbf{w}^{(t)}-\mathbf{w}^{(t+1)}\rangle\le\frac{\|\beta^{(t+1)}-\beta^{(t)}\|}{4\sigma}\\
+\frac{\|\mathbf{w}^{(t+1)}-\mathbf{w}^{(t)}\|^2 m}{4\tau}.
\end{aligned}$$

Putting these estimations into (22) and arranging the terms yield that

$$\begin{aligned}
&\left(\frac{1}{m}+\frac{1}{2\sigma m}\right)\mathbb{E}\big[\|\beta^{(t+1)}-\beta^*\|^2\big]+\left(\lambda+\frac{1}{2\tau}\right)\\
&\mathbb{E}\big[\|\mathbf{w}^{(t+1)}-\mathbf{w}^*\|^2\big]+\frac{1}{2\tau}\mathbb{E}\big[\|\mathbf{w}^{(t+1)}-\mathbf{w}^{(t)}\|^2\big]\\
&+\mathbb{E}\big[\langle u^{t+1}-u^*,\mathbf{w}^{(t+1)}-\mathbf{w}^{(t)}\rangle\big]\\
&\le\Big(\frac{1}{m}+\frac{1}{2\sigma m}-\frac{1}{n}\Big)\mathbb{E}\big[\|\beta^{(t)}-\beta^*\|\big]+\frac{1}{2\tau}\mathbb{E}\big[\|\mathbf{w}^{(t)}-\mathbf{w}^*\|^2\big]\\
&+\theta\left(\frac{1}{2\tau}\mathbb{E}\big[\|\mathbf{w}^{(t)}-\mathbf{w}^{(t-1)}\|^2\big]+\mathbb{E}\big[\langle u^t-u^*,\mathbf{w}^{(t)}-\mathbf{w}^{(t-1)}\rangle\big]\right). \qquad (22)
\end{aligned}$$

Choosing that $\sigma=\frac{(n-m)+\sqrt{(n-m)^2+4n\kappa^2 m/\lambda}}{8m\kappa^2}$, $\tau=\frac{1}{4\sigma\kappa^2}$ and $\theta=1-\frac{\lambda}{\lambda+2\sigma\kappa^2}$ implies that

$$\left(\frac{1}{m}+\frac{1}{2\sigma m}-\frac{1}{n}\right)=\theta\left(1+\frac{1}{2\sigma}\right)\ \text{ and }\ \frac{1}{2\tau}=\theta\left(\lambda+\frac{1}{2\tau}\right). \qquad (23)$$

Letting

$$\begin{aligned}
\triangle_t=&\left(\frac{1}{m}+\frac{1}{2\sigma m}\right)\mathbb{E}\big[\|\beta^{(t)}-\beta^*\|^2\big]+\left(\lambda+\frac{1}{2\tau}\right)\mathbb{E}\big[\|\mathbf{w}^{(t)}-\mathbf{w}^*\|^2\big]\\
&+\frac{1}{2\tau}\mathbb{E}\big[\|\mathbf{w}^{(t)}-\mathbf{w}^{(t-1)}\|^2\big]+\mathbb{E}\big[\langle u^t-u^*,\mathbf{w}^{(t)}-\mathbf{w}^{(t-1)}\rangle\big],
\end{aligned}$$

we know from (22) and (23) that $\triangle_{t+1}\le\theta\,\triangle_t$. Using the exactly argument as in (21), there holds

$$\begin{aligned}
&|\langle u^t-u^*,\mathbf{w}^{(t)}-\mathbf{w}^{(t-1)}\rangle|\le\frac{\|\mathbf{w}^{(t)}-\mathbf{w}^{(t-1)}\|^2}{4\tau}\\
&+\frac{\|(\beta^{(t)}-\beta^*)^\top X\|^2}{n^2/\tau}\le\frac{\|\mathbf{w}^{(t)}-\mathbf{w}^{(t-1)}\|^2}{4\tau}+\frac{\|(\beta^{(t)}-\beta^*)^\top X\|}{4n\sigma\kappa^2}\\
&\le\frac{\|\mathbf{w}^{(t)}-\mathbf{w}^{(t-1)}\|^2}{4\tau}+\frac{\|\beta^{(t)}-\beta^*\|}{4n\sigma}, \qquad (24)
\end{aligned}$$

which implies, for any t, that

$$\begin{aligned}
\triangle_t\ge&\left(\frac{1}{m}+\frac{1}{4\sigma m}\right)\mathbb{E}\big[\|\beta^{(t)}-\beta^*\|^2\big]\\
&+\left(\lambda+\frac{1}{2\tau}\right)\mathbb{E}\big[\|\mathbf{w}^{(t)}-\mathbf{w}^*\|^2\big]+\frac{1}{4\tau}\mathbb{E}\big[\|\mathbf{w}^{(t)}-\mathbf{w}^{(t-1)}\|^2\big]\ge 0.
\end{aligned} \qquad (25)$$

Consequently,

$$\begin{aligned}
\triangle_{t+1}\ &\le\theta^t\triangle_0=\theta^t\left(\left(\frac{1}{m}+\frac{1}{2\sigma m}\right)\|\beta^{(0)}-\beta^*\|\right.\\
&\left.+\left(\lambda+\frac{1}{2\tau}\right)\|\mathbf{w}^{(0)}-\mathbf{w}^*\|^2\right).
\end{aligned}$$

Combining this with the inequality (25) yields the desired result.

5. EXPERIMENTS

In this section, we report the experimental evaluations of SPDAM and compare it with existing state-of-the-art learning algorithms for AUC optimization and convergence rate.

5.1. Comparison Algorithms

We conduct comprehensive studies by comparing the proposed algorithm with other AUC optimization algorithms for both online and batch scenarios. Specifically, the algorithms considered in our experiments include:

- **SPDAM**: The proposed stochastic primal-dual algorithm for AUC maximization.

- **regSOLAM**: The regularized online projected gradient descent algorithm for AUC maximization.
- **OPAUC**: The one-pass AUC optimization algorithm with square loss function [18].
- **OAMseq**: The OAM algorithm with reservoir sampling and sequential updating method [22].
- **OAMgra**: The OAM algorithm with reservoir sampling and online gradient updating method [22].
- **Online Uni-Exp**: Online learning algorithm which optimizes the (weighted) univariate exponential loss [7].
- **B-SVM-OR**: A batch learning algorithm which optimizes the pairwise hinge loss [32].
- **B-LS-SVM**: A batch learning algorithm which optimizes the pairwise square loss.

It should be noted that OAMseq, OAMgra, and OPAUC are the state-of-the-art methods for AUC maximization in online settings. The algorithm regSOLAM is a modified version of our previous work that includes a regularization term and it achieves a similar convergence with only modified constants. We also reformulate the bound R in terms of the regularization parameter λ. Assume $\kappa = \sup_{x \in \mathcal{X}} \|x\| < \infty$, and recall that $\|\mathbf{w}\| \leq R$. By assuming that $\mathbf{w}^*$ is the optimal $\mathbf{w}$ then we have the following:

$$\frac{\lambda}{2}\|\mathbf{w}^*\|^2 \leq \mathbb{E}\Big[(1 - \mathbf{w}^\top(x - x'))^2 | y = 1, y' = -1\Big] + \frac{\lambda}{2}\|\mathbf{w}\|^2$$

By letting $\mathbf{w} = \mathbf{0}$ and recalling that $\|\mathbf{w}\| \leq R$, we can very easily see that: $R \leq \sqrt{\frac{2}{\lambda}}$. We make these changes to ensure a fair comparison with SPDAM.

TABLE 2 | Basic information about the benchmark datasets used in the experiments.

Datasets	♯inst	♯feat	Datasets	♯inst	♯feat
diabetes	768	8	fourclass	862	2
german	1,000	24	splice	3,175	60
usps	9,298	256	a9a	32,561	123
mnist	60,000	780	acoustic	78,823	50
ijcnn1	141,691	22	covtype	581,012	54
sector	9,619	55,197	news20	15,935	62,061

5.2. Experimental Testbed and Setup

To examine the performance of the proposed SPDAM algorithm in comparison to state-of-the-art methods, we conduct experiments on 11 benchmark datasets. **Table 2** shows the details of each of the datasets. All of these datasets are available for download from the LIBSVM and UCI machine learning repository. Note that some of the datasets (*mnist*, *covtype*, etc.) are multi-class, which we converted to binary data by randomly partitioning the data into two groups, where each group includes the same number of classes.

For the experiments, the features were normalized by taking $x_i \leftarrow \frac{x_i - \text{mean}(x_i)}{\|x_i\|}$ for the large datasets and $x_i \leftarrow \frac{x_i}{\|x_i\|}$ for the small datasets (*diabetes*, *fourclass*, and *german*). For each dataset, the data is randomly partitioned into 5-folds (4 are for training and 1 is for testing). We generate this partition for each dataset 5 times. This results in 25 runs for each dataset for which we use to calculate the average AUC score and standard deviation. To determine the proper parameter for each dataset, we conduct 5-fold cross validation on the training sets to determine the parameter $\lambda \in 10^{[-5:1]}$ for SPDAM and for regSOLAM the learning rate $\zeta \in [1:9:100]$ and the regularization parameter $\lambda \in 10^{[-5:5]}$ were found by a grid search. The buffer size for OAMseq and OAMgra is 100 as suggested [22]. All experiments for SPDAM and regSOLAM were conducted with MATLAB.

5.3. Evaluation of SPDAM and regSOLAM on Benchmark Datasets

Classification performances on the testing dataset of all methods are given in **Table 3**. These results show that SPDAM and

TABLE 3 | Comparison of the testing AUC values (mean±std.) on the evaluated datasets.

Datasets	SPDAM	regSOLAM	OPAUC	OAM$_{\text{seq}}$	OAM$_{\text{gra}}$	online Uni-Exp	B-SVM-OR	B-LS-SVM
diabetes	0.8275 ± 0.0302	0.8140 ± 0.0330	0.8309 ± 0.0350	0.8264 ± 0.0367	0.8262 ± 0.0338	0.8215 ± 0.0309	0.8326 ± 0.0328	0.8325 ± 0.0329
fourclass	0.8223 ± 0.0275	0.8222 ± 0.0276	0.8310 ± 0.0251	0.8306 ± 0.0247	0.8295 ± 0.0251	0.8281 ± 0.0305	0.8305 ± 0.0311	0.8309 ± 0.0309
german	0.7959 ± 0.0265	0.7830 ± 0.0247	0.7978 ± 0.0347	0.7747 ± 0.0411	0.7723 ± 0.0358	0.7908 ± 0.0367	0.7935 ± 0.0348	0.7994 ± 0.0343
splice	0.9227 ± 0.0128	0.9237 ± 0.0090	0.9232 ± 0.0099	0.8594 ± 0.0194	0.8864 ± 0.0166	0.8931 ± 0.0213	0.9239 ± 0.0089	0.9245 ± 0.0092
usps	0.9854 ± 0.0019	0.9848 ± 0.0021	0.9620 ± 0.0040	0.9310 ± 0.0159	0.9348 ± 0.0122	0.9538 ± 0.0045	0.9630 ± 0.0047	0.9634 ± 0.0045
a9a	0.8967 ± 0.0032	0.8970 ± 0.0048	0.9002 ± 0.0047	0.8420 ± 0.0174	0.8571 ± 0.0173	0.9005 ± 0.0024	0.9009 ± 0.0036	0.8982 ± 0.0028
mnist	0.9552 ± 0.0011	0.9599 ± 0.0014	0.9242 ± 0.0021	0.8615 ± 0.0087	0.8643 ± 0.0112	0.7932 ± 0.0245	0.9340 ± 0.0020	0.9336 ± 0.0025
acoustic	0.8119 ± 0.0039	0.8114 ± 0.0035	0.8192 ± 0.0032	0.7113 ± 0.0590	0.7711 ± 0.0217	0.8171 ± 0.0034	0.8262 ± 0.0032	0.8210 ± 0.0033
ijcnn1	0.9132 ± 0.0016	0.9108 ± 0.0030	0.9269 ± 0.0021	0.9209 ± 0.0079	0.9100 ± 0.0092	0.9264 ± 0.0035	0.9337 ± 0.0024	0.9320 ± 0.0037
covtype	0.9409 ± 0.0011	0.9332 ± 0.0020	0.8244 ± 0.0014	0.7361 ± 0.0317	0.7403 ± 0.0289	0.8236 ± 0.0017	0.8248 ± 0.0013	0.8222 ± 0.0014
sector	0.9406 ± 0.0062	0.9734 ± 0.0036	0.9292 ± 0.0081	0.9163 ± 0.0087	0.9043 ± 0.0100	0.9215 ± 0.0034	–	–

To accelerate the experiments, the value for sector was determined after five runs instead of 25 for the other data sets. The performances of OPAUC, OAMseq, OAMgra, online Uni-Exp, B-SVM-OR, and B-LS-SVM were taken from Gao et al. [18].

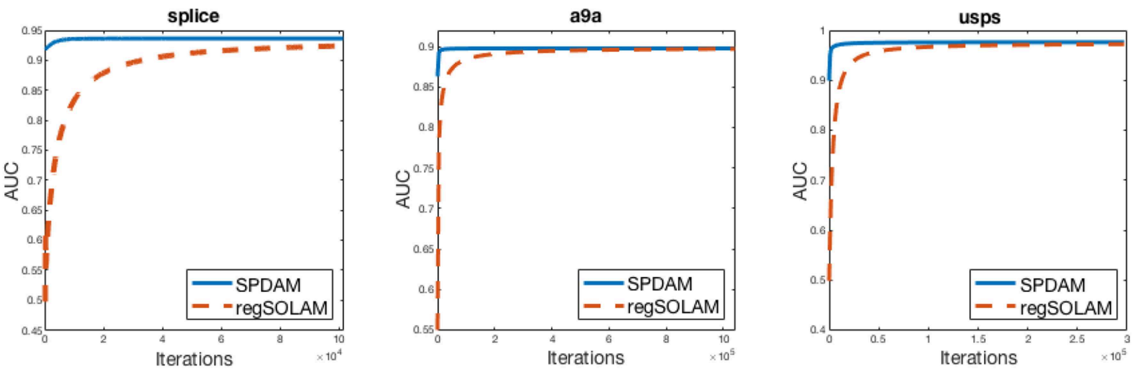

FIGURE 1 | AUC vs. Iteration curves of SPDAM against regSOLAM. For SPDAM, 10% of the data was chosen for a batch size. The optimal value of the parameter λ from SPDAM was used in regSOLAM.

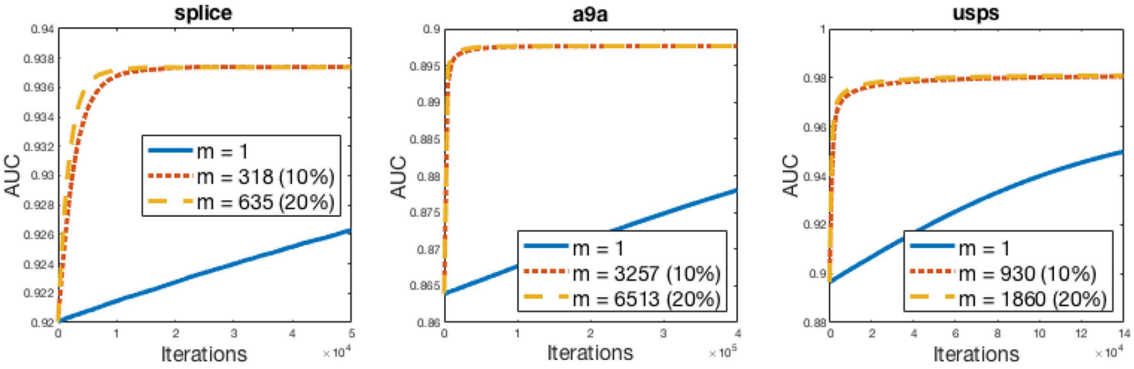

FIGURE 2 | AUC vs. Iteration curves of SPDAM algorithm for various batch sizes. The batch size is a percentage of the number of samples.

regSOLAM both achieve similar performances as other state-of-the-art online and offline methods based on AUC maximization. In some cases, SPDAM and regSOLAM perform better than some of the other online learning algorithms. There is a significant improvement in the text classification dataset *mnist* and *covtype*. The difference in performance of SPDAM and regSOLAM could be due to the fact since the data is randomly partitioned into two classes, the value of p could be resulting in a higher AUC score.

However, the main advantage of SPDAM over regSOLAM is the running time performance. SPDAM has a linear convergence rate while regSOLAM has a $\mathcal{O}(\frac{1}{\sqrt{t}})$ convergence. The theory tells us that SPDAM should be faster than regSOLAM. In **Figure 1**, we show AUC vs. Iterations for SPDAM against regSOLAM over 3 datasets. The figures show that SPDAM converges faster in comparison to regSOLAM, while maintaining a similar competitive performance as from **Table 3**.

In order to obtain this convergence rate, it is important to pick a large enough batch size (m). As from Theorem 4.1, the value of θ needs to be small for ensuring that SPDAM converges quickly. To ensure a fast convergence, the relationship between σ and θ should be examined. For θ to be small, σ should also be small which can be made possible by increasing the batch size m. If the batch size is too small, SPDAM will result in very poor performance. **Figure 2** demonstrates SPDAM on various batch sizes and shows that selecting a larger batch size ensures a faster rate of convergence. A batch size of 10% is sufficient so that SPDAM converges faster than regSOLAM.

6. CONCLUSION

In this paper, we proposed a stochastic primal-dual algorithm for AUC optimization [18, 22] based upon our previous work that AUC maximization is equivalent to a stochastic saddle point problem. By letting the distribution of ρ as in (7) be uniform, the proposed SPDAM algorithm is shown both theoretically and by experiments that the algorithm achieves a linear convergence rate. This makes SPDAM, given that a large enough batch size is used, faster than regSOLAM. If the batch size is not sufficiently large, SPDAM has poor performance.

There are several research directions for future work. First, the convergence was established using the duality gap associated with the stochastic SPP formulation (7). It would be interesting to establish the strong convergence of the output $\bar{\mathbf{w}}_T$ of the regSOLAM algorithm to its optimal solution of the actual AUC optimization problem (3). Secondly, the SPP formulation (3.1) holds for the least square loss. We do not know if the same formulation holds true for other loss functions such as the logistic regression or the hinge loss.

DATA AVAILABILITY

Publicly available datasets were analyzed in this study. This data can be found here: https://archive.ics.uci.edu/ml/index.php.

AUTHOR CONTRIBUTIONS

All authors listed have made a substantial, direct and intellectual contribution to the work, and approved it for publication.

FUNDING

This work is supported by NSF grant (#1816227) and was supported by a grant from the Simons Foundation (#422504), and the Presidential Innovation Fund for Research and Scholarship (PIFRS) from SUNY Albany.

ACKNOWLEDGMENTS

This manuscript is a significant extension of work that first appeared at NIPS 2016 [25].

REFERENCES

1. Elkan C. The foundations of cost-sensitive learning. In: *International Joint Conference on Artificial Intelligence*. Vol. 17. Seattle, WA: Lawrence Erlbaum Associates Ltd (2001). p. 973–8.
2. Metz CE. Basic principles of ROC analysis. In: Freeman LM, Blaufox MD, editors. *Seminars in Nuclear Medicine*. Vol. 8. Amsterdam: Elsevier (1978). p. 283–98.
3. Hanley JA, McNeil BJ. The meaning and use of the area under of receiver operating characteristic (roc) curve. *Radiology*. (1982) 143:29–36. doi: 10.1148/radiology.143.1.7063747
4. Fawcett T. ROC graphs: notes and practical considerations for researchers. *Mach Learn*. (2004) 31:1–38.
5. Cortes C, Mohri M. AUC optimization vs. error rate minimization. In: *Neural Information Processing Systems*. Vancouver, BC (2003).
6. Joachims T. A support vector method for multivariate performance measures. In: *International Conference on Machine Learning*. Bonn (2005).
7. Kotlowski W, Dembczynski K, Hüllermeier E. Bipartite ranking through minimization of univariate loss. In: *International Conference on Machine Learning*. Bellevue, WA (2011).
8. Rakotomamonjy A. Optimizing area under Roc curve with SVMs. In: *1st International Workshop on ROC Analysis in Artificial Intelligence*. Valencia (2004).
9. Bach FR, Moulines E. Non-asymptotic analysis of stochastic approximation algorithms for machine learning. In: *Neural Information Processing Systems.* Granada (2011).
10. Bottou L, LeCun Y. Large scale online learning. In: *Neural Information Processing Systems.* (2003). Available online at: http://papers.nips.cc/paper/2365-large-scale-online-learning
11. Cesa-Bianchi N, Conconi A, Gentile C. On the generalization ability of on-line learning algorithms. *IEEE Trans Inform Theory.* (2004) 50:2050–7. doi: 10.1109/TIT.2004.833339
12. Rakhlin A, Shamir O, Sridharan K. Making gradient descent optimal for strongly convex stochastic optimization. In: *International Conference on Machine Learning*. Edinburgh (2012).
13. Ying Y, Pontil M. Online gradient descent learning algorithms. *Found Comput Math.* (2008) 8:561–96. doi: 10.1007/s10208-006-0237-y
14. Zinkevich M. Online convex programming and generalized infinitesimal gradient ascent. In: *International Conference on Machine Learning.* Washington, DC (2003).
15. Nemirovski A, Juditsky A, Lan G, Shapiro A. Robust stochastic approximation approach to stochastic programming. *SIAM J Optim.* (2009) 19:1574–609. doi: 10.1137/070704277
16. Yu W, Lin Q, Yang T. Doubly stochastic primal-dual coordinate method for regularized empirical risk minimization with factorized data. *CoRR.* (2015) abs/1508.03390. Available online at: http://arxiv.org/abs/1508.03390
17. Herschtal A, Raskutti B. Optimising area under the ROC curve using gradient descent. In: *Proceedings of the Twenty-First International Conference on Machine Learning*. Banff, AB: ACM (2004). p. 49.
18. Gao W, Jin R, Zhu S, Zhou ZH. One-pass AUC optimization. In: *International Conference on Machine Learning.* Atlanta, GA (2013).
19. Kar P, Sriperumbudur BK, Jain P, Karnick H. On the generalization ability of online learning algorithms for pairwise loss functions. In: *International Conference on Machine Learning*. Atlanta, GA (2013).
20. Wang Y, Khardon R, Pechyony D, Jones R. Generalization bounds for online learning algorithms with pairwise loss functions. In: *COLT*. Edinburgh (2012).
21. Ying Y, Zhou DX. Online pairwise learning algorithms. *Neural Comput.* (2016) 28:743–77. doi: 10.1162/NECO_a_00817
22. Zhao P, Hoi SCH, Jin R, Yang T. Online AUC maximization. In: *International Conference on Machine Learning*. Bellevue, WA (2011).
23. Ding Y, Zhao P, Hoi SCH, Ong Y. Adaptive subgradient methods for online AUC maximization. *CoRR*. (2016) abs/1602.00351. Available online at: http://arxiv.org/abs/1602.00351
24. Gultekin S, Saha A, Ratnaparkhi A, Paisley J. MBA: mini-batch AUC optimization. *CoRR*. (2018) abs/1805.11221. Available online at: http://arxiv.org/abs/1805.11221
25. Ying Y, Wen L, Lyu S. Stochastic online AUC maximization. In: Lee DD, Sugiyama M, Luxburg UV, Guyon I, Garnett R, editors. *Advances in Neural Information Processing Systems 29*. Curran Associates, Inc. (2016). p. 451–9. Available online at: http://papers.nips.cc/paper/6065-stochastic-online-auc-maximization.pdf
26. Liu M, Zhang X, Chen Z, Wang X, Yang T. Fast stochastic AUC maximization with $O(1/n)$-convergence rate. In: Dy J, Krause A, editors. *Proceedings of the 35th International Conference on Machine Learning. vol. 80 of Proceedings of Machine Learning Research.* Stockholm: PMLR (2018). p. 3189–97. Available online at: http://proceedings.mlr.press/v80/liu18g.html
27. Rosasco L, Villa S, Vũ BC. Convergence of stochastic proximal gradient algorithm. *arXiv:14035074.* (2014).
28. Natole M Jr, Ying Y, Lyu S. Stochastic proximal algorithms for AUC maximization. In: Dy J, Krause A, editors. *Proceedings of the 35th International Conference on Machine Learning. vol. 80 of Proceedings of Machine Learning Research.* Stockholm: PMLR (2018). p. 3710–9. Available online at: http://proceedings.mlr.press/v80/natole18a.html
29. Clemencon S, Lugosi G, Vayatis N. Ranking and empirical minimization of U-statistics. *Ann Stat.* (2008) 36:844–74. doi: 10.1214/009052607000000910
30. Gao W, Zhou ZH. On the consistency of AUC pairwise optimization. In: *International Joint Conference on Artificial Intelligence.* Buenos Aires (2015).
31. Zhang Y, Lin X. Stochastic primal-dual coordinate method for regularized empirical risk minimization. In: *International Conference on Machine Learning*. Lille (2015). p. 353–61.
32. Joachims T. Training linear SVMs in linear time. In: *Proceedings of the Twelfth ACM SIGKDD International Conference on Knowledge Discovery and Data Mining.* Philadelphia, PA (2006). p. 217–26.

Conflict of Interest Statement: The authors declare that the research was conducted in the absence of any commercial or financial relationships that could be construed as a potential conflict of interest.

frontiers in Physics

MINI REVIEW
published: 06 August 2019
doi: 10.3389/fphy.2019.00112

Anomalous Diffusion in Random-Walks With Memory-Induced Relocations

Axel Masó-Puigdellosas, Daniel Campos and Vicenç Méndez*

Grup de Física Estadística, Departament de Física, Facultat de Ciències, Edifici Cc, Universitat Autònoma de Barcelona, Barcelona, Spain

In this minireview we present the main results regarding the transport properties of stochastic movement with relocations to known positions. To do so, we formulate the problem in a general manner to see several cases extensively studied during the last years as particular situations within a framework of random walks with memory. We focus on (i) stochastic motion with resets to its initial position followed by a waiting period, and (ii) diffusive motion with memory-driven relocations to previously visited positions. For both of them we show how the overall transport regime may be actively modified by the details of the relocation mechanism.

Keywords: stochastic movement, resets, relocations, anomalous diffusion, random walk

Edited by:
Ralf Metzler,
University of Potsdam, Germany

Reviewed by:
Shlomire Reuveni,
Tel Aviv University, Israel
Denis Grebenkov,
Centre National de la Recherche
Scientifique (CNRS), France

****Correspondence:***
Axel Masó-Puigdellosas
axel.maso@uab.cat

Specialty section:
This article was submitted to
Interdisciplinary Physics,
a section of the journal
Frontiers in Physics

Received: *30 April 2019*
Accepted: *18 July 2019*
Published: *06 August 2019*

Citation:
Masó-Puigdellosas A, Campos D and Méndez V (2019) Anomalous Diffusion in Random-Walks With Memory-Induced Relocations. Front. Phys. 7:112. doi: 10.3389/fphy.2019.00112

1. INTRODUCTION

While Brownian movement is characterized by the well-known diffusive scaling $\langle x^2 \rangle \sim t$, alternative (anomalous) scalings can be obtained when the local motion of the particles is highly non-stationary or somehow governed by heavy-tailed (e.g., power-law) statistics, for instance, in the distribution of the local displacements [1]. The physical mechanisms responsible for such non-standard statistics are wide-ranging, including interaction with the underlying media or with an external force/field, as well as internal mechanisms. In the present mini-review, we focus in the latter case and explore recent advances that have been achieved in exploring anomalous properties of random walk processes when particles are assumed to possess some level of internal memory, such that their displacements are conditioned by the information acquired during its ongoing trajectory. While the framework of random-walks with memory includes many different models (as self-avoiding walks [2], elephant or alzheimer random-walks [3, 4], infotactic strategies [5],...) we focus here in the particular case where particles use their memory from time to time to relocate to known, or familiar, positions in the domain.

As a first case of interest, relocations to the initial position (resets) have been recurrently studied in recent years. One-dimensional unbounded diffusion with resets happening at a constant rate was initially introduced in [6]. Originally its interest was focused on their ability to make the mean first passage time finite, with a minimum value found for an intermediate reset rate [7–10]. However, it has been subsequently shown that their intrinsic transport properties are also of interest. For example, as a consequence of such resetting, dispersal is asymptotically suppressed and a steady state is reached. Thereafter, this property has been confirmed by numerous works on Markovian resets in different contexts, as multi-dimensional diffusion [11], coagulation-diffusion processes [12], confined diffusion [13, 14], diffusion with a refractory period after the resets [15], anomalous subdiffusion [16, 17], monotonic stochastic motion [18, 19], continuous-time random walk (CTRW) velocity models [20], the telegraphic process [21], and underdamped Brownian motion [22]. Likewise, in [23], a steady state is shown to appear when a diffusion process is restarted at a time-dependent rate and in [24] power-law reset time probability density functions (pdf) are considered and conditions for a steady state to exist are found. Finally, general conditions on the reset time pdf for the appearance of a steady state have been found in [25, 26].

In contrast with the aforementioned cases, where a steady state is reached, some works have shown that unbounded dispersal is still possible at a population level when the reset time is governed by heavy-tailed distributions so making resets less and less frequent with time (see [20, 25–27]). Particularly, in [15, 27] it is shown that the diffusivity of a walker which resets its position followed by a residence or refractory period at the origin is strongly dependent on the tail of the reset and residence time pdfs. Also, asymptotic transport appears when the resetting is soft [17], meaning that the walker is relocated to the origin but the other properties of the motion (e.g., a dynamic diffusion coefficient) are not renewed.

Alternatively, random walks with relocations to any previously visited place have been seen to modify the transport regime of a given motion process. In [28] it was proved that if such relocations are equiprobable among all visited sites in the past, then unbounded dispersal is not suppressed as in the resetting case but becomes ultraslow, with a mean squared displacement (MSD) that grows logarithmically [i.e., $\langle x^2(t)\rangle \sim \ln(t)$], a result that is kept when relocation events follow a time-continuous dynamics [28–30]. This can be generalized to include a weight function for the memory to chose the relocation position; in such case, the MSD of the process can exhibit a range of behaviors, from diffusive or sub-diffusive to logarithmic, as a function of the distribution [31]. Also, a rich variety of transport regimes have been proved to arise in the continuous time and space version of this model [29], ranging from an ultraslow growth $\langle x^2(t)\rangle \sim \ln(\ln(t))$ to the diffusive scaling. Finally, a more specific relocation mechanism consisting of stochastically taking the walker to the maximum position attained in the past has also been proven to also let the motion spread [32].

In the following, we employ a general framework that includes these two types of models (resets and/or relocations to visited sites) as particular cases, and so allows us to review the results mentioned above from the unified perspective of random-walks with memory-induced jumps, and detect opportunities of research in the field for the near future. We focus our efforts on recovering the different transport regimes mentioned above, so illustrating the capacity of internal memory to modify the scaling properties governing the transport regime of the process.

2. GENERAL FRAMEWORK

The framework we consider here follows a time dynamics based on the alternation between two states (one for standard motion and another for relocations), an approach which is quite usual in models of random walks with memory [27, 33]. First, a normal state ($i = 1$) where the walker motion is governed by a given by a jump length distribution and a probability time distribution, as in the classical CTRW. The duration of this state is determined by a given pdf $\varphi_1(t)$. Second, a memory-induced state ($i = 2$) which results from introducing a relocation to a particular position without explicit dependence of memory and waiting there until a new normal period is started. The relocation position is chosen from a generalized relocation distribution $p_0(x, t)$. After the relocation takes place, we assume that there exists a *refractory*, or waiting, period during which the particle remains at the position of relocation, governed by another pdf denoted as $\varphi_2(t)$.

If the walker starts at $t = 0$ from position $x = 0$ at state $i = 1$, the transition probability $j_1(x, t)$ from state $i = 2$ to $i = 1$ at position x and the transition probability $j_2(x, t)$ from state $i = 1$ to $i = 2$ at x will follow, respectively:

$$j_1(x,t) = \delta(x)\delta(t) + \int_0^t j_2(x,t-t')\varphi_2(t')dt' \tag{2.1}$$

$$j_2(x,t) = p_0(x,t)\int_{-\infty}^{+\infty} dx' \int_0^t j_1(x',t-t')\varphi_1(t')dt'. \tag{2.2}$$

Let us now introduce the spatial dynamics for both states. In the normal state, the motion can be described by a general propagator $P(x, t; x', t')$, being the probability of finding the walker at point x at time t if it was at point x' at time t'. Otherwise, in the memory-induced state the walker stays at the relocation position x', so its "propagator" reduces to $\delta(x - x')$. As a whole, the pdf of the particles in state $i = 1$ and $i = 2$ at time t, respectively read

$$\rho_1(x,t) = \int_{-\infty}^{+\infty} dx' \int_0^t dt' j_1(x',t-t')\varphi_1^*(t')P(x,t';x',0) \tag{2.3}$$

$$\rho_2(x,t) = \int_{-\infty}^{+\infty} dx' \int_0^t dt' j_2(x',t-t')\varphi_2^*(t')\delta(x-x'), \tag{2.4}$$

where $\varphi_i^*(t) \equiv \int_t^\infty \varphi_i(t')dt'$, for $i = \{1, 2\}$. The meaning of the first equation can be stated as follows: the pdf for particles in the memory-free state ($i = 1$) is described by the propagator $P(x, t'; x', 0)$, provided the system entered this state at time $t - t'$ at any position x', and it has remained in that state (i.e., without relocating) for the subsequent time t'. Equation (2.4) represents the equivalent for the memory-induced state, with the position described by the delta function $\delta(x-x')$ instead of the propagator.

3. SPATIAL DISPERSAL WITH RESETS

Resets can be defined as relocations which are used by the particle to come back from time to time to its initial position, an idea which can be satisfactorily adapted to study situations like animal foraging [10, 34], searches on the Internet [35, 36] or genetic networks [37, 38], and the kinetics of chemical reactions [39, 40] or molecular proofreading [41, 42]. Using the general formalism in the previous section, this corresponds to a time-independent relocation distribution $p_0(x, t) = \delta(x)$. Also, for the sake of simplicity we can restrict our analysis to propagators which are space homogenous, such that motion in the memory-free state satisfies $P(x, t; x', 0) = P(x - x', t; 0, 0) \equiv P(x - x', t)$.

Performing the Fourier-Laplace transform of the Equations (2.1–2.4) above and solving for the MSD of the overall propagator as $\langle x^2(t)\rangle \equiv \int_{-\infty}^{\infty} dx\, x^2 \rho(x,t) = \int_{-\infty}^{\infty} dx\, x^2 \left(\rho_1(x,t) + \rho_2(x,t)\right)$, it can be found that

$$\mathcal{L}\left[\langle x^2(t)\rangle\right] = \frac{\mathcal{L}\left[\varphi_1^*(t)\langle x^2(t)\rangle_P\right]}{1-\hat{\varphi}_1(s)\hat{\varphi}_2(s)}, \tag{3.1}$$

where $\mathcal{L}[f(t)] = \hat{f}(s) \equiv \int_0^{\infty} e^{-st} f(t)dt$ represents the Laplace transform of $f(t)$, and $\langle x^2(t)\rangle_P$ is the MSD of the propagator $P(x,t;x_0,0)$ by assuming that it is symmetric in space.

Seminal works on random walks with resets were focused on the situation where the process restarts immediately after the reset happens, i.e., $\varphi_2(t) = \delta(t)$ [6, 7]. In such case, it is known that if the memory-free propagation scales as $\langle x^2(t)\rangle_P \sim t^p$ and the resets are Markovian [i.e., $\varphi_1(t) = re^{-rt}$], a stationary state is always reached (so, there is propagation failure), and the relaxation to that stationary situation can be also characterized [43]. This scenario, where the resetting is strong enough to localize the walker around the origin, has been later studied from different perspectives. In some cases, a modified Fokker-Planck equation formalism [6, 11–14, 21, 22] has been employed to study Markovian resetting in, for instance, the diffusion equation [6], the Telegrapher's equation [21] and the underdamped Brownian motion equation [22]. Other works have found this same result by interpreting resets as a renewal of the motion and consequently building a renewal master equation for the overall pdf as done in the general formalism herein [16–20].

Otherwise, for the same propagation scaling but a long-tailed statistics of reset times with diverging first moment ($\varphi_1(t) \sim t^{-1-\gamma_1}$, with $0 < \gamma_1 < 1$), the overall MSD scales also as $\langle x^2(t)\rangle \sim t^p$. Therefore, the properties of the memory-free movement can be modified or not depending on the specific properties of the refractory or waiting time. This was found in [25] for diffusive motion (i.e., $p = 1$) and later in [26] for the general case.

The model turns out to be more interesting, however, when the resting time after the resets is non-zero, this is, for a non-trivial choice of the waiting time pdf as $\varphi_2(t) \sim t^{-1-\gamma_2}$. This scenario, which has been recently studied in [10, 15, 27] from a renewal perspective, yields a wide range of situations for the asymptotic behavior of the overall MSD in the case when memory-free propagation scales again as $\langle x^2(t)\rangle_P \sim t^p$. Depending on the finiteness/infiniteness of the moments of $\varphi_1(t)$ and $\varphi_2(t)$, the following cases can be identified:

(i) $\gamma_1 > 1, \gamma_2 > 1$. The propagation ceases and a stationary state is reached as for the non-resting period case, yielding

$$\langle x^2(t)\rangle \sim \text{const.}$$

(ii) $\gamma_1 > 1, 0 < \gamma_2 < 1$. The propagation ceases and the system tends to collapse toward the origin.

$$\langle x^2(t)\rangle \sim t^{\gamma_2 - 1}$$

(iii) $0 < \gamma_1 < 1, \gamma_2 > 1$. The propagation is only affected by the resetting mechanism in a multiplicative factor, but it does not affect the scaling:

$$\langle x^2(t)\rangle \sim t^p$$

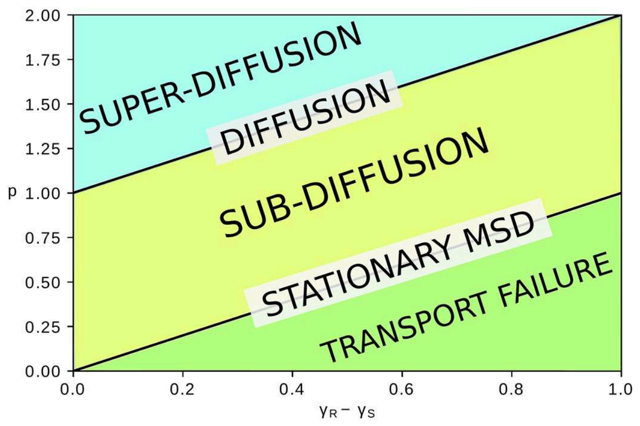

FIGURE 1 | Schematic plot of the different overall transport regimes in terms of the transport regime of the movement process *p* and the difference between the decaying exponents of the reset and residence time pdfs $\gamma_1 - \gamma_2$, corresponding to case (iv) in the main text. In the blue region the overall behavior is super-diffusive. In the yellow region it is sub-diffusive and the green represents the values for which we have transport failure. We can see that, for instance, an originally super-diffusive process ($p > 1$) can become sub-diffusive (yellow region) with the properly chosen tail exponents.

(iv) $0 < \gamma_1 < 1, 0 < \gamma_2 < 1$. The propagation is actively modified by the resetting mechanism when the tail of $\varphi_2 \sim t^{-1-\gamma_2}$ is longer than the tail of $\varphi_1 \sim t^{-1-\gamma_1}$, i.e., $\gamma_2 < \gamma_1$. Otherwise, when $\gamma_2 \geq \gamma_1$, the overall process behaves as in case iii). In short,

$$\langle x^2(t)\rangle \sim t^{p-(\gamma_1-\gamma_2)\theta(\gamma_1-\gamma_2)},$$

where $\theta(\gamma_1 - \gamma_2)$ denotes the Heaviside function.

According to this, scenario iv) turns out to be particularly interesting and all its casuistic is visually summarized in **Figure 1**. When the resting period is asymptotically longer than the active period, the diffusivity of the propagation is reduced by a factor $\gamma_1 - \gamma_2$ as a result of the competition between the heavy-tailed effects of the movement and the refractory period. This, for instance, may turn a superdiffusive (or diffusive) process into subdiffusive by only tuning the asymptotic decay of the active and resting times pdf.

In the light of what we have seen in this section, some questions regarding the asymptotic transport properties of motion with resetting remain still unanswered. For instance, without the residence time after the resetting, it seems that resetting either leaves the transport regim unaltered or it makes the transport cease and a stationary state is reached. Is there any resetting mechanism able to smoothly modify the transport regime of the motion? Also, resetting has been mainly treated as an internal mechanism of the motion. What would be the overall dynamics of a set of walkers which interact to suddenly reset their individual position? Despite this has been shown to be hard from an analytical point of view [44], it would be extremely interesting for the description of many ecological systems.

4. SPATIAL DISPERSAL WITH RELOCATIONS TO VISITED PLACES

Relocation processes in which particles are allowed to return to already visited places is another case of interest for which the properties of the overall MSD have been recurrently explored [28, 30, 31, 45]. If expressed in terms of the general framework presented in section II, this case would correspond to a relocation distribution of the type

$$p_0(x,t) = \frac{\int_0^t \phi(t')\rho(x,t')}{\int_0^t \phi(t')dt'}, \tag{4.1}$$

where $\phi(t)$ is a memory function which weights all possible relocation places as a function of the time elapsed since they were visited. This is, if $\phi(t)$ is an increasing function, then relocation to recent positions is more likely to occur, which would implicitly assume that memory is a vanishing process. On the other hand, if $\phi(t)$ is a decreasing function of time then the initial positions are the most probable ones. Finally, one could even recover the resetting mechanism by choosing $\phi(t) \sim \delta(t)$.

Since the mathematical treatment for a general situation as a function of $\phi(t)$ becomes cumbersome, we can restrict ourselves to Markovian relocations [so $\varphi_1(t) = re^{-rt}$] and mule resting times after the relocation, $\varphi_2(t) = \delta(t)$. For this particularly simple case, the four general Equations (2.1–2.4) lead to the following implicit solution for the overall MSD; if the propagation is diffusive with $\langle x^2(t)\rangle_P = 2Dt$, we get

$$\mathcal{L}\left[x^2(t)\right] = \frac{2D}{s(r+s)} + \frac{r}{r+s}\mathcal{L}\left[\frac{\int_0^t \phi(t')\langle x^2(t')\rangle}{\int_0^t \phi(t')dt'}\right]. \tag{4.2}$$

From this expression, the long time behavior of the MSD can be deduced for different weight functions for the memory; this has been done, using a relatively different perspective, in [29]. There it is shown that up to five different regimes emerge, which illustrates the rich variety of the model:

i) $\phi(t) \sim t^{-a}$, with $a > 1$. The transport ceases and a stationary state is reached.

$$\langle x^2(t)\rangle \sim \text{const}.$$

ii) $\phi(t) \sim t^{-a}$, with $a = 1$. The transport becomes extremely slow.

$$\langle x^2(t)\rangle \sim \ln(\ln(t))$$

iii) $\phi(t) \sim t^{-a}$, with $a < 1$. The transport becomes ultra slow.

$$\langle x^2(t)\rangle \sim \ln(t)$$

iv) $\phi(t) \sim e^{t^b}$, with $0 < b \leq 1$. The transport becomes subdiffusive when $b < 1$ and it is not affected by the memory for $b = 1$.

$$\langle x^2(t)\rangle \sim t^b$$

v) $\phi(t) \sim e^{t^b}$, with $1 < b$. The transport is not qualitatively affected by the memory, so it remains diffusive.

$$\langle x^2(t)\rangle \sim t.$$

These results have progressively been found during the last years. While case (iii) was originally found in [28] and later in [30], scalings (iv) and (iv) were found in [31] and, finally, all the asymptotic scalings derived herein were found in [29]. Likewise, transitions between different transport regimes have can possibly emerge as a consequence of spatial [46] or temporal [45] heterogeneities in the resetting process.

This range of situations is already obtained for fixed (and particularly simple) forms of $\varphi_1(t)$ and $\varphi_2(t)$, while the situation is susceptible to become even more complex as more general pdfs are taken into account. All this enlights the theoretical interest of the memory-induced mechanism as a way to reproduce different propagation regimes.

5. FUTURE PERSPECTIVES

Mostly inspired by the movement of biological individuals and other systems of intelligent walkers, random-walk models with memory-induced relocations (either resets or relocation to visited places) have been widely explored in recent years. In this minireview we have tried to condense the current knowledge we have about their transport properties in order to illustrate the richness of macroscopic transport properties they are able to yield. New situations of interest can arise in the future as long as different choices for the relocation distribution $p_0(x,t)$ in Equation (2.2) are explored instead of the two (resetting, uniform relocation) reviewed here. This may include the case of resetting to a distribution of fixed points, visited or not (a topic which has also received attention in the biological literature [47, 48]), or a relocation dynamics based on returns to those sites that were more beneficial in the past (so introducing an additional variable representing food available or assigning a value to the visited sites). As long as more general models and conclusions are obtained, a meaningful comparison to real data from animals or other organisms can represent a promising way to explore memory capacities in these living systems; or, alternatively, they can also become a useful tool to study the properties of active matter when subject to memory effects [49]. So, we envision that the following years will probably witness an increasing interest of researchers for the intricate interplays between memory and transport properties.

AUTHOR CONTRIBUTIONS

All authors listed have made a substantial, direct and intellectual contribution to the work, and approved it for publication.

FUNDING

This research has been supported by the Spanish government through Grant No. CGL2016-78156-C2-2-R.

REFERENCES

1. Méndez V, Campos D, Bartumeus F. *Stochastic Foundations in Movement Ecology*. Berlin; Heidelberg: Springer-Verlag (2014).
2. Madras N, Slade G. *The Self-Avoiding Walk*. Basel: Birkhuser (1996).
3. Schütz GM, Trimper S. Elephants can always remember: exact long-range memory effects in a non-Markovian random walk. *Phys Rev E*. (2004) **70**:045101. doi: 10.1103/PhysRevE.70.045101
4. Cressoni JC, Viswanathan GM, Ferreira AS, da Silva MAA. Alzheimer random walk model: two previously overlooked diffusion regimes. *Phys Rev E*. (2012) **86**:042101. doi: 10.1103/PhysRevE.86.042101
5. Vergassola M, Villermaux E, Shraiman BI. "Infotaxis" as a strategy for searching without gradients. *Nature*. (2007) **445**:406–9. doi: 10.1038/nature05464
6. Evans MR, Majumdar SN. Diffusion with stochastic resetting. *Phys Rev Lett*. (2011) **106**:160601. doi: 10.1103/PhysRevLett.106.160601
7. Evans MR, Majumdar SN. Diffusion with optimal resetting. *J Phys A Math Theor*. (2011) **44**:435001. doi: 10.1088/1751-8113/44/43/435001
8. Pal A, Reuveni S. First passage under restart. *Phys Rev Lett*. (2017) **118**:030603. doi: 10.1103/PhysRevLett.118.030603
9. Chechkin A, Sokolov IM. Random search with resetting: a unified renewal approach. *Phys Rev Lett*. (2018) **121**:050601. doi: 10.1103/PhysRevLett.121.050601
10. Pal A, Kuśmierz L, Reuveni S. Home-range search provides advantage under high uncertainty. *arXiv [Preprint]*. (2019) arXiv:190606987.
11. Evans MR, Majumdar SN. Diffusion with resetting in arbitrary spatial dimension. *J Phys A Math Theor*. (2014) **47**:285001. doi: 10.1088/1751-8113/47/28/285001
12. Durang X, Henkel M, Park H. The statistical mechanics of the coagulation–diffusion process with a stochastic reset. *J Phys A Math Theor*. (2014) **47**:045002. doi: 10.1088/1751-8113/47/4/045002
13. Pal A. Diffusion in a potential landscape with stochastic resetting. *Phys Rev E*. (2015) **91**:012113. doi: 10.1103/PhysRevE.91.012113
14. Christou C, Schadschneider A. Diffusion with resetting in bounded domains. *J Phys A Math Theor*. (2015) **48**:285003. doi: 10.1088/1751-8113/48/28/285003
15. Evans MR, Majumdar SN. Effects of refractory period on stochastic resetting. *J Phys A Math Theor*. (2018) **52**:01LT01. doi: 10.1088/1751-8121/aaf080
16. Shkilev VP. Continuous-time random walk under time-dependent resetting. *Phys Rev E*. (2017) **96**:012126. doi: 10.1103/PhysRevE.96.012126
17. Kuśmierz L, Gudowska-Nowak E. Subdiffusive continuous-time random walks with stochastic resetting. *Phys Rev E*. (2019) **99**:052116. doi: 10.1103/PhysRevE.99.052116
18. Montero M, Villarroel J. Monotonic continuous-time random walks with drift and stochastic reset events. *Phys Rev E*. (2013) **87**:012116. doi: 10.1103/PhysRevE.87.012116
19. Montero M, Masó-Puigdellosas A, Villarroel J. Continuous-time random walks with reset events. *Eur Phys J B*. (2017) **90**:176. doi: 10.1140/epjb/e2017-80348-4
20. Méndez V, Campos D. Characterization of stationary states in random walks with stochastic resetting. *Phys Rev E*. (2016) **93**:022106. doi: 10.1103/PhysRevE.93.022106
21. Masoliver J. Telegraphic processes with stochastic resetting. *Phys Rev E*. (2019) **99**:012121. doi: 10.1103/PhysRevE.99.012121
22. Gupta D. Stochastic resetting in underdamped Brownian motion. *J Stat Mech Theory Exp*. (2019) **2019**:033212. doi: 10.1088/1742-5468/ab054a
23. Pal A, Kundu A, Evans MR. Diffusion under time-dependent resetting. *J Phys A Math Theor*. (2016) **49**:225001. doi: 10.1088/1751-8113/49/22/225001
24. Nagar A, Gupta S. Diffusion with stochastic resetting at power-law times. *Phys Rev E*. (2016) **93**:060102. doi: 10.1103/PhysRevE.93.060102
25. Eule S, Metzger JJ. Non-equilibrium steady states of stochastic processes with intermittent resetting. *N J Phys*. (2016) **18**:033006. doi: 10.1088/1367-2630/18/3/033006
26. Masó-Puigdellosas A, Campos D, Méndez V. Transport properties and first-arrival statistics of random motion with stochastic reset times. *Phys Rev E*. (2019) **99**:012141. doi: 10.1103/PhysRevE.99.012141
27. Masó-Puigdellosas A, Campos D, Méndez V. Stochastic movement subject to a reset-and-residence mechanism: transport properties and first arrival statistics. *J Stat Mech Theory Exp*. (2019) **2019**:033201. doi: 10.1088/1742-5468/ab02f3
28. Boyer D, Solis-Salas C. Random walks with preferential relocations to places visited in the past and their application to biology. *Phys Rev Lett*. (2014) **112**:240601. doi: 10.1103/PhysRevLett.112.240601
29. Boyer D, Evans MR, Majumdar SN. Long time scaling behaviour for diffusion with resetting and memory. *J Stat Mech Theory Exp*. (2017) **2017**:023208. doi: 10.1088/1742-5468/aa58b6
30. Campos D, Méndez V. Recurrence time correlations in random walks with preferential relocation to visited places. *Phys Rev E*. (2019) **99**:062137. doi: 10.1103/PhysRevE.99.062137
31. Boyer D, Romo-Cruz JCR. Solvable random-walk model with memory and its relations with Markovian models of anomalous diffusion. *Phys Rev E*. (2014) **90**:042136. doi: 10.1103/PhysRevE.90.042136
32. Majumdar SN, Sabhapandit S, Schehr G. Random walk with random resetting to the maximum position. *Phys. Rev. E*. (2015) **92**:052126. doi: 10.1103/PhysRevE.92.05212
33. Kumar N, Harbola U. Memory induced anomalous dynamics in a random walker with internal states. *J Stat Mech Theory Exp*. (2018) **2018**:103207. doi: 10.1088/1742-5468/aae59b
34. Campos D, Méndez V. Phase transitions in optimal search times: how random walkers should combine resetting and flight scales. *Phys Rev E*. (2015) **92**:062115. doi: 10.1103/PhysRevE.92.062115
35. Villén-Altamirano M, Villén-Altamirano J. RESTART: a method for accelerating rare event simulations. In: *Queueing, Performance and Control in ATM: Proceedings of the 13th International Teletraffic Congress*. Copenhagen (1991).
36. Tong H, Faloutsos C, Pan JY. Random walk with restart: fast solutions and applications. *Knowl Inform Syst*. (2008) **14**:327–46. doi: 10.1007/s10115-007-0094-2
37. Köhler S, Bauer S, Horn D, Robinson PN. Walking the interactome for prioritization of candidate disease genes. *Am J Hum Genet*. (2008) **82**:949–58. doi: 10.1016/j.ajhg.2008.02.013
38. Li L, Wang Y, An L, Kong X, Huang T. A network-based method using a random walk with restart algorithm and screening tests to identify novel genes associated with Menière's disease. *PLoS ONE*. (2017) **12**:1–19. doi: 10.1371/journal.pone.0182592
39. Reuveni S, Urbakh M, Klafter J. Role of substrate unbinding in Michaelis–Menten enzymatic reactions. *Proc Natl Acad Sci USA*. (2014) **111**:4391–6. doi: 10.1073/pnas.1318122111
40. Reuveni S. Optimal stochastic restart renders fluctuations in first passage times universal. *Phys Rev Lett*. (2016) **116**:170601. doi: 10.1103/PhysRevLett.116.170601
41. Bar-Ziv R, Tlusty T, Libchaber A. Protein–DNA computation by stochastic assembly cascade. *Proc Natl Acad Sci USA*. (2002) **99**:11589–92. doi: 10.1073/pnas.162369099
42. Murugan A, Huse DA, Leibler S. Speed, dissipation, and error in kinetic proofreading. *Proc Natl Acad Sci USA*. (2012) **109**:12034–9. doi: 10.1073/pnas.1119911109
43. Majumdar SN, Sabhapandit S, Schehr G. Dynamical transition in the temporal relaxation of stochastic processes under resetting. *Phys Rev E*. (2015) **91**:052131. doi: 10.1103/PhysRevE.91.052131
44. Falcao R, Evans MR. Interacting Brownian motion with resetting. *J Stat Mech Theory Exp*. (2017) **2017**:023204. doi: 10.1088/1742-5468/aa569c
45. Falcón-Cortés A, Boyer D, Giuggioli L, Majumdar NS. Localization transition induced by learning in random searches. *Phys Rev Lett*. (2017) **119**:140603. doi: 10.1103/PhysRevLett.119.140603

46. Boyer D, Falcón-Cortés A, Giuggioli L, Majumdar SN. Anderson-like localization transition of random walks with resetting. *J Stat Mech Theory Exp.* (2019) **2019**:053204. doi: 10.1088/1742-5468/ab16c2
47. Gautestad A. Memory matters: influence from a cognitive map on animal space use. *J Theor Biol.* (2011) **287**:26–36. doi: 10.1016/j.jtbi.2011.07.010
48. Gautestad A. *ANIMAL SPACE USE: Memory Effects, Scaling Complexity, and Biophysical Model Coherence*. Indianapolis, IN: Dog Ear Publishing (2015).
49. Falcón-Cortés A, Boyer D, Ramos-Fernández G. Collective learning from individual experiences and information transfer during group foraging. *J Roy Soc Interface.* (2019) **16**:20180803. doi: 10.1098/rsif.2018.0803

Conflict of Interest Statement: The authors declare that the research was conducted in the absence of any commercial or financial relationships that could be construed as a potential conflict of interest.

frontiers in Physics

ORIGINAL RESEARCH
published: 03 September 2019
doi: 10.3389/fphy.2019.00119

Transient Anomalous Diffusion in a Heterogeneous Environment

Andrew J. Spakowitz[1,2,3,4]*

[1] Department of Chemical Engineering, Stanford University, Stanford, CA, United States, [2] Department of Materials Science and Engineering, Stanford University, Stanford, CA, United States, [3] Department of Applied Physics, Stanford University, Stanford, CA, United States, [4] Biophysics Program, Stanford University, Stanford, CA, United States

This work provides an analytical model for the diffusive motion of particles in a heterogeneous environment where the diffusivity varies with position. The model for diffusivity describes the environment as being homogeneous with randomly positioned pockets of larger diffusivity. This general framework for heterogeneity is amenable to a systematic expansion of the Green's function, and we employ a diagrammatic approach to identify common terms in this expansion. Upon collecting a common family of these diagrams, we arrive at an analytical expression for the particle Green's function that captures the spatially varying diffusivity. The resulting Green's function is used to analyze anomalous diffusion and kurtosis for varying levels of heterogeneity, and we compare these results with numerical simulations to confirm their validity. These results act as a basis for analysis of a range of diffusive phenomena in heterogeneous materials and living cells.

Keywords: diffusion, heterogeneity, non-Gaussian statistics, soft materials, transport in living cells

Edited by:
Ralf Metzler,
University of Potsdam, Germany

Reviewed by:
Flavio Seno,
University of Padova, Italy
Marco G. Mazza,
Max-Planck-Institute for Dynamics and Self-Organisation, Max Planck Society (MPG), Germany
Denis Grebenkov,
Centre National de la Recherche Scientifique (CNRS), France

Correspondence:
Andrew J. Spakowitz
ajspakow@stanford.edu

Specialty section:
This article was submitted to Interdisciplinary Physics, a section of the journal Frontiers in Physics

Received: *30 May 2019*
Accepted: *13 August 2019*
Published: *03 September 2019*

Citation:
Spakowitz AJ (2019) Transient Anomalous Diffusion in a Heterogeneous Environment. Front. Phys. 7:119. doi: 10.3389/fphy.2019.00119

INTRODUCTION

Brownian motion of microscopic objects [1–3] is a ubiquitous phenomenon that plays a significant role in virtually all molecular processes. Predictive understanding of the statistical behavior of objects undergoing Brownian motion is essential to our ability to determine and control the outcome of processes that fundamentally rely on stochastic motion at the molecular level. Given the general nature of Brownian motion, it is essential to establish a mathematical framework that is transferable to a diverse range of materials with varying microscopic structural characteristics.

Foundational studies of Brownian motion [1, 2, 4] establish a mathematical approach for predicting trajectory statistics in a homogeneous environment, thus capturing diffusive random-walk processes described by Gaussian statistics. However, all materials exhibit microscopic heterogeneity at length scales approaching that of individual chemical units (i.e., approaching atomic scales), and a broad range of materials, including glasses, gels, and other amorphous solids, exhibit heterogeneity across a broad range of length scales [5–11]. Furthermore, experimental measurements of particle motion in living cells reveal anomalous diffusive transport [12–25] that is tied to a range of physical effects, including heterogeneity and cell-to-cell variability [26] as well as viscoelasticity [26–29], dynamic arrest due to glassy disorder [11, 19], and active biological processes [9, 17, 25, 30]. Heterogeneity in soft materials and living cells results in non-Gaussian statistics for the step distribution over a range of time scales [8, 9, 26, 31–33], which acts as a signature for heterogeneous diffusion.

Theoretical modeling of heterogeneous diffusion provides fundamental insight into the impact of spatially varying diffusivity. Homogenization [34–38] and effective medium theory [39–47] are powerful analytical approaches to modeling spatially varying diffusivity. Such approaches leverage a systematic averaging of the microscopic heterogeneity as an effective large-scale medium, resulting in predictions for the effective diffusion at large length scales. However, the initial diffusive transport is distinct from the behavior in this effective medium. Thus, the behavior across broad time scales exhibits both the initial sampling of the local environment and the long-time sampling of the surrounding effective medium.

To capture this temporal evolution of the effective diffusivity, theoretical approaches employ frameworks that allow the diffusivity to stochastically change with time, dubbed a "diffusing diffusivity" [48–51]. This approach has been valuable in interpreting particle dynamics in living cells across a broad range of time scales, where the particles generally transition from complex heavy-tailed statistics to effective Gaussian behavior [8, 9, 26, 31–33]. However, the microscopic interpretation of the diffusing diffusivity picture is not straightforward. Thus, an analytical treatment that directly relates the specific microscopic structural heterogeneity to particle diffusion across all time scales would be valuable in establishing a fundamental understanding of heterogeneous transport. Such a development would impact a broad range of soft-materials and biological phenomena with varying microscopic structural characteristics.

Our work provides an analytical approach to determining the Green's function for diffusion in a spatially varying environment. We present an exact solution for the Green's function for an arbitrary spatial diffusivity function. We then define a heterogeneous diffusivity model with randomly positioned pockets of large diffusivity in an otherwise homogeneous background. Based on this model, we develop a systematic approach to determining the diffusivity-averaged Green's function over a range of degrees of heterogeneity. This approach applies a diagrammatic representation of the terms in the exact solution. We exploit this diagrammatic representation to collect like-powered terms in the strength of heterogeneity, resulting in an analytical expression for the Green's function.

Our solution is then used to analyze the transient anomalous diffusion of particles in a heterogeneous environment. We also analyze the temporal evolution of the kurtosis as a signature of the underlying non-Gaussian nature of the step distribution. These results demonstrate the signature feature of heterogeneous diffusion, where a particle transitions from sampling its local environment before transitioning to exploring the surrounding effective medium. These results provide a new framework for interpreting the temporal evolution of diffusive transport in complex heterogeneous materials and living cells.

THEORY

We consider the diffusion of a particle in a heterogeneous environment (in d dimensions) with a spatially varying diffusivity $D(\vec{r})$. The transport of the particle is defined by the Green's function $G(\vec{r}|\vec{r}_0; t)$, which gives the probability that a particle that begins at position $\vec{r}_0$ and time $t = 0$ is located at $\vec{r}$ at time t. The Green's function G is governed by the Smoluchowski equation

$$\frac{\partial G(\vec{r}|\vec{r}_0; t)}{\partial t} = \vec{\nabla} \cdot \left[D(\vec{r}) \vec{\nabla} G(\vec{r}|\vec{r}_0; t) \right] \tag{1}$$

with the initial condition

$$G(\vec{r}|\vec{r}_0; t = 0) = \delta(\vec{r} - \vec{r}_0). \tag{2}$$

We perform a Laplace transform from time t to the Laplace variable s and a Fourier transform from position $\vec{r}$ to Fourier variable $\vec{k}$. We then arrive at the expression

$$\hat{\tilde{G}}(\vec{k}; s) = \frac{\exp(i\vec{k} \cdot \vec{r}_0)}{s} - \frac{1}{(2\pi)^d} \frac{1}{s} \int d\vec{k}_1 (\vec{k} \cdot \vec{k}_1) \tilde{D}(\vec{k} - \vec{k}_1) \hat{\tilde{G}}(\vec{k}_1; s), \tag{3}$$

where the tilde indicates a Fourier-transformed function and the hat indicates a Laplace-transformed function.

The current form of $\hat{\tilde{G}}$ is transcendental (i.e., $\hat{\tilde{G}}$ is a function of $\hat{\tilde{G}}$), and an explicit expression for $\hat{\tilde{G}}(\vec{k}; s)$ requires recursive insertion of Equation (3) into itself. This leads to a general form

$$\hat{\tilde{G}}(\vec{k}; s) = \exp(i\vec{k} \cdot \vec{r}_0) \sum_{n=0}^{\infty} \frac{(-1)^n}{s^{n+1}} D_n(\vec{k}). \tag{4}$$

The k-dependent terms D_n represent the contributions from spatially varying diffusivity at various powers of $\tilde{D}$. The expressions for D_n up to $n = 3$ are given by

$$D_0 = 1, \tag{5}$$

$$D_1 = \frac{1}{(2\pi)^d} \int d\vec{k}_1 (\vec{k} \cdot \vec{k}_1) \tilde{D}(\vec{k} - \vec{k}_1), \tag{6}$$

$$D_2 = \frac{1}{(2\pi)^{2d}} \int d\vec{k}_1 d\vec{k}_2 (\vec{k} \cdot \vec{k}_1)(\vec{k}_1 \cdot \vec{k}_2) \tilde{D}(\vec{k} - \vec{k}_1) \tilde{D}(\vec{k}_1 - \vec{k}_2) \tag{7}$$

$$\begin{aligned} D_3 = {} & \frac{1}{(2\pi)^{3d}} \int d\vec{k}_1 d\vec{k}_2 d\vec{k}_3 (\vec{k} \cdot \vec{k}_1)(\vec{k}_1 \cdot \vec{k}_2)(\vec{k}_2 \cdot \vec{k}_3) \tilde{D}(\vec{k} - \vec{k}_1) \\ & \tilde{D}(\vec{k}_1 - \vec{k}_2) \tilde{D}(\vec{k}_2 - \vec{k}_3), \end{aligned} \tag{8}$$

and the general expression for D_n is given by

$$\begin{aligned} D_n = {} & \frac{1}{(2\pi)^{nd}} \int \prod_{i=1}^{n} d\vec{k}_i (\vec{k} \cdot \vec{k}_1)(\vec{k}_1 \cdot \vec{k}_2) \ldots (\vec{k}_{n-1} \cdot \vec{k}_n) \tilde{D}(\vec{k} - \vec{k}_1) \\ & \tilde{D}(\vec{k}_1 - \vec{k}_2) \ldots \tilde{D}(\vec{k}_{n-1} - \vec{k}_n). \end{aligned} \tag{9}$$

Thus, the nth term D_n contains n factors of $\tilde{D}$ and n integrals over the Fourier variables $\vec{k}_i$.

This result is valid for any spatially varying diffusivity $D(\vec{r})$. We now specialize our discussion to a model for heterogeneity where the diffusivity $D(\vec{r})$ has a homogeneous component with M localized pockets of larger diffusivity. We focus our analysis on the diffusivity

$$D(\vec{r}) = 1 + \sum_{i=1}^{M} \delta \exp\left(-\frac{1}{2\sigma^2} |\vec{r} - \vec{c}_i|^2 \right), \tag{10}$$

where the ith pocket is centered at $\vec{c}_i$. Each pocket contributes magnitude δ to the diffusivity, and the spread σ defines the radial size of the pocket. In this model, we assume each pocket has the same contribution δ and spread σ. However, variability in these parameters are easily inserted into the model. The Fourier-transformed diffusivity $\tilde{D}(\vec{k})$ is given by

$$\tilde{D}(\vec{k}) = (2\pi)^d \delta(\vec{k}) + (2\pi)^{d/2} \delta \sigma^d \sum_{i=1}^{M} \exp\left(-\frac{1}{2}\sigma^2 k^2 + i\vec{k}\cdot\vec{c}_i\right), \tag{11}$$

and we define the rescaled magnitude $\delta_\sigma = (2\pi)^{d/2}\delta\sigma^d$ to simplify our notation, and we define $k = \left|\vec{k}\right|$. We note that our definition of diffusivity is dimensionless, which implies that time t and position $\vec{r}$ are also dimensionless.

This framework provides a basis for determining the Green's function for a fixed system configuration, defined by $\vec{c}_i$. We now consider the case where we average the Green's function over an ensemble of system realizations, i.e., average over diffusivity configurations $\vec{c}_i$. In this work, we assume the configuration is randomly distributed with no spatial correlations between pockets. We define a diffusivity average of the quantity A to be

$$\langle A \rangle_D = \frac{1}{V^M} \int \prod_{i=1}^{M} d\vec{c}_i A(D), \tag{12}$$

where V is the system volume, which is assumed to be very large relative to the displacements that are considered. This average is akin to determining the step distributions from individual realizations of the heterogeneity and then averaging these together. In this regard, the diffusivity average still captures heterogeneity as experienced by individual trajectories. Thus, the treatment does not assume the step distribution captures a homogenized environment at all time scales.

The ensemble average Green's function is written as

$$\langle \hat{\tilde{G}}(\vec{k};s) \rangle_D = \sum_{n=0}^{\infty} \frac{(-1)^n}{s^{n+1}} \langle D_n(\vec{k}) \rangle_D, \tag{13}$$

where we set the initial position $\vec{r}_0$ to the origin without loss of generality (since the ensemble average exhibits translational invariance). Within the nth term $\langle D_n(\vec{k})\rangle_D$, we shift the $\vec{k}$ integrals by defining $\vec{k}_i'$ through the expression $\vec{k}_i = \vec{k} + \sum_{j=1}^{i} \vec{k}_j'$, which gives $\vec{k}_i - \vec{k}_{i-1} = \vec{k}_i'$. Thus, we now reset the arguments of the spatially varying diffusivity $\tilde{D}(\vec{k}_{i-1} - \vec{k}_i)$ to $\tilde{D}(\vec{k}_i')$.

The ensemble average of the nth term now requires us to evaluate $\langle \tilde{D}(\vec{k}_1')\tilde{D}(\vec{k}_2')\ldots\tilde{D}(\vec{k}_n')\rangle_D$. This average involves integrals over $\vec{c}_i$, leading to delta functions in the $\vec{k}_i'$. Each factor of $\tilde{D}$ contains a summation over the M pockets. For example, the $n = 2$ term contains the factor

$$\begin{aligned}
\langle \tilde{D}(\vec{k}_1')\tilde{D}(\vec{k}_2')\rangle_D = {} & \frac{1}{V^M}\int \prod_{i=1}^{M} dc_i \Big[(2\pi)^d \delta(\vec{k}_1') \\
& + \delta_\sigma \sum_{j=1}^{M} \exp\left(-\frac{1}{2}\sigma^2 k_1'^2 + i\vec{k}_1'\cdot\vec{c}_j\right)\Big] \\
& \times \Big[(2\pi)^d \delta(\vec{k}_2') + \delta_\sigma \sum_{k=1}^{M} \exp \\
& \left(-\frac{1}{2}\sigma^2 k_2'^2 + i\vec{k}_2'\cdot\vec{c}_k\right)\Big] \\
= {} & (1+\rho\delta_\sigma)^2 (2\pi)^{2d} \delta(\vec{k}_1')\delta(\vec{k}_2') \\
& + \rho\delta_\sigma^2 (2\pi)^d \delta(\vec{k}_1' + \vec{k}_2') \exp\left(-\sigma^2 k_1'^2\right),
\end{aligned} \tag{14}$$

where $k = \left|\vec{k}\right|$. In Equation (14), we define the pocket density $\rho = M/V$ as the number of pockets per unit volume. Details of this derivation are found in the **Appendix**. This leads to selection rules for the k-vectors in the integrals that simplify the evaluation of $\langle D_n \rangle_D$.

We visualize the selection rules by adopting a diagrammatic representation. For $\langle D_n\rangle_D$, the $\vec{k}_i'$ are sequentially listed as dots on a line, and an arc is drawn between each $\vec{k}_i'$ that appear together in a delta function. **Figure 1A** shows a selection diagram of the two $\vec{k}_i'$ that appear within $\langle D_2\rangle_D$, explicitly derived in Equation (14). The first diagram shows two self loops that each contribute a factor $(1+\rho\delta_\sigma)(2\pi)^d\delta(\vec{k}_i')$. The second diagram shows a single arc between $\vec{k}_1'$ and $\vec{k}_2'$ that contributes a factor of $\rho\delta_\sigma^2(2\pi)^d\delta(\vec{k}_1' + \vec{k}_2')\exp\left(-\sigma^2 k_1'^2\right)$.

Our diagrammatic representation provides a visual framework for identifying all contributions that have common factors. **Figure 1B** shows all of the selection diagrams that appear in $\langle D_3\rangle_D$. These diagrams can be sorted according to powers of $(1+\rho\delta_\sigma)$, ρ, and δ_σ. The first diagram is order $(1+\rho\delta_\sigma)^3$, since there are three self loops and no arcs. The second, third, and fourth diagrams scale as $(1+\rho\delta_\sigma)\rho\delta_\sigma^2$, and the fifth diagram scales as $\rho\delta_\sigma^3$.

We identify the irreducible diagrams as those that cannot be decomposed into a subset of other diagrams. Within **Figure 1B**, the diagrams of order $(1+\rho\delta_\sigma)\rho\delta_\sigma^2$ can be categorized into whether the diagram can be split into two distinct contributions. The second and third diagrams are both composed of a separate arc and self loop. When represented mathematically, both of these diagrams result in a product of terms that are separate from each other, i.e., they are reducible. However, the fourth diagram results in a single term that cannot be reduced into a product.

We determine the sum of all of the irreducible diagrams that up to order $\rho\delta_\sigma^2$, which is the lowest order contribution beyond order $(1+\rho\delta_\sigma)$. First, we identify the sum of all self loops g_0 to be given by

$$g_0 = \sum_{n=0}^{\infty} \frac{(-1)^n}{s^{n+1}} (1+\rho\delta_\sigma)^n k^{2n} = \frac{1}{s + (1+\rho\delta_\sigma)k^2} = \frac{1}{s + D_0 k^2}, \tag{15}$$

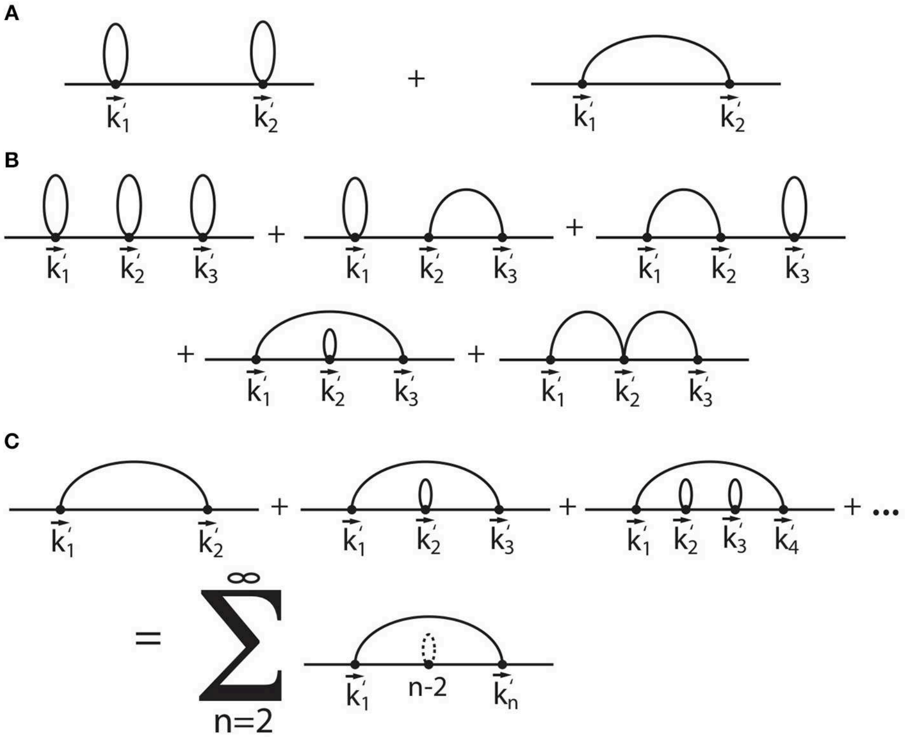

FIGURE 1 | Diagrammatic representation of the expansion terms $\langle D_n(\vec{k})\rangle_D$ within the Fourier-Laplace transformed Green's function $\langle \hat{\hat{G}}(\vec{k};s)\rangle_D$ (Equation 13). The diagrams in **(A)** represent the selection rules for $\langle D_2\rangle_D$, and the diagrams in **(B)** identify the selection rules for $\langle D_3\rangle_D$. The infinite sum of diagrams found in **(C)** represent the set of irreducible diagrams Δg_1 (Equation 16) that form the basis for the lowest-order correction due to heterogeneity.

where we have identified $D_0 = 1+\rho\delta_\sigma$ as the zero-time diffusivity (explained further below), and $k = \left|\vec{k}\right|$. **Figure 1C** shows the sum of all diagrams at the order $\rho\delta_\sigma^2$ that are irreducible. The summation of these diagrams results in the mathematical expression for the correction term

$$\begin{aligned}\Delta g_1 &= \sum_{n=2}^{\infty} \frac{(-1)^n}{s^{n+1}} D_0^{n-2} \rho\delta_\sigma^2 \frac{1}{(2\pi)^d} \\ &\quad \int d\vec{k}_1' [\vec{k}\cdot(\vec{k}+\vec{k}_1')]^2 \left|\vec{k}+\vec{k}_1'\right|^{2(n-2)} \exp\left(-\sigma^2 k_1'^2\right) \\ &= \frac{\rho\delta_\sigma^2}{s^2}\frac{1}{(2\pi)^d}\int d\vec{k}_1' \frac{[\vec{k}\cdot(\vec{k}+\vec{k}_1')]^2}{s+D_0\left|\vec{k}+\vec{k}_1'\right|^2}\exp\left(-\sigma^2 k_1'^2\right). \quad (16)\end{aligned}$$

The two irreducible sets of diagrams g_0 and Δg_1 form the basis for the lowest-order correction to the Green's function due to heterogeneity. The combination of all possible diagrams that include both self loops and single arcs results in the approximate expression for the Green's function

$$\begin{aligned}\langle\hat{\hat{G}}\rangle_D &\approx \sum_{n=0}^{\infty} g_0\left(s^2 g_0 \Delta g_1\right)^n = \frac{1}{s+D_0k^2-s^2\Delta g_1} \\ &= \frac{1}{s+D_0k^2-\frac{\rho\delta_\sigma^2}{(2\pi)^d}\int d\vec{k}_1'\frac{[\vec{k}\cdot(\vec{k}+\vec{k}_1')]^2}{s+D_0(\vec{k}+\vec{k}_1')^2}\exp\left(-\sigma^2k_1'^2\right)}. \quad (17)\end{aligned}$$

This result forms the basis for our subsequent analyses. For this discussion, we focus our attention on 3-dimensional diffusion. Though, our results are amenable to analysis in arbitrary dimensions.

The Green's function $\langle\hat{\hat{G}}\rangle_D$ adopts a form that reflects a mathematical structure that is notably non-Gaussian. The expansion of the Green's function in Equation (13) is reminiscent of a straight-forward moment-based expansion, particularly if the expansion terms scale as $\langle D_n\rangle_D \sim k^{2n}$. This is precisely the outcome if only the self-loop diagrams are included (i.e., $\Delta g_1 = 0$). The resulting expression for $\langle\hat{\hat{G}}\rangle_D$ is the Fourier-Laplace transform of the Gaussian distribution. Inclusion of the correction Δg_1 results in non-Gaussian contributions to the Green's function that reveal the underlying role of heterogeneity in the diffusive transport.

The Green's function $\langle\hat{\hat{G}}\rangle_D$ can be used to determine various statistical averages of the diffusivity-averaged motion of the particles. In other words, the statistical behavior of the particle motion after averaging over an ensemble of heterogeneous diffusivities. Here, we consider the $2n$-th moment of the distribution projected onto the z-axis in our 3-dimensional space, given by

$$\langle\langle z^{2n}\rangle\rangle_D = (-1)^n \mathcal{L}^{-1}_{s\to t}\left[\lim_{k\to 0}\frac{\partial^{2n}\langle\hat{\hat{G}}\rangle_D}{\partial k^{2n}}\right], \quad (18)$$

where the two sets of angle brackets ($\langle\langle z^{2n}\rangle\rangle_D$) indicates a statistical average over both an ensemble of trajectories and an ensemble of diffusivities D. In Equation (18), the operator $\mathcal{L}^{-1}_{s\to t}$ indicates a Laplace inversion from the Laplace variable s to time t. From our results in Equation (17), we find the expressions for the second and fourth moments to be

$$\langle\langle z^2\rangle\rangle_D = 2D_0 t - \frac{1}{6\pi^{3/2}}\frac{\rho\delta_\sigma^2}{\sigma D_0^2}\left(\tau - 1 + \frac{1}{\sqrt{2\tau+1}}\right), \tag{19}$$

$$\begin{aligned}\langle\langle z^4\rangle\rangle_D = {} & 12D_0^2t^2 - \frac{4}{\pi^{3/2}}\frac{\sigma\rho\delta_\sigma^2}{D_0^2}\left[\tau^2 - \frac{12}{5}\tau - \frac{11}{5} + 2\sqrt{2\tau+1}\right. \\ & \left. + \frac{1}{2}\frac{1}{\sqrt{2\tau+1}} - \frac{3}{10}\frac{1}{(2\tau+1)^{3/2}}\right] \\ & + \frac{1}{12\pi^3}\left(\frac{\rho\delta_\sigma^2}{\sigma D_0^2}\right)^2\left[\tau^2 - 4\tau - 2 + 2\sqrt{2\tau+1}\right. \\ & - \frac{2}{\sqrt{2\tau+1}} \\ & \left. + \frac{2}{(2\tau+1)^{3/2}} + \frac{2\tau(4\tau^2+6\tau+3)}{(\tau+1)(2\tau+1)^{3/2}}\right].\end{aligned} \tag{20}$$

We define the diffusive time $\tau = t/t_\sigma$, where $t_\sigma = 2\sigma^2/D_0$ gives the time scale for diffusion to a distance of order σ (i.e., the scale of heterogeneity). Notably, corrections to normal diffusion due to heterogeneity naturally depend on the time scale for diffusion to a distance comparable to the length scale of the heterogeneity. These results form the basis of our subsequent analyses of diffusive transport in a heterogeneous environment.

RESULTS AND DISCUSSION

In this work, we explore the statistical behavior of particle motion in a heterogeneous environment, as defined by our random diffusivity model (Equation 10). We first consider the mean-square displacement (MSD) of particle diffusion $\langle\langle r^2\rangle\rangle_D = 3\langle\langle z^2\rangle\rangle_D$. **Figure 2** shows the mean-square displacement for diffusion in a heterogeneous environment with $\delta = 5$, $D_0 = 2$ (i.e., $\rho = 1/\delta_\sigma$), and $\sigma = 1/2$. For this set of parameters, the heterogeneity time scale $t_\sigma = 2\sigma^2/D_0 = 1/4$ results in the relationship $\tau = 4t$.

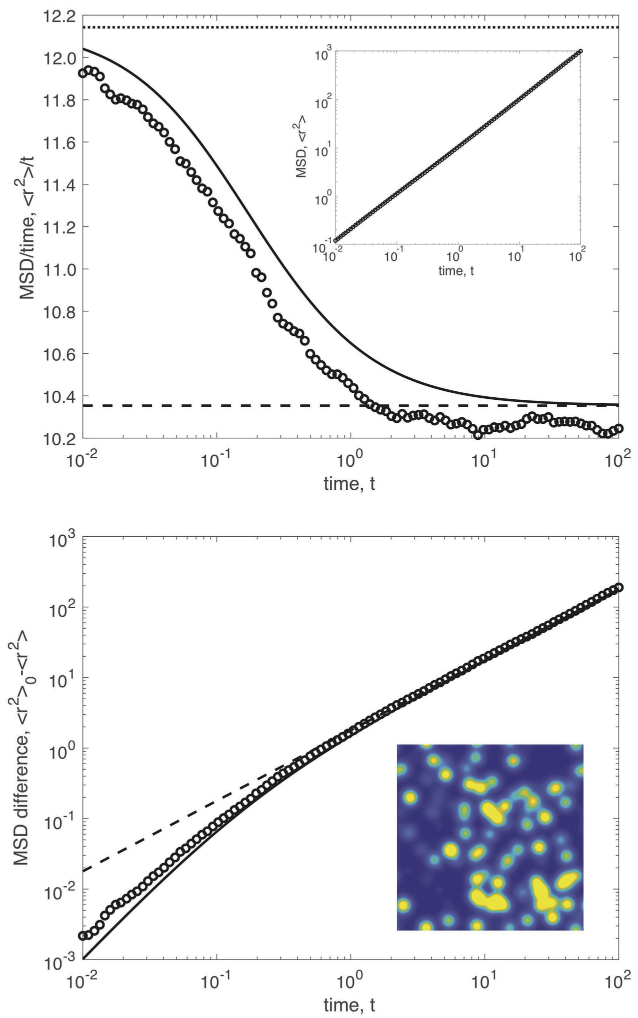

FIGURE 2 | The mean-square displacement (MSD) for particle diffusion in a heterogeneous environment. The top plot shows the ratio MSD/t $\langle\langle r^2\rangle\rangle_D$ (solid curve) vs. time for heterogeneous diffusivity with $\delta = 5$, $D_0 = 2$ (i.e., $\rho = 1/\delta_\sigma$), and $\sigma = 1/2$. The dotted curved indicates the short-time MSD $\langle\langle r^2\rangle\rangle_D^{(0)}$, and the dashed curve shows the long-time MSD $\langle\langle r^2\rangle\rangle_D^{(\infty)}$. Results from numerical simulations are shown as dots. The inset plot shows the MSD before dividing by time. The bottom plot shows the MSD difference $\langle\langle r^2\rangle\rangle_D^{(0)} - \langle\langle r^2\rangle\rangle_D$. The inset image shows a realization of the diffusivity with color scaling from blue ($D = 1$) to yellow ($D = 5$).

To validate our analytical theory, we perform numerical simulations of particle diffusion in a heterogeneous environment based on our model for microscopic heterogeneity. We define the position-dependent diffusivity $D(\vec{r})$ in a square box of length Δ by randomly selecting the positions $\vec{c}_i$ (for $i = 1, \ldots, M$) for a given pocket density $\rho = M/\Delta^3$, and the position-dependent diffusivity $D(\vec{r})$ is defined by Equation (10). The simulations are performed with periodic boundary conditions to capture an effectively infinite medium, and we set $\Delta = 10$ for our simulations, which is determined to be adequate to capture the long-time dynamics (i.e., all results shown are insensitive to this choice of Δ). We perform Brownian dynamics simulations using the discrete-time algorithm for particle displacement with time-step Δt, given by

$$\vec{r}(t+\Delta t) = \vec{r}(t) + \left[\sqrt{2D(\vec{r}(t))\Delta t}\right]\vec{u} + \left[\frac{1}{2}\vec{u}\cdot\vec{\nabla}D(\vec{r}(t))\Delta t\right]\vec{u}, \tag{21}$$

where $\vec{u}$ is a 3-dimensional vector with components selected from a Gaussian distribution with unit variance.

The top plot of **Figure 2** shows $\langle\langle r^2\rangle\rangle_D$ with an inset that shows a realization of the heterogeneous diffusivity (blue indicating $D = 1$ to yellow indicating $D = 5$). The solid curve shows our analytical result, given by Equation (19). **Figure 2** also contains results from numerical simulations (dots). The short-time MSD $\langle\langle r^2\rangle\rangle_D^{(0)} = 6D_0t$ is indicated by the dotted line, where $D_0 = 1 + \rho\delta_\sigma$. The long-time MSD $\langle\langle r^2\rangle\rangle_D^{(\infty)} = 6D_\infty t$ is

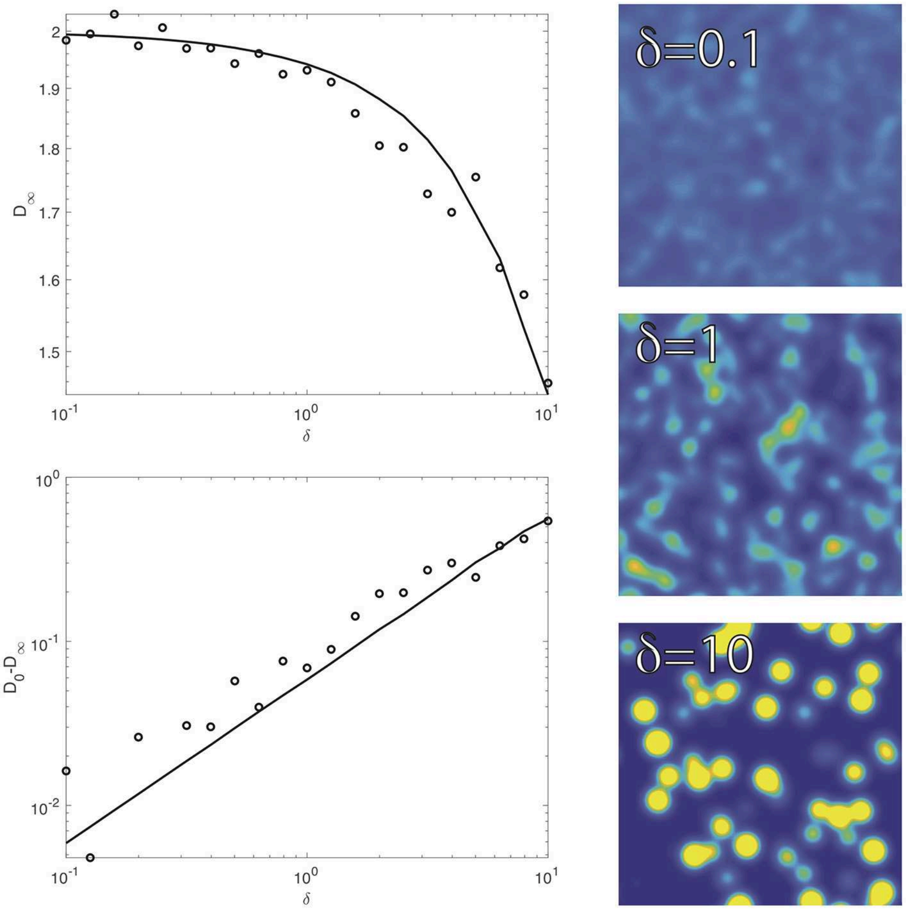

FIGURE 3 | The long-time diffusivity D_∞ and the diffusivity difference $D_0 - D_\infty$ over a range of the strength of heterogeneity δ (with fixed $D_0 = 2$ and $\sigma = 1/2$). The solid curves show our analytical theory, and the dots give results from numerical simulations. The right images show realizations of the heterogeneous diffusivity over the range of δ in the plots (same color scaling as **Figure 2**).

shown as a dashed line, where $D_\infty = D_0 - \rho\delta_\sigma^2/(24\pi^{3/2}\sigma^3 D_0)$. The influence of heterogeneity on the mean-square displacement is relatively modest over the broad range of timescales in **Figure 2**. The bottom plot shows the MSD difference $\langle\langle r^2\rangle\rangle_D^{(0)} - \langle\langle r^2\rangle\rangle_D$ to clearly show the comparison between our analytical theory and the numerical simulations over the entire range of times.

The short-time diffusivity D_0 is governed by the motion of the particle within a local environment. Thus, the particle is not yet able to sample the surrounding heterogeneity. In this regard, the diffusivity difference $D_0 - D_\infty$ is a measure of the impact of heterogeneity on the particle motion. **Figure 3** shows a plot of the long-time diffusivity D_∞ (top plot) and the diffusivity difference $D_0 - D_\infty$ (bottom plot) over of range of the strength of heterogeneity δ. The right images in **Figure 3** show realizations of the diffusivity over the range of values of δ within the plots. The results in **Figure 3** have a fixed short-time diffusivity $D_0 = 1 + \rho\delta_\sigma = 2$. Thus, the density ρ decreases with increasing δ to maintain an equivalent D_0. In **Figure 3**, the length scale of heterogeneity is $\sigma = 1/2$, and the dots indicate results from our numerical simulations as a check of our analytical theory.

Our results thus far suggest that our analytical results are valid within the range of the heterogeneity parameters explored in **Figures 2**, **3**. However, the impact of heterogeneity on the mean-square displacement is somewhat modest (see **Figure 2**). Experimental measurements of MSD may exhibit considerable noise due to measurement precision and insufficient sampling over both an ensemble of trajectories and an ensemble of diffusivity samples. In this regard, MSD may be insufficient to characterize the heterogeneity. Furthermore, many physical or biological processes are dependent on statistical metrics that are not weighted heavily in the MSD. In this regard, a statistical quantity that represents higher moments of the distribution would better represent the impact of heterogeneity.

We turn to the kurtosis as a metric that reveals the impact of heterogeneity on diffusive transport. The kurtosis represents the lowest-order metric that determines to what extent the step distribution deviates from a Gaussian distribution, which is the expectation for diffusion in a homogeneous environment. We define the excess kurtosis κ as

$$\kappa = \frac{\langle\langle z^4\rangle\rangle_D}{\langle\langle z^2\rangle\rangle_D^2} - 3, \tag{22}$$

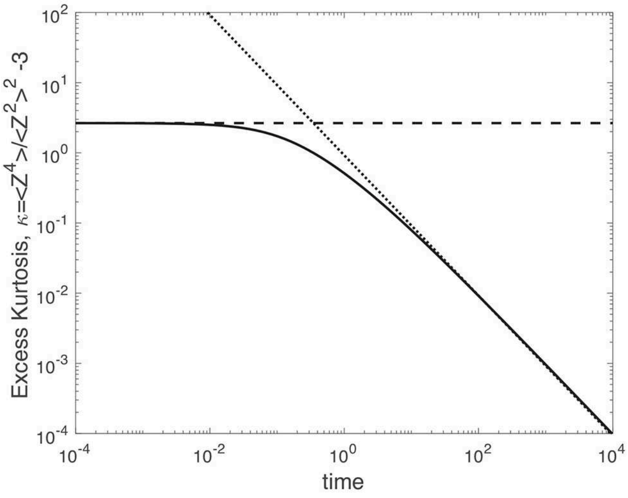

FIGURE 4 | The excess kurtosis κ vs. time for $\delta = 10$, $D_0 = 2$, and $\sigma = 2$. The dashed curve indicates the short-time behavior of the excess kurtosis based on our model for heterogeneity. The dotted curve gives the long-time relaxation of the excess kurtosis to zero.

where $\langle\langle z^2\rangle\rangle_D$ and $\langle\langle z^4\rangle\rangle_D$ are given by Equations (19) and (20), respectively. The excess kurtosis is zero for a Gaussian distribution. Positive values of κ indicate a heavy-tailed distribution that implies trajectories that are significantly more mobile than a random walk with an averaged diffusivity.

Figure 4 shows the excess kurtosis vs. time for $\delta = 10, D_0 = 2$, and $\sigma = 2$ (note, $t_\sigma = 1/4$). Our results demonstrate two regimes. At short time, the excess kurtosis κ exhibits a short-time plateau that represents the excess kurtosis that arises from averaging over an ensemble of quenched diffusivities that are selected from the statistical distribution of our model (discussed further below). At long times, the excess kurtosis κ relaxes to zero as $\kappa \sim \tau^{-1}$. This asymptotic behavior suggests that individual trajectories within a fixed diffusivity realization have sufficiently sampled their surrounding microenvironments and now experience an effective diffusivity D_∞. As a result, the individual trajectories are random walk at long time scales, and the D-averaged step distribution tends to a Gaussian.

At short times, the particles are unable to sufficiently explore their surrounding environment. Thus, the diffusivity of each particle is dictated by the random-selected diffusivity of its initial position. The statistical distribution for the diffusivity at a fixed point (here given by the origin) is given by

$$P_D(D) = \frac{1}{V^M}\int \prod_{i=1}^{M} d\vec{c}_i\,\delta\left[D - 1 - \delta\sum_{k=1}^{M}\exp\left(-\frac{1}{2\sigma^2}c_k^2\right)\right], \tag{23}$$

which captures the contributions of the pockets as a superposition of Dirac delta distributions. We perform a Laplace transform from D to u, and upon taking the limit $M, V \to \infty$ such that $M/V = \rho$, we arrive at the Laplace-transformed D-distribution

$$\hat{P}_D = \exp\left[-u + (2\pi)^{3/2}\rho\sigma^3\sum_{n=1}^{\infty}\frac{(-1)^n}{n!\,n^{3/2}}\delta^n u^n\right]. \tag{24}$$

From this distribution, we determine the first two moments of the local diffusivity, given by

$$\langle D\rangle_D = -\lim_{u\to 0}\left(\frac{d\hat{P}_D}{du}\right) = 1 + \rho\delta_\sigma = D_0, \tag{25}$$

$$\begin{aligned}\langle D^2\rangle_D &= \lim_{u\to 0}\left(\frac{d^2\hat{P}_D}{du^2}\right) = (1+\rho\delta_\sigma)^2 + \pi^{3/2}\rho\delta^2\sigma^3 \\ &= D_0^2 + \frac{\rho\delta_\sigma^2}{2\pi^{3/2}\sigma^3}.\end{aligned} \tag{26}$$

These statistical quantities capture the instantaneous environment that a particle experiences prior to diffusion into a surrounding microenvironment.

The short-time behavior of the excess kurtosis is given by

$$\kappa^{(0)} = \frac{12\langle D^2\rangle_D t^2}{(2\langle D\rangle_D t)^2} - 3 = 3\left(\frac{\langle D^2\rangle_D}{\langle D\rangle_D^2} - 1\right) = \frac{3\rho\delta_\sigma^2}{2\pi^{3/2}\sigma^3 D_0^2}. \tag{27}$$

This short-time behavior coincides with the dashed curve in **Figure 4**. For the parameters in **Figure 4**, the short-time excess kurtosis is given by $\kappa^{(0)} = 2.652$. For reference, the value of the excess kurtosis for a Laplace distribution [52, 53] is $\kappa = 9$. The Laplace distribution is of particular interest for cellular transport [26, 31, 32, 54], since the step distribution in both yeast cells and bacterial cells trends from a Laplace distribution to a Gaussian distribution with increasing time [26].

CONCLUSIONS

Our solutions for the Green's function provide insight into the impact of microscopic heterogeneity of diffusive transport across a broad range of time scales. At short time scales, the particles explore the local environment around their initial position. The local diffusivity is randomly determined from the distribution of diffusivities from the specific model of heterogeneity. With increasing time, the stochastic trajectories of the particles lead to a transition to the exploration of a spatially averaged environment. The time scale of this transition is naturally linked to the time scale of diffusion to a distance defined by the correlation length of the heterogeneity. The excess kurtosis exhibits a short-time, non-zero value that implies a heavy-tailed step distribution associated with the distribution of initial diffusivities, and the excess kurtosis decays to zero as the diffusive transport leads to exploration of the surrounding effective medium, implying a Gaussian step distribution at long times.

Further refinement of the model can be developed by including higher order loop diagrams in the expansion. The structure of our diagrammatic representation is akin to Feynman diagrams commonly employed in quantum field theory and condensed matter physics [55, 56]. Notably, one can extend our approach to include higher-order diagrams, or alternatively, one can employ renormalization group methods to determine a renormalized one-loop contribution [55] based on the structure of the solutions presented in this manuscript. These developments would improve the level of accuracy of our solutions, particular in the limit of large heterogeneity ($\delta \gg 1$). However, the agreement between numerical simulations and our results presented in this manuscript suggest the solutions are not limited to conditions where $\delta \ll 1$, and the results presented here are not strictly limited to conditions of weak heterogeneity.

Heterogeneity is prevalent in a range of soft materials, particularly in living cells. We specifically note the observed heterogeneity of the organization of chromosomal DNA within eukaryotic nuclei [57–61]. Underlying the observed heterogeneity is the physical segregation of chromosomes into compartments due to epigenetic modifications to the proteins that packaged the DNA, which is captured by models that incorporate incompatibility between segments in a chromosome polymer [62–68]. The connection between spatial segregation of chromosomes and the dynamics and accessibility of regulatory proteins [69–71] remains a challenging problem that would shed light on the structure-function relationships in chromosome biology. This work provides a valuable analytical approach to analyzing heterogeneous transport in the complex environment of the nucleus that may be valuable in establishing these connections.

DATA AVAILABILITY

The datasets generated for this study are available on request to the corresponding author.

AUTHOR CONTRIBUTIONS

AS performed the research and wrote the manuscript.

FUNDING

Financial support for this work was provided by the National Science Foundation, Physics of Living Systems Program (PHY-1707751).

SUPPLEMENTARY MATERIAL

The Supplementary Material for this article can be found online at: https://www.frontiersin.org/articles/10.3389/fphy.2019.00119/full#supplementary-material

REFERENCES

1. Von Smoluchowski M. Drei vortrage uber diffusion. Brownsche bewegung und koagulation von kolloidteilchen. *Z Phys.* (1916) **17**:557–585.
2. Fick A. Eber diffusion. *Ann Phys.* (1855) **170**:59–86.
3. Einstein A. Investigations on the theory of the Brownian movement.*Ann. D. Phys.* (1905) **17**:549.
4. Perrin J. Mouvement brownien et realite moleculaire. *Ann. de Chim. Phys.* (1909) **18**:5–114.
5. Munder MC, Midtvedt D, Franzmann T, Nulske E, Otto O, Herbig M, et al. A pH-driven transition of the cytoplasm from a fluid-to a solid-like state promotes entry into dormancy. *eLife.* (2016) **5**:e09347. doi: 10.7554/eLife.09347
6. Valentine MT, Kaplan PD, Thota D, Crocker JC, Gisler T, Prudâhomme RK, et al. Investigating the microenvironments of inhomogeneous soft materials with multiple particle tracking. *Phys Rev E.* (2001) **64**:061506. doi: 10.1103/PhysRevE.64.061506
7. Kegel WK, van Blaaderen A. Direct observation of dynamical heterogeneities in colloidal hard-sphere suspensions. *Science.* (2000) **287**:290–3. doi: 10.1126/science.287.5451.290
8. Burov S, Jeon J-H, Metzler R, Barkai E. Single particle tracking in systems showing anomalous diffusion: the role of weak ergodicity breaking. *Phys Chem Chem Phys.* (2011) **13**:1800–12. doi: 10.1039/c0cp01879a
9. Toyota T, Head DA, Schmidt CF, Mizuno D. Non-Gaussian athermal fluctuations in active gels. *Soft Matter.* (2011) **7**:3234–9. doi: 10.1039/C0SM00925C
10. Cao J. Single molecule tracking of heterogeneous diffusion. *Phys Rev E.* (2001) **63**:041101. doi: 10.1103/PhysRevE.63.041101
11. Weeks ER, Crocker JC, Levitt AC, Schofield A, Weitz DA. Three-dimensional direct imaging of structural relaxation near the colloidal glass transition. *Science.* (2000) **287**:627–31. doi: 10.1126/science.287.5453.627
12. Joyner RP, Tang JH, Helenius J, Dultz E, Brune C, Holt LJ, et al. A glucose-starvation response regulates the diffusion of macromolecules. *eLife.* (2016) **5**:e09376. doi: 10.7554/eLife.09376
13. Duits MH, Li Y, Vanapalli SA, Mugele F. Mapping of spatiotemporal heterogeneous particle dynamics in living cells. *Phys Rev E.* (2009) **79**:051910. doi: 10.1103/PhysRevE.79.051910
14. Guo M, Ehrlicher AJ, Jensen MH, Renz M, Moore JR, Goldman RD, et al. Probing the stochastic, motor-driven properties of the cytoplasm using force spectrum microscopy. *Cell.* (2014) **158**:822–32. doi: 10.1016/j.cell.2014.06.051
15. Fodor É, Guo M, Gov N, Visco P, Weitz D, van Wijland F. Activity driven fluctuations in living cells. *arXiv preprint* (2015) arXiv:1505.06489. doi: 10.1209/0295-5075/110/48005
16. Knight SC, Xie L, Deng W, Guglielmi B, Witkowsky LB, Bosanac L, et al. Dynamics of CRISPR-Cas9 genome interrogation in living cells. *Science.* (2015) **350**:823–6. doi: 10.1126/science.aac6572
17. Bursac P, Fabry B, Trepat X, Lenormand G, Butler JP, Wang N, et al. Cytoskeleton dynamics: fluctuations within the network. *Biochem Biophys Res Commun.* (2007) **355**:324–30. doi: 10.1016/j.bbrc.2007.01.191
18. Wirtz D. Particle-tracking microrheology of living cells: principles and applications. *Ann Rev Biophys.* (2009) **38**:301–26. doi: 10.1146/annurev.biophys.050708.133724
19. Parry BR, Surovtsev IV, Cabeen MT, O'Hern CS, Dufresne ER, Jacobs-Wagner C. The bacterial cytoplasm has glass-like properties and is fluidized by metabolic activity. *Cell.* (2014) **156**:183–94. doi: 10.1016/j.cell.2013.11.028
20. Stylianidou S, Kuwada NJ, Wiggins PA. Cytoplasmic dynamics reveals two modes of nucleoid-dependent mobility. *Biophys J.* (2014) **107**:2684–92. doi: 10.1016/j.bpj.2014.10.030
21. Hajjoul H, Mathon J, Ranchon H, Goiffon I, Mozziconacci J, Albert B, et al. High-throughput chromatin motion tracking in living yeast reveals the flexibility of the fiber throughout the genome. *Genome Res.* (2013) **23**:1829–38. doi: 10.1101/gr.157008.113
22. Backlund MP, Joyner R, Weis K, Moerner W. Correlations of three-dimensional motion of chromosomal loci in yeast revealed by the double-helix point spread function microscope. *Mol Biol Cell.* (2014) **25**:3619–29. doi: 10.1091/mbc.E14-06-1127
23. Backlund MP, Joyner R, Moerner W. Chromosomal locus tracking with proper accounting of static and dynamic errors. *Phys Rev E.* (2015) **91**:062716. doi: 10.1103/PhysRevE.91.062716
24. Golding I, Cox EC. RNA dynamics in live *Escherichia coli* cells. *Proc Natl Acad Sci USA.* (2004) **101**:11310–5. doi: 10.1073/pnas.0404443101
25. Silva MS, Stuhrmann B, Betz T, Koenderink GH. Time-resolved microrheology of actively remodeling actomyosin networks. *New J Phys.* (2014) **16**:075010. doi: 10.1088/1367-2630/16/7/075010
26. Lampo TJ, Stylianidou S, Backlund MP, Wiggins PA, Spakowitz AJ. Cytoplasmic RNA-protein particles exhibit non-Gaussian subdiffusive behavior. *Biophys J.* (2017) **112**:532–42. doi: 10.1016/j.bpj.2016.11.3208
27. Weber S, Theriot J, Spakowitz A. Subdiffusive motion of a polymer composed of subdiffusive monomers. *Phys Rev E.* (2010) **82**:011913. doi: 10.1103/PhysRevE.82.011913
28. Weber S, Spakowitz A, Theriot J. Bacterial chromosomal loci move subdiffusively through a viscoelastic cytoplasm. *Phys Rev Lett.* (2010) **104**:238102. doi: 10.1103/PhysRevLett.104.238102
29. Weber SC, Thompson MA, Moerner WE, Spakowitz AJ, Theriot JA. Analytical tools to distinguish the effects of localization error, confinement, and medium

elasticity on the velocity autocorrelation function. *Biophys J.* (2012) **102**:2443–50. doi: 10.1016/j.bpj.2012.03.062

30. Weber SC, Spakowitz AJ, Theriot JA. Nonthermal ATP-dependent fluctuations contribute to the *in vivo* motion of chromosomal loci. *Proc Natl Acad Sci USA.* (2012) **109**:7338–43. doi: 10.1073/pnas.1119505109
31. Wang B, Anthony SM, Bae SC, Granick S. Anomalous yet Brownian. *Proc Natl Acad Sci USA.* (2009) **106**:15160–4. doi: 10.1073/pnas.0903554106
32. Wang B, Kuo J, Bae SC, Granick S. When Brownian diffusion is not Gaussian. *Nat Mater.* (2012) **11**:481–5. doi: 10.1038/nmat3308
33. Ghosh SK, Cherstvy AG, Grebenkov DS, Metzler R. Anomalous, non-Gaussian tracer diffusion in crowded two-dimensional environments. *New J Phys.* (2016) **18**:013027. doi: 10.1088/1367-2630/18/1/013027
34. Papanicolaou GC. *Surveys in Applied Mathematics*. New York, NY: Springer (1995), 205–53.
35. Stevens A, Papanicolaou G, Heinze S. Variational principles for propagation speeds in inhomogeneous media. *SIAM J Appl Math.* (2001) **62**:129–48. doi: 10.1137/S0036139999361148
36. Lewandowska J, Laurent J-P. Homogenization modeling and parametric study of moisture transfer in an unsaturated heterogeneous porous medium. *Transport Porous Med.* (2001) **45**:319–43. doi: 10.1023/A:1012450327408
37. Auriault J-L, Lewandowska J. Effective diffusion coefficient: from homogenization to experiment. *Transport Porous Med.* (1997) **27**:205–23.
38. Avellaneda M. Homogenization and renormalization: the mathematics of multi-scale random media and turbulent diffusion. *Dyn Syst Probab Methods Partial Differ Equat.* (1996) **31**:251–68.
39. Novikov DS, Kiselev VG. Effective medium theory of a diffusion-weighted signal. *NMR Biomed.* (2010) **23**:682–97. doi: 10.1002/nbm.1584
40. Alonso S, Kapral R, Bär M. Effective medium theory for reaction rates and diffusion coefficients of heterogeneous systems. *Phys Rev Lett.* (2009) **102**:238302. doi: 10.1103/PhysRevLett.102.238302
41. Kröner E. *Micromechanics and Inhomogeneity*. New York, NY: Springer (1990), 197–211.
42. Alonso S, Baer M, Kapral R. Effective medium approach for heterogeneous reaction-diffusion media. *J Chem Phys.* (2009) **131**:214102. doi: 10.1063/1.3265987
43. Duan H, Karihaloo B, Wang J, Yi X. Effective conductivities of heterogeneous media containing multiple inclusions with various spatial distributions. *Phys Rev B.* (2006) **73**:174203. doi: 10.1103/PhysRevB.73.174203
44. Sahimi M, Tsotsis TT. Transient diffusion and conduction in heterogeneous media: beyond the classical effective-medium approximation. *Ind Eng Chem Res.* (1997) **36**:3043–52.
45. Chang H-C. Multi-scale analysis of effective transport in periodic heterogeneous media. *Chem Eng Commun.* (1982) **15**:83–91.
46. Akanni K, Evans J, Abramson I. Effective transport coefficients in heterogeneous media. *Chem Eng Sci.* (1987) **42**:1945–54.
47. Saez AE, Otero CJ, Rusinek I. The effective homogeneous behavior of heterogeneous porous media. *Transport Porous Med.* (1989) **4**:213–38.
48. Chubynsky MV, Slater GW. Diffusing diffusivity: a model for anomalous, yet Brownian, diffusion. *Phys Rev Lett.* (2014) **113**:098302. doi: 10.1103/PhysRevLett.113.098302
49. Metzler R, Jeon J-H, Cherstvy AG, Barkai E. Anomalous diffusion models and their properties: non-stationarity, non-ergodicity, and ageing at the centenary of single particle tracking. *Phys Chem Chem Phys.* (2014) **16**:24128–64. doi: 10.1039/C4CP03465A
50. Cherstvy AG, Metzler R. Anomalous diffusion in time-fluctuating non-stationary diffusivity landscapes. *Phys Chem Chem Phys.* (2016) **18**:23840–52. doi: 10.1039/C6CP03101C
51. Chechkin AV, Seno F, Metzler R, Sokolov IM. Brownian yet non-Gaussian diffusion: from superstatistics to subordination of diffusing diffusivities. *Phys Rev X.* (2017) **7**:021002. doi: 10.1103/PhysRevX.7.021002
52. Kozubowski TJ, Meerschaert MM, Podgorski K. Fractional Laplace motion. *Adv Appl Probab.* (2006) **38**:451–64. doi: 10.1017/S000186780000104X
53. Kotz S, Kozubowski T, Podgorski K. *The Laplace Distribution and Generalizations: A Revisit With Applications to Communications, Exonomics, Engineering, and Finance*. New York, NY: Springer (2001).
54. Phillies GDJ. In complex fluids the Gaussian diffusion approximation is generally invalid. *Soft matter.* (2015) **11**:580–6. doi: 10.1039/C4SM02506G
55. Amit DJ, Martin-Mayor V. *Field Theory, The Renormalization Group, and Critical Phenomena: Graphs to Computers 3rd Edn*. Singapore: World Scientific Publishing Company (2005).
56. Peskin ME. *An Introduction to Quantum Field Theory*. Boca Raton, FL: CRC Press (2018).
57. Grewal SI, Moazed D. Heterochromatin and epigenetic control of gene expression. *Science.* (2003) **301**:798–802. doi: 10.1126/science.1086887
58. Lieberman-Aiden E, Van Berkum NL, Williams L, Imakaev M, Ragoczy T, Telling A, et al. Comprehensive mapping of long-range interactions reveals folding principles of the human genome. *Science.* (2009) **326**:289–93. doi: 10.1126/science.1181369
59. Zidovska A, Weitz DA, Mitchison TJ. Micron-scale coherence in interphase chromatin dynamics. *Proc Natl Acad Sci USA*. (2013) **110**:15555–60. doi: 10.1073/pnas.1220313110
60. Rao SS, Huntley MH, Durand NC, Stamenova EK, Bochkov ID, Robinson JT, et al. A 3D map of the human genome at kilobase resolution reveals principles of chromatin looping. *Cell.* (2014) **159**:1665–80. doi: 10.1016/j.cell.2014.11.021
61. Ou HD, Phan S, Deerinck TJ, Thor A, Ellisman MH, O'shea CC. ChromEMT: visualizing 3D chromatin structure and compaction in interphase and mitotic cells. *Science.* (2017) **357**:eaag0025. doi: 10.1126/science.aag0025
62. Jost D, Carrivain P, Cavalli G, Vaillant C. Modeling epigenome folding: formation and dynamics of topologically associated chromatin domains. *Nucleic Acids Res.* (2014) **42**:9553–61. doi: 10.1093/nar/gku698
63. Chiariello AM, Annunziatella C, Bianco S, Esposito A, Nicodemi M. Polymer physics of chromosome large-scale 3D organisation. *Sci Rep.* (2016) **6**:29775. doi: 10.1038/srep29775
64. Michieletto D, Orlandini E, Marenduzzo D. Polymer model with epigenetic recoloring reveals a pathway for the de novo establishment and 3D organization of chromatin domains. *Phys Rev X.* (2016) **6**:041047. doi: 10.1103/PhysRevX.6.041047
65. Di Pierro M, Zhang B, Aiden EL, Wolynes PG, Onuchic JN. Transferable model for chromosome architecture. *Proc Natl Acad Sci USA*. (2016) **113**:12168–73. doi: 10.1073/pnas.1613607113
66. Di Pierro M, Cheng RR, Aiden EL, Wolynes PG, Onuchic JN. *De novo* prediction of human chromosome structures: Epigenetic marking patterns encode genome architecture. *Proc Natl Acad Sci USA.* (2017) **114**:12126–31. doi: 10.1073/pnas.1714980114
67. MacPherson Q, Beltran B, Spakowitz AJ. Bottom-up modeling of chromatin segregation due to epigenetic modifications. *Proc Natl Acad Sci USA*. (2018) **115**:12739–44. doi: 10.1073/pnas.1812268115
68. Nuebler J, Fudenberg G, Imakaev M, Abdennur N, Mirny LA. Chromatin organization by an interplay of loop extrusion and compartmental segregation. *Proc Natl Acad Sci USA*. (2018) **115**:E6697–706. doi: 10.1073/pnas.1717730115
69. de la Rosa MAD, Koslover EF, Mulligan PJ, Spakowitz AJ. Dynamic strategies for target-site search by DNA-binding proteins. *Biophys J.* (2010) **98**:2943–53. doi: 10.1016/j.bpj.2010.02.055
70. Koslover EF, de la Rosa MAD, Spakowitz AJ. Theoretical and computational modeling of target-site search kinetics *in vitro* and *in vivo*. *Biophys J.* (2011) **101**:856–65. doi: 10.1016/j.bpj.2011.06.066
71. Koslover EF, de la Rosa MD, Spakowitz AJ. Crowding and hopping in a protein's diffusive transport on DNA. *J Phys A Math Theor.* (2017) **50**:074005. doi: 10.1088/1751-8121/aa53ee

Conflict of Interest Statement: The author declares that the research was conducted in the absence of any commercial or financial relationships that could be construed as a potential conflict of interest.

ORIGINAL RESEARCH
published: 04 September 2019
doi: 10.3389/fphy.2019.00122

Drag Force for Asymmetrically Grafted Colloids in Polymer Solutions

Matthias Werner[1,2], **Paolo Margaretti**[1] **and Anna Maciołek**[1,3]*

[1] Department of Inhomogeneous Condensed Matter, Max-Planck-Institut für Intelligente Systeme, Stuttgart, Germany, [2] IV. Institut für Theoretische Physik, Universität Stuttgart, Stuttgart, Germany, [3] Institute of Physical Chemistry, Polish Academy of Sciences, Warsaw, Poland

We consider the situation in which a colloidal particle modifies locally the solvent leading to a spatially dependent viscosity. This situation is typical for colloidal particles in crowded environment, for example DNA-grafted particles in a polymer solution, or a hot particle which implies a temperature gradient to a viscous liquid. By means of suitable approximations we calculate the dependence of the friction force on the profile of the local viscosity. Our results show that in the case of axially symmetric viscosity profile the friction force is sensitive to the anisotropy of the viscous profile whereas it is not sensitive to for-ahead asymmetries. Our results are crucial for active microrheology measurements where tracer particles are pulled through complex fluids.

Keywords: crowded environments, polymer solution, drag force, anisotropic viscosity, transport phenomena and fluid mechanics, functionalized colloids

Edited by:
Ralf Metzler,
University of Potsdam, Germany

Reviewed by:
Rajarshi Chakrabarti,
Indian Institute of Technology Bombay, India
Enzo Orlandini,
University of Padova, Italy

***Correspondence:**
Anna Maciołek
maciolek@is.mpg.de

Specialty section:
This article was submitted to Interdisciplinary Physics, a section of the journal Frontiers in Physics

Received: *25 June 2019*
Accepted: *14 August 2019*
Published: *04 September 2019*

Citation:
Werner M, Margaretti P and Maciołek A (2019) Drag Force for Asymmetrically Grafted Colloids in Polymer Solutions. Front. Phys. 7:122. doi: 10.3389/fphy.2019.00122

1. INTRODUCTION

Particles in the nanometer size range coated with polymers are of growing importance for rather diverse applications [1]. In hybrid materials such as nanocomposites, the use of polymers grafted to nanoparticles is widely exploit to suppress aggregation of particles and to enhance their dispersion and mixing into solvent or matrix. The nanoparticles coated with DNA are used for building highly sensitive probes or drug carriers in biological systems [2, 3] and to assemble crystals and other structures of numerous morphologies [4].

In the absence of external driving, the transport of nanobjects in the fluid environment is dominated by diffusion, a process due to random molecular motion excited by thermal fluctuations [5–7]. Diffusion of isolated spherical nanoparticle in the simple molecular liquids is well-described by the Fick's law, which says that the mean-square displacement changes linearly in time. The rate of this change, the translational diffusion coefficient D_t, is related to the macroscopic viscosity of the solvent η_m (as measured rheometer) via Stokes-Sutherland-Einstein (SSE) relation [6, 8]; $D_t = k_B T/\zeta_m$ where ζ_m is the hydrodynamic drag coefficient given by the Stokes equation $\zeta_m = 6\pi\eta_m R$. In this equation R is the hydrodynamic radius of diffusing particle, k_B is the Boltzmann constant and T is the temperature.

However, various experiments [9–20] and simulation studies [21–23] show that diffusion of nano-sized particles in complex fluids is not accurately described by Fick's law and that the SSE relation is violated in certain regimes of parameters. For polymer solutions, these parameters involve the size of the particle and the polymer length scales [24, 25]. For example, if the particle size is comparable to or smaller than the characteristic length scale in a polymer solution, its diffusion is significantly faster than the one predicted based on the macroscopic viscosity [13, 17, 18]. This is because on such length scales the nanoparticle does not experience the homogeneous continuum medium with high viscosity, rather, the individual polymer chains or blobs and their fluctuations as well as entanglements influence its dynamics.

Grafting nanoparticles with macromolecules, such as polymers or DNA, complicates their interactions with the complex medium and, therefore, stronger deviations from the SSE relation are expected. These deviations can be tested in rheological experiments [26] by measuring the drag force. The experiments for a bare (non-grafted) colloid in DNA solutions demonstrated that by using optical tweezers it is possible to move a particle through a highly monodispersed polymer solution at a given velocity as well as to measure the drag force on the colloid with piconewton resolution at the same time [26].

Here we provide a theoretical prediction for a drag force based on the assumption that interactions between grafted particle and the complex medium result in an effective spatially dependent viscosity. A similar idea was used by Tuinier et al. [27], Fan et al. [28, 29], and Feng et al. [30] to calculate the hydrodynamic resistance force for a bare spherical particle in a non-adsorbing polymer solution, where polymer depletion results in a reduced polymer concentration near the particle surface. Using the concept of local viscosity [31], the polymer concentration profile was related to the viscosity profile near a spherical particle. Hydrodynamics was formulated by the modified Stokes equation with non-uniform spherically symmetric viscosity, which was solved by a regular perturbation approximation using the Green function method.

In the present paper, we extend this analysis to account for anisotropic viscosity profile around a spherical particle, which may result from anisotropically grafted nanoparticles in a non-adsorbing polymer solution (see **Figure 1**). Such anisotropically grafted nanoparticles, e.g., DNA-grafted Janus particles can be manufactured [33–35]. They provide a basic structural element that can be used to produce useful nanoparticle clusters of different topologies through DNA-based self-assembly [33–35]. The concept of anisotropic viscosity might also be applicable for describing the transport of protein through the nuclear pore complex, where the transporting protein encounters heterogeneous polymer brush or gel like environment [36–38].

Because the concentration profile of free polymers in the solution depends on the length of grafted macromolecules and on the grafting density [32], an anisotropic grafting changes the depletion zone around the particle, which leads to anisotropic polymer concentration and thus to anisotropic effective viscosity. We assume that the particle is dragged slow enough such that the polymer solution can adiabatically follow the motion of the colloid. This means that the advective transport rate must be smaller than the diffusive transport rate of the polymers, which can be expressed via the Peclét number $Pe = l_p u/D_p \ll 1$, where l_p is the characteristic length scale of the polymer, u the characteristic velocity of the solvent u, and D_p diffusivity of the polymers. Further, we assume that the characteristic length scale of the variation of polymer concentration is bigger than the length of an effective statistical chain element. This assures a sufficiently large number of chain elements in small volume element to apply the concept of local viscosity [31]. Solving the modified Stokes equations with a spatial-dependent viscosity of a general form is not easy—even within a regular perturbation approximation. However, for the axisymmetric systems some simplifications occur. For axisymmetric Stokes equations with constant viscosity, translational and rotational motion are decoupled. For translational motion a scalar stream function, which transforms vectorial equations to the scalar ones is well-established. We demonstrate that these properties also hold for the modified Stokes equations with axisymmetric viscosity profile and provide a formalism to calculate the drag force experienced by a translating particle.

Our paper is structured as follows. In section 2, we present the extended Stokes equations with the spatially dependent viscosity and introduce the perturbation calculation scheme. In section 3 the drag force for the axisymmetric systems is calculated and analyzed for various grafting geometries. We conclude in section 5.

2. MODEL

2.1. Extended Stokes Equation

The Stokes equations are valid for small Reynolds numbers $Re = \rho ul/\eta \ll 1$, where ρ is the density of the fluid, u is the characteristic velocity of the flow, and l is the characteristic length scale of the particle. This assures that viscous forces dominate the inertial forces. The stationary incompressible Stokes equations with spatially dependent viscosity $\eta(\boldsymbol{r})$ are given by

$$\nabla \cdot \boldsymbol{\tau} = 0\,, \qquad \nabla \cdot \boldsymbol{v} = 0\,, \tag{1}$$

where $\boldsymbol{\tau} = -p\boldsymbol{I} + 2\eta(\boldsymbol{r})\boldsymbol{\Delta}$ the stress tensor, p is a pressure and $\boldsymbol{\Delta} = \left[\nabla \boldsymbol{v} + (\nabla \boldsymbol{v})^T\right]/2$ is the strain rate. The superscript T denotes the transposed of a tensor, $\boldsymbol{I}$ is the identity matrix. Expanding the divergence in the momentum equation one obtains an additional term, which is proportional to the gradient of the viscosity

$$0 = -\nabla p + \eta(\nabla^2 \boldsymbol{v}) + (\nabla \eta) \cdot \left[\nabla \boldsymbol{v} + (\nabla \boldsymbol{v})^T\right]. \tag{2}$$

We consider a quiescent, unbounded fluid which is dragged by a particle with no-slip and vanishing far-field boundary conditions:

$$\boldsymbol{v} = \boldsymbol{U} + \boldsymbol{\Omega} \times (\boldsymbol{r}_p - \boldsymbol{r}_c)\,, \qquad \boldsymbol{r} \in \Sigma_p \tag{3a}$$

$$\boldsymbol{v} \to 0\,, \quad p \to 0\,, \qquad |\boldsymbol{r}| \to \infty\,. \tag{3b}$$

where Σ_p is the particle surface and $\boldsymbol{r}_p$ is a point on the particle surface Σ_p. The particle is translating with velocity $\boldsymbol{U}$ and rotating with angular velocity $\boldsymbol{\Omega}$, which requires a force $\boldsymbol{F}$ and a torque $\boldsymbol{T}$ acting on the particle. The angular motion of the particle is described in a coordinate system fixed to the particle at $\boldsymbol{r}_c$.

The drag force on the particle is determined by the force acting on the particle surface Σ_p, which corresponds to the momentum flux through the surface

$$\boldsymbol{F} = \int_{\Sigma_p} \mathrm{dS}\, \boldsymbol{\tau} \cdot \boldsymbol{n}\,, \tag{4}$$

where $\boldsymbol{n}$ is the surface normal vector. In the following all quantities are represented in dimensionless units: $\boldsymbol{v} \propto U$, $\boldsymbol{\Omega} \propto U/a$, $\boldsymbol{\tau} \propto \bar{\eta}U/a$ and $\boldsymbol{p} \propto \bar{\eta}U/a$, where a is the particle radius and $\bar{\eta}$ is the bulk viscosity. Accordingly, the drag force and viscosity are also dimensionless.

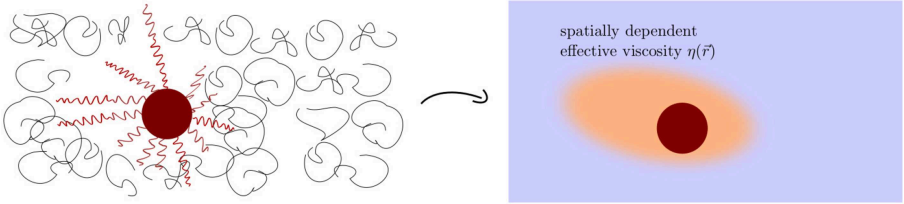

FIGURE 1 | Sketch of an anisotropic polymer concentration profile around a DNA-grafted colloid in a non-adsorbing polymer solution. The concentration profile of the free polymers depends on the grafting density and length of the DNA strings [32]. The anisotropic concentration profile leads to a non-uniform viscosity variation. We want to stress that the system is in equilibrium and there is no netforce.

2.2. Small Viscosity Variations

We consider an expansion of the system in small viscosity perturbations of order $\mathcal{O}(\epsilon)$

$$\eta = 1 + \epsilon\eta_1 + \epsilon^2\eta_2 + \mathcal{O}(\epsilon^3) \tag{5a}$$

$$\boldsymbol{v} = \boldsymbol{v}_0 + \epsilon\boldsymbol{v}_1 + \epsilon^2\boldsymbol{v}_2 + \mathcal{O}(\epsilon^3) \tag{5b}$$

$$p = p_0 + \epsilon p_1 + \epsilon^2 p_2 + \mathcal{O}(\epsilon^3). \tag{5c}$$

The fluid velocity at the surface of the particle is determined by the leading order velocity field $\boldsymbol{v}_0$. Thus, the higher order fluid velocity fields at the surface must vanish. The far-field condition of the quiescent fluid requires that both the pressure and the velocity fields have to vanish at infinity.

We expand the stationary Stokes equations in small viscosity variations of order ϵ. The leading order system $\mathcal{O}(\epsilon^0)$ is given by

$$-\nabla p_0 + \nabla^2\boldsymbol{v}_0 = 0\,, \qquad 0 = \nabla\cdot\boldsymbol{v}_0 \tag{6a}$$

$$\boldsymbol{v}_0 = \boldsymbol{U} + \boldsymbol{\Omega}\times(\boldsymbol{r}_p - \boldsymbol{r}_c)\,, \qquad \boldsymbol{r}\in\Sigma_p \tag{6b}$$

$$\boldsymbol{v}_0,\, p_0 \to 0\,, \qquad |\boldsymbol{r}|\to\infty \tag{6c}$$

and the first order system $\mathcal{O}(\epsilon^1)$

$$-\nabla p_1 + \nabla^2\boldsymbol{v}_1 = -\eta_1\nabla^2\boldsymbol{v}_0 + \nabla\eta_1\cdot\left[\nabla\boldsymbol{v}_0 + (\nabla\boldsymbol{v}_0)^T\right] \tag{7a}$$

$$0 = \nabla\cdot\boldsymbol{v}_1 \tag{7b}$$

$$\boldsymbol{v}_1 = 0\,,\;\; \boldsymbol{r}\in\Sigma_p \tag{7c}$$

$$\boldsymbol{v}_1,\, p_1 \to 0\,,\;\; |\boldsymbol{r}|\to\infty \tag{7d}$$

The leading order solutions fulfill common Stokes equations with constant viscosity.

3. AXISYMMETRIC SYSTEMS

Axisymmetric systems possess at least one axis of rotational symmetry, which we choose to be parallel to $\boldsymbol{e}_z$. We use spherical coordinates $\{r,\theta,\phi\}$ with the corresponding orthonormal basis $\{\hat{\boldsymbol{r}},\boldsymbol{e}_\theta,\boldsymbol{e}_\phi\}$ and the origin located at the center of the particle. Due to the rotational symmetry the system is independent of the azimuthal angle ϕ. Thus, the viscosity $\eta(r,\theta)$ is a function of radial distance r and the polar angle θ. Accordingly, the $\hat{\boldsymbol{r}}$- and $\boldsymbol{e}_\theta$-components of the extended Stokes equations Equation (1) depend on the components v_r and v_θ of the fluid velocity, whereas the $\boldsymbol{e}_\phi$-component of Equation (1) depends only on v_ϕ. The velocity field of the fluid for translational motion of the particle $\boldsymbol{U} \parallel \boldsymbol{e}_z$ is determined by $\{v_r, v_\theta\}$ and for rotational motion $\boldsymbol{\Omega} \parallel \boldsymbol{e}_z$ is determined by v_ϕ. These properties are summarized in **Figure 2**.

For axisymmetric Stokes equations translational and rotational motion are decoupled. For translational motion a scalar stream function formalism is well-established to simplify the vectorial equation to a scalar one (see, e.g., Happel and Brenner [39]). This formalism can be extended to a non-uniform viscosity as long as it is axisymmetric (see **Appendix A**). In the following we focus on translational motion of a particle in an axisymmetric system which is characterized by the particle velocity $\boldsymbol{U}$.

3.1. Leading Order Solution

The leading order axisymmetric momentum equation [see (A5) in the **Appendix A**] is the same as for the homogeneous system. So the stream function (see Equation A1) for the leading order system is [39]

$$\psi_0(r,\theta) = \frac{1}{4}r^2\sin^2\theta\left[\left(\frac{1}{r}\right)^3 - \frac{3}{r}\right]. \tag{8}$$

The corresponding velocity field is given by

$$v_{r0} = \cos\theta\left[\frac{3}{2r} - \frac{1}{2}\left(\frac{1}{r}\right)^3\right] \tag{9a}$$

$$v_{\theta 0} = -\sin\theta\left[\frac{3}{4r} + \frac{1}{4}\left(\frac{1}{r}\right)^3\right]. \tag{9b}$$

As expected, the leading order decay of the velocity is $\propto 1/r$. The pressure is determined by integration

$$\nabla p_0 = \nabla^2\boldsymbol{v}_0\,, \qquad \Rightarrow \qquad p_0(r,\theta) = \frac{3}{2}\frac{\cos\theta}{r^2}\,.$$

3.2. First Order Solution

For the first order velocity field we use Equations (B3) (see **Appendix B**), which correspond to the stream function ansatz (B2). In order to determine the first order pressure contribution

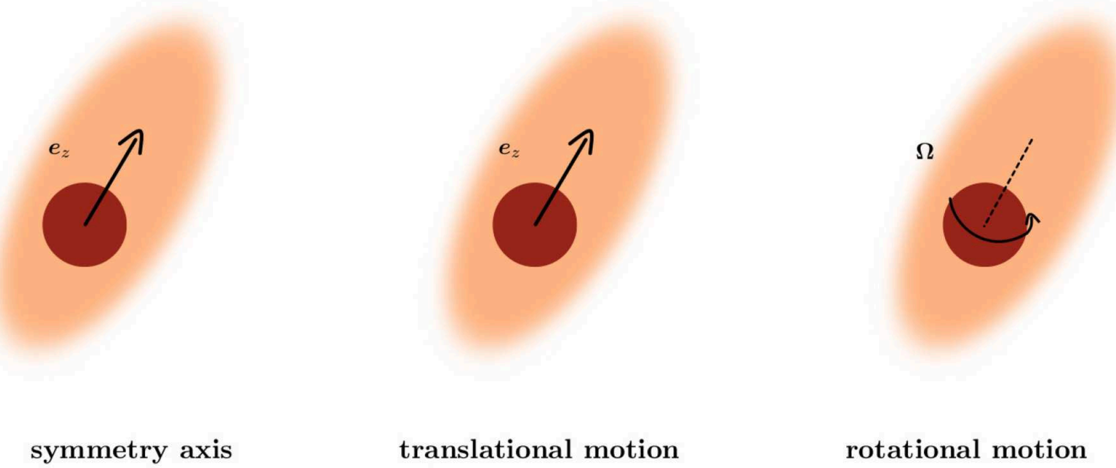

FIGURE 2 | Short summary of the decoupling of translational and rotational motion of the extended Stokes equations for an axisymmetric system. The velocity field of the fluid for translational motion of the particle $\boldsymbol{U} \parallel \boldsymbol{e_z}$ is determined by $\{v_r, v_\theta\}$ and for rotational motion $\boldsymbol{\Omega} \parallel \boldsymbol{e_z}$ is determined by v_ϕ.

$p_1(r=1,\theta)$ at the particle surface, we exploit the $\boldsymbol{e}_\theta$-component of the stationary Stokes equation

$$\nabla \cdot \boldsymbol{\tau}_{|\boldsymbol{e}_\theta} = 0 \quad \Rightarrow \quad \frac{1}{r}\frac{\partial p}{\partial \theta} = \nabla \cdot \Big(\eta(r=1,\theta)[\nabla \boldsymbol{v} + (\nabla \boldsymbol{v})^T]\Big)_{|\boldsymbol{e}_\theta}. \tag{10}$$

Using the stream function relations for $\boldsymbol{v}_0$ (9) and $\boldsymbol{v}_1$ (B3) we integrate over θ to obtain the pressure at the surface $r=1$

$$\begin{aligned} p_1(r=1,\theta) = {} & \sum_{n\geq 3} f_n^{(3)}(r=1)\int \frac{\mathscr{I}_n}{\sin\theta}\mathrm{d}\theta - \frac{1}{2}f_2^{(3)}(r=1)\cos\theta \\ & - \frac{3}{2}\int \left(\eta_1(r=1,\theta) - \frac{\partial \eta_1(r,\theta)}{\partial r}\right)_{r=1} \sin\theta \mathrm{d}\theta + c(r). \end{aligned} \tag{11}$$

The integration constant $c(r)$ does not contribute to the drag force. Here, superscript (i) defines the *ith* derivative.

3.3. Drag Force

The drag force on the particle is calculated by integrating the stress tensor over the particle surface (see Equation 4). First, we derive an expression for the forces $\boldsymbol{f}_s(r,\theta)$ at the particle surface $r=1$

$$\boldsymbol{f_s}(r=1,\theta) = \boldsymbol{\tau}\cdot\hat{\boldsymbol{r}} = -p\,\hat{\boldsymbol{r}} + 2\,\eta(r=1,\theta)\,\boldsymbol{\Delta}\cdot\hat{\boldsymbol{r}} \tag{12}$$

($\hat{\boldsymbol{r}}$ is a vector normal to the surface denoted in Equation 4 by $\boldsymbol{n}$). Up to the first order, the surface force can be expressed as $\boldsymbol{f}_s = \boldsymbol{f}_{s0} + \epsilon \boldsymbol{f}_{s1}$. Using solutions for zero and first order velocities and pressures derived above, we find

$$\begin{aligned} \boldsymbol{f_s}\,|_{\hat{\boldsymbol{r}}} = \boldsymbol{f}_{0s}\,|_{\hat{\boldsymbol{r}}} - \epsilon\Big\{ & \overbrace{\sum_{n\geq 3} f_n^{(3)}(r=1)\int \frac{\mathscr{I}_n}{\sin\theta}\mathrm{d}\theta}^{\text{vanish under surface integration}} + \frac{1}{2}f_2^{(3)}(r=1)\cos\theta \\ & + \frac{3}{2}\int\left(\eta_1(r=1,\theta) - \frac{\partial \eta_1(r,\theta)}{\partial r}\,|_{r=1}\right)\sin\theta\mathrm{d}\theta\Big\} \end{aligned} \tag{13a}$$

$$\begin{aligned} \boldsymbol{f_s}\,|_{\boldsymbol{e}_\theta} = \boldsymbol{f}_{0s}\,|_{\boldsymbol{e}_\theta} + \epsilon\Big\{ & \overbrace{\sum_{n\geq 3} f_n^{(2)}(r=1)\frac{\mathscr{I}_n}{\sin\theta}}^{\text{vanish under surface integration}} \\ & + \frac{1}{2}f_2^{(2)}(r=1)\sin\theta + \frac{3}{2}\eta_1(r=1,\theta)\sin\theta\Big\}. \end{aligned} \tag{13b}$$

In the leading order, $\boldsymbol{f}_{s0}\,|_{\hat{\boldsymbol{r}}} = -3/2\cos\theta$ and $\boldsymbol{f}_{0s}\,|_{\boldsymbol{e}_\theta} = 3/2\sin\theta$. It turns out that the orthogonal component $\boldsymbol{f}_s \cdot \hat{\boldsymbol{r}}$ of the surface force is determined by the pressure whereas the tangential component $\boldsymbol{f}_s \cdot \boldsymbol{e}_\theta$ is determined by the shear force contribution.

The last step to calculate the drag force $\boldsymbol{F}$ is to integrate the surface forces over the whole surface of the particle $\boldsymbol{F} = \int_{\Sigma_p} \mathrm{d}S\boldsymbol{f}_s$. Due to the symmetry of the system the drag force is aligned parallel to the symmetry axis $\boldsymbol{e}_z$. The resolved part of the surface force $\boldsymbol{f}_s$ in $\boldsymbol{e}_z$ direction is obtained by using $\boldsymbol{e}_z = \hat{\boldsymbol{r}}\cos\theta$ and $\boldsymbol{e}_z = -\boldsymbol{e}_\theta\sin\theta$. Performing partial integration and applying the orthogonality of Gegenbauer functions (C2) as well as relation (C3) (see **Appendix C**) the drag force can be expressed as

$$\Rightarrow \quad F_z = -6\pi + \epsilon 2\pi\Big\{\frac{f_2^{(3)}(r=1)}{3} \tag{14a}$$

$$- \frac{3}{4}\int_0^\theta \left(\eta_1(r=1,\theta) - \frac{\partial \eta_1(r,\theta)}{\partial r}\Big|_{r=1}\right)\sin^3\theta\mathrm{d}\theta \tag{14b}$$

$$+ \epsilon 2\pi\Big\{ - \frac{2f_2^{(2)}(r=1)}{3} - \frac{3}{2}\int_0^\pi \eta_1(r=1,\theta)\sin^3\theta\mathrm{d}\theta\Big\} \tag{14c}$$

The first line (14a) is the leading order drag force corresponding to a sphere and a homogeneous viscosity. The negative sign shows that the force is opposite to the particle moving direction. It turns out that in the leading order, the pressure contributes 1/3 and the shear force 2/3 of the total drag force. The last two lines (14b) and (14c), give the first order correction to the drag force. The contribution of the first order pressure at the surface is shown in line (14b) and the first order shear force contribution is shown in line (14c). Equation (13) implies that only the second Gegenbauer coefficient f_2 is needed to calculate the first order drag force. A general solution for f_2 can be provided by the Green function of the ODE (14) with $n = 2$, which has a form

$$\left(\frac{\partial^4}{\partial r^4} - \frac{4}{r^2}\frac{\partial^2}{\partial r^2} + \frac{8}{r^3}\frac{\partial}{\partial r} - \frac{12}{r^4} + \frac{4}{r^4}\right) f_2(r) = R_2(r). \tag{15}$$

For a sphere in an unbounded quiescent fluid with vanishing velocity at the sphere surface, this Green function has been calculated by Tuinier et al. [28]:

$$\begin{aligned} G_1(r,r') = &\left(\frac{-r'^4}{30r} + \frac{r}{6}r'^2 + \frac{1}{12}\left(\frac{r'}{r} + \frac{r}{r'}\right)\right. \\ &\left. -\frac{r\,r'}{4} - \frac{1}{20r\,r'}\right),\ 1 < r' < r \\ G_2(r,r') = &\left(\frac{-r^4}{30r'} + \frac{r'}{6}r^2 + \frac{1}{12}\left(\frac{r}{r'} + \frac{r'}{r}\right)\right. \\ &\left. -\frac{r'\,r}{4} - \frac{1}{20r'\,r}\right),\ r < r' < \infty. \end{aligned} \tag{16}$$

The coefficient f_2 is obtained via integration of the Green function and the second Gegenbauer mode of the inhomogeneity $R_2(r)$

$$f_2(r) = \int_1^r G_1(r,r')R_2(r')\mathrm{d}r' + \int_r^\infty G_2(r,r')R_2(r')\mathrm{d}r'. \tag{17}$$

It satisfies the following boundary conditions: at the sphere surface $f_2(r = 1) = 0, f_2^{(1)}(r = 1) = 0$, and in far-field $\lim\limits_{r\to\infty} :\ f_2(r)/r^2 = 0,\ f_2^{(1)}(r)/r = 0$. All integrands in (17) are smooth functions, therefore, even if for a given r-dependence of the viscosity an analytical solution does not exist, the integrals can be easily calculated using the standard quadrature method. For the first order drag force, also the derivatives $f^{(2)}(r = 1)$ and $f^{(3)}(r = 1)$ at the surface of the sphere are needed. Considering the Leibnitz rule and the continuity of the given Green function up to the second derivative, the derivatives of f_2 at the surface are

$$\lim_{r\to 1} f_2^{(k)}(r) = \int_1^\infty G_2^{(k)}(r = 1, r')R_2(r')\mathrm{d}r' \tag{18}$$

$$G_2^{(3)}(r = 1, r') = -\frac{1}{2r'} - \frac{r'}{2}, \quad G_2^{(2)}(r = 1, r') = -\frac{1}{2r'} + \frac{r'}{2}$$

3.3.1. Multipol Representation

In order to proceed, we represent the first order viscosity variation in Equation (5a) as a multipole expansion with r-dependent coefficients

$$\eta_1(\boldsymbol{r}) = m(r) + \boldsymbol{d}(r)\cdot\hat{\boldsymbol{r}} + \boldsymbol{Q}(r) : \frac{3\hat{\boldsymbol{r}}\hat{\boldsymbol{r}} - \boldsymbol{I}}{2} + \dots. \tag{19}$$

In the above, the symbol ":" denotes the double dot product. The projections of the viscosity variation are: the monopole $m(r) = \frac{1}{4\pi}\int \sin\theta \mathrm{d}\theta \mathrm{d}\phi\, \eta_1(\boldsymbol{r})$, the dipole $\boldsymbol{d}(r) = \frac{3}{4\pi}\int \sin\theta \mathrm{d}\theta \mathrm{d}\phi\, \hat{\boldsymbol{r}}\eta_1(\boldsymbol{r})$ and the quadrupole $\boldsymbol{Q}(r) = \frac{5}{8\pi}\int \sin\theta \mathrm{d}\theta \mathrm{d}\phi\, \eta_1(\boldsymbol{r})(3\hat{\boldsymbol{r}}\hat{\boldsymbol{r}} - \boldsymbol{I})$. The quadrupole matrix $\boldsymbol{Q}$ is traceless and symmetric by definition. It follows that the second Gegenbauer coefficient $R_2(r)$ of the inhomogeneity $h_1(r,\theta)$ in Equation (B4) depends on the monopole and quadrupole contributions to the axisymmetric viscosity but does not depend on the dipole contribution. Thus, for the total drag force $\boldsymbol{F}$ one has

$$\begin{aligned} F_z = -6\pi\, \Bigg\{ & 1 + \epsilon\left[\frac{1}{2}\, m(r = 1) - \frac{1}{6}\, m^{(1)}(r = 1)\right] \\ & -\frac{\epsilon}{6}\left[Q_{33}(r = 1) - Q_{33}^{(1)}(r = 1)\right] \\ & +\frac{\epsilon}{12}\int_1^\infty \mathrm{d}r'\mathscr{G}(r')\Big[-r'\left(1 + 3r'^2\right) m^{(1)}(r') + r'^2 Q_{33}^{(2)}(r')\Big] \\ & +\frac{\epsilon}{12}\int_1^\infty \mathrm{d}r'\mathscr{G}(r')\Big[r'\left(1 + 3r'^2\right) Q_{33}^{(1)}(r') - r'^2 Q_{33}^{(2)}(r') \\ & -18Q_{33}(r') + 9r'(1 - r'^2)Q_{33}^{(1)}(r')\Big]\Bigg\}. \end{aligned} \tag{20}$$

In the above

$$\mathscr{G}(r') \equiv \left(\frac{1}{r'^6} - \frac{3}{r'^4}\right), \quad \int_1^\infty \mathrm{d}r'\mathscr{G}(r') = -\frac{4}{5}.$$

This result includes the solution of Tuinier et al. [28] for isotropic viscosity variations $\eta_1(r)$.

4. ANALYSIS

We start the analysis of our result for the drag force with the general case of viscosity variations that decay beyond a certain length scale. The decay of viscosity variations is expected because the overall polymer concentration profile approaches its bulk value sufficiently far away from the grafted particle. Specifically, we assume that each multipole mode n of η_1 decays beyond the (possibly different) length scale d_n. Since merely the first three multipoles are relevant, we have

$$m(r) = Z_0(r; d_0)\cdot m \tag{21}$$

$$\boldsymbol{d}(r) = Z_1(r; d_1)\cdot \boldsymbol{d} \tag{22}$$

$$\boldsymbol{Q}(r) = Z_2(r; d_2)\cdot \boldsymbol{Q}. \tag{23}$$

In order to grasp the basics of the role of the viscosity profile on the drag force on the colloid, we follow Tuinier and Taniguchi [31] and consider the decay profile of the following functional form:

$$Z_n(r; d_n) = 1 - \tanh^2\left(\frac{r - 1}{d_n}\right), \tag{24}$$

with the properties $Z_n(r = 1; d_n) = 1$, $Z_n^{(1)}(r = 1; d_n) = 0$, and $\lim\limits_{r\to\infty} Z_n(r; d_n) = 0$. An example of the decay profile is shown in **Figure 3** for different values of d.

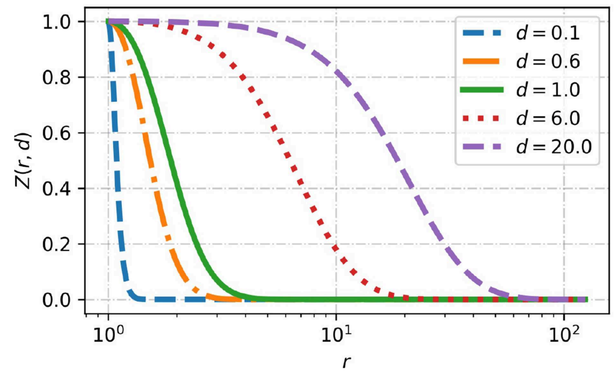

FIGURE 3 | The decay profile $Z(r; d)$ next to the particle surface $r = 1$ is plotted for different $d \in \{0.1, 0.6, 1, 8, 20\}$. $d < 1$ corresponds to a fast decay compared to the particle size and $d > 1$ corresponds to a slow decay.

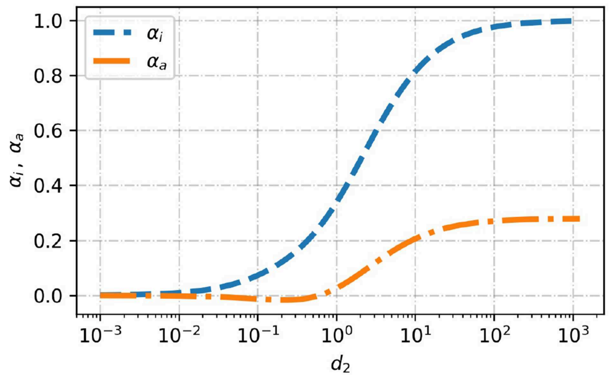

FIGURE 4 | Dimensionless drag force due to a solely monopole contribution, α_i (see Equation 27), and solely due to quadrupole contribution, α_a (see Equation 29), as a function of the dimensionless decay length, d_2.

The drag force can be represented in terms of an isotropic viscosity contribution $\epsilon m \alpha_i(d)$ and the anisotropic viscosity contributions $\epsilon Q_{33}\, \alpha_a(d)$ as follows:

$$\frac{F_z}{-6\pi} = 1 + \epsilon \Big[m\, \alpha_i(d_0) + Q_{33}\, \alpha_a(d_2) \Big] \tag{25}$$

with

$$\alpha_i(d) = \frac{1}{2} + \frac{1}{12} \int_1^\infty \mathrm{d}r' \mathscr{G}(r') \Big[-r' \left(1 + 3r'^2\right) Z_0^{(1)}(r', d) + r'^2 Z_0^{(2)}(r', d) \Big] \tag{26}$$

$$\alpha_a(d) = -\frac{1}{6} + \frac{1}{12} \int_1^\infty \mathrm{d}r' \mathscr{G}(r') \Big[r' \left(10 - 6r'^2\right) Z_2^{(1)}(r', d) - r'^2 Z_2^{(1)}(r', d) - 18 Z_2(r', d) \Big]. \tag{27}$$

In **Figure 4** we plot the forces α_i and α_a as function of the decay length $d \in [10^{-3}, 10^3]$. As expected, for variations very quickly decaying with the distance from the sphere, i.e., for ($d \ll 1$), both functions vanish and the drag force is similar to a particle in a homogeneous solution. Thus, in this limit the viscosity variation is negligible. On the other hand, in the limit of very slow decays ($d \gg 1$)

$$\lim_{d\to\infty} \alpha_i = 1\,, \quad \lim_{d\to\infty} \alpha_a = \frac{7}{25} \tag{28}$$

the solution correspond to the case of viscosity variations that depend only on the angle θ.

In between there is a transition region from short length scales to long length scales. The isotropic viscosity variation is the main contribution to the drag force. The contribution from the anisotropic viscosity variation is weaker. At $d \approx 1$ the anisotropic contribution becomes negligibly small because α_a shows a zero crossing in that region. Thus, up to the first order the drag force is independent of anisotropic viscosity variations that decay on the length scale of the particle. In order to get a better understanding of the zero crossing we look at the specific quadrupole like viscosity variation $\mathbf{Q} = [(-1, 0, 0), (0, -1, 0), (0, 0, 2)]/2$, which is shown in **Figure 5** for $d_2 \in \{0.3, 7\}$. This specific viscosity variation does not change the net viscosity. The viscosity in front and at the back of the particle is increased whereas at the waist it is decreased. The corresponding drag force is increased for $d_2 > 1$ and decreased for $d_2 < 1$. In a more general context this indicates that higher viscosity at the back and front of a particle leads to larger drag force if the viscosity variation decays on a longer length scale compared to the length scale of the particle and to a weaker drag force if the variation decays on a shorter length scale compared to the length scale of the particle.

4.1. Analysis of the Velocity Mode $\boldsymbol{v}_d$

Our formalism allows us to analyze how the velocity field adapts to modulations in the local viscosity. In the following we focus on the dependence of the local velocity field on the local viscosity for anisotropic viscosity profiles (isotropic profiles have been analyzed in Fan et al. [28]). In this case only the quadrupolar component of the viscosity profile (with magnitude given by $Q_{33} = l_2$, where l_2 is the coefficient of the projection of η_1 on the second Legendre mode[1]) affects the translational friction, thus we study the velocity field variations which are related to those viscosity variations and call them $\boldsymbol{v}_d \propto \epsilon l_2$.

In **Figure 7** we show the velocity field variation $\boldsymbol{v}_d$ (calculated using Equation 16) for different decay length of the quadrupolar contribution $d_2 \in \{0.1, 1, 8, 20\}$ (in units of ϵl_2). For each decay d_2 two figures are shown. The semi-logarithmic plot gives information about the long ranged velocity field v_{dz} along the lines $\theta = 0$ and $\theta = \pi/2$ whereas the vector-density-plot indicates the absolute value of the velocity component $|\boldsymbol{v}_d|$ and the arrows give additional information about the direction of the velocity variation. For comparison the leading order velocity field is shown in **Figure 6**.

---

[1] A function f defined on the interval $[-1, 1]$ can be represented in Legendre's polynomials $f(x) = \sum_{n\geq 0} l_n P_n(x)$. The coefficients l_n are the projections onto the corresponding Legendre's mode $\frac{2n+1}{2} \langle f \mid P_n \rangle_P = l_n$.

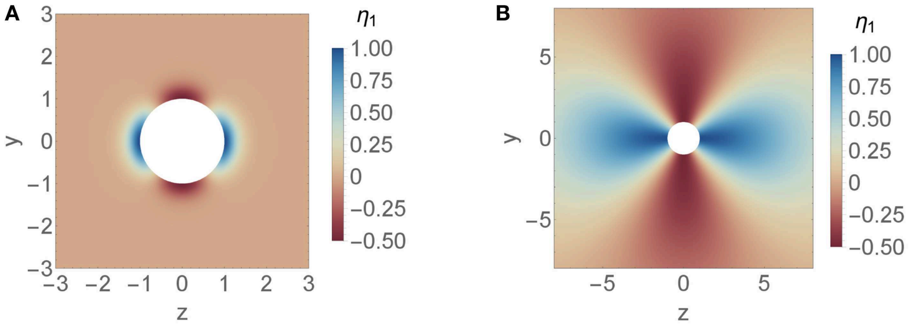

FIGURE 5 | Axisymmetric, quadrupolar viscosity variation $\boldsymbol{Q} = [(-1, 0, 0), (0, -1, 0), (0, 0, 2)]/2$ around a spherical particle with length scale decay **(A)** $d_2 = 0.3$ and **(B)** $d_2 = 7$.

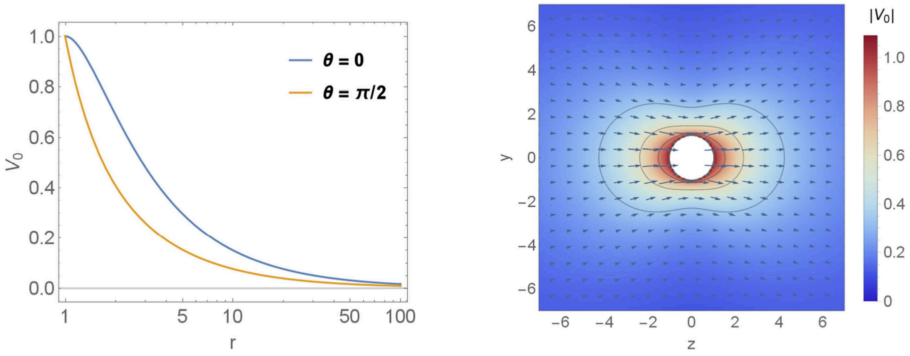

FIGURE 6 | Velocity profiles. The leading order velocity field is shown in two plots. The first one is a semi-logarithmic plot which gives information about the long ranged velocity field v_0 decay parallel to the symmetry axis. Therefore we calculated v_0 along the lines $\theta = 0$ and $\theta = \pi/2$. The second one is a vector-density-plot which indicates the absolute value of $|\boldsymbol{v}_0|$ and the arrows give additional information about the direction of the velocity field. The particle is denoted by the white sphere in the middle of the plot and it is moving to the right parallel to $\boldsymbol{e}_z$.

In the semi-logarithmic plot we see the algebraic decay of the velocity field and at the surface $r = 1$ the dimensionless velocity of the particle $v \propto 1$. Thus, a positive sign in the semi-logarithmic plot as well as arrows with positive z-component corresponds to an increase of the velocity field. On the other hand, a negative sign in the semi-logarithmic plot as well as arrows with negative z-component corresponds to a decrease of the velocity field. For short ranged viscosity variations $d_2 \lesssim 1$ the semi-logarithmic plot is negative as shown in the top right panel of **Figure 7**. Thus, the velocity variation decreases the velocity field. For viscosity variations of the particle length scale $d_2 \approx 1$ (middle left panel of **Figure 7**) the semi-logarithmic plot is mainly positive except close to the particle surface. Hence, the velocity variation increases the velocity field. This property is maintained in the far-field for long ranged viscosity variations. Finally, in the bottom right panel of **Figure 7** the vector-density-plot shows two velocity regions which are separated by a crossover area (*blue area*) with very small velocity variations. The first region is close to the particle surface. Here the fluid velocity is reduced compared to the homogeneous case. The second region is outside the crossover area and increases the velocity field. With increasing length scale of the viscosity variation d the layers get stretched.

4.2. Janus and Quadrupole Particles

We consider a spherical particle that is anisotropically grafted with polymer chains in a polymer suspension. The grafted polymers induce an anisotropic depletion zone of suspended polymers whose width is controlled by the mutual interaction between the grafted and suspended polymers. In the following we assume that the motion of the particle occurs on time scales τ_{particle} that are much larger than the relaxation time of the polymers ($\tau_{\text{particle}} \gg \tau_{\text{polymer}}$), i.e., the Peclét number $Pe = l_p u/D_p \ll 1$.

Under these conditions the semi empirical Martin Equation [40] can be used to relate the local polymer concentration to a local viscosity:

$$\eta_p/\eta_s = 1 + [\eta] c_b \rho(\boldsymbol{r})\, \mathrm{e}^{k_H [\eta] c_b \rho(\boldsymbol{r})} . \tag{29}$$

where ρ is the dimensionless, normalized total polymer (i.e., grafted plus suspended polymers) concentration profile, η_s is the viscosity of the solvent, k_H is the Huggins coefficient, which is specific for a given polymer-solvent combination. The intrinsic viscosity $[\eta]$ is approximately the inverse of the polymer overlap concentration $1/c_b^*$ in the bulk, which corresponds to the hydrodynamic volume of a polymer chain in solution per unit

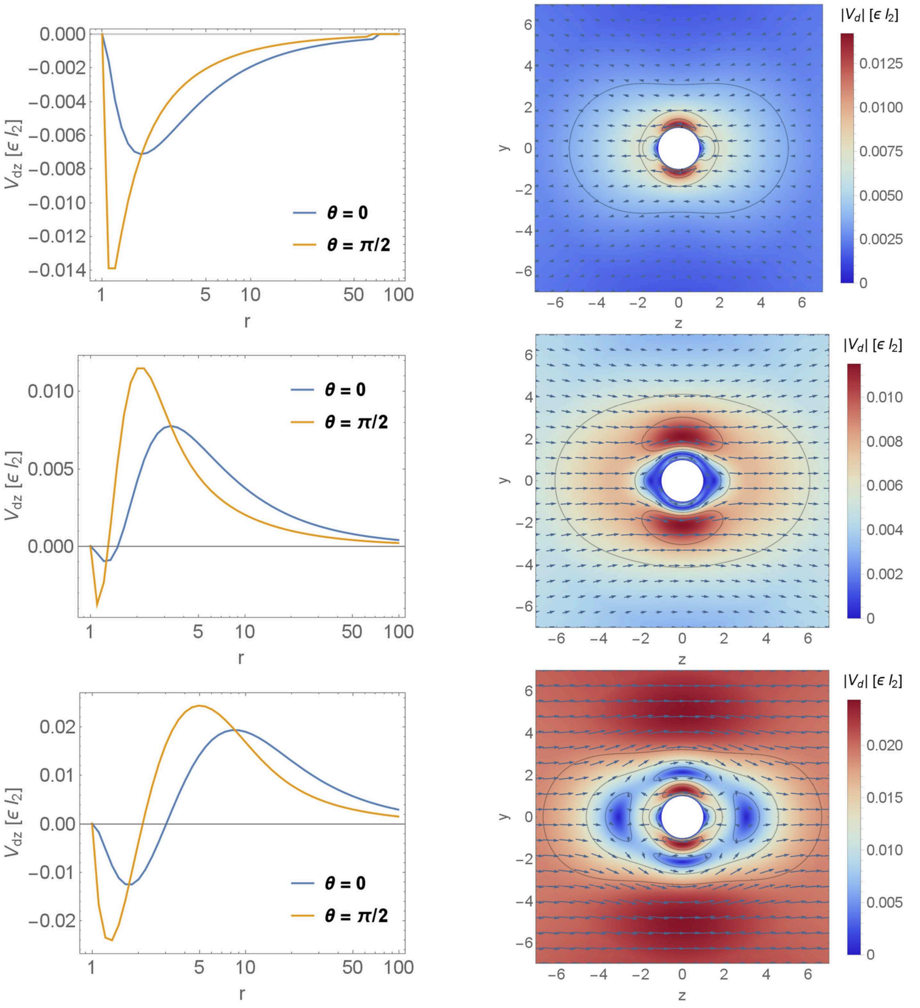

FIGURE 7 | Velocity profiles. The velocity field variation $\boldsymbol{v}_d$ is shown for different decays of the viscosity variation $d_2 \in \{0.1, 1, 8\}$ top to bottom, respectively. Each velocity field is shown in two plots. The first one is a semi-logarithmic plot which gives information about the long ranged velocity field v_{dz} decay parallel to the symmetry axis. Therefore we calculated v_{dz} along the lines $\theta = 0$ and $\theta = \pi/2$. The second one is a vector-density-plot which indicates the absolute value of $|\boldsymbol{v}_d|$ and the arrows give additional information about the direction of the velocity variation. The particle is denoted by the white sphere in the middle of the plot and it is moving to the right parallel to $\boldsymbol{e}_z$.

mass. We expand the Martin equation for small variations of the polymer concentration profile $c_b\rho(\boldsymbol{r})$, which is in the dilute regime $\epsilon = c_b[\eta] \ll 1$

$$\eta_p/\eta_s = 1 + \epsilon\rho(\boldsymbol{r}) + \epsilon^2 k_H\,\rho(\boldsymbol{r})^2 \,. \tag{30}$$

We identify $\eta_1 = \rho$.

Now, we discuss the following (physically realizable) grafting geometries [33–35]:

- **isotropic:** bare particle – index $'i'$;
- **dipolar grafting:** a Janus like particle – index $'j'$;
- **quadrupolar grafting** two cases
  - dominant length scale at back and front – index $'q'$;
  - dominant length scale at the waist – index $'q_2'$;

which are defined by the following concentration profiles

$$\rho_i = R(r,d) \tag{31}$$

$$\rho_j = \frac{\big(R(r,d_1) + R(r,d)\big)}{2} + \frac{\big(R(r,d) - R(r,d_1)\big)}{2}\cos\theta \tag{32}$$

$$\rho_q = \frac{\big(R(r,d_1) + R(r,d)\big)}{2} + \frac{R(r,d) - R(r,d_1)}{2}(3\cos^2\theta - 1)/2 \tag{33}$$

$$\rho_{q2} = \frac{\big(R(r,d_1) + R(r,d)\big)}{2} + \frac{R(r,d_1) - R(r,d)}{2}(3\cos^2\theta - 1)/2\,. \tag{34}$$

The lowest monopoles of the viscosity corresponding to these concentration profiles are:

$$m_i(r) = R(r,d) \tag{35}$$

$$m_{j,q}(r) = \frac{\big(R(r,d_1) + R(r,d)\big)}{2} \tag{36}$$

$$\boldsymbol{d}_j(r) = \frac{R(r,d) - R(r,d_1)}{2} \cdot \boldsymbol{d} \tag{37}$$

$$\mathbf{Q}_q(r) = \frac{R(r,d) - R(r,d_1)}{2} \cdot \mathbf{Q} \tag{38}$$

$$\mathbf{Q}_{q2}(r) = \frac{R(r,d_1) - R(r,d)}{2} \cdot \mathbf{Q}\,. \tag{39}$$

We assume that near a surface of the bare particle polymers are depleted, which corresponds to the polymer concentration profile [41]

$$R(r,d) = \tanh^2\left(\frac{r-1}{d}\right). \tag{40}$$

The polymer concentration profile ρ_j next to a Janus like colloidal particle is shown in **Figure 8A**. The polymer concentration profile for the two cases ρ_q, ρ_{q2} of quadrupolar grafting are shown in **Figures 8A,C**.

We calculate the drag force for different length scales $d \in [0.01, 50]$ of the depletion zone at the grafted sides and compare it to the isotropic case. The length scale of the depletion zone at one hemisphere of the dipolar grafted particle, the waist of the quadrupolar back-front grafted particle $'q'$ as well as the back and front of the waist grafted particle $('q_2')$ are fixed at $d_1 = 1$ or at $d_1 = 0.01$.

The results for the first order correction to the drag force $F_{z,1} = (F_z - 1)/(-6\pi)$ (in units of ϵ) are shown in **Figure 9** for two cases: (1) $d_1 = 1$ and (2) $d_1 = 0.01$. One can see that for all cases $F_{z,1}$ is positive, i.e., the total drag force always increase, and that the first order correction decays monotonically upon increasing the decay length d. Because the dipolar part of the axisymmetric viscosity variations does not contribute to the first order correction to the drag force, for the Janus like grafting $F_{z,1}$ is determined by the monopol part (36). For the quadrupolar grafting both monopol and quadrupole viscosity variations contribute to $F_{z,1}$. By the choice of the polymer concentration profiles, at $d_1 = d$ the drag force $F_{z,1}$ for all cases of grafted particles equals the one for the bare particle. If $d_1 < d$, i.e., when the grafting induce a larger depletion zone, the first order correction to the drag force is smaller than that for a bare particle. If d_1 or d are <1, $F_{z,1}$ is almost the same for all three cases of grafting. For $d > d_1$, the back-front grafting leads to a weaker $F_{z,1}$ than the waist grafting.

5. CONCLUSIONS

We have characterized the friction force of colloidal particles dragged across a fluid that show an inhomogeneous and anisotropic viscosity profile. We have derived closed formulas for both the drag force as well as for the velocity profile. In order to rationalize our results we have expressed the local viscosity profile in terms of its multipole expansion. As expected, we found that the drag force is sensitive to the amplitude of the monopole, i.e., the drag force increases upon increasing the average viscosity. Interestingly, higher order multipoles have quite different roles. In fact, our results show that the drag force is insensitive to the amplitude of the dipole, i.e., for a fore-and-aft asymmetric particle pulling it back and forwards leads to the same drag force. In contrast, the drag force is sensitive to the amplitude of the quadrupole. In particular, we found that a proper choice of the quadrupole orientation (i.e., with higher viscosity on the waist and lower on the axis of motion) with a long decay, $d \gg 1$ leads to a net *reduction* of the drag force. We emphasize that such a reduction occurs with "fixed" average viscosity, i.e., at fixed monopole contribution. Hence this is a genuine effect of the anisotropic viscosity distribution and cannot be reduced to a simple reduction of the average drag. Moreover, the sign of this contribution can be switched by changing either the sign of the quadrupole, i.e., moving the higher viscosity from the waist of the particle to the axis of motion, or by reducing the decay length, $d \ll 1$.

We have analyzed the cases of physically plausible grafting shown in **Figure 7** in more detail. Interestingly, we found that the net drag force can be controlled by tuning the relative magnitude of the monopole and quadrupole contribution to the density of the grafted polymers (see **Figure 8**). In particular, our results show that for the Janus grafting the anisotropic grafting can both reduce and enhance the drag force as compared to the isotropic case. In contrast, for the

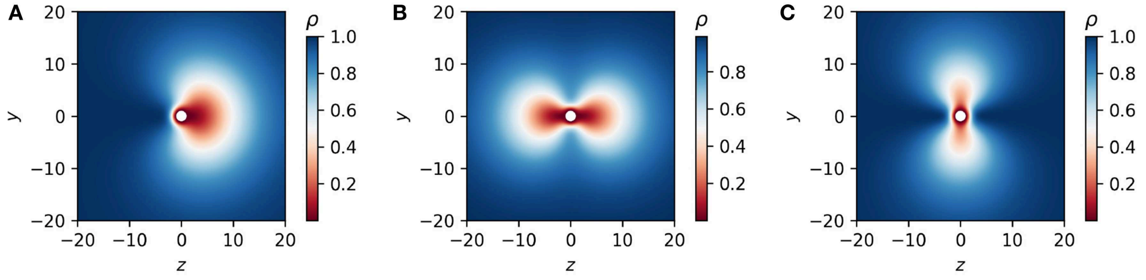

FIGURE 8 | Concentration profile ρ (see Equation 32) next to a dipolar grafted (Janus-like) colloidal particle **(A)**, next to a quadrupolar back-front grafted colloidal particle **(B)**, and a quadrupolar waist grafted particle **(C)**. The length scale of the depletion zone at one hemisphere of the dipolar grafted particle and at the waist (back front) of the quadrupolar grafted particle is fixed at ($d_1 = 1$) whereas at the other parts of the particle it is fixed at $d = 10$.

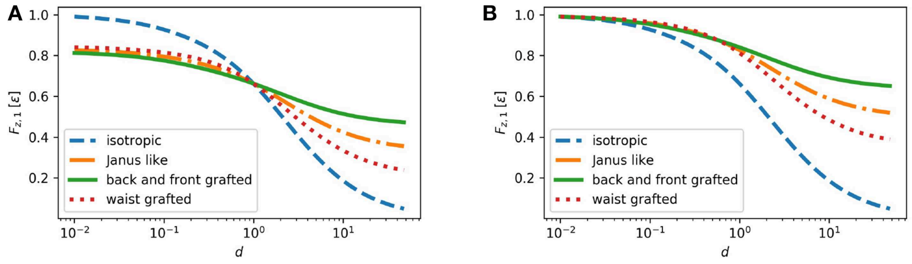

FIGURE 9 | The first order correction to the drag force $F_{Z,1} = (F_Z - 1)/(-6\pi)$ (see Equation 25) for three cases of the grafting geometry as defined by Equations (32–34) compared to the case of isotropic (bare) particle Equation (31). Polymer concentration profiles corresponding to the drag force for the Janus and back-front quadrupolar grafting in **(A)** are shown, respectively, in panels **(A,B)** in **Figure 8**.

case of back-front grafting the net effect of the anisotropic contribution is to enhance the drag force as compared to the isotropic case.

Concerning the velocity profile, we have shown that the inhomogeneous and anisotropic viscosity profile induces quite involved modulations in the velocity field. Interestingly, the modulations of the velocity profile can oppose t the main flow. Due to our perturbation approach, the magnitude of these modulations are tiny. In this perspective, our results are pinpointing the relevance of the modulations in the viscosity that, possibly, may persist also for stronger variations of the viscosity. We have truncated our expansion at first order since, typically, this is also the leading order when the perturbation parameter is small. Indeed this is the case for monopole and quadrupole contributions to the density of grafted polymers. Interestingly, dipole contributions to the density distribution, at linear order, do not affect the effective friction. Therefore, for the dipolar contribution a higher order expansion is required. Since this quadratic contribution is relevant only when the monopole and quadrupole are vanishing small, we have decided to disregard this contribution in the present manuscript and to focus on the leading contributions, namely monopole and quadrupole. We plan to investigate higher order contribution (and hence also dipole ones) in forthcoming works. Results of Fan et al. [28] suggest that they may be relevant for variations at short length scales.

DATA AVAILABILITY

The datasets generated for this study are available on request to the corresponding author.

AUTHOR CONTRIBUTIONS

MW, PM, and AM contributed conception and design of the study. MW wrote the first draft. AM rewrote several sections. All authors contributed to manuscript revision.

ACKNOWLEDGMENTS

The work of AM was partially supported by Polish National Science Center (Harmonia Grant No. 2015/18/M/ST3/0403).

SUPPLEMENTARY MATERIAL

The Supplementary Material for this article can be found online at: https://www.frontiersin.org/articles/10.3389/fphy.2019.00122/full#supplementary-material

REFERENCES

1. Mezzenga R, Ruokolainen J. Nanocomposites: nanoparticles in the right place. *Nat Mater.* (2009) **8**:926–8. doi: 10.1038/nmat2576
2. Rosi NL, Mirkin CA. Nanostructures in biodiagnostics. *Chem Rev.* (2009) **105**:1547. doi: 10.1021/cr030067f
3. Tiwari PM, Vig K, Dennis VA, Singh SR. Functionalized gold nanoparticles and their biomedical applications. *Nanomaterials.* (2011) **1**:31–62. doi: 10.3390/nano1010031
4. Nykypanchuk D, Maye MM, van der Lelie D, Gang O. DNA-guided crystallization of colloidal nanoparticles. *Nature.* (2008) **451**:549–52. doi: 10.1038/nature06560
5. Brown R. In: Bennett JJ, Hardwicke R, editors. *The Miscellaneous Botanical Works of Robert Brown.* Vol. 1. London (1866). p. 463–86.
6. Einstein A. *Investigations on the Theory of the Brownian Movement.* New York, NY: Dover (1956).
7. Smoluchowski M. Zur kinetischen theorie der brownschen molekularbewegung und der suspensionen. *Ann Phys.* (1906) **21**:756–80.
8. Sutherland W. A dynamical theory of diffusion for non-electrolytes and the molecular mass of albumin. *Philos Mag.* (1905) **9**:781–85.
9. Odijk T. Depletion theory of protein transport in semi-dilute polymer solutions. *Biophys J.* (2000).**79**:2314–21. doi: 10.1016/S0006-3495(00)76477-0
10. Kalwarczyk T, Sozanski K, Ochab-Marcinek A, Szymanski J, Tabaka M, Hou S, et al. Motion of nanoprobes in complex liquids within the framework of the length-scale dependent viscosity model. *Adv Colloid Interface Sci.* (2015) **223**:55–63. doi: 10.1016/j.cis.2015.06.007
11. Wong IY, Gardel ML, Reichman DR, Weeks ER, Valentine MT, Bausch AR, et al. Anomalous diffusion probes microstructure dynamics of entangled F-actin networks. *Phys Rev Lett.* (2004) **92**:178101. doi: 10.1103/PhysRevLett.92.178101
12. Banks DS, Fradin C. Anomalous diffusion of proteins due to molecular crowding. *Biophys J.* (2005) **89**:2960–71. doi: 10.1529/biophysj.104.051078
13. Tuteja A, Mackay ME, Narayan S, Asokan S, Wong MS. Hydroxylated quantum dots as luminescent probes for *in situ* hybridization. *Nano Lett.* (2006) **7**:1276–81. doi: 10.1021/nl070192x

14. Saxton MJ. A biological interpretation of transient anomalous. *Biophys J.* (2007) **92**:1178–91. doi: 10.1529/biophysj.106.092619
15. Grabowski CA, Adhikary B, Mukhopadhyay A. Dynamics of gold nanoparticles in a polymer melt. *Appl Phys Lett.* (2009) **94**:021903. doi: 10.1063/1.3070533
16. Ziębacz N, Wieczorek SA, Kalwarczyk T, Fiałkowski M, Hołyst R. Crossover regime for the diffusion of nanoparticles in polyethylene glycol solutions: influence of the depletion layer. *Soft Matter.* (2011) **7**:7181–6. doi: 10.1039/C0SM01357A
17. Kohli I, Mukhopadhyay A. Diffusion of nanoparticles in semidilute polymer solutions: effect of different length scales. *Macromolecules.* (2012) **45**:6143–9. doi: 10.1021/ma301237r
18. Guo H, Bourret G, Lennox RB, Sutton M, Harden JL, Leheny RL. Entanglement-controlled subdiffusion of nanoparticles within concentrated polymer solutions. *Phys Rev Lett.* (2012) **109**:055901. doi: 10.1103/PhysRevLett.109.055901
19. Chapman CD, Lee K, Henze D, Smith DE, Robertson- Anderson RM. Onset of non-continuum effects in microrheology of entangled polymer solutions. *Macromolecules.* (2014) **47**:1181–6. doi: 10.1021/ma401615m
20. Grabowski CA, Mukhopadhyay A. Size effect of nanoparticle diffusion in a polymer melt. *Macromolecules.* (2014) **47**:7238–42. doi: 10.1021/ma501670u
21. Ganesa V, Pryamitsyn V, Surve M, Narayanan B. Noncontinuum effects in nanoparticle dynamics in polymers. *J Chem Phys.* (2006) **124**:221102. doi: 10.1063/1.2209241
22. Liu J, Cao D, Zhang L. Molecular dynamics study on nanoparticle diffusion in polymer melts: a test of the stokes Einstein law. *J Phys Chem C.* (2008) **112**:6653–661. doi: 10.1021/jp800474t
23. Kalathi JT, Yamamoto U, Grest GS, Schweizer KS, Kumar SK. Nanoparticle diffusion in polymer nanocomposites. *Phys Rev Lett.* (2014) **112**:108301. doi: 10.1103/PhysRevLett.112.108301
24. de Gennes PG. *Scaling Concepts in Polymer Physics.* Ithaca, NY: Cornel University Press (1979).
25. Rubinstein M, Colby RH. *Polymer Physics.* New York, NY: Oxford University Press (2003).
26. Gutsche C, Elmahdy MM, Kegler K, Semenov I, Stangner T, Otto O, et al. Micro-rheology on (polymer-grafted) colloids using optical tweezers. *J Phys.* (2011) **23**:184114. doi: 10.1088/0953-8984/23/18/184114
27. Tuinier R, Dhont JKG, Fan TH. How depletion affects sphere motion through solutions containing macromolecules. *Europhys Lett.* (2006) **75**:929–35. doi: 10.1209/epl/i2006-10200-0
28. Fan TH, Xie B, Tuinier R. Asymptotic analysis of tracer diffusivity in nonadsorbing polymer solutions. *Phys Rev E.* (2007) **76**:051405. doi: 10.1103/PhysRevE.76.051405
29. Fan TH, Dhont JKG, Tuinier R. Motion of a sphere through a polymer solution. *Phys Rev E.* (2007) **75**:011803. doi: 10.1103/PhysRevE.75.011803
30. Feng X, Chen A, Wang J, Zhao N, Hou Z. Understanding protein diffusion in polymer solutions: a hydration with depletion model. *J Phys Chem B.* (2016) **120**:10114–23. doi: 10.1021/acs.jpcb.6b06248
31. Tuinier R, Taniguchi T. Polymer depletion-induced slip near an interface. *J Phys.* (2005) **17**:L9–14. doi: 10.1088/0953-8984/17/2/l01
32. Wijmans CM, Zhulina EB, Fleer GJ. Effect of free polymer on the structure of a polymer brush and interaction between two polymer brushes. *Macromolecules.* (1994) **27**:3238–48. doi: 10.1021/ma00090a017
33. Maye M, Nykypanchuk D, Cuisinier M, van der Lelie D, Gang O. Stepwise surface encoding for high-throughput assembly of nanoclusters. *Nat Mater.* (2009) **8**:388–91. doi: 10.1038/nmat2421
34. Vivek MP, Steven DH. Nanoparticle assembly: DNA provides control. *Nat Mater.* (2009) **8**:346–6. doi: 10.1038/nmat2436
35. Lattuada M, Hatton TA. Synthesis, properties and applications of Janus nanoparticles. *Nano Today.* (2011) **6**:286–308. doi: 10.1016/j.nantod.2011.04.008
36. Chakrabarti R, Debnath A, Sebastian KL. Diffusion in an elastic medium: a model for macromolecule transport across the nuclear pore complex. *Phys A.* (2014) **404**:65–78. doi: 10.1016/j.physa.2014.02.059
37. Mair A, Tung C, Cacciuto A, Coluzza I. Translocation of a globular polymer through a hairy pore. *J Mol Liquids.* (2018) **265**:603–10. doi: 10.1016/j.molliq.2018.06.009
38. Chakrabarti R, Kesselheim S, Košovan P, Holm C. Tracer diffusion in a crowded cylindrical channel. *Phys Rev E.* (2013) **87**: 062709. doi: 10.1103/PhysRevE.87.062709
39. Happel J, Brenner H. *Low Reynolds Number Hydrodynamics.* The Hague: Martinus Nijhoff (1983).
40. Weissberg SG, Simha R, Rothman S. Viscosities of very dilute polymer solutions. *J Res Natl Bur Stand.* (1951) **47**:2257.
41. Fleer GJ, Skvortsov AM, Tuinier R. Mean-field equation for the depletion thickness. *Macromolecules.* (2003) **36**:7857–72. doi: 10.1021/ma0345145

Conflict of Interest Statement: The authors declare that the research was conducted in the absence of any commercial or financial relationships that could be construed as a potential conflict of interest.

frontiers in Physics

ORIGINAL RESEARCH
published: 06 September 2019
doi: 10.3389/fphy.2019.00123

Gaussian Processes in Complex Media: New Vistas on Anomalous Diffusion

Francesco Di Tullio[1,2], *Paolo Paradisi*[2,3], *Renato Spigler*[1] *and Gianni Pagnini*[2,4]*

[1] Department of Mathematics and Physics, Roma Tre University, Rome, Italy, [2] BCAM–Basque Center for Applied Mathematics, Bilbao, Spain, [3] ISTI-CNR, Institute of Information Science and Technologies "A. Faedo", Pisa, Italy, [4] Ikerbasque–Basque Foundation for Science, Bilbao, Spain

Normal or Brownian diffusion is historically identified by the linear growth in time of the variance and by a Gaussian shape of the displacement distribution. Processes departing from the at least one of the above conditions defines anomalous diffusion, thus a nonlinear growth in time of the variance and/or a non-Gaussian displacement distribution. Motivated by the idea that anomalous diffusion emerges from standard diffusion when it occurs in a complex medium, we discuss a number of anomalous diffusion models for strongly heterogeneous systems. These models are based on Gaussian processes and characterized by a population of scales, population that takes into account the medium heterogeneity. In particular, we discuss diffusion processes whose probability density function solves space- and time-fractional diffusion equations through a proper population of time-scales or a proper population of length-scales. The considered modeling approaches are: the continuous time random walk, the generalized gray Brownian motion, and the time-subordinated process. The results show that the same fractional diffusion follows from different populations when different Gaussian processes are considered. The different populations have the common feature of a large spreading in the scale values, related to power-law decay in the distribution of population itself. This suggests the key role of medium properties, embodied in the population of scales, in the determination of the proper stochastic process underlying the given heterogeneous medium.

Keywords: anomalous diffusion, fractional diffusion, complex medium, Gaussian process, heterogeneity, continuous time random walk, generalized gray Brownian motion, time-subordinated process

Edited by:
Carlos Mejía-Monasterio, Polytechnic University of Madrid, Spain

Reviewed by:
Marcin Magdziarz, Wroclaw University of Science and Technology, Poland
Allbens Picardi Faria Atman, Federal Center for Technological Education of Minas Gerais, Brazil

***Correspondence:**
Gianni Pagnini
gpagnini@bcamath.org

Specialty section:
This article was submitted to Interdisciplinary Physics, a section of the journal Frontiers in Physics

Received: *01 June 2019*
Accepted: *14 August 2019*
Published: *06 September 2019*

Citation:
Di Tullio F, Paradisi P, Spigler R and Pagnini G (2019) Gaussian Processes in Complex Media: New Vistas on Anomalous Diffusion. Front. Phys. 7:123. doi: 10.3389/fphy.2019.00123

1. INTRODUCTION

Normal diffusion has been widely investigated by means of different modeling approaches, such as:

conservation of mass, constitutive laws, random walks based on central limit theorem (CLT), stochastic models, i.e., Wiener process, Langevin equation, Fokker–Planck equation, and other Markovian Master equations [1–3]. The adjective *normal* highlights that a Gaussian-based process is considered.

However, many natural phenomena show a diffusive behavior that cannot be modeled by classical methods based on the CLT or linear and/or local constitutive laws. This is a ubiquitous observation in life sciences, soft condensed matter, geophysics and ecology, among others. These phenomena are generally labeled with the term *anomalous diffusion* in order to distinguish them from normal diffusion. In this last case, when assumptions of the CLT are satisfied, i.e., independence of random variables and finiteness of variances, the mean square displacement (MSD) of diffusing particles increases linearly in time. Conversely, departures from the CLT determine the emergence of anomalous diffusion. There are numerous experimental measurements in which the MSD scales with a non-linear power-law in time. These processes are successfully modeled through Fractional Calculus (see, e.g., [4–6]), so that the corresponding processes are referred to as *Fractional Diffusion* [7–16].

Anomalous diffusion is ubiquitously observed in many complex systems, ranging from turbulence [17, 18], plasma physics [19, 20] to soft matter, e.g., the cell cytoplasm, membrane, and nucleus [21–30] and neuro-physiological systems [31, 32]. In particular, the analysis of highly accurate data of single particle tracking (SPT), which are nowadays available thanks to the great instrumental advancement in fluorescence-based microscopy [33], has allowed to reveal the clear emergence of anomalous diffusion in many biological systems [27, 34–37].

As a consequence, the debate on the understanding of the most suitable microscopic model explaining the observed statistical features of SPT has taken momentum in the scientific community. The emergence of long-range correlations and anomalous diffusion asks for stochastic models departing from the classical Brownian motion based on the Gaussian-Wiener process and the standard random walk [1, 3]. At first, the main debate has been focused on whether the best stochastic approach should be one based on time-continuous trajectories, i.e., fractional Brownian motion (FBM), or to discontinuous trajectories characterized by jump events, i.e., continuous time random walk (CTRW) (see, e.g., [38] for a short discussion). However, both stochastic models, FBM and CTRW, do not describe the observed features of the SPT data. As a consequence, this implies that the above two minimal models (FBM and CTRW) do not take into account some microscopic dynamics affecting the particle motion and determining the emergence of long-range correlations, anomalous diffusion, non-Gaussian power-law distributions, ergodicity breaking, and aging [38].

For this reason, the scientific community is now focusing on the role of the system's heterogeneity, which was at first neglected in the above mentioned modeling approaches. Superstatistics [39–43] is probably the first model where heterogeneity is taken into account through a time modulation of a fast relaxing variable by a slow, adiabatic, variable. Many authors follow the main idea of superstatistics, developing stochastic models that try to go beyond superstatistics itself. This is obtained by developing an explicit stochastic dynamics for the adiabatic modulating variables characterizing the superstatistical models [44, 45]. Along this line, an interesting approach is the recently proposed diffusing diffusivity model (DDM) [46–50]. Approaches similar to superstatistics have also been proposed to model the inter-event times in point processes [51–54], which describe the intermittent events at the basis of event-driven diffusion processes, e.g., CTRWs where the inter-event time distribution is modulated by an external perturbation [41, 54, 55].

Other authors follow a somewhat different approach based on random-scaled Gaussian processes (RSGPs) [38, 56–59], which are physically based on a recently proposed model where inter-particle heterogeneity is explicity described through a population of scales characterizing the dynamical parameters of particle diffusive motion. This modeling approach has been denoted as heterogeneous ensemble of Brownian particles (HEBP) and has been developed on the basis of a Langevin model [57–59]. The HEBP model is then based on the Gaussian-Wiener process and, thus, on trajectories that are strongly continuous in the stochastic sense [60], while anomalous diffusion emerge as a consequence of heterogeneity. Fractional diffusion can be also interpreted as a consequence of complex heterogeneity in the underlying medium, where a classical diffusion takes place for the single particle. According to this approach, fractional diffusion emerges from the population of scales characterizing the medium. Interestingly, for a given stationary Gaussian process, the displacement distribution is uniquely related to the distribution of scales in the considered population. Thus, the observed diffusion properties can be used to guess the properties of the underlying diffusing medium.

All the above mentioned stochastic models where fractional diffusion follows from medium heterogeneity are essentially based on processes with continuous trajectories. Conversely, sudden transition events play a crucial role in the diffusing dynamics in many complex systems. Further, the role of microscopic models with smooth trajectories (Gaussian-based processes) and of event-based models with discontinuous trajectories in biological diffusion is not yet clear.

For this reason, we here propose, discuss, and review different models based on different Gaussian processes, whose parameters are characterized by a population of time or length scales. These models include stochastic processes with both time-continuous single particle trajectories and discontinuous trajectories with crucial jump events. We show that proper choices of the populations lead to space- or time-fractional diffusion. In this paper we propose and discuss a further development of the Master thesis by FDT [61].

The paper is organized as follows. In section 6 we propose and discuss two different Markovian CTRWs with population of time or length scales. In sections 3 and 4 we discuss RSGPs and subordination processes, respectively. Finally, in section 5 we give a brief discussion and draw some conclusions.

2. CONTINUOUS TIME RANDOM WALK (CTRW)

2.1. The Approach of Continuous Time Random Walk to Study Diffusion Processes

2.1.1. Basic Formulation of the CTRW

For the purposes of the present paper we briefly report some fundamentals on the CTRW. It is well-known that the CTRW is a successful approach to study diffusion processes. It considers the trajectories of discrete particles within a discrete space, according to the original formulation [7, 62, 63], or within a continuous underlying space, according to more recent studies [64, 65].

The trajectory of each particle is considered to be governed by the joint probability density function (PDF) $\varphi(\delta r, \delta t)$ of making a jump of length δr in the time interval δt. If the particle is located in r' at time t' and the position r is the particle position after a inter-event time (IET) δt, then: $r = r' + \delta r$, and $t = t' + \delta t$. The times t and t' are occurrence times of crucial jump events. In the basic theory of CTRW, these events are mutually independent and, thus, the IETs are statistically independent random variables whose features are described in the framework of renewal theory [51–54]. The marginal jump PDF $\lambda(\delta r)$ and the marginal waiting-time PDF $\psi(\tau)$ are, respectively

$$\lambda(\delta r) = \int_0^\infty \varphi(\delta r, \tau)\, d\tau\,, \qquad \psi(\tau) = \sum_{\delta r} \varphi(\delta r, \tau)\,. \tag{1}$$

The integral $\int_0^\tau \psi(\xi)\, d\xi$ is the probability that at least one step is made $(0,\tau)$ [64, 66]. Therefore, the probability that a given waiting time between two consecutive jumps is greater or equal to τ is:

$$\Psi(\tau) = 1 - \int_0^\tau \psi(\xi)\, d\xi = \int_\tau^\infty \psi(\xi)\, d\xi\,, \tag{2}$$

and upon differentiation: [64, 66]

$$\frac{d\Psi}{d\tau} = \frac{d}{d\tau}\left(1 - \int_0^\tau \psi(\xi)\, d\xi\right) = -\psi(\tau)\,. \tag{3}$$

Following Klafter et al. [62], the PDF $\eta(r,t)$ for a particle to arriving in r in the time interval from t to $t + \delta t$ is

$$\eta(r,t) = \sum_{r'} \int_0^t \eta(r',t')\varphi(r - r', t - t')\, dt' + \delta(t)\delta(r)\,, \tag{4}$$

where the initial condition is stated at $t = 0$ in $r = 0$. Hence, the PDF for a particle to be in r at time t is [62, 63]

$$p(r,t) = \int_0^t \eta(r, t - t')\Psi(t')\, dt' = \int_0^t \eta(r,\zeta)\Psi(t - \zeta)\, d\zeta\,. \tag{5}$$

Finally, by using (4), the PDF $p(r,t)$ is given by the following integral equation [62]

$$\begin{aligned} p(r;t) &= \delta(r)\Psi(t) + \sum_{r'} \int_0^t \int_0^\tau \eta(r', \tau - t')\varphi(r - r', t - \tau)\Psi(t')\, dt' d\tau \\ &= \delta(r)\Psi(t) + \sum_{r'} \int_0^t p(r',\tau)\varphi(r - r', t - \tau)\, d\tau\,. \end{aligned} \tag{6}$$

2.1.2. The Uncoupled Case and the Memory Effects

The simplest case of the CTRW modeling is the uncoupled case, i.e., the case when the jumps and the waiting times are statistically independent and it holds $\varphi(\delta r, \tau) = \lambda(\delta r)\psi(\tau)$. In this case Equation (6) can be re-arranged as [7]

$$p(r,t) = \delta(r)\Psi(t) + \int_0^t \psi(t - \tau) \sum_{r'} \lambda(r - r')p(r',\tau)\, d\tau\,. \tag{7}$$

For our purposes we rewrite Equation (7) in the Fourier–Laplace domain. The standard Laplace and Fourier transforms for sufficiently well-behaved functions are, respectively

$$\widetilde{g}(s) = \int_0^\infty \mathrm{e}^{-st} g(t)\, dt\,, \quad \widehat{f}(k) = \sum_r \mathrm{e}^{i\,k\cdot r} f(r)\,. \tag{8}$$

Then the Laplace transform of formula (6) is

$$\widetilde{p}(r,s) = \frac{1 - \widetilde{\psi}(s)}{s} + \widetilde{\psi}(s) \sum_{r'} \lambda(r - r')\widetilde{p}(r',s)\,. \tag{9}$$

Now, after Fourier transform, we have that the Fourier–Laplace transform of the solution of (6) is

$$\widehat{\widetilde{p}}(k,s) = \frac{1 - \widetilde{\psi}(s)}{s} + \widetilde{\psi}(s)\widehat{\lambda}(k)\widehat{\widetilde{p}}(k,s)\,, \tag{10}$$

and then, after re-arrangement, the above equation becomes

$$\widehat{\widetilde{p}}(k,s) = \frac{1 - \widetilde{\psi}(s)}{s\,[1 - \widehat{\lambda}(k)\widetilde{\psi}(s)]}\,. \tag{11}$$

According to Mainardi et al. [64], formula (11) can be written in the alternative form

$$\widetilde{\Phi}(s)\left[s\,\widehat{\widetilde{p}}(k,s) - 1\right] = \left[\widehat{\lambda}(k) - 1\right]\widehat{\widetilde{p}}(k,s)\,, \tag{12}$$

where

$$\widetilde{\Phi}(s) = \frac{1 - \widetilde{\psi}(s)}{s\,\widetilde{\psi}(s)} = \frac{\widetilde{\Psi}(s)}{\widetilde{\psi}(s)} = \frac{\widetilde{\Psi}(s)}{1 - s\,\widetilde{\Psi}(s)}\,. \tag{13}$$

After Fourier–Laplace anti-transforming, relation (12) gives

$$\int_0^t \Phi(t - \tau)\frac{\partial p}{\partial \tau}\, d\tau = -p(r,t) + \sum_{r'} \lambda(r - r')p(r',t)\,, \tag{14}$$

where it is evident the memory effect due to the auxiliary function $\Phi(\tau)$.

2.1.3. The Markovian CTRW Model

A Markovian model is obtained from (14) when $\Phi(\tau) = \delta(\tau)$. This implies that $\widetilde{\Phi}(s) = 1$ and, from the second equality in (13), it holds $\widetilde{\Psi}(s) = \widetilde{\psi}(s)$ and $\Psi(\tau) = \psi(\tau)$. The functions $\Psi(\tau)$ and $\psi(\tau)$ are related by (3), then a CTRW model is Markovian if

$$\Psi(\tau) = \mathrm{e}^{-\tau}\,, \tag{15}$$

and the resulting Markovian master equation is

$$\frac{\partial p}{\partial t} = -p(r,t) + \sum_{r'} \lambda(r - r')p(r',t)\,, \quad p(r,0) = \delta(r)\,. \tag{16}$$

On the contrary, when $\Psi(\tau)$ is not an exponential function the resulting CTRW model is non-Markovian.

2.2. Markovian CTRW Model With a Population of Time-Scales

Let the functions $\lambda_n(\delta r)$ and $\psi_n(\tau)$ be the n-fold convolutions of the jump and of the waiting-time PDFs, respectively. The most general solution of (6) can be written as [63, 65]

$$p(r,t) = \sum_{n=0}^{\infty} P(n,t)\lambda_n(r)\,, \tag{17}$$

where $P(n,t)$ is the probability of n jumps occurring up to time t:

$$P(n,t) = \int_0^t \psi_n(t-\tau)\Psi(\tau)\,d\tau\,. \tag{18}$$

In particular, since $\Psi(\tau)$ is, by definition, the probability that the particle remains fixed $(0,\tau)$, then it holds $\psi_0(\tau) = \delta(\tau)$ and [63]

$$P(0,t) = \int_0^t \delta(\tau)\Psi(\tau)\,d\tau = \Psi(t)\,. \tag{19}$$

Let us consider a heterogeneous condition. Hence, for any Markovian trajectory, the waiting-time τ is scaled by a proper timescale T. This timescale is taken to be a random variable following a proper distribution. In particular, the survival probability $\Psi(\tau)$ for each single Markovian trajectory is:

$$\Psi_M(\tau/T) = \mathrm{e}^{-\tau/T}\,, \tag{20}$$

where the index M has been added to remark that it is the survival probability corresponding to the Markovian case. In this case the random walk goes on according to the standard iteration procedure with the same meaning for the symbols, but the random waiting time τ is driven by the rescaled PDF $\psi(\tau)$. The characteristic function of the particle PDF turns out to be

$$\widehat{p}(k,t/T_0) = \int_0^{\infty} \widehat{p}_M(k,t/T)f(T/T_0,t)\,dT/T_0\,, \tag{21}$$

where $p_M(r,t)$ refers to the Markovian PDF, and $f(T/T_0,t)/T_0$ is the distribution of the random timescale T such that $\int_0^{\infty} f(T/T_0,t)\,dT/T_0 = 1$ and T_0 is the effective observed timescale. The single timescale case is recovered when $f(T/T_0,t)/T_0 = \delta(T-T_0)$.

Hence, by Fourier inversion and by using formula (17) for the Markovian PDF $p_M(r,t)$, it follows

$$p(r,t/T_0) = \sum_{n=0}^{\infty}\left[\int_0^{\infty} P_M(n,t/T_0)f(T/T_0,t)\,dT/T_0\right]\lambda_n(r)\,. \tag{22}$$

To conclude, the combination of (17) and (22) gives

$$P(n,t/T_0) = \int_0^{\infty} P_M(n,t/T)f(T/T_0,t)\,dT/T_0\,, \tag{23}$$

and setting $n=0$ it holds the following

$$\begin{aligned} P(0,t/T_0) &= \int_0^{\infty} P_M(0,t/T)f(T/T_0,t)\,dT/T_0 \\ &= \int_0^{\infty}\int_0^t \psi_0(t-\tau)\Psi_M(t/T)d\tau f(T/T_0,t)\,dT/T_0 \\ &= \int_0^{\infty}\int_0^t \delta_0(t-\tau)\Psi_M(t/T)d\tau f(T/T_0,t)\,dT/T_0 \\ &= \int_0^{\infty} \Psi_M(t/T)f(T/T_0,t)\,dT/T_0 = \Psi(t/T_0)\,. \end{aligned} \tag{24}$$

Let hereinafter be $T_0 = 1$ for simplicity. In their pioneering work [7], derived the following fundamental result:
if the survival probability $\Psi(\tau)$ is a function of the Mittag–Leffler type, i.e.

$$\Psi(\tau) = E_\beta(-\tau^\beta) = \sum_{n=0}^{\infty}\frac{(-1)^n\tau^{\beta n}}{\Gamma(\beta n+1)}\,, \quad 0<\beta<1\,, \tag{25}$$

the particle PDF $p(r;t)$ solves the time-fractional diffusion equation, i.e., equation (A.1) with $\alpha = 2$. Therefore, from (24) and (25) it follows that, for any T-distribution $f(T,t)$ such that the following integral holds

$$\int_0^{\infty} \mathrm{e}^{-t/T} f(T,t)\,dT = E_\beta(-t^\beta)\,, \quad 0<\beta<1\,, \tag{26}$$

the resulting process is a time-fractional diffusion process.

In particular, in the *stationary* case there is a unique the time-scale distribution, i.e., $f(T,t) = f_S(T)$. In fact, it is well-known that it holds [6]

$$\int_0^{\infty} \mathrm{e}^{-ty} K_\beta(y)\,dy = E_\beta(-t^\beta)\,, \quad 0<\beta<1\,, \tag{27}$$

where

$$K_\beta(y) = \frac{1}{\pi}\frac{y^{\beta-1}\sin(\beta\pi)}{1+2y^\beta\cos(\beta\pi)+y^{2\beta}}\,, \tag{28}$$

and, by comparing of (26) and (27), the *stationary* timescale distribution $f_S(T)$ turns out to be [67]

$$f_S(T) = \frac{1}{T^2}K_\beta\left(\frac{1}{T}\right)\,. \tag{29}$$

It is worth noting that the K_β, defined in (28), is the fundamental solution of the space-time fractional diffusion equation (A.1) when space and time fractional orders of derivation are equal each other and equal to β and when the asymmetry parameter assumes the extremal value, in which case the distribution has support solely on the positive real axis [11]. This case is also known as neutral diffusion [68, 69]. In the Markovian limit, i.e., $\beta = 1$, it holds $K_\beta(y) = \sin\pi/[\pi\,(y-1)^2] \to \delta(y-1)$ and a single timescale follows.

Concerning the waiting time PDF $\psi(t)$, we observe that, from formula (24) for the survival probability $\Psi(t)$ and from (3), we have

$$\psi(t) = -\frac{d\Psi(t)}{dt} = -\frac{d}{dt}\left(\int_0^\infty \Psi_M(t/T) f_s(T) dT\right). \tag{30}$$

By the fact that the involved functions are the exponential function Ψ_M and the normalized distribution $f_S(T)$, the following equality holds

$$\frac{d}{dt}\left(\int_0^\infty \Psi_M(t/T) f_S(T)\, dT\right) = \int_0^\infty \frac{d}{dt}\Psi_M(t/T) f_S(T)\, dT\,. \tag{31}$$

Finally, we can write the rescaled PDF $\psi(t)$ as.

$$\begin{aligned}\psi(t) &= -\frac{d\Psi(t)}{dt} = -\frac{d}{dt}\left(\int_0^\infty \Psi_M(t/T) f_S(T)\, dT\right)\\ &= -\int_0^\infty \frac{d}{dt}\Psi_M(t/T) f_S(T)\, dT = -\int_0^\infty \frac{d}{dt}\mathrm{e}^{-t/T} f_S(T)\, dT\\ &= \int_0^\infty \frac{1}{T}\mathrm{e}^{-t/T} f_S(T)\, dT\\ &= \int_0^\infty \Psi_M(t/T) f_S(T)\, \frac{dT}{T}\,. \end{aligned} \tag{32}$$

2.3. Markovian CTRW Model With a Population of Length-Scales

In this section we consider the case of a Markovian CTRW model with a population of length-scales. Hence, the space variable r is scaled by a proper distributed length-scale ℓ and the ratio r/ℓ is a distributed variable because ℓ is a distributed variable. The characteristic function of the particle PDF turns out to be

$$\widehat{p}(k/\ell_0, t) = \int_0^\infty \widehat{p}_G(k\ell, t) q(\ell/\ell_0)\, d\ell/\ell_0\,, \tag{33}$$

where $p_G(r, t)$ is the PDF of the Gaussian CTRW model and $q(\ell/\ell_0)/\ell_0$ is the distribution of the length-scale ℓ such that

$$\int_0^\infty q(\ell/\ell_0)\, d\ell/\ell_0 = 1\,, \tag{34}$$

and ℓ_0 is the effective observed length-scale. The case with a single length-scale is recovered when $q(\ell/\ell_0)/\ell_0 = \delta(\ell - \ell_0)$. Hereinafter we consider $\ell_0 = 1$.

Let the jump PDF be

$$\lambda(r - r') = \frac{\partial}{\partial r}\Lambda(r - r')\,, \tag{35}$$

where $\Lambda(r - r')$ is the cumulative distribution function of jumps, then we have

$$\Lambda(r - r') = \int_0^\infty \Lambda_G\left(\frac{r - r'}{\ell}\right) q(\ell)\, d\ell\,, \tag{36}$$

where $q(\ell)$ is the distribution of the length-scale and $\Lambda_G(r - r')$ is the cumulative distribution function of Gaussian jumps. Assuming $q(\ell)$ such that $\Lambda_G((r - r')/\ell)q(\ell)$ is integrable and differentiable and it holds $\left|\frac{\partial}{\partial r}\Lambda_G((r - r')/\ell)q(\ell)/\ell\right| \le g(\ell)$, with $g(\ell)$ integrable, then we have

$$\begin{aligned}\lambda(r - r') &= \frac{\partial}{\partial r}\Lambda(r - r') = \int_0^\infty \frac{\partial}{\partial r}\Lambda_G\left(\frac{r - r'}{\ell}\right) q(\ell)\, d\ell\\ &= \int_0^\infty \lambda_G\left(\frac{r - r'}{\ell}\right) q(\ell)\, \frac{d\ell}{\ell}\,. \end{aligned} \tag{37}$$

The PDF $p(r;\, t)$ of the process under consideration results to be

$$\begin{aligned}p(r;\, t) &= \delta(r)\Psi(t) + \sum_{r'} \int_0^t p(r', \tau)\lambda(r - r')\psi_M(t - \tau)\, d\tau\\ &= \delta(r)\Psi(t) + \sum_{r'} \int_0^t p(r', \tau)\left[\int_0^\infty \lambda_G\left(\frac{r - r'}{\ell}\right)\frac{q(\ell)}{\ell} d\ell\right]\psi_M(t - \tau)\, d\tau\,. \end{aligned} \tag{38}$$

Now, we want to find an explicit formula for $q(\ell)$ and we proceed considering the Fourier transform of the above equation, i.e.,

$$\widehat{p}(k, t) = \Psi_M(t) + \int_0^t \widehat{p}(k, \tau)\widehat{\lambda}(k)\psi_M(t - \tau)\, d\tau\,, \tag{39}$$

or analogously

$$\widehat{p}(k, t) = \Psi(t) + \int_0^t \widehat{p}(k, \tau)\left[\int_0^\infty \widehat{\lambda}_G(k\ell)\, q(\ell)\, d\ell\right]\psi_M(t - \tau)\, d\tau\,. \tag{40}$$

Reminding that in the Markovian case the survival probability is $\Psi_M(t) = \mathrm{e}^{-t}$ and the waiting time PDF $\psi(t) = \mathrm{e}^{-t}$, Equation (40) becomes

$$\widehat{p}(k, t) = \mathrm{e}^{-t} + \widehat{\lambda}(k)\mathrm{e}^{-t}\int_0^t \mathrm{e}^{\tau}\widehat{p}(k, \tau)\, d\tau\,, \tag{41}$$

and the following relation holds

$$\widehat{\lambda}(k) = \frac{\widehat{p}(k, t) - \mathrm{e}^{-t}}{\mathrm{e}^{-t}\displaystyle\int_0^t \mathrm{e}^{\tau}\widehat{p}(k, \tau)\, d\tau}\,. \tag{42}$$

Considering Equation (11) in the Markovian case (that is $\beta = 1$), we have

$$\widehat{\widetilde{p}}(k, s) = \frac{1}{1 + s - \widehat{\lambda}(k)}\,, \tag{43}$$

and after Laplace anti-transforming we obtain

$$\widehat{p}(k, t) = \mathrm{e}^{-(1 - \widehat{\lambda}(k))t}\,, \tag{44}$$

that is the general expression for $\widehat{p}(k, t)$. Since $|\widehat{\lambda_G}(k)| \le 1$ from the proprieties of characteristic functions, then also $|\widehat{\lambda}(k)| \le 1$, i.e.,

$$|\widehat{\lambda}(k)| \le \int_0^\infty |\widehat{\lambda}_G(k)| q(\ell)\, d\ell \le \int_0^\infty q(\ell)\, d\ell = 1\,. \tag{45}$$

Hence, the above general representation of $\widehat{p}(k,t)$ shows that $\widehat{p}(k,t)$ is a characteristic function for all $t \in \mathbb{R}^+$ and $k \in \mathbb{R}$ because it holds

$$\mathrm{e}^{-(1-\widehat{\lambda}(k))t} \le 1\,. \tag{46}$$

The explicit expression of $\widehat{\lambda}(k)$ can also be obtained. We know that the Gaussian density for jumps λ_G comes from an unbiased random walk in one-dimension. In this random walk, a particle starts from the origin and, at each time step Δt, makes a jump $\pm\Delta x$ to the left or the right with equal probability. We call $P_{h,n}$ the probability that the particle will be in point $x = h\sigma_G$ at the time $t = n\Delta t$. In this simple case we have

$$P_{h,n} = \frac{1}{2}P_{h-1,n-1} + \frac{1}{2}P_{h+1,n-1}\,, \tag{47}$$

assuming $P_{0,0} = 1$. The characteristic function for this binomial formulation is

$$\widehat{\lambda}_G(k) = \sum_{h=-n}^{n} \mathcal{P}(X = \sigma_G\, h)\, \mathrm{e}^{ik\sigma_G h}\,, \tag{48}$$

that n even becomes

$$\begin{aligned}
\widehat{\lambda}_G(k) &= \sum_{h=-\frac{n}{2}}^{n/2} \mathcal{P}(X = \sigma_G\, 2h)\mathrm{e}^{ik\sigma_G 2h} \\
&= \sum_{h=-\frac{n}{2}}^{n/2} \frac{n!}{\left(\frac{n+2h}{2}\right)!\left(\frac{n-2h}{2}\right)!}\left(\frac{1}{2}\right)^{\frac{n+2h}{2}}\left(\frac{1}{2}\right)^{\frac{n-2h}{2}} \mathrm{e}^{ik\sigma_G 2h} \\
&= \frac{1}{2^n}\sum_{h=-\frac{n}{2}}^{n/2}\binom{n}{\frac{n+2h}{2}}\mathrm{e}^{ik\sigma_G 2h} = \frac{1}{2^n}\sum_{k=0}^{n}\binom{n}{k}\mathrm{e}^{ik\sigma_G(2k-n)} \\
&= \frac{1}{2^n}\sum_{k=0}^{n}\binom{n}{k}\mathrm{e}^{ik\sigma_G k}\mathrm{e}^{-ik\sigma_G(n-k)} = \left(\frac{\mathrm{e}^{ik\sigma_G} + \mathrm{e}^{-ik\sigma_G}}{2}\right)^n \\
&= \cos(\sigma_G k)^n\,.
\end{aligned} \tag{49}$$

Finally, the characteristic function $\widehat{\lambda}(k)$ turns out to be.

$$\widehat{\lambda}(k) = \int_0^\infty \cos(\sigma_G k\ell)q(\ell)\,d\ell = \int_0^\infty \cos(k\ell)\frac{1}{\sigma_G}q\left(\frac{\ell}{\sigma_G}\right)d\ell\,. \tag{50}$$

2.3.1. Comparison With the Green Function of the Space-Fractional Diffusion Equation

We recall that the Fourier transform of the Lévy stable density $L_\alpha^0(x;t)$ that solves the space-fractional diffusion equation, i.e., Equation (A.1) with $\beta = 1$, is

$$\begin{aligned}
\widehat{L}_\alpha^0(kt^{1/\alpha}) &= \int_{-\infty}^{\infty} \mathrm{e}^{ikt^{1/\alpha}\zeta} L_\alpha^0(\zeta)\,d\zeta \\
&= 2\int_0^\infty \cos(kt^{1/\alpha}\zeta)L_\alpha^0(\zeta)\,d\zeta = \mathrm{e}^{-|k|^\alpha t}\,.
\end{aligned} \tag{51}$$

If we compare the above relation with Equation (50), we obtain also the following consistent pair $\widehat{\lambda}(k)$ and $q(\ell)$:

$$\widehat{\lambda}(k) = \widehat{L}_\alpha^0(k)\,, \quad \frac{1}{\sigma_G}q\left(\frac{\ell}{\sigma_G}\right) = 2L_\alpha^0(\ell)\,. \tag{52}$$

Moreover, this choice is consistent also with the proprieties of unitary initial value for the characteristic function and of normalization for the PDF, i.e.,

$$\widehat{\lambda}(k)\bigg|_{k=0} = \mathrm{e}^{-|k|^\alpha}\bigg|_{k=0} = 1\,, \tag{53}$$

and

$$\begin{aligned}
\widehat{\lambda}(k)\bigg|_{k=0} &= \int_0^\infty \cos(\sigma_G k\ell)q(\ell)d\ell\bigg|_{k=0} = \int_0^\infty q(\ell)d\ell \\
&= \int_0^\infty \cos(k\ell)\frac{1}{\sigma_G}q\left(\frac{\ell}{\sigma_G}\right)d\ell\bigg|_{k=0} = \int_0^\infty \frac{1}{\sigma_G}q\left(\frac{\ell}{\sigma_G}\right)d\ell \\
&= 2\int_0^\infty L_\alpha^0(x) = \int_{-\infty}^{\infty} L_\alpha^0(x) = 1\,.
\end{aligned} \tag{54}$$

In general for $k \in \mathbb{R}$ it holds

$$\begin{aligned}
\widehat{p}(k,t) &= \mathrm{e}^{-(1-\widehat{\lambda}(k))t} = \mathrm{e}^{-(1-\mathrm{e}^{-|k|^\alpha})t} \\
&= \exp\left\{t\sum_{n=1}^{\infty}\frac{(-1)^n}{n!}|k|^{\alpha n}\right\} = \prod_{n=1}^{\infty}\mathrm{e}^{\frac{(-1)^n}{n!}|k|^{\alpha n}t}\,.
\end{aligned} \tag{55}$$

In the limit $|k| \ll 1$ the characteristic function $\widehat{p}(k,t)$ results to be

$$\begin{aligned}
\widehat{p}(k,t) &= \mathrm{e}^{-(1-\widehat{\lambda}(k))t} \\
&= \mathrm{e}^{-(|k|^\alpha - \frac{|k|^{2\alpha}}{2} + \frac{|k|^{3\alpha}}{6} + \ldots)t} \simeq \mathrm{e}^{-|k|^\alpha t}(1 + O(t|k|^{2\alpha})).
\end{aligned} \tag{56}$$

Then, for $|k| \ll 1$, it holds

$$\widehat{p}(k;t) \simeq \widehat{L}_\alpha^0(kt^{1/\alpha}). \tag{57}$$

Hence the characteristic function of the considered process is a Lévy stable density, that is the fundamental solution of the space-fractional diffusion equation. To conclude, since a characteristic function corresponds to a unique distribution and *vice versa*, in the considered limit ($k \ll 1$) the PDF $p(r - r'; t)$ is a Lévy stable density.

3. RANDOMLY-SCALED GAUSSIAN PROCESSES

Let us denote a randomly-scaled Gaussian process (RSGP) as a stochastic process defined by the product of a Gaussian process times a non-negative random variable. In general, the one-point one-time PDF is not sufficient to characterize a stochastic process. There are infinitely many stochastic processes that follow the same one-dimensional distribution and, thus, solve the same Cauchy problem for the associated diffusion/master equation describing the time evolution of the PDF. However, in RSGPs, this indeterminacy is solved by the choice of the Gaussian process that is fully characterized for given first and second moments.

In this paper we consider a special class of RSGPs called generalized gray Brownian motion (ggBm), that is defined by using the fractional Brownian motion as Gaussian process [70–75]. For other form of randomly-scaled Gaussian process we refer the reader to Sliusarenko et al. [59]. Hence, we consider the following class of processes:

$$X_{\alpha,\beta}(t) = \ell\, B^H(t)\,, \quad 0 < \beta \le 1\,, \quad 0 < \alpha \le 2\,, \tag{58}$$

where $B^H(t)$ is the fBm process with Hurst exponent $0 < H < 1$, and then with power law variance t^{2H}.

The application of this approach to fractional diffusion is based on the correspondence of the PDFs resulting from the product of two independent random variables with the PDFs resulting from the integral representation formula (A.10).

Let define Z_1 and Z_2 as two real independent random variables: $z_1 \in \mathbb{R}$ and $z_2 \in \mathbb{R}^+$. The associated PDFs are $p_1(z_1)$ and $p_2(z_2)$, respectively. Let Z be the random variable obtained by the product of Z_1 and Z_2^γ, i.e., $Z = Z_1 Z_2^\gamma$. Denoting with $p(z)$ the PDF of Z, it results:

$$p(z) = \int_0^\infty p_1\left(\frac{z}{\lambda^\gamma}\right) p_2(\lambda)\, \frac{d\lambda}{\lambda^\gamma}\,. \tag{59}$$

Comparing the above formula with the integral representation formula (A.10), and applying the change of variables $z = xt^{-\gamma\omega}$ and $\lambda = \tau t^{-\omega}$, the integral representation (71) is recovered from (59) by setting:

$$\begin{aligned} &\frac{1}{t^{\gamma\omega}} p \left(\frac{x}{t^{\gamma\omega}}\right) \equiv p(x;t)\,, \quad \frac{1}{\tau^\gamma} p_1\left(\frac{x}{\tau^\gamma}\right) \equiv \psi(x;\tau)\\ &\frac{1}{t^\omega} p_2 \left(\frac{\tau}{t^\omega}\right) \equiv \varphi(\tau;t)\,. \end{aligned} \tag{60}$$

Then, by identifying functions and parameters as

$$p(z) \equiv K^0_{\alpha,\beta}(z)\,, \qquad p_1(z_1) \equiv G(z_1)\,, \qquad p_2(z_2) \equiv K^{-\alpha/2}_{\alpha/2,\beta}(z_2)\,, \tag{61}$$

$$\gamma = \frac{1}{2}\,, \qquad \omega = \frac{2\beta}{\alpha}\,, \qquad \gamma\omega = \frac{\beta}{\alpha}\,, \tag{62}$$

formula (59) reduces to the integral formula (A.10) for the symmetric space-time fractional diffusion equation. In terms of random variables it follows that [56]

$$Z = Xt^{-\beta/\alpha} \quad \text{and} \quad Z = Z_1 Z_2^{1/2}\,, \tag{63}$$

hence it holds

$$X = Zt^{\beta/\alpha} = Z_1 t^{\beta/\alpha} Z_2^{1/2}\,. \tag{64}$$

Since $p_1(z_1) \equiv G(z_1)$, Z_1 is a Gaussian random variable. Consequently, the variable $Z_1 t^{\beta/\alpha}$ is Gaussian with variance proportional to $t^{2\beta/\alpha}$. Hence, we chose the fBm with $0 < H = \beta/\alpha < 1$ as a Gaussian process with consistent power law variance. Furthermore, the random variable $Z_2 = \Lambda_{\alpha/2,\beta}$ is distributed according to $p_2(z_2) \equiv K^{-\alpha/2}_{\alpha/2,\beta}(z_2)$. Finally, we have the process

$$\begin{aligned} &X_{\alpha,\beta}(t) = \sqrt{\Lambda_{\alpha/2,\beta}}\, B^H(t)\,, \quad 0 < \beta < 1\,, \quad 0 < \alpha < 2\,,\\ &0 < H = \beta/\alpha < 1\,. \end{aligned} \tag{65}$$

where $\ell = \sqrt{\Lambda_{\alpha/2,\beta}}$ is an independent constant non-negative random variable distributed according to the PDF $K^{-\alpha/2}_{\alpha/2,\beta}(\lambda)$, $\lambda \ge 0$, that is a special case of (A.7). The process defined above is the solution of the space-time fractional diffusion Equation (A.1) in the symmetric case. This means that the one-time one-point PDF of $X_{\alpha,\beta}(t)$ is the fundamental solution of Equation (A.1) in the symmetric case, namely the PDF $K^0_{\alpha,\beta}(x;t)$ defined in (A.10).

The space-fractional diffusion is recovered when $\beta = 1$, in fact by using formula (A.7) with $t = 1$, we have

$$\begin{aligned} K^{-\alpha/2}_{\alpha/2,1}(\lambda) &= \int_0^\infty M_1(\tau) L^{-\alpha/2}_{\alpha/2}(\lambda;\tau)\; d\tau\\ &= \int_0^\infty \delta(1-\tau) L^{-\alpha/2}_{\alpha/2}(\lambda;\tau)\, d\tau = L^{-\alpha/2}_{\alpha/2}(\lambda)\,. \end{aligned} \tag{66}$$

Here we are interested in the distribution of $\ell = \sqrt{\Lambda_{\alpha/2,1}}$ then, by normalization condition, the PDF of ℓ results to be

$$q(\ell) = 2\ell L^{-\alpha/2}_{\alpha/2}(\ell^2)\,. \tag{67}$$

Analogously, the time-fractional diffusion is recovered when $\alpha = 2$, in fact by using formula (A.7) with $t = 1$, we have

$$\begin{aligned} K^{-1}_{1,\beta}(\lambda) &= \int_0^\infty M_\beta(\tau) L^{-1}_1(\lambda;\tau)\; d\tau\\ &= \int_0^\infty M_\beta(\tau)\delta(\lambda-\tau)\, d\tau = M_\beta(\lambda)\,, \end{aligned} \tag{68}$$

and the corresponding PDF of ℓ is

$$q(\ell) = 2\ell M_\beta(\ell^2)\,. \tag{69}$$

4. TIME-SUBORDINATION FOR GAUSSIAN PROCESSES

Another approach proposed to model the emergence of fractional and, more in general, anomalous diffusion in complex media is the time-subordination of a otherwise standard diffusion process (see, e.g., [15, 76, 77]). Even when the time-subordination procedure is applied to a Gaussian process, the PDF of the resulting process is no longer Gaussian, and the particle MSD has a non-linear time dependence. Let $Y(\tau)$, $\tau > 0$, be a stochastic process. Time-subordination is defined by the following expression:

$$X(t) = Y(Q(t))\,. \tag{70}$$

Thus, time-subordination follows from the randomization of the time clock in a stochastic process $Y(\tau)$, i.e., by using a new clock $\tau = Q(t)$, being $Q(t)$ a random process with non-negative increments. The resulting process $Y(Q(t))$ is said to be subordinated to $Y(\tau)$. This is called the *parent process*, while $Q(t)$ is called the *directing process*, so that it is said that $Y(\tau)$ it is directed by $Q(t)$ [78].

In diffusion processes, the parameter τ is named *operational time*. The process $t = t(\tau)$, which is the inverse of $\tau = Q(t)$, is called the *leading process* [15, 79]. It is worth noting that, in general, $X(t)$ is non-Markovian, even when the parent process $Y(\tau)$ is Markovian. At the macroscopic level, i.e., in terms of the particle PDF, the subordination process $X(t)$ is described by the following expression:

$$p(x;\,t) = \int_0^\infty \psi(x;\,\tau)\varphi(\tau;\,t)\,d\tau\,, \tag{71}$$

where $p(x;\,t)$ is the PDF of $X(t)$, $\psi(x;\,\tau)$ the PDF of $Y(\tau)$ and $\varphi(\tau;\,t)$ the PDF of $Q(t)$. In the following, the PDFs are self-similar, i.e., have a scaling property. Similarly to the approaches previously described, we introduce a population of time-scales T with distribution function $f(T)$ for the subordinated process $Y(\tau)$. Then parameter τ is now determined by the process $Q(t/T)$.

By comparing (71) and (A.10) we have

$$p(x;\,t) \equiv K^0_{\alpha,\beta}(x;\,t)\,, \quad \psi(x;\,\tau) \equiv G(x;\,\tau) = \frac{1}{\tau^{1/2}} G\left(\frac{x}{\tau^{1/2}}\right)\,,$$
$$\varphi(\tau;\,t) \equiv K^{-\alpha/2}_{\alpha/2,\beta}(\tau;\,t)\,. \tag{72}$$

Hence, the integral representation (71) turns out to be

$$K^0_{2,\beta}(x;\,t) = \int_0^\infty \frac{1}{Q(t/T)^{1/2}} G\left(\frac{x}{Q(t/T)^{1/2}}\right) K^{-\alpha/2}_{\alpha/2,\beta}(Q(t/\tau);\,t)\frac{dQ}{dT}\,dT\,. \tag{73}$$

In the case of space-fractional diffusion, from formula (A.11) we observe that the scaling property gives $Q(t/T) = (t/T)^{1/\alpha}$, and $f(T)$ results to be

$$f(T) = L^{-\alpha/2}_{\alpha/2}\left(\frac{1}{T^{1/\alpha}}\right)\frac{1}{\alpha T^{1/\alpha+1}}\,. \tag{74}$$

Analogously, in the case of time-fractional diffusion, from formula (A.12) we observe that the scaling

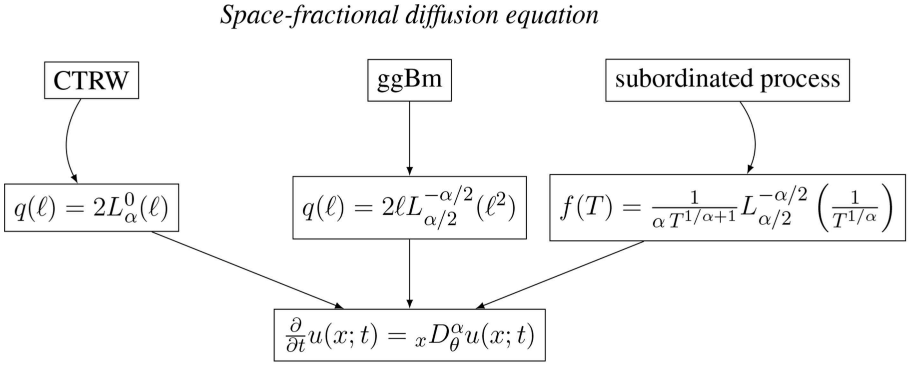

FIGURE 1 | Schematic picture of the three stochastic processes in heterogenous media leading to the same space-fractional diffusion equation for the 1-point 1-time PDF.

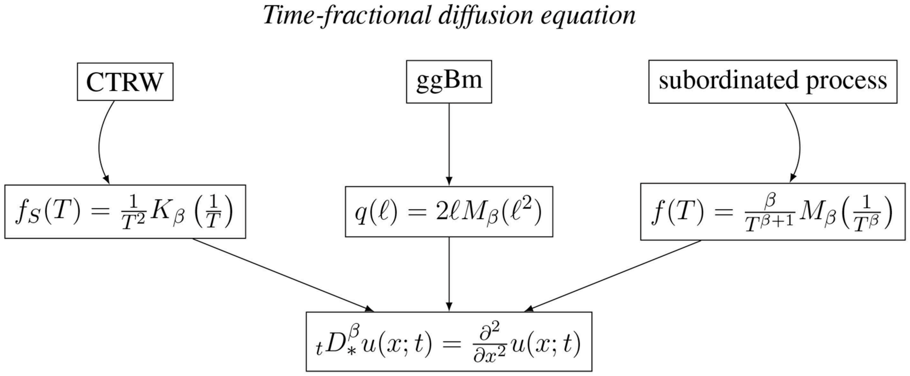

FIGURE 2 | Schematic picture of the three stochastic processes in heterogenous media leading to the same time-fractional diffusion equation for the 1-point 1-time PDF.

property gives $Q(t/T) = (t/T)^{\beta}$, and $f(T)$ results to be

$$f(T) = M_{\beta}\left(\frac{1}{T^{\beta}}\right)\frac{\beta}{T^{\beta+1}}\,. \tag{75}$$

5. CONCLUSIONS

In this paper we studied a framework for explaining the emergence of anomalous diffusion in media characterized by random structures. In particular, we considered three different modeling approaches based on Gaussian processes but displaying a population of scales. The main idea is that the deviation from Gaussianity is indeed an indirect estimation of the population of the scales that characterize the medium where the diffusion takes place. We discussed the cases of space- and time-fractional diffusion through the CTRW, the ggBm and time-subordinated process.

The introduction of a population of scales significantly affects the particle PDF. The same fractional diffusion follows from different populations of scales when different Gaussian processes are considered. This suggests that the same macroscopic fractional process can be experimentally observed in different systems displaying different populations of scales and, consequently, driven by different underlying mesoscopic Gaussian processes. In **Figures 1**, **2** we give a synthetic picture of the three processes here described, all leading to the macroscopic space- or time-fractional diffusion equations.

When a macroscopic fractional process is experimentally observed, the simultaneous measurement of the population of scales embodies a selection criterion for the corresponding mesoscopic (and maybe not experimentally detectable) underlying Gaussian process. The same holds in the other way round, when a macroscopic fractional process is experimentally observed in place of a specific Gaussian process theoretically and/or experimentally expected, and then the deviation from Gaussianity embodies an indirect measurement of the population of the scales.

In general, this framework can be adopted for studying the presence and the characterization of impurities, as well as of obstacles, in a given complex medium. These results highlight the key role of the properties of the medium, embodied by the population of the scales, in the determination of the proper stochastic process for a given medium. The present research and our final claim aim to analyze and provide an explanation to the role and the effects of the system's configuration (environment plus particles) on the emergence of deviations from Gaussianity. In this respect, the present results add a contribution to similar existing literature concerning, for example, the dependence on system's configuration of the emergence of nonextensive statistical mechanics in confined granular media [80], or the emergence of processes modeled by fractional linear diffusion or by integer non-linear diffusion accordingly to different settings of CTRW simulations [81].

DATA AVAILABILITY

All datasets generated for this study are included in the manuscript and the **Supplementary Files**.

AUTHOR CONTRIBUTIONS

GP, PP, FD, and RS discussed the main ideas and took care of the text. The research presented in this paper and, in particular, the mathematical derivation of the models has been carried out at BCAM, Bilbao, and was developed by FD for his Master Thesis in Mathematics, Roma Tre University, under the supervision of GP and RS. GP wrote the Appendix in **Supplementary Material**.

FUNDING

This research was supported by the Basque Government through the BERC 2014–2017 and BERC 2018–2021 programs, and by the Spanish Ministry of Economy and Competitiveness MINECO through BCAM Severo Ochoa excellence accreditations SEV-2013-0323 and SEV-2017-0718 and through project MTM2016-76016-R MIP.

ACKNOWLEDGMENTS

The authors would like to acknowledge Francesco Mainardi for his motivating attitude to the scientific research and his positive example to human relations that are at the basis of this collaborative research.

SUPPLEMENTARY MATERIAL

The Supplementary Material for this article can be found online at: https://www.frontiersin.org/articles/10.3389/fphy.2019.00123/full#supplementary-material

REFERENCES

1. van Kampen NG. *Stochastic Processes in Physics and Chemistry.* Amsterdam: North-Holland (1981).
2. Risken H. *The Fokker-Planck Equation. Methods of Solution and Applications.* 2nd Edn. Berlin; Heidelberg: Springer-Verlag (1989).
3. Gardiner CW. *Handbook of Stochastic Methods for Physics, Chemistry and the Natural Sciences.* 2nd Edn. Berlin; Heidelberg: Springer-Verlag (1990).
4. Sneddon IN. *The Use of Operators of Fractional Integration in Applied Mathematics.* Warszawa: RWN - Polish Science Publishers (1979).
5. Samko SG, Kilbas AA, Marichev OI. *Fractional Integrals and Derivatives: Theory and Applications.* Gordon and Breach Science Publishers (1993). Philadelphia, PA: Reprinted 2002 by Taylor & Francis Books Ltd, London.
6. Mainardi F. *Fractional Calculus and Waves in Linear Viscoelasticity.* London: Imperial College Press (2010).
7. Hilfer R, Anton L. Fractional master equations and fractal time random walks. *Phys Rev E.* (1995) **51**:R848–51. doi: 10.1103/PhysRevE.51.R848
8. Mainardi F. Fractional relaxation-oscillation and fractional diffusion-wave phenomena. *Chaos Solit Fract*. (1996) **7**:1461–77. doi: 10.1016/0960-0779(95)00125-5

9. Klafter J, Lim SC, Metzler R. *Fractional Dynamics: Recent Advances*. Singapore: World Scientific (2011).
10. Metzler R, Klafter J. The random walk's guide to anomalous diffusion: a fractional dynamics approach. *Phys Rep.* (2000) **339**:1–77. doi: 10.1016/S0370-1573(00)00070-3
11. Mainardi F, Luchko Y, Pagnini G. The fundamental solution of the space-time fractional diffusion equation. *Fract Calc Appl Anal.* (2001) **4**:153–92.
12. Mainardi F, Pagnini G. The Wright functions as solutions of the time-fractional diffusion equations. *Appl Math Comput.* (2003) **141**:51–62. doi: 10.1016/S0096-3003(02)00320-X
13. Mainardi F, Pagnini G, Saxena RK. Fox H functions in fractional diffusion. *J Comput Appl Math.* (2005) **178**:321–1. doi: 10.1016/j.cam.2004.08.006
14. Mainardi F, Pagnini G. The role of the Fox–Wright functions in fractional sub-diffusion of distributed order. *J Comput Appl Math.* (2007) **207**:245–57. doi: 10.1016/j.cam.2006.10.014
15. Gorenflo R, Mainardi F. Subordination pathways to fractional diffusion. *Eur Phys J.* (2011) **193**:119–32. doi: 10.1140/epjst/e2011-01386-2
16. Paradisi P. Fractional calculus in statistical physics: the case of time fractional diffusion equation. *Comm Appl Ind Math.* (2015) **6**:e530. doi: 10.1685/journal.caim.530
17. Paradisi P, Cesari R, Donateo A, Contini D, Allegrini P. Scaling laws of diffusion and time intermittency generated by coherent structures in atmospheric turbulence. N*onlinear Proc Geoph.* (2012) **19**:113–26. doi: 10.5194/npg-19-113-2012
18. Paradisi P, Cesari R, Donateo A, Contini D, Allegrini P. Diffusion scaling in event-driven random walks: an application to turbulence. *Rep Math Phys.* (2012) **70**:205–20. doi: 10.1016/S0034-4877(12)60040-8
19. del Castillo-Negrete D. Fractional diffusion in plasma turbulence. *Phys Plasmas.* (2004) **11**:3854–64. doi: 10.1063/1.1767097
20. del Castillo-Negrete D, Carreras BA, Lynch VE. Nondiffusive transport in plasma turbulence: a fractional diffusion approach. *Phys Rev Lett.* (2005) **94**:065003. doi: 10.1103/PhysRevLett.94.065003
21. Tolić-Nørrelykke IM, Munteanu EL, Thon G, Odderhede L, Berg-Sørensen K. Anomalous diffusion in living yeast cells. *Phys Rev Lett.* (2004) **93**:078102. doi: 10.1103/PhysRevLett.93.078102
22. Golding I, Cox EC. Physical nature of bacterial cytoplasm. *Phys Rev Lett.* (2006) **96**:098102. doi: 10.1103/PhysRevLett.96.098102
23. Bronstein I, Israel Y, Kepten E, Mai S, Shav-Tal Y, Barkai E, et al. Transient anomalous diffusion of telomeres in the nucleus of mammalian cells. *Phys Rev Lett.* (2009) **103**:018102. doi: 10.1103/PhysRevLett.103.018102
24. Zaid IM, Lomholt MA, Metzler R. How subdiffusion changes the kinetics of binding to a surface. *Biophys J.* (2009) **97**:710–21. doi: 10.1016/j.bpj.2009.05.022
25. Gal N, Lechtman-Goldstein D, Weihs D. Particle tracking in living cells: a review of the mean square displacement method and beyond. *Rheol Acta.* (2013) **52**:425–3. doi: 10.1007/s00397-013-0694-6
26. Javer A, Kuwada NJ, Long Z, Benza VG, Dorfman KD, Wiggins PA, et al. Persistent super-diffusive motion of Escherichia coli chromosomal loci. *Nat Commun.* (2014) **5**:3854. doi: 10.1038/ncomms4854
27. Metzler R, Jeon JH, Cherstvy AG. Non–Brownian diffusion in lipid membranes: experiments and simulations. *Biochim Biophys Acta.* (2016) **1858**:2451–67. doi: 10.1016/j.bbamem.2016.01.022
28. Pöschke P, Sokolov IM, Nepomnyashchy AA, Zaks MA. Anomalous transport in cellular flows: the role of initial conditions and aging. *Phys Rev E.* (2016) **94**:032128. doi: 10.1103/PhysRevE.94.032128
29. Stadler L, Weiss M. Non-equilibrium forces drive the anomalous diffusion of telomeres in the nucleus of mammalian cells. *New J Phys.* (2017) **19**:113048. doi: 10.1088/1367-2630/aa8fe1
30. Pierro MD, Potoyan DA, Wolynes PG, Onuchic JN. Anomalous diffusion, spatial coherence, and viscoelasticity from the energy landscape of human chromosomes. *Proc Natl Acad Sci USA.* (2018) **115**:7753–8. doi: 10.1073/pnas.1806297115
31. Allegrini P, Paradisi P, Menicucci D, Laurino M, Piarulli A, et al. Self-organized dynamical complexity in human wakefulness and sleep: different critical brain-activity feedback for conscious and unconscious states. *Phys Rev E.* (2015) **92**:032808. doi: 10.1103/PhysRevE.92.032808
32. Paradisi P, Allegrini P. Intermittency-driven complexity in signal processing. In: Barbieri R, Scilingo EP, Valenza G, editors. *Complexity and Nonlinearity in Cardiovascular Signals*. Cham: Springer (2017). p. 161–96.
33. Manzo C, Garcia-Parajo MF. A review of progress in single particle tracking: from methods to biophysical insights. *Rep Progr Phys.* (2015) **78**:124601. doi: 10.1088/0034-4885/78/12/124601
34. Burov S, Jeon JH, Metzler R, Barkai E. Single particle tracking in systems showing anomalous diffusion: the role of weak ergodicity breaking. *Phys Chem Chem Phys.* (2011) **13**:1800–2. doi: 10.1039/c0cp01879a
35. Javanainen M, Hammaren H, Monticelli L, Jeon JH, Miettinen MS, Martinez-Seara H, et al. Anomalous and normal diffusion of proteins and lipids in crowded lipid membranes. *Faraday Discuss.* (2012) **161**:397–417. doi: 10.1039/C2FD20085F
36. Metzler R, Jeon JH, Cherstvy AG, Barkai E. Anomalous diffusion models and their properties: non-stationarity, non-ergodicity, and ageing at the centenary of single particle tracking. *Phys Chem Chem Phys.* (2014) **16**:24128. doi: 10.1039/C4CP03465A
37. Jeon JH, Javanainen M, Martinez-Seara H, Metzler R, Vattulainen I. Protein crowding in lipid bilayers gives rise to non-Gaussian anomalous lateral diffusion of phospholipids and proteins. *Phys Rev X.* (2016) **6**:021006. doi: 10.1103/PhysRevX.6.021006
38. Molina-García D, Minh Pham T, Paradisi P, Manzo C, Pagnini G. Fractional kinetics emerging from ergodicity breaking in random media. *Phys Rev E.* (2016) **94**:052147. doi: 10.1103/PhysRevE.94.052147
39. Beck C. Dynamical foundations of nonextensive statistical mechanics. *Phys Rev Lett.* (2001) **87**:180601. doi: 10.1103/PhysRevLett.87.180601
40. Beck C, Cohen EGD. Superstatistics. *Phys A.* (2003) **322**:267–75. doi: 10.1016/S0378-4371(03)00019-0
41. Allegrini P, Barbi F, Grigolini P, Paradisi P. Renewal, modulation, and superstatistics in times series. *Phys Rev E Stat Nonlin Soft Matter Phys.* (2006) **73**(4 Pt 2):046136. doi: 10.1103/PhysRevE.73.046136
42. Paradisi P, Cesari R, Grigolini P. Superstatistics and renewal critical events. *Cent Eur J Phys.* (2009) **7**:421–31. doi: 10.2478/s11534-009-0069-x
43. Van Der Straeten E, Beck C. Superstatistical fluctuations in time series: applications to share-price dynamics and turbulence. *Phys Rev E.* (2009) **80**:036108. doi: 10.1103/PhysRevE.80.036108
44. Massignan P, Manzo C, Torreno-Pina J, García-Parajo M, Lewenstein M, Lapeyre G Jr. Nonergodic subdiffusion from Brownian motion in an inhomogeneous medium. *Phys Rev Lett.* (2014) **112**:150603. doi: 10.1103/PhysRevLett.112.150603
45. Manzo C, Torreno-Pina JA, Massignan P, Lapeyre GJ, Lewenstein M, Garcia–Parajo MF. Weak ergodicity breaking of receptor motion in living cells stemming from random diffusivity. *Phys Rev X.* (2015) **5**:011021. doi: 10.1103/PhysRevX.5.011021
46. Chubynsky MV, Slater GW. Diffusing diffusivity: a model for anomalous, yet brownian, diffusion. *Phys Rev Lett.* (2014) **113**:098302. doi: 10.1103/PhysRevLett.113.098302
47. Chechkin AV, Seno F, Metzler R, Sokolov IM. Brownian yet non-Gaussian diffusion: from superstatistics to subordination of diffusing diffusivities. *Phys Rev X.* (2017) **7**:021002. doi: 10.1103/PhysRevX.7.021002
48. Jain R, Sebastian KL. Diffusing diffusivity: a new derivation and comparison with simulations. *J Chem Sci.* (2017) **129**:929–37. doi: 10.1007/s12039-017-1308-0
49. Lanoiselée Y, Grebenkov DS. A model of non-Gaussian diffusion in heterogeneous media. *J Phys A Math Theor.* (2018) **51**:145602. doi: 10.1088/1751-8121/aab15f
50. Sposini V, Chechkin AV, Seno F, Pagnini G, Metzler R. Random diffusivity from stochastic equations: comparison of two models for Brownian yet non-Gaussian diffusion. *New J Phys.* (2018) **20**:043044. doi: 10.1088/1367-2630/aab696
51. Cox DR. *Renewal Theory*. London: Methuen & Co. Ltd. (1962).
52. Bianco S, Grigolini P, Paradisi P. A fluctuating environment as a source of periodic modulation. *Chem Phys Lett.* (2007) **438**:336–40. doi: 10.1016/j.cplett.2007.03.013
53. Paradisi P, Grigolini P, Bianco S, Akin OC. Renewal aging in non-homogeneous Poisson processes with periodic rate modulation. *Int J Bif Chaos.* (2008) **18**:2681–91. doi: 10.1142/S0218127408021890

54. Akin OC, Paradisi P, Grigolini P. Perturbation-induced emergence of Poisson-like behavior in non-Poisson systems. *J Stat Mech Theory Exp.* (2009) **2009**:P01013. doi: 10.1088/1742-5468/2009/01/P01013
55. Akin OC, Paradisi P, Grigolini P. Periodic trend and fluctuations: the case of strong correlation. *Phys A.* (2006) **371**:157–70. doi: 10.1016/j.physa.2006.04.054
56. Pagnini G, Paradisi P. A stochastic solution with Gaussian stationary increments of the symmetric space-time fractional diffusion equation. *Fract Calc Appl Anal.* (2016) **19**:408–40. doi: 10.1515/fca-2016-0022
57. Vitali S, Sposini V, Sliusarenko O, Paradisi P, Castellani G, Pagnini G. Langevin equation in complex media and anomalous diffusion. *J R Soc Interface.* (2018) **15**:20180282. doi: 10.1098/rsif.2018.0282
58. D′Ovidio M, Vitali S, Sposini V, Sliusarenko O, Paradisi P, Castellani G, et al. Centre-of-mass like superposition of Ornstein-Uhlenbeck processes: a pathway to non-autonomous stochastic differential equations and to fractional diffusion. *Fract Calc Appl Anal.* (2018) **21**:1420–35. doi: 10.1515/fca-2018-0074
59. Sliusarenko OY, Vitali S, Sposini V, Paradisi P, Chechkin A, Castellani G, et al. Finite-energy Lévy-type motion through heterogeneous ensemble of Brownian particles. *J Phys A.* (2019) **52**:095601. doi: 10.1088/1751-8121/aafe90
60. Kloeden PE, Platen E. *Numerical solution of Stochastic Differential Equations.* Springer-Verlag (1992).
61. Di Tullio F. *Fractional diffusion in random media on the basis of Gaussian stochastic processes.* Master Thesis in Mathematics, University of Roma Tre, Rome, Italy (2016).
62. Klafter J, Blumen A, Shlesinger MF. Stochastic pathway to anomalous diffusion. *Phys Rev A.* (1987) **35**:3081–5. doi: 10.1103/PhysRevA.35.3081
63. Montroll EW, Weiss GH. Random walks on lattices. II. *J Math Phys.* (1965) **6**:167–81. doi: 10.1063/1.1704269
64. Mainardi F, Raberto M, Gorenflo R, Scalas E. Fractional calculus and continuous-time finance II: the waiting-time distribution. *Phys A.* (2000) **287**:468–81. doi: 10.1016/S0378-4371(00)00386-1
65. Scalas E, Gorenflo R, Mainardi F. Uncoupled continuous-time random walks: solution and limiting behavior of the master equation. *Phys Rev E.* (2004) **69**:011107. doi: 10.1103/PhysRevE.69.011107
66. Scalas E, Gorenflo R, Mainardi F. Fractional calculus and continuous-time finance. *Phys A.* (2000) **284**:376–84. doi: 10.1016/S0378-4371(00)00255-7
67. Pagnini G. Short note on the emergence of fractional kinetics. *Phys A.* (2014) **409**:29–34. doi: 10.1016/j.physa.2014.03.079
68. Metzler R, Nonnenmacher TF. Space- and time-fractional diffusion and wave equations, fractional Fokker-Planck equations, and physical motivation. *Chem Phys.* (2002) **284**:67–90. doi: 10.1016/S0301-0104(02)00537-2
69. Luchko Y. Models of the neutral-fractional anomalous diffusion and their analysis. *AIP Conf Proc.* (2012) **1493**:626–32. doi: 10.1063/1.4765552
70. Mura A, Taqqu MS, Mainardi F. Non-Markovian diffusion equations and processes: analysis and simulations. *Phys A.* (2008) **387**:5033–64. doi: 10.1016/j.physa.2008.04.035
71. Mura A, Pagnini G. Characterizations and simulations of a class of stochastic processes to model anomalous diffusion. *J Phys A Math Theor.* (2008) **41**:285003. doi: 10.1088/1751-8113/41/28/285003
72. Mura A, Mainardi F. A class of self-similar stochastic processes with stationary increments to model anomalous diffusion in physics. *Integr Transf Spec F.* (2009) **20**:185–98. doi: 10.1080/10652460802567517
73. Pagnini G, Mura A, Mainardi F. Generalized fractional master equation for self-similar stochastic processes modelling anomalous diffusion. *Int J Stoch Anal.* (2012) **2012**:427383. doi: 10.1155/2012/427383
74. Pagnini G, Mura A, Mainardi F. Two-particle anomalous diffusion: probability density functions and self-similar stochastic processes. *Philos Trans R Soc A.* (2013) **371**:20120154. doi: 10.1098/rsta.2012.0154
75. Pagnini G. Erdélyi–Kober fractional diffusion. *Fract Calc Appl Anal.* (2012) **15**:117–27. doi: 10.2478/s13540-012-0008-1
76. Mainardi F, Pagnini G, Gorenflo R. Mellin transform and subordination laws in fractional diffusion processes. *Fract Calc Appl Anal.* (2003) **6**:441–59.
77. Mainardi F, Pagnini G, Gorenflo R. Mellin convolution for subordinated stable processes. *J Math Sci.* (2006) **132**:637–42. doi: 10.1007/s10958-006-0008-y
78. Feller W. *An Introduction to Probability Theory and its Applications, Vol. 2.* 2nd Edn. New York, NY: Wiley (1971).
79. Gorenflo R, Mainardi F. Parametric subordination in fractional diffusion processes. In: Klafter J, Lim SC, Metzler R, editors. *Fractional Dynamics. Recent Advances*. Singapore: World Scientific (2012). p. 227–61.
80. Combe G, Richefeu V, Stasiak M, Atman APF. Experimental validation of a nonextensive scaling law in confined granular media. *Phys Rev Lett.* (2015) **115**:238301. doi: 10.1103/PhysRevLett.115.238301
81. Pereira APP, Fernandes JP, Atman APF, Acebal JL. Parameter calibration between models and simulations: connecting linear and non-linear descriptions of anomalous diffusion. *Phys A.* (2018) **509**:369–82. doi: 10.1016/j.physa.2018.06.025
82. Mainardi F, Mura A, Pagnini G. The M-Wright function in time-fractional diffusion processes: a tutorial survey. *Int J Differ Equat.* (2010) **2010**:104505. doi: 10.1155/2010/104505
83. Mainardi F, Mura A, Pagnini G. The functions of the Wright type in fractional calculus. *Lect Notes Semin Interdisc Matemat.* (2010) **9**:111–28.
84. Cahoy DO. On the parametrization of the M-Wright function. *Far East J Theor Stat.* (2011) **34**:155–64.
85. Cahoy DO. Estimation and simulation for the M-Wright function. *Commun Stat-Theor M.* (2012) **41**:1466–77. doi: 10.1080/03610926.2010.543299
86. Cahoy DO. Moment estimators for the two-parameter M-Wright distribution. *Comput Stat.* (2012) **27**:487–97. doi: 10.1007/s00180-011-0269-x
87. Pagnini G. The M-Wright function as a generalization of the Gaussian density for fractional diffusion processes. *Fract Calc Appl Anal.* (2013) **16**:436–53. doi: 10.2478/s13540-013-0027-6
88. Pagnini G, Scalas E. Historical notes on the M-Wright/Mainardi function. *Commun Appl Indus Math.* (2004) **6**:e496. doi: 10.1685/journal.caim.496

Conflict of Interest Statement: The authors declare that the research was conducted in the absence of any commercial or financial relationships that could be construed as a potential conflict of interest.

frontiers in Physics

ORIGINAL RESEARCH
published: 18 September 2019
doi: 10.3389/fphy.2019.00129

From Micro-to-Macro: How the Movement Statistics of Individual Walkers Affect the Formation of Segregated Territories in the Territorial Random Walk Model

Seeralan Sarvaharman[1], *Alexandro Heiblum Robles*[2] *and Luca Giuggioli*[1,3]*

[1] *Department of Engineering Mathematics, University of Bristol, Bristol, United Kingdom,* [2] *Foro Consultivo Científico y Tecnológico, Mexico City, Mexico,* [3] *Bristol Centre for Complexity Sciences, University of Bristol, Bristol, United Kingdom*

Animal territoriality is a widespread phenomena in many vertebrate species. In mammals it is often associated with territorial marking with which individuals make their presence conspicuous to others by leaving trace of their passage, often in the form of deposited scent. A simple interaction mechanism consisting of retreating upon the encounter of a foreign scent is sufficient to observe the emergence of territorial patterns at the population level. With the introduction of the so-called territorial random walk model this local avoidance mechanism coupled with a simple diffusive movement of the individuals has been shown to generate long-lasting patterns of segregation at much larger spatial scales. To shed further light on the micro-to-macro connection of this collective movement model we study how the movement statistics of the individuals affect the formation of the segregated scented territories. We represent individual animals as correlated random walkers and we analyse the spatial ordering of the population as a function of the length of time a scent mark remains active after deposition and as a function of the degree of correlation of the movement steps. For low and intermediate correlation strength we find that territories undergo a liquid-hexatic-solid transition as active scent time is increased. Increased spatial order also appears by increasing the correlation strength but only if well away from the ballistic limit. We ascribe this non-monotonic dependence to the coverage efficiency of the individual walkers mainly controlled by the correlation and the mobility of the territories mainly controlled by the active scent time.

Keywords: territorial random walk, correlated random walk, KTHNY melting, topological defects, animal territoriality

Edited by:
Ralf Metzler,
University of Potsdam, Germany

Reviewed by:
Diego R. Amancio,
University of São Paulo, Brazil
Muktish Acharyya,
Presidency University, India

***Correspondence:**
Luca Giuggioli
luca.giuggioli@bristol.ac.uk

Specialty section:
This article was submitted to Interdisciplinary Physics, a section of the journal Frontiers in Physics

Received: *17 June 2019*
Accepted: *27 August 2019*
Published: *18 September 2019*

Citation:
Sarvaharman S, Heiblum Robles A and Giuggioli L (2019) From Micro-to-Macro: How the Movement Statistics of Individual Walkers Affect the Formation of Segregated Territories in the Territorial Random Walk Model. Front. Phys. 7:129. doi: 10.3389/fphy.2019.00129

1. INTRODUCTION AND BACKGROUND

In biology it is rather common to find a system in which the underlying movement of its constituent parts is not diffusive, often owed to the out-of-equilibrium nature of the processes involved. Examples of anomalous transport can be found at all scales: from the active and passive microrheology of various nanoparticles inside the molecularly crowded environment of cells [1] and the two stage diffusion of macromolecules on cell membranes [2, 3] to the superdiffusive displacement of epithelial cells [4], and all the way to the anomalous dynamics of whole organism while foraging randomly [5] or during memory biased search [6, 7].

Among the cited biological examples characterized by anomalous diffusion we have focused for this special issue on the movement of whole organisms and on the collective effects of many such organisms spatially excluding one another. Our interest here lies in understanding how the local statistical features of the movement of individual animals affect the emergence of the collective patterns at the population level. We choose a movement statistics that becomes random at long time scales, but retains a degree of persistence at shorter time scales, the so-called correlated random walker [8], a paradigmatic movement model in animal ecology [9, 10]. Among the forms of spatial exclusion or avoidance we are particularly interested in a very common behavior of vertebrate populations in 2D: the subdivision of the terrain into spatially segregated regions [11]. When these regions are of exclusive ownership of a single individual or a single family unit they are called territories [12, 13].

The purposes of territoriality change from species to species or even throughout the year [14]. These include, roosting, mating, nesting, and harboring resources. Accordingly the interaction mechanisms that animals rely upon to form and maintain these territories are quite rich and depend on the type of signals that animals exchange. Broadly speaking one may distinguish them between direct and indirect, that is whether the time scale for the signals to travel from the emitter to the receiver is short or long relative to the time scale for the emitter to move. Examples of direct interactions, often employed by birds [15], is the use of visual displays and audio calls. In this case the signal of the emitter is detected by the receiver nearly instantaneously. Examples of indirect interaction, used by a large number of mammals [16], is the use of olfactory cues. In this case the scent that an animal deposits is nearly static. For the period over which the scent remains detectable, which could be a long time after deposition, the environment retains the memory of the passage of the emitter. Any individual that comes in close proximity to the deposited scent becomes a receiver and acquires information about the (past) presence of the emitter.

In this study we analyse a specific case of olfactory-based territorial formation, often called conspecific avoidance, whereby animals mark the terrain wherever they go, and other individuals passing by respond to these olfactory cues by retreating from the region or area where foreign scent was encountered. This indirect animal interaction, that occurs through the modification of the environment, is called stigmergy [17]. It is a common form of interaction in eusocial insects [18], but it has been shown to occur also in territorial animals [19].

The mathematical study of scent-marked territorial patterns has a relatively long history dating back to the early '90s when the first reaction-diffusion model representing a pair of animals avoiding each other scent was formulated [20]. This model coupled the occupation probability of two Brownian walkers tethered to their respective den or burrow and their scent profiles. It was later generalized to include the effects of landscape heterogeneity and animal movement responses and applied to movement data on wolves and coyotes [21].

In subsequent modeling studies on the formation of scented territories a different approach was followed [22]. That approach becomes necessary when one aims to account for the sharp spatial dependence of the interaction. In these cases the field nature of the interaction potentials (or forces), which tacitly assumes that they are defined at every point in space, may not be adequate. It is more convenient to account for the interaction dynamics through localized walls or spatial partitions representing the deposited scent [23]. By doing so one remains faithful to the biology of scent-marking species for which individuals react to the encounter of foreign scent only if it is informative, that is only if the deposition occurred before a certain time in the past [see e.g., Alberts [24]].

As this approach requires tracking the movement and interaction of the entire population to determine the time-dependent position of each animal and the age of the scent deposited, it was formulated as an individual based model [22]. This increased complexity, however, allows to consider animals that do not have a den or a burrow as well as to study the emergence of territorial patterns as a collective phenomena rather than a two-body problem between neighboring individuals.

The collective movement model of territory formation, termed the territorial random walk (TRW) model [23], lends itself naturally to questions on the nature of the emerging patterns, e.g., if macroscopic order and/or disorder phases appear and how the microscopy of the movement and interaction rules influence the emergence of the macroscopic patterns. Along these lines a very recent investigation on the presence of order-disorder phase transitions in the TRW model as a function of the scent decay time and the population density has been conducted [25]. In that study it has been shown that the emerging territorial patterns display a solid to liquid melting scenario analogous to the one supported by the Kosterlitz-Thouless-Halperin-Nelson-Young (KTHNY) theory of melting [26–28], with the appearance of an intermediate partially ordered phase, called *hexatic*, due to the importance of geometrical arrangements of the first six neighbors.

Here we extend that analysis by considering a more realistic movement model for the individual animals. We modify the movement statistics of the animal by representing them as correlated random walkers and we ask how the "microscopic" movement of the individuals alters the collective dynamics of the system and the order-disorder scenario.

The paper is organized as follows. In section 2 we introduce the model and we present details of the stochastic simulations and the thermalization of the system. The analysis has two parts to it. At the "microscopic" level, that is at the level of the individuals, we study the influence of the persistence of the walk on the variance of the occupation probability, that is the mean square displacement (MSD). This is presented in section 3 together with an analysis of the spatial coverage of each walker in its own territory. As we scale up to the level of the territories, we analyse the effects of the animal movement statistics on the appearance of ordered phases in the system. This is dealt with in section 4. And finally section 5 presents concluding remarks.

2. THE CORRELATED TERRITORIAL RANDOM WALKER MODEL

The correlated territorial random walker (cTRW) model, an extension of the TRW model, is a lattice-based collective movement model where individuals move with some degree of persistence, that is the movement direction at each time step depends on the previous step direction. The model can be run in any dimension and in discrete or continuous time. For computational efficiency we have run it in discrete time and we have only analyzed the 2D case. To study the structure of the emerging territories it is important not to introduce spatial frustration effects and we have thus used a triangular lattice with periodic boundary conditions.

In the absence of interactions a walker's steps are correlated. To model the persistent random walk on a triangular lattice we start from a continuous turning angle variable $\theta \in (-\pi, \pi]$, and we create six bins of width $\frac{\pi}{3}$ for each of the turns a walker can make. The angle θ is then drawn randomly from a wrapped Cauchy distribution, $\mathcal{C}(\theta) = \left(1-\rho^2\right)\left[2\pi\left(1+\rho^2-2\rho\cos(\theta)\right)\right]^{-1}$ where $-\pi \leq \theta < \pi$ and ρ is the persistence parameter, or the mean cosine of the distribution. It indicates the tendency of a walker to continue to move in the same direction from where it came from at the previous step. In the limit $\rho \to 0$, the distribution reduces to $\mathcal{C}(\theta) = \frac{1}{2\pi}$ i.e., the turning angles are uniformly distributed and the movement of the walker becomes random. The opposite limit corresponds to the ballistic case $\mathcal{C}(\theta) \to \delta(\theta)$, where $\delta(\theta)$ is the Dirac delta function as $\rho \to 1$.

Avoidance between individuals occurs as follows. As animals deposit marks wherever they go, at each time step any individual may encounter one of its own marks or may step on a lattice site with one or multiple foreign marks. When an animal encounters its own marks, no interaction occurs. On the other hand upon encountering a foreign mark within a time period shorter or equal to the so called active scent time T_A from when it was deposited, an interaction occurs. In order to avoid intruding further into neighboring territories. An interaction consists of one of three types of retreat at the following time step. These are in order of preference, first toward a neighboring site with no scent marks, second toward a neighboring site with the animal's own scent and lastly in the rare case where neither of the previous options are available the animal moves randomly to one of the six neighboring sites. At the subsequent step the animal reorients itself with a new direction chosen at random between the six potential choices.

As a result of the above interactions, foreign scents serve as spatial barriers effectively making individuals avoid entering further into others' territories. At any given time t a territory is represented by all the sites that contain an active scent of a specific animal. Alternatively it represents the sites an individual has visited within the interval $(t - T_A, t)$. Except at the boundaries, where a given territory may overlap with one or more neighboring ones, the avoidance of region recently visited by other individuals create spatially segregated areas of exclusive ownership for each animal.

The spatio-temporal dynamics of the territories can be fast and slow depending on the choice of parameters, which are, respectively, the inverse of the population density or specific volume $\nu = L^2/N$ where L^2 is the domain size, the active scent time T_A and the persistence parameter ρ. With small T_A and large ν one observes highly mobile and morphing territories as exclusion interactions are not very frequent. The opposite happens with large T_A and small ν as interactions occur more frequently.

The dependence on the initial condition of the system is dealt with by running simulations and waiting for the system to thermalize before making any spatial and/or temporal measurement on appropriate quantities of the system. The thermalization is performed as follows. Two different initial conditions are used. The first is initialized with the scent profile tessellating the available space, i.e., the territory of each walker is a perfect hexagon with all boundary lattice sites overlapping with the neighboring territories. The second is initialized with randomly distributed walkers with no scent profile. The two are left to run until the standard deviation of the territory size across the entire population converges to the same value in the two cases. When that happens the system is deemed to be thermalized.

Rather than exploring the dynamics for different population density we have selected an intermediate value of ν, namely $\nu = 48$ for multiple reasons. On one hand the rich (slow and fast) dynamics can be attained within a limited range of T_A values so that disordered and ordered phases of the system could be observed and studied as a function of ρ. For smaller population densities, as interactions become more infrequent, it becomes harder to observe spatial ordering and we have thus not explored the regime with larger ν. On the other hand smaller values of ν makes the computation very expensive and makes it harder to reach thermalization except for very small values of T_A.

The specific range and resolution of the parameter space $\rho - T_A$ with $\nu = 48$ has been as follows. The active scent time T_A has been chosen in the range between 89 and 1,424 with a resolution of 89, except for specific cases detailed in the figure captions. For the correlation parameter ρ we have used the values 0, 0.15, 0.35, 0.55, 0.75, and 0.95. To ensure that the territories, with the appropriate choice of T_A, can tessellate with equal hexagons the 2D domain, the linear domain size (with periodic boundary conditions) is set to $L = 1200$ with $N = 3 \times 10^4$, which corresponds to $\nu = 48$, although we have also used smaller domains e.g., in section 3.

3. PARTIAL "CAGING" AND SPATIAL COVERAGE OF THE INDIVIDUAL WALKERS

The spatial exclusion of the scented territories is a complex collective phenomenon whereby an animal remains confined in certain region of space depending on when and where foreign marks as well as its own marks have been deposited. But this confinement is only partial since a mark has a lifetime and

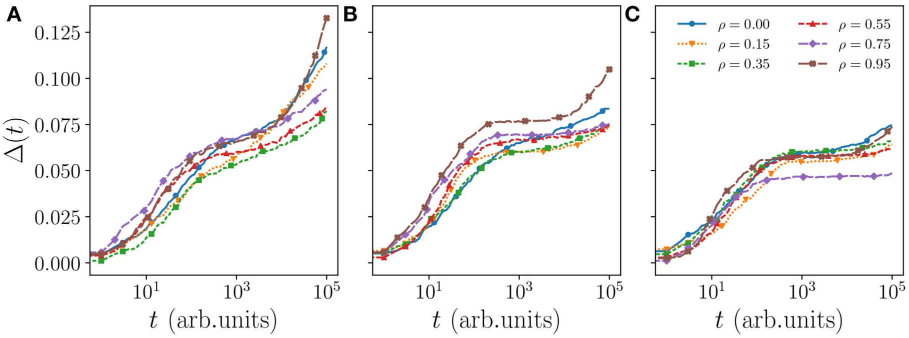

FIGURE 1 | MSD $\Delta(t)$ of a walker in a system with $\nu = 48$ and $L = 120$, where each curve is a snapshot average. The active scent times (T_A) for panels **(A–C)** are 712, 1,068, and 1,424, respectively. At short timescale the walkers tend to exhibit superdiffusion indicated by the $\Delta(t) \propto t^{\alpha}$ relationship where $\alpha > 1$. For intermediate timescales the dynamics of the walkers are governed by the mobility of their territories. High values of T_A yield slowly moving territories and increase in caging caused by neighbors. This caging saturation is highly sensitive to the correlation of the walkers (see **Figure A2**) while the time spent at the caging saturation before increasing again is related to the coverage efficiency of the walker.

disappears unless an animal remarks that same location within T_A steps. Animals may thus be trapped for some time before escaping. It is possible to observe such partial "caging" by plotting the MSD as a function of time. We do so in **Figure 1** where we draw the normalized MSD for $T_A = 712$, 1,068, and 1,424 for various values of ρ by averaging over all individuals in one simulation (after the system has thermalized). The MSD plots for $T_A = 1$ and $T_A = 89$ are additionally shown in **Figure A1**. We term these snapshot averages to distinguish them from ensemble averages when multiple copies of the system are run.

In moving from panel (a) to (b) and (c) in the figure, that is by increasing T_A, one clearly observes a reduced growth of the curves at intermediate times for each value of ρ. Since a long-time saturating MSD is expected whenever a walker roams inside a finite domain [29], the flattening of the MSD at intermediate times is a manifestation of increased caging from the neighbors. As marks remain active for longer they make the territories progressively less mobile and the MSD curves start increasing again at later times.

A comparison of different values of ρ within the same panel shows that this caging effect becomes stronger—curves remain flat for longer time—for larger ρ except when one approaches the ballistic regime. This is clearly visible in panel (c) when $T_A = 1,424$ where this non-monotonicity as a function of ρ can be seen more clearly. There also appears some non-monotonic dependence of the intermediate-time saturation value of the MSD, but this non-monotonicity is only apparent. As we have verified and shown in **Figure A2** in the appendix, the intermediate saturation of the MSD is highly erratic as it is very sensitive to the actual shape of the occupation probability for each animal. We consider the time it takes the MSD curve to start increasing again the more significant feature, and to understand the non-monotonicity as a function of ρ we look in detail at the walker spatial coverage.

Considering initially a fixed finite domain, for a walk to improve spatial coverage it needs to reduce spatial oversampling, which clearly happens by increasing ρ. However, in a confined domain, when the degree of correlation is too large, the walker would retrace back its steps thus increasing again the sampling of lattice sites already visited. It is well known in fact that the mean coverage time of an independent walker in a finite domain can be minimized for intermediate values of walk persistence [30, 31].

To test whether this understanding suffices to explain the non-monotonic ρ dependence of the caging effect, we study the walkers' spatial coverage in the cTRW model. As territories are mobile and change shape, we cannot compare values of coverage time for each walker. However, it is possible to obtain information about the efficiency of spatial coverage by plotting the average number of sites an individual covers in a time T_A as a function of ρ. The outcome is shown in **Figure 2** where we have plotted C_p, the fraction of sites covered in a time T_A, for different values of ρ and T_A. From the figure it is evident that the partial coverage of the terrain is maximal for intermediate values of ρ and for T_A sufficiently large. As T_A affects the size of the confining domain, the correlation parameter that maximizes coverage depends on how long marks remain on the terrain.

4. SPATIAL ORDERING OF THE EMERGING TERRITORIES

The interaction dynamics of the individual walkers have a long lasting effects on the spatial structure that emerges in the population, as was shown in the case of the simpler TRW model [25]. The spatial ordering of the emerging territories is dictated by the "caging" effect whose size corresponds to the size of the territory. To analyse the spatial ordering as a function of ρ and T_A we look at the system with a coarser temporal and spatial resolution because no order is present at distances smaller than the size of the territory. We neglect the dynamics of the walkers and look at the territory centroids over a T_A time resolution. As territorial centroids are calculated only by considering the mean position of all lattice sites with active scent every T_A steps, we obtain a coarse-grained (continuous-space) mesoscopic time-dependent description of the cTRW model.

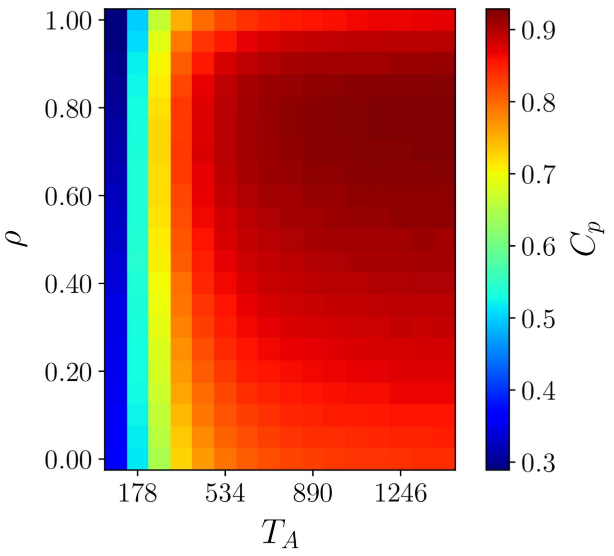

FIGURE 2 | The fraction of the territory defined at time t covered within T_A time steps by walkers as a function of the correlation parameter ρ, and the active scent time T_A. For each pair of ρ and T_A a snapshot average is taken on a thermalized system with $L = 120$ and $\nu = 48$. For very low T_A the territories are highly volatile, i.e., within a T_A time window the territories are no longer the ones defined at time t which results in low C_p independent of ρ. For higher values of T_A the territories are less mobile and we see the maximization of territory coverage for an intermediate values of ρ.

4.1. The Pair Correlation Function

For a coarse measure of spatial ordering, we plot in **Figure 3** the pair correlation function [32], $g(r) = \nu\langle\sum_{i\neq 0}\delta(|\vec{r} - \vec{r}_i|)\rangle$, where $\delta(z)$ is the Dirac delta function, as a function of the centroid distance $r = |\vec{r}|$ for different ρ and T_A values. In particle systems the pair correlation function gives the likelihood of finding a neighboring particle as a function of distance relative to the ideal gas case. In an ideal gas, $g(r)$ equals 1 for any r as individual particles do not interact with each other and are equally likely to be anywhere in space. A value of zero indicates instead the impossibility of having another particle at that distance in space, e.g., for hard-core interaction of particles of radius σ, $g(r)$ remains zero for all distances up to $r = 2\sigma$. Except for extremely small values of T_A, the emerging territories in our model have an effective hard core interaction as can be observed for any of the curves in **Figure 3**. Those curves remain close to zero up to 2σ where $\sigma = a\sqrt{\nu}/2$, with a the lattice spacing, represents the distance between two evenly spaced centroids when hexagonal territories tessellate the entire domain (see explicit calculation for σ in Heiblum Robles and Giuggioli [25]). A rise from zero to the value one with no evident oscillations would be indicative of a gas with purely hard-core particles. On the other hand a rise beyond the value one with subsequent damped oscillations toward one represents the arrangement of other particles into "shells" of neighbors with the decay pointing to the radial distance over which such spatial ordering persists. Two phases may have qualitatively these characteristics: a liquid but also a hexatic phase. While it is not possible to distinguish a liquid from a hexatic phase from a pair correlation plot, it is possible to determine the appearance of a solid phase because the shells of neighbors are not arranged anymore radially. As a solid possesses hexagonally arranged particles, the radial symmetry is not present anymore and the smoothness of peaks and troughs in the pair correlation function is lost.

A feature that can be evinced by looking at **Figure 3** is that the solid phase for sufficiently large T_A appears for intermediate values of persistence ρ. This is particularly evident in panel (b) where the system has radial symmetry at $\rho = 0$, but then loses it as it approaches $\rho = 0.3$, and then regains it beyond $\rho = 0.55$. In panel (c) although the system is already in a solid phase at $\rho = 0$, the shape of the various $g(r)$ plots also points to a progressive loss, even though only slightly, of radial symmetry as ρ is increased to 0.55, whereas radial symmetry is present when $\rho = 0.75$. This interesting dependence of the appearance of a solid phase depending both on the value of ρ and T_A matches qualitatively the region in parameter space where the coverage efficiency of an individual is maximized, displayed earlier in **Figure 2**.

The partial coverage analysis in conjunction with the pair correlation plots indicate that an animal, for a given size of its own territory, that is for a given value of the active scent time T_A, may select the most appropriate correlation statistics to be able to remark the majority of the scented terrain in T_A steps. When that occurs, it implies that the neighbors are kept outside of the terrain that the animal defends. This in turns makes the territories less mobile, reducing the chance of having territory shape far from hexagonal and with large variability in sizes, and the entire population possess a bigger spatial order.

While **Figures 2**, **3** brings good evidence on how the microscopy of the movement statistics affect the emerging spatial order of the territories for small and intermediate ρ values, it does not seem a viable explanation for large values of ρ. From **Figure 2** one would expect in fact a very high order also for $\rho = 0.95$ and high T_A, but that does not appear to be the case in **Figure 3C**. However, the system may still possess a great degree of order if it were in an hexatic phase. To determine if that is the case, we first try to use appropriate order parameters that should help us to map out more precisely when the system is in a solid phase as well as to distinguish between a liquid and a hexatic phase as a function of ρ and T_A.

4.2. Order Parameters

In Heiblum Robles and Giuggioli [25] some of the present authors have brought support for a continuous solid-hexatic-liquid transition akin to the KTHNY theory of melting as a function of T_A in the TRW model. Starting from a very high T_A in a perfect crystal configuration, by decreasing T_A below a certain value makes the system loose translational order even though it retains orientational order and no phase coexistence has been observed, the transition being continuous. With a further decrease of T_A the system looses also the orientational order to become liquid. We have extended these results by constructing the orientational and translational order parameters as a function both of ρ and T_A.

We use the so-called local bond-orientational parameter [32] $\psi_6(\ell) = \frac{1}{N_\ell}\sum_j^{N_\ell}\exp(i\,6\theta_{\ell,j})$, where $\theta_{\ell,j}$ is the angle that particle ℓ,

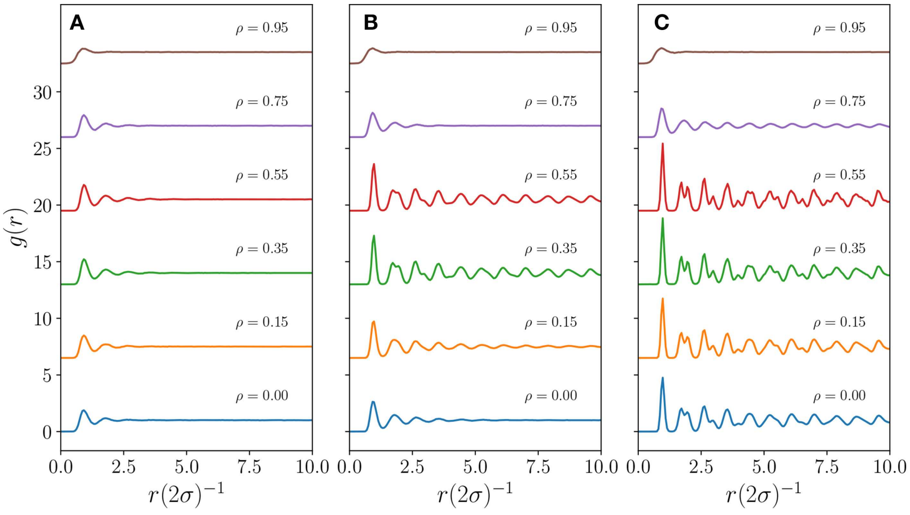

FIGURE 3 | The pair correlation function $g(r)$ for a system with $L = 1,200$, $\nu = 48$. Moving from panel **(A–C)**, the T_A values are 712, 1,068, and 1,424, respectively. Within each panel, the $g(r)$ function has been shifted upwards from zero for visualization purposes. For the case $\rho = 0$ we have used the results from a previous study and as such the T_A values are not precisely the same as the one used for the cases when $\rho \neq 0$; they are 707, 1,070, and 1,409 for panels **(A–C)**, respectively. These differences do not take away from the qualitative differences presented here.

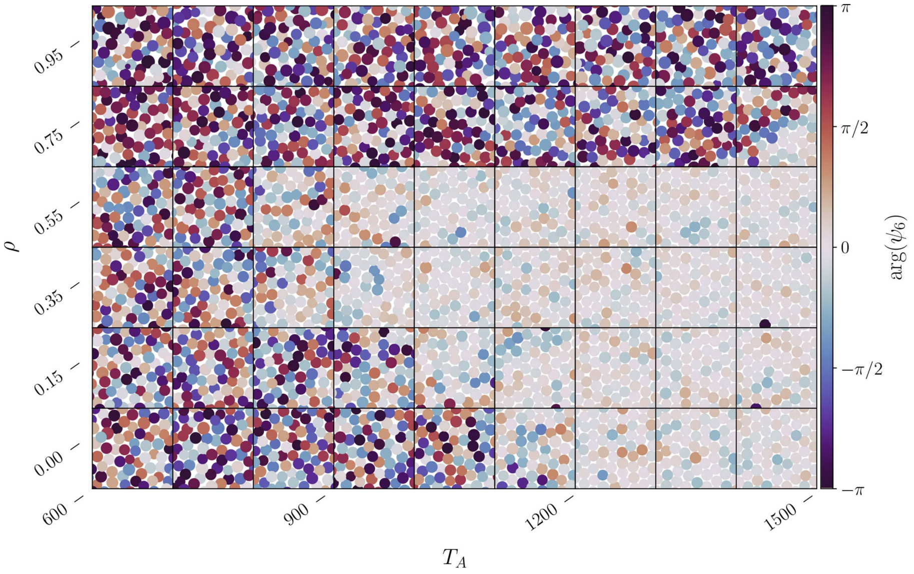

FIGURE 4 | Change in the local bond orientational parameter $\psi_6(\ell)$ for each territory centroid located at $\vec{r}_\ell$ as a function of ρ and T_A. The color of the centroid is determined by $\arg(\psi_6(\ell))$, while the size of each centroid is proportional to the size of its territory. The system parameters are $L = 1,200$ and $\nu = 48$. Each subplot represents subdomain with width $L_S = 50$, a small fraction of the L^2 domain, taken at a random location and at some random time after thermalization.

located at $\vec{r}_\ell$, makes with the j-th neighbor relative to a reference axis, and the j-summation is over the N_ℓ neighbors, the latter obtained through the Voronoi construction [33]. In a perfect crystal, $N_\ell = 6$ and $\theta_{\ell,j} = \frac{\pi}{6}$, hence $\psi_6(\ell) = 1$. In **Figure 4** we visualize qualitatively the changes in orientational order of the system by plotting the argument of the orientational order parameter, $\arg(\psi_6)$, for each territory centroid. The orientational ordering of the system, that is when $\psi_6 \rightarrow 1$, corresponds to when $\arg(\psi_6) \rightarrow 0$. From the various subplots one clearly notices that for a given ρ, if one increases T_A, the hexatic phase does not always appear. It is also evident that for $T_A < 800$ the system cannot reach the hexatic phase independently of the correlation parameter. On the other hand for intermediate values of T_A, e.g., for a given T_A in the range 800–1,100, the system is in a liquid state but then becomes eventually hexatic with sufficiently large ρ, and then liquid again

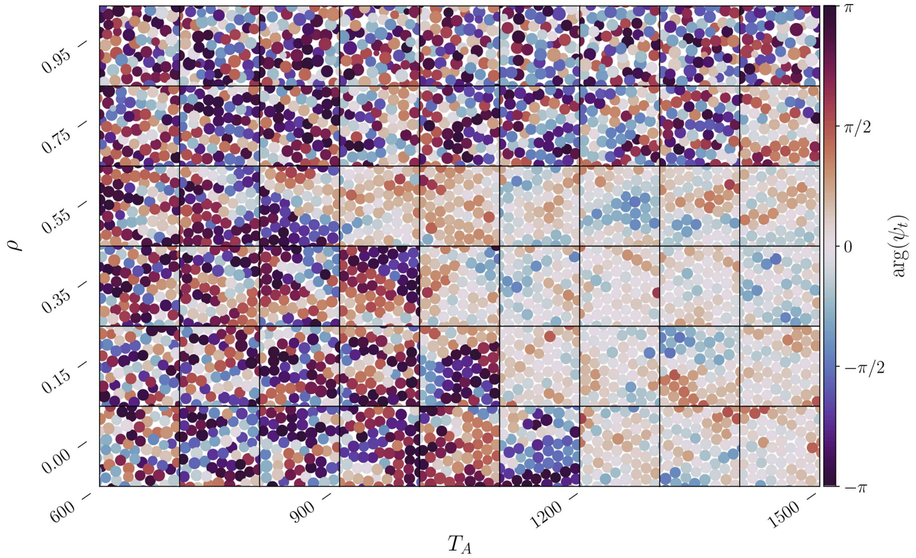

FIGURE 5 | Change in the local translational order parameter $\psi_t(\ell)$ for each territory centroid located at $\vec{r}_\ell$ as a function of ρ and T_A for the system parameters utilized in **Figure 4**. The color of the centroid is determined by $\arg(\psi_t(\ell))$, while the size of each centroid is proportional to the size of its territory. Each subplot represents subdomain with width $L_S = 50$, a small fraction of the L^2 domain, taken at a random location and at some random time after thermalization.

with further increase in ρ. These findings support the pair correlation analysis depicted in **Figure 3** and, in addition, they might also give a better idea of whether the system is in an hexatic or a liquid phase, which was not possible by looking only at $g(r)$.

Within the range of where the bond-orientational parameter appears to indicate a hexatic phase, the system may actually be in a solid phase. This can be determined by analyzing the local translational order parameter $\psi_t(\ell) = \exp(i\vec{G}\cdot\Delta\vec{r}_\ell)$, where $\vec{G}$ is one of the two reciprocal vectors of the simple hexagonal lattice and $\Delta\vec{r}_\ell$ is the displacement of the ℓ-th territorial centroid from its ideal lattice site if it were a perfect crystal ($\psi_t(\ell) = 1$). The result of such an analysis is shown in **Figure 5** where we plot the argument of the local translational order parameter $\arg(\psi_t(\vec{r}_\ell))$ for each territory. The subplots point to the appearance of a solid phase for intermediate values of ρ and sufficiently large values of T_A, which is when the system is also hexatic when one compares (**Figure 4**).

Given the limited resolution we have employed for the parameters of the system, ρ in particular, it is hard to identify the precise region in parameter space where phase transitions occur. However, by comparing **Figures 4**, **5** a small hexatic region may exist in a narrow region of parameter space, potentially for $1,100 \lesssim T_A \lesssim 1,300$ when $\rho = 0.15$, for $900 \lesssim T_A \lesssim 1,200$ when $\rho = 0.35$, and for $900 \lesssim T_A \lesssim 1,200$ when $\rho = 0.55$. This hexatic region should thus be limited on the left by the liquid-hexatic transition and on the right by an hexatic-solid transition.

To try to confirm these qualitative findings we construct the global bond-orientational order parameter $\Psi_6 = \left|(1/N)\sum_\ell \psi_6(\ell)\right|$ and the global translational order parameter $\Psi_t = \left|(1/N)\sum_\ell \psi_t(\ell)\right|$ and calculate their susceptibility, $\chi_6 = N\langle(\Psi_6 - \langle\Psi_6\rangle)^2\rangle$ and $\chi_t = N\langle(\Psi_t - \langle\Psi_t\rangle)^2\rangle$ [32, 34], respectively, as a function of T_A. In **Figure 6** we show the outcome of that analysis, which does not, however, help us to identify precisely the transition points. We thus turn to the analysis of topological defects to help us pinpoint the hexatic region in phase space.

4.3. Topological Defect Analysis

Two types of topological defects accompany the KTHNY melting scenario, namely dislocations and disclinations. Dislocations are translational defects, which destroy long range translational order when are isolated or free. On the other hand, disclinations are orientational defects, which destroy the long range orientational order when they are free. In a perfect 2D hexagonal crystal all atoms have six neighbors. Disclination cores have only 7 or more neighbors whereas antidisclination cores have 5 or less neighbors [35, 36]. For a 2D crystal, an isolated tightly bound 5–7 fold disclination pair is a dislocation [32]. In an imperfect solid, dislocation defects are always found in pairs because they do not destroy long range order as shown in **Figure C1** for our cTRW model.

According to the KTHNY theory of defect induced melting, by increasing temperature the system first undergoes a continuous transition from a solid where only pairs of dislocations are possible, to a hexatic phase where the pairs of dislocations "unbind" spawning free dislocations (see in **Figure C1** an example of how a free disclination destroys the orientational order in the cTRW model). These free dislocations result in the loss of long range translational order found in crystals. With further increase in temperature the system then undergoes another continuous transition from hexatic to liquid where the

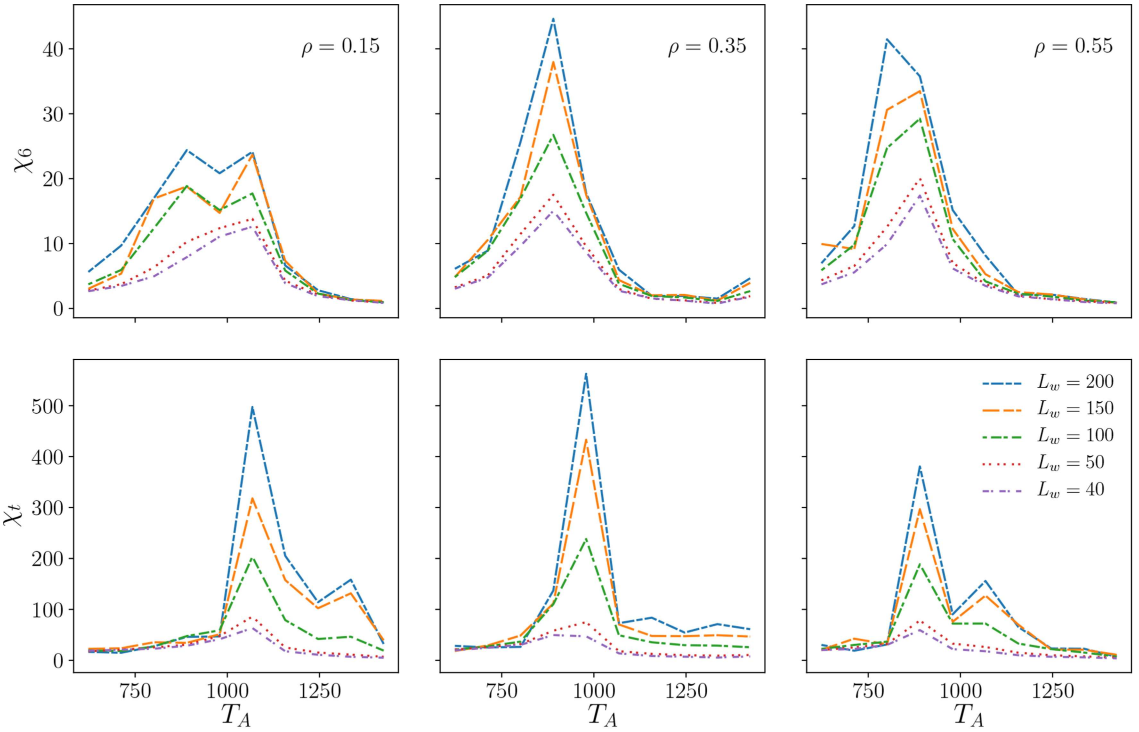

FIGURE 6 | The susceptibilities χ_6 and χ_t of the global order parameters Ψ_6, Ψ_t, respectively. A system with parameters $L = 1,200$ and $\nu = 48$ was subdivided into square subdomains of widths L_W. For each of these subdomains the global order parameters and the susceptibilities are computed and then a variance of those measurements is taken.

dislocations themselves unbind resulting in free disclinations and the loss of long range orientational order [37, 38].

We analyse these topological defects in our cTRW model by considering their fraction λ in the system shown in **Figure 7**. For each type of defect λ is their number relative to the total number of centroids. Looking sequentially at panels (a) to (d) in **Figure 7** one can see that as free disclinations drop significantly there is a sharp increase of dislocations signaling the onset of the liquid-hexatic transition at around, respectively, $T_A = 870$, 890, 712, and 712. The hexatic phase appears once there are no free disclinations in the system. The faster decay of the free dislocations vs. the dislocation pairs that is observed by increasing T_A is indicative of the fact that free dislocations are binding together to form pairs of dislocations. Once free dislocations disappear the system has entered the solid phase. By looking at these values of T_A when free disclinations disappear (hexatic) and free dislocations disappear (solid) we are able to identify the hexatic region in the $T_A - \rho$ parameter space as shown in **Table 1**.

Once in the solid phase with further increase of T_A the system approaches progressively the perfect crystalline arrangement by shedding paired dislocations. For the case $\rho = 0.75$ there is the possibility that ordered phases exist but one ought to look at values of T_A beyond those considered here. On the other hand, when $\rho = 0.95$ the defects show no sign of decaying. This results from the breaking down of the centroid coarse-graining analysis, which is further discussed in the following section.

4.4. Territory Fragmentation

While the previous sections have shed light on the links between the movement statistics of the walkers and the phases of the territorial system for $\rho \leq 0.55$, we have a less clear picture of what occurs for large ρ. While stronger correlation implies that an animal would cross its own territory more quickly, it does not necessarily mean that the terrain is covered more efficiently. On the contrary the coverage efficiency is expected to decrease beyond a certain value of ρ as demonstrated in the ideal scenario of **Figure B1**. With neighboring individuals not covering efficiently their own territories, an animal spending more time at the boundaries has more chance to carve away part of the terrain recently occupied by its own neighbors. In so doing the territorial shapes become less and less convex as ρ is increased.

With further increase in ρ at any given time an animal may have its own scented territory separated into multiple *islands*, which are sets of contiguous lattice sites that contain the scent of one walker only. Those islands where a walker is not present are cut off quickly from its owner and get absorbed by neighboring territories. While islands get created and decay away continuously, we expect the rate at which they form to become larger than the rate at which they dissolve beyond a certain value of ρ. When that happens the centroid of an animal territory could easily be located in between multiple islands, in areas that are also covered by the scent of other individuals, or even outside its own scented region when the territory shape

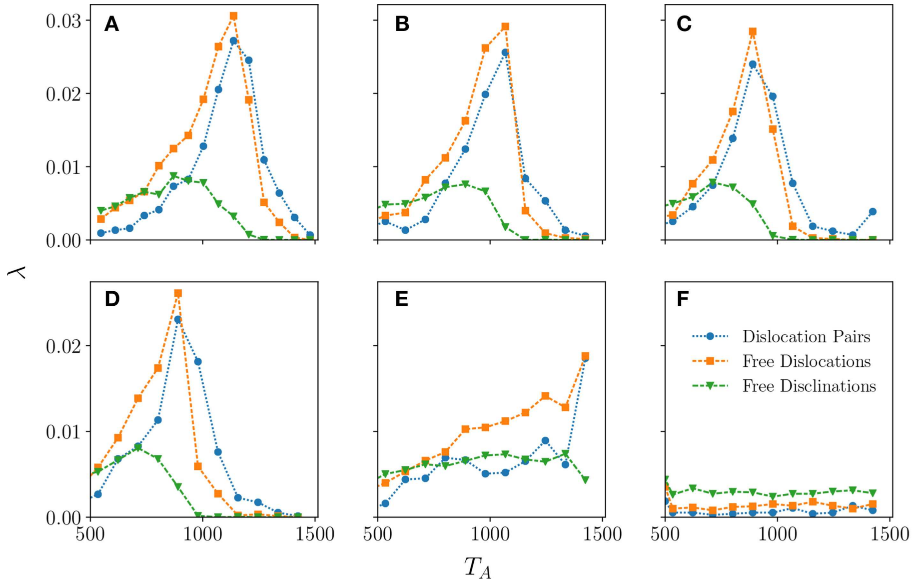

FIGURE 7 | The fraction, λ of each of the defect types considered as a function of T_A for thermalized systems with parameters $L = 1,200$ and $\nu = 48$. The absence of free disclinations marks the transition from liquid to hexatic phase, while the absence of free dislocations is indicative of the system having transitioned into the solid phase from the hexatic phase. The panels **(A–F)** correspond, respectively, to $\rho = 0.00$, 0.15, 0.35, 0.55, 0.75, and 0.95. Defects with different number of neighbors are at least two orders of magnitude smaller than the ones drawn and we have omitted plotting them.

TABLE 1 | Approximate phase regions in T_A for each value of ρ extracted from the appearance/disappearance of topological defects (see **Figure 7**).

ρ	Hexatic region (T_A)	Solid region (T_A)
0.00	1273–1409	>1409
0.15	1157–1335	>1335
0.35	1068–1157	>1157
0.55	979–1157	>1157

Within the hexatic region there are free dislocation defects but no free disclination defects, whereas in the solid region there are pairs of dislocation defects but no free dislocation defects.

is highly concave. In these cases the centroid analysis, utilized in previous sections to identify the phases of the system, is not appropriate any more and there are no biological meaningful ways to define a territorial centroid.

We can, however, quantify the degree of fragmentation as a function of the system parameters by considering the ratio $\kappa = N/I$ where N is the number animals in the system and I is the total number of islands. This fragmentation index is plotted in **Figure 8**. For low T_A values, traces of past presence of an individual get lost quickly, and thus it is not so frequent for an animal to encounter foreign scent. While such encounters increase as T_A gets larger, potentially reducing I, they are rare and are thus relatively independent of how straight the animal movement trajectories are. Beyond a certain value of T_A foreign scent encounter events become very frequent and the rate of increase is affected by the shape of the territories. For $\rho \lesssim 0.75$ the encounters occur mainly at boundary sites and thus further increase in T_A does not change the number of islands in the system, which remains at $\kappa = 1$ when the number of islands corresponds to the number of territories. This is not the case for $\rho > 0.75$ where the number of islands becomes larger than N.

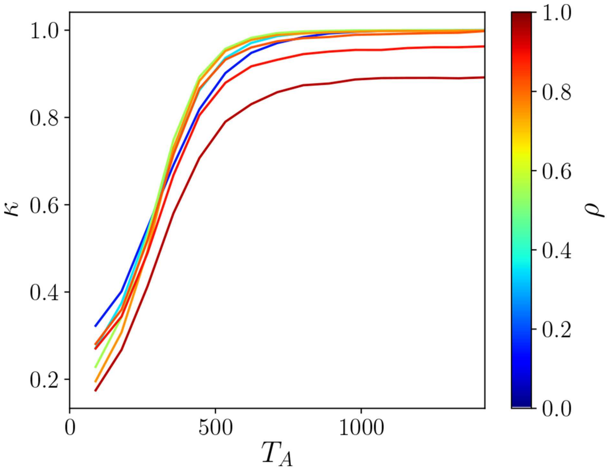

FIGURE 8 | The fragmentation index κ as a function of the active scent time T_A for thermalized systems with parameters $L = 1,200$ and $\nu = 48$. With $\rho \lesssim 0.75$, at low T_A values the territories are concave and as a result are more prone to fragmentation resulting in low κ. As the T_A is increased, the territories become more convex becoming more resistant to fragmentation resulting in $\kappa = 1$ for $T_A \gtrsim 800$. On the other hand, for $\rho \gtrsim 0.75$ fragmentation persists in the system regardless of T_A.

The appearance of fragmented territories for $\rho \gtrsim 0.75$ as shown in **Figure 8** helps us interpret **Figures 4**, **5** when $\rho \geq 0.5$, which indicated the presence of a fluid for any T_A. In light of

Figure 8 it is clear that we cannot conclude that for larger T_A no ordered phase appears because the territory centroids are not an appropriate coarse grained representation of the animal scented territories. Although we believe that an analysis that takes into account the actual shape of the territories might help us develop other ways to identify order in fragmented terrain, we have decided not to perform such investigation here given the heavy computational cost that such a study would entail.

5. CONCLUSIONS

Territoriality is a common behavior in natural populations as it allows individual animals or family units to defend resources being food, shelter, or mates. We have studied here the case where the mechanisms through which animals defend their resources is via leaving trace of their passage on the terrain. For our theoretical analysis we have used a collective movement model recently employed to study red fox movement data [39] called the territorial random walk model. We have extended its prediction by determining how the individual movement statistics affect territory formation at the population level. And we have focused in particular on relaxing the diffusive assumption allowing the walkers to have a variable degree of correlation in their movement steps.

By studying the main parameters of the systems, namely the degree of correlation of the walk ρ and the active scent time T_A, we have brought evidence pointing to the existence of the KTHNY melting scenario with liquid, hexatic and solid phases. We have identified the coverage efficiency of an individual territory, which is controlled by ρ and T_A, as the micro level behavior that explains why different phases of territories are present at the macro level.

As the movement of the individuals becomes more correlated i.e., by increasing ρ from 0, they increase territory coverage. Individuals are able to re-scent more quickly and more readily defend their territory from neighbors. Territories are less mobile and the whole system becomes more ordered.

Beyond an intermediate degree of correlation, that is for high values of ρ, the walkers are not only inefficient at covering their own territory, but also spend more time at the borders. Their increased presence at the borders gives them more opportunities to take over neighboring territories. This results in large variation in the shape and size of territories and ultimately their fragmentation. In this scenario, the coarse grained approximation is no longer suitable to determine the spatial ordering.

Moreover, we have demonstrated how it may be useful to look at the presence of different types of topological defects to pinpoint phase transitions in the correlated territorial random walk model. As thermodynamic limits represent a big abstraction from the realm of biological systems we believe that this latter part of our analysis will be instrumental to determine empirically the spatial order of an actual population of territorial animals. With the recent development in animal tracking [40] it is in fact realistic to have in the near future simultaneous highly resolved movement data of neighboring territorial individuals from which defect densities and movement correlation statistics can be extracted.

Applications of this study extend beyond an ecological context. For example, in multi-robot online area coverage [31] tasks such as surveillance, search and harvesting [41–44] involve coordinating a large number of robots. In such cases the natural approach is to use a decentralized controller [45]. The observations and insights of this study may help refine stigmergic control systems that have been successfully demonstrated in previous studies [46, 47]. As an avenue for future research, it might be interesting to study the difference of the cTRW model on scale-free and small-world networks and compare it the bioinspired machine learning models used for semi-supervised learning [48, 49].

DATA AVAILABILITY

The datasets generated for this study are available on request to the corresponding author. Data used can be found at https://www.dropbox.com/sh/06ts5rwb922yqwk/AADeY66Q_7fqn5axMKcCK-Tra?dl=0.

AUTHOR CONTRIBUTIONS

LG designed the study and wrote the paper. SS and AH created the computational code. SS analyzed the data.

FUNDING

LG and SS acknowledge funding from, respectively, the Engineering and Physical Research Council Grant nos. EP/I013717/1 and S108151-111.

SUPPLEMENTARY MATERIAL

The Supplementary Material for this article can be found online at: https://www.frontiersin.org/articles/10.3389/fphy.2019.00129/full#supplementary-material

REFERENCES

1. Goychuk I, Kharchenko VO, Metzler R. How molecular motors work in the crowded environment of living cells: coexistence and efficiency of normal and anomalous transport. *PLoS ONE*. (2014) **9**:e91700. doi: 10.1371/journal.pone.0091700
2. Kusumi A, Nakada C, Ritchie K, Murase K, Suzuki K, Murakoshi H, et al. Paradigm shift of the plasma membrane concept from the two-dimensional continuum fluid to the partitioned fluid: high-speed single-molecule tracking of membrane molecules. *Annu Rev Biophys Biomol Struct*. (2005) **34**:351–78. doi: 10.1146/annurev.biophys.34.040204.144637
3. Kenkre VM, Giuggioli L, Kalay Z. Molecular motion in cell membranes: analytic study of fence-hindered random walks. *Phys Rev E*. (2008) **77**:051907. doi: 10.1103/PhysRevE.77.051907

4. Dieterich P, Klages R, Preuss R, Schwab A. Anomalous dynamics of cell migration. *Proc Natl Acad Sci USA*. (2008) **105**:459–63. doi: 10.1073/pnas.0707603105
5. Viswanathan GM, da Luz MGE, Raposo EP, Stanley HE. *The Physics of Foraging: An Introduction to Random Searches and Biological Encounters*. Carmbridge: Cambridge Univ. Press (2011).
6. Boyer D, Crofoot MC, Walsh PD. Non-random walks in monkeys and humans. *J Roy Soc Interface*. (2011) **9**:842–7. doi: 10.1098/rsif.2011.0582
7. Falcón-Cortés A, Boyer D, Giuggioli L, Majumdar SN. Localization transition induced by learning in random searches. *Phys Rev Lett*. (2017) **119**:140603. doi: 10.1103/PhysRevLett.119.140603
8. Goldstein S. On diffusion by discontinuous movements, and on the telegraph equation. *Q J Mech Appl Math*. (1951) **4**:129–56. doi: 10.1093/qjmam/4.2.129
9. Codling EA, Planck MJ, Benhamou S. Random walk models in biology. *J Roy Soc Interface*. (2008) **95**:813–34. doi: 10.1098/rsif.2008.0014
10. Benhamou S. Of scales and stationarity in animal movements. *Ecol Lett*. (2014) **17**:261–72. doi: 10.1111/ele.12225
11. Brown JL, Orians GH. Spacing patterns in mobile animals. *Ann Rev Ecol Syst*. (1970) **1**:239–62. doi: 10.1146/annurev.es.01.110170.001323
12. Burt WH. Territoriality and home range concepts as applied to mammals. *J Mammal*. (1943) **24**:346–52.
13. Maher CA, Lott DF. Definitions of territoriality used in the study of variation in vertebrate spacing systems. *Anim Behav*. (1995) **49**:1581–97.
14. Adams ES. Approaches to the study of territory size and shape. *Ann Rev Ecol Syst*. (2001) **32**:277–303. doi: 10.1146/annurev.ecolsys.32.081501.114034
15. Davies NB, Houston AI. Territory economics. In: Krebs JR, Davies NB, editors. *Behavioural Ecology: An Evolutionary Approach, 2nd ed.* Oxford: Blackwell Sci. (1984). p. 148–69.
16. Gosling LM, Roberts SC. Scent-marking by male mammals: cheat-proof signals to competitors and mates. *Adv Stud Behav*. (2001) **30**:169–217. doi: 10.1016/S0065-3454(01)80007-3
17. Grassé PP. La reconstruction du nid et les coordinations interindividuelles chez Bellicositermes natalensis et Cubitermes sp. La théorie de la stigmergie: essai dÕinterprétation du comportement des termites constructeurs. *Insec Soc*. (1959) **6**:41–83.
18. Theraulaz G, Bonabeau E. A brief history of stigmergy. *Artificial Life*. (1999) **5**:97–116.
19. Giuggioli L, Potts JR, Rubenstein DI, Levin SA. Stigmergy, collective actions, and animal social spacing. *Proc Natl Acad Sci USA*. (2013) **110**:16904–9. doi: 10.1073/pnas.1307071110
20. Lewis MA, Murray JD. Modelling territoriality and wolf-deer interactions. *Ecology*. (1993) **366**:738–40.
21. Moorcroft PR, Lewis MA. *Mechanistic Home Range Analysis*. Princeton, NJ: Princeton University Press (2006).
22. Giuggioli L, Potts JR, Harris S. Animal interactions and the emergence of territoriality. *PLoS Comput Biol*. (2011) **7**:e1002008. doi: 10.1371/journal.pcbi.1002008
23. Giuggioli L, Kenkre VM. Consequences of animal interactions on their dynamics: emergence of home ranges and territoriality. *Mov Ecol*. (2014) **2**:20. doi: 10.1186/s40462-014-0020-7
24. Alberts AC. Constraints on the design of chemical communication systems in terrestrial vertebrates. *Am Nat*. (1992) **139**:S62–89.
25. Heiblum Robles A, Giuggioli L. Phase transitions in stigmergic territorial systems. *Phys Rev E*. (2018) **98**:042115. doi: 10.1103/PhysRevE.98.042115
26. Halperin BI, Nelson DR. Theory of two-dimensional melting. *Phys Rev Lett*. (1978) **41**:121–4.
27. Kosterllitz DJ, Thouless JM. Ordering, metastability and phase transitions in two-dimensional systems. *J Phys C Solid State Phys*. (1973) **1181**:1181–203.
28. Young AP. Melting and the vector Coulomb gas in two dimensions. *Phys Rev B*. (1979) **19**:1855–66.
29. Giuggioli L, Abramson G, Kenkre VM, Parmenter RR, Yates TL. Theory of home range estimation from displacement measurements of animal populations. *J Theor Biol*. (2006) **240**:126–35. doi: 10.1016/j.jtbi.2005.09.002
30. Chupeau M, Bénichou O, Voituriez R. Cover times of random searches. *Nat Phys*. (2015) **11**:844. doi: 10.1038/nphys3413
31. Giuggioli L, Arye I, Heiblum Robles A, Kaminka GA. From ants to birds: a novel bio-inspired approach to online area coverage. In: Groß R, Kolling A, Berman S, Frazzoli E, Martinoli A, Matsuno F, et al., editors. *Distributed Autonomous Robotic Systems: The 13th International Symposium*. Cham: Springer International Publishing (2018). p. 31–43.
32. Binder K, Kob W. *Glassy Materials and Disordered Solids: An Introduction to Their Statistical Mechanics*. Singapore: World scientific (2011).
33. Fraser DP, Zuckermann MJ, Mouritsen OG. Simulation technique for hard-disk models in two dimensions. *Phys Rev A*. (1990) **42**:3186.
34. Jaster A. Computer simulations of the two-dimensional melting transition using hard disks. *Phys Rev E*. (1999) **59**:2594.
35. Harris WF. Disclinations. *Sci Ame*. (1977) **237**:130–45.
36. DeWit R. Relation between dislocations and disclinations. *J Appl Phys*. (1971) **42**:3304–8.
37. Qi W, Gantapara AP, Dijkstra M. Two-stage melting induced by dislocations and grain boundaries in monolayers of hard spheres. *Soft Matter*. (2014) **10**:5449. doi: 10.1039/C4SM00125G
38. Quinn RA, Goree J. Experimental test of two-dimensional melting through disclination unbinding. *Phys Rev E*. (2001) **64**:051404. doi: 10.1103/PhysRevE.64.051404
39. Potts JR, Harris S, Giuggioli L. Quantifying behavioral changes in territorial animals caused by sudden population declines. *Am Nat*. (2013) **182**:E73–82. doi: 10.1086/671260
40. Nathan RM, Giuggioli L. A milestone for movement ecology research. *Move Ecol*. (2013) **1**:1. doi: 10.1186/2051-3933-1-1
41. Schneider-Fontán M, Matarić MJ. Territorial multi-robot task division. *IEEE Trans Robot Automat*. (1998) **14**:815–22.
42. Larionova S, Almeida N, Marques L, De Almeida AT. Olfactory coordinated area coverage. *Autonom Robots*. (2006) **20**:251–60. doi: 10.1007/s10514-006-7099-7
43. Paull L, Saeedi S, Seto M, Li H. Sensor-driven online coverage planning for autonomous underwater vehicles. *IEEE/ASME Trans Mechat*. (2013) **18**:1827–38. doi: 10.1109/TMECH.2012.2213607
44. Fazli P, Davoodi A, MacKworth AK. Multi-robot repeated area coverage. *Autonom Robot*. (2013) **34**:251–76. doi: 10.1007/s10514-012-9319-7
45. Marjovi A, Nunes JG, Marques L, De Almeida A. Multi-robot exploration and fire searching. In: *2009 IEEE/RSJ International Conference on Intelligent Robots and Systems, IROS 2009*. St. Louis, MO: IEEE. (2009). p. 1929–34. doi: 10.1109/IROS.2009.5354598
46. Scheidt D, Stipes J. Cooperating unmanned vehicles. In: *Proceedings 2005 IEEE Networking, Sensing and Control, 2005*. Tucson, AZ: IEEE (2005). p. 326–31.
47. Stipes J, Hawthorne R, Scheidt D, Pacifico D. Cooperative localization and mapping. In: *2006 IEEE International Conference on Networking, Sensing and Control*. Fort Lauderdale, FL: IEEE (2006). p. 596–601.
48. de Arruda HF, Silva FN, Costa LdF, Amancio DR. Knowledge acquisition: a complex networks approach. *Inform Sci*. (2017) **421**:154–66. doi: 10.1016/j.ins.2017.08.091
49. Lima TS, de Arruda HF, Silva FN, Comin CH, Amancio DR, Costa LdF. The dynamics of knowledge acquisition via self-learning in complex networks. *Chaos Interdiscipl J Nonlinear Sci*. (2018) **28**:083106. doi: 10.1063/1.5027007

Conflict of Interest Statement: The authors declare that the research was conducted in the absence of any commercial or financial relationships that could be construed as a potential conflict of interest.

frontiers in Physics

ORIGINAL RESEARCH
published: 18 September 2019
doi: 10.3389/fphy.2019.00120

Transient Anomalous Diffusion in Run-and-Tumble Dynamics

M. Reza Shaebani* and Heiko Rieger*

Department of Theoretical Physics, Center for Biophysics, Saarland University, Saarbrücken, Germany

We study the stochastic dynamics of a particle with two distinct motility states. Each one is characterized by two parameters: one represents the average speed and the other represents the persistence quantifying the tendency to maintain the current direction of motion. We consider a run-and-tumble process, which is a combination of an active fast motility mode (persistent motion) and a passive slow mode (diffusion). Assuming stochastic transitions between the two motility states, we derive an analytical expression for the time evolution of the mean square displacement. The interplay of the key parameters and the initial conditions as for instance the probability of initially starting in the run or tumble state leads to a variety of transient regimes of anomalous transport on different time scales before approaching the asymptotic diffusive dynamics. We estimate the crossover time to the long-term diffusive regime and prove that the asymptotic diffusion constant is independent of initially starting in the run or tumble state.

Keywords: anomalous diffusion, run-and-tumble, persistent random walk, active motion, transient dynamics

Edited by:
Ralf Metzler,
University of Potsdam, Germany

Reviewed by:
Rainer Klages,
Queen Mary University of London, United Kingdom
Jae-Hyung Jeon,
Pohang University of Science and Technology, South Korea
Aleksei Chechkin,
Kharkov Institute of Physics and Technology, Ukraine

****Correspondence:***
M. Reza Shaebani
shaebani@lusi.uni-sb.de
Heiko Rieger
h.rieger@mx.uni-saarland.de

Specialty section:
This article was submitted to Interdisciplinary Physics, a section of the journal Frontiers in Physics

Received: *01 May 2019*
Accepted: *13 August 2019*
Published: *18 September 2019*

Citation:
Shaebani MR and Rieger H (2019) Transient Anomalous Diffusion in Run-and-Tumble Dynamics. Front. Phys. 7:120. doi: 10.3389/fphy.2019.00120

1. INTRODUCTION

Many transport processes in nature involve distinct motility states. Of particular interest is the run-and-tumble process, which consists of alternating phases of fast active and slow passive motion. Prominent examples are bacterial species that swim when their flagella form a bundle and synchronize their rotation. The bundle is disrupted and swimming stops when some of the flagella stochastically change their rotational direction. In the absence of rotating bundle, the bacterium moves diffusively until it manages to re-form the bundle and actively move forward again [1, 2]. The run-and-tumble dynamics is beneficial for bacteria as it allows them to react to the environmental changes by adjusting their average run time or speed [3], change their direction of motion, perform an efficient search [4–7], or optimize their navigation [8, 9].

Another example is the motion of molecular motors along cytoskeletal filaments. When motor proteins bind to filaments, they perform a number of steps until they randomly unbind and experience diffusion in the crowded cytoplasm. While the efficiency of long-distance cargo delivery requires high motor processivity (i.e., the tendency to continue the motion along the filament), the slow diffusive mode during unbinding periods is also vital for cellular functions which depend on the localization of the reactants [10–13]. The processivity of the motors (and thus the unbinding probability) depends on the type of motor and filament [14, 15] and the presence of particular proteins or binding domains in the surrounding medium [16–18]. On the other hand other factors, such as cell crowding, may affect the binding probability. Therefore, the switching probabilities between active run and tumble states are generally asymmetric. By ignoring the microscopic details of stepping on filaments, coarse-grained random walk models have been employed to study the two-state dynamics of molecular motors [19–22]. Dentritic immune cells also move persistently (migration phase) interrupted by slow phases for antigen uptake [23]. There have been many other locomotive patterns in biological and non-living systems investigated via models with distinct states of motility [24–33]. For instance, the problem of searcher proteins finding a specific target site over a DNA strand has been studied by multi-state stochastic processes [34–36].

The particle trajectories obtained from experiments often comprise a set of recorded positions of the particle, from which the successive directions of motion can be deduced. These directions are correlated on short time scales for active motions. However, the trajectory eventually gets randomized and the asymptotic dynamics is diffusive, with a diffusion constant D_{asymp} that depends on the particle velocity and persistency [37, 38]. One expects a similar long-term behavior for a mixture of run and tumble dynamics as well. The question arises how the transient short time dynamics, the crossover time to asymptotic diffusion, and D_{asymp} depend on the run and tumble velocities and the switching probabilities between the two states. It is also unclear how the overall dynamics is influenced by the choice of the initial conditions, like the probabilities to start either in the run or tumble state, which are parameters that can be extracted from experimental data.

Here, we present a two-state model for the run-and-tumble dynamics with spontaneous switchings between the states of motility. By deriving an analytical expression for the time evolution of the mean square displacement, we show how the interplay between the run and tumble velocities, the transition probabilities, and the initial conditions leads to various anomalous transport regimes on short and intermediate time scales. We particularly clarify how the probability of starting from run or tumble state diversifies the transient anomalous regimes of motion, and verify that the long-term diffusion constant D_{asymp} does not depend on the choice of the initial conditions.

2. MODEL

We develop a stochastic model for the run-and-tumble dynamics with spontaneous transitions between the motility states. We consider a two-state random walk in discrete time and continuous space with the following characteristics: The *run* phase is a persistent random walk with persistency p and mean speed v_{R}. The dynamics in the *tumble* phase is an ordinary diffusion with the mean speed v_{T}. The asymmetric transition probabilities from run to tumble phase and vice versa are denoted, respectively, by $f_{\text{R}\to\text{T}}$ and $f_{\text{T}\to\text{R}}$. As a result of constant transition probabilities, the run and tumble times are exponentially distributed in our model. This restriction can be relaxed by introducing time-dependent transition probabilities (Shaebani and Sadjadi, submitted). To characterize the persistency of the run phase, we use the probability distribution $F_{\text{R}}(\theta)$ of directional changes along the trajectory in the run phase. The directional persistence can be characterized by the persistency parameter $p=\int_{-\pi}^{\pi}\text{d}\theta \quad e^{\text{i}\theta}F_{\text{R}}(\theta)$, which leads to $p=\langle\cos\theta\rangle$ for symmetric distributions with respect to the arrival direction. Thus, p ranges from 0 for pure diffusion to 1 for ballistic motion and reflects the average curvature of the run trajectories. Similarly, we define $F_{\text{T}}(\theta)$ for the probability distribution of directional changes along the trajectory in the tumble phase, and $F_{\text{R}\to\text{T}}(\theta)$ and $F_{\text{T}\to\text{R}}(\theta)$ for the directional changes when switching between the states occurs (see **Figure 1A**). In the tumble phase (i.e., an ordinary diffusion), the probability distribution of directional changes is isotropically distributed ($F_{\text{T}}(\theta)=\frac{1}{2\pi}$), leading to a zero persistency.

The run-and-tumble stochastic process can be described in discrete time by introducing the probability densities $P_t^R(x,y|\alpha)$ and $P_t^T(x,y|\alpha)$ to find the particle at position (x,y) arriving along the direction α at time t in the run and tumble states, respectively. α is defined with respect to a given reference direction, as shown in **Figure 1B**. Denoting the time interval between consecutive recorded positions of the particle by Δt, the following set of master equations describe the dynamical evolution of the probability densities

$$\begin{aligned}
&P_{t+\Delta t}^R(x,y|\alpha) = \\
&(1-f_{\text{R}\to\text{T}})\int_{-\pi}^{\pi} d\gamma\, F_{\text{R}}(\alpha-\gamma) P_t^R(x-v_{\text{R}}\Delta t\cos\alpha, y-v_{\text{R}}\Delta t\sin\alpha|\gamma) \\
&+f_{\text{T}\to\text{R}}\int_{-\pi}^{\pi} d\gamma\, F_{\text{T}\to\text{R}}(\alpha-\gamma) P_t^T(x-v_{\text{R}}\Delta t\cos\alpha, y-v_{\text{R}}\Delta t\sin\alpha|\gamma), \\
\\
&P_{t+\Delta t}^T(x,y|\alpha) = \\
&(1-f_{\text{T}\to\text{R}})\int_{-\pi}^{\pi} d\gamma\, F_{\text{T}}(\alpha-\gamma) P_t^T(x-v_{\text{T}}\Delta t\cos\alpha, y-v_{\text{T}}\Delta t\sin\alpha|\gamma) \\
&+f_{\text{R}\to\text{T}}\int_{-\pi}^{\pi} d\gamma\, F_{\text{R}\to\text{T}}\, P_t^R(x-v_{\text{T}}\Delta t\cos\alpha, y-v_{\text{T}}\Delta t\sin\alpha|\gamma).
\end{aligned} \tag{1}$$

Each of the two terms on the right-hand side of the equations represents the possibility of being in one of the two states in the previous time step (see **Figure 1B** for the particle trajectory during two successive steps). The probability of starting the motion in the run or tumble phase is denoted by P_0^R and P_0^T, respectively (with $P_0^T=1-P_0^R$). The change in the direction of motion $\theta=\alpha-\gamma$ with respect to the arrival direction is randomly chosen according to the turning-angle distribution $F_{\text{R}}(\theta)$ or $F_{\text{T}}(\theta)$ in the run or tumble state, respectively. Both distributions are symmetric with respect to the arrival direction (i.e., left-right symmetric in 2D). We assume for simplicity that the directional change during the transition between the two states follows the turning-angle distribution of the new state, corresponding to $F_{\text{R}\to\text{T}}(\theta)=F_{\text{T}}(\theta)$ and $F_{\text{T}\to\text{R}}(\theta)=F_{\text{R}}(\theta)$. However, in general one should consider independent turning-angle distributions with non-zero mean for $F_{\text{R}\to\text{T}}(\theta)$ and $F_{\text{T}\to\text{R}}(\theta)$ as, for instance, a sharp change in the direction of motion of *E. coli* or *Bacillus Subtilis* when switching from tumbling to running is observed [1, 2, 6].

The total probability density $P_{t+\Delta t}(x,y|\alpha)$ to find the particle at position (x,y) arriving along the direction α at time $t+\Delta t$ is given by $P_{t+\Delta t}(x,y|\alpha) = P_{t+\Delta t}^R(x,y|\alpha) + P_{t+\Delta t}^T(x,y|\alpha)$. Using the Fourier transform of the probability density in each state h ($h\in\{R,T\}$), defined as

$$P_{t+\Delta t}^h(\boldsymbol{k}|m) \equiv \int_{-\pi}^{\pi}\text{d}\alpha\, e^{im\alpha}\int\text{d}y\int\text{d}x\; e^{i\boldsymbol{k}\cdot\boldsymbol{r}} P_{t+\Delta t}^h(x,y|\alpha), \tag{2}$$

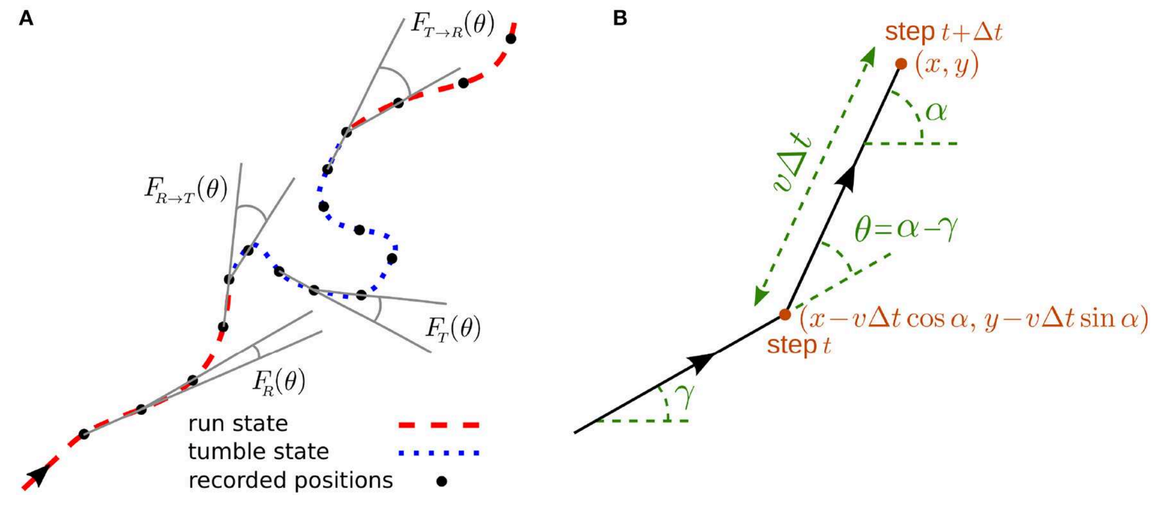

FIGURE 1 | (A) A sample trajectory with run-and-tumble dynamics. Typical turning angles for different types of turning-angle distributions introduced in the model are shown. **(B)** Trajectory of the walker during two successive steps.

the Fourier transform of the total probability density is given by $P_{t+\Delta t}(\boldsymbol{k}|m) = P^R_{t+\Delta t}(\boldsymbol{k}|m) + P^T_{t+\Delta t}(\boldsymbol{k}|m)$, from which the moments of displacement can be calculated as

$$\langle x^{j_1} y^{j_2}\rangle(t{+}\Delta t) \equiv \int \mathrm{d}\alpha \int \mathrm{d}y \int \mathrm{d}x \; x^{j_1} y^{j_2} P_{t+\Delta t}(x,y|\alpha)$$
$$= (-i)^{j_1+j_2} \frac{\partial^{j_1+j_2} P_{t+\Delta t}(k_x,k_y|m=0)}{\partial k_x^{j_1}\,\partial k_y^{j_2}}\bigg|_{(k_x,k_y)=(0,0)}. \qquad (3)$$

By means of a Fourier-z-transform technique, it is possible to solve the master equations (1) to obtain the time evolution of the moments of displacement [38–40]. Here we briefly explain the procedure to calculate the mean square displacement (MSD) as the main quantity of interest. From Equation (3), the MSD is given as

$$\langle r^2\rangle(t{+}\Delta t) = (-i)^2 \frac{\partial^2 P_{t+\Delta t}(k,\phi{=}0|m{=}0)}{\partial k^2}\bigg|_{k=0}, \qquad (4)$$

where (k,ϕ) is the polar representation of $\boldsymbol{k}$. Assuming $F_{\mathrm{R\to T}}(\theta){=}F_{\mathrm{T}}(\theta){=}\frac{1}{2\pi}$ and $F_{\mathrm{T\to R}}(\theta){=}F_{\mathrm{R}}(\theta)$, their Fourier transforms are $F_{\mathrm{R\to T}}(m){=}F_{\mathrm{T}}(m){=}\frac{1}{2\pi}\int_{-\pi}^{\pi}\mathrm{d}\theta\, e^{im\theta}$ and $F_{\mathrm{T\to R}}(\theta){=}F_{\mathrm{R}}(m){=}\int_{-\pi}^{\pi}\mathrm{d}\theta\;\, e^{im\theta} F_{\mathrm{R}}(\theta)$. Next we apply the Fourier transformation on the master equations (1). For example, the first master equation after Fourier transform reads

$$\begin{aligned} &P^R_{t+\Delta t}(k,\phi|m) = \\ &(1{-}f_{\mathrm{R\to T}})\int \mathrm{d}\alpha\, e^{im\alpha} \int d\gamma\, F_{\mathrm{R}}(\alpha{-}\gamma) \int \mathrm{d}y \int \mathrm{d}x\, e^{i\boldsymbol{k}\cdot\boldsymbol{r}} \\ &P^R_t(x{-}v_{\mathrm{R}}\Delta t\cos\alpha, y{-}v_{\mathrm{R}}\Delta t\sin\alpha|\gamma) \\ &+f_{\mathrm{T\to R}} \int \mathrm{d}\alpha\, e^{im\alpha} \int d\gamma\, F_{\mathrm{T\to R}}(\alpha{-}\gamma) \int \mathrm{d}y \int \mathrm{d}x\, e^{i\boldsymbol{k}\cdot\boldsymbol{r}} P^T_t \\ &(x{-}v_{\mathrm{R}}\Delta t\cos\alpha, y{-}v_{\mathrm{R}}\Delta t\sin\alpha|\gamma). \end{aligned} \qquad (5)$$

Then by using the qth order Bessel's function

$$J_q(z) = \frac{1}{2\pi\, i^q}\int_{-\pi}^{\pi}\mathrm{d}\alpha\;\, e^{iz\cos\alpha} e^{-iq\alpha},$$

replacing $e^{ikv_{\mathrm{R}}\Delta t\cos(\alpha-\phi)}$ with $\int_{-\pi}^{\pi} d\beta e^{ikv_{\mathrm{R}}\Delta t\cos\beta}\delta(\beta{-}(\alpha{-}\phi))$, and using

$$\delta(\beta{-}(\alpha{-}\phi)) = \frac{1}{2\pi}\sum_{q=-\infty}^{\infty} e^{-iq(\beta-(\alpha-\phi))},$$

it follows that

$$\begin{aligned} P^{\mathrm{R}}_{t+\Delta t}(k,\phi|m) = &\sum_{q=-\infty}^{\infty} i^q\, e^{-iq\phi} J_q(k\, v_{\mathrm{R}}\Delta t)\, \times \\ &\Big[(1{-}f_{\mathrm{R\to T}})\, F_{\mathrm{R}}(m{+}q)\, P^{\mathrm{R}}_t(k,\phi|m{+}q) \\ &+f_{\mathrm{T\to R}}\; F_{\mathrm{R}}(m{+}q)\, P^{\mathrm{T}}_t(k,\phi|m{+}q)\Big]. \end{aligned} \qquad (6)$$

$P^R_{t+\Delta t}(k,\phi|m)$ can be expanded as a Taylor series

$$\begin{aligned} P^R_{t+\Delta t}(k,\phi|m) = &\; Q^R_{0,t+\Delta t}(\phi|m) + i\,k\,v_{\mathrm{R}}\,\Delta t\, Q^R_{1,t+\Delta t}(\phi|m) \\ &-\frac{1}{2}k^2\, v^2_{\mathrm{R}}\,(\Delta t)^2\, Q^R_{2,t+\Delta t}(\phi|m) + \cdots. \end{aligned} \qquad (7)$$

We expand both sides of Equation (6) and collect all terms with the same power in k. As a result, recursion relations for the Taylor expansion coefficients can be obtained. For instance, for the terms with power 0 in k one finds

$$\begin{aligned} Q^{\mathrm{R}}_{0,t+\Delta t}(\phi|m) \;=\; &(1{-}f_{\mathrm{R\to T}})F_{\mathrm{R}}(m)Q^{\mathrm{R}}_{0,t}(\phi|m) \\ &+f_{\mathrm{T\to R}}\; F_{\mathrm{R}}(m)\; Q^{\mathrm{T}}_{0,t}(\phi|m). \end{aligned} \qquad (8)$$

Similarly, the expansion coefficients of terms with higher powers in k can be calculated and the procedure is repeated for the second master equation in (1). As a result, a set of coupled equations is obtained for each expansion coefficient, connecting time steps $t{+}\Delta t$ and t. Applying a z-transform $Q(z){=}\sum_{t=0}^{\infty} Q_t z^{-t}$ enables one to solve these sets of equations. Particularly the coefficients of terms with power 2 in k, i.e., $Q_2^{\mathrm{R}}(z,\phi|m)$ and $Q_2^{\mathrm{T}}(z,\phi|m)$, are useful to calculate the MSD

$$\langle r^2\rangle(z) = 2(\Delta t)^2 \Big(v_{\mathrm{R}}^2\, Q_2^{\mathrm{R}}(z,0|0){+}v_{\mathrm{T}}^2\, Q_2^{\mathrm{T}}(z,0|0)\Big). \tag{9}$$

Finally we obtain the following exact expression for the MSD in z space

$$\begin{aligned}\langle r^2\rangle(z) ={}&\left[\frac{z(1{-}f_{\mathrm{R\to T}}{-}f_{\mathrm{T\to R}})P_0^R}{z{-}1{+}f_{\mathrm{R\to T}}{+}f_{\mathrm{T\to R}}}+\frac{z^2 f_{\mathrm{T\to R}}}{G_0(z)}\right]\left[\frac{2z^2}{(z{-}1)G_1(z)}-\frac{1}{(z{-}1}\right]v_{\mathrm{R}}^2\,(\Delta t)^2\\ &+\left[\frac{-z(1{-}f_{\mathrm{R\to T}}{-}f_{\mathrm{T\to R}})P_0^R}{z{-}1{+}f_{\mathrm{R\to T}}{+}f_{\mathrm{T\to R}}}+\frac{z^2(1{-}f_{\mathrm{T\to R}})}{G_0(z)}-\frac{z(1{-}f_{\mathrm{T\to R}}{-}f_{\mathrm{R\to T}})}{G_0(z)}\right]\\ &\times\left[\frac{2z\left[z{-}(1{-}f_{\mathrm{R\to T}})p\right]}{(z{-}1)G_1(z)}v_{\mathrm{T}}^2+\frac{2z}{(z{-}1)G_1(z)}f_{\mathrm{T\to R}}\,p\,v_{\mathrm{R}}v_{\mathrm{T}}-\frac{1}{z{-}1}v_{\mathrm{T}}^2\right](\Delta t)^2,\end{aligned} \tag{10}$$

where $G_0(z){=}(z{-}1)(z{-}1{+}f_{\mathrm{T\to R}}{+}f_{\mathrm{R\to T}})$ and $G_1(z){=}z\big(z{-}(1{-}f_{\mathrm{R\to T}})\,p\big)$. By inverse z-transforming Equation (10), the MSD can be obtained as a function of time. The resulting general expression for the MSD $\langle r^2\rangle(t)$ is lengthy and depends on the run persistency p, the speeds v_{R} and v_{T}, the transition probabilities $f_{\mathrm{R\to T}}$ and $f_{\mathrm{T\to R}}$, and the probability of initially starting in the run P_0^R or tumble state $P_0^T{=}1{-}P_0^R$. $\langle r^2\rangle(t)$ typically consists of linear and exponentially decaying terms with t as well as time-independent terms, as shown in the following in the special case of constant velocity and the initial condition of starting in the run state. By choosing $\Delta t{=}1$, $v_{\mathrm{R}}{=}v_{\mathrm{T}}{=}1$, and the initial condition $P_0^R{=}1$, the general expression of $\langle r^2\rangle(t)$ reduces to.

$$\begin{aligned}\langle r^2\rangle(t)={}&\frac{\Big(p\big((f_{\mathrm{T\to R}}{-}1)f_{\mathrm{R\to T}}{+}f_{\mathrm{T\to R}}{+}f_{\mathrm{R\to T}}^2\big){+}f_{\mathrm{T\to R}}{+}f_{\mathrm{R\to T}}\Big)}{p\,(f_{\mathrm{R\to T}}{-}1)(f_{\mathrm{T\to R}}{+}f_{\mathrm{R\to T}}){+}f_{\mathrm{T\to R}}{+}f_{\mathrm{R\to T}}}\,t\,-\\ &\frac{2\,p\,(f_{\mathrm{R\to T}}{-}1)\big(f_{\mathrm{R\to T}}p(f_{\mathrm{T\to R}}{+}f_{\mathrm{R\to T}}{-}2){+}f_{\mathrm{T\to R}}{+}f_{\mathrm{R\to T}}{+}p{-}1\big)\big(p(1{-}f_{\mathrm{R\to T}})\big)^t}{\big(p(f_{\mathrm{R\to T}}{-}1){+}1\big)^2(f_{\mathrm{T\to R}}{-}f_{\mathrm{R\to T}}p{+}f_{\mathrm{R\to T}}{+}p{-}1)}\\ &+\frac{2\,p\,f_{\mathrm{R\to T}}(1{-}f_{\mathrm{T\to R}}{-}f_{\mathrm{R\to T}})^{t+2}}{(f_{\mathrm{T\to R}}{+}f_{\mathrm{R\to T}})^2(f_{\mathrm{T\to R}}{-}f_{\mathrm{R\to T}}p{+}f_{\mathrm{R\to T}}{+}p{-}1)}+\\ &\frac{\Big(p\big((f_{\mathrm{T\to R}}{-}1)f_{\mathrm{R\to T}}{+}f_{\mathrm{T\to R}}{+}f_{\mathrm{R\to T}}^2\big){+}f_{\mathrm{T\to R}}{+}f_{\mathrm{R\to T}}\Big)}{p\,(f_{\mathrm{R\to T}}{-}1)(f_{\mathrm{T\to R}}{+}f_{\mathrm{R\to T}}){+}f_{\mathrm{T\to R}}{+}f_{\mathrm{R\to T}}}-\\ &\frac{2\,p\big((f_{\mathrm{T\to R}}{+}f_{\mathrm{R\to T}})^2{-}f_{\mathrm{R\to T}}\big){+}(f_{\mathrm{T\to R}}{+}f_{\mathrm{R\to T}})^2}{\big(p\,(f_{\mathrm{R\to T}}{-}1)(f_{\mathrm{T\to R}}{+}f_{\mathrm{R\to T}}){+}f_{\mathrm{T\to R}}{+}f_{\mathrm{R\to T}}\big)^2}+\\ &\frac{p^2(f_{\mathrm{R\to T}}{-}1)\Big((f_{\mathrm{T\to R}}{+}f_{\mathrm{R\to T}})\big(f_{\mathrm{T\to R}}(f_{\mathrm{R\to T}}{-}1){+}(f_{\mathrm{R\to T}}{-}3)f_{\mathrm{R\to T}}\big){+}2f_{\mathrm{R\to T}}\Big)}{\big(p\,(f_{\mathrm{R\to T}}{-}1)(f_{\mathrm{T\to R}}{+}f_{\mathrm{R\to T}}){+}f_{\mathrm{T\to R}}{+}f_{\mathrm{R\to T}}\big)^2}.\end{aligned} \tag{11}$$

3. RESULTS AND DISCUSSION

We first investigate the time evolution of the MSD for different values of the key parameters p, v_{R}, v_{T}, $f_{\mathrm{R\to T}}$, $f_{\mathrm{T\to R}}$, and P_0^R. As a simple check, the expression (10) for $f_{\mathrm{R\to T}}{=}0, f_{\mathrm{T\to R}}{=}1, v_{\mathrm{T}}{=}0$, and $P_0^R{=}1$ reduces to

$$\langle r^2\rangle(z) = \frac{v_{\mathrm{R}}^2\, z\,(z{+}p)}{(z{-}1)^2\,(z{-}p)}(\Delta t)^2, \tag{12}$$

and by inverse z-transforming, the MSD for a single-state persistent random walk [37, 41]

$$\langle r^2\rangle(t) = (\Delta t)^2 v_{\mathrm{R}}^2\Big[\frac{1{+}p}{1{-}p}\,t + 2p\,\frac{p^t{-}1}{(1{-}p)^2}\Big] \tag{13}$$

is recovered. In **Figure 2**, we show how the MSD evolves in time for different values of the key parameters. We plot the general expression of $\langle r^2\rangle(t)$, obtained from the inverse z-transforming of Equation (10), and validate the analytical predictions by Monte Carlo simulations. A wide range of different types of anomalous dynamics can be observed on varying the parameters. While the short-time dynamics is typically superdiffusion (due to the combination of active and passive motion) and the long-term dynamics is diffusion in all cases, transitions between sub-, ordinary, and super-diffusion occur on short and intermediate time scales. For some parameter values, the exponential terms of the MSD rapidly decay while the linear term is not yet big enough compared to the time-independent terms. In such a case, the constant terms dominate at intermediate time scales leading to the observed slow dynamics in this regime. The asymptotic dynamics is however diffusive since the linear term eventually dominates. It can also be seen that the crossover time to asymptotic diffusion varies by several orders of magnitude upon changing the parameter values. The crossover time can be characterized as the time at which the exponentially decreasing terms in $\langle r^2\rangle(t)$ become smaller than the terms which survive at long times. We find that the convergence of the MSD to its asymptotic diffusive form can be described by the sum of two exponential functions

$$\langle r^2\rangle(t){-}\langle r^2\rangle(t{\to}\infty) \sim B_1\,\mathrm{e}^{-t/t_{c_1}} + B_2\,\mathrm{e}^{-t/t_{c_2}}, \tag{14}$$

with the characteristic times $t_{c_1}{=}\dfrac{1}{|\ln(1{-}f_{\mathrm{R\to T}}{-}f_{\mathrm{T\to R}})|}$ and $t_{c_2}{=}\dfrac{1}{|\ln\big(p(1{-}f_{\mathrm{R\to T}})\big)|}$. The prefactors B_1 and B_2 are functions of p, v_{R}, v_{T}, $f_{\mathrm{R\to T}}$, $f_{\mathrm{T\to R}}$, and P_0^R. **Figure 3** shows how the characteristic times t_{c_1} and t_{c_2} vary upon changing the key parameters. Although the slopes of the exponential decays in Equation (14) are solely determined by the transition probabilities $f_{\mathrm{R\to T}}$ and $f_{\mathrm{T\to R}}$ and the run persistency p, the crossover time to the asymptotic diffusive dynamics is also influenced by the other dynamic parameters of the model through the prefactors B_1 and B_2. For example, for the set of parameter values $p{=}0.9$, $v_{\mathrm{R}}{=}10$, $v_{\mathrm{T}}{=}0.1$, $f_{\mathrm{R\to T}}{=}0.1$, and $f_{\mathrm{T\to R}}{=}0.01$, the convergence time (with 5% accuracy) to the asymptotic dynamics for $P_0^R = 1$ is nearly twice as long as for $P_0^R = 0$.

Figure 2 also shows that the asymptotic diffusion constant D_{asymp} varies by changing the key parameters. The differences

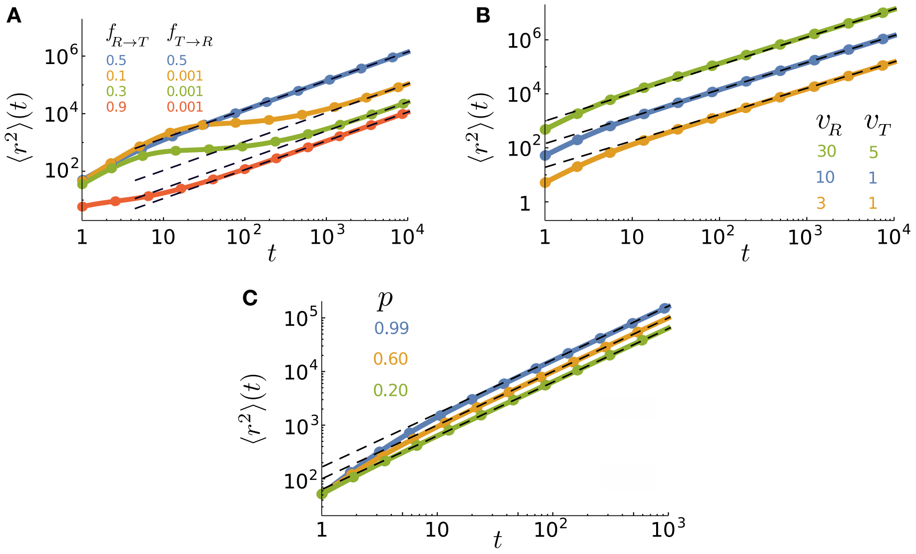

FIGURE 2 | Time evolution of the MSD for various **(A)** transition probabilities, **(B)** speeds, and **(C)** persistencies. The parameter values (unless varied) are taken to be p=0.9, v_{R}=10, v_{T}=1, Δt=1, $f_{\mathrm{R\to T}}$=0.5, $f_{\mathrm{T\to R}}$=0.5, and P_0^R=0.5. The lines are obtained from the inverse z-transform of Equation (10) and symbols denote simulation results. The dashed lines represent the asymptotic diffusion regime.

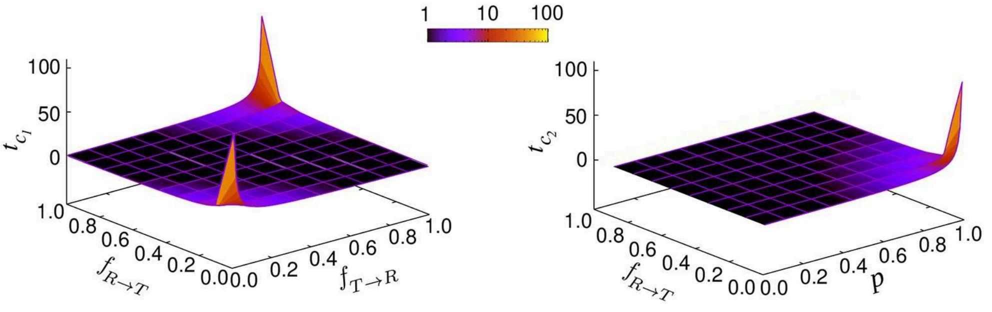

FIGURE 3 | Characteristic times t_{c_1} and t_{c_2} in terms of the transition probabilities $f_{\mathrm{R\to T}}$ and $f_{\mathrm{T\to R}}$ and run persistency p.

in the y-intercept of the dashed (asymptotic) lines in log-log plots reflect the sensitivity of D_{asymp} to the model parameters. By inverse z-transforming of Equation (10) and taking the limit $t\to\infty$, we obtain D_{asymp} (i.e., the coefficient of the term linear in time) in the general form as

$$D_{\text{asymp}} = \frac{1}{4}\,\Delta t\,\frac{2f_{\mathrm{T\to R}}f_{\mathrm{R\to T}}\,p\,v_{\mathrm{T}}\,v_{\mathrm{R}}+f_{\mathrm{T\to R}}\,v_{\mathrm{R}}^2\big(1+p(1-f_{\mathrm{R\to T}})\big)+f_{\mathrm{R\to T}}\,v_{\mathrm{T}}^2\big(1-p(1-f_{\mathrm{R\to T}})\big)}{(f_{\mathrm{T\to R}}+f_{\mathrm{R\to T}})\big(1-p(1-f_{\mathrm{R\to T}})\big)}. \quad (15)$$

While the diffusion coefficient trivially increases with the speed, its dependency on $f_{\mathrm{R\to T}}$, $f_{\mathrm{T\to R}}$, and p is more complicated and shown in **Figure 4**. D_{asymp} varies by several orders of magnitude as a function of these parameters. Under the specific condition $F_{\mathrm{R\to T}}(\theta)=F_{\mathrm{T}}(\theta)=\delta(\theta)$ and $F_{\mathrm{T\to R}}(\theta)=F_{\mathrm{R}}(\theta)$ and $v_{\mathrm{T}}=0$, the walker stops when entering the tumble phase without changing its arrival direction and it returns smoothly to the run phase without experiencing a kick (i.e., a sharp change in the direction of motion). Motor-driven transport along cytoskeletal filaments in crowded cytoplasm exhibits such a run-and-pause dynamics [21, 42]. In this case, one obtains

$$D_{\text{asymp}}^{\text{run-pause}} = \frac{1}{4}\,\Delta t\,v_{\mathrm{R}}^2\,\frac{1+p}{1-p}\,\frac{f_{\mathrm{T\to R}}}{f_{\mathrm{T\to R}}+f_{\mathrm{R\to T}}}. \quad (16)$$

In the limit $p\to 1$ the trajectory becomes nearly straight implying that the randomization time and the covered area until reaching the asymptotic diffusive regime (and thus D_{asymp}) diverge.

Interestingly, D_{asymp} in Equation (15) is independent of P_0^R and P_0^T, i.e., the initial condition of starting the motion in the run or tumble state. Thus, the analytical results predict that the asymptotic diffusive dynamics, characterized by the linear time-dependence

$$\langle r^2\rangle(t\to\infty) = 4D_{\text{asymp}}\,t, \quad (17)$$

does not depend on the initial conditions. In **Figure 5** we present the simulation results for several values of P_0^R. At long times, all

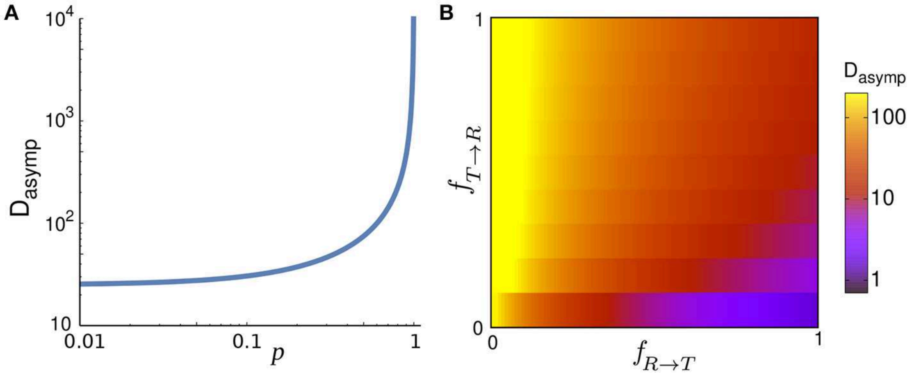

FIGURE 4 | **(A)** Asymptotic diffusion coefficient D_{asymp} as a function of the run persistency p for $v_{\text{R}}=10$, $v_{\text{T}}=1$, $\Delta t=1$, $f_{\text{R}\to\text{T}}=0.001$, and $f_{\text{T}\to\text{R}}=0.9$. **(B)** D_{asymp} in the space of transition probabilities $f_{\text{R}\to\text{T}}$ and $f_{\text{T}\to\text{R}}$ for $v_{\text{R}}=10$, $v_{\text{T}}=1$, $\Delta t=1$, and $p=0.9$.

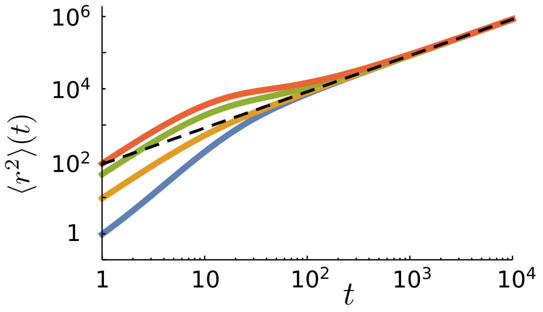

FIGURE 5 | The mean square displacement as a function of time for different values of the probability P_0^R of initially starting in the run state in simulations (from top to bottom: P_0^R=1.0, 0.5, 0.1, 0.0). Other parameter values: $p=0.9$, $v_{\text{R}}=10$, $v_{\text{T}}=0.1$, $f_{\text{R}\to\text{T}}=0.1$, and $f_{\text{T}\to\text{R}}=0.01$. The dashed line represents the analytical prediction via Equation (17) for the same parameter values.

curves merge and follow the analytical prediction Equation (17). Note that only the linear term in time is independent of P_0^R and the exponentially decaying and time-independent terms in the MSD depend on the initial conditions (see e.g., Equation 12). The walker keeps initially for some time its memory of the initial direction and state of motion. However, the influence of the P_0^R-dependent terms vanishes in the limit $t\to\infty$ and the time dependence of the MSD approaches the asymptotic linear form Equation (17).

The short time dynamics is, however, strongly influenced by the choice of the initial conditions. **Figure 5** shows that the initial slope of the MSD curve varies with P_0^R. One can assign an initial anomalous exponent κ to the MSD curve by fitting the power-law $\langle r^2\rangle \sim t^\kappa$. By choosing the first two data points of the MSD curve, the fitting leads to $\langle r^2\rangle(t{=}2)/\langle r^2\rangle(t{=}1)=2^\kappa$. Thus, the initial anomalous exponent κ can be deduced from the MSD at t=1, 2 as

$$\kappa = \ln\left[\frac{\langle r^2\rangle(t{=}2)}{\langle r^2\rangle(t{=}1)}\right]/\ln 2, \tag{18}$$

After replacing the MSD at t=1, 2 obtained from Equation (10) we get

$$\begin{aligned}\kappa = \ln\Bigg[\bigg[&\Big(2-2P_0^R+(3-f_{\text{T}\to\text{R}}-f_{\text{R}\to\text{T}})\big(f_{\text{T}\to\text{R}}(P_0^R-1)+f_{\text{R}\to\text{T}}P_0^R\big)\Big)v_{\text{T}}^2\\ &+2f_{\text{T}\to\text{R}}\big(1-f_{\text{T}\to\text{R}}+(f_{\text{T}\to\text{R}}+f_{\text{R}\to\text{T}}-1)P_0^R\big)\,p\,v_{\text{T}}\,v_{\text{R}}\\ &+\Big(2P_0^R+(-3+f_{\text{T}\to\text{R}}+f_{\text{R}\to\text{T}})\big(f_{\text{T}\to\text{R}}(P_0^R-1)+f_{\text{R}\to\text{T}}P_0^R\big)\\ &+2(f_{\text{R}\to\text{T}}-1)\big(-f_{\text{T}\to\text{R}}+(f_{\text{T}\to\text{R}}+f_{\text{R}\to\text{T}}-1)P_0^R\big)p\Big)v_{\text{R}}^2\bigg]/\\ &\Big[\big(1-f_{\text{T}\to\text{R}}-(1-f_{\text{T}\to\text{R}}-f_{\text{R}\to\text{T}})P_0^R\big)v_{\text{T}}^2+\big(f_{\text{T}\to\text{R}}+(1-f_{\text{T}\to\text{R}}-f_{\text{R}\to\text{T}})P_0^R\big)v_{\text{R}}^2\Big]\Bigg]/\ln 2.\end{aligned} \tag{19}$$

Figure 6A shows the influence of the initial conditions on the initial anomalous exponent for a given set of parameters. Note that the monotonic growth of κ with P_0^R does not hold in general, as we observed decreasing as well as non-monotonic dependencies by varying other parameter values. However, κ increases monotonically with p in all parameter regimes as shown in **Figure 6B**. Moreover, **Figures 6C,D** show that κ also varies widely with the speed and transition probabilities. Because of combining an active run state ($0<p<1$) and normal diffusion (tumble state), κ remains above 1 (superdiffusion). However, by generalizing the run state to include subdiffusive motion (i.e., when $-1<p<1$), κ can decrease below 1.

To better understand the role of the initial conditions, we note that the steady probabilities P^R_{steady} and P^T_{steady} of finding the particle in each of the two states are determined by the transition probabilities $f_{\text{R}\to\text{T}}$ and $f_{\text{T}\to\text{R}}$. Therefore, the influence of the initial condition of starting the motion in any of the two states gradually vanishes as the probabilities $P^R(t)$ and $P^T(t)$ of finding the particle in the run or tumble state gradually approach their steady values. By considering a discrete time Markov process with transition probabilities $f_{\text{R}\to\text{T}}$ and $f_{\text{T}\to\text{R}}$, the probabilities at time t can be obtained from those at time $t-1$ as

$$\big(P^R(t), P^T(t)\big) = \big(P^R(t-1), P^T(t-1)\big)\begin{bmatrix}1-f_{\text{R}\to\text{T}} & f_{\text{R}\to\text{T}}\\ f_{\text{T}\to\text{R}} & 1-f_{\text{T}\to\text{R}}\end{bmatrix}. \tag{20}$$

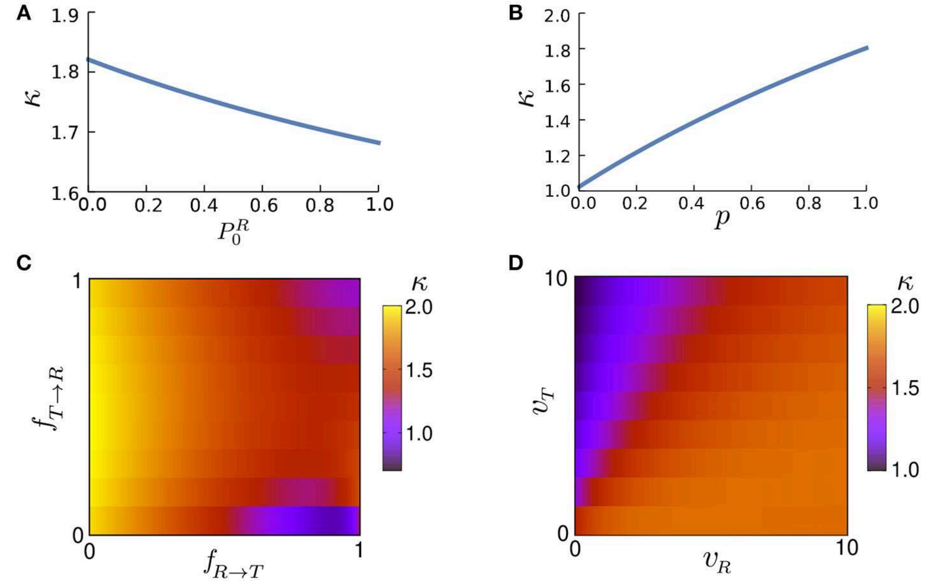

FIGURE 6 | The anomalous exponent κ vs. **(A)** the initial condition of motion P_0^R, **(B)** run persistency p, **(C)** transition probabilities $f_{\mathrm{R\to T}}$ and $f_{\mathrm{T\to R}}$, and **(D)** speeds v_{R} and v_{T} via Equation (19). The parameter values (unless varied) are taken to be p=0.9, v_{R}=10, v_{T}=1, Δt=1, $f_{\mathrm{R\to T}}$=0.3, $f_{\mathrm{T\to R}}$=0.5, and P_0^R=0.5.

By applying this relation recursively, one can derive the probabilities at time t based on the initial probabilities

$$\begin{aligned}\Big(P^R(t),P^T(t)\Big) &= \Big(P_0^R,P_0^T\Big)\begin{bmatrix}1-f_{\mathrm{R\to T}} & f_{\mathrm{R\to T}}\\ f_{\mathrm{T\to R}} & 1-f_{\mathrm{T\to R}}\end{bmatrix}^t \qquad (21)\\ &= \Big(P_0^R,P_0^T\Big)\frac{1}{f_{\mathrm{R\to T}}+f_{\mathrm{T\to R}}}\end{aligned}$$
$$\begin{bmatrix}f_{\mathrm{T\to R}}+f_{\mathrm{R\to T}}(1-f_{\mathrm{T\to R}}-f_{\mathrm{R\to T}})^t & f_{\mathrm{R\to T}}\Big(1-(1-f_{\mathrm{T\to R}}-f_{\mathrm{R\to T}})^t\Big)\\ f_{\mathrm{T\to R}}\Big(1-(1-f_{\mathrm{T\to R}}-f_{\mathrm{R\to T}})^t\Big) & f_{\mathrm{R\to T}}+f_{\mathrm{T\to R}}(1-f_{\mathrm{T\to R}}-f_{\mathrm{R\to T}})^t\end{bmatrix}.$$

Thus the evolution of $P^R(t)$ and $P^T(t)$ obeys

$$\begin{aligned}P^R(t) &= \frac{f_{\mathrm{T\to R}}}{f_{\mathrm{T\to R}}+f_{\mathrm{R\to T}}}+\frac{\Big(1-f_{\mathrm{T\to R}}-f_{\mathrm{R\to T}}\Big)^t}{f_{\mathrm{T\to R}}+f_{\mathrm{R\to T}}}\\ &\quad\Big(f_{\mathrm{R\to T}}P_0^R-f_{\mathrm{T\to R}}(1-P_0^R)\Big),\\ P^T(t) &= \frac{f_{\mathrm{R\to T}}}{f_{\mathrm{T\to R}}+f_{\mathrm{R\to T}}}-\frac{\Big(1-f_{\mathrm{T\to R}}-f_{\mathrm{R\to T}}\Big)^t}{f_{\mathrm{T\to R}}+f_{\mathrm{R\to T}}}\\ &\quad\Big(f_{\mathrm{R\to T}}P_0^R-f_{\mathrm{T\to R}}(1-P_0^R)\Big), \qquad (22)\end{aligned}$$

leading to the steady probabilities $P^R_{\text{steady}}=\frac{f_{\mathrm{T\to R}}}{f_{\mathrm{T\to R}}+f_{\mathrm{R\to T}}}$ and $P^T_{\text{steady}}=\frac{f_{\mathrm{R\to T}}}{f_{\mathrm{T\to R}}+f_{\mathrm{R\to T}}}$. If one starts with the initial condition $P_0^R=P^R_{\text{steady}}$, the system is immediately equilibrated. Otherwise, the choice of the initial conditions affects the short-time dynamics and diversifies the transient anomalous diffusive regimes. According to Equation (22), the relaxation of the probabilities toward their steady values follow an exponential decay $P^R(t)$, $P^T(t)$ $\sim$ e^{-t/t_m} with $t_m=\frac{1}{|\ln(1-f_{\mathrm{R\to T}}-f_{\mathrm{T\to R}})|}$. While the characteristic relaxation time of the probabilities solely depends on the transition probabilities, the characteristic time for the crossover to asymptotic dynamics is influenced additionally by the run persistency, as we showed previously in Equation (14).

Therefore, there are two independent relaxation times $t_m(=t_{c_1})$ and t_{c_2}. In case these differ substantially, two distinct crossovers in the time evolution of the MSD may be observed in general as can be seen in **Figure 2A**.

4. CONCLUSION

We presented a persistent random walk model to study the stochastic dynamics of particles with active fast and passive slow motility modes. We derived an exact analytical expression for the mean square displacement, which allows to analyze the transient anomalous transport regimes on short time scales and also to extract the characteristics of the asymptotic diffusive motion such as the crossover time and the long-term diffusion constant. In particular we showed that while the choice of the initial conditions influences the anomalous diffusion at short times, the asymptotic behavior remains independent of it and is entirely controlled by the run persistency, the velocities of the run and tumble states and the transition probabilities between the two states.

DATA AVAILABILITY

All datasets generated for this study are included in the manuscript and the Supplementary Files.

AUTHOR CONTRIBUTIONS

MS and HR designed the study, performed the analysis, and wrote the manuscript.

FUNDING

This work was financially supported by the German Research Foundation (DFG) within the Collaborative Research Center SFB 1027 (A3, A7).

REFERENCES

1. Berg HC. *E. coli in Motion*. New York, NY: Springer Verlag (2004).
2. Berg HC, Brown DA. Chemotaxis in *Escherichia coli* analysed by three-dimensional tracking. *Nature*. (1972) **239**:500–4. doi: 10.1038/239500a0
3. Patteson AE, Gopinath A, Goulian M, Arratia PE. Running and tumbling with *E. coli* in polymeric solutions. *Sci Rep*. (2015) **5**:15761. doi: 10.1038/srep15761
4. Bartumeus F, Levin SA. Fractal reorientation clocks: linking animal behavior to statistical patterns of search. *Proc Natl Acad Sci USA*. (2008) **105**:19072–7. doi: 10.1073/pnas.0801926105
5. Bénichou O, Coppey M, Moreau M, Suet PH, Voituriez R. Optimal search strategies for hidden targets. *Phys Rev Lett*. (2005) **94**:198101. doi: 10.1103/PhysRevLett.94.198101
6. Najafi J, Shaebani MR, John T, Altegoer F, Bange G, Wagner C. Flagellar number governs bacterial spreading and transport efficiency. *Sci Adv*. (2018) **4**:eaar6425. doi: 10.1126/sciadv.aar6425
7. Bénichou O, Loverdo C, Moreau M, Voituriez R. Intermittent search strategies. *Rev Mod Phys*. (2011) **83**:81–129. doi: 10.1103/RevModPhys.83.81
8. Wadhams GH, Armitage JP. Making sense of it all: bacterial chemotaxis. *Nat Rev Mol Cell Biol*. (2004) **5**:1024–37. doi: 10.1038/nrm1524
9. Taktikos J, Stark H, Zaburdaev V. How the motility pattern of bacteria affects their dispersal and chemotaxis. *PLoS ONE*. (2014) **8**:e81936. doi: 10.1371/journal.pone.0081936
10. Weigel AV, Simon B, Tamkun MM, Krapf D. Ergodic and nonergodic processes coexist in the plasma membrane as observed by single-molecule tracking. *Proc Natl Acad Sci USA*. (2011) 108:6438–43. doi: 10.1073/pnas.1016325108
11. Guigas G, Weiss M. Sampling the ell with anomalous diffusion-the discovery of slowness. *Biophys J*. (2008) **94**:90–4. doi: 10.1529/biophysj.107.117044
12. Golding I, Cox EC. Physical nature of bacterial cytoplasm. *Phys Rev Lett*. (2006) **96**:098102. doi: 10.1103/PhysRevLett.96.098102
13. Sereshki LE, Lomholt MA, Metzler R. A solution to the subdiffusion-efficiency paradox: Inactive states enhance reaction efficiency at subdiffusion conditions in living cells. *EPL*. (2012) **97**:20008. doi: 10.1209/0295-5075/97/20008
14. Ali MY, Krementsova EB, Kennedy GG, Mahaffy R, Pollard TD, Trybus KM, et al. Myosin Va maneuvers through actin intersections and diffuses along microtubules. *Proc Natl Acad Sci USA*. (2007) **104**:4332–6. doi: 10.1073/pnas.0611471104
15. Shiroguchi K, Kinosita K. Myosin V walks by lever action and brownian motion. *Science*. (2007) 316:1208–12. doi: 10.1126/science.1140468
16. Vershinin M, Carter BC, Razafsky DS, King SJ, Gross SP. Multiple-motor based transport and its regulation by Tau. *Proc Natl Acad Sci USA*. (2007) **104**:87–92. doi: 10.1073/pnas.0607919104
17. Okada Y, Higuchi H, Hirokawa N. Processivity of the single-headed kinesin KIF1A through biased binding to tubulin. *Nature*. (2003) **424**:574–7. doi: 10.1038/nature01804
18. Culver-Hanlon TL, Lex SA, Stephens AD, Quintyne NJ, King SJ. A microtubule-binding domain in dynactin increases dynein processivity by skating along microtubules. *Nat Cell Biol*. (2006) **8**:264–70. doi: 10.1038/ncb1370
19. Klumpp S, Lipowsky R. Active diffusion of motor particles. *Phys Rev Lett*. (2005) **95**:268102. doi: 10.1103/PhysRevLett.95.268102
20. Lipowsky R, Klumpp S. Life is motion: multiscale motility of molecular motors. *Physica A*. (2005) **352**:53–112. doi: 10.1016/j.physa.2004.12.034
21. Hafner AE, Santen L, Rieger H, Shaebani MR. Run-and-pause dynamics of cytoskeletal motor proteins. *Sci Rep*. (2016) **6**:37162. doi: 10.1038/srep37162
22. Pinkoviezky I, Gov NS. Transport dynamics of molecular motors that switch between an active and inactive state. *Phys Rev E*. (2013) **88**:022714. doi: 10.1103/PhysRevE.88.022714
23. Chabaud M, Heuzé ML, Bretou M, Vargas P, Maiuri P, Solanes P, et al. Cell migration and antigen capture are antagonistic processes coupled by myosin II in dendritic cells. *Nat Commun*. (2015) **6**:7526. doi: 10.1038/ncomms8526
24. Bressloff PC, Newby JM. Stochastic models of intracellular transport. *Rev Mod Phys*. (2013) **85**:135–96. doi: 10.1103/RevModPhys.85.135
25. Höfling F, Franosch T. Anomalous transport in the crowded world of biological cells. *Rep Prog Phys*. (2013) **76**:046602. doi: 10.1088/0034-4885/76/4/046602
26. Jose R, Santen L, Shaebani MR. Trapping in and escape from branched structures of neuronal dendrites. *Biophys J*. (2018) **115**:2014–25. doi: 10.1016/j.bpj.2018.09.029
27. Angelani L. Averaged run-and-tumble walks. *EPL*. (2013) **102**:20004. doi: 10.1209/0295-5075/102/20004
28. Soto R, Golestanian R. Run-and-tumble dynamics in a crowded environment: persistent exclusion process for swimmers. *Phys Rev E*. (2014) **89**:012706. doi: 10.1103/PhysRevE.89.012706
29. Shaebani MR, Pasula A, Ott A, Santen L. Tracking of plus-ends reveals microtubule functional diversity in different cell types. *Sci Rep*. (2016) **6**:30285. doi: 10.1038/srep30285
30. Theves M, Taktikos J, Zaburdaev V, Stark H, Beta C. A bacterial swimmer with two alternating speeds of propagation. *Biophys J*. (2013) **105**:1915–24. doi: 10.1016/j.bpj.2013.08.047
31. Shaebani MR, Jose R, Sand C, Santen L. Unraveling the structure of treelike networks from first-passage times of lazy random walkers. *Phys Rev E*. (2018) **98**:042315. doi: 10.1103/PhysRevE.98.042315
32. Elgeti J, Gompper G. Run-and-tumble dynamics of self-propelled particles in confinement. *EPL*. (2015) **109**:58003. doi: 10.1209/0295-5075/109/58003
33. Thiel F, Schimansky-Geier L, Sokolov IM. Anomalous diffusion in run-and-tumble motion. *Phys Rev E*. (2012) **86**:021117. doi: 10.1103/PhysRevE.86.021117
34. Berg OG, Winter RB, Von Hippel PH. Diffusion-driven mechanisms of protein translocation on nucleic acids. 1. Models and theory. *Biochemistry*. (1981) **20**:6929–48. doi: 10.1021/bi00527a028
35. Meroz Y, Eliazar I, Klafter J. Facilitated diffusion in a crowded environment: from kinetics to stochastics. *J Phys A*. (2009) **42**:434012. doi: 10.1088/1751-8113/42/43/434012
36. Bauer M, Metzler R. Generalized facilitated diffusion model for DNA-binding proteins with search and recognition states. *Biophy J*. (2012) **102**:2321–30. doi: 10.1016/j.bpj.2012.04.008
37. Nossal R, Weiss GH. A descriptive theory of cell migration on surfaces. *J Theor Biol*. (1974) **47**:103–13. doi: 10.1016/0022-5193(74)90101-5
38. Sadjadi Z, Shaebani MR, Rieger H, Santen L. Persistent-random-walk approach to anomalous transport of self-propelled particles. *Phys Rev E*. (2015) **91**:062715. doi: 10.1103/PhysRevE.91.062715
39. Sadjadi Z, Miri M, Shaebani MR, Nakhaee S. Diffusive transport of light in a two-dimensional disordered packing of disks: analytical approach to transport mean free path. *Phys Rev E*. (2008) **78**:031121. doi: 10.1103/PhysRevE.78.031121

40. Shaebani MR, Sadjadi Z, Sokolov IM, Rieger H, Santen L. Anomalous diffusion of self-propelled particles in directed random environments. *Phys Rev E*. (2014) **90**:030701. doi: 10.1103/PhysRevE.90.030701
41. Tierno P, Shaebani MR. Enhanced diffusion and anomalous transport of magnetic colloids driven above a two-state flashing potential. *Soft Matter*. (2016) **12**:3398–405. doi: 10.1039/C6SM00237D
42. Song MS, Moon HC, Jeon JH, Park HY. Neuronal messenger ribonucleoprotein transport follows an aging Lévy walk. *Nat Commun*. (2018) **9**:344. doi: 10.1038/s41467-017-02700-z

Conflict of Interest Statement: The authors declare that the research was conducted in the absence of any commercial or financial relationships that could be construed as a potential conflict of interest.

frontiers in Physics

ORIGINAL RESEARCH
published: 24 September 2019
doi: 10.3389/fphy.2019.00124

Polymerization Induces Non-Gaussian Diffusion

Fulvio Baldovin*†, Enzo Orlandini† and Flavio Seno†

Dipartimento di FIsica e Astronomia e Sezione INFN di Padova, Universita' di Padova, Padua, Italy

Recent theoretical modeling offers a unified picture for the description of stochastic processes characterized by a crossover from anomalous to normal behavior. This is particularly welcome, as a growing number of experiments suggest the crossover to be a common feature shared by many systems: in some cases the anomalous part of the dynamics amounts to a Brownian yet non-Gaussian diffusion; more generally, both the diffusion exponent and the distribution may deviate from normal behavior in the initial part of the process. Since proposed theories work at a mesoscopic scale invoking the subordination of diffusivities, it is of primary importance to bridge these representations with a more fundamental, "microscopic" description. We argue that the dynamical behavior of macromolecules during simple polymerization processes provide suitable setups in which analytic, numerical, and particle-tracking experiments can be contrasted at such a scope. Specifically, we demonstrate that Brownian yet non-Gaussian diffusion of the center of mass of a polymer is a direct consequence of the polymerization process. Through the kurtosis, we characterize the early-stage non-Gaussian behavior within a phase diagram, and we also put forward an estimation for the crossover time to ordinary Brownian motion.

Keywords: polymer dynamics, polymerization process, anomalous diffusion, non-Gaussian, crossover to Gaussian

OPEN ACCESS

Edited by:
Carlos Mejía-Monasterio,
Polytechnic University of
Madrid, Spain

Reviewed by:
Gleb Oshanin,
Sorbonne Universités, France
Haroldo Valentin Ribeiro,
State University of Maringá, Brazil
Aljaz Godec,
Max Planck Institute for Biophysical
Chemistry, Germany

Correspondence:
Fulvio Baldovin
baldovin@pd.infn.it

†These authors have contributed
equally to this work

Specialty section:
This article was submitted to
Interdisciplinary Physics,
a section of the journal
Frontiers in Physics

Received: *05 July 2019*
Accepted: *15 August 2019*
Published: *24 September 2019*

Citation:
Baldovin F, Orlandini E and Seno F
(2019) Polymerization Induces
Non-Gaussian Diffusion.
Front. Phys. 7:124.
doi: 10.3389/fphy.2019.00124

1. INTRODUCTION

Diffusion in crowded and complex systems such as biological cells is usually very heterogeneous, and anomalous behavior—where the mean square displacement of tracers varies non linearly with time—is envisaged [1–3]. Over the last few years a new class of diffusive processes has been reported, where the mean square displacement is found to grow linearly in time like in standard, Brownian diffusion, but with a corresponding probability density function (PDF) which is strongly non-Gaussian [4–16]. This behavior, termed Brownian yet non-Gaussian diffusion [6, 8], occurs quite robustly in a wide range of systems, including beads diffusing on lipid tubes [6] or in networks [6, 7], the motion of tracers in colloidal, polymeric or active suspensions [4, 17–19] and in biological cells [12, 20, 21], as well as the motion of individuals in heterogeneous populations such as nematodes [5]. Similar effects on the PDF are also observed in the anomalous diffusion [22] of labeled messenger RNA molecules in living *E.coli* and *S.cervisiae* cells. In the majority of cases, at larger time the form of the PDF crosses over to the normal, Gaussian one. Therefore, such change cannot be simply due to the heterogeneity of the tracers, unless some of their properties vary with time. More plausibly, the anomalous-to-Gaussian transition might be induced by temporal fluctuations of the diffusion coefficient, due to rearrangements of properties of tracers or of the surrounding medium. To mimic such behaviors, models in which the diffusion varies with time by obeying a stochastic equation have been introduced and solved both analytically and numerically.

These models are referred in the literature as "diffusing diffusivity models" [23–32], and it has been shown that for short times they are intimately related to the idea of superstatistics [33]. In the latter approach, an ensemble of particles is assumed to be characterized by different diffusion coefficients and it is then described as a mixture of Gaussian PDFs, weighted by the distribution of the diffusivities. As a result, the ensemble dynamics is still Brownian, yet the PDF of particle displacements corresponds to a Gaussian mixture and it is thus not Gaussian anymore.

Although diffusing diffusivity models qualitatively reproduce the experimental observations, they work at a mesoscopic scale and without a visible connection to the underlying molecular processes. It is therefore becoming increasingly relevant to find strategies that bridge the gap between the paradigm of diffusing diffusivity and the microscopic realm, in order to fully understand this form of anomalous diffusion. In this paper we show how the diffusion of polymers during a polymerization process offers one possible mechanism to realize this connection[1]. It is well known from polymer theory [36] that the motion of the center of mass of a linear chain is Brownian, but with a diffusivity constant which is inversely proportional to N^{α}, where N is the number of monomers and α an exponent ranging from 1/2 (Rouse model) to 2 (reptation model). During an equilibrated polymerization processes the number N fluctuates in time and its statistics can be obtained through the exact solution of its stationary master equation. By using a continuous approximation for this temporally homogeneous birth-death Markov process [37], it emerges that in the limit of large systems such process converges to an Ornstein-Uhlenbeck, as it is assumed in most of the diffusing diffusivity models [24]. The time scale of the Ornstein-Uhlenbeck process is linearly proportional to the volume of the system and this guarantees that the non-Gaussian behavior can be accessible experimentally by tuning such parameter.

2. POLYMERIZATION PROCESS

Polymers are made of relatively simple subunits (monomers) assembled with one another through different mechanisms and geometries. The result is a macromolecule which may contain from a few tens (in the case oligomers), to several thousand monomer units [38], or even millions as in the case of DNA and RNA molecules. From a biological point of view, the polymerization process occurs regularly either within or outside the cell [39]. In particular, cells might trigger polymerization by several mechanisms such as the *de novo* nucleation of new filaments, the uncapping of existing barbed ends (actin) and rescuing a depolymerizing filament (commonly observed for microtubules).

In order to guarantee the existence of equilibrium conditions, here we consider a polymerization process occurring in a closed volume with a fixed total number of monomers N_t. For sake of simplicity, in what follows we suppose that one filament only can nucleate and that subunits may bind reversibly onto both ends of the chain. At each end, the addition and deletion of monomers can be represented as [40]

$$A_N + A_1 \underset{k_-}{\overset{k_+}{\rightleftharpoons}} A_{N+1}\,, \tag{1}$$

where A_N is the filament with N subunits, and k_+, k_- are the rate constants for association and dissociation, respectively. Hence,

$$N_t = N(t) + M(t)\,, \tag{2}$$

where $M(t) = c(t)\,V$ is the number of monomeric subunits, c its concentration and V the system volume. The probability of a filament with n monomers at time t given n_0 units at time t_0, $P_N(n,t|n_0,t_0)$ satisfies the (forward) master equation of a temporally homogeneous birth-death Markov process [37]:

$$\begin{aligned}\partial_t P_N(n,t|n_0,t_0) = &\left[W_-(n+1)\,P_N(n+1,t|n_0,t_0)\right.\\ &\left.-W_+(n)\,P_N(n,t|n_0,t_0)\right]\\ &+\left[W_+(n-1)\,P_N(n-1,t|n_0,t_0)\right.\\ &\left.-W_-(n)\,P_N(n,t|n_0,t_0)\right]\end{aligned}\,, \tag{3}$$

with stepping functions

$$\begin{aligned}&W_+(n) = 2k_+\,c(n) \quad (1 \le n \le N_t)\,,\\ &W_-(1) = 0\,, \quad W_-(2) = k_-\,, \quad W_-(n) = 2k_- \quad (3 \le n \le N_t)\,,\end{aligned} \tag{4}$$

and $c(n) = (N_t - n)/V$. Through these choices, we are assuming with certainty the existence in solution of a filament with at least one monomer. The factor 2 in W_+ models a linear polymer which grows at both ends without developing branching; W_- is instead concerned with the possible bonds which may break down. Equilibrium is reached under detailed balance $W_-(n) = W_+(n)$ $(3 \le n \le N_t)$, corresponding to a polymer composed by

$$N_{eq} = N_t - \frac{k_-}{k_+}\,V \equiv \lambda\,N_t \tag{5}$$

monomers, and to a number

$$M_{eq} = \frac{k_-}{k_+}\,V \equiv (1-\lambda)\,N_t \tag{6}$$

of single monomers in solution. We remark that the rate constants k_+, k_- are specific to the polymerization chemical reactions. Given a certain kind of polymer, the average polymer size and the average number of single monomers in solution are thus controlled by the total number of subunits N_t and by the volume of the system V, which are quantities easily controlled in experiments. In the following analysis, we find it convenient to replace the volume with the fraction $0 < \lambda < 1$ of N_t that compose the polymer at equilibrium; clearly, $V = (1-\lambda)\,N_t\,k_+/k_-$.

As we prove in the **Appendix**, for any given N_t and independently from n_0, the stationary solution $P_N(n) \equiv \lim_{t\to\infty} P_N(n,t|n_0,t_0)$ reads

---

[1] Along different lines, connections between polymerization processes and anomalous diffusion have been pointed out in Oshanin and Moreau [34] and Sposini et al. [35].

$$
\begin{aligned}
P_N(1) &= \frac{1}{\mathcal{N}(N_\mathrm{t},\lambda)}\,\frac{(1-\lambda)\,N_\mathrm{t}}{2\,(N_\mathrm{t}-1)}\\
P_N(2) &= \frac{1}{\mathcal{N}(N_\mathrm{t},\lambda)}\\
P_N(n) &= \frac{2}{\mathcal{N}(N_\mathrm{t},\lambda)}\,\frac{(N_\mathrm{t}-2)!}{\left[(1-\lambda)\,N_\mathrm{t}\right]^{N_\mathrm{t}-2}}\,\frac{\left[(1-\lambda)\,N_\mathrm{t}\right]^{N_\mathrm{t}-n}}{(N_\mathrm{t}-n)!}\ (3\leq n\leq N_\mathrm{t}),
\end{aligned}
\tag{7}
$$

with a normalization factor

$$
\mathcal{N}(N_\mathrm{t},\lambda) = \frac{N_\mathrm{t}\left[(11-4\lambda)\,\lambda-9\right]+2}{2(N_\mathrm{t}-1)} + \frac{2\,(N_\mathrm{t}-2)!}{\left[(1-\lambda)\,N_\mathrm{t}\right]^{N_\mathrm{t}-2}}\,\frac{\Gamma(N_\mathrm{t}+1,(1-\lambda)\,N_\mathrm{t})}{\Gamma(N_\mathrm{t}+1)}\ \mathrm{e}^{(1-\lambda)\,N_\mathrm{t}}\,, \tag{8}
$$

$\Gamma(\cdot,\cdot)$ being the upper incomplete gamma function [41],

$$
\Gamma(N_\mathrm{t}+1,(1-\lambda)\,N_\mathrm{t}) \equiv \int_{(1-\lambda)\,N_\mathrm{t}}^{\infty} \mathrm{d}t\, t^{N_\mathrm{t}}\,\mathrm{e}^{-t}\,, \tag{9}
$$

and $\Gamma(\cdot)$ the Euler gamma function. We may observe that with $(1-\lambda)\,N_\mathrm{t} \to 0$ the two Gamma functions in the normalization factor become equal and simplify to 1; in this limit, probabilities for small n are suppressed. Indeed, in section 4 we show that $P_N(n)$ becomes close to a Gaussian for large λ and N_t. In view of the inverse power-law relation with the diffusion coefficient of the center of mass, it is however the behavior for small n which affects the probability of large diffusivities, triggering in turn strong deviations from ordinary diffusion which are described in the following Section.

3. BROWNIAN YET NON-GAUSSIAN DIFFUSION OF THE CENTER OF MASS

From polymer physics we know that the center of mass $\boldsymbol{R}_G$ of a macromolecules with N subunits diffuses with a coefficient $D(N) = D_0/N^\alpha$, D_0 being a diffusion coefficient specific of the considered subunit. This means

$$
\mathrm{d}\boldsymbol{R}_G(t) = \sqrt{6\,D(N(t))}\,\mathrm{d}\boldsymbol{B}(t)\,, \tag{10}
$$

with $\boldsymbol{B}(t)$ a (three-dimensional) Wiener process (Brownian motion). Reference values for the exponent α are:

- $\alpha = 1/2$ in the Rouse model [36, 42], where the polymer is composed of N equivalent beads with neither excluded-volume nor hydrodynamic interaction;
- $\alpha = 1$ for the Zimm model [36, 43], where hydrodynamic is taken into account;
- $\alpha = 2$ for the reptation model which describes tagged polymer motion in entangled polymer solutions [36, 44].

In view of the previous analysis, we understand that polymerization confers a random character to $\boldsymbol{R}_G$, providing a clear microscopic origin to the "diffusing diffusivity" process we are going to detail next.

From Equation (7) we readily obtain the stationary distribution for the diffusion coefficient of the polymer's center of mass,

$$
\begin{aligned}
P_D(D_n) &= \sum_{n'=1}^{N_\mathrm{t}} P_N(n')\,\delta_{D_n,\frac{D_0}{n'^\alpha}}\\
&= P_N\left(\frac{D_0^\alpha}{D_n^\alpha}\right)\quad (1\leq n\leq N_\mathrm{t},\ D_n = D_0/n^\alpha)\,,
\end{aligned}
\tag{11}
$$

and its first moment

$$
D_\mathrm{av} \equiv \mathbb{E}[D_n] = \sum_{n=1}^{N_\mathrm{t}} P_D(D_n)\,D_n\,. \tag{12}
$$

Imagine now to perform a particle-tracking experiment at constant N_t and V and to monitor the position of $\boldsymbol{R}_G$ in stationary conditions. At a given initial instant the polymer possesses a size n, and thus a diffusion coefficient $D_n = D_0/n^\alpha$ with probability given by Equation (12). For time smaller than the characteristic decay τ of the autocorrelation of the process $N(t)$, the experimental PDF amounts then to a Gaussian mixture (also called "superstatistics") [6, 23, 33] weighted by Equation (12). In addition, its second moment grows linearly with time as in the ordinary Brownian motion. Such a phenomenon of "Brownian yet non Gaussian diffusion" [6, 8] has been recently modeled at a mesoscopic scale in terms of diffusing diffusivity models [23–32]. It is only at time larger than τ that ordinary (Gaussian) Brownian motion is recovered, with a diffusion coefficient D_av. Before giving an estimate of τ for our model (see next section), we study the early time non-Gaussianity in the full phase diagram $[N_\mathrm{t},\lambda]$, together with its dependence on α.

The non-Gaussian behavior distinctive of $\boldsymbol{R}_G(t)$ at time $0 \leq t \ll \tau$ can be properly characterized by referring to one of its Cartesian coordinates, say x. The PDF of the x-displacements takes the form

$$
p_X(x,t) = \sum_{n=1}^{N_\mathrm{t}} P_N\left(\frac{D_0^\alpha}{D_n^\alpha}\right)\frac{\exp\left(-\frac{x^2}{4\pi\,D_n t}\right)}{\sqrt{4\pi\,D_n t}}\,. \tag{13}
$$

In **Figure 1** we plot Equation (13) for $\alpha = 1$ and different values of λ and N_t. At first sight, non-Gaussianity increases with decreasing N_t and λ; below we however show that the behavior is not monotonic. To measure deviations from Gaussianity we consider the kurtosis of $p_X(x,t)$,

$$
\kappa \equiv \frac{\mathbb{E}\left[(X-\mathbb{E}[X])^4\right]}{\left(\mathbb{E}\left[(X-\mathbb{E}[X])^2\right]\right)^2} \tag{14}
$$

($\kappa = 3$ for any Gaussian variable). In our case it is straightforward to see that

$$
\kappa = 3\,\frac{\mathbb{E}\left[D^2\right]}{(\mathbb{E}\,[D])^2} = 3\,\frac{\mathbb{E}\left[N^{-2\alpha}\right]}{\left(\mathbb{E}\left[N^{-\alpha}\right]\right)^2}\,, \tag{15}
$$

independently of D_0. Notice instead the strong dependence of κ from α; moreover, $\kappa > 3$ (positive excess kurtosis or leptokurtic

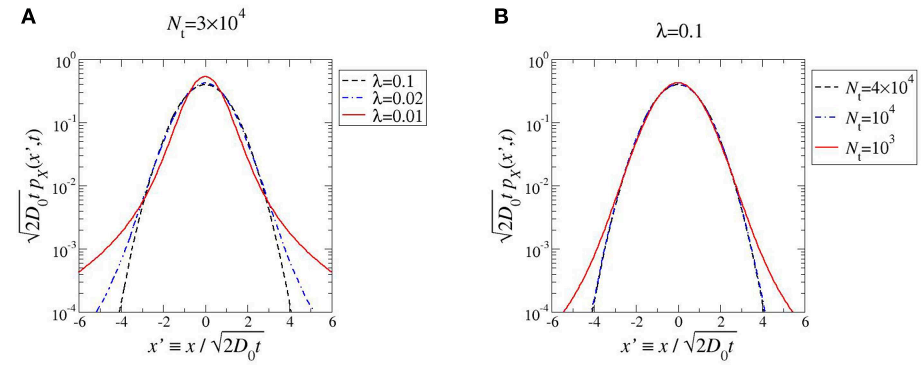

FIGURE 1 | PDF of the x-coordinate of $\boldsymbol{R}_G$ for $0 \le t \ll \tau$, at fixed N_t **(A)**, and fixed λ **(B)**. The PDF is rescaled such that the variance is unity; recall that in a log-linear plot Gaussian PDFs have parabolic shape. In both cases, $\alpha = 1$.

PDF). In order to illustrate regions of more pronounced non-Gaussianity and to discuss their dependence on α in **Figure 2** we draw the kurtosis level curves within a (λ, N_t)-phase diagram. Note that, for a given pair (N_t, λ), higher values of the exponent α give rise to larger kurtosis (compare **Figures 2A,B**).

As quoted, by looking at the plots in **Figure 1** one may expect the kurtosis to steadily increase by decreasing λ and N_t. The structure of the phase diagram implies instead the existence of a maximum kurtosis, both at given λ and N_t. Indeed, for any horizontal or vertical line traced through the phase diagram (**Figure 2**) it is possible to find a family of kurtosis level curves each intersecting the line in two distinct points. Between each couple of intersection points the kurtosis first raises and then decreases, thus reaching a maximum value. This is highlighted in **Figure 3**. Albeit within a small portion of the phase space, the maximum kurtosis can be extremely high, as reported in **Figure 4**; for instance, $k_{\max} \simeq 40$ corresponds to an average polymer size of order $N_{eq} \simeq 350$ with $N_t \simeq 10^4$.

4. CROSSOVER TO BROWNIAN, GAUSSIAN DIFFUSION

The stationary distribution in Equation (7) is exact, but it does not provide information about the decay time-scale τ of initial conditions for the process $N(t)$. To get such an insight, we next workout a continuous approximation for the polymerization process. In the gedankenexperiment reported above, τ is the persistence time scale of the randomly chosen initial diffusion coefficient for $\boldsymbol{R}_G$, corresponding in turn to the typical duration of the leptokurtic PDF for the diffusion of the center of mass.

We start by noticing that around equilibrium, for $N_t \gg 1$ and $N_{eq} \gg M_{eq}$ (large λ), $N(t)$ can be approximated as a continuous Markov process with Langevin equation [37]

$$\mathrm{d}N(t) = 2\frac{k_+}{V}\left[N_{eq} - N(t)\right]\,\mathrm{d}t + \sqrt{2\frac{k_+}{V}\left[2N_t - N_{eq} - N(t)\right]}\,\mathrm{d}B(t)\,, \tag{16}$$

where $B(t)$ is a Wiener process (Brownian motion). Taking further advantage of the large N_{eq} assumption, we then introduce the rescaled quantity $\widetilde{N} \equiv N/N_{eq}$, obeying

$$\mathrm{d}\widetilde{N}(t) = 2\frac{k_+}{V}\left[1 - \widetilde{N}(t)\right]\,\mathrm{d}t + \left(\frac{1}{N_{eq}}\right)^{1/2}\sqrt{2\frac{k_+}{V}\left[2\frac{N_t}{N_{eq}} - 1 - \widetilde{N}(t)\right]}\,\mathrm{d}B(t)\,, \tag{17}$$

to which we may apply the *weak noise approximation*. Indeed, one may straightforwardly prove [37] that for large N_{eq} Equation (18) is satisfied by the approximate solution

$$\widetilde{N}(t) \simeq \widetilde{n}(t) + \left(\frac{1}{N_{eq}}\right)^{1/2} Y(t)\,, \tag{18}$$

with $\widetilde{n}(t)$ a deterministic process satisfying

$$\frac{\mathrm{d}\widetilde{n}(t)}{\mathrm{d}t} = 2\frac{k_+}{V}\left[1 - \widetilde{n}(t)\right]\,, \tag{19}$$

and $Y(t)$ the stochastic process defined by the Langevin equation

$$\mathrm{d}Y(t) = -2\frac{k_+}{V}\,Y(t)\,\mathrm{d}t + \sqrt{2\frac{k_+}{V}\left[2\frac{N_t}{N_{eq}} - 1 - \widetilde{n}(t)\right]}\,\mathrm{d}B(t)\,. \tag{20}$$

The solution of the deterministic process,

$$\widetilde{n}(t) = 1 + \left[\widetilde{n}(0) - 1\right]\mathrm{e}^{-\frac{t}{\tau}}\,, \tag{21}$$

asymptotically tends to 1 with a characteristic decay time

$$\tau \equiv \frac{V}{2k_+} = \frac{(1-\lambda)\,N_t}{2k_-}\,. \tag{22}$$

Correspondingly, the long-time behavior of $Y(t)$ is that of an Ornstein-Uhlenbeck process:

$$Y(t \to \infty) = \mathbb{N}\left(0, \frac{N_t}{N_{eq}} - 1\right)\,, \tag{23}$$

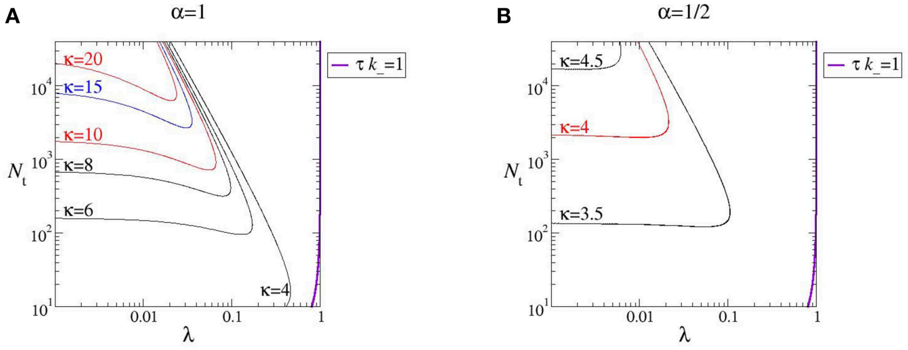

FIGURE 2 | Phase diagram of the early-stage non-Gaussianity for **(A)** $\alpha = 1$ and **(B)** $\alpha = 1/2$. The thick, violet, line at the right end of both plots corresponds to $\tau k_- = 1$ (please refer to text for details).

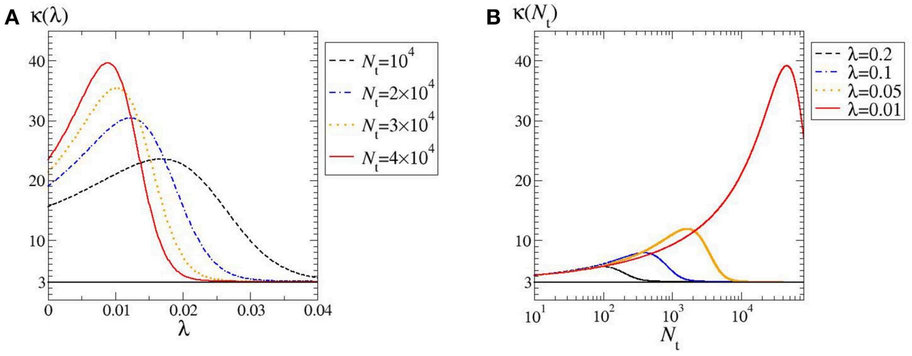

FIGURE 3 | Kurtosis as a function of: **(A)** λ; **(B)** N_t. In both cases, $\alpha = 1$.

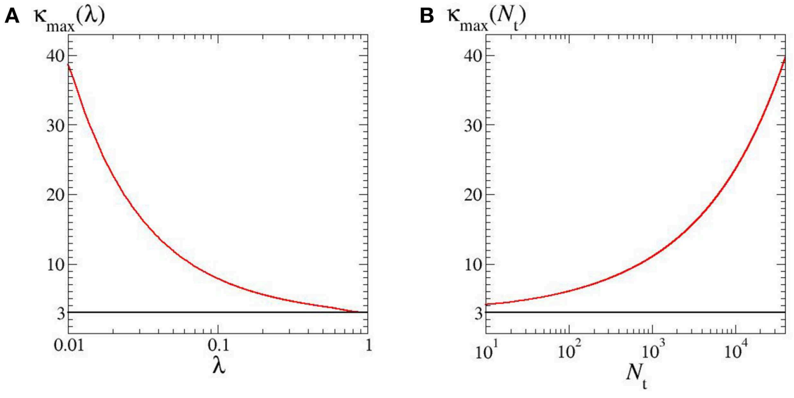

FIGURE 4 | Maximum kurtosis as a function of: **(A)** λ; **(B)** N_t. In both cases, $\alpha = 1$.

where $\mathbb{N}(\mu, \sigma^2)$ is a Gaussian variable with mean μ and variance σ^2. Hence, the stationary solution of $\widetilde{N}$ is

$$\widetilde{N}(t \to \infty) = \mathbb{N}\left(1, \frac{M_{\text{eq}}}{N_{\text{eq}}^2}\right) . \tag{24}$$

For the polymer size $N = \widetilde{N}\, N_{\text{eq}}$, this implies

$$N(t \to \infty) = \mathbb{N}\left(N_{\text{eq}}, M_{\text{eq}}\right) . \tag{25}$$

We thus appreciate that, to be self consistent, the continuous approximation requires large values of N_t to blur out discreteness, and $N_{\text{eq}} \gg M_{\text{eq}}$ so that the

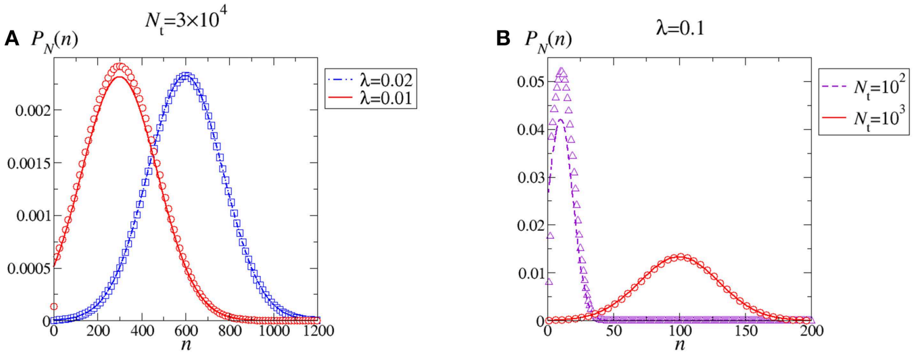

FIGURE 5 | Stationary PDF of the polymerization process. Comparison between the exact PDF in Equation (7) (symbols) and the continuous, weak noise approximation associated to Equation (25) (curves). Values for the parameters N_t and λ have been chosen to facilitate comparison with **Figure 1**. Specifically, continuous red curves correspond to choices in **Figure 1**. By decreasing either λ at fixed N_t **(A)** or N_t at fixed λ **(B)** the weak noise approximation breaks down.

negative support of the Gaussian PDF corresponds to a negligible probability. **Figure 5** shows that when N_t and λ are both large the weak noise approximation of the stationary distribution $P_N(n)$ is almost indistinguishable from the exact solution. On the other hand, decreasing either N_t or λ the approximation fails concomitantly with the fact that the Gaussian probability of negative n-values becomes significant. Depending on the specific cut in phase-space, the approximation may or may not work well in correspondence to the maximum kurtosis (compare red full lines in **Figures 5A,B**).

When applicable, the important result conveyed by the continuous, weak noise approximation is that through Equation (22) it establishes the time scale of the decay of the autocorrelation of $N(t)$. It would be nice to give an explicit representation of τ in terms of the control parameters (λ, N_t); however, Equation (22) shows that it further depends on the dissociation rate constant k_-, which is specific to the chosen polymer. To get a qualitative insight, in **Figure 2** we have added the line

$$\tau\, k_- = \frac{(1-\lambda)\, N_t}{2} = 1\,, \tag{26}$$

representing the locus of points for which τ is equal to the inverse of k_-. Notice that the largest kurtosis level curve lay at the left of the line, a region which is also characterized by $\tau > 1/k_-$. Hence, the farther left of the line the longer lasts the Brownian yet non-Gaussian diffusion stage.

5. CONCLUSIONS

We have been able to analytically characterize the stochastic motion of the center of mass of a fluctuating filament undergoing a simple polymerization process. Depending on experimentally accessible parameters such as the the total monomers in the solution N_t and the system volume V (equivalently, the fraction λ of total monomers composing the filament in equilibrium), the center of mass displays at early times a Brownian, yet non-Gaussian, diffusion. To our knowledge, this is one of the first example in which this anomalous behavior is directly linked to a microscopic prototype: the effect originates from the fluctuations of N (due to polymerization) and from the relation $D(N) = D_0/N^\alpha$ which distinguishes many microscopic models of polymeric diffusion. By studying the kurtosis of the early-time displacement PDF along the x-coordinate we quantified deviations from Gaussian behavior in the phase diagram (λ, N_t), highlighting the dependence on the exponent α. Remarkably, the kurtosis is not monotonic and displays a maximum at either λ or N_t fixed. Finally, on the basis of a continuum (weak noise) approximation for the stochastic process $N(t)$, we put forward an estimation for the time $\tau(\lambda, N_t)$ at which the anomalous behavior crosses over to ordinary Brownian motion. Since the weak noise approximation is not applicable in the whole (λ, N_t) phase diagram, and also in view of the non-monotonic behavior of the kurtosis, further studies approaching the determination of τ are welcome.

In parallel with the analytical results, we proposed a *gedankenexperiment* in which the anomalous behavior could be detected. As a further perspective, we may notice that if we shift the focus on the diffusion of a tagged monomer (in place of the center of mass of the polymer), in the early stage of the process a *subdiffusive* behavior coupled to non-Gaussianity is expected to be observed, with a crossover to a Brownian regime at the Rouse time [36]. This analysis is intended to be the subject of future work.

In conclusion, we believe that this work provides a valuable analytical backdrop to Brownian yet non-Gaussian diffusion, a fascinating phenomenon reported to occur in many physical systems. To fully understand this anomalous behavior, it is essential to ground it on a microscopic spring. This is the case for the presented model, but we are confident than others more will come along these lines.

DATA AVAILABILITY

The datasets generated for this study are available on request to the corresponding author.

AUTHOR CONTRIBUTIONS

All authors listed have made a substantial, direct and intellectual contribution to the work, and approved it for publication.

FUNDING

FB and FS acknowledge financial support from a 2019 PRD project of the Physics and Astronomy Department of the University of Padova, Italy (BIRD 191017).

ACKNOWLEDGMENTS

The authors would like to thank M. Baiesi, G. Falasco, and A.L. Stella for useful discussions.

SUPPLEMENTARY MATERIAL

The Supplementary Material for this article can be found online at: https://www.frontiersin.org/articles/10.3389/fphy.2019.00124/full#supplementary-material

REFERENCES

1. Metzler R, Klafter J. The random walk's guide to anomalous diffusion: a fractional dynamics approach. *Phys Rep*. (2000) **339**:1–77. doi: 10.1016/S0370-1573(00)00070-3
2. Sanabria H, Kubota Y, Waxham MN. Multiple diffusion mechanisms due to nanostructuring in crowded environments. *Biophys J*. (2007) **92**:313–22. doi: 10.1529/biophysj.106.090498
3. Höfling F, Franosch T. Anomalous transport in the crowded world of biological cells. *Rep Prog Phys*. (2013) **76**:046602. doi: 10.1088/0034-4885/76/4/046602
4. Weeks ER, Crocker JC, Levitt AC, Schofield A, Weitz DA. Three-dimensional direct imaging of structural relaxation near the colloidal glass transition. *Science*. (2000) **287**:627–31. doi: 10.1126/science.287.5453.627
5. Hapca S, Crawford JW, Young IM. Anomalous diffusion of heterogeneous populations characterized by normal diffusion at the individual level. *J R Soc Interf*. (2008) **6**:111–22. doi: 10.1098/rsif.2008.0261
6. Wang B, Anthony SM, Bae SC, Granick S. Anomalous yet brownian. *Proc Natl Acad Sci U.S.A*. (2009) **106**:15160–4. doi: 10.1073/pnas.0903554106
7. Toyota T, Head DA, Schmidt CF, Mizuno D. Non-Gaussian athermal fluctuations in active gels. *Soft Matter*. (2011) **7**:3234–9. doi: 10.1039/c0sm00925c
8. Wang B, Kuo J, Bae SC, Granick S. When Brownian diffusion is not Gaussian. *Nat Mater*. (2012) **11**:481. doi: 10.1038/nmat3308
9. Guan J, Wang B, Granick S. Even hard-sphere colloidal suspensions display Fickian yet non-Gaussian diffusion. *ACS Nano*. (2014) **8**:3331–6. doi: 10.1021/nn405476t
10. Ghosh SK, Cherstvy AG, Metzler R. Deformation propagation in responsive polymer network films. *J Chem Phys*. (2014) **141**:08B6141. doi: 10.1063/1.4893056
11. Wang D, Hu R, Skaug MJ, Schwartz DK. Temporally anticorrelated motion of nanoparticles at a liquid interface. *J Phys Chem Lett*. (2014) **6**:54–9. doi: 10.1021/jz502210c
12. Stylianidou S, Kuwada NJ, Wiggins PA. Cytoplasmic dynamics reveals two modes of nucleoid-dependent mobility. *Biophys J*. (2014) **107**:2684–92. doi: 10.1016/j.bpj.2014.10.030
13. Samanta N, Chakrabarti R. Tracer diffusion in a sea of polymers with binding zones: mobile vs. frozen traps. *Soft Matter*. (2016) **12**:8554–63. doi: 10.1039/C6SM01943A
14. Dutta S, Chakrabarti J. Anomalous dynamical responses in a driven system. *Europhys Lett*. (2016) **116**:38001. doi: 10.1209/0295-5075/116/38001
15. Metzler R. Gaussianity fair: the riddle of anomalous yet non-Gaussian diffusion. *Biophys J*. (2017) **112**:413. doi: 10.1016/j.bpj.2016.12.019
16. Cherstvy AG, Nagel O, Beta C, Metzler R. Non-Gaussianity, population heterogeneity, and transient superdiffusion in the spreading dynamics of amoeboid cells. *Phys Chem Chem Phys*. (2018) **20**:23034–54. doi: 10.1039/C8CP04254C
17. Kegel WK, van Blaaderen A. Direct observation of dynamical heterogeneities in colloidal hard-sphere suspensions. *Science*. (2000) **287**:290–3. doi: 10.1126/science.287.5451.290
18. Leptos KC, Guasto JS, Gollub JP, Pesci AI, Goldstein RE. Dynamics of enhanced tracer diffusion in suspensions of swimming eukaryotic microorganisms. *Phys Rev Lett*. (2009) **103**:198103. doi: 10.1103/PhysRevLett.103.198103
19. Xue C, Zheng X, Chen K, Tian Y, Hu G. Probing non-Gaussianity in confined diffusion of nanoparticles. *J Phys Chem Lett*. (2016) **7**:514–9. doi: 10.1021/acs.jpclett.5b02624
20. Parry BR, Surovtsev IV, Cabeen MT, OHern CS, Dufresne ER, Jacobs-Wagner C. The bacterial cytoplasm has glass-like properties and is fluidized by metabolic activity. *Cell*. (2014) **156**:183–94. doi: 10.1016/j.cell.2013.11.028
21. Munder MC, Midtvedt D, Franzmann T, Nüske E, Otto O, Herbig M, et al. A pH-driven transition of the cytoplasm from a fluid-to a solid-like state promotes entry into dormancy. *Elife*. (2016) **5**:e09347. doi: 10.7554/eLife.09347
22. Lampo TJ, Stylianidou S, Backlund MP, Wiggins PA, Spakowitz AJ. Cytoplasmic RNA-protein particles exhibit non-Gaussian subdiffusive behavior. *Biophys J*. (2017) **112**:532–42. doi: 10.1016/j.bpj.2016.11.3208
23. Chubynsky MV, Slater GW. Diffusing diffusivity: a model for anomalous, yet Brownian, diffusion. *Phys Rev Lett*. (2014) **113**:098302. doi: 10.1103/PhysRevLett.113.098302
24. Chechkin AV, Seno F, Metzler R, Sokolov IM. Brownian yet non-Gaussian diffusion: from superstatistics to subordination of diffusing diffusivities. *Phys Rev X*. (2017) **7**:021002. doi: 10.1103/PhysRevX.7.021002
25. Jain R, Sebastian K. Diffusing diffusivity: a new derivation and comparison with simulations. *J Chem Sci*. (2017) **129**:929–37. doi: 10.1007/s12039-017-1308-0
26. Jain R, Sebastian K. Diffusing diffusivity: rotational diffusion in two and three dimensions. *J Chem Phys*. (2017) **146**:214102. doi: 10.1063/1.4984085
27. Tyagi N, Cherayil BJ. Non-Gaussian Brownian diffusion in dynamically disordered thermal environments. *J Phys Chem B*. (2017) **121**:7204–9. doi: 10.1021/acs.jpcb.7b03870
28. Matse M, Chubynsky MV, Bechhoefer J. Test of the diffusing-diffusivity mechanism using near-wall colloidal dynamics. *Phys Rev E*. (2017) **96**:042604. doi: 10.1103/PhysRevE.96.042604
29. Jain R, Sebastian K. Diffusing diffusivity: fractional Brownian oscillator model for subdiffusion and its solution. *Phys Rev E*. (2018) **98**:052138. doi: 10.1103/PhysRevE.98.052138
30. Sposini V, Chechkin AV, Seno F, Pagnini G, Metzler R. Random diffusivity from stochastic equations: comparison of two models for Brownian yet non-Gaussian diffusion. *New J Phys*. (2018) **20**:043044. doi: 10.1088/1367-2630/aab696
31. Sposini V, Chechkin A, Metzler R. First passage statistics for diffusing diffusivity. *J Phys A*. (2018) **52**:04LT01. doi: 10.1088/1751-8121/aaf6ff
32. Grebenkov D. A unifying approach to first-passage time distributions in diffusing diffusivity and switching diffusion models. *J Phys A Math Theor*. (2019) 52:174001. doi: 10.1088/1751-8121/ab0dae
33. Beck C, Cohen EG. Superstatistics. *Physica A*. (2003) **322**:267–75. doi: 10.1016/S0378-4371(03)00019-0
34. Oshanin G, Moreau M. Influence of transport limitations on the kinetics of homopolymerization reactions. *J Chem Phys*. (1995) **102**:2977–85. doi: 10.1063/1.468606
35. Sposini V, Metzler R, Oshanin G. Single-trajectory spectral analysis of scaled Brownian motion. *New J Phys*. (2019) **21**:073043–2985. doi: 10.1088/1367-2630/ab2f52

36. Doi M, Edwards SF. *The Theory of Polymer Dynamics.* Vol. 73. Oxford: Oxford University Press (1992).
37. Gillespie DT. *Markov Processes: An Introduction for Physical Scientists*. San Diego, CA: Academic Press (1992).
38. Flory PJ. Thermodynamics of high polymer solutions. *J Chem Phys*. (1942) **10**:51–61. doi: 10.1063/1.1723621
39. Paul R. Modeling biological cells. *Chem Modell.* (2012) **9**:61–91. doi: 10.1039/9781849734790-00061
40. Boal DH. *Mechanics of the Cell*. Cambridge: Cambridge University Press (2002).
41. Abramowitz M, Stegun IA. *Handbook of Mathematical Functions: With Formulas, Graphs, and Mathematical Tables*. Vol. 55. Washington, DC: Courier Corporation (1965).
42. Weber SC, Spakowitz AJ, Theriot JA. Bacterial chromosomal loci move subdiffusively through a viscoelastic cytoplasm. *Phys Rev Lett*. (2010) **104**:238102. doi: 10.1103/PhysRevLett.104.238102
43. Ermak DL, McCammon JA. Brownian dynamics with hydrodynamic interactions. *J Chem Phys*. (1978) **69**:1352–60. doi: 10.1063/1.436761
44. Doi M, Edwards S. Dynamics of concentrated polymer systems. Part 1. Brownian motion in the equilibrium state. *J Chem Soc Far Trans 2 Mol Chem Phys*. (1978) **74**:1789–801. doi: 10.1039/F29787401789

Conflict of Interest Statement: The authors declare that the research was conducted in the absence of any commercial or financial relationships that could be construed as a potential conflict of interest.

frontiers in Physics

ORIGINAL RESEARCH
published: 09 October 2019
doi: 10.3389/fphy.2019.00148

Rectification of Bacterial Diffusion in Microfluidic Labyrinths

Ariane Weber[1,2], *Marco Bahrs*[3], *Zahra Alirezaeizanjani*[3], *Xingyu Zhang*[1,2], *Carsten Beta*[3]* *and Vasily Zaburdaev*[1,2]*

[1] *Department Biologie, Friedrich-Alexander-Universität Erlangen-Nürnberg, Erlangen, Germany,* [2] *Max-Planck-Zentrum für Physik und Medizin, Erlangen, Germany,* [3] *Institut für Physik und Astronomie, Universität Potsdam, Potsdam, Germany*

In nature as well as in the context of infection and medical applications, bacteria often have to move in highly complex environments such as soil or tissues. Previous studies have shown that bacteria strongly interact with their surroundings and are often guided by confinements. Here, we investigate theoretically how the dispersal of swimming bacteria can be augmented by microfluidic environments and validate our theoretical predictions experimentally. We consider a system of bacteria performing the prototypical run-and-tumble motion inside a labyrinth with square lattice geometry. Narrow channels between the square obstacles limit the possibility of bacteria to reorient during tumbling events to an area where channels cross. Thus, by varying the geometry of the lattice it might be possible to control the dispersal of cells. We present a theoretical model quantifying diffusive spreading of a run-and-tumble random walker in a square lattice. Numerical simulations validate our theoretical predictions for the dependence of the diffusion coefficient on the lattice geometry. We show that bacteria moving in square labyrinths exhibit enhanced dispersal as compared to unconfined cells. Importantly, confinement significantly extends the duration of the phase with strongly non-Gaussian diffusion, when the geometry of channels is imprinted in the density profiles of spreading cells. Finally, in good agreement with our theoretical findings, we observe the predicted behaviors in experiments with *E. coli* bacteria swimming in a square lattice labyrinth created in a microfluidic device. Altogether, our comprehensive understanding of bacterial dispersal in a simple two-dimensional labyrinth makes the first step toward the analysis of more complex geometries relevant for real world applications.

Keywords: diffusion, rectification, random walk, bacteria, confinement

Edited by:
Jürgen Vollmer,
Universität Leipzig, Germany

Reviewed by:
Chengyi Xia,
Tianjin University of Technology, China
Nuno A. M. Araújo,
University of Lisbon, Portugal
Anupam Sengupta,
University of Luxembourg,
Luxembourg

***Correspondence:**
Carsten Beta
beta@uni-potsdam.de
Vasily Zaburdaev
vasily.zaburdaev@fau.de

Specialty section:
This article was submitted to
Interdisciplinary Physics,
a section of the journal
Frontiers in Physics

Received: *02 June 2019*
Accepted: *19 September 2019*
Published: *09 October 2019*

Citation:
Weber A, Bahrs M, Alirezaeizanjani Z,
Zhang X, Beta C and Zaburdaev V
(2019) Rectification of Bacterial
Diffusion in Microfluidic Labyrinths.
Front. Phys. 7:148.
doi: 10.3389/fphy.2019.00148

1. INTRODUCTION

Bacteria are ubiquitous on our planet. They inhabit diverse environments such as soil, oceans, hot springs and the human body, where they may cause infections or serve to establish a natural flora [1]. Being adapted to such a broad spectrum of habitats, bacteria show different forms of locomotion, depending on their specific needs [2, 3]. The motility apparatus and patterns of many different bacterial species have been described and extensively analyzed [4–6]. This experimental work has also been accompanied by theoretical efforts abstracting the motion of cells to random walks or modeling it as diffusion of active particles [7–9]. A significant number of studies exists on how bacteria move, by which mechanic and hydrodynamic forces the motility is driven and what the underlying molecular mechanisms are [10–12]. However, the motion of bacteria is strongly influenced by their surroundings, which often spatially restrict their spreading in natural habitats. Therefore, the behavior of bacteria in confinement has also been investigated [13], for example bacteria moving through narrow channels [14–18] or porous media [19, 20]. For active particles moving in channel confinements [21] or obstacle lattices [22, 23] theoretical models also exist. In specific confinements, these studies reported more persistent motion of bacteria and thus an enhanced diffusion [23].

Studying bacterial behaviors in narrow channels or complex labyrinths is of great medicinal relevance. It can help to better understand the spreading of bacteria during infection, where cells have to move inside of the body through natural constrictions with narrow spacing like blood vessels or the extracellular matrix [24]. On the other hand, it can also help in the design and evaluation of new therapeutic methods like targeted treatment of cancer by genetically modified bacteria, which are used to transport the drugs to the tumor or synthesize the drug on-site [25, 26].

In general, dispersal of bacteria in a complex environment is a result of an intricate interplay of confinement geometry and cell motility pattern. Here, we study the diffusive spreading of swimming bacteria with the well-known run-and-tumble pattern in a square labyrinth. This is probably the simplest possible geometry, which allows for analytical treatment and at the same time provides interesting and nontrivial results. Results obtained from this simplified model will complement the existing literature by offering possible reasoning for previously reported properties of bacterial motion in confinement. Constituting the first step in understanding the spreading of bacteria in complex environments, these results can be applied to problems in various areas dealing with directed transport of bacteria. Microbial enhanced oil recovery, for example, relies on the ability of bacteria to penetrate porous media. To optimize the recovery process, the spreading of the bacteria through the corresponding environment has to be optimal [27, 28]. Also, in ecological sciences, more precisely in the process of bioremediation by bioaugmentation, bacteria have to pass through complex environments to remove organic contaminants from soil and ground water [29]. In medicine, furthermore, quantifying the spreading of bacteria inside the human body—a complex network of tissue as well as lymphatic and blood vessels—helps to better understand the spreading of infections [24] and also to develop new therapies [30], as for example the targeted treatment of cancer [26].

Bacteria performing run-and-tumble motion alternate phases of almost straight swimming with tumbling events, when the cell turns and reorients its swimming direction [31]. On a macroscopic scale, that leads to a random walk like behavior and diffusive spreading of cells. By putting cells in a labyrinth, we anticipate that the reorientation process may be hindered when bacteria are in the channels between the obstacles [32]. However, in the crossings, there is more room available to tumble and cells may choose a new random direction. This provides a mechanism of how the labyrinth can rectify the diffusion of bacteria, which we aim to investigate in this paper. Using theoretical estimates, simulations and experimental data, we are able to show that bacteria disperse faster inside the labyrinth than in a spatially unrestricted environment. For the spreading inside the labyrinth, the diffusion coefficient depends in a nontrivial way on the parameters of the underlying lattice structure. For small times, the bacteria show a pronounced ballistic-like, non-Gaussian dispersal. In this regime, which lasts longer than for unrestricted motion, the bacterial density keeps memory of the underlying lattice geometry. At larger times, the memory of the geometry is lost and the density of bacteria attains an isotropic Gaussian profile. Thus, the underlying geometry of the labyrinth can greatly influence the dispersal of the bacteria on experimentally relevant time scales.

The paper is organized as follows. We start by describing our model system of *E. coli* bacteria swimming in a labyrinth. We then introduce a theoretical model and derive the estimates for the diffusion coefficient in a labyrinth with square lattice geometry (for a detailed derivation please refer to the **Supplementary Material**). After validating the theoretical predictions by numerical simulations we compare our results with experimental data on *E. coli* swimming in microfluidic labyrinths.

2. MODEL SETUP

2.1. Swimming Bacteria in a Labyrinth

In this work, we consider *E. coli* bacteria as a well studied model organism but also as a widely used model in synthetic biology and thus in applications, for example, for the on-site synthesis of anti-cancer drugs. *E. coli* swim in a fluid environment by means of flagella and perform the well known run-and-tumble motion. This motion consists of periods of almost straight runs, interrupted by tumbles. The times between consecutive tumbling events follow an exponential distribution [7]. During the runs, multiple flagella, rotating in the same direction, are arranged as a bundle and push the cell forward. If at least one flagellum starts to rotate in the opposite direction and dissociates from the bundle, the run is shortly interrupted and the tumbling bacterium chooses a new random direction for the next run [31, 33]. Since the flagella have the length of several cell-bodies [33], the bacterium needs enough space to enable the dissociation and rearrangement of the flagellar bundle as well as the cell reorientation. Thus, in a lattice structure with sufficiently narrow channels, the bacteria may not be able to change their direction during the tumble, but continue to swim forward [32, 34]. This behavior is illustrated in **Figure 1**. The lattice is defined by the parameters b, w and h, being the side length of the square obstacles, the width of the channels between two obstacles and the height of the channels, respectively. By using a sufficiently small channel width w and height h, we can potentially forbid tumble events with a change of the swimming direction inside of the channels between the obstacles and reduce the effective spreading of the bacteria to two dimensions of the x/y-plane. Thus, in theoretical considerations and simulations, we disregard the z-direction. In the model, bacteria move inside of a square lattice defined by b and w, in which they are only able to change their moving direction in the crossings of two channels. If a

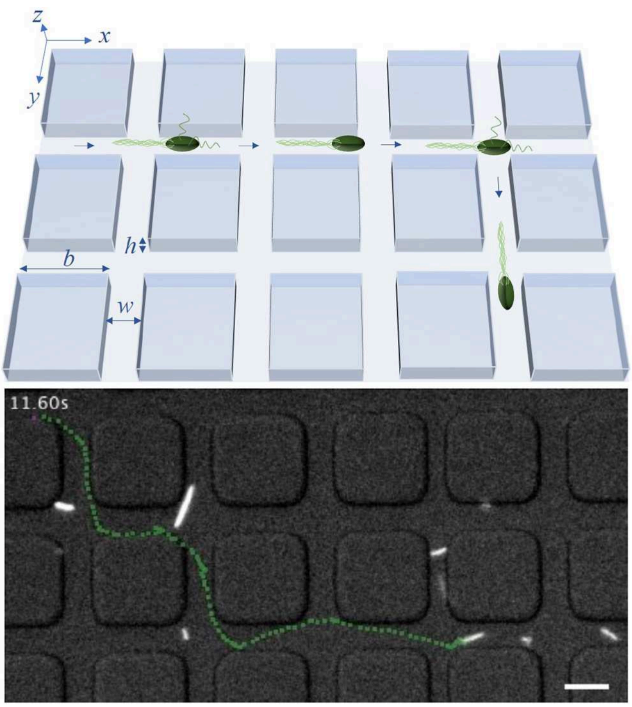

FIGURE 1 | Model system: An illustration of the bacterial motility pattern within a lattice with channel width *w*, height *h* and side length of obstacles *b* (upper row) and a trajectory, marked in green, of a tracked bacterium inside a labyrinth with $b = 20\,\mu\mathrm{m}$ and $w = 8\,\mu\mathrm{m}$ (lower row). The scale bar in the lower row corresponds to $10\,\mu\mathrm{m}$. In experiments, *w* and *h* are equal, restricting the effective spreading of bacteria to two dimensions. Times between consecutive tumble events follow an exponential distribution with mean τ_0. In the model, tumbling events may lead to directional change only within crossings of two channels separating the squares.

tumbling event happens in a crossing, the bacteria can turn right, left, backward or continue their path forward.

2.2. Run-and-Tumble Pattern

Generally, when modeling the run-and-tumble motion, the bacteria are assumed to move in straight lines with constant velocity v_0 during runs. Here, we will neglect rotational diffusion as the channel confinement naturally limits its effect (see, however, section 5). During tumbling events, the bacterium changes its direction by turning at a random angle with respect to its prior running direction. Usually, the bacteria turn left or right with equal probability and thus, the turning angle distribution considers only angles between 0° and 180° [7]. In the simplest case, the turning angle distribution is considered to be uniform. The free-swimming *E. coli* bacteria, however, have a tendency toward smaller turning angles ϕ, with an average $\phi_0 \approx 70^\circ$ [35], resulting in a more persistent motion. The time between consecutive tumbling events is random and well approximated by an exponential distribution with the mean $\tau_0 \approx 1\,\mathrm{s}$ [36]. The duration of tumbles is one order of magnitude shorter than that of runs [35] and is usually neglected in the modeling. The run-and-tumble motion for large times, due to the exponential distribution of run times, is a memoryless random walk. Therefore, on time scales much larger than the mean run time, the mean squared displacement (MSD) of an ensemble of swimming bacteria is linearly proportional to time and can be quantified by the diffusion coefficient *D*. In the diffusive regime of the dispersal, the MSD $\langle \boldsymbol{r}(t)^2\rangle$ in two dimensions can be written as [7]

$$\langle \boldsymbol{r}(t)^2\rangle = 4D_0 t, \text{ with } D_0 = \frac{\langle r^2\rangle}{4\langle \tau\rangle}. \tag{1}$$

Here, $\langle r^2\rangle$ is the mean squared run length and $\langle\tau\rangle$ is the mean run time. As runs happen with constant velocity v_0 (for freely swimming *E. coli* $v_0 \approx 20\,\mu\mathrm{m\,s^{-1}}$), we have $\langle r^2\rangle = v_0^2\langle\tau^2\rangle$. Thus, the diffusion coefficient depends on the first and the second moment of the run time distribution. For the unconstrained but two-dimensional run-and-tumble motion, bacteria are assumed to move freely without spatial restrictions. If they also show no bias in the choice of the turning angle during a reorientation event, we have $\langle\tau\rangle = \tau_0$ and $\langle\tau^2\rangle = 2\tau_0^2$, due to the exponential distribution of run times with mean τ_0. Thus, the diffusion coefficient D_0 for this case becomes

$$D_0 = \frac{v_0^2\tau_0}{2}. \tag{2}$$

When generalizing this result to the run-and-tumble motion of *E. coli*, the directional persistence exhibited by the bacterium has to be taken into account. This persistence can be incorporated by rescaling the average run time with the factor $(1-\cos\phi_0)^{-1}$ (see [37] and **Supplementary Material** for details) resulting in

$$\langle\tau\rangle = \widetilde{\tau} = \frac{\tau_0}{1-\cos\phi_0}.$$

Thus, the diffusion coefficient D_e for the dispersal of *E. coli* in two dimensions is

$$D_e = \frac{v_0^2\tau_0}{2\,(1-\cos\phi_0)}, \tag{3}$$

which for the above mentioned parameters results in $D_e \approx 300\,\mu\mathrm{m^2\,s^{-1}}$. Moreover, an analytical description of the MSD, valid also for small times, can be calculated in this general case by using the Green-Kubo relation [37, 38] yielding

$$\langle \boldsymbol{r}(t)^2\rangle = 2v_0^2\widetilde{\tau}^2\left(\frac{t}{\widetilde{\tau}} - 1 + \mathrm{e}^{-\frac{t}{\widetilde{\tau}}}\right). \tag{4}$$

This result describes ballistic-like dispersal of cells for times comparable to $\widetilde{\tau}$ and diffusive motion at larger times.

3. THEORETICAL ESTIMATES OF DIFFUSION PROPERTIES

3.1. Run-and-Tumble in a Lattice With Uniform Turning Angle Distribution

We now consider the movement of run-and-tumbling bacteria in a labyrinth with square lattice geometry– the two-dimensional equivalent of the system illustrated in **Figure 1**. Here, we assume the width of the channel between two obstacles w to be small enough to inhibit reorientation events in the channels. Therefore, the bacteria can only change their swimming direction inside of the crossings. Since bacteria swimming without spatial confinement exhibit run times following an exponential distribution with mean τ_0, we can calculate the probability to tumble inside of a crossing of width w, P_w, as:

$$P_w = \frac{1}{\tau_0}\int_0^{\frac{w}{v_0}} \mathrm{e}^{-\frac{\tau}{\tau_0}}\,d\tau = 1 - \mathrm{e}^{-\frac{w}{v_0\tau_0}}.$$

Correspondingly, the probability of not tumbling in the crossing is $1 - P_w$. Thus, the probability of the first tumble to occur in the k-th crossing is given by the product of the probability not to tumble in the first $k-1$ crossings and the probability to tumble in the k-th:

$$P_k = \mathrm{e}^{-\frac{(k-1)w}{v_0\tau_0}}\left(1 - \mathrm{e}^{-\frac{w}{v_0\tau_0}}\right).$$

In the model, we assume that in each crossing only one tumbling event can occur (see below). As for the unrestricted case, we still expect the dispersal to become a diffusive process after multiple reorientation events. However, this now takes much longer time, as reorientations are only possible in the crossings.

We first consider the tumbling process with uniform turning angle distribution, where all four possible directions (forward, right, backward and left) are equally probable after a tumbling event in a crossing. To determine the diffusion coefficient D, as defined in Equation (1), the first two moments of the run time distribution have to be calculated. Since the bacteria are only able to perform reorientation events inside of the crossings and not in the channels connecting them, the relation $\langle\tau\rangle = \tau_0$ of the unrestricted case does not hold anymore. Assuming the bacteria to start in the middle of one crossing at $t = 0$ and tumbling events to occur on average also in the middle of crossings, the run times now have to be multiples of the time needed to travel from the center of one crossing to the next, $\tau_{bw} = \frac{b+w}{v_0}$, with lattice parameters b and w. Thus, the moments of the run time can be calculated as

$$\begin{aligned}
\langle\tau\rangle &= \sum_{k=1}^{\infty} k\tau_{bw}P_k = \sum_{k=1}^{\infty} k\tau_{bw}\mathrm{e}^{-\frac{(k-1)w}{v_0\tau_0}}\left(1 - \mathrm{e}^{-\frac{w}{v_0\tau_0}}\right)\\
&= \frac{\tau_{bw}}{1 - \mathrm{e}^{-\frac{w}{v_0\tau_0}}},\\
\left\langle\tau^2\right\rangle &= \sum_{k=1}^{\infty} k^2\tau_{bw}^2P_k = \sum_{k=1}^{\infty} k^2\tau_{bw}^2\mathrm{e}^{-\frac{(k-1)w}{v_0\tau_0}}\left(1 - \mathrm{e}^{-\frac{w}{v_0\tau_0}}\right)\\
&= \frac{\tau_{bw}^2\mathrm{e}^{\frac{w}{v_0\tau_0}}\left(1 + \mathrm{e}^{\frac{w}{v_0\tau_0}}\right)}{\left(\mathrm{e}^{\frac{w}{v_0\tau_0}} - 1\right)^2}.
\end{aligned}$$

Plugging the above expressions into Equation (1) the diffusion coefficient D_l in the labyrinth becomes

$$D_l = \frac{1}{4}\tau_{bw}v_0^2\coth\left[\frac{w}{2v_0\tau_0}\right]. \tag{5}$$

Comparing the diffusion coefficient of the spatially unrestricted walk, given in Equation (2), to our estimate of the walk inside the labyrinth in Equation (5), we see that the ratio

$$\frac{D_l}{D_0} = \frac{\tau_{bw}}{2\tau_0}\coth\left[\frac{w}{2v_0\tau_0}\right]$$

depends on the lattice and motility parameters. The ratio becomes larger for smaller channel width w and bigger side length of the obstacles b. This behavior is also emphasized in the approximation of the ratio for small channel widths w with $w \ll v_0\tau_0$, where $\frac{D_l}{D_0} \approx 1 + \frac{b}{w}$. Thus, in the model, for relevant lattice and motility parameters, we get a higher diffusion coefficient in the labyrinth and consequently faster spreading.

3.2. Run-and-Tumble in a Lattice With Nonuniform Turning Angle Distribution

To consider bacteria exhibiting a nonuniform distribution of turning angles after a tumbling event, the diffusion coefficient has to be modified to include a term accounting for the nonuniformity, similarly to what was done in Equation (3) for the spatially unrestricted walk. For the motion inside the labyrinth, this can be performed as follows. By considering the walk as steps from one crossing to the next, the mean run time $\langle\tau\rangle$ becomes

$$\langle\tau\rangle = \tau_{bw} = \frac{b+w}{v_0}$$

and $\langle\tau^2\rangle = \tau_{bw}^2$. To account for the nonuniform turning angle distribution, we introduce an additional factor B to the formula of the diffusion coefficient. In the square labyrinth, the bacterium can only go in four different directions (forward, right, backward and left), therefore this factor will depend on the four corresponding probabilities p_f, p_r, p_b and p_l, determined by the turning angle distribution. The probability to go forward after a tumbling event p_f, for example, will be the probability that a bacterium swimming outside the labyrinth turns in an angle between 0° and 45° after a tumble. However, as we defined the run time in a crossing-oriented way, to calculate the factor B, we need to consider the bacterial behavior in each crossing, not only in the crossings in which a tumbling event happens. Given the probabilities p_f, p_r, p_b and p_l after a tumbling event and the exponentially distributed run time, the corresponding turning probabilities defined for every passed crossing are

$$\widetilde{p}_f = \mathrm{e}^{-\frac{w}{v_0\tau_0}} + \left(1 - \mathrm{e}^{-\frac{w}{v_0\tau_0}}\right)p_f, \tag{6}$$

$$\widetilde{p}_r = \left(1 - \mathrm{e}^{-\frac{w}{v_0\tau_0}}\right)p_r, \tag{7}$$

$$\widetilde{p}_b = \left(1 - \mathrm{e}^{-\frac{w}{v_0\tau_0}}\right)p_b, \tag{8}$$

$$\widetilde{p}_l = \left(1 - \mathrm{e}^{-\frac{w}{v_0\tau_0}}\right)p_l. \tag{9}$$

Assuming the probability to go right and left to be the same, as done by considering only angles between 0° and 180°, we find B to depend only on $\widetilde{p}_f$ and $\widetilde{p}_b$ as

$$B(\widetilde{p}_f, \widetilde{p}_b) = \frac{1 + \widetilde{p}_f - \widetilde{p}_b}{1 - \widetilde{p}_f + \widetilde{p}_b}.$$

With this, the diffusion coefficient D_{lb} can be written down:

$$D_{lb} = \frac{1}{4}\tau_{bw} v_0^2 \frac{1+\widetilde{p}_f-\widetilde{p}_b}{1-\widetilde{p}_f+\widetilde{p}_b}.$$

Here too, by comparing this result to the diffusion coefficient for the unrestricted walk, Equation (3), we see that the bacteria swimming inside the lattice structure are spreading faster. We can also evaluate the effect of the nonuniformity of the turning angle distribution on the diffusion inside the labyrinth, by looking at the ratio

$$\frac{D_{lb}}{D_l} = \frac{1+\widetilde{p}_f-\widetilde{p}_b}{\left(1-\widetilde{p}_f+\widetilde{p}_b\right)\coth\left[\frac{w}{2v_0\tau_0}\right]} = \frac{1+\left(p_f-p_b\right)\tanh\left[\frac{w}{2v_0\tau_0}\right]}{1-p_f+p_b}.$$

Here, v_0, τ_0 and w are the same for both systems. Thus, the ratio depends on the two probabilities p_f and p_b. As expected, for the case with uniform turning angle distribution, i.e., $p_f = p_b$, the ratio becomes one. For a higher probability to go forward, $p_f > p_b$, it will, in contrast, become greater than one, corresponding to facilitated diffusion through directional persistence. If $p_f < p_b$ instead, the dispersal with uniform turning angle distribution is faster.

It is important to note here, that our theoretical predictions are made for the long-time asymptotics of the diffusive regime. In principle, Equation (4) could have been used with the mean of the run time calculated for the labyrinth as an approximation of the ballistic regime of the dispersal. However, it is derived under the assumption of exponentially distributed run times, which, in the case of the random walk in the labyrinth, is not fulfilled. It might give a much better agreement to the actual MSD measured in computer simulations or in the experiment for small times, but it would still not be exact. That is why, for the remaining of the paper, we will primarily focus on the asymptotic diffusive regime.

Now that we quantitatively understand the properties of the long-time diffusion, we turn to numerical simulations to test our predictions. In particular, it is interesting to see how the dispersal process occurs at shorter times and what the effect of several simplifying assumptions of the analytical approach is.

4. SIMULATIONS OF 2D BACTERIAL DISPERSAL IN LATTICE

In the simulations, all bacteria generally start their walk at the origin $(0, 0)$, which is located in the middle of the same crossing. However, in section 5 we will also consider random starting points. To facilitate computations we use an event-driven algorithm. At each step, a random variable representing the run time is drawn from an exponential distribution with mean τ_0, which is used to determine the position of the next tumble. However, the directional change of the tumbling event happens only if the bacterium is inside of a crossing, as depicted in **Figure 1**. In the case of a uniform turning angle distribution, all four directions are chosen with equal probability. In contrast to the theoretical derivation, multiple tumbles in one crossing are allowed in simulations. For a quantitative evaluation of the effect of multiple tumbles on the diffusion coefficient (see **Figure S2**).

4.1. Diffusive Properties

The results of the simulations are summarized in **Figure 2**. As can be seen in **Figures 2A,B**, the trajectories and bacterial densities have a pronounced square outline at small times (upper row), while acquiring a circular shape at larger times (lower row). This indicates that at the beginning, the bacterial motion is greatly influenced by the geometry of the labyrinth. The clearly seen boundary of the density profile is the ballistic front determined by the constant and finite velocity of the bacteria v_0 as $|x| + |y| = v_0 T$, where T is the measurement time. At a given moment in time, the total distance traveled along the x- and y-directions of the labyrinth cannot exceed the value of $v_0 T$. Trajectories which end up at the front are those where no two steps were done in opposite directions. The effect of ballistic fronts is not frequently mentioned in the context of normal diffusion. However, as this example shows (see also experimental results below), the density of diffusing particles may carry on the information about the underlying lattice for an extended period of time. This effect can be even more dramatic in the case of anomalous diffusion [39]. This behavior is also illustrated in the x-projection of the 2D density of the bacteria shown in **Figure 2C**. The density of the bacteria keeps memory of the underlying geometry at small times but then loses it at larger times and becomes isotropic after many reorientation events. In this diffusive regime, at large times, the bacterial density also quantitatively agrees with the analytical prediction of a Gaussian distribution, shown as red dashed line, validating the theoretical description for the long-time diffusion in the labyrinth. In **Figure 2D**, presenting the mean squared displacement of the bacteria as a function of time, it can be seen that the bacteria indeed exhibit nearly ballistic motion with $\langle \boldsymbol{r}(t)^2 \rangle \propto t^2$ at the beginning and then switch to a diffusive regime with $\langle \boldsymbol{r}(t)^2 \rangle \propto t$, where the derived estimates for the diffusion coefficient are confirmed. At large times, numerical and theoretical curves for the MSD are linear with the same slope, which directly corresponds to the diffusion coefficient. We also clearly see that the slope of the MSD of the walk within the labyrinth is higher than for a walk without spatial restrictions, thus further confirming the hypothesis of facilitated diffusion in the lattice.

4.2. Dependence of Diffusion Coefficient on Lattice Parameters

To further test the level of agreement between our theoretical estimates for the diffusion coefficient and the simulation results, we compared these for a range of different parameters determining the geometry of the lattice and evaluated the dependence of the diffusion coefficient on b—the side length of the obstacles—and on w—the width of the channels between two obstacles. In **Figure 3A**, it can be seen that for three different channel widths w the diffusion coefficient shows a linear dependence on the side length b and can be rescaled onto a single master curve (see inset) with $\widetilde{D}$ being

$$\widetilde{D}_l(b) = \frac{D_l(b)}{\coth\left[\frac{w}{2v_0\tau_0}\right]} - \frac{wv_0}{4} = \frac{bv_0}{4}. \qquad (10)$$

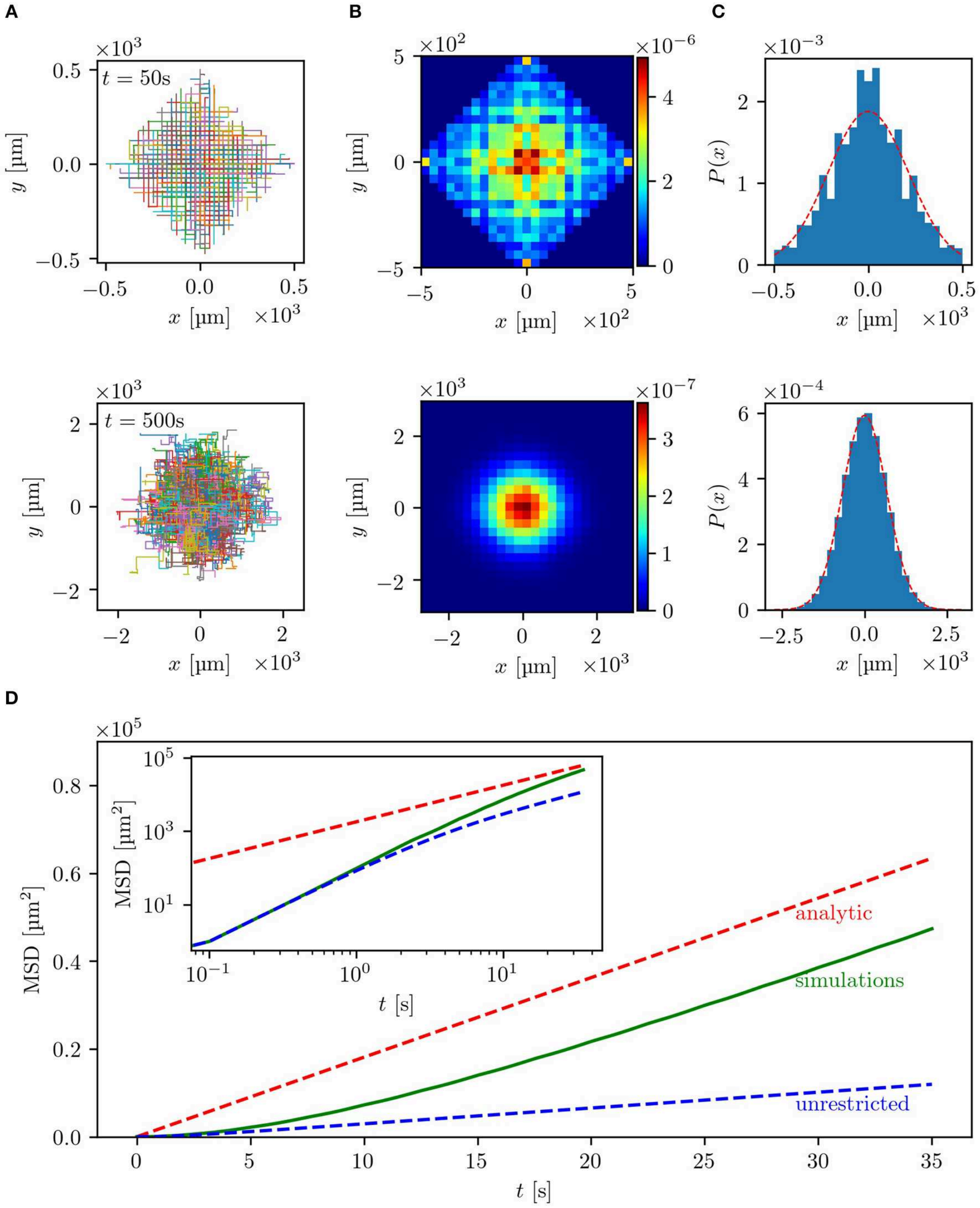

FIGURE 2 | Results of the simulations with uniform turning angle distribution in a lattice with $b = 20\,\mu\text{m}$ and $w = 5\,\mu\text{m}$: **(A)** depicts the trajectories of 500 bacteria for small times, $t = 50\,\text{s}$ (upper row), and large times, $t = 500\,\text{s}$ (lower row). In **(B)** the two-dimensional histograms of the particle density for the same time scales used in **(A)** for 10^5 bacteria are shown. The particle density projected on the x-axis, also for 10^5 bacteria, is plotted in **(C)** with the red dashed line representing the analytical solution $P(x) = \left(4\pi D_{lb}t\right)^{-1/2} \exp\left(-x^2/4D_{lb}t\right)$. For small times the underlying geometry has strong influence on the bacterial spreading, while for large times the distribution becomes isotropic. In **(D)** the mean squared displacement of 10^5 bacteria is shown in linear scale, while the inset shows the double logarithmic plot. The red dashed line represents the theoretical estimate introduced in section 3.1 and the green line the empirical MSD of the simulated bacteria. The blue dashed line corresponds to the same random walk without spatial restrictions, which can be described by Equation (4), where $\phi_0 = 90^\circ$ due to the uniform turning angle distribution. The theoretical estimates match the simulated MSD for large times. Guiding the bacteria through a lattice of channels significantly enhances the dispersal as compared to an unrestricted motion.

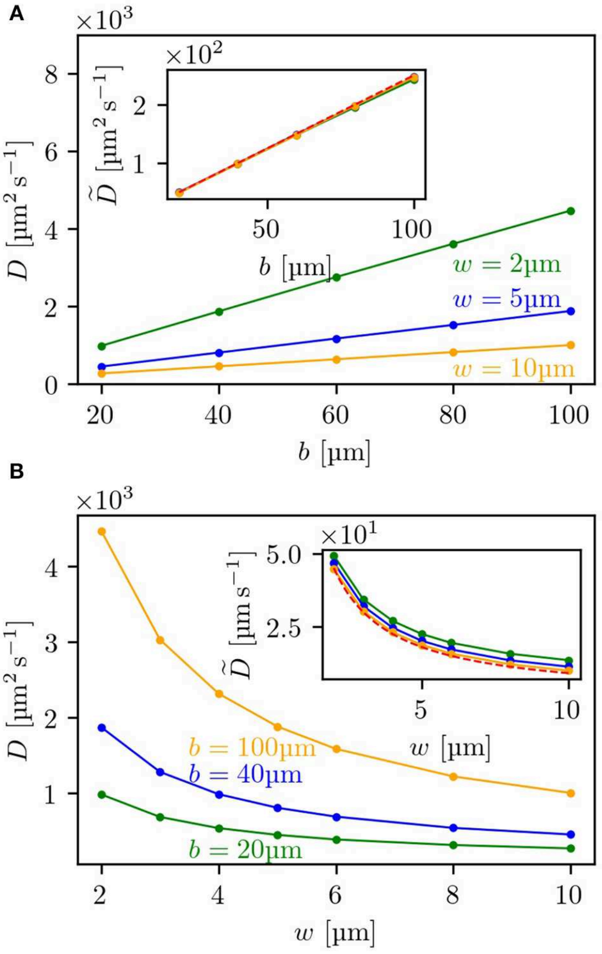

FIGURE 3 | Dependence of the diffusion coefficient on lattice parameters: **(A)** depicts the dependence of the diffusion coefficient in the labyrinth D_l on the side length b of the obstacles for three different channel widths w, **(B)** the dependence on w for three different values of b. Both insets show the rescaled diffusion coefficients as given by Equation (10) for **(A)**, and by Equation (11) for **(B)**. The red dashed line shows the corresponding analytical expression. For each measurement 5,000 bacteria were each simulated to perform 2,000 tumbling events.

As shown in the inset, the rescaled curves of the simulated diffusion coefficients all coincide with the analytical expression. Similarly, for the dependence on the channel width w, the predicted diffusion coefficient matches—as presented in **Figure 3B**—the simulation results for three different side lengths b and can also be rescaled to one master curve, shown as inset. Here, the scaled diffusion coefficient $\widetilde{D}$ is defined as:

$$\widetilde{D}_l(w) = \frac{D_l(w)}{b} = \frac{1}{4} v_0 \coth\left[\frac{w}{2v_0\tau_0}\right] + \frac{w}{4b} v_0 \coth\left[\frac{w}{2v_0\tau_0}\right]$$
$$\simeq \frac{1}{4} v_0 \coth\left[\frac{w}{2v_0\tau_0}\right].$$

In the expression for $\widetilde{D}_l(w)$ a factor of $\frac{w}{b}$ is still included, which makes it not completely independent of the parameter b. However, for $w/b \ll 1$ this term becomes small and can be neglected. Thus, with increasing b, the rescaled curves for the simulations shown in the inset of **Figure 3B** converge to the analytical expression, so that the curve for $b = 100$ µm already agrees with the theoretical prediction. This very good agreement between simulation results and analytical expressions also suggests that multiple tumbles in the crossing included in simulations but neglected in theory are not making a significant contribution for the range of tested parameters (see also **Figure S2**).

5. INTRODUCING A NONUNIFORM TURNING ANGLE DISTRIBUTION: COMPARISON OF SIMULATIONS AND EXPERIMENTS

After verifying the analytical solutions for the case with a uniform turning angle distribution during tumbles, we now switch to the system with a nonuniform turning angle distribution. To test our theory and its practical applicability we implemented the nonuniformity of the turning angle distribution after a tumbling event in a crossing in simulations and compared these results to experimental data [40].

The experiments were performed by using microfluidic devices with a lattice geometry of obstacles with a side length $b = 20$ µm and with two channel widths w and heights h of 5 µm and 8 µm. For these dimensions, some tumbling events of the bacteria inside the channels between two obstacles were observed. Fluorescently labeled *E. coli* were imaged with an inverted fluorescence microscope. Thereby, trajectories in the range of 2.5–20 s could be recorded and analyzed. An example trajectory of one *E. coli* bacterium swimming in a labyrinth with $w = 5$ µm can be seen in the **Supplementary Movie**. The simulation parameters were adjusted to the experimentally observed values. More precisely, the turning angle distribution after a reorientation event and the mean run time were taken from measurements of bacteria moving without geometric restrictions in the x/y-plane but with a vertical constraint at a height of $h = 5$ µm or $h = 8$ µm, respectively. This confinement to effectively two dimensions changes the motility parameters, e.g., the velocity v_0 and turning angle distribution, compared to bacteria freely swimming in three dimensions. In the 5 µm channels the bacteria swim with a mean run time $\tau_0 = 1.8$ s, while in the 8 µm channels with $\tau_0 = 1.7$ s. For both channel widths a velocity $v_0 \approx 10$ µm s^{-1} was measured. By splitting the histogram of turning angles (see **Supplementary Material**) into the domains 0°-45°, 45°-135° and 135°-180°, we determine the turning probabilities in the labyrinth $p_f \approx 0.1, p_r \approx 0.3, p_l \approx 0.3, p_b \approx 0.3$. Further information on how the experiments and simulations were performed can be found in the section 7. In **Figure 4**, side-by-side comparisons between simulations and experiments for $w = 8$ µm are shown (for $w = 5$ µm see **Figure S3**). As basis for the comparisons, we chose the trajectories themselves, the MSD and the decision making behavior at the crossings. Since the longest trajectory length measured in the experiments was

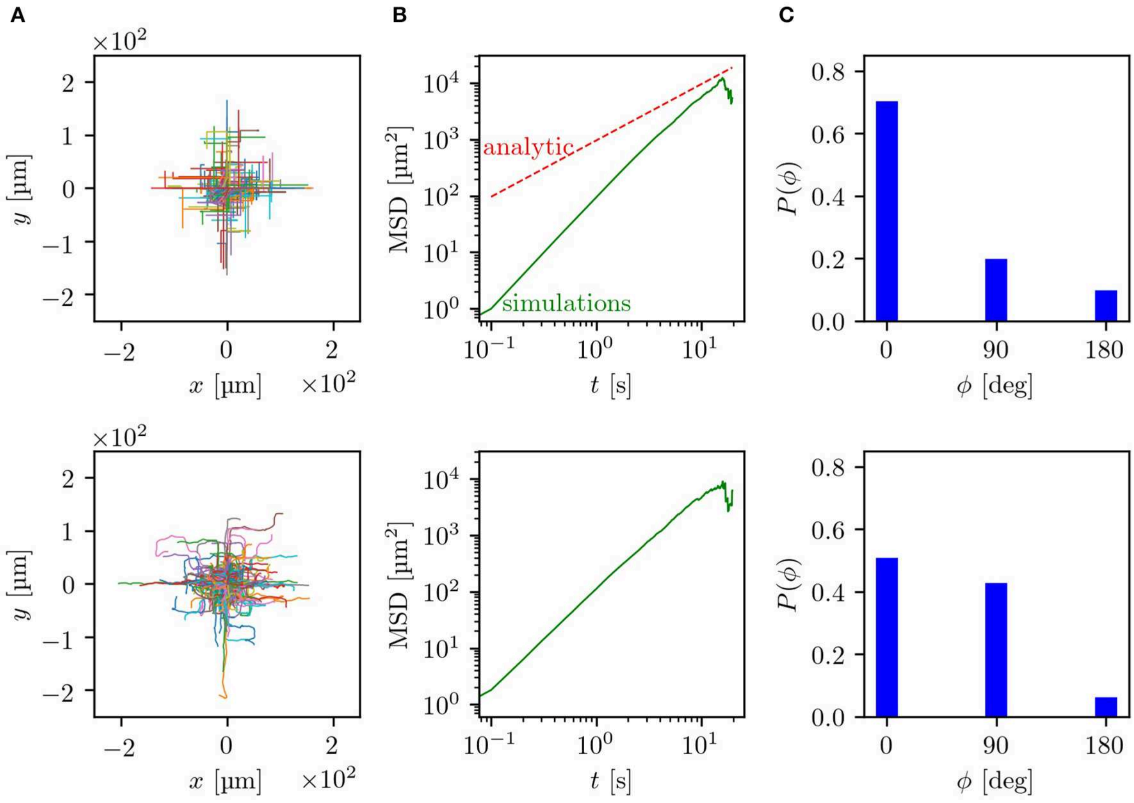

FIGURE 4 | Comparison between simulation results (upper row) and experiments (lower row) for a lattice with $b = 20\,\mu\mathrm{m}$ and $w = 8\,\mu\mathrm{m}$: **(A)** compares the trajectories, starting at a random position in the lattice, which are centered to the zero point. **(B)** Shows the mean squared displacements in double logarithmic plots, where the green line displays the simulated and measured MSD while the red dashed line corresponds to the analytical prediction. **(C)** Displays the probabilities for turning decisions at each crossing. Parameters of simulations are chosen to match experimental data as discussed in the section 7.

around 20 s, the time scale of the comparisons lies, according to our estimates, in the regime of ballistic motion with $\langle \boldsymbol{r}(t)^2 \rangle \propto t^2$. Contrasting both sets of trajectories, shown in **Figure 4A**, it can be observed that both simulations and experiments show evidence of the underlying geometry resembling a ballistic front with the typical $|x| + |y| = v_0 T$ shape. In experiments, hence also in simulations, the trajectories are of different lengths and start at an arbitrary point in the labyrinth. Because of this, both the outlines of obstacles and the ballistic fronts are smeared out in comparison to **Figure 2A**. The distance traveled by the bacteria is quantified by the MSD and shown in double logarithmic display in **Figure 4B**. Here, it can be seen that the simulated curve reproduces the overall trend of the experimental curve and also quantitatively agrees with the experimental data. This becomes even more evident in the direct comparison between the simulated and experimental MSD shown in **Figures S4, S5**. Interestingly, in the experiments, we can track bacterial decisions at every crossing, plot the histogram of the chosen directions and compare it to simulation results, as shown in **Figure 4C**. Here, we see that the simulations reproduce the overall tendency of the decision distributions measured in the experiments. The smaller probability to go forward paired with the higher probability to go right or left in experiments compared to the simulations, can be attributed to smooth directional changes in the crossings due to rotational diffusion, without tumbling events happening. Thus, it would be predicted that in narrower channels the effect of rotational diffusion deflecting the cell from straight motion should be weaker. Indeed, we see that in 5 µm channels (see **Figure S3**), the probability to continue forward approaches the theoretical value. The otherwise good agreement between experiments and simulations suggests that by taking the angle distribution of x/y-unrestricted motion we can reproduce the behavior inside the labyrinth. Here, we should note that the numerical simulations achieve good agreement with experimental data without any fitting parameters. All values and distributions were obtained directly from experiments. Finally, we provide the results of a control experiment, comparing the dispersal of bacteria in the labyrinth and outside the labyrinth. We see a clear effect of enhanced diffusion in agreement with the predictions of the model, see **Figure S5**. Thus, our theoretical model of the diffusion through a square lattice of channels proves to be a reasonable simplification covering the most significant features of experimentally observed bacterial behavior inside of a microfluidic labyrinth.

6. DISCUSSION

We analyzed the process of bacterial dispersal in a labyrinth of channels with square geometry. Narrow channels between the obstacles guide the motion of bacteria and prevent them from changing the swimming direction. The reorientation events can, however, happen in the channel crossings. By modeling this system as a two-dimensional random walk with exponentially distributed run times we provided analytical expressions for the diffusion constants quantifying large time asymptotics of bacterial dispersal in the labyrinth. The main theoretical predictions are an enhanced diffusion constant for smaller channel widths and larger obstacle sizes and a prolonged regime of non-Gaussian diffusion where the geometry of the channels is imprinted in the density of bacteria spreading in the labyrinth. Here, we focused on the two-dimensional geometry to be able to compare our results to experiments. However, a generalization of the developed theoretical and numerical approaches to higher dimensions is rather straightforward.

To assess the practical applicability of the model we specialized it to describe the run-and-tumble motion of *E. coli* with a nonuniform turning angle distribution. We then compared both simulations and theory to experimental data, collected by tracking *E. coli* bacteria in microfluidic labyrinths with lattice geometry. Thereby, we were able to quantitatively verify our theoretical results and demonstrate that our approach can serve as an adequate model of bacterial dispersal in simple labyrinth geometries.

Our results suggest that the developed model can be used to theoretically analyze the behavior of bacteria in an environment with lattice structure. Understanding the dispersal of bacteria in these rather simple geometries can help to evaluate the usability of *E. coli* as a transport bacterium for on-site treatments in more complex environments as well as in other fields like ecology and industrial processes. Our future work will include the analysis of other geometries, for example a hexagonal lattice, and the evaluation of different bacteria species and motility patterns, for example the run-and-reverse pattern of *Pseudomonas putida* or run-reverse-flick of *Vibrio alginolyticus* bacteria. Another interesting task will be the analysis of the effects of different chemical landscapes, e.g., a concentration gradient of a chemoattractant, on the diffusive properties of the bacteria. Additionally, in the future, the diffusion mechanism of bacteria in lattice structures can be further extended to interpret the evolution of game strategies in square lattices [41, 42].

7. MATERIALS AND METHODS

7.1. Microfluidic Experiments

7.1.1. Cell Culturing

The GFP-expressing *E.coli* AW405 strain was cultured overnight in rich liquid LB medium ($10\,\mathrm{g\,L^{-1}}$ Tryptone, $5\,\mathrm{g\,L^{-1}}$ NaCl, $5\,\mathrm{g\,L^{-1}}$ Yeast Extract, pH 7.0) including $100\,\mu\mathrm{g\,ml^{-1}}$ ampicillin at 37 °C on a rotary shaker at 200 rpm. The cell suspension from the overnight culture was diluted 1:100 with fresh LB, and grown to an OD_{600} of 0.6. The cells were washed by centrifugation (1500 g at 20 °C for 2 min) and resuspended in motility buffer ($11.2\,\mathrm{g\,L^{-1}}$ K_2HPO_4, $4.8\,\mathrm{g\,L^{-1}}$ KH_2PO_4, $3.93\,\mathrm{g\,L^{-1}}$ NaCl, $0.029\,\mathrm{g\,L^{-1}}$ EDTA and $0.5\,\mathrm{g\,L^{-1}}$ glucose; pH 7.0).

7.1.2. Cell Imaging and Tracking

The cells were infused into microfluidic chips (for details about the fabrication see **Supplementary Material**). The chips had two wide chambers connected by a maze-like mid-section (see **Figure S1**). This region was made of periodically arranged square structures with a side-length of 20 μm. In this study, two different chips were fabricated with different widths of the channels in the maze (5 μm and 8 μm). The cells freely swam in the wide chambers and occasionally entered the maze and explored this region as well. The GFP-expressing cells were visualized in the chips using an IX71 inverted microscope equipped with a 20X UPLFLN-PH objective (both Olympus, Japan) and an Orca Flash 4.0 CMOS camera (Hamamatsu Photonics, Japan). Two image stacks were acquired at 10 fps over 3 min for each chip. The 5 μm data set contains 45 trajectories with a total length of 409 s. The 8 μm data set consists of 346 trajectories with a total length of 2,231 s.

A custom Matlab program based on the Image Processing Toolbox (version R2015a, The MathWorks, USA) together with the open source image analysis platform Fiji were used to process the image sequences. For each image stack, the images projected into a single image by taking the median value for each pixel over stack. The median image was subtracted from each frame to eliminate non-moving objects including dead cells. A despeckle filter was then applied to correct the noise at the CMOS-sensor of the camera. Afterward, the high frequency noise in the images was filtered out by a Gaussian blur filter. The filtered images were binarized by using maximum entropy thresholding following Kapur et al. [43]. The binary images were further processed to find connected regions in the images using the built-in function *bwconncomp*. The *regionprops* function was used to determine the size and centroid of the objects. Finally, the centroid position was tracked utilizing the algorithms by Crocker and Grier [44].

7.2. Simulation

All simulations have been implemented as event-driven algorithms in Python 3.7 using the freely available packages NumPy and matplotlib. Simulations used in section 4 were performed on an unbounded domain with channels being located on the intervals $[k(b+w)-sign(k)\frac{w}{2}, k(b+w)+sign(k)\frac{w}{2}]$ with $k \in \mathbb{Z}$ in x- as well as in y-direction. Therein all bacteria start their walk at zero at time $t = 0$ positioned in the middle of the same crossing in a random direction $\vec{d}$ taken from a uniform distribution. For each bacterium, N tumbling events are simulated. At each step a random variable τ is drawn from an exponential distribution with mean τ_0 representing the run time until the next tumbling event. Using the constant speed v_0 the new position $\vec{x}_i$ of the bacterium is determined from its prior position $\vec{x}_{i-1}$ as $\vec{x}_i = \vec{x}_{i-1} + \vec{d}\tau v_0$. Only if this lies inside a crossing, a new walking direction $\vec{d}$ (forward, right, backward, left) is randomly drawn from a uniform distribution and used as the direction of the next step. The variable parameters are set to be equal to the experimentally determined values. These are in the two-dimensional confinement a mean run time $\tau_0 = 1.8\,\mathrm{s}$, a constant speed $v_0 = 10\,\mu\mathrm{m\,s}^{-1}$ and a side length $b = 20\,\mu\mathrm{m}$ of the obstacles for a width $w = 5\,\mu\mathrm{m}$ of the channels, and $\tau_0 = 1.7\,\mathrm{s}$, $v_0 = 10\,\mu\mathrm{m\,s}^{-1}$, $b = 20\,\mu\mathrm{m}$ for a channel width $w = 8\,\mu\mathrm{m}$. In Section 5, instead of a uniform distribution, the experimentally determined turning angle distribution (see **Figure S6**) for bacterial movement with spatial restrictions only in the z-plane has been used. By taking the probability to turn in an angle between 0° and 45° in the two-dimensional unrestricted case, the probability to go forward p_f is set to be $p_f = 0.1$. For the probability to go right p_r and to go left p_l the relation $p_r = p_l = 0.3$ holds, being each approximately half of the probability to take an angle between 45° and 135° in the unrestricted experiments. Finally, the probability to turn backwards p_b is $p_b = 0.3$, corresponding to the probability to turn in an angle between 135° and 180°. Also, here the simulated bacteria do not start in the middle of one crossing at $t = 0$, but at a random place inside the lattice. To plot the trajectories—as done in **Figure 4A**—the trajectories were centered to the zero position. For both comparisons, i.e., for $w = 5\,\mu\mathrm{m}$ and $w = 8\,\mu\mathrm{m}$, the same number of trajectories and same trajectory lengths were simulated as were tracked in experiments.

DATA AVAILABILITY STATEMENT

The datasets generated and analyzed for this study can be found under the doi: 10.5281/zenodo.3367324.

AUTHOR CONTRIBUTIONS

AW performed numerical simulations, analyzed the data, and wrote the manuscript. All coauthors contributed to the conception and design of the study and to writing the manuscript. XZ and VZ provided analytical results. MB performed the experiments. MB and ZA analyzed the experimental data. CB designed the experimental research.

FUNDING

MB, ZA, and CB gratefully acknowledge financial support by the research training group GRK 1558 funded by Deutsche Forschungsgemeinschaft.

ACKNOWLEDGMENTS

We thank Hui-Shun Kuan and Tim Klingberg for stimulating discussions and Marius Hintsche for support with the experiments and the cell tracking algorithm.

SUPPLEMENTARY MATERIAL

The Supplementary Material for this article can be found online at: https://www.frontiersin.org/articles/10.3389/fphy.2019.00148/full#supplementary-material

Supplementary Movie | Bacteria swimming in square labyrinth.

REFERENCES

1. Turnbaugh PJ, Ley RE, Hamady M, Fraser-Liggett CM, Knight R, Gordon JI. The human microbiome project. *Nature.* (2007) **449**:804. doi: 10.1038/nature06244
2. Mitchell JG, Kogure K. Bacterial motility: links to the environment and a driving force for microbial physics. FEMS Microbiol Ecol. (2006) **55**:3–16. doi: 10.1111/j.1574-6941.2005.00003.x
3. Jarrell KF, McBride MJ. The surprisingly diverse ways that prokaryotes move. *Nat Rev Microbiol*. (2008) **6**:466. doi: 10.1038/nrmicro1900
4. Johansen JE, Pinhassi J, Blackburn N, Zweifel UL, Hagström Å. Variability in motility characteristics among marine bacteria. *Aquat Microb Ecol*. (2002) **28**:229–37. doi: 10.3354/ame028229
5. Bardy SL, Ng SY, Jarrell KF. Prokaryotic motility structures. *Microbiology.* (2003) **149**:295–304. doi: 10.1099/mic.0.25948-0
6. Berg HC. The rotary motor of bacterial flagella. *Annu Rev Biochem*. (2003) **72**:19–54. doi: 10.1146/annurev.biochem.72.121801.161737
7. Berg HC. *Random Walks in Biology*. Princeton, NJ: Princeton University Press (1993).
8. Fürth R. Die brownsche Bewegung bei Berücksichtigung einer Persistenz der Bewegungsrichtung. Mit Anwendungen auf die Bewegung lebender Infusorien. *Zeitschrift für Physik A Hadrons and Nuclei.* (1920) **2**:244–56. doi: 10.1007/BF01328731
9. Tailleur J, Cates M. Statistical mechanics of interacting run-and-tumble bacteria. *Phys Rev Lett.* (2008) **100**:218103. doi: 10.1103/PhysRevLett.100.218103
10. Lauga E. Bacterial hydrodynamics. *Annu Rev Fluid Mech*. (2016) **48**:105–30. doi: 10.1146/annurev-fluid-122414-034606
11. DeRosier DJ. The turn of the screw: the bacterial flagellar motor. *Cell.* (1998) **93**:17–20. doi: 10.1016/S0092-8674(00)81141-1
12. Lighthill J. Flagellar hydrodynamics. *SIAM Rev*. (1976) **18**:161–230. doi: 10.1137/1018040
13. Bechinger C, Di Leonardo R, Löwen H, Reichhardt C, Volpe G, Volpe G. Active particles in complex and crowded environments. *Rev Mod Phys*. (2016) **88**:045006. doi: 10.1103/RevModPhys.88.045006
14. Männik J, Driessen R, Galajda P, Keymer JE, Dekker C. Bacterial growth and motility in sub-micron constrictions. *Proc Natl Acad Sci USA*. (2009) **106**:14861–6. doi: 10.1073/pnas.0907542106
15. Libberton B, Binz M, Van Zalinge H, Nicolau DV. Efficiency of the flagellar propulsion of *Escherichia coli* in confined microfluidic geometries. *Phys Rev E.* (2019) **99**:012408. doi: 10.1103/PhysRevE.99.012408
16. Wioland H, Lushi E, Goldstein RE. Directed collective motion of bacteria under channel confinement. *New J Phys*. (2016) **18**:075002. doi: 10.1088/1367-2630/18/7/075002
17. Theves M, Taktikos J, Zaburdaev V, Stark H, Beta C. Random walk patterns of a soil bacterium in open and confined environments. *Europhys Lett*. (2015) **109**:28007. doi: 10.1209/0295-5075/109/28007
18. Raatz M, Hintsche M, Bahrs M, Theves M, Beta C. Swimming patterns of a polarly flagellated bacterium in environments of increasing complexity. *Eur Phys J Spec Top*. (2015) **224**:1185–98. doi: 10.1140/epjst/e2015-02454-3
19. Sosa-Hernández JE, Santillán M, Santana-Solano J. Motility of *Escherichia coli* in a quasi-two-dimensional porous medium. *Phys Rev E.* (2017) **95**:032404. doi: 10.1103/PhysRevE.95.032404
20. Bhattacharjee T, Datta SS. Bacterial hopping and trapping in porous media. *Nat Commun*. (2019) **10**:2075. doi: 10.1038/s41467-019-10115-1
21. Elgeti J, Gompper G. Run-and-tumble dynamics of self-propelled particles in confinement. *Europhys Lett*. (2015) **109**:58003. doi: 10.1209/0295-5075/109/58003
22. Jakuszeit T, Croze OA, Bell S. Diffusion of active particles in a complex environment: role of surface scattering. *Phys Rev E.* (2019) **99**:012610. doi: 10.1103/PhysRevE.99.012610
23. Pattanayak S, Das R, Kumar M, Mishra S. Enhanced dynamics of active Brownian particles in periodic obstacle arrays and corrugated channels. *Eur Phys J E.* (2019) **42**:62. doi: 10.1140/epje/i2019-11826-7

24. Ribet D, Cossart P. How bacterial pathogens colonize their hosts and invade deeper tissues. *Microbes Infect*. (2015) **17**:173–83. doi: 10.1016/j.micinf.2015.01.004
25. Forbes NS. Engineering the perfect (bacterial) cancer therapy. *Nat Rev Cancer*. (2010) **10**:785. doi: 10.1038/nrc2934
26. Patyar S, Joshi R, Byrav DP, Prakash A, Medhi B, Das B. Bacteria in cancer therapy: a novel experimental strategy. *J Biomed Sci*. (2010) **17**:21. doi: 10.1186/1423-0127-17-21
27. Jang LK, Chang PW, Findley JE, Yen TF. Selection of bacteria with favorable transport properties through porous rock for the application of microbial-enhanced oil recovery. *Appl Environ Microbiol*. (1983) **46**:1066–72.
28. Al-Sulaimani H, Joshi S, Al-Wahaibi Y, Al-Bahry S, Elshafie A, Al-Bemani A. Microbial biotechnology for enhancing oil recovery: current developments and future prospects. *Biotechnol Bioinf Bioeng*. (2011) **1**:147–58.
29. Zhong H, Liu G, Jiang Y, Yang J, Liu Y, Yang X, et al. Transport of bacteria in porous media and its enhancement by surfactants for bioaugmentation: a review. *Biotechnol Adv*. (2017) **35**:490–504. doi: 10.1016/j.biotechadv.2017.03.009
30. Akin D, Sturgis J, Ragheb K, Sherman D, Burkholder K, Robinson JP, et al. Bacteria-mediated delivery of nanoparticles and cargo into cells. *Nat Nanotechnol*. (2007) **2**:441. doi: 10.1038/nnano.2007.149
31. Berg HC. *E. coli in Motion*. New York, NY: Springer Science & Business Media (2008).
32. Molaei M, Barry M, Stocker R, Sheng J. Failed escape: solid surfaces prevent tumbling of *Escherichia coli*. *Phys Rev Lett*. (2014) **113**:068103. doi: 10.1103/PhysRevLett.113.068103
33. Turner L, Ryu WS, Berg HC. Real-time imaging of fluorescent flagellar filaments. *J Bacteriol*. (2000) **182**:2793–801. doi: 10.1128/JB.182.10.2793-2801.2000
34. Biondi SA, Quinn JA, Goldfine H. Random motility of swimming bacteria in restricted geometries. *AIChE J*. (1998) **44**:1923–9. doi: 10.1002/aic.690440822
35. Berg HC, Brown DA. Chemotaxis in *Escherichia coli* analysed by three-dimensional tracking. *Nature*. (1972) **239**:500. doi: 10.1038/239500a0
36. Phillips BR, Quinn JA, Goldfine H. Random motility of swimming bacteria: single cells compared to cell populations. *AIChE J*. (1994) **40**:334–48. doi: 10.1002/aic.690400212
37. Lovely PS, Dahlquist F. Statistical measures of bacterial motility and chemotaxis. *J Theor Biol*. (1975) **50**:477–96. doi: 10.1016/0022-5193(75)90094-6
38. Taktikos J, Stark H, Zaburdaev V. How the motility pattern of bacteria affects their dispersal and chemotaxis. *PLoS ONE*. (2013) **8**:e81936. doi: 10.1371/journal.pone.0081936
39. Zaburdaev V, Fouxon I, Denisov S, Barkai E. Superdiffusive dispersals impart the geometry of underlying random walks. *Phys Rev Lett*. (2016) **117**:270601. doi: 10.1103/PhysRevLett.117.270601
40. Bahrs M. *Diffusive spreading of Escherichia coli and Pseudomonas putida in complex environments* (Master thesis). Universität Potsdam, Potsdam, Germany (2017).
41. Chen Mh, Wang L, Wang J, Sun Sw, Xia Cy. Impact of individual response strategy on the spatial public goods game within mobile agents. *Appl Math Comput*. (2015) **251**:192–202. doi: 10.1016/j.amc.2014.11.052
42. Chen MH, Wang L, Sun SW, Wang J, Xia CY. Evolution of cooperation in the spatial public goods game with adaptive reputation assortment. *Phys Lett A*. (2016) **380**:40–7. doi: 10.1016/j.physleta.2015.09.047
43. Kapur JN, Sahoo PK, Wong AKC. A new method for gray-level picture thresholding using the entropy of the histogram. *Comput Vis Graph*. (1985) **29**:273–85. doi: 10.1016/0734-189X(85)90125-2
44. Crocker JC, Grier DG. Methods of digital video microscopy for colloidal studies. *J Coll Interfat Sci*. (1996) **179**:298–310. doi: 10.1006/jcis.1996.0217

Conflict of Interest: The authors declare that the research was conducted in the absence of any commercial or financial relationships that could be construed as a potential conflict of interest.

frontiers in Physics

ORIGINAL RESEARCH
published: 18 October 2019
doi: 10.3389/fphy.2019.00143

Langevin Dynamics Driven by a Telegraphic Active Noise

Jaegon Um[†], *Taegeun Song*[†] *and Jae-Hyung Jeon*[*]

Department of Physics, Pohang University of Science and Technology (POSTECH), Pohang, South Korea

Self-propelled or active particles are referred to as the entities which exhibit anomalous transport violating the fluctuation-dissipation theorem by means of taking up an athermal energy source from the environment. Currently, a variety of active particles and their transport patterns have been quantified based on novel experimental tools such as single-particle tracking. However, the comprehensive theoretical understanding for these processes remains challenging. Effectively the stochastic dynamics of these active particles can be modeled as a Langevin dynamics driven by a particular class of active noise. In this work, we investigate the corresponding Langevin dynamics under a telegraphic active noise. By both analytical and computational approaches, we study in detail the transport and nonequilibrium properties of this process in terms of physical observables such as the velocity autocorrelation, heat current, and the mean squared displacement. It is shown that depending on the properties of the amplitude and duration time of the telegraphic noise various transport patterns emerge. Comparison with other active dynamics models such as the run-and-tumble and Lévy walks is also presented.

Keywords: active bath, anomalous diffusion, Langevin dynamics, telegraphic noise, Lévy walks, run-and-tumble

Edited by:
Carlos Mejía-Monasterio,
Polytechnic University of Madrid, Spain

Reviewed by:
Punyabrata Pradhan,
S.N. Bose National Centre for Basic Sciences, India
Luciano Calheiros Lapas,
Universidade Federal da Integração Latino-Americana, Brazil

***Correspondence:**
Jae-Hyung Jeon
jeonjh@postech.ac.kr

[†] *These authors have contributed equally to this work as co-first authors*

Specialty section:
This article was submitted to Interdisciplinary Physics, a section of the journal Frontiers in Physics

Received: *16 June 2019*
Accepted: *13 September 2019*
Published: *18 October 2019*

Citation:
Um J, Song T and Jeon J-H (2019) Langevin Dynamics Driven by a Telegraphic Active Noise. Front. Phys. 7:143. doi: 10.3389/fphy.2019.00143

1. INTRODUCTION

Anomalous diffusion disobeying the fluctuation-dissipation theorem has been widely observed in active systems. Prominent examples are the motor-driven transport in living cells, crawling and swimming dynamics of a cell in free or confined space, the motion of artificial micro-swimmers like Janus particles, and the diffusion of an enzyme during catalysis [1–3]. It can be understood that these active dynamics, typically observed on a mesoscopic time & length scale, are collective phenomena resulted from complicated, myriad interactions among the components comprising the system in the presence of nonequilibrium energy sources. A currently attracting issue is to model the stochastic dynamics of individual active (self-propelled) particles at a coarse-grained level, in which a physical picture is that a single particle is immersed in an active bath, i.e., a heat bath in the presence of an extra nonequilibrium noise [4–8]. A closely connected issue to this problem in other fields is the study of quantifying superdiffusion in the complex (biological) systems [9]. Examples include the motor-driven transport of bio-materials in a cell [10, 11], the run-and-tumble motion of a bacterium [12], foraging motion of motile cells and animals [13], anomalous diffusion of ultracold atoms [14], and the dispersal of a banknote [15]. It has been shown that the displacement distributions often follow a (truncated) Lévy distribution and, thus, the models in the class of continuous-time random walks such as the Lévy flights and Lévy walks explain essential features of the observed stochastic dynamics [16]. In this description, the effect of the active or out-of-equilibrium noise is implicitly taken into account in the PDFs of displacement lengths and/or sojourn times.

In the above studies of the active anomalous diffusion, its stochastic dynamics is often modeled by the Langevin equation of the following form:

$$m\dot{v} = -\gamma v + \xi(t) + f(t). \tag{1}$$

This equation describes the dynamics of a particle of mass $m(=1)$ in a viscous heat bath comprised of passive and active noises. $\xi(t)$ is a thermal (gaussian) noise satisfying the zero mean ($\langle\xi\rangle = 0$) and the variance $\langle\xi(t)\xi(t')\rangle = 2\gamma\beta^{-1}\delta(t-t')$ [γ: frictional coefficient, $\beta = 1/k_B\mathcal{T}$ the inverse temperature where k_B is the Boltzmann constant and $\mathcal{T}$ is the absolute temperature]. The active noise $f(t)$ is responsible for the nonequilibrium source in the system, of which statistical properties characterize the nature of active dynamics under consideration. Here, it is assumed that the two noises are independent each other such that the nonequilibrium environment caused by the active noise does not seriously change the characteristics of $\xi(t)$. For a representative example, the tracer dynamics in an active bath containing *E Coli* micro-swimmers was modeled with the gaussian colored noise $f_{\rm OU}(t)$, often referred to as the Ornstein-Ulenbeck noise, characterized by $\langle f_{\rm OU}\rangle = 0$ and $\langle f_{\rm OU}(t')f_{\rm OU}(t'+t)\rangle \propto \exp(-t/t_c)$ [17]. Regarding subdiffusive or superdiffusive dynamics of the particles embedded in a crowded, viscoelastic medium, their stochastic dynamics can be modeled with fractional gaussian noise $f_H(t)$ [18] having a power-law decaying autocorrelation $\langle f_H(t')f_H(t'+t)\rangle \propto (2H-1)t^{-1+2H}$ with the Hurst exponent H ($0 < H < 1$) [19–23]. For animal or self-propelled particles (e.g., molecular-motor-driven cargo) exhibiting Lévy statistics, the f is a Lévy noise having the characteristics $\mathcal{P}(f) \propto 1/f^{1+\mu}$ [24, 25].

In this work, we investigate the stochastic dynamics of single particles governed by Equation 1 with a telegraphic (i.e., step-like) noise $f(t)$ as illustrated in **Figure 1**. Here the characteristics of the noise is described by its PDFs of noise amplitude $\mathcal{P}(f)$ and of duration time $P(\tau)$. It is noted that by adjusting the PDFs $P(\tau)$ and $\mathcal{P}(f)$ our nonequilibrium noise $f(t)$ can become a shot-noise [26, 27] as well as a dichotomous noise [26, 28]. Hence, in general our model links these two distinct noises. Furthermore, we show that our model with $P(\tau) \sim 1/\tau^{1+\alpha}$ ($0 < \alpha < 2$) serves a model for a Lévy walk superimposed with the thermal noise.

The current paper is organized as follows. In section 2 we present our path integral approach to solve the Langevin equation 1 with a telegraphic active force $f(t)$. Dynamic quantities such as the velocity autocorrelation, heat rate, and the mean-square displacement (MSD) are derived in the underdamped level. Then we introduce the overdamped version of Equation 1 and investigate in detail the long-time dynamics of the particle. In section 3 complementary numerical study is provided. Here we generate the active force $f(t)$ for a few distinct cases of $P(\tau)$ and simulate the corresponding Langevin equations. The results are compared and explained with the analytic studies in section 2. Lastly, in section 4, we summarize the main results with a discussion on the connection between our Langevin model and other active dynamics models.

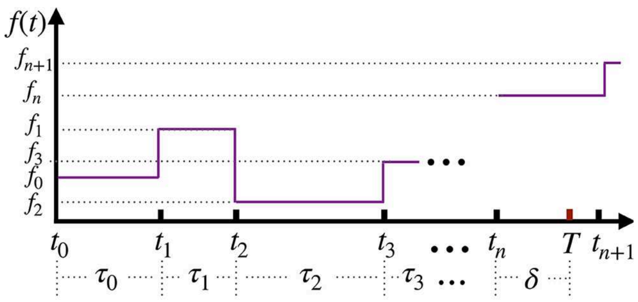

FIGURE 1 | The schematic description of the telegraphic active noise $f(t)$ considered in our Langevin equation 1. The protocol of the noise is given by $f(t) = f_i$ for $t \in [t_i, t_{i+1}]$, where the noise strength f_i and the duration time $\tau_i \equiv t_{i+1} - t_i$ are random variables specifying the statistical properties of $f(t)$. It is a renewal process such that the sequences of $\{f_i\}$ and $\{\tau_i\}$ are i.i.d.s obtained from the PDF $\mathcal{P}(f)$ and $P(\tau)$, respectively.

2. LANGEVIN DYNAMICS

In section 2 we analytically investigate the active dynamics of our Langevin model 1 under a telegraphic noise $f(t)$. Prior to this, we briefly look at the autocorrelation property of $f(t)$ and also introduce useful truncated statistics that used throughout the paper. In section 2.2 our path integral formalism to the Langevin equation 1 is presented with several analytic main results. In section 2.3 we propose the overdamped version of the original Langevin equation 1 and explicitly derive transport quantities for the three distinct types of $f(t)$ (introduced in **Table 1**).

2.1. Noise Correlation of *f*(*t*)

A given time series of a telegraphic noise $f(t)$ can be uniquely defined by its duration time sequence $\{\tau_i\}$ and the amplitude $\{f_i\}$, see **Figure 1**. First, let us consider the ensemble-averaged autocorrelation of $f(t)$, denoted as $\langle f(t)f(t+\Delta t)\rangle_{f_i,\tau_i}$. In this expression, the symbol of $\langle\cdot\rangle_{f_i,\tau_i}$ represents the average over the active noise $f(t)$ for the noise amplitudes f_i and the duration times τ_i. Since the PDFs $\mathcal{P}(f)$ and $P(\tau)$ are independent, the corresponding two averages are independent. Exploiting this property, let us first calculate the f_i-averaged autocorrelation function $\langle f(t)f(t+\Delta t)\rangle_{f_i}$ for a given sequence $\{\tau_i\}$. In this case, the corresponding active noise $f(t)$s have the same transition events, given by the $\{\tau_i\}$, so that the number of transitions n until T is determined by the inequality $\sum_{i=0}^{n-1}\tau_i < T < \sum_{i=0}^{n}\tau_i$. For this set of $f(t)$s, the noise-amplitude averaged autocorrelation is given by

$$\begin{aligned}\langle f(t)f(t+\Delta t)\rangle_{f_i} &= \sigma\sum_{i=0}^{n-1}\Theta(t-t_i)\Theta(t_{i+1}-t-\Delta t)\\ &\quad+\sigma\Theta(t-t_n)\Theta(T-t-\Delta t)\end{aligned} \tag{2}$$

where $\Theta(x)$ is the Heaviside step function [$\Theta(x) = 1$ for $x > 0$, otherwise zero] and $\langle f_l f_m\rangle_{f_i} = \sigma\delta_{lm}$ is used.

To get the full ensemble-averaged autocorrelation, one has to average Equation 2 over all possible sequences of $\{\tau_i\}$. This average can be effectively obtained by performing the

TABLE 1 | The three duration time PDFs considered in our telegraphic noise *f*(*t*) and their statistical properties.

Statistics	$P_T(\tau)$	$[\tau]_T$	$\overline{\langle f(t)f(t+\Delta)\rangle}$ $(T \to \infty)$
Poissonian	$\frac{1}{\tau_c(1-e^{-T/\tau_c})}e^{-\tau/\tau_c}$	$\tau_c - \frac{T}{(e^{T/\tau_c}-1)}$	$\sigma e^{-\Delta/\tau_c}$
Gaussian	$\sqrt{\frac{2}{\pi\sigma_\tau^2 A_0^2}}e^{-(\tau-\tau_c)^2/2\sigma_\tau^2}$	$\tau_c - \sqrt{\frac{2\sigma_\tau^2}{\pi A_0^2}}e^{-(T-\tau_c)^2/2\sigma_\tau^2}$ $-\sqrt{+\frac{2\sigma_\tau^2}{\pi A_0^2}}e^{-\tau_c^2/2\sigma_\tau^2}$	$\sigma B_0\sqrt{\frac{\pi}{2}}e^{-\tau_c^2/2\sigma_\tau^2}\,\mathrm{Erfc}[\frac{\Delta-\tau_c}{\sqrt{2\sigma_\tau^2}}](\tau_c-\Delta)$ $+\,\sigma\sigma_\tau B_0 e^{-\Delta(\Delta-2\tau_c)/2\sigma_\tau^2}$
Power-law	$\frac{\alpha}{(\tau_m^{-\alpha}-T^{-\alpha})}\tau^{-(1+\alpha)}$	$\frac{\alpha}{\alpha-1}\tau_m\left[1-\left(\frac{\tau_m}{T}\right)^{\alpha-1}\right]$	$\frac{\sigma}{\alpha}\left(\frac{\tau_m}{\Delta}\right)^{\alpha-1}$

In the above expressions, $A_0 = Erf\left[(T-\tau_c)/\sqrt{2\sigma_\tau^2}\right] + Erf\left[\tau_c/\sqrt{2\sigma_\tau^2}\right]$, $B_0 = 2/\left[2\sigma_\tau + \sqrt{2\pi\tau_c^2}e^{\tau_c^2/2\sigma_\tau^2}\left(1+Erf[\tau_c/\sqrt{2\sigma_\tau^2}]\right)\right]$.

time average of Equation 2 with an assumption that T is sufficiently large enough to have many transition events (n is large). For nonequilibrium systems this ergodic relation may not be generally guaranteed [1, 4, 29], but we have numerically confirmed this for the telegraphic active noises investigated in this study. We leave the ergodicity test and further discussions in the **Appendix A2.C**. Accordingly, we obtain the expression

$$\begin{aligned}\overline{\langle f(t)f(t+\Delta t)\rangle_{f_i}} &= \frac{\sigma}{T-\Delta t}\int_0^{T-\Delta t} dt\,\langle f(t)f(t+\Delta t)\rangle_{f_i}\,,\\ &= \frac{\sigma}{T-\Delta t}\left[\sum_{i=0}^{n-1}(\tau_i-\Delta t)\,\Theta(\tau_i-\Delta t)\right.\\ &\quad\left.+(\eta-\Delta t)\,\Theta(\eta-\Delta t)\right]\,, \end{aligned} \tag{3}$$

where $\eta = T - \sum_{i=0}^{n-1}\tau_i$. To evaluate the finite summation in the above expression, we define the average number of events $N(\gg 1)$ in the time window $[0,\ T]$ where $N = T/[\tau]_T$ and $[\tau]_T$ is the mean duration time of τ_i in $[0,\ T]$, given by the self-consistent equation

$$[\tau]_T = \int_0^T d\tau\,\tau P_T(\tau)\,. \tag{4}$$

Here, $P_T(\tau)$ is the truncated PDF defined in the interval $[0,\ T]$ from the original one $P(\tau)$, i.e., $P_T(\tau) = P(\tau)/\left[\int_0^T d\tau\,P(\tau)\right]$. Note that N (or n) is large, so we are allowed to replace the summation in Equation 3 by $\frac{1}{n}\sum_{i=0}^{n-1} \to \int_0^T d\tau P_T(\tau)$. Then, using $n \approx N$ and $\Delta t/[\tau]_T \ll N$, we obtain the time-averaged autocorrelation function

$$\overline{\langle f(t)f(t+\Delta t)\rangle_{f_i}} = \frac{\sigma}{[\tau]_T}\int_{\Delta t}^T d\tau\;(\tau-\Delta t)\,P_T(\tau)\,. \tag{5}$$

For the definition and the autocorrelation properties of the three types of $f(t)$ considered in this work, refer to **Table 1**. It is noted that the time-averaged expression 5 is valid and fulfills ergodicity since the duration time PDF of $f(t)$ in our study has a finite mean. Our study below is restricted to this case.

2.2. Path Integral Formalism and the Underdamped Langevin Dynamics

Analogously to section 2.1, let us start to solve the Langevin equation 1 with $f(t)$ observed in $[0,\ T]$ under the condition that the sequences of $\{f_i\}$ and $\{\tau_i\}$ were predetermined.

First, consider the particle dynamics for an infinitesimal time interval $\delta t(\ll 1)$ during which the $f(t)$ is a constant. In this case, according to Onsager and Machlup [30], the propagator of v is given by

$$\Pi\left[v'|v\right] = \sqrt{\frac{\beta}{4\pi\gamma\delta t}}\exp\left[-\frac{\left(v'-v+\gamma v\delta t-f_i\delta t\right)^2}{4\gamma\beta^{-1}\delta t}\right] \tag{6}$$

where $v = v(t)$, $v' = v(t+\delta t)$, and $f(t) = f_i$. Next, we look for the propagator Π of $v(t)$ and $v(t+\Delta t)$ for an arbitrary time interval Δt during which $f(t)$ is allowed to have multiple transitions. With a given $f(t)$, it can be shown that the propagator is written as [31]

$$\Pi\left[v'|v\right] = \sqrt{\frac{\beta}{2\pi w(\Delta t)}}\exp\left[-\frac{\left(v'-e^{-\gamma\Delta t}v-\lambda(t',t)\right)^2}{2\beta^{-1}w(\Delta t)}\right] \tag{7}$$

where $w(\Delta t) = \left(1-e^{-2\gamma\Delta t}\right)$ and $\lambda(t',t)$ is the convolution integral of $f(t)$, given by

$$\lambda(t',t) = \int_t^{t'} ds\,e^{-\gamma(t'-s)}f(s)\,. \tag{8}$$

The derivation of Equation 7 is described in the **Appendix A1**. For example, when $t_i < t < t_{i+1}$ and $t_j < t' < t_{j+1}$ $(i < j)$, $\lambda(t',t)$ reads

$$\begin{aligned}\lambda(t',t) &= \lambda_i(t)e^{-\gamma(t'-t_{i+1})} + e^{-\gamma(t'-t_j)}\sum_{k=i+1}^{j-1}\lambda_k\prod_{l=k+1}^{j-1}e^{-\gamma\tau_l}\\ &\quad+\frac{f_j}{\gamma}\left(1-e^{-\gamma(t'-t_j)}\right)\,,\end{aligned} \tag{9}$$

where $\lambda_k = \lambda_k(t_k)$ is given by

$$\lambda_k = \frac{f_k}{\gamma}\left(1-e^{-\gamma(t_{k+1}-t_k)}\right) = \frac{f_k}{\gamma}\left(1-e^{-\gamma\tau_k}\right) \tag{10}$$

and $\lambda_i(t) = \frac{f_i}{\gamma}\left(1 - e^{-\gamma(t_{i+1}-t)}\right)$. If $f(t)$ has no transition event in $[t,\ t']$ where $t_i < t < t' < t_{i+1}$, Equation 9 is reduced to $\lambda(t',t) = \frac{f_i}{\gamma}\left(1 - e^{-\gamma(t'-t)}\right)$. Given $\lambda(t,t_0)$, the conditional PDF of v is similarly obtained with the initial condition $p(v_0|\lambda) = \delta(v_0)$ as

$$p\left(v|\lambda(t,t_0)\right) = \sqrt{\frac{\beta}{2\pi w(t-t_0)}}\exp\left[-\frac{\left(v-\lambda(t,t_0)\right)^2}{2\beta^{-1}w(t-t_0)}\right]. \quad (11)$$

Heat is defined as the energy gain from a heat bath to the particle. Heat rate is given by [32]

$$\dot{Q} = -(-\gamma v + \xi)\circ v, \quad (12)$$

where $\circ$ denotes the Stratonovich calculus. Using $(-\gamma v+\xi)\circ v = (-\gamma v+\xi)(v+(1/2)\dot{v}\,dt)$ and averaging over the thermal noise, we obtain the conditional heat rate, $\langle\dot{Q}\rangle_\xi$, where $\langle\cdot\rangle_\xi$ stands for the thermal average over ξ for given protocol $f(t)$,

$$\langle\dot{Q}\rangle_\xi = \gamma\langle v^2\rangle_\xi - \frac{1}{2}\langle\xi^2\rangle_\xi\,dt = \gamma\left(\langle v^2\rangle_\xi - \beta^{-1}\right). \quad (13)$$

Here, the equal-time correlation function in Equation 13 is given by $\langle v^2\rangle_\xi = \int dv\, v^2 p\left(v|\lambda(t,t_0)\right)$, which reads

$$\langle v^2(t)\rangle_\xi = \beta^{-1}w(t-t_0) + [\lambda(t,t_0)]^2. \quad (14)$$

In R.H.S, the first term explains the relaxation kinetics toward thermal equilibrium and the second term describes the energy input from the active force $f(t)$. In the limit of $t\to\infty$, $w(t-t_0)\to 1$ at which the heat rate $\langle\dot{Q}\rangle_\xi$ becomes $\gamma\left[\lambda(t,t_0)\right]^2$.

The average over the noise amplitude (f_i) can be further evaluated on the condition that the sequence $\{\tau_i\}$ is quenched. About the active force term $\lambda^2(t,t_0)$, its averaged quantity over $\mathcal{P}(f)$ is calculated to

$$\begin{aligned}\langle\left[\lambda(t,t_0)\right]^2\rangle_{\xi,f_i} &= \frac{\sigma}{\gamma^2}e^{-2\gamma(t-t_i)}\sum_{k=0}^{i-1}\left(1-e^{-\gamma\tau_k}\right)^2\prod_{l=k+1}^{i-1}e^{-2\gamma\tau_l}\\ &\quad+\frac{\sigma}{\gamma^2}\left(1-e^{-\gamma(t-t_i)}\right)^2, \end{aligned}\quad (15)$$

where the index i represents the transition time (of $f(t)$) specifying $t_i < t < t_{i+1}$. The notation $\langle\cdot\rangle_{\xi,f_i}$ denotes the average over both the thermal noise $\xi(t)$ and the amplitude f_i of $f(t)$, henceforth. From this relation, we identify that the averaged heat rate has the relation

$$\langle\dot{Q}(t\to\infty)\rangle_{\xi,f_i} = \lim_{t\to\infty}\gamma\langle\left[\lambda(t,t_0)\right]^2\rangle_{\xi,f_i}. \quad (16)$$

This relation tells that the system has a non-vanishing heat rate (at $t\to\infty$) from the telegraphic noise; it acts as a non-conservative force to the system, driving the particle out of equilibrium constantly and leading to a non-vanishing heat rate. According to Equation 15, however, there is an exceptional case where the heat rate can be vanishing. This happens in the limit of $[\tau]_T\to 0$ where all the exponential terms in Equation 15 are unity (τ_k, τ_l, and $t-t_i$ go to zero). In this case, the telegraphic noise is no longer telegraphic and the effect of $f(t)$ to the system is negligible compared to the thermal noise.

Using Equation 15, the noise-amplitude averaged v^2 is given by

$$\langle v^2(t)\rangle_{\xi,f_i} = \beta^{-1}w(t-t_0) + \langle[\lambda(t,t_0)]^2\rangle_{\xi,f_i}. \quad (17)$$

As time is increased to infinity, both terms of $w(t-t_0)$ and $\lambda^2(t,t_0)$ decay out and v^2 reaches a stationary value. This value can be evaluated in the limit of $t-t_0\to\infty$ where, in Equation 15, τ_i in the exponential terms are approximated to $[\tau]_T$, yielding $\sum_{k=0}^{i-1}\left(1-e^{-\gamma\tau_k}\right)^2\prod_{l=k+1}^{i-1}e^{-2\gamma\tau_l} \approx \left(1-e^{-\gamma[\tau]_T}\right)^2\sum_{k=0}^{\infty}e^{-2k\gamma[\tau]_T} = (1-e^{-\gamma[\tau]_T})/(1+e^{-\gamma[\tau]_T})$. Subsequently, we further perform the average over the duration time $\{\tau_i\}$ by way of time-averaging and finally obtain the time-averaged $\overline{\langle v^2\rangle_{\xi,f_i}}$ at $t\to\infty$

$$\overline{\langle v^2\rangle_{\xi,f_i}} = \beta^{-1} + \frac{\sigma}{\gamma^2}\left(1 - \frac{1-e^{-\gamma[\tau]_T}}{\gamma[\tau]_T}\right). \quad (18)$$

This result will be confirmed in section 3 by the numerical study.

Velocity autocorrelation function (VACF) for $v = v(t)$ and $v' = v(t+\Delta t)$ for a given $f(t)$ can be obtained from the propagator (Equation 7), which is

$$\langle vv'\rangle_\xi = e^{-\gamma\Delta t}\langle v^2\rangle_\xi + \lambda(t',t)\lambda(t,t_0). \quad (19)$$

The noise-amplitude averaged VACF is then found to be

$$\begin{aligned}\langle v'v\rangle_{\xi,f_i} &= e^{-\gamma\Delta t}\left[\beta^{-1}w(t-t_0)\right.\\ &\quad\left.+\langle\left[\lambda(t,t_0)\right]^2\rangle_{\xi,f_i}\right] + \langle\lambda(t',t)\lambda(t,t_0)\rangle_{\xi,f_i}\end{aligned}\quad (20)$$

where $\langle\lambda(t',t)\lambda(t,t_0)\rangle$ means

$$\langle\lambda(t',t)\lambda(t,t_0)\rangle_{\xi,f_i} = \frac{\sigma}{\gamma^2}e^{-\gamma(t'-t_{i+1})}\left(1-e^{-\gamma(t_{i+1}-t)}\right)\left(1-e^{-\gamma(t-t_i)}\right) \quad (21)$$

for $t_i < t < t_{i+1} < t'$ and

$$\langle\lambda(t',t)\lambda(t,t_0)\rangle_{\xi,f_i} = \frac{\sigma}{\gamma^2}\left(1-e^{-\gamma(t'-t)}\right)\left(1-e^{-\gamma(t-t_i)}\right) \quad (22)$$

for $t_i < t < t' < t_{i+1}$.

The mean squared displacement (MSD) of the particle in the interval $[t,\ t+\Delta t]$ can be obtained via the double integral of VACF

$$\langle[\Delta x(\Delta t;t)]^2\rangle_{\xi,f_i} = \int_t^{t+\Delta t}ds\int_t^{t+\Delta t}du\,\langle v(s)v(u)\rangle_{\xi,f_i}. \quad (23)$$

Within a short time interval $\Delta t \ll 1$, Equation 23 can be expanded to

$$\langle\Delta x^2\rangle_{\xi,f_i} \approx \left\langle\left(\frac{v(t)+v(t+\Delta t)}{2}\right)^2\right\rangle_{\xi,f_i}\Delta t^2. \quad (24)$$

Using $\left[v(t)+v(t+\Delta t)\right]/2 \approx v+\dot{v}\Delta t/2$, we obtain the MSD up to the next leading order,

$$\langle \Delta x^2\rangle_{\xi,f_i} \approx \langle v^2\rangle_{\xi,f_i}\Delta t^2 + \left[\frac{\langle \lambda(t,t_0)f(t)\rangle_{\xi,f_i}}{2} + \gamma\beta^{-1} - \gamma\langle v^2\rangle_{\xi,f_i}\right]\Delta t^3. \quad (25)$$

This result suggests that the MSD always starts to grow ballistically in the beginning where the amplitude $\langle v^2\rangle_{\xi,f_i}$ is given by Equation 18.

For the other extreme limit of $\Delta t \to \infty$ together with $t \gg t_0$, we find that up to the order of $1/\gamma^3$ the MSD, Equation 23, grows with Δt in the form of

$$\langle \Delta x^2\rangle_{\xi,f_i} \approx \frac{2\beta^{-1}}{\gamma}\Delta t - \frac{2\beta^{-1}}{\gamma^2} + \frac{\sigma}{\gamma^2}\sum_{i=1}^{n}\left[\tau_i^2 + \frac{4\tau_i}{\gamma}e^{-\gamma\tau_i}\right]. \quad (26)$$

Here, the boundary terms are neglected and n is the number of events in $[t, t+\Delta t]$. This is the expression for a quenched sequence of $\{\tau_i\}$. Equation 26 suggests that in the long-time limit where $\Delta t \gg \gamma^{-1}$ (which is the momentum relaxation time m/γ) the MSD dynamics is eventually determined by the first linear term (thermal) and the sum of τ_i^2 (active). The active part term can be reasonably rewritten as $\sum_{i=1}^{n}\tau_i^2 \to n[\tau^2]_T \approx ([\tau^2]_T/[\tau]_T)\Delta t$. Therefore, the second moment of duration time plays a crucial role in the long-time transport. Further development will be presented in the following section 2.3.

Equation 26 also suggests that the long-time limit dynamics of our underdamped Langevin model can be alternatively obtained by taking the overdamped limit: $\gamma \to \infty$ (or $m/\gamma \to 0$) while $1/[\beta\gamma]$ and σ/γ^2 keep finite. It is shown below that the MSD Equation 26 in this limit is identical to the MSD (Equation 35) of the overdamped version of the original underdamped Langevin equation 1. In the following section, we introduce this overdamped Langevin equation and investigate its MSD dynamics in a precise manner.

2.3. Overdamped Limit

Using the rescaled noises, $\tilde{\xi} = \xi/\gamma$ and $\tilde{f}(t) = f(t)/\gamma$, from our Langevin equation 1 we obtain the equation of motion for the overdamped dynamics as such

$$\dot{x} = \tilde{\xi} + \tilde{f}(t), \quad (27)$$

where the gaussian white noise has the autocorrelation property $\langle\tilde{\xi}(t)\tilde{\xi}(t')\rangle = 2D\delta(t-t')$ with $D = \beta^{-1}/\gamma$. Akin to the $v(t)$ in the underdamped case, when the time series of $\tilde{f}(t)$ is given, the PDF for $x(t)$ is evaluated to

$$p\left(x|\tilde{\lambda}(t,t_0)\right) = \sqrt{\frac{1}{4\pi Dt}}\exp\left[-\frac{\left(x-\tilde{\lambda}(t,t_0)\right)^2}{4Dt}\right], \quad (28)$$

where $x(t_0)=0$ and

$$\tilde{\lambda}(t,t_0) = \int_{t_0}^{t} ds\tilde{f}(s). \quad (29)$$

Therefore, $\tilde{\lambda}(t,t_0)$ means the mean drifted distance for given $f(t)$ and the PDF of $x(t)$ is a gaussian distribution centered at $\tilde{\lambda}(t,t_0)$. However, the noise-averaged PDF of x has a complicated structure beyond the simple gaussian. This will be discussed with the simulation in the next section. In the special case where $P(\tau) = e^{-\tau/\tau_c}/\tau_c$ and the two-state amplitude $\mathcal{P}(\tilde{f}) = \frac{1}{2}\delta(\tilde{f}-\tilde{f}_0) + \frac{1}{2}\delta(\tilde{f}+\tilde{f}_0)$, $\tilde{f}(t)$ can be treated as a dichotomous noise switching between the two states with a constant transition rate $(2\tau_c)^{-1}$. This model was analytically studied in a recent work [33] within the approach using a generalized telegrapher's equation.

In the limit of $\gamma/m \gg 1$ (while $1/[\beta\gamma]$ and σ/γ^2 are finite), we find that the heat rate $\langle\dot{Q}\rangle_{\xi,f_i}$ in Equation 16 is reduced to $\langle\dot{Q}\rangle_{\xi,f_i} = \gamma\tilde{\sigma}$. The same conclusion is drawn from the overdamped equation, Equation 27, yielding

$$\langle\dot{Q}\rangle_{\tilde{\xi},\tilde{f}_i} = \left\langle\left(\gamma\dot{x} - \gamma\tilde{\xi}\right)\circ\dot{x}\right\rangle_{\tilde{\xi},\tilde{f}_i} = \gamma\tilde{\sigma} \quad (30)$$

where $\langle\cdot\rangle_{\tilde{\xi},\tilde{f}_i}$ denotes the double average over the thermal noise $\tilde{\xi}$ and the amplitude $\tilde{f}_i$ of the active noise $\tilde{f}(t)$. The PDF Equation 28 tells that the MSD is given by

$$\langle\Delta x^2(\Delta t;t)\rangle_{\tilde{\xi}} = 2D\Delta t + \left[\tilde{\lambda}(t',t)\right]^2, \quad (31)$$

where $t' = t+\Delta t$. By performing the average of Equation 31 over the noise amplitude $\mathcal{P}(f)$, we obtain

$$\langle\Delta x^2\rangle_{\tilde{\xi},\tilde{f}_i} = 2D\Delta t + \tilde{\sigma}\left[(t'-t_j)^2 + \sum_{k=i+1}^{j-1}\tau_k^2 + (t_{i+1}-t)^2\right] \quad (32)$$

where $t_i < t < t_{i+1}$ and $t_j < t' < t_{j+1}$ $(i<j)$; for $t_i = t_j$, $\langle\Delta x^2\rangle_{\tilde{\xi},\tilde{f}_i} = 2D\Delta t + \tilde{\sigma}\Delta t^2$.

From Equation 32, we finally find the analytic form of MSD averaged over the noise duration time with $P(\tau)$. Direct evaluation of the τ-average on Equation 32 is, however, not straightforward. In this work, we obtain this average by self-averaging Equation 32 over time at the large-T limit. This task is essentially same as finding the time-averaged MSD of Equation 32

$$\overline{\langle\Delta x^2\rangle_{\tilde{\xi},\tilde{f}_i}} = \frac{1}{T-\Delta t}\int_0^{T-\Delta t} dt\langle[\Delta x(\Delta t;t)]^2\rangle_{\tilde{\xi},\tilde{f}_i}. \quad (33)$$

To calculate this, we follow the trick used in finding the autocorrelation of $f(t)$. Consider a sequence $\{\tau_0,\ldots,\tau_n\}$ where n is the last event satisfying $\sum_{i=0}^{n-1}\tau_i < T < \sum_{i=0}^{n}\tau_i$. In the assumption of periodic B.C. (where the sequence of τ_i in $[0,\ \Delta t]$ appears again in $[T-\Delta t,\ T]$), we find that Equation 33 is evaluated to

$$\overline{\langle\Delta x^2\rangle_{\tilde{\xi},\tilde{f}_i}} \equiv \overline{\langle\Delta x^2\rangle} = 2D\Delta t + \frac{\tilde{\sigma}}{T-\Delta t}\left[\sum_{\tau_i<\Delta t}\left(\tau_i^2\Delta t - \frac{\tau_i^3}{3}\right) + \sum_{\tau_i>\Delta t}\left(\tau_i\Delta t^2 - \frac{\Delta t^3}{3}\right)\right]. \quad (34)$$

From now on, for simplicity, we drop the subscript $\tilde{\xi}, \tilde{f}_i$ in expressing the multiple average of $\overline{\langle \cdot \rangle_{\tilde{\xi}, \tilde{f}_i}}$. In the long observation time limit where $n \gg 1$, the statistics is sufficient enough so as to replace the summation above by integral with the truncated PDF $P_T(\tau)$ defined in $[0,\ T]$, see **Table 1**. Using this, we obtain the expression of the fully averaged MSD in terms of $P_T(\tau)$ as

$$\overline{\langle \Delta x^2 \rangle} = 2D\Delta t + \frac{\tilde{\sigma}}{[\tau]_T} \left[\int_0^{\Delta t} d\tau\, P_T(\tau) \left(\tau^2 \Delta t - \frac{\tau^3}{3} \right) + \int_{\Delta t}^{T} d\tau\, P_T(\tau) \left(\tau \Delta t^2 - \frac{\Delta t^3}{3} \right) \right] \quad (35)$$

where $[\tau]_T = \int_0^T d\tau\, \tau\, P_T(\tau)$ is the average duration time observed in $[0,\ T]$.

2.3.1. Poissonian and Gaussian PDFs

Plugging the corresponding $P_T(\tau)$s in **Table 1** into Equation 35 we can in principle obtain the explicit form of the time-averaged MSDs (not shown). For $P(\tau)$s having a well-defined time scale $\tau_s(\sim\ [\tau]_T)$, the MSD is shown to have the following universal structures at the two extreme time scales:

$$\overline{\langle \Delta x^2 \rangle} \approx \begin{cases} 2D\Delta t + \tilde{\sigma}\,\Delta t^2 - \frac{\tilde{\sigma}}{3[\tau]_T} \Delta t^3\,, & \Delta t \ll \tau_s \\ 2D\Delta t + \frac{\tilde{\sigma}[\tau^2]_T}{[\tau]_T} \Delta t - \frac{\tilde{\sigma}[\tau^3]_T}{3[\tau]_T}\,, & \Delta t \gg \tau_s \end{cases}. \quad (36)$$

The result suggests that the overdamped dynamics have the Fickian behavior at both limiting time scales, with different diffusivities. For $\Delta t \ll \tau_s$, the active noise effects negligibly, where the particle has the bare diffusivity D. For the opposite limit of $\Delta t \gg \tau_s$, the particle ultimately attains a larger Fickian transport with an apparent diffusivity

$$D_L = D + \frac{\tilde{\sigma}[\tau^2]_T}{2[\tau]_T}. \quad (37)$$

Detailed information about the profile of $P(\tau)$ is irrelevant for the nature of long-time transport; it only affects D_L through the first and second moments of the duration time. An example belonging to this class is the two-state active system with a constant transition rate $(2\tau_c)^{-1}$ introduced in Malakar et al. [33]. This system can be modeled in our Langevin description with $P(\tau) = \tau_c^{-1} e^{-\tau/\tau_c}$ and $\tilde{f}_i = \pm \tilde{f}_0$. For this model, we analytically evaluate the MSD 35 with $T \to \infty$ and obtain the identical form of MSD reported in Malakar et al. [33]

$$\overline{\langle \Delta x^2 \rangle} = 2(D + \tau_c \tilde{f}_0^2)\Delta t - 2\tau_c^2 \tilde{f}_0^2 (1 - e^{-\Delta t/\tau_c}). \quad (38)$$

This expression shows that, for $\Delta t \ll \tau_c$, $\overline{\langle \Delta x^2 \rangle} = 2D\Delta t + \tilde{f}_0^2 \Delta t^2 - \frac{\tilde{f}_0^2}{3\tau_c} \Delta t^3$ while, for $\Delta t \gg \tau_c$, $\overline{\langle \Delta x^2 \rangle} = 2(D + \tau_c \tilde{f}_0^2)\Delta t - 2\tau_c^2 \tilde{f}_0^2$ where the apparent diffusivity is $D + \tau_c \tilde{f}_0^2$. These results are reproduced by plugging $[\tau^q]_{T\to\infty} = \tau_c^{-1} \int_0^\infty \tau^q e^{-t/\tau_c}$ into Equations 36 and 37.

2.3.2. Power-Law PDFs

Considering $P_T(\tau) \propto \tau^{-1-\alpha}$ in $[\tau_m,\ T]$, the finite-time expectations, $[\tau]_T$ and $[\tau^2]_T$, are obtained in terms of α, T, and τ_m (**Table 1**). For the large-time limit of $\Delta t \to \infty$, we obtain the asymptotic scaling relations of MSD depending on α:

$$\overline{\langle \Delta x^2 \rangle} \approx \begin{cases} a_1 + a_2 \Delta t^\alpha + a_3 \Delta t + a_4 \Delta t^2\,, & 0 < \alpha \le 1 \\ b_1 + b_2 \Delta t + b_3 \Delta t^{3-\alpha}\,, & 1 < \alpha \le 2 \\ c_1 + c_2 \Delta t^{3-\alpha} + c_3 \Delta t\,, & 2 < \alpha \le 3 \\ d_1 + d_2 \Delta t\,, & 3 < \alpha \end{cases}. \quad (39)$$

Here, $\{a_i\}$, $\{b_i\}$, $\{c_i\}$, and $\{d_i\}$ are constants expressed with α, D, and other time constants (we omit providing these lengthy expressions except for $c_3 = d_2 = 2D_L$). The above expression explains that the long-time motion is akin to that of the Lévy walk [9], sensitively depending on the value of α. For a heavy-tailed PDF of a diverging mean $[\tau]_T \sim T^{1-\alpha}$ $(0 < \alpha < 1)$, the ballistic dynamics dominates over the other corrections as Δt approaches to T. For $1 < \alpha \le 2$, the mean duration time is finite ($[\tau]_T = \alpha\tau_m/(\alpha - 1)$), but the second moment is diverging ($[\tau^2]_T \sim T^{2-\alpha}$). In this case, the long-time dynamics is ultimately governed by the sub-ballistic superdiffusion term of $\Delta t^{3-\alpha}$. These superdiffusive dynamics in the range of α between 0 and 2 can emerge for a particle in a fluid in the hydrodynamic regime [9, 34, 35]. For all $\alpha > 2$, the first and second moments of τ are all finite, which, thus, results in the Fickian long-time dynamics ($\sim \Delta t$) as in the cases of poissonian and gaussian PDFs. In this case, the long-time diffusivity D_L has exactly the same expression in Equation 37. As a special case, for α in between 2 and 3, the divergence of $[\tau^3]_T$ gives the nonvanishing correction term $c_2 \Delta t^{3-\alpha}$ (see Equation 36); however, this term is sublinear and negligible compared to the Fickian term Δt at large times.

3. NUMERICAL RESULTS

In this section, we perform the Langevin dynamics simulation of Equation 1 and elucidate the transport dynamics with the theoretical expectations presented in the previous section. In our simulation study, we consider the three distinct $f(t)$ governed by $P(\tau)$ of a poissonian, gaussian, and of a power-law, respectively. The specific functional form of these PDFs used in our study is presented in **Table 1**, with information about their autocorrelation properties. **Figure 2** shows sample time series of $f(t)$ generated in our simulation where the noise amplitude was chosen from a uniform $\mathcal{P}(f)$ in the interval $[-f_0,\ f_0]$ for all simulations, otherwise specified. Further information on the simulation procedure is provided in the **Appendices A2**, **A3**.

3.1. Dynamics of $v^2(t)$

In **Figure 3** we plot the relaxation of $\langle v^2(t) \rangle_{\xi, f_i, \tau_i}$ (black) from 10^5 sample trajectories of the Langevin equation 1 for the three distinct $f(t)$ (see the Caption for further information). Here, in simulation, the full ensemble-averaged v^2, $\langle v^2(t) \rangle_{\xi, f_i, \tau_i}$, is evaluated via the average over the thermal noise as well as the amplitude and duration time of $f(t)$.The data is compared with the theoretical curve (red) of $\langle v^2(t) \rangle_{\xi, f_i, \tau_i}$, which is computationally obtained from Equation (17) with the average

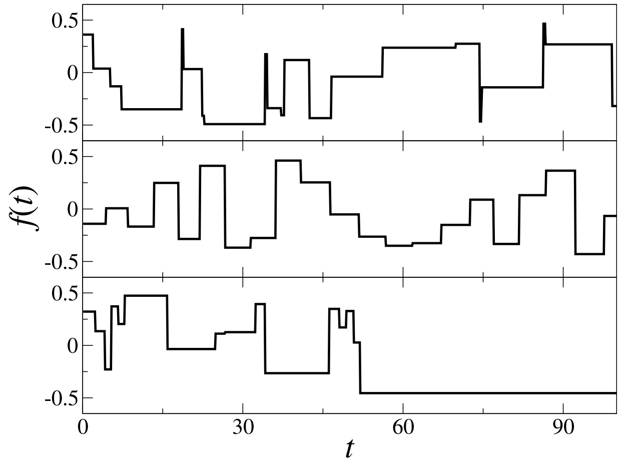

FIGURE 2 | Time trace of the telegraphic noise $f(t)$ generated in simulation. From Top to Bottom the sample noise was generated from the duration time PDFs: poissonian $P(\tau) \propto e^{-\tau/\tau_c}$, gaussian $P(\tau) \propto e^{-(\tau-\tau_c)^2/2\sigma_\tau^2}$, and power-lawed $P(\tau) \propto \tau^{-(1+\alpha)}$. The parameters we used are $\tau_c = 5$, $\sigma_\tau = 0.5$, $\alpha = 1.2$, and the unit time step 0.01, which gives the theoretical values for $[\tau]_{T\to\infty} (\equiv \int_0^{T\to\infty} d\tau\, \tau P(\tau)) = 5$ (poissonian, gaussian) and 6 (power-law). The noise strength f_i was chosen from a uniform distribution in the interval of $[-0.5, 0.5]$.

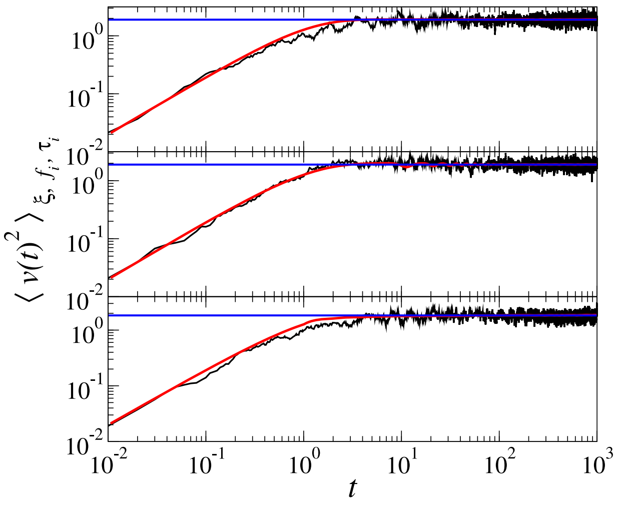

FIGURE 3 | Relaxation dynamics of $\langle v^2(t)\rangle_{\xi,f_i,\tau_i}$. From Top to Bottom they are the cases with $f(t)$ of a poissonian, gaussian, and a power-law $P(\tau)$, respectively. The simulation data (black) were obtained by solving the Langevin Equation 1 with timestep $\delta t = 0.01$, $v_0 = 0$, and the total observation window $T = 2000$. Two theoretical lines are compared to the data: $\langle v^2(t)\rangle_{\xi,f_i,\tau_i}$ (red) obtained from Equation 17 with the additional numerical average over $\{\tau_i\}$ and the stationary value (blue) Equation 18. In the simulation, we used the parameters: $m = \beta = \gamma = 1$, $\tau_c = 10$ and $\sigma_\tau = 1$ for the poissonian and gaussian PDFs, and $\alpha = 1.2$ (producing $[\tau]_T = 5.7$) for the power-law PDF. For all cases, $\mathcal{P}(f)$ is a uniform distribution in $[-\sqrt{3}, \sqrt{3}]$. The units in our Langevin simulation of Equation 1 are: $[x] = 1/\sqrt{\beta\sigma}$, $[t] = \sqrt{m/(\beta\sigma)}$.

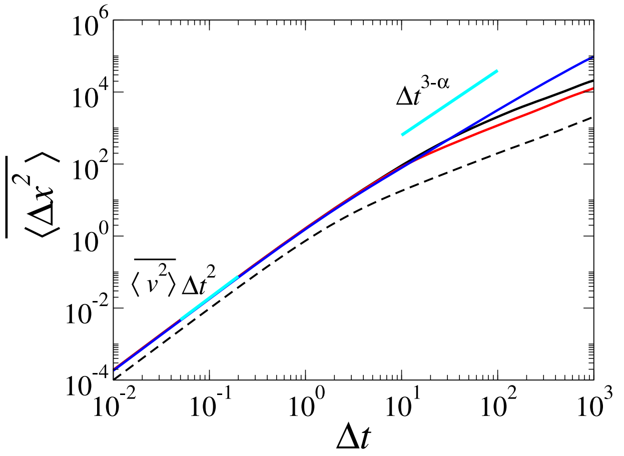

FIGURE 4 | Time-averaged MSDs. The three solid curves correspond to the case of $P(\tau)$, respectively, the poissonian (black), gaussian (red), and the power-law (blue). For reference, the underdamped Brownian particle with $f(t) = 0$ is plotted together (dashed). Additionally, the theoretical expectation (thick cyan) of $\overline{\langle v^2 \rangle}\Delta t^2$, Equation 18, is overlaid with the simulation data. The simulations were carried out based on the equation of motion 1 with $v_0 = 0$, timestep $\delta t = 0.01$, and with 10^5 random realizations of $f(t)$. The same parameter values used in **Figure 3**. The basic units are: $[x] = 1/\sqrt{\beta\sigma}$, $[t] = \sqrt{m/(\beta\sigma)}$.

over $\{\tau_i\}$. The stationary value of $\langle v^2(t \to \infty)\rangle_{\xi,f_i,\tau_i}$ is approximately given by Equation 18 (blue). For all cases, the data are excellently explained by our analytical counterparts.

3.2. MSD

In **Figure 4** we plot the full ensemble-averaged MSDs over random realizations of the noise strength $\{f_i\}$ as well as the duration time $\{\tau_i\}$ for the three cases of f. At the underdamped timescale, as predicted in Equation 25, the MSDs have the ballistic scaling with the same amplitude for all cases. We confirm that this amplitude corresponds to $\overline{\langle v^2 \rangle_{\xi,f_i}}$ given by the formula (Equation 18), cyan line. For comparison, in this plot, the ordinary Langevin dynamics at $f = 0$ is added (dashed). It is seen that the particle under f of the poissonian and gaussian PDFs has the Fickian dynamics at large times (after the momentum relaxation). This is explained by Equation 18. Compared to the ordinary Langevin particle at $f = 0$ the long-time diffusivity is increased to D_L (Equation 18). Under the $f(t)$ of a power-law, the particle is shown to eventually attain a sub-ballistic superdiffusion of the anomaly exponent $3 - \alpha$ in the range of α in $(1, 2)$. This is expected in our analysis (Equation 39) for the overdamped dynamics of the particle.

Additionally, we simulate the overdamped Langevin equation 27 and obtain, in **Figure 5**, the fully averaged MSDs for the three cases of f. In the plot, the gray dots show sample time-averaged MSDs from individual trajectories and their average curve over 10^6 ensemble is depicted with solid red line. This MSD is overlaid with our theoretical expression (Equation 35) explaining the full-time (overdamped) dynamics with information of $P(\tau)$. It confirms that our analytic theory correctly explains the overdamped dynamics in the full range of time. Here, the MSD initially grows as $2D\Delta t$ (plotted as cyan). Then the MSD has a cross-over at $\Delta t \sim [\tau]_T$ and beyond it reaches the

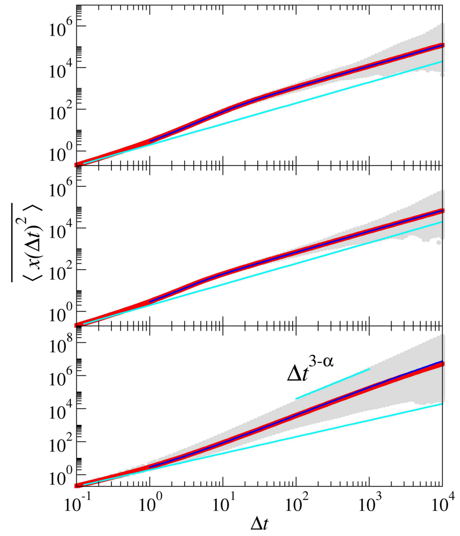

FIGURE 5 | Time-averaged MSDs for the overdamped Langevin dynamics from Equation 27. From Top to Bottom the cases for the poissonian, gaussian, and the power-law PDFs of $P(\tau)$, respectively. Gray dots show the time-averaged MSD curves from single trajectories generated from simulation and the solid (red) line represents their average over 10^6 realizations. Blue lines are the theoretical curves of Equation 35. The Langevin simulation was carried out with timestep $\delta t = 0.01$, $D = 1$, and $T = 10^5$. For the $f(t)$ the same PDFs of $\mathcal{P}(f)$ and $P(\tau)$ informed in **Figures 3**, **4** were used. The units in our overdamped Langevin simulation (Equation 27) are: $[x] = D/\sqrt{\tilde{\sigma}}$, $[t] = D/\tilde{\sigma}$.

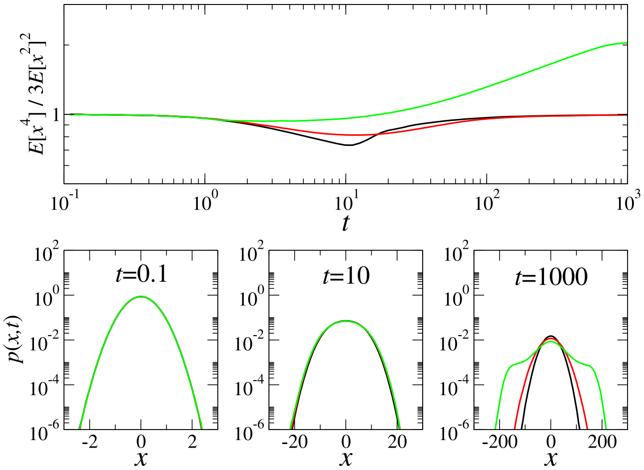

FIGURE 6 | Gaussianity test **(Top)** and the corresponding displacement PDFs $p(x,t)$ **(Bottom)** for the overdamped Langevin motion of Equation (27). In the panels, each line represents, respectively, the result for the poissonian (red), gaussian (black), and the power-law (green) PDF of $P(\tau)$. Parameters in $P(\tau)$ were used as in the previous simulation for MSDs. The displacement PDFs were obtained from 10^8 simulation runs with $T = 10^4$, $\delta t = 0.001$, and $D = \tilde{\sigma} = 1$. The basic units are: $[x] = D/\sqrt{\tilde{\sigma}}$, $[t] = D/\tilde{\sigma}$.

large-time limit. For the poissonian and gaussian PDFs the large-time motion is Fickian with the increased diffusivity D_L. Consistently with **Figure 4**, for the overdamped Langevin model of Equation (27) a superdiffusion of $\Delta t^{3-\alpha}$ is observed for the power-law PDF.

3.3. Displacement PDFs and Gaussianity

In **Figure 6** (Bottom) we present the displacement PDFs, $p(x,t)$, for the active dynamics shown in our overdamped Langevin model Equation 27. The PDFs are obtained for the three distinct $P(\tau)$s and for three MSD regimes (Left: short-time, Middle: cross-over, Right: long-time). Top panel in **Figure 6** shows the evolution of the non-gaussian parameter $\mathrm{E}[x^4(t)]/(3\mathrm{E}[x^2(t)]^2)$ (where $\mathrm{E}[x^m(t)] \equiv \int dx x^m p(x,t)$) [1], which is zero for a gaussian process. Comparing with the MSD in **Figure 5**, we see that the displacement PDF has the unique feature in each regime: Namely, when the particle dynamics is Fickian with D, the displacement PDF is gaussian. Entering the cross-over regime, the MSD has a transient superdiffusion where the $p(x,t)$ most deviates from the gaussianity. In the long-time regime, interestingly, the $p(x,t)$ recovers the gaussian property for the poissonian and gaussian $P(\tau)$s which exhibits the Fickian dynamics with D_L, although the particle is constantly under a nonequilibrium state due to $f(t)$. For the power-law $P(\tau)$ ($\alpha = 1.2$), leading to the long-time superdiffusion in MSD, the displacement is severely deviated from gaussianity because of the violation of the central limit theorem (CLT). Note that our power-law $P(\tau)$, different from the former two PDFs, is a heavy-tailed PDF having the diverging second moment $\int d\tau \tau^2 P(\tau) = \infty$. Thus, the variance of typical displacement due to $f(t)$ over one event, $\tilde{\lambda}(t, t+\tau) = \frac{f}{\gamma}\tau$, diverges (see Equation 29) and breaks down the CLT. We learn from this result that the $P(\tau)$ not only determines the long-time dynamics but also affects the gaussianity.

We investigate the effect of $\mathcal{P}(f)$ on the gaussianity. For this purpose, we simulate the cases where $\mathcal{P}(f)$s are two-stated and gaussian under the three $P(\tau)$s considered. **Figure 7** presents the evolution of the non-gaussian parameter for the corresponding Langevin dynamics. From Top to Bottom, the panels show the results for the poissonian, gaussian, and the power-law $P(\tau)$, respectively. In each panel, the three curves indicate those from a uniform (red), a two-state (green), and a gaussian (black) $\mathcal{P}(f)$. The figure shows two interesting observations. The Langevin dynamics (Equation 27) is always gaussian for all times, irrespective of $P(\tau)$, if $\mathcal{P}(f)$ is gaussian; otherwise, it exhibits qualitatively the same feature shown in **Figure 6**, where the long-time motion eventually attains gaussianity for the poissonian and gaussian $P(\tau)$ while it is non-gaussian for the heavy-tailed $P(\tau)$. Previously, similar studies on the gaussianity for the processes described by a generalized Langevin equation were reported in Oliveira et al. [29] and Lapas et al. [36].

4. DISCUSSION AND CONCLUSIONS

In this work, we investigated the dynamics of a Brownian particle in the presence of a telegraphic random force $f(t)$, which acts as a nonequilibrium noise from the environment and mimics the active force experienced in an active bath. We presented an analytic method to solve the Langevin equation 1 for a given telegraphic time series of $f(t)$ and theoretically studied the active dynamics of the particle in terms of the velocity autocorrelation, heat rate, and the MSD. Analytic expressions of these observables were derived within a proper approximation for three distinct types of $f(t)$ having a poissonian, gaussian, and a power-law PDFs of the noise duration time $P(\tau)$. To complement this analytic study, we simulated the corresponding Langevin active systems and computationally investigated the same physical observables that fully averaged over the noise amplitude and duration time. It was validated that the numerically observed dynamic behaviors are quantitatively well explained by the analytic results.

It turns out that in the presence of the telegraphic $f(t)$ the heat rate is nonzero for all times, which implies the imbalance between thermal fluctuation and dissipation due to the $f(t)$. The effect of the active noise is present not only in the FDT violation but also in the long-time apparent diffusivity D_L. It was shown that $D_L > D(= \beta^{-1}/\gamma)$ (see Equation 37) where the difference $D_L - D$ is proportional to the strength of $f(t)$ as shown in $\langle \dot{Q} \rangle$, as long as the variance of duration time is finite: If this diverges, D_L diverges as well and the transport becomes anomalous (superdiffusive).

4.1. Active Particle Under Confinement

We emphasize that our current model essentially describes the transport dynamics of an active particle under confinement. Consider the overdamped Langevin dynamics of a particle under a confining harmonic potential in the presence of the active telegraphic force $f(t)$. The equation of motion reads

$$\gamma \dot{x} = -\kappa x + \xi(t) + f(t)\,, \qquad (40)$$

where κ is the stiffness constant of the harmonic potential such as the optical trap. By replacing $v \to x$, $\gamma \to \kappa/\gamma$, $\sigma \to \sigma/\gamma^2$, and $\beta \to \kappa\beta$, our original Langevin equation 1 is mapped to Equation 40. Therefore, by analogy, all the analytic results presented in our work can be applied to this problem. For instance, the autocorrelation of $x(t)$ can be directly read off from Equations 14 and 19. It is inferred that the MSD grows linearly as $\overline{\langle \Delta x^2 \rangle} \sim \Delta t$ at the beginning, approaching to

$$\overline{\langle \Delta x^2 \rangle} \approx 2(\beta\kappa)^{-1} + 2\frac{\sigma}{\kappa^2}\left(1 - \frac{1 - e^{-\kappa[\tau]_T/\gamma}}{\kappa[\tau]_T/\gamma}\right) \qquad (41)$$

as $\Delta t \to \infty$.

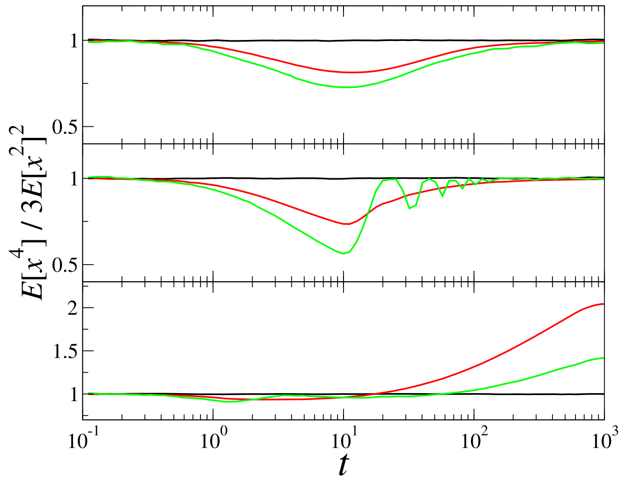

FIGURE 7 | The effect of $\mathcal{P}(f)$ on the gaussianity of the overdamped Langevin dynamics Equation (27). Three models of $\mathcal{P}(f)$ are the uniform distribution $\mathcal{P}(f) = 1/(2\sqrt{3})$ in $[-\sqrt{3}, \sqrt{3}]$ (red), the gaussian $\mathcal{P}(f) = \exp(-f^2/2)/\sqrt{2\pi}$ (black), and the two-state $\mathcal{P}(f) = \frac{1}{2}\delta(f+1) + \frac{1}{2}\delta(f-1)$ (green). From Top to Bottom, the panels show the non-gaussian parameters for the three models under the $P(\tau)$: poissonian (Top), gaussian (Middle), and the power-law (Bottom). The simulation parameters are same as in **Figure 6**.

4.2. The Run-and-Tumble Dynamics

The locomotion dynamics of bacterial micro-swimmers has been investigated with great interest in the viewpoint of a self-propelled particle [2, 19, 33, 37–40]. Our Langevin model and the presented study of the model provide an insight into the so-called run-and-tumble dynamics of bacteria. In our model, the run and tumble states can be represented by a telegraphic noise $f(t)$ having the zero state of $f_i = 0$. The simplest case is the three-state model allowing only the discrete amplitudes $f_i = -f_0, 0, +f_0$. A continuous model expanding the three-state model can be $\mathcal{P}(f) = q\delta(f) + (1-q)\mathcal{P}_r(f)$ with a ratio q $(0 < q < 1)$. $\mathcal{P}_r(f)$ is a normalized bimodal PDF for the run states. With a proper $\mathcal{P}(f)$ and $P(\tau)$, the experimentally observed run-and-tumble dynamics can be quantitatively explained. Typically, the run-and-tumble dynamics is modeled with a time-independent constant transition rate between the two phases [41, 42]. In our model, this is the case governed by the poissonian $P(\tau)$. It is inferred from our study that this type of run-and-tumble dynamics eventually reaches the Fickian regime, as consistent with previous experimental and theoretical studies [42–44]. We also anticipate that even if the transition rate is weakly time-dependent (i.e., the gaussian $P(\tau)$ in our model) the long-time Fickian dynamics is still present. Namely, for any $P(\tau)$ having a well-defined cutoff timescale, the Fickian dynamics is universal. Another interesting feature is that before this Fickian nonequilibrium state is reached a superdiffusive dynamics can be transiently observed, as seen

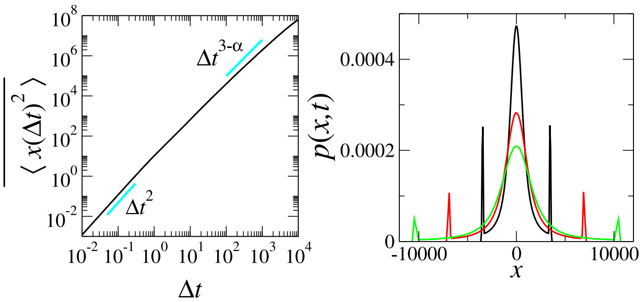

FIGURE 8 | MSD **(Left)** and $p(x,t)$ **(Right)** of the overdamped Langevin model Equation 27 for the two-state model of $f_i(=\pm 1)$. The $p(x,t)$ are plotted at t = 8,000 (black), 9,000 (red), and 10,000 (green). For the duration time, the power-law PDF with $\alpha = 1.2$ was used. The simulation details were same as in **Figure 5**. The data were obtained from 10^5 simulation runs. The basic units are: $[x] = D/\sqrt{\tilde{\sigma}}$, $[t] = D/\tilde{\sigma}$.

in **Figure 5**. For the power-law PDFs of the run and tumble times, their long-time dynamics may vary from the ballistic over a sub-ballistic superdiffusion to the Fickian depending on the power-law exponent α. A superdiffusive dynamics of swarming *B. subtilis*, $\overline{\langle \Delta x^2 \rangle} \sim \Delta t^{1.6}$, reported in [45] may be an example of this type.

4.3. Connection to Lévy Walks

As commented above and also seen in Equation 39, our Langevin model with a power-law $P(\tau)$ are intimately related to the Lévy walk model. Especially, if the active force only has two states ($f_i = -f_0, +f_0$), our overdamped Langevin model Equation 27 describes a Lévy walk in the presence of thermal noise. Conceptually, this model can be understood as a noisy continuous-time random walks introduced in Song et al. [4] and Jeon et al. [46]. The thermal effect yields the linear growth of MSD ($\sim \Delta t$) at the beginning, otherwise absent, before the ballistic regime appears in the intermediate regime. At large times the thermal noise will be ignored and the well-known Lévy walk dynamics emerge. In **Figure 8**, we simulate this noisy Lévy walk process in our overdamped Langevin model with the power-law $P(\tau)$ of $\alpha = 1.2$. The simulation procedure is the same as that of our overdamped model with the power-law $P(\tau)$ (in **Figures 5**, **6**) but the continuous amplitude PDF is replaced to $\mathcal{P}(f) = \frac{1}{2}\delta(f + f_0) + \frac{1}{2}\delta(f - f_0)$. Further information on the simulation is provided in the Appendix and the Caption in **Figure 8**. The simulated Langevin process is consistent with a sub-ballistic Lévy walk with the sojourn time power-law PDF of $1 < \alpha < 2$ [9]. The MSD at large times grows as $\sim \Delta t^{3-\alpha}$ expected in the sub-ballistic Lévy walk [9, 45, 47]. The $p(x,t)$s exhibit the sharp peaks at the end of the distribution, which originates from the ballistic front of a Lévy walk representing the cases that the first active noise remains survived until the measurement time t [9]. A small difference is the spread of the ballistic front shown in $p(x,t)$ (**Figure 8**, Right). This broadening is the outcome of thermal noise. The survival probability of the ballistic front $\Psi_s(t) = \int_t^\infty P(\tau)d\tau$ decays as a power-law of $t^{-\alpha}$. The average survival time of the first active noise $\int dtt\Psi_s(t)$ is finite for all $\alpha > 1$. Thus, the peaks eventually decay out with time, as seen in **Figure 8** (Right), and the $p(x,t)$ becomes a unimodal distribution. It is worths comparing our noisy Lévy walk with the two-state transition model introduced by Malakar et al. [33]. The latter model can be understood as a variant of our noisy Lévy walk where the power-law $P(\tau)$ is replaced to the poissonian PDF. In this case, as shown in section 2.3, the long-time diffusion dynamics becomes Fickian with an apparent diffusivity 37 after the cross-over superdiffusive regime. The $p(x,t)$ of this model can have the sharp peaks (the ballistic front) at the tails in the cross-over regime if the thermal noise is sufficiently weak. The multi-modal distribution eventually returns to a gaussian distribution in the long-time Fickian regime [33]. This is in agreement with the gaussianity behavior of our corresponding model shown in **Figure 7** [the two-state $\mathcal{P}(f)$ & poissonian $P(\tau)$].

Finally, we note in passing that for the power-law PDFs our active process will suffer the aging dynamics. This aging effect will be investigated in depth as further work.

DATA AVAILABILITY STATEMENT

The appendix of this paper is included in the manuscript/**Supplementary Files**.

AUTHOR CONTRIBUTIONS

JU, TS, and J-HJ designed the model, performed the analytic and computational invetigations, and wrote the paper together.

FUNDING

This work was supported by the National Research Foundation (NRF) of Korea through No. 2017R1D1A1B03030872 (JU), No. 2017R1D1A1B03034600 (TS), and No. 2017R1C1B2007555 (J-HJ).

SUPPLEMENTARY MATERIAL

The Supplementary Material for this article can be found online at: https://www.frontiersin.org/articles/10.3389/fphy.2019.00143/full#supplementary-material

REFERENCES

1. Metzler R, Jeon JH, Cherstvy AG, Barkai E. Anomalous diffusion models and their properties: non-stationarity, non-ergodicity, and ageing at the centenary of single particle tracking. *Phys Chem Chem Phys.* (2014) **16**:24128–64. doi: 10.1039/C4CP03465A
2. Bechinger C, Di Leonardo R, Löwen H, Reichhardt C, Volpe G, Volpe G. Active particles in complex and crowded environments. *Rev Mod Phys.* (2016) **88**:045006. doi: 10.1103/RevModPhys.88.045006
3. Riedel C, Gabizon R, Wilson CAM, Hamadani K, Tsekouras K, Marqusee S, et al. The heat released during catalytic turnover enhances the diffusion of an enzyme. *Nature.* (2014) **517**:227–30. doi: 10.1038/nature14043
4. Song MS, Moon HC, Jeon JH, Park HY. Neuronal messenger ribonucleoprotein transport follows an aging Lévy walk. *Nat Commun.* (2018) **9**:344. doi: 10.1038/s41467-017-02700-z
5. Wu XL, Libchaber A. Particle Diffusion in a Quasi-Two-Dimensional Bacterial Bath. *Phys Rev Lett.* (2000) **84**:3017–20. doi: 10.1103/PhysRevLett.84.3017
6. Fodor E, Hayakawa H, Tailleur J, van Wijland F. Non-Gaussian noise without memory in active matter. *Phys Rev E.* (2018) **98**:062610. doi: 10.1103/PhysRevE.98.062610
7. Chen DTN, Lau AWC, Hough LA, Islam MF, Goulian M, Lubensky TC, et al. Fluctuations and rheology in active bacterial suspensions. *Phys Rev Lett.* (2007) **99**:148302. doi: 10.1103/PhysRevLett.99.148302
8. Dev S, Chatterjee S. Run-and-tumble motion with steplike responses to a stochastic input. *Phys Rev E.* (2019) **99**:012402. doi: 10.1103/PhysRevE.99.012402
9. Zaburdaev V, Denisov S, Klafter J. Lévy walks. *Rev Mod Phys.* (2015) **87**:483–530. doi: 10.1103/RevModPhys.87.483
10. Gal N, Weihs D. Experimental evidence of strong anomalous diffusion in living cells. *Phys Rev E.* (2010) **81**:020903. doi: 10.1103/PhysRevE.81.020903

11. Chen K, Wang B, Granick S. Memoryless self-reinforcing directionality in endosomal active transport within living cells. *Nat Mater*. (2015) **14**:589–93. doi: 10.1038/nmat4239
12. Berg HC, Borowski A, De Vivie ER. *E. coli* in Motion. In: *Biological and Medical Physics, Biomedical Engineering*. Springer (2004).
13. Ramos-Fernandez G, Mateos J, Miramontes O, Germinal C, Larralde H, Ayala-Orozco B. Lévy walk patterns in the foraging movements of spider monkeys (*Ateles geoffroyi*). *Behav Ecol Sociobiol*. (2003) **55**:223–30. doi: 10.1007/s00265-003-0700-6
14. Sagi Y, Brook M, Almog I, Davidson N. Observation of anomalous diffusion and fractional self-similarity in one dimension. *Phys Rev Lett*. (2012) **108**:093002. doi: 10.1103/PhysRevLett.108.093002
15. Brockmann D, Hufnagel L, Geisel T. The scaling laws of human travel. *Nature*. (2006) **439**:462–5. doi: 10.1038/nature04292
16. Reynolds AM, Rhodes CJ. The Lévy flight paradigm: random search patterns and mechanisms. *Ecology*. (2009) **90**:877–87. doi: 10.1890/08-0153.1
17. Chaki S, Chakrabarti R. Enhanced diffusion, swelling, and slow reconfiguration of a single chain in non-Gaussian active bath. *J Chem Phys*. (2019) **150:**094902. doi: 10.1063/1.5086152
18. Mandelbrot B, Van Ness J. Fractional brownian motions, fractional noises and applications. *SIAM Rev*. (1968) **10**:422–37. doi: 10.1137/1010093
19. Barthelemy P, Bertolotti J, Wiersma DS. A Lévy flight for light. *Nature*. (2008) **453**:495–8. doi: 10.1038/nature06948
20. Jeon JH, Monne HMS, Javanainen M, Metzler R. Anomalous diffusion of phospholipids and cholesterols in a lipid bilayer and its origins. *Phys Rev Lett*. (2012) **109**:188103. doi: 10.1103/PhysRevLett.109.188103
21. Ernst D, Hellmann M, Köhler J, Weiss M. Fractional Brownian motion in crowded fluids. *Soft Matt*. (2012) **8**:4886–9. doi: 10.1039/c2sm25220a
22. Weiss M. Single-particle tracking data reveal anticorrelated fractional Brownian motion in crowded fluids. *Phys Rev E*. (2013) **88**:010101. doi: 10.1103/PhysRevE.88.010101
23. Weber SC, Spakowitz AJ, Theriot JA. Bacterial chromosomal loci move subdiffusively through a viscoelastic cytoplasm. *Phys Rev Lett*. (2010) **104**:238102. doi: 10.1103/PhysRevLett.104.238102
24. Jespersen S, Metzler R, Fogedby HC. Lévy flights in external force fields: langevin and fractional Fokker-Planck equations and their solutions. *Phys Rev E*. (1999) **59**:2736. doi: 10.1103/PhysRevE.59.2736
25. Lisowski B, Valenti D, Spagnolo B, Bier M, Gudowska-Nowak E. Stepping molecular motor amid Lévy white noise. *Phys Rev E*. (2015) **91**:042713. doi: 10.1103/PhysRevE.91.042713
26. Van Den Broeck C. On the relation between white shot noise, Gaussian white noise, and the dichotomic Markov process. *J Stat Phys*. (1983) **31**:467–83. doi: 10.1007/BF01019494
27. Luczka J. Non-Markovian stochastic processes: colored noise. *Chaos*. (2005) **15**:026107. doi: 10.1063/1.1860471
28. Barik D, Ghosh PK, Ray DS. Langevin dynamics with dichotomous noise: direct simulation and applications. *J Stat Mech*. (2006) **2006**:P03010. doi: 10.1088/1742-5468/2006/03/P03010
29. Oliveira FA, Ferreira RMS, Lapas LC, Vainstein MH. Anomalous diffusion: a basic mechanism for the evolution of inhomogeneous systems. *Front Phys*. (2019) **7**:18. doi: 10.3389/fphy.2019.00018
30. Onsager L, Machlup S. Fluctuations and irreversible processes. *Phys Rev*. (1953) **91**:1505–12. doi: 10.1103/PhysRev.91.1505
31. Kwon C, Um J, Park H. Information thermodynamics for a multi-feedback process with time delay. *Europhys Lett*. (2017) **117:**10011. doi: 10.1209/0295-5075/117/10011
32. Sekimoto K. Langevin equation and thermodynamics. *Prog Theor Phys Suppl*. (1998) **130**:17–27. doi: 10.1143/PTPS.130.17
33. Malakar K, Jemseena V, Kundu A, Kumar V, Sabhapandit S, Majumdar SN, et al. Steady state, relaxation and first-passage properties of a run-and-tumble particle in one-dimension. *J Stat Mech*. (2018) 043215. doi: 10.1088/1742-5468/aab84f
34. Hayot F. Lévy walk in lattice-gas hydrodynamics. *Phys Rev A*. (1991) **43**:806–10. doi: 10.1103/PhysRevA.43.806
35. Solomon TH, Weeks ER, Swinney HL. Observation of anomalous diffusion and Lévy flights in a two-dimensional rotating flow. *Phys Rev Lett*. (1993) **71**:3975–8. doi: 10.1103/PhysRevLett.71.3975
36. Lapas LC, Costa IVL, Vainstein MH, Oliveira FA. Entropy, non-ergodicity and non-Gaussian behaviour in ballistic transport. *Europhys Lett*. (2007) **77**:37004. doi: 10.1209/0295-5075/77/37004
37. Cates ME, Tailleur J. Motility-induced phase separation. *Annu Rev Condens Matt Phys*. (2015) **6**:219–44. doi: 10.1146/annurev-conmatphys-031214-014710
38. Darnton NC, Turner L, Rojevsky S, Berg HC. Dynamics of bacterial swarming. *Biophys J*. (2010) **98**:2082–90. doi: 10.1016/j.bpj.2010.01.053
39. Di Leonardo R, Angelani L, Dell'Arciprete D, Ruocco G, Iebba V, Schippa S, et al. Bacterial ratchet motors. *Proc Natl Acad Sci USA*. (2010) **107**:9541–5. doi: 10.1073/pnas.0910426107
40. Saragosti J, Calvez V, Bournaveas N, Perthame B, Buguin A, Silberzan P. Directional persistence of chemotactic bacteria in a traveling concentration wave. *Proc Natl Acad Sci USA*. (2011) **108**:16235–40. doi: 10.1073/pnas.1101996108
41. Najafi J, Shaebani MR, John T, Altegoer F, Bange G, Wagner C. Flagellar number governs bacterial spreading and transport efficiency. *Sci Adv*. (2018) **4**:eaar6425. doi: 10.1126/sciadv.aar6425
42. Lee M, Szuttor K, Holm C. A computational model for bacterial run-and-tumble motion. *J Chem Phys*. (2019) **150**:174111. doi: 10.1063/1.5085836
43. Thiel F, Schimansky-Geier L, Sokolov IM. Anomalous diffusion in run-and-tumble motion. *Phys Rev E*. (2012) **86**:021117. doi: 10.1103/PhysRevE.86.021117
44. Fier G, Hansmann D, Buceta RC. Langevin equations for the run-and-tumble of swimming bacteria. *Soft Matt*. (2018) **14**:3945–54. doi: 10.1039/C8SM00252E
45. Ariel G, Rabani A, Benisty S, Partridge JD, Harshey RM, Be'er A. Swarming bacteria migrate by Lévy Walk. *Nat Commun*. (2015) **6**:8396. doi: 10.1038/ncomms9396
46. Jeon JH, Barkai E, Metzler R. Noisy continuous time random walks. *J Chem Phys*. (2013) **139**:121916. doi: 10.1063/1.4816635
47. Froemberg D, Barkai E. Time-averaged Einstein relation and fluctuating diffusivities for the Lévy walk. *Phys Rev E*. (2013) **87**:030104. doi: 10.1103/PhysRevE.87.030104

Conflict of Interest: The authors declare that the research was conducted in the absence of any commercial or financial relationships that could be construed as a potential conflict of interest.

frontiers in Physics

REVIEW
published: 05 November 2019
doi: 10.3389/fphy.2019.00159

Anomalous Heat Transport in One Dimensional Systems: A Description Using Non-local Fractional-Type Diffusion Equation

Abhishek Dhar[1], *Anupam Kundu*[1]* *and Aritra Kundu*[2]

[1] International Centre for Theoretical Sciences, Tata Institute of Fundamental Research, Bengaluru, India, [2] Raman Research Institute, Bengaluru, India

It has been observed in many numerical simulations, experiments and from various theoretical treatments that heat transport in one-dimensional systems of interacting particles cannot be described by the phenomenological Fourier's law. The picture that has emerged from studies over the last few years is that Fourier's law gets replaced by a spatially non-local linear equation wherein the current at a point gets contributions from temperature gradients in other parts of the system. Correspondingly the usual heat diffusion equation gets replaced by a non-local fractional-type diffusion equation. In this review, we describe the various theoretical approaches which lead to this framework and also discuss recent progress on this problem.

Keywords: fractional diffusion equation, Levy walks, anomalous heat transport, fluctuating hydrodynamics, heat conduction

Edited by:
Carlos Mejía-Monasterio,
Polytechnic University of Madrid,
Spain

Reviewed by:
Stefano Lepri,
Italian National Research Council
(CNR), Italy
Tarcísio Marciano Rocha Filho,
University of Brasilia, Brazil

Correspondence:
Anupam Kundu
anupam.kundu@icts.res.in

Specialty section:
This article was submitted to
Interdisciplinary Physics,
a section of the journal
Frontiers in Physics

Received: *18 June 2019*
Accepted: *30 September 2019*
Published: *05 November 2019*

Citation:
Dhar A, Kundu A and Kundu A (2019)
Anomalous Heat Transport in One
Dimensional Systems: A Description
Using Non-local Fractional-Type
Diffusion Equation. Front. Phys. 7:159.
doi: 10.3389/fphy.2019.00159

1. INTRODUCTION

Transport of heat through materials is a paradigmatic example of non-equilibrium phenomena [1–3]. When an extended system is attached to two reservoirs of different temperatures at its two ends, an energy current flows through the body from hot region to cold region. At the macroscopic level this phenomena is described by the phenomenological Fourier's law. Considering transport in one dimensional systems, Fourier's law states that the local heat current density $j(x,t)$ inside a system at point x at time t is proportional to the gradient of the local temperature $T(x,t)$:

$$j = -\kappa \frac{\partial T(x,t)}{\partial x} \tag{1}$$

where κ is referred to as the thermal conductivity of the material. This law implies diffusive transfer of energy. To see this we note that the local energy density $e(x,t)$ in a one dimensional system satisfies the continuity equation $\partial e(x,t)/\partial t = -\partial j(x,t)/\partial x$. Inserting Equation (1) in this continuity equation, and using the relation between the local energy density and the local temperature $c_v = \partial e/\partial T$ (where c_v represents the specific heat per unit volume), one finds the heat diffusion equation

$$\frac{\partial T(x,t)}{\partial t} = \frac{\kappa}{c_v}\frac{\partial^2 T(x,t)}{\partial x^2}, \tag{2}$$

where we assume (for simplicity) no variation of κ with temperature. In usual three dimensional systems, the heat diffusion equation takes the form $\partial_t T(\mathbf{x},t) = (\kappa/c_v)\nabla^2 T(\mathbf{x},t)$ and describes the evolution of the temperature field in bulk systems. The phenomenological macroscopic description provided by the equations in (1) and (2) has been used extensively to describe heat transfer phenomena in a wide class of physical systems.

A natural question is to ask if it is possible to derive or establish Fourier's phenomenological law theoretically, starting from a complete microscopic description. The issue of deriving Fourier's law has been a long standing question and a very active field of research [1]. Several theoretical as well as large scale numerical studies have been performed on different mathematical model systems to understand the necessary and sufficient conditions needed in the microscopic description to validate Fourier's law at the macroscopic level [2–4]. Surprisingly, these studies suggest that Fourier's law is probably not valid in many one-dimensional systems and one finds that the thermal conductivity κ diverges with system size N as $\kappa \sim N^{\alpha}$ where $0 < \alpha < 1$ [2–12]. This is referred to as anomalous heat transport (AHT). For $\alpha = 0$, the transport is classified as being diffusive while $\alpha = 1$ is referred to as ballistic transport [2, 3]. Recent developments in technology has made it possible to verify some of these theoretical predictions experimentally as well as numerically in real physical systems, such as nano-structures, polymers, semiconductor films etc. [13–20], and these have provided further motivation and new directions of study.

Two approaches have mainly been used to look for signatures of anomalous heat transport (AHT): (i) the open system set-up in which a system is connected to heat reservoirs at different temperatures T_L and T_R at the two ends and (ii) the closed system set-up in which the isolated system is prepared in thermal equilibrium at temperature T and evolves according to Hamiltonian dynamics (or sometimes stochastic dynamics with same conservation laws). In the open system set-up, one usually considers the non-equilibrium steady state (NESS) and measures directly the steady state heat current j and the temperature profile $T(x)$ in a finite system of N particles. For small $\Delta T = T_L - T_R$, one finds the system size scaling $j \sim N^{\alpha-1}$ (implying $\kappa \sim N^{\alpha}$) and a *non-linear* temperature profile. These are in contrast with Fourier's law which would predict $j \sim N^{-1}$ and a linear temperature profile. In the closed system set-up the idea is to look at the spreading of a heat pulse in a system in equilibrium. From linear response theory we expect that this would evolve in the same way as dynamical correlations of energy fluctuations in equilibrium. Studies on spreading of pulses and energy correlations in systems with AHT show that the process is super-diffusive, with scaling functions described by Lévy distributions [8, 21, 22]. This contrasts systems described by Fourier's law where we expect diffusion and Gaussian propagators. Note that we expect in fact that the thermal conductivity κ obtained in non-equilibrium measurements should be related to equilibrium energy current auto-correlation functions via the Green-Kubo formula [3, 23, 24]. This leads to the understanding of AHT as arising from the fact that the non-integrable long time tails in the auto-correlation function of the total current lead to the divergence of the thermal conductivity.

The natural question that arises for understanding systems with AHT is to find the replacements of Fourier's law in Equation (1) and the heat diffusion equation in Equation (2). The picture that has emerged from studies over the last few years [4, 25–37] is that Fourier's law gets replaced by a spatially non-local but linear equation wherein the current at a point gets contributions from temperature gradients in other parts of the system. This has the form

$$j(x,t) = -\int dx'\, K(x,x')\, \frac{\partial T(x',t)}{\partial x'}, \tag{3}$$

where now the thermal conductivity is replaced by the non-local kernel $K(x,x')$. This then leads to a corresponding non-local fractional-type equation for the time evolution of $T(x,t)$. An important difference from the heat diffusion equation is that the fractional-type equation takes different forms in the closed system set-up (infinite domain) and the open system set-up (finite domain). In the infinite domain the evolution of a localized temperature pulse is described by a fractional-type diffusion equation

$$\partial_t T(x,t) = -\bar{\kappa}(-\Delta)^{\nu/2} T(x,t), \tag{4}$$

where the fractional operator should be interpreted by its action on plane wave basis states: $(-\Delta)^{\nu/2} e^{ikx} = |k|^{\nu}\, e^{ikx}$, with $1 < \nu < 2$. However it should be noted that the corresponding Lévy-stable distribution is valid only over the scale $x \lesssim t^{1/\nu}$. As we will see, the evolution of a heat pulse is restricted to a domain $|x| < ct$, determined by the sound speed c. For the open system, the precise form of the fractional equation is dependent on the details of boundary conditions. In this review we discuss these developments as well as open questions.

The plan of the review is as follows. In section 2 we discuss the various signatures of AHT in the closed and open set-ups. In section 3 we discuss two theoretical approaches that have been used to understand various aspects of anomalous transport. One of these is a phenomenological approach based on the idea that the heat carriers perform Lévy walks instead of random walk. The second approach is a microscopic one, though still phenomenological, and is based on fluctuating hydrodynamics and applicable to Hamiltonian systems. For a class of stochastic models, it has been possible to provide a complete microscopic derivation of the fractional heat equation in the context of both the closed and open system set-ups. These results are described in section 4. In the last part of this section we address the difficult issue of treating arbitrary boundary conditions and discuss a heuristic formulation that uses linear response ideas and fluctuating hydrodynamics to arrive at a general form of the kernel $K(x,x')$ in Equation (3). Finally we conclude in section 5 with a summary of the results presented and some of the outstanding open questions.

2. SIGNATURES OF ANOMALOUS HEAT TRANSPORT

In the theoretical study of anomalous energy transport in one dimension, one usually considers simple yet non-trivial model systems of interacting particles. Let us consider N particles of unit masses, with positions and momenta given respectively, by

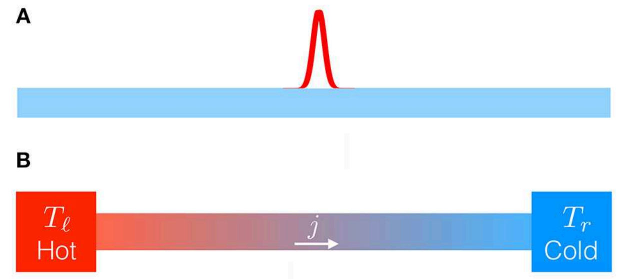

FIGURE 1 | Schematic illustration of the **(A)** closed system set-up and the **(B)** open system set-up, commonly used to study heat transport. In **(A)**, a localized heat pulse is introduced at some point in a system in thermal equilibrium and its subsequent time-evolution is observed. In **(B)**, the system is attached to two heat reservoirs at different temperatures and the NESS properties, such as current and temperature profile are studied.

q_ℓ and p_ℓ, for $\ell = 1, 2, \ldots, N$. One often starts with the following microscopic Hamiltonian:

$$H = \sum_{\ell=1}^{N} \frac{p_\ell^2}{2} + \sum_{\ell=0}^{N} V(q_{\ell+1} - q_\ell), \tag{5}$$

where $V(r)$ is a nearest neighbor interaction potential, and the extra variables q_0 and q_{N+1} are introduced to incorporate different boundary conditions (BC). For example, fixed BC corresponds to $q_0 = 0, q_{N+1} = 0$ while free BC corresponds to setting $q_0 = q_1$, $q_{N+1} = q_N$. The particles in the bulk of the system satisfy Hamiltonian equations of motion

$$\dot{q}_\ell = \partial_{p_\ell} H, \; \dot{p}_\ell = -\partial_{q_\ell} H \,, \;\; \ell = 1, 2, \ldots N. \tag{6}$$

One of the well-studied choices for the potential is to take $V(r) = k_2 r^2/2 + k_3 r^3/3 + k_4 r^4/4$ which leads to the Fermi-Pasta-Ulam-Tsingou (FPUT) model. Another popular choice is the alternate mass hard particle gas which is not in the standard form of Equation (5). In this model one considers a chain of point particles with masses which alternate between two fixed values, say m_1, m_2, and which collide via elastic collisions conserving energy and momentum. For generic interaction potentials $V(r)$ it is expected that the system has three conserved quantities, namely volume of the system (alternatively the total number of particles), total momentum and total energy. Corresponding to each conserved quantity one can write a local continuity equation. For instance, the local energy defined on bulk points as

$$e(\ell, t) = \frac{p_\ell^2}{2} + \frac{1}{2}[V(q_{\ell+1} - q_\ell) + V(q_\ell - q_{\ell-1})], \tag{7}$$

satisfies a continuity equation

$$\begin{aligned} \partial_t e(\ell, t) &= j(\ell, t) - j(\ell+1, t), \\ \text{where} \;\; j\ell(t) &= -\frac{1}{2}(p_{\ell-1} + p_\ell) V'(q_\ell - q_{\ell-1}) \,. \end{aligned} \tag{8}$$

This equation gives a microscopic definition of the energy current. For quadratic $V(r)$, i.e., harmonic chains, there are a macroscopic number of conserved quantities and transport becomes ballistic. In this case a number of studies have considered augmenting the Hamiltonian dynamics with a stochastic component such that the system again has only three conserved quantities [9, 29–31]. In this case one again recovers the typical features of anomalous transport and several exact results are possible. In this review we will discuss results for both Hamiltonian and stochastic systems.

There are two possible approaches for studying transport properties of a system [3, 4]. A schematic of the two set-ups is shown in **Figure 1**:

A. Closed system set-up—in this case, an isolated system is prepared in thermal equilibrium at some temperature T described by the canonical distribution

$$P(\mathbf{q}, \mathbf{p}) = \frac{e^{-H(\mathbf{q},\mathbf{p})/T}}{Z} \,, \tag{9}$$

where $Z = \int d\mathbf{q} d\mathbf{p} e^{-H/T}$ is the partition function. For any initial condition chosen from this distribution the system evolves according to the pure Hamiltonian dynamics (or the conservative stochastic dynamics). Transport properties are usually probed by studying the form of spatio-temporal correlation functions of the conserved quantities (volume, momentum, energy) or the decay with time of the energy current auto-correlation function. Another approach that has been used is to study the spreading of an initially localized perturbation in the equilibrated system (see **Figure 1A**). In the closed system set-up one takes the system to be infinite or, in numerical studies, N to be sufficiently large such that the correlations are not affected by the boundaries at the maximum observation times.

B. Open system set-up—in this case, one considers finite systems attached at the two boundaries to heat reservoirs at different temperatures (see **Figure 1B**). The heat reservoirs are modeled by adding extra force terms to the usual Hamiltonian equations of motion of the boundary particles. One of the standard choices is to consider Langevin type baths, wherein the additional forces consist of a dissipative term and a white noise term, which are related via a fluctuation-dissipation relation. The system is "open" in the sense that energy can flow in and out of the system, though we note that locally in the bulk we still have energy conservation. When the temperatures of the heat reservoirs are different, the system eventually reaches a NESS in which a heat current flows across the system. The main focus of this approach has been to search for anomalous features in the NESS by looking at observables, such as the heat current $j = \langle j(x, t) \rangle_{open}^{neq}$ and temperature profile obtained from $T(x) = \langle p_x^2 \rangle_{open}^{neq}$ (the averages are computed in the NESS). There have also been attempts to understand the relaxation to NESS and look at correlations and large deviation properties of the NESS.

In the following sub-sections, we describe various signatures of AHT observed in both these set-ups.

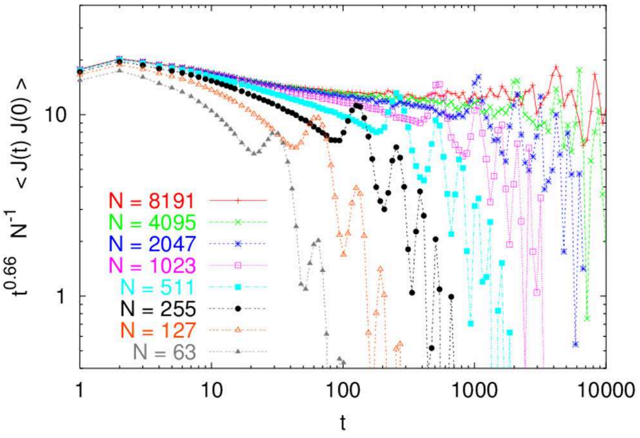

FIGURE 2 | Total scaled heat current auto-correlation, $t^{0.66}N^{-1}\langle J(t)J(0)\rangle$, in the alternate mass hard particle gas for mass ratio 2.2 and $T = 2.0$ (adapted from Grassberger et al. with permission from [7] Copyright (2002) by American Physical Society).

2.1. Signatures in the Closed System Set-Up

- **Slow decay of energy current auto-correlations**: A commonly followed approach for determining the N dependence of j or equivalently the thermal conductivity κ, is to use the *closed system Green-Kubo (GK) formula* [23, 24]:

$$\kappa = \frac{1}{k_B T^2} \lim_{\tau\to\infty} \lim_{N\to\infty} \frac{1}{N} \int_0^{\tau} dt\ \langle J(t)J(0)\rangle^{eq}_{closed}, \qquad (10)$$

  where $J(t) = \sum_x j(x,t)$, with $j(x,t)$ defined in Equation (8), is the total current in the system. The average $\langle \dots \rangle^{eq}_{closed}$ is evaluated with initial conditions chosen from a thermal distribution and time-evolution given by the closed system dynamics. This formula relates the thermal conductivity κ to the integral of the equilibrium heat current auto-correlation function $C_J(t) = N^{-1}\langle J(t)J(0)\rangle^{eq}_{closed}$. Numerical simulations as well as several theoretical treatments find that $C_J(t)$ in a closed system generically decays with time as a power law $C_J(t) \sim t^{\alpha-1}$ with $0 \leq \alpha \leq 1$ [2, 3, 7, 9, 12, 33, 38–51]. As an example we show in **Figure 2** data from simulations [7] of the alternate mass hard particle gas, where we see a decay with $\alpha \approx 0.33$. Such a power-law time dependence implies, from Equation (10), a divergent thermal conductivity. To see the dependence on system size one heuristically puts a cutoff $t_N \sim N$ in the upper limit of the time integral, the argument being that this is the time taken by sound modes to explore the full system of size N. Performing the time integral in Equation (10) with this cut-off, one finally gets $\kappa \sim N^{\alpha}$. An interesting example where this procedure fails has been pointed out in a recent work [52, 53].
- **Super-diffusive spreading of initially localized energy pulse**: Here one looks at the spreading of a localized energy pulse in a thermally equilibrated system. One takes an initial configuration chosen from a thermal distribution with average local energy $e_0 = \langle e(x)\rangle^{eq}_{closed}$, uniform across the system.

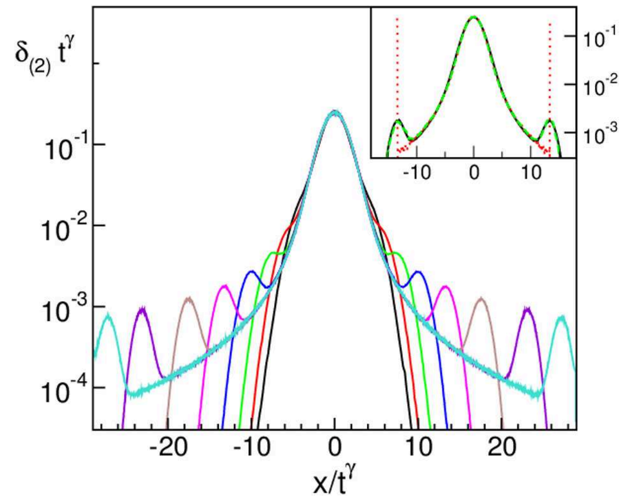

FIGURE 3 | Scaled perturbation profiles at times $t = 40, 80, 160, 320, 640, 1,280, 2,560$, and $3,840$, with $\gamma = 3/5$. The profiles have been obtained by averaging over large number of realizations. In the inset, the profile at $t = 640$ (solid line) is compared with the propagators of a Lévy walk with an exponent $\nu = 5/3$ with a fixed velocity $v = 1$ (dotted line) or with velocity chosen from a Gaussian distribution with mean 1 and variance 0.036 (dashed line) (adapted from Cipriani et al. with permission from [8] Copyright (2005) by American Physical Society).

Imagine putting an extra amount of energy ϵ_0 to a few particles in a region inside the bulk to create a pulse of excess energy locally. As the system evolves according to the closed system dynamics, this localized energy perturbation starts spreading across the system. Let $\epsilon(x,t)$ represent the excess energy density (above e_0) at the point x and at time t (averaged over the initial distribution). This quantity starts as a δ-function at $t = 0$ and then starts spreading with time. Note that $\int dx\ \epsilon(x,t) = \epsilon_0$, the total injected energy is conserved under the closed system dynamics. For a diffusive system, the perturbation would evolve according to the diffusion equation $\partial\epsilon(x,t)/\partial t = D\partial^2\epsilon(x,t)/\partial x^2$ and in macroscopic length-time scales, the perturbation profile at time t would be given by a Gaussian

$$\epsilon(x,t) = \epsilon_0\, \frac{e^{-x^2/4Dt}}{\sqrt{4\pi Dt}}. \qquad (11)$$

For a system with AHT, one instead finds the following scaling form [4, 8]

$$\epsilon(x,t) = \frac{1}{t^{\gamma}}\, \mathcal{G}\left(\frac{x}{t^{\gamma}}\right), \quad \text{for } x \lesssim t, \qquad (12)$$

with a scaling exponent $1/2 < \gamma < 1$. The two limits $\gamma = 1/2$ and 1 correspond respectively to diffusive and ballistic transport. In **Figure 3** we show results for energy pulse spreading obtained in [8] for the alternate mass hard particle gas model. The main plot shows the scaling $x \sim t^{\gamma}$, with $\gamma = 3/5$ of the central part of the distribution. The central part of the distribution was found to fit to the Lévy function which is the propagator of Equation (4) with $\mu = 1/\gamma$. The mean square deviation (MSD) defined as

$$\sigma_e^2(t) = \int dx\, x^2\, \epsilon(x,t), \tag{13}$$

with mean taken as zero, was seen to scale as $\sigma_e^2(t) \sim t^\beta$, with $\beta = 4/3$, as opposed to a diffusive system with $\beta = 1$. It was also noted that the MSD width exponent, β, is related to the thermal conductivity exponent α as $\beta = 1 + \alpha$ (see section 3.1.2 for details). To compute the MSD and relate the exponents β and γ is a somewhat subtle issue and requires one to note that the scaling function is valid in the bulk region $|x| \lesssim t$, beyond which $\epsilon(x,t)$ decays rapidly (see discussion in section (3.1.1) in the context of Lévy-walk model). From properties of the Lévy distribution one gets, in the regime $t^\gamma << x \lesssim t$, the scaling form $\mathcal{G}(u) \sim 1/u^{1+1/\gamma}$. Using these asymptotics and computing $\sigma_e^2(t) = \int_0^t dx\, x^2\, t^{-\gamma}\mathcal{G}(x/t^\gamma)$ gives us the leading behavior $\sigma^2(t) \sim t^{3-1/\gamma}$ which then leads to the relation $\beta = 3 - 1/\gamma$. Observations from several other numerical simulations have confirmed the super-diffusive behavior [8, 54–59].

- **Super-diffusive evolution of density correlations**: The anomalous signature discussed in the previous point can also be observed alternatively by looking at the spreading of the equilibrium spatio-temporal correlation function of the energy density $e(x,t)$ defined as

$$C_e(x,t) = \langle e(x,t)e(0,0)\rangle - \langle e(x,t)\rangle\langle e(0,0)\rangle, \tag{14}$$

where the average is taken over the equilibrium initial conditions. For diffusive systems this correlation has the Gaussian form in Equation (11), while for systems with AHT this has the scaling form in Equation (12) and one again has super-diffusive growth of the MSD [21], now defined as

$$\sigma_c^2(t) = \frac{1}{k_B T}\int dx\, x^2\, C_e(x,t). \tag{15}$$

This MSD can be related to $\sigma_e^2(t)$ defined above, using linear response theory and both have $\sim t^\beta$ scaling. In the case of AHT, observing the scaling form in Equation (12) usually requires one to subtract contributions of sound modes which travel ballistically. The theory of non-linear fluctuating hydrodynamics (NFH) provides a framework in which one can systematically describe the super-diffusive scaling of the correlation [22, 47, 60–63]. This theory is based on writing hydrodynamic equations for the conserved quantities in the system which for the Hamiltonian in Equation (5) are the total energy, total momentum and the total number of particles (or volume). This framework of NFH is discussed in detail in section 3.2. A connection can be made between the super-diffusive scaling ($\sigma_c^2(t) \sim t^\beta$) of the energy correlations and the power-law decay, $\sim t^{\alpha-1}$, of the current-current correlations [4, 58, 59], which can be seen as follows. Starting from the continuity equation for energy, one can obtain the relation [61, 62] on the infinite line

$$\frac{\partial^2 C_e(x,t)}{\partial t^2} = \frac{\partial^2 \langle j(x,t)j(0,0)\rangle}{\partial x^2}\,. \tag{16}$$

Multiplying by x^2 on both sides and integrating over all the range of x one gets

$$\frac{d^2\sigma_c^2(t)}{dt^2} = \frac{1}{k_B T}\langle J(t)j(0,0)\rangle = \frac{C_J(t)}{k_B T}\,. \tag{17}$$

Assuming the expected forms $\sigma^2(t) \sim t^\beta$ and $C_J(t) \sim t^{\alpha-1}$ we get the relation $\alpha = \beta - 1$.

2.2. Signatures in the Open System Set-Up

- **Diverging thermal conductivity**: As discussed above in the open system set-up, one connects the system at the two boundaries to heat reservoirs at unequal temperatures $T_\ell \neq T_r$. A common model for baths is to write Langevin dynamics for the boundary particles involving dissipation and noise term satisfying the fluctuation-dissipation relation. For a chain of interacting particles described by the Hamiltonian in Equation (5) the equations of motion for the boundary particles would read

$$\dot{p}_1 = f_1 - \lambda p_1 + \xi_\ell(t), \tag{18}$$
$$\dot{p}_N = f_N - \lambda p_N + \xi_r(t), \tag{19}$$

where $f_i = -\partial H/\partial q_i$. The noise terms $\xi_{\ell,r}$ are Gaussian white noise terms, with zero mean and correlations $\langle \xi_\ell(t)\xi_\ell(t')\rangle = 2\lambda T_\ell \delta(t-t')$ and $\langle \xi_r(t)\xi_r(t')\rangle = 2\lambda T_r \delta(t-t')$. The remaining particles evolve according to Equation (6). After a long time the system reaches a non-equilibrium steady state (NESS) and we can measure the steady state current j as average of the local current $j(x,t)$ defined through Equation (8). In the steady state this will be independent of time as well as the bond where we measure the current. One can then check if the system size N scaling of this steady state current j has the expected form $j \sim N^{\alpha-1}$, where $\alpha < 1$ for anomalous systems. Alternatively one can define the $\kappa = jN/(T_\ell - T_r)$ and see how this scales with N. For a large class of non-linear interaction potentials, it has been observed that the thermal conductivity $\kappa \sim N^\alpha$ with $0 < \alpha < 1$ for large N [6, 7, 10, 11, 63, 64]. As an example, we show in **Figure 4** data from [10] for the FPUT-β chain, where one finds $\alpha \approx 0.33$.
- **Non-linear temperature profile**: The local temperature at a site on the lattice can be defined through the relation $T_i = \langle p_i^2/m\rangle$, where the average is taken in the NESS. For diffusive systems, the temperature profile obtained would be linear for small $\Delta T = T_\ell - T_r$, as expected from solving Fourier's law with a constant κ. It is important to note that non-linear temperature profiles can also be obtained in case of diffusive transport if the thermal conductivity κ is temperature-dependent and ΔT is large. On the other hand, for many systems with AHT, one finds a strongly non-linear temperature profile even when ΔT is made arbitrary small [5, 10, 11, 26, 34, 36, 65]. Quite often the profiles are characterized by divergent slopes at the boundaries. In **Figure 5** we show the temperature profile in the FPUT-β model and one can see the characteristic non-linear nature. Note that the definition of local temperature makes sense (and is useful) only if this temperature predicts correctly other local observables, for

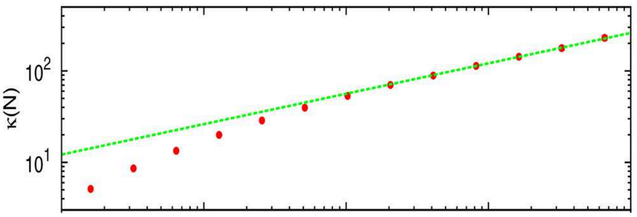

FIGURE 4 | FPUT-β model: Results for conductivity κ vs. N for $T_\ell = 2.0$ and $T_r = 0.5$. The last five points fit to a slope of 0.333 ± 0.004 (adapted from Mai et al. with permission from [10] Copyright (2007) by American Physical Society).

example higher moments of the velocity. This was also verified in [10] and also shown in **Figure 5**. Typically one finds that the temperature difference $\delta T(x) = |T_\ell - T(x)|$ scales as $(\delta x)^\mu$, with distance δx from the boundary, where $0 < \mu \leq 1$. The exponent μ has been referred to as the meniscus exponent [66]. This exponent is non-universal in the sense that it depends on details of boundary conditions, unlike the conductivity exponent α.

- **Green-Kubo-type relation for open systems**: Analogous to the Green-Kubo formula in the closed system set-up given by Equation (10), an exact formula exists in the open system set-up that relates the current response to a small temperature difference $\Delta T = T_\ell - T_r$. This is given by [67]

$$\lim_{\Delta T \to 0} \frac{j}{\Delta T} = \frac{1}{K_B T^2 N^2} \int_0^\infty dt \, \langle J(t) J(0) \rangle_{open}^{eq} \,. \qquad (20)$$

The time auto-correlation $\langle J(t)J(0)\rangle_{open}^{eq}$ is computed by averaging over equilibrium initial conditions as well as the open system dynamics which includes the stochastic baths (at equal temperatures). This formula is valid for a finite size system. We note that for systems with AHT, unlike with Equation (10), in the open set-up we do not require the use of an upper cut-off $t_N \sim N$ for estimating the size dependence of conductivity. In this case the linear response current can be evaluated directly from Equation (20) for any finite system of size N and thereby one can verify the form $j/\Delta T \sim N^{\alpha-1}$. This approach has been discussed for example in [63, 64]. It was observed in [64] that, for the so-called random collision model studied by them, both $\langle J(t)J(0)\rangle_{closed}^{eq}$ and $\langle J(t)J(0)\rangle_{open}^{eq}$ showed a $t^{-2/3}$ decay at times $t \lesssim N$. However, the exponential decay for the open case begins at $t_N \sim N$ while for the closed system (with periodic boundary conditions) this begins at $t_N \sim N^{3/2}$. This was understood as arising from the time scale associated to the spreading of sound modes. Note that if we put the cut-off $t_N \sim N^{3/2}$ as the upper limit in the time-integral of Equation (10) then we would get the wrong conductivity exponent. In order to get the correct exponent in the closed system set-up, one has to by hand set the cut-off at $t_N \sim N$ based on consideration of the practical transport set-up which has baths at the boundaries.

Recently, in a model system of AHT the relation in Equation (3) has been established using the above formula and a heuristic approach based on fluctuating hydrodynamics [36]. An explicit expression of the kernel was obtained for a specific model, using which one can understand the divergence of κ as well as the singular features in the temperature profile. A detailed discussion of this method is given later in section 4.2.3.

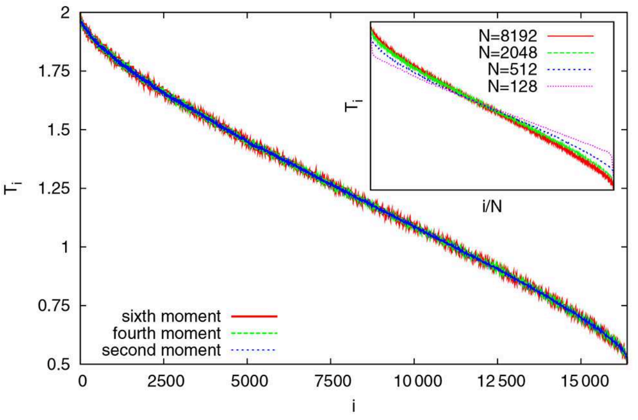

FIGURE 5 | FPUT-β model: Kinetic temperature profile for a system with $N = 16384$, $T_\ell = 2.0$, $T_r = 0.5$. Assuming a Gaussian local velocity distribution, the temperatures as defined from the first three even moments are shown; their agreement vindicates the assumed Gaussian velocity distribution. (Inset) Normalized temperature profiles for different N (adapted from Mai et al. with permission from [10] Copyright (2007) by American Physical Society).

3. PHENOMENOLOGICAL APPROACHES FOR ANOMALOUS HEAT TRANSPORT

In this section we will discuss two different approaches that have tried to understand the various aspects of AHT mentioned above. The first is a completely heuristic approach where one assumes that the heat carriers perform Lévy walks instead of random walk which is expected for diffusive heat transfer. This method has been used to explain spreading of localized energy pulses, steady state properties and current fluctuations [8, 39, 57, 66, 68–71]. The second approach is a microscopic one where one starts by writing hydrodynamic equations for the conserved quantities of the Hamiltonian dynamics. One then phenomenologically adds noise and dissipation terms satisfying fluctuation dissipation relations and this allows one to study equilibrium fluctuations in the system. In particular, using the formalism of fluctuating hydrodynamics, one can compute dynamical correlation functions which contain information on AHT.

3.1. Lévy Walk Description of Anomalous Heat Transport

3.1.1. Lévy Walk Description in the Closed Set-Up

In this description one thinks of energy as being carried by Lévy walkers, each of which carry a fixed amount of energy. It follows that the local energy density and energy current at any point can be taken to be directly proportional to, respectively, the particle density and current. Let us also assume that the local temperature is proportional to the local energy density and hence to the density of particles.

Definition of the Lévy walk [72–74]: At each step of the walk, a particle chooses a time of flight τ from a specified distribution, $\phi(\tau)$, and then moves a distance $x = c\tau$ at a fixed speed c, with equal probability in either direction. More generally one can consider the velocity c to be drawn from a distribution. Let $P(x,t)dx$ denote the probability that the particle is in the interval $(x, x+dx)$ at time t. Note that $P(x,t)$ also includes events where the particle is crossing the interval $(x, x+dx)$, in addition to the events in which the particle lands in the interval at time t. If a particle starts at the origin at time $t = 0$, the probability $P(x,t)$ satisfies

$$\begin{aligned} P(x,t) = {} & \frac{1}{2}\psi(t)\delta(|x|-ct) + \frac{1}{2}\int_0^t d\tau\phi(\tau)\,[P(x-c\tau, t-\tau) \\ & + P(x+c\tau, t-\tau)], \end{aligned} \tag{21}$$

where $\psi(\tau) = \int_\tau^\infty d\tau'\ \phi(\tau')$ is the probability of choosing a time of flight $\geq \tau$. Here we consider Lévy walkers with a time-of-flight distribution

$$\phi(t) = \frac{\nu}{t_o}\frac{1}{(1+t/t_o)^{\nu+1}}\ ,\quad 1 < \nu < 2, \tag{22}$$

which decays, at large times, like a power law $\phi(t) \simeq A\ t^{-\nu-1}$ with $A = \nu t_0^\nu$. For this range of ν the mean flight time $\langle t\rangle = \int_0^\infty dt\ t\ \phi(t) = t_0/(\nu-1)$ is finite but $\langle t^2\rangle = \infty$.

Some properties of the Lévy walk: Taking the Fourier Laplace transform $\widetilde{P}(k,s) = \int_{-\infty}^\infty dx \int_0^\infty\ dt\ P(x,t)\ e^{ikx-st}$ we get

$$\widetilde{P}(k,s) = \frac{\widetilde{\psi}(s-ick) + \widetilde{\psi}(s+ick)}{2 - \widetilde{\phi}(s-ick) - \widetilde{\phi}(s+ick)}, \tag{23}$$

where $\widetilde{\phi}(s) = \int_0^\infty dt e^{-st}\phi(t)$ and $\widetilde{\psi}(s) = \int_0^\infty dt e^{-st}\psi(t) = [1-\widetilde{\phi}(s)]/s$.

For asymptotic properties it is useful to find the form of $\widetilde{P}(k,s)$ for small k, s. The Laplace transform $\widetilde{\phi}$ is given by:

$$\widetilde{\phi}(s) = \int_0^\infty dt\ e^{-st}\ \phi(t) = 1 - \langle t\rangle\ s + b\ \nu(st_o)^\nu + \cdots, \tag{24}$$

$$\text{where } b = \frac{1}{\nu(\nu-1)}\int_0^\infty dz\ e^{-z}z^{1-\nu} = \frac{1}{\nu(\nu-1)}\Gamma(2-\nu),$$

and $\Gamma(u)$ is the Gamma-function. Hence we get:

$$\widetilde{P}(k,s) = \frac{1 - d[(s-ick)^{\nu-1} + (s+ick)^{\nu-1}]}{s - d[(s-ick)^\nu + (s+ick)^\nu]}\ , \tag{25}$$

where $d = bA/(2\langle t\rangle)$. Taking the inverse Fourier-Laplace transform of this gives us the propagator of the Lévy walk on the infinite line. This corresponds to a pulse whose central region is a Lévy-stable distribution with a scaling $x \sim t^{1/\nu}$. This can be seen by expanding Equation (25) for $ck/s << 1$ to get $\widetilde{P}(k,s) = [s - c\cos(\nu\pi/2)(ck)^\nu]^{-1}$. The difference with the Lévy-stable distribution is that the Lévy-walk propagator has ballistic peaks of magnitude $t^{1-\nu}$ at $x = \pm ct$ and vanishes outside this. The overall behavior of the propagator is as follows [72]:

$$\begin{aligned} P(x,t) & \sim t^{-1/\nu}\ \exp\left(\frac{-ax^2}{t^{2/\nu}}\right) && |x| \lesssim t^{1/\nu} \\ & \sim t\ x^{-\nu-1} && t^{1/\nu} \lesssim |x| < ct \\ & \sim t^{1-\nu} && |x| = ct \\ & = 0 && |x| > ct. \end{aligned} \tag{26}$$

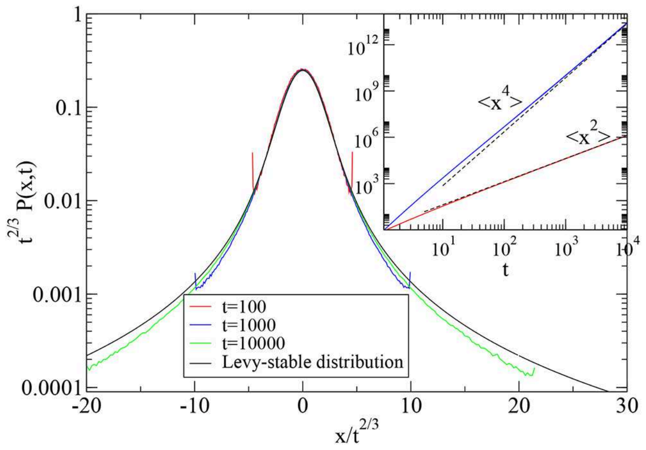

FIGURE 6 | Plot of the scaled distribution $t^{2/3}P(x,t)$ vs. $x/t^{2/3}$ of the Lévy walk on the open line for $\nu = 3/2$ at three different times. Also shown is a plot of the Lévy-stable distribution. The inset shows a plot of the mean square displacement and the fourth moment and a comparison with the exact asymptotic forms (dashed lines) given by Equations (27, 28). In all plots the time t_o and c are set to one.

The time evolution of the Lévy-walk propagator, obtained from direct simulations of the Lévy walk, is shown in **Figure 6**. We also plot the Lévy-stable distribution obtained by taking the Fourier transform of $P(k,t) = e^{-c\cos(\nu\pi/2)|k|^\nu t}$.

Various moments of the distribution can be found using the relation $\langle x^n\rangle(t) = (d^n/d(ik)^n)\int_{-\infty}^\infty dk e^{ikx}P(x,t)\Big|_{k=0}$, or its Laplace transform given by $\langle x^n\rangle(s) = (d^n/d(ik)^n)\ \widetilde{P}(k,s)\ \Big|_{k=0}$. Using Equation (25) we get in particular the following leading behavior

$$\langle x^2\rangle_c \simeq \frac{2\ A\ c^2}{(3-\nu)(2-\nu)\nu\ \langle\tau\rangle}\ t^\beta, \quad \beta = 3-\nu\ , \tag{27}$$

$$\langle x^4\rangle_c \simeq \frac{4\ A\ c^4}{(5-\nu)(4-\nu)\nu\ \langle\tau\rangle}\ t^{\beta+2}\ . \tag{28}$$

We see that for $1 < \nu < 2$ the motion is super-diffusive [73, 74]. The most interesting characteristics to note about the Lévy walk are the fact that the probability distribution has finite support ($|x| \leq ct$), in the bulk it coincides with the Lévy distribution with scaling $x \sim t^{1/\nu}$ and finally the mean square displacement

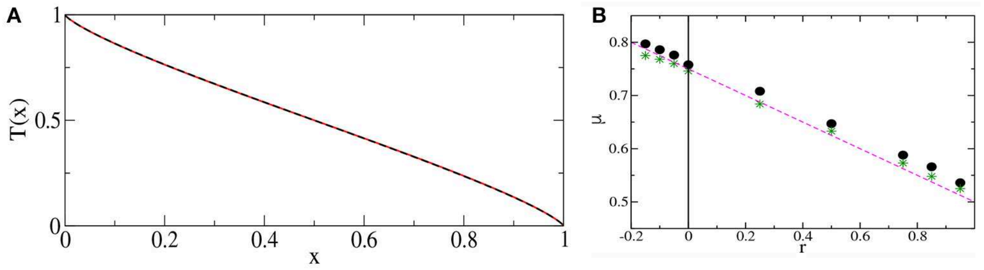

FIGURE 7 | (A) Temperature profile of the oscillator chain with conservative noise with free boundary condition and $\lambda = \gamma = 1$ (solid line) and solution of the master equation with reflection coefficient $R = -0.1$ (dashed line) (reprinted from Lepri and Politi [66]). **(B)** Dependence of the meniscus exponent μ on the reflection probability r for $\nu = 3/2$. Note that r in this figure is denoted by R in this review. Full circles and stars are measures from fitting of $P(x)$ and $Q(x)$, respectively (see text). The dashed line is given by formula (29) (adapted from Lepri and Politi with permission from [66] Copyright (2011) by American Physical Society).

(MSD) $\langle x^2 \rangle \sim t^\beta$ with $\beta = 3 - \nu$. Note that the usual Lévy stable distribution has a diverging second moment, however the Lévy walk has a finite MSD and this follows from the finite support $|x| \leq ct$ of the corresponding distribution. Indeed, on using this cutoff and the power-law form of the Lévy near the cut-off (see Equation 26) gives us the expected scaling exponent $\beta = 3 - \nu$.

Lévy walks and AHT: The first proposal suggesting the Lévy walk model to describe anomalous heat transport was made in [68]. This idea was tested for a microscopic model in [8] where it was shown that the spreading of a heat pulse in a thermally prepared alternate mass hard particle gas was super-diffusive and is well-described by the Lévy walk model. In **Figure 3** we show the evolution of a localized perturbation. The main plot shows the $x \sim t^{3/5}$ scaling of the central part of the distribution while the inset shows a fit to the expected Lévy distribution (for a LW with $\nu = 5/3$) with a single fitting parameter. It was also shown that the MSD of the energy has the scaling $\sim t^{4/3}$ as expected from the relation $\beta = 3 - \nu$ for LW. Finally it was proposed using linear response ideas that the exponent β and the conductivity exponent α should be related as $\alpha = \beta - 1$ which gives $\alpha = 1/3$ for the present system. This agrees with known results for the alternate mass hard particle gas. The validity of the Lévy walk description of pulse propagation was further verified in [39] for a hard particle gas interacting via a square well-potential and in [57] for the FPUT chain. All these cases were described by the same Lévy-walk exponent $\nu = 5/3$.

3.1.2. Lévy Walk Description of the Open Set-Up

We now discuss the case of the open system consisting of a finite segment $(0, L)$ that is connected to two reservoirs at the ends. The use of the Lévy walk model to study NESS properties in AHT was first proposed in Lepri and Politi [66] where the authors considered a finite lattice of N sites containing a collection of Lévy walkers. The system was connected at it's two ends to infinite reservoirs that contained sources emitting Lévy walkers at fixed constant rates. A Lévy walker crosses from the reservoir into system with probability one, but while exiting from system into reservoir, it can get reflected with probability R. A particle exiting the reservoir is eliminated. The authors in Lepri and Politi [66] considered a discrete version and studied this problem numerically. The strategy was to write appropriate master equations for the probability evolution and obtain the steady state solution numerically. One of the main observations in the paper was that the NESS profile for $P(x)$ was non-linear and was singular at the boundaries. In **Figure 7A** we show a plot of the profile for the case $R = -0.1$, compared with simulation results for the temperature profile in the momentum exchange model (HCME), with free BC and a specific choice of exchange rate. One sees very good agreement. As noted in section 2.2 in the context of temperature profiles in systems with AHT, one can define a "meniscus" exponent, μ, through the observed scaling form $P(x) \sim (\delta x)^\mu$ for small distances δx from any boundary. Based on their numerical observations (see **Figure 7B**) the authors in [66] conjecture the relation

$$\mu = \frac{\nu}{2} + R\left(\frac{\nu}{2} - 1\right). \tag{29}$$

It was noted in [66] that the value $R = -0.1$ was unphysical but made mathematical sense in the master equation (see [66] for further discussions on this point) and gave the best agreement with the momentum exchange simulation profile.

Some exact results were obtained for the Lévy walk model with particle reservoirs, for the special case of perfectly transmitting boundary walls (i.e., $R = 0$) [69] which we now describe. We note that for the Lévy walker, at any given time, a particle could either be passing over a point x or could have landed precisely at the point. Hence, in addition to the probability density $P(x, t)$, it is convenient to define the probability $Q(x, t)dxdt$ that a particle lands precisely between x to $x + dx$ in the time interval $(t, t + dt)$. We now specify the boundary conditions required to set up a non-equilibrium current carrying steady state. For this, we consider the region $x \leq 0$ as the left reservoir with $Q(x, t) = Q_l$ for all points in this region. Similarly, we set $Q(x, t) = Q_r$ in the region $x \geq L$ corresponding to the right reservoir. In the steady state, the distributions become time-independent and $Q(x, t) = Q(x)$, $P(x, t) = P(x)$ satisfy [69]

$$\begin{aligned} Q(x) &= \int_0^L dy\, \frac{1}{2c}\phi(|x-y|/c)\, Q(y) + \frac{Q_l}{2}\psi(x/c) \\ &\quad + \frac{Q_r}{2}\psi[(L-x)/c], \end{aligned} \tag{30}$$

$$P(x) = \int_0^L dy \frac{1}{2c}\psi(|x-y|/c)\, Q(y) + \frac{Q_l}{2}\chi(x/c)$$

$$+\frac{Q_r}{2}\chi\left[(L-x)/c\right], \tag{31}$$

where $\psi(t)=\int_t^\infty d\tau\ \phi(\tau)$ and $\chi(t)=\int_t^\infty d\tau\,\psi(\tau)$ as mentioned earlier after Equation (21). The terms on the right hand side of the above equation for $Q(x)$ represent different contributions. The first term represents the contributions from walkers that start from various points y and land at x. The second and the third term represent contributions from walkers starting, respectively, from left and right reservoirs and landing at x. Similarly, the terms on the right hand side of Equation (31) for $P(x)$ can also be interpreted in the same way except now, events in which the walkers are passing over x, in addition to the events in which they land at x at a given time, also contribute.

Interestingly, it turns out that the problem of finding $Q(x)$ can be related to the problem of the escape probability [75] of a Lévy walker on the interval $(0, L)$. Let $H(x)$ denote the probability with which a Lévy walker, starting at position x, arrives at the left reservoir (region $x < 0$) before arriving at the right reservoir (region $x > L$). It can be shown that $H(x)$ satisfies [69]

$$H(x)=\int_0^L dy\ \frac{1}{2c}\phi(|x-y|/c)\ H(y)+\frac{1}{2}\psi(x/c). \tag{32}$$

The probability $Q(x)$ can now be expressed in terms of $H(x)$ as $Q(x)=(Q_l-Q_r)H(x)+Q_r$, which can be checked easily to satisfy Equation (30).

If one considers a Lévy flight with distribution $\rho(z)=[\phi(z/c)+\phi(-z/c)]/(2c)$ of steps z, the probability $H(x)$ that starting at x, the flight hits first the left bath satisfies exactly Equation (32). Hence by following the same mathematical steps as in [75] to study equations, such as (30) or (32), one can show that, in the large L limit, the solution $Q(x)$ of (30) [and $H(x)$ of (32)] satisfies

$$\int_0^L dy\ \psi(|x-y|/c)\ \mathrm{Sgn}(x-y)Q'(y)=0\,. \tag{33}$$

with $Q(0)=Q_l$ and $Q(L)=Q_r$ [and $H(0)=1$ and $H(1)=0$ for (32)] with a solution of (33), for a $\phi(\tau)$ decaying as in (22), which satisfies

$$Q'(x)=-B[x(L-x)]^{\nu/2-1}\,. \tag{34}$$

We can integrate this equation to get $Q(x)$, with the integration constant and B being then determined from the boundary conditions $Q(0)=Q_l$ and $Q(L)=Q_r$. One finally obtains

$$Q(x)\ =\ Q_l+(Q_r-Q_l)\,\mathbb{G}\left(\frac{x}{L}\right),$$

$$\text{where } \mathbb{G}(z)=\frac{2\Gamma(\nu)}{\nu\Gamma(\nu/2)^2}\ z^{\nu/2}\ {}_2F_1\left(1-\frac{\nu}{2},\frac{\nu}{2},1+\frac{\nu}{2},z\right), \tag{35}$$

and ${}_2F_1\left(a,b,c,z\right)$ is the hypergeometric function. For large L, the right hand side of Equation (31) is dominated by the range $|y-x|\ll L$ and therefore

$$P(x)=\chi(0)Q(x)=\langle\tau\rangle Q(x)\,. \tag{36}$$

The exact results of Equations (34) have been verified in [69] from direct numerical solution of Equations (30, 31) and it was noted that the density profiles were similar to the temperature profiles seen in AHT.

Next we discuss the steady state current $j(x)$ which is given by

$$j(x)=\frac{1}{2}\int_{-\infty}^{\infty} dy\ Q(x-y)\ \mathrm{Sgn}(y)\ \psi(|y|/c). \tag{37}$$

This can be seen to be the difference between the flow from left to right and from right to left. The contribution from $0<y<\infty$ to the integral corresponds to particles crossing the point x from left to right which is obtained by multiplying the density of particles at $x-y$ with the probability $\psi(y/c)$ that they have a flight time larger than y/c. The contribution from $-\infty<y<0$ to the integral corresponds to a similar right-to-left current. After performing a partial integration and using the boundary conditions $Q(0)=Q_l$ and $Q(L)=Q_r$, one obtains

$$j(x)=-\frac{c}{2}\int_0^L dy\ \chi(|x-y|/c)\ Q'(y)\,. \tag{38}$$

Using Equation (33) it is easy to see that $dj/dx=0$ which implies that the current in the steady state is independent of x, as expected. Hence, evaluating the current at $x=0$ and using Equation (34), we get for large L

$$j\simeq(Q_l-Q_r)\,\frac{A\ c^{\nu}\ \Gamma(\nu)\ \Gamma(1-\frac{\nu}{2})}{2\ \nu(\nu-1)\ \Gamma(\frac{\nu}{2})}\ L^{\alpha-1},\quad \alpha=2-\nu. \tag{39}$$

From Equation (27) we then get the relation $\alpha=\beta-1$, between the conductivity exponent of AHT and the MSD exponent for Lévy-walk diffusion. This relation for Lévy diffusion was pointed out in [68] and verified in simulations in 1*D* heat conduction models [8, 21]. A derivation based on linear response theory has been given in [59]. Finite size corrections to the results in Equations (34, 39) were recently obtained in [76].

In the large L limit by using Equation (36) in Equation (38) we obtain

$$j=-\frac{c}{2\langle\tau\rangle}\int_0^L dy\ \chi(|x-y|/c)P'(y). \tag{40}$$

Above equation is the analog of Fourier's law Equation (1) with the important difference that in the linear response regime the current at a point gets contributions from the temperature gradients at other parts of the system as well.

The above treatment can be generalized for arbitrary values of the reflection probability R [37] and this leads to the following general non-local form of the current

$$j\ =\ -\frac{c}{2\langle\tau\rangle}\int_0^L dy\ \chi_R(x,y)P'(y)\,, \tag{41}$$

$$\text{where } \chi_R(x,y)\ =\ \sum_{n=-\infty}^{\infty}\left[R^{|2n|}\chi\left(\frac{|2nL+y-x|}{c}\right)-R^{|2n+1|}\chi\left(\frac{|2nL+y+x|}{c}\right)\right]. \tag{42}$$

Remarkably we note that for $\nu = 3/2$ ($\alpha = 2 - \nu = 1/2$), the expression above is identical to the expression for $\mathcal{K}_R(v, v')$ with $v = x/L, v' = y/L$, given later in Equation (112).

3.2. Non-linear Fluctuating Hydrodynamics Description of Anomalous Heat Transport

We now discuss a completely different approach for understanding AHT. In this approach the starting point is the Hamiltonian dynamics of the system. The idea is to consider the effective dynamics of the slow conserved fields using some coarse graining. One finds that the evolution of small fluctuations around equilibrium can be described by fluctuating hydrodynamics. Solving these equations using mode coupling theory, detailed predictions can be made on the form of equilibrium spatio-temporal correlation functions of the conserved fields. In particular, we will see that it predicts the super-diffusive spreading of energy perturbations with Lévy-law scaling, and the slow decay of energy current auto-correlation functions. We will here describe the theory for generic anharmonic systems with three conserved quantities, namely volume, momentum, energy [61], and present some numerical results which verify the predictions of the theory.

Let us consider N particles of unit masses with positions and momenta denoted by $\{q(\ell), p(\ell)\}$, for $\ell = 1, \ldots, N$. The particles move on a ring of size L so that we have the boundary conditions $q(N+1) = q(1) + L$ and $p(N+1) = p(1)$. The Hamiltonian is taken to be

$$H = \sum_{\ell=1}^{N} \epsilon(\ell), \quad \epsilon(\ell) = \frac{p^2(\ell)}{2} + V[r(\ell)], \tag{43}$$

where we have defined the stretch variables $r(\ell) = q(\ell+1) - q(\ell)$. It is easy to see from the Hamiltonian equations of motion that stretch $r(\ell)$, momentum $p(\ell)$, and energy $\epsilon(\ell)$ are locally conserved and hence satisfy corresponding continuity equations. In the continuum limit, these equations take the form

$$\begin{aligned} \frac{\partial r(x,t)}{\partial t} &= \frac{\partial p(x,t)}{\partial x}, \\ \frac{\partial p(x,t)}{\partial t} &= -\frac{\partial P(x,t)}{\partial x}, \\ \frac{\partial e(x,t)}{\partial t} &= -\frac{\partial}{\partial x}\left[p(x,t)P(x,t)\right], \end{aligned} \tag{44}$$

where the label index ℓ has been denoted by the corresponding continuous variable x and $P(x) = -V'(x)$ is the local force. Assume that the system starts in a state of thermal equilibrium at zero total average momentum characterized by the temperature ($T = \beta^{-1}$) and pressure (P), which fix the the average energy and average stretch of the chain. The distribution corresponding to this ensemble is

$$\begin{aligned} \mathcal{P}(\{p(x), r(x)\}) &= \prod_x \frac{e^{-\beta[p_x^2/2 + V(r_x) + Pr_x]}}{Z_x}, \\ Z_x &= \int_{-\infty}^{\infty} dp \int_{-\infty}^{\infty} dr e^{-\beta[p^2/2 + V(r) + Pr]}. \end{aligned} \tag{45}$$

Since the fields $r(x,t)$, $p(x,t)$, and $e(x,t)$ satisfy continuity equations, they evolve slowly suggesting a slowly evolving local equilibrium picture. We consider small fluctuations of the conserved quantities about their equilibrium values, $u_1(x,t) = r(x,t) - \langle r \rangle_{eq}$, $u_2(x,t) = p(x,t)$, and $u_3(x,t) = \epsilon(x,t) - \langle \epsilon \rangle_{eq}$. Inserting these into Equation (44) one obtains $\partial_t u_\alpha = -\partial_x j_\alpha$, where j_α are the corresponding Euler currents which are functions of u_αs. Expanding these currents to second order in the fields as $j_\alpha = \sum_\beta A_{\alpha\beta} u_\beta + \sum_{\beta,\gamma} H^\alpha_{\beta\gamma} u_\beta u_\gamma$, and then adding dissipation and noise terms (to ensure thermal equilibration) one arrives at the following noisy hydrodynamic equations

$$\partial_t u_\alpha = -\partial_x \left[A_{\alpha\beta} u_\beta + H^\alpha_{\beta\gamma} u_\beta u_\gamma - \partial_x \widetilde{D}_{\alpha\beta} u_\beta + \widetilde{B}_{\alpha\beta} \xi_\beta \right], \tag{46}$$

where repeated indices are summed over. The noise and the dissipation matrices, $\widetilde{B}, \widetilde{D}$, are related to each other by the fluctuation-dissipation relation $\widetilde{D}C + C\widetilde{D} = \widetilde{B}\widetilde{B}^T$, where the matrix C corresponds to equilibrium correlations and its elements are $C_{\alpha\beta}(x) = \langle u_\alpha(x,0) u_\beta(0,0) \rangle$.

It is useful to define normal modes of the linearized equations (dropping u^2 terms in Equation 46) through the transformation $(\phi_-, \phi_0, \phi_+) = \vec{\phi} = R\vec{u}$, where the matrix R acts only on the component index and diagonalizes A, *i.e.* $RAR^{-1} = \mathrm{diag}(-c, 0, c)$. The diagonal form implies that there are two sound modes, $\phi_\pm$, traveling at speed c in opposite directions and one stationary but decaying heat mode, ϕ_0. The quantities of interest are the equilibrium spatio-temporal correlation functions $C_{ss'}(x,t) = \langle \phi_s(x,t) \phi_{s'}(0,0) \rangle$, where $s, s' = -, 0, +$. Because the modes separate linearly in time, one argues that at large times the off-diagonal matrix elements of the correlator are small compared to the diagonal ones and that the dynamics of the diagonal terms decouples into three single component equations. After including the non-linearity it is seen that to leading order the equations for sound modes have self-coupling terms of the form $\phi_\pm^2$. These then have the structure of the noisy Burgers equation, for which the exact scaling function, denoted by f_{KPZ}, are known. For the heat peak the self-coupling coefficient vanishes for any interaction potential. Thus, one has to study the sub-leading corrections, and calculations using the mode-coupling approximation result in the symmetric Lévy walk distribution, with a cut-off at $x = ct$. While this is an approximation, it seems to be very accurate. For the generic case of non-zero pressure, *i.e.* $P \neq 0$, which corresponds either to asymmetric inter-particle potentials or to an externally applied stress, the prediction for the left moving, resp. right moving, sound peaks, and the heat mode are

$$\begin{aligned} C_{--}(x,t) &= \frac{1}{(\lambda_s t)^{2/3}} f_{\mathrm{KPZ}} \left[\frac{(x+ct)}{(\lambda_s t)^{2/3}} \right], \\ C_{++}(x,t) &= \frac{1}{(\lambda_s t)^{2/3}} f_{\mathrm{KPZ}} \left[\frac{(x-ct)}{(\lambda_s t)^{2/3}} \right], \end{aligned} \tag{47}$$

$$C_{00}(x,t) = \frac{1}{(\lambda_e t)^{3/5}} f_{\mathrm{LW}}^{5/3} \left[\frac{x}{(\lambda_e t)^{3/5}} \right], \tag{48}$$

where $f_{\mathrm{KPZ}}(x)$ is the KPZ scaling function discussed in [61, 77], and tabulated in [78]. The scaling function $f_{\mathrm{LW}}^{\nu}(x)$ is given by the Fourier transform of the Lévy characteristic function $e^{-|k|^{\nu}}$, with a cut-off at $x = ct$. The scaling parameters λ_s and λ_e are known explicitly. On the other hand for an even potential at zero pressure, i.e., $P = 0$, all self-coupling coefficients vanish. As a result the scaling solutions within mode-coupling approximation change and one obtains

$$\begin{aligned} C_{--}(x,t) &= \frac{1}{(\lambda_s^0 t)^{1/2}} f_{\mathrm{G}}\left[\frac{(x+ct)}{(\lambda_s^0 t)^{1/2}}\right], \\ C_{++}(x,t) &= \frac{1}{(\lambda_s^0 t)^{1/2}} f_{\mathrm{G}}\left[\frac{(x-ct)}{(\lambda_s^0 t)^{1/2}}\right], \end{aligned} \tag{49}$$

$$C_{00}(x,t) = \frac{1}{(\lambda_e^0 t)^{2/3}} f_{\mathrm{LW}}^{3/2}\left[\frac{x}{(\lambda_e^0 t)^{2/3}}\right], \tag{50}$$

where $f_{\mathrm{G}}(x)$ is the unit Gaussian with zero mean. The scaling parameters λ_s^0 is not known from microscopics while λ_e^0 is known explicitly in terms of λ_s^0.

Here we present molecular dynamics simulation results for the FPUT chain that were obtained in [63] which verify the predictions of NFH. In **Figure 8**, top panel, the two-point correlation functions $C_{00}(x,t)$, $C_{++}(x,t)$ and $C_{--}(x,t)$ are plotted as a function of x for three values of time $t = 800,\ 2,400$ and $3,200$. The parameters used in this plot are $k_2 = 1.0, k_3 = 2.0, k_4 = 1.0, T = 5.0, P = 1.0$ for which one gets $c = 1.80293$ and we also see there is a good separation of the heat and sound modes. In **Figure 8**, bottom panel we also find an excellent collapse of the heat mode and the sound mode data with the expected scalings. The scaled data for the heat mode fits very well to the Lévy-scaling function whereas the same for the sound-mode still shows some asymmetry but is quite close to the KPZ function. The numerically estimated values of the constants $\lambda_{s,e}$ are $\lambda_s = 0.46$ and $\lambda_e = 5.86$. These are in close agreement to the theoretically obtained values $\lambda_s = 0.396$ and $\lambda_e = 5.89$.

4. STOCHASTIC MODELS: EXACT RESULTS ON FRACTIONAL EQUATION DESCRIPTION

It is now well-understood that conservation laws play an important role in observation of super-diffusive transport in one-dimensional systems. As we saw in the previous section, NFH provides some understanding of the emergence of Lévy-walk behavior, which seems to capture several aspects of anomalous transport. However, providing a completely rigorous microscopic derivation of the Lévy-walk picture in a Hamiltonian model has been difficult, though there have been some attempts [79]. While generic non-linear Hamiltonian models are difficult to analyze, analytical results have been obtained for harmonic chains whose Hamiltonian dynamics is perturbed by stochastic noise that breaks integrability of the system [9, 30, 52]. These stochastic models attempt to mimic non-linear chains and for these models, several exact results both in the closed system set-up and the open system set-up have been obtained. In particular one can rigorously establish non-local response relation Equation (3) and the fractional diffusion equation Equation (4). There are two widely studied stochastic models which we discuss below.

4.1. Harmonic Chain With Volume Exchange

This model is defined on a one dimensional lattice where each site carries a "stretch" variable $\eta_i,\ i \in \mathbb{Z}$ and the energy of the system is $E = \sum_i \eta_i^2$. The dynamics has two parts: (a) a deterministic part given by $\frac{d\eta_i}{dt} = \eta_{i+1} - \eta_{i-1}$ and (b) a stochastic exchange part where ηs from any two randomly chosen neighboring sites, are exchanged at a constant rate γ. We refer to this model as Harmonic chain with volume exchange (HCVE). This model was introduced in [30] where it was shown that the energy current auto-correlation decays as $\sim 1/\sqrt{t}$, implying super-diffusive transport. It is easy to see that this system has only two conserved quantities namely, the total "volume" $\sum_i \eta_i$ and the total energy $\sum_i \eta_i^2$. The evolution of the density fields corresponding to these conserved quantities at the macroscopic length and time scales was studied in [62] using NFH, where it has been shown that this model has two normal modes - one diffusive sound mode and a $\frac{3}{2}$-asymmetric Lévy heat mode. Subsequently, it was rigorously shown that the local energy density $e(x,t)$ satisfies a (3/4)-skew-fractional Equation [31]

$$\begin{aligned} \partial_t e(x,t) &= -\frac{1}{\sqrt{2\gamma}} \mathbb{L}_{\infty}^{\nu} e(x,t), \ \text{ for } x \in (-\infty, \infty), \\ \text{where } \mathbb{L}_{\infty}^{\nu} &= [(-\Delta)^{3/4} - \nabla(-\Delta)^{1/4}], \end{aligned} \tag{51}$$

with Δ as the usual Laplacian operator. In the Fourier domain, defined by $e(k,t) = \int_{-\infty}^{\infty} e(x,t) e^{ixk} dx$, the above equation reads as

$$\partial_t e(k,t) = -\frac{1}{\sqrt{2\gamma}} |k|^{3/2} [1 - i \ \mathrm{sgn}(k)] \ e(k,t). \tag{52}$$

Note that for the diffusive case the analog of the above equation would be $\partial_t e(k,t) = -Dk^2 \ e(k,t)$. The above results suggest that, in the open set-up where the system is connected to two reservoirs at different temperatures, this model would exhibit anomalous scaling of the steady state current j with system size N. In [30], it has been numerically shown that indeed $j \sim 1/\sqrt{N}$. Recently, an understanding of the open system was achieved using the fractional equation description, which we now discuss [34]. An aspect that we will point out here is that the fractional-equation-type description in the open-set up is strongly dependent on boundary conditions (fixed or free or mixed).

For the open system case, we consider a finite lattice of size N, connected to two thermal reservoirs at temperatures T_ℓ and T_r on the left and right boundaries. The dynamics of the $\eta_i,\ i = 1, 2, \ldots, N$ now gets modified to

$$\begin{aligned} \frac{d\eta_i}{dt} &= \eta_{i+1} - \eta_{i-1} + \delta_{i,1} \Big(-\lambda \eta_1 \\ &\quad + \sqrt{2\lambda T_\ell} \xi_\ell(t) \Big) + \delta_{i,N} \Big(-\lambda \eta_N \\ &\quad + \sqrt{2\lambda T_r} \xi_r(t) \Big) \\ &\quad + \text{stochastic exchange at rate } \gamma. \end{aligned} \tag{53}$$

The Langevin terms at the boundaries $i = 1$ and $i = N$ appear due to the baths and $\xi_{\ell,r}(t)$ are independent Gaussian

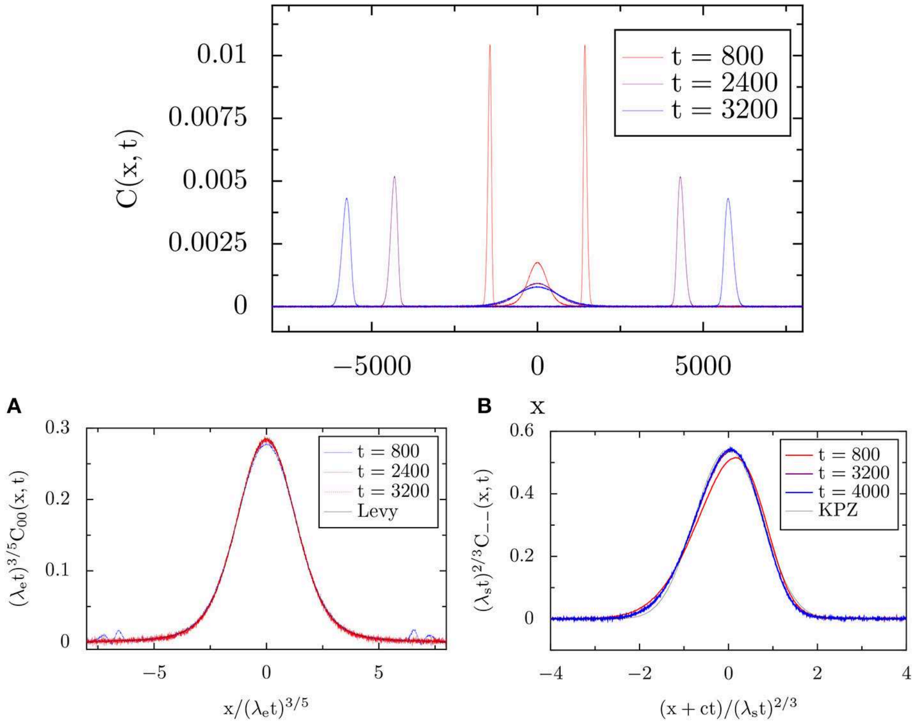

FIGURE 8 | (Top) Plots of the heat mode correlation $C_{00}(x,t)$ (central peaks) and the sound mode correlations $C_{++}(x,t)$ and $C_{--}(x,t)$ (right and left moving peaks) in the FPUT chain, at three different times, for the parameter set with $k_2 = 1.0, k_3 = 2.0, k_4 = 1.0, T = 5.0, P = 1.0$, and system size 16,384. The speed of sound was $c = 1.80293$. We see that the heat and sound modes are well-separated. The numerical data in this plot were obtained by averaging over around $10^6 - 10^7$ initial conditions. (Bottom) The heat mode **(A)** and the left moving sound mode **(B)** correlations, respectively, $C_{00}(x,t)$ by $C_{--}(x,t)$ are plotted at different times, using a Lévy-type-scaling for the heat mode and KPZ-type scaling for the sound mode. Here we observe a very good collapse of the data at different times. Moreover, we observe a good fit to the Lévy-stable distribution with $\lambda_e = 5.86$ and a reasonable fit to the KPZ scaling function, with $\lambda_s = 0.46$. The parameters used in this plot are $k_2 = 1.0, k_3 = 2.0, k_4 = 1.0, T = 5.0, P = 1.0$ (adapted from Das et al. with permission from [63] Copyright (2014) by American Physical Society).

white noises with mean zero and unit variance. We consider fixed boundary conditions $\eta_0 = \eta_{N+1} = 0$.

Our main interest is to obtain an equation in this finite system, analogous to Equation (51), to describe the evolution equation of the temperature profile. To do this we first define the local temperature $T_i(t) = \langle \eta_i^2(t) \rangle$ and the off-diagonal correlations $C_{i,j}(t) = \langle \eta_i(t)\eta_j(t) \rangle$, $i \neq j$, which characterize the non-equilibrium state of the system. Interestingly, it turns out that the equations for two point correlations do not depend on higher order correlations and this property leads to the model's solvability. The evolution of these quantities in the bulk $(2 < i, j < N-1)$ can be obtained from Equation (53) as:

$$\begin{aligned} \dot{C}_{ij} &= C_{i+1,j} - C_{i-1,j} + C_{i,j+1} - C_{i,j-1} \\ &\quad + \gamma[C_{i-1,j} + C_{i+1,j} + C_{i,j-1} + C_{i,j+1} - 4C_{i,j}], \\ \dot{C}_{i,i+1} &= T_{i+1} - C_{i-1,i+1} + C_{i,i+2} - T_i \\ &\quad + \gamma[C_{i-1,i+1} + C_{i,i+2} - 2C_{i,i+1}], \\ \dot{T}_i &= 2[C_{i,i+1} - C_{i-1,i}] + \gamma[T_{i+1} + T_{i-1} - 2T_i]. \end{aligned} \tag{54}$$

The equations involving the boundary terms are given in Priyanka et al. [34]. Note that in an infinite system, we get the same set of equations with $i, j \in \mathbb{Z}$. For the finite open system, solving the above equations exactly seems to be difficult. However, it was observed numerically [34] that for large N the temperature field $T_i(t)$ scales as $T_i(t) = \mathcal{T}\left(\frac{i}{N}, \frac{t}{N^{3/2}}\right)$ and the correlation field $C_{i,j}(t)$ scales as $C_{i,j}(t) = \frac{1}{\sqrt{N}}\mathcal{C}\left(\frac{|i-j|}{\sqrt{N}}, \frac{i+j}{2N}, \frac{t}{N^{3/2}}\right), i \neq j$. Inserting these into (54), and expanding in powers of $1/\sqrt{N}$, we find at leading order the following equations

$$\partial_v \mathcal{C}(u,v,\tau) = -\gamma \partial_u^2 \mathcal{C}(u,v,\tau), \tag{55}$$

$$\partial_v \mathcal{T}(v,\tau) = -2\gamma \left[\partial_u \mathcal{C}(u,v,\tau)\right]_{u=0}, \tag{56}$$

$$\partial_\tau \mathcal{T}(v,\tau) = 2\partial_v \mathcal{C}(0,v,\tau), \tag{57}$$

where the scaling variables $u = |i-j|/\sqrt{N}, v = (i+j)/2N, \tau = t/N^{3/2}$ are defined over $\{0 \leq u \leq \infty;\ 0 \leq v \leq 1;\ 0 \leq \tau \leq \infty\}$.

Note that for the isolated infinite system, one can follow the same procedure as above, but now replacing the scale parameter $1/N \rightarrow a$ where a is the lattice spacing, to obtain the same set of Equations (55–57) with a different domain $\{-\infty \leq u \leq \infty; -\infty \leq v \leq \infty\}$. These equations can be solved by Fourier transforms to get a skew fractional evolution equation for $\mathcal{T}(v,\tau)$ of the same form as Equation (52). Defining Fourier

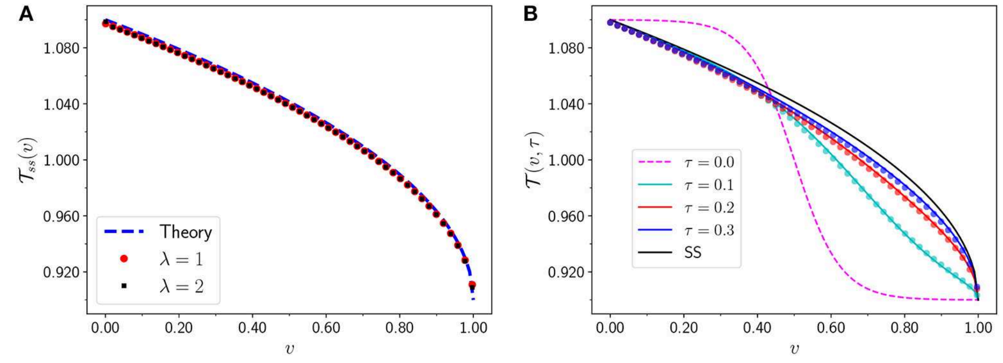

FIGURE 9 | (A) Steady state temperature of HCVE model ($\mathcal{T}_{ss}$) as given by Equation (66) (blue dashed line) is compared with numerical simulations for parameters $\omega = \gamma = 1, T_\ell = 1.1, T_r = 0.9$, and $N = 1,024$, and for two different choice of λ. **(B)** Numerical verification of the evolution of the temperature profiles $\mathcal{T}(v, \tau)$ given by Equation (71) (solid lines), starting from a non-stationary profile (dashed line). The points indicate simulation results for parameters are $\lambda = \gamma = 1, T_\ell = 1.1, T_r = 0.9$ and $N = 2{,}048$ (adapted from Kundu et al. with permission from [34] Copyright (2018) by American Physical Society).

transforms $\mathcal{T}(v, \tau) = \int_{-\infty}^{\infty} dk \hat{\mathcal{T}}(\tau) e^{-ikv}/(2\pi)$ and $\mathcal{C}(u, v, \tau) = \int_{-\infty}^{\infty} dk \hat{\mathcal{C}}_k(u, \tau) e^{-ikv}/(2\pi)$ in the variable v, we get

$$\partial_u^2 \hat{\mathcal{C}}_k(u, \tau) = \frac{ik}{\gamma} \hat{\mathcal{C}}_k(u, \tau), \tag{58}$$

$$ik \hat{\mathcal{T}}_k(\tau) = 2\gamma \left[\partial_u \hat{\mathcal{C}}_k(u, \tau) \right]_{u=0}, \tag{59}$$

$$\partial_\tau \hat{\mathcal{T}}_k(\tau) = -2ik \hat{\mathcal{C}}_k(0, \tau) . \tag{60}$$

Solving the first Equation (58), with the condition that correlations vanish at $u = \pm\infty$, we get

$$\hat{\mathcal{C}}_k(u, \tau) = A_k(\tau) \exp\left[-(1 + i\mathrm{Sgn}(k)) \frac{|k|^{1/2}}{\sqrt{2\gamma}} |u| \right] \tag{61}$$

The Equation (59) relates the constant A_k to $\hat{\mathcal{T}}_k$:

$$A_k(\tau) = -\frac{ik(1 - i\mathrm{Sgn(k)})}{2\sqrt{2\gamma|k|}} \hat{\mathcal{T}}_k. \tag{62}$$

Using Equations (61, 62) in Equation (60) we get the infinite line equation in Equation (52).

We now go back to the open system case where the solution is more non-trivial. To solve these equations in the open set-up, we proceed as for the regular diffusive heat equation, and write the solution as sum of a steady state part and a relaxation part

$$\mathcal{T}(v, \tau) = \mathcal{T}_{ss}(v) + \mathcal{T}_r(z, \tau) \tag{63}$$

$$\mathcal{C}(u, v, \tau) = \mathcal{C}_{ss}(u, v) + \mathcal{C}_r(u, z, \tau), \tag{64}$$

where we have defined $z = 1 - v$. We note that under this transformation, the "anti-diffusion" Equation (55), becomes a diffusion equation, with v as the time variable and z the space variable. The relaxation part satisfies the equations given in Equations (55, 56, 57), while the steady state part satisfies these equations but with $\partial_\tau \mathcal{T}_{ss}(v) = 0$. The boundary conditions for the steady state part are given by Priyanka et al. [34]

$$\mathcal{C}_{ss}(u, z \to 0) = 0,\ \mathcal{C}_{ss}(u \to \infty, z) = 0,\ \mathcal{C}_{ss}(u = 0, z) = J/2.$$

$$\mathcal{T}_{ss}(v = 0) = T_\ell,\ \mathcal{T}_{ss}(v = 1) = T_r, \tag{65}$$

where we have used Equation (57) to identify $J = 2\mathcal{C}_{ss}(u = 0, z)$ as the NESS current which gets determined by the boundary conditions for $\mathcal{T}_{ss}(v)$. In terms of the original unscaled variables, the true current is given by $j_{ss} = J/\sqrt{N}$. The solution of the steady state equations is given by Priyanka et al. [34]

$$\begin{aligned} \mathcal{T}_{ss}(v) &= T_r + (T_\ell - T_r)\sqrt{1 - v}, \\ \mathcal{C}_{ss}(u, v) &= -\frac{T_\ell - T_r}{4}\sqrt{\frac{\pi}{\gamma}}\,\mathrm{erfc}\left(\frac{u}{\sqrt{4\gamma(1 - v)}} \right), \\ J &= \frac{T_\ell - T_r}{2}\sqrt{\frac{\pi}{\gamma}}. \end{aligned} \tag{66}$$

In **Figure 9A**, we show a comparison of the above result for steady state temperature profile with those obtained from direct simulations of the microscopic model, and we see very good agreement. It is interesting to note that the temperature profile is non-symmetric under space reversal as the microscopic model itself does not have such symmetry. This fact is also reflected in hydrodynamics where this shows in the existence of a single sound mode.

For the relaxation part we look for solutions which satisfy the initial condition $\mathcal{T}_r(z, 0)$, $\mathcal{C}_r(u, z, \tau = 0) = 0$ and boundary conditions $\mathcal{C}_r(u, z, \tau)|_{u \to \infty} = 0$, $\mathcal{T}_r(0, \tau) = \mathcal{T}_r(1, \tau) = 0$. The solution of the "anti-diffusion" Equation (55), with z as time variable, with the boundary condition (56) can be obtained as [34]

$$\mathcal{C}_r(u, z, \tau) = -\int_0^z \frac{\exp\left(-\frac{u^2}{4\gamma(z - z')}\right)}{\sqrt{4\pi\gamma(z - z')}} \frac{\partial \mathcal{T}_r(z', \tau)}{\partial z'} dz'. \tag{67}$$

Using this in (56) then gives finally the evolution equation for the temperature field

$$\partial_\tau \mathcal{T}_r(z, \tau) = \frac{1}{\sqrt{\pi\gamma}} \partial_z \left[\int_0^z dz' \frac{\partial_{z'} \mathcal{T}_r(z', \tau)}{\sqrt{z - z'}} \right], \tag{68}$$

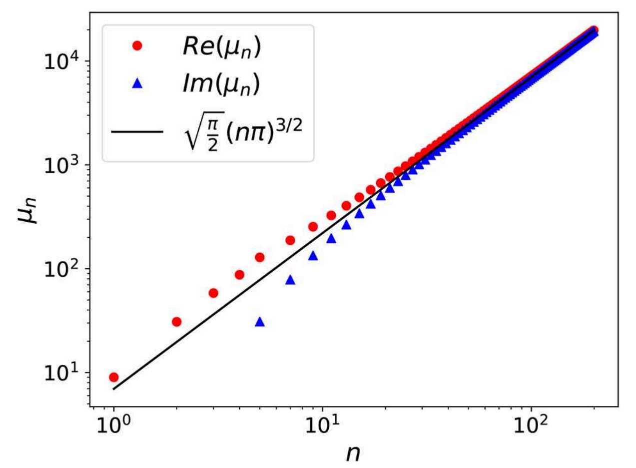

FIGURE 10 | The real and imaginary part of the alternate eigenvalues for the matrix $\mathbb{L}^\nu$ in Equation (70). The first 4 eigenvalues are completely real and distinct. The higher eigenvalue comes in complex conjugate pairs. For large $\mu_n \sim (n\pi)^{3/2}(1 \pm i)$. For smaller n, there is a deviation from asymptotic scaling due to finite definition of the operator (adapted from Kundu et al. with permission from [34] Copyright (2018) by American Physical Society).

inside the domain $0 \le z \le 1$. This is a non-local equation which can be recognized as a continuity equation $\partial_\tau \mathcal{T}_r(z,\tau) = -\partial_z j(z,\tau)$ where the current j is precisely in the form stated in Equation (3). This is the open-system analog of Equation (51). For the infinite system, a similar computation leads to Equation (68) but with the lower limit of integration replaced by $z = -\infty$, and by taking Fourier transforms, this can be shown to reduce to Equation (52).

We now proceed to solve Equation (68) to find the temperature evolution. It is natural to expand the temperature profile $\mathcal{T}_r(z,\tau)$ in a basis set satisfying Dirichlet boundary conditions, and we choose the set $\alpha_n(z) = \sqrt{2}\sin(n\pi z)$, $n = 1,2,3\dots$. Substituting $\mathcal{T}_r(z,\tau) = \sum_n \hat{\mathcal{T}}_n(\tau)\alpha_n(z)$ in Equation (68), we get

$$\sum_n \dot{\hat{\mathcal{T}}}_n \alpha_n(z) = \kappa \sum_n \hat{\mathcal{T}}_n(\tau)(n\pi)\partial_z \int_0^z \frac{\phi_n(z')}{\sqrt{z-z'}}dz'. \tag{69}$$

Further we expand the function $f_n(z) = \partial_z \int_0^z \phi_n(z')/\sqrt{z-z'}dz' = \sum_{l=1} \zeta_{nl}\alpha_l(z)$ where $\zeta_{nl} = \int_0^1 dz\, f_n(z)\, \alpha_l(z)$. Using orthogonality, we get

$$|\, \dot{\hat{\mathcal{T}}}\, \rangle = \kappa\, \mathbb{L}^\nu |\, \hat{\mathcal{T}}\, \rangle, \tag{70}$$

where $\mathbb{L}^\nu_{nl} = (n\pi)\zeta_{nl}$ and the column vector $|\, \mathcal{T}\, \rangle$ has elements $\hat{\mathcal{T}}_n = \langle \alpha_n | \hat{\mathcal{T}} \rangle$. The above equation is an infinite-dimensional matrix representation of the non-local Equation (68). To solve this, we diagonalize the matrix $\mathbb{L}^\nu$ as $\mathbb{R}^{-1}\mathbb{L}^\nu\mathbb{R} = \boldsymbol{\mu}$, which gives the time dependent solution as $|\, \hat{\mathcal{T}}(\tau)\, \rangle = \mathbb{R}e^{\kappa\boldsymbol{\mu}\tau}\mathbb{R}^{-1}|\, \hat{\mathcal{T}}(0)\, \rangle$ where $\mathbb{R}_{n,l} = \langle \alpha_n | \psi_l \rangle$ denotes the n-th element of the l-th right-eigenvector of the matrix $\mathbb{L}^\nu$ and the diagonal matrix μ contains the corresponding eigenvalue μ_l. The matrix $\mathbb{L}^\nu$ is real but non-symmetric and it has left eigenvectors $\langle \chi_l |$ whose elements are given by $\langle \chi_l | \alpha_n \rangle = \mathbb{R}^{-1}_{l,n}$. The formal solution for the temperature field $\mathcal{T}_r(z,\tau)$ can then be written as

$$\begin{aligned} \mathcal{T}_r(z,\tau) &= \sum_n \hat{\mathcal{T}}_n(\tau)\alpha_n(z) \\ &= \sum_{n,m,l} \mathbb{R}_{n,l}e^{\kappa\mu_l\tau}\mathbb{R}^{-1}_{l,m}\left[\int_0^1 dz'\mathcal{T}_r(z',0)\alpha_m(z')\right]\alpha_n(z) \\ &= \int_0^1 dz'\left[\sum_l \psi_l(z)\chi_l(z')e^{\kappa\mu_l\tau}\right]\mathcal{T}_r(z',0), \end{aligned} \tag{71}$$

where $\psi_l(z) = \langle z|\psi_l\rangle = \sum_n \mathbb{R}_{nl}\alpha_n(z)$ and $\chi_l(z) = \langle \chi_l | z \rangle = \sum_n \mathbb{R}^{-1}_{ln}\alpha_n(z)$. Finding the eigenspectrum of the matrix $\mathbb{L}^\nu$ is a difficult problem as the matrix is infinite-dimensional and non-symmetric. However, one can truncate the matrix at some order and diagonalize it numerically, assuming that the spectrum converges with increasing truncation order. In [34] the authors used this approach to compute the eigenspectrum and thereby study the time evolution of the temperature profile. This is shown in **Figure 9B**. The spectrum is shown in **Figure 10** where it is seen that for large n, $\mu_n \sim \sqrt{\frac{\pi}{2}}|n\pi|^{3/2}(1 \pm i)$ which is similar to the spectrum of the non-local operator $\mathbb{L}^\nu$ in Equation (52) describing the evolution in infinite system. In **Figure 11** we show the left and right eigenvectors $\chi_n(z) = \sum_{l=1}\mathbb{R}^{-1}_{nl}\alpha_l(z)$ and $\psi_n(z) = \sum_{l=1}\mathbb{R}_{ln}\alpha_l(z)$, respectively, corresponding to the first eight eigenvalues. One observes that the eigenvectors corresponding to the first four eigenvalues are real whereas the eigenvectors corresponding to the eigenvalues with $n > 4$ are complex and come in conjugate pairs.

4.2. Harmonic Chain With Momentum Exchange

In the previous section we discussed transport in the HCVE model which has two conserved quantities, namely volume and energy. In this section, we discuss heat transport in the harmonic chain momentum exchange (HCME) model which has three conserved quantities, namely volume, momentum and energy, that are the same as the ones in usual anharmonic chains with Hamiltonian dynamics [3, 4]. The model consists of a harmonic chain of particles each of unit mass and described by the degrees of freedom q_i, p_i, with $i \in \mathbb{Z}$, corresponding respectively to position and momentum. As for the HCVE system, the dynamics of the HCME model also has two parts: (i) the usual deterministic part given by the Hamiltonian equations $\dot{q}_i = p_i$, $\dot{p}_i = \omega^2(q_{i+1} - 2q_i + q_{i-1})$, $i \in \mathbb{Z}$, where ω is the strength of the harmonic interaction and (ii) a stochastic part consisting of exchanges of momenta between neighboring particles (chosen at random) occurring with rate γ. In the absence of the stochastic exchange, the underlying Hamiltonian dynamics is integrable and the transport in this system is ballistic due to the absence of any scattering mechanism. The stochastic exchange introduces a momentum conserving scattering mechanism, which should make the transport behavior non-ballistic. However, it turns out that the stochastic mixing is not sufficient to make the transport behavior diffusive. It has been shown rigorously that the energy current correlation in equilibrium of an infinite chain

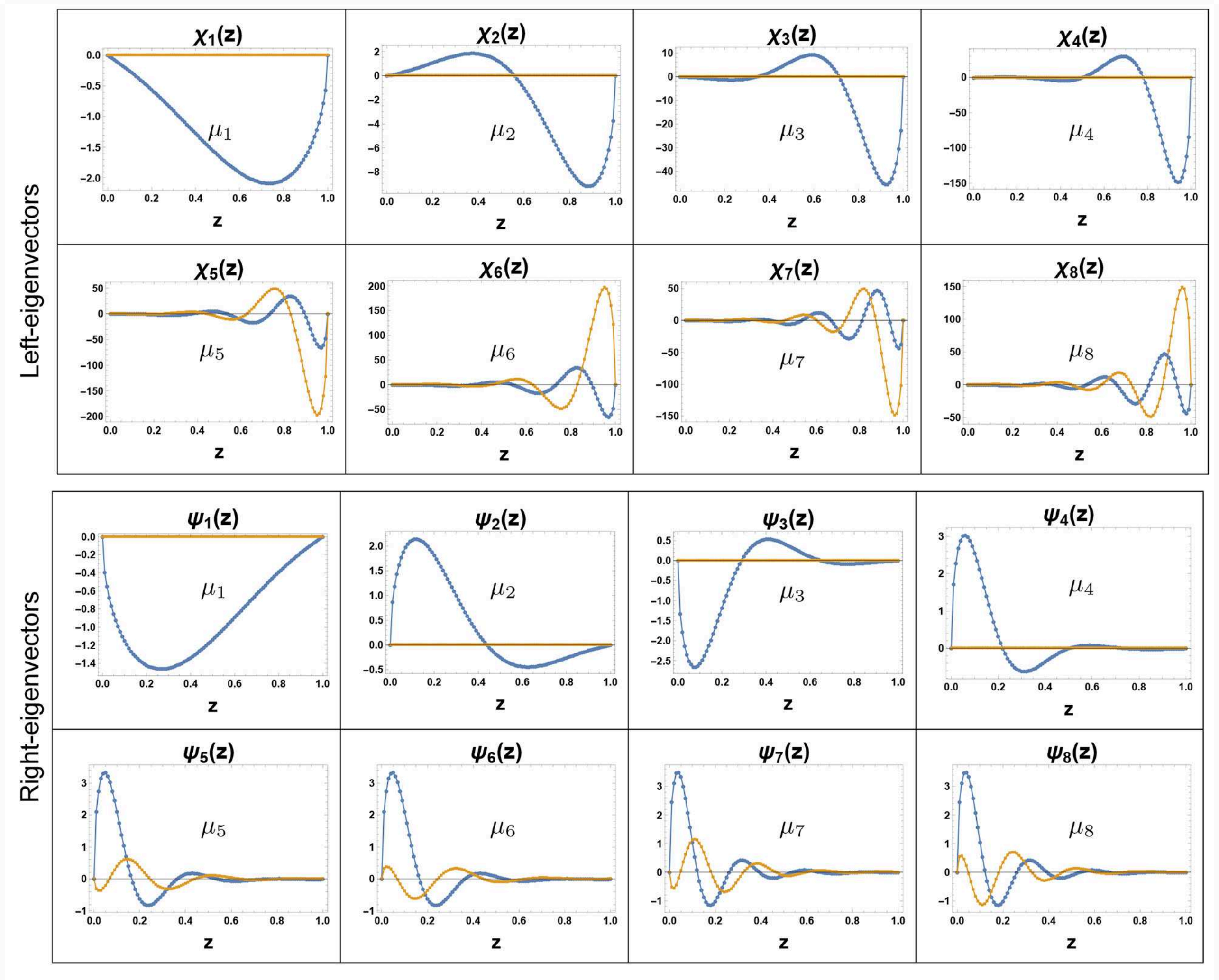

FIGURE 11 | Left and right eigenvectors of matrix $\mathbb{L}^{v}$ in Equation (70) for $n = 1, 2, 3, 4, 5, 6, 7, 8$. The real parts are indicated by blue lines while orange denotes the imaginary part. Note that the eigenvectors corresponding to the real eigenvalues ($n = 1, 2, 3, 4$) are also real where the eigenvectors corresponding to complex eigenvalues ($n = 5, 6, 7, 8 \ldots$) are complex (adapted from Kundu et al. with permission from [34] Copyright (2018) by American Physical Society).

decays as $t^{-1/2}$ similar to that in the HCVE model [9]. This, through the closed system GK formula in Equation (10), implies the anomalous system size scaling of the steady state current as $j \sim N^{-1/2}$.

The HCME dynamics conserves the following three quantities: (a) total stretch $\sum_i r_i$ where $r_i = q_{i+1} - q_i$, (b) total momentum $\sum_i p_i$ and (c) the total energy $\sum_i e_i$ with $e_i = p_i^2/2 + \omega^2 r_i^2/2$. As a consequence, the corresponding local densities evolve slowly in the macroscopic length and time scales. In [29], it has been analytically shown that the local energy density $e(x, t)$ in the isolated system evolves according to the following fractional diffusion equation

$$\partial_t e(x,t) = -\bar{\kappa}(-\Delta)^{3/4} e(x,t), \quad -\infty < x < \infty,$$
$$\text{where } \bar{\kappa} = \frac{\omega^{3/2}}{2\sqrt{2\gamma}}, \tag{72}$$

and the fractional operator in Fourier space is represented by $(-\Delta)^{3/4} e^{ikx} = |k|^{3/2}\, e^{ikx}$. The NESS of this system was analyzed in detail in [26–28] where the scaling $j \sim N^{-1/2}$ and a closed form for the non-linear temperature profile were established. More recently the fractional-equation-type description of this system in the open set-up was further discussed in [37]. We summarize below some of these results for the open system. We first discuss the steady state and relaxation properties which is followed by the discussion on the evolution of the fluctuations and in the end we discuss the role of boundary conditions.

4.2.1. Typical Behavior of Temperature, Current, and Other Correlations

In the open system HCME set-up, the two ends are attached to two reservoirs at temperatures T_ℓ and T_r. The equations of motion are now modified by adding Langevin forces to the 1st and the Nth particles:

$$\begin{aligned}\dot{q}_i &= p_i,\\ \dot{p}_i &= (1-\delta_{i,1}-\delta_{i,N})\omega^2(q_{i+1}-2q_i+q_{i-1})\\ &\quad+\delta_{i,1}[\omega^2(q_2-\zeta q_1)-\lambda p_1+\sqrt{2\lambda T_\ell}\xi_1]\\ &\quad+\delta_{i,N}[\omega^2(q_{N-1}-\zeta q_N)-\lambda p_N+\sqrt{2\lambda T_r}\xi_N],\\ &\quad+\text{stochastic exchange of momenta at rate }\gamma, \end{aligned} \tag{73}$$

for $i = 1, 2 \ldots, N$, where $\xi_{1,N}$ are independent Gaussian white noises with mean zero and unit variance, λ is the friction coefficient, and the parameter ζ has been introduced to describe different boundary conditions. Free boundary conditions correspond to $\zeta = 1$ while fixed boundary conditions are given by $\zeta = 2$. We will first discuss the fixed boundary case, i.e., $\zeta = 2$.

We will be interested not only in NESS properties, such as the form of the temperature profile and the current scaling with system size but also in the temporal evolution of the temperature from some arbitrary initial profile to the steady state form. As in the case of the HCVE model, the analytical tractability of the HCME system comes from the fact that the evolution of the two-point correlations is given by a closed set of equations. The two point correlations include $\mathbf{U}_{i,j} = \langle q_i q_j\rangle$, $\mathbf{V}_{i,j} = \langle p_i p_j\rangle$, and $\mathbf{Z}_{i,j} = \langle q_i p_j\rangle$ and the local temperature defined as $T_i(t) = \langle p_i^2\rangle$ consists of the diagonal elements of $\mathbf{V}$. For these, one obtains a set of coupled linear equations, similar in form to Equation (54), which one needs to solve with appropriate boundary and initial conditions. The number of equations in this case is much larger than the HCVE case and hence it is even more difficult to solve them analytically for finite N. Observations from numerical solutions of these equations reveal [27] that for large N, the temperature field T_i and the correlations $\mathbf{z}^+_{i,j} = \left(\mathbf{Z}_{i,j} - \mathbf{Z}_{i-1,j} + \mathbf{Z}_{j,i} - \mathbf{Z}_{j-1,i}\right)/2$ show the following scaling behaviors: $T_i(t) = \mathcal{T}(i/N, t/N^{3/2})$ and $\mathbf{z}^+_{i,j} = \frac{1}{\sqrt{N}}\mathcal{C}\left((|i-j|)/N^{1/2}, (i+j)/2N, t/N^{3/2}\right)$. Hence, for large N it is instructive to construct solutions of these scaling forms. Inserting these scaling forms in the discrete equations of the two point correlations and taking the large N limit one finds, at leading order in $1/\sqrt{N}$, the following partial differential equations [27]

$$\gamma^2\partial_u^4\mathcal{C}(u,v,\tau) = \omega^2\partial_v^2\mathcal{C}(u,v,\tau), \tag{74}$$

$$\partial_v T(v,\tau) = -2\gamma\,\partial_u\mathcal{C}(u,v,\tau)\big|_{u\to 0}, \tag{75}$$

$$\partial_\tau T(v,\tau) = \omega^2\partial_v\mathcal{C}(u,v,\tau)|_{u\to 0}, \tag{76}$$

where the scaling variables $u = |i-j|/\sqrt{N}, v = (i+j)/2N, \tau = t/N^{3/2}$ are defined over the domain $u \in [0,\infty)$ and $v \in [0,1]$ with boundary conditions $\mathcal{C}(u,0,\tau) = \mathcal{C}(u,1,\tau) = 0, \mathcal{C}(\infty,v,\tau) = 0, \partial_u^3 C(0,v,\tau) = 0$ and $T(0,\tau) = T_\ell$ and $T(1,\tau) = T_r$. We again note that for the isolated infinite system, one can follow the same procedure as above, but now replacing the scale parameter $1/N \to a$ where a is the lattice spacing, to obtain the same set of Equations (74–76) with a different domain $\{-\infty \le u \le \infty;\ -\infty \le v \le \infty\}$. Defining Fourier transforms $\mathcal{T}(v,\tau) = \int_{-\infty}^{\infty} dk\hat{\mathcal{T}}_k(\tau)e^{-ikv}/(2\pi)$ and $\mathcal{C}(u,\tau) = \int_{-\infty}^{\infty} dk\hat{\mathcal{C}}_k(u,\tau)e^{-ikv}/(2\pi)$ in the variable v, we get

$$\partial_u^4\hat{\mathcal{C}}_k(u,\tau) = -\frac{\omega^2k^2}{\gamma^2}\hat{\mathcal{C}}_k(u,\tau), \tag{77}$$

$$ik\hat{\mathcal{T}}_k(\tau) = 2\gamma\,\partial_u\hat{\mathcal{C}}_k(u,\tau)\big|_{u=0}, \tag{78}$$

$$\partial_\tau\hat{\mathcal{T}}_k(\tau) = -ik\omega^2\hat{\mathcal{C}}_k(0,\tau)\,. \tag{79}$$

Solving the first Equation (77), with the condition that correlations vanish at $u = \pm\infty$, $\partial_u^3\mathcal{C}(u=0,v,\tau) = 0$ and requiring that $\hat{\mathcal{C}}_k(u,\tau)$ is real [since $\mathcal{C}(u,v,\tau) = \mathcal{C}(u,-v,\tau)$], we get

$$\begin{aligned}\hat{\mathcal{C}}_k(u,\tau) &= A_k(\tau)\left[\cos\left(\sqrt{\frac{\omega}{2\gamma}}|k|^{1/2}u\right)\right.\\ &\quad\left.-\sin\left(\sqrt{\frac{\omega}{2\gamma}}|k|^{1/2}u\right)\right]\exp\left(-\sqrt{\frac{\omega}{2\gamma}}|k|^{1/2}|u|\right)\end{aligned} \tag{80}$$

The Equation (78) relates the constant A_k to $\hat{\mathcal{T}}_k$:

$$A_k(\tau) = -\frac{ik}{2\sqrt{2\gamma\omega|k|}}\hat{\mathcal{T}}_k. \tag{81}$$

Using Equations (80, 81) in Equation (79) we get

$$\partial_\tau\hat{\mathcal{T}}_k(\tau) = -\frac{\omega^{3/2}}{2\sqrt{2\gamma}}|k|^{3/2}\hat{\mathcal{T}}_k(\tau)\,, \tag{82}$$

which is the Fourier representation of Equation (72), with $\bar{\kappa} = \omega^{3/2}/2\sqrt{2\gamma}$.

We now go back to the open system case where the solution is more non-trivial. The boundary conditions for this case are given by $\mathcal{C}(u,0,\tau) = \mathcal{C}(u,1,\tau) = 0, \mathcal{C}(\infty,v,\tau) = 0, \partial_u^3 C(0,v,\tau) = 0$ and $T(0,\tau) = T_\ell$ and $T(1,\tau) = T_r$ (see [27, 37]). Note that the domain of the v variable in [27] is $v \in (-1,1)$.

In the steady state, the analytical solutions of these equations [with $\partial_\tau T(v,\tau) = 0$] were obtained in [26] and are given by

$$\begin{aligned}\mathcal{T}_{ss}(v) &= \overline{T} + \Delta T\Theta(v),\ \text{ where }\ \Theta(v)\\ &= \frac{\pi^{3/2}}{[\sqrt{8}-1]\zeta(3/2)}\sum_{n\ odd}\frac{\phi_n(v)}{\lambda_n^{3/4}},\end{aligned} \tag{83}$$

$$\begin{aligned}\mathcal{C}_{ss}(u,v) &= -\frac{\Delta T\sqrt{\pi}}{2\sqrt{\omega\gamma}[\sqrt{8}-1]\zeta(3/2)}\sum_{n\ odd}\exp\left(-\sqrt{\frac{n\pi\omega}{2\gamma}}u\right)\\ &\quad\left[\cos\left(\sqrt{\frac{n\pi\omega}{2\gamma}}u\right)-\sin\left(\sqrt{\frac{n\pi\omega}{2\gamma}}u\right)\right]\frac{\sin(n\pi v)}{n},\end{aligned} \tag{84}$$

where $\overline{T} = (T_\ell + T_r)/2$, $\Delta T = T_\ell - T_r$ and $\phi_n(v) = \delta_{n,0} + (1-\delta_{n,0})\sqrt{2}\cos(n\pi v)$ for $n \ge 0$. From Equation (76) we see that the current $J = -\omega^2\mathcal{C}(u,v,\tau)|_{u\to 0}$ is given by

$$J = \frac{(\omega\pi)^{3/2}}{8\sqrt{\gamma}[\sqrt{8}-1]\zeta(3/2)}\Delta T\,. \tag{85}$$

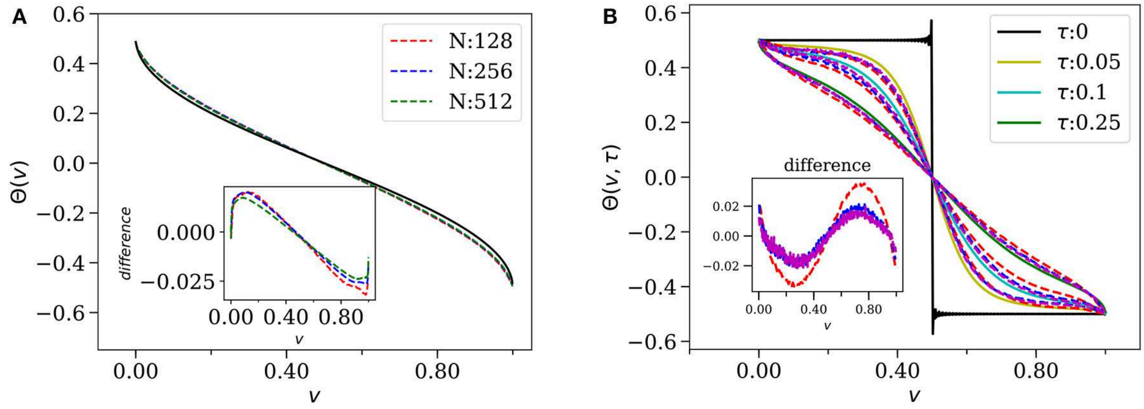

FIGURE 12 | (A) Comparison of temperature profiles obtained theoretically from Equation (83) (solid black line) with the same obtained from direct numerical simulations of microscopic system for $N = 128, 256, 512$. The agreement between theory and numerics becomes better for larger N as can be seen in the inset where the difference between theoretical curve (Equation 83) and simulation data are plotted for various system sizes. **(B)** Time evolution of temperature starting from an initial step profile. The function $\Theta(v, \tau) = [\mathcal{T}(v, \tau) - \bar{T}]/\Delta T$, with $\mathcal{T}(v, \tau)$ given by Equation (93), is plotted and compared with direct numerical simulations. The dashed lines indicate simulation results for the time-evolution in HCME at different scaled times (τ), for system sizes $N = 128$ (red), $N = 256$ (blue), $N = 512$ (magenta), while the solid lines are obtained from the theory. The boundary temperatures were fixed at $T_\ell = 1.5$ and $T_r = 0.5$ (adapted from Kundu et al. with permission from [37] Copyright SISSA Medialab Srl, IOP Publishing).

Note that both the temperature profile and the current are independent of the friction coefficient λ. This is true only for the special case of fixed boundary conditions. Note also that the temperature profile in the steady state is intrinsically non-linear as can be seen in **Figure 12A** where one observes excellent agreement with data from simulations of the microscopic dynamics in Equation (73). It can be shown that the temperature profile at both boundaries scales as $\sim (\delta v)^\mu$ with $\mu = 1/2$ where δv is the distance from the boundary [26]. This singular behavior of $T_{ss}(v)$ is a common signature of anomalous transport and it is characterized by the meniscus exponent μ. The value of μ however is non-universal and depends strongly on the boundary conditions. We will discuss this in section 4.2.3.

To solve for the approach toward the above steady state results, we proceed as for the HCVE model. Separating the relaxation part and the steady state part we write

$$\mathcal{C}(u, v, \tau) = \mathcal{C}_{ss}(u, v) + \mathcal{C}_r(u, v, \tau), \tag{86}$$

$$\mathcal{T}(v, \tau) = \mathcal{T}_{ss}(v) + \mathcal{T}_r(v, \tau). \tag{87}$$

Since the relaxation parts satisfy Dirichlet boundary conditions $\mathcal{C}_r(u, 0, \tau) = \mathcal{C}_r(u, 1, \tau) = 0$ and $\mathcal{T}_r(0, \tau) = \mathcal{T}_r(1, \tau) = 0$, we expand them in the Dirichlet basis $\alpha_n(v) = \sqrt{2}\sin(n\pi v)$ for $n = 1, 2, 3, \ldots$ as

$$\mathcal{C}_r(u, v, \tau) = \sum_{n=1}^{\infty} \hat{\mathcal{C}}_n(u, \tau)\alpha_n(v), \tag{88}$$

$$\mathcal{T}_r(v, \tau) = \sum_{n=1}^{\infty} \hat{\mathcal{T}}_n(\tau)\alpha_n(v)\,. \tag{89}$$

After inserting these expansions in Equations (74–76) and using the orthogonality property of the $\alpha_n(v)$ functions, one gets the following (infinite order) matrix equation for the evolution of the components $\hat{\mathcal{T}}_n$:

$$\dot{\hat{\mathcal{T}}}_n = -\bar{\kappa}\sum_{l=1}^{\infty}\mathbb{L}^p_{nl}\hat{\mathcal{T}}_l, \quad n = 1, 2, \ldots, \infty,$$

$$\text{where: } \mathbb{L}^p_{nl} = \left[\mathcal{S}\Lambda^{3/4}\mathcal{S}^\dagger\right]_{nl}, \tag{90}$$

with $\mathcal{S}_{nl} = \langle \alpha_n | \phi_l \rangle = \int_0^1 dz \alpha_n(z)\phi_l(z)$, $\Lambda_{nl} = \lambda_n\delta_{nl}$ is a diagonal matrix with $\lambda_n = (n\pi)^2$ and the constant $\bar{\kappa} = \omega^{3/2}/(2\sqrt{2\gamma})$. In the position basis, the above equation can be written as

$$\partial_\tau \mathcal{T}(v, \tau) = -\bar{\kappa}\mathbb{L}^p\mathcal{T}(v, \tau), \tag{91}$$

where the operator $\mathbb{L}^p$ is represented as

$$\begin{aligned}\mathbb{L}^p_{nl} &= \left[\mathcal{S}\Lambda^{3/4}\mathcal{S}^\dagger\right]_{nl} \\ &= \langle\, \alpha_n \,|\left[\sum_{m=0}^{\infty}\lambda_m^{3/4}|\, \phi_m \,\rangle\langle\, \phi_m \,|\right]|\, \alpha_l \,\rangle, \;\; \forall\;\; n, l = 1, 2, \ldots, \infty\end{aligned}$$

From this representation one can identify the action of $\mathbb{L}^p$ on the set of basis functions ϕ_m (which satisfy Neumann boundary conditions) [4, 37].

$$\mathbb{L}^p |\, \phi_m \,\rangle = \lambda_m^{3/4} |\, \phi_m \,\rangle\,. \tag{92}$$

For the time evolution we need the eigenspectrum of $\mathbb{L}^p$ with Dirichlet boundary conditions. The eigenstates $\psi_n(y)$ and eigenvalues μ_n can be obtained by diagonalizing the matrix $\mathbb{L}^p_{nm}$ in Equation (90). In [27] the spectrum was obtained numerically by diagonalizing truncated form of the infinite-dimensional matrix $\mathbb{L}^p$. An alternate method was recently proposed in [37]

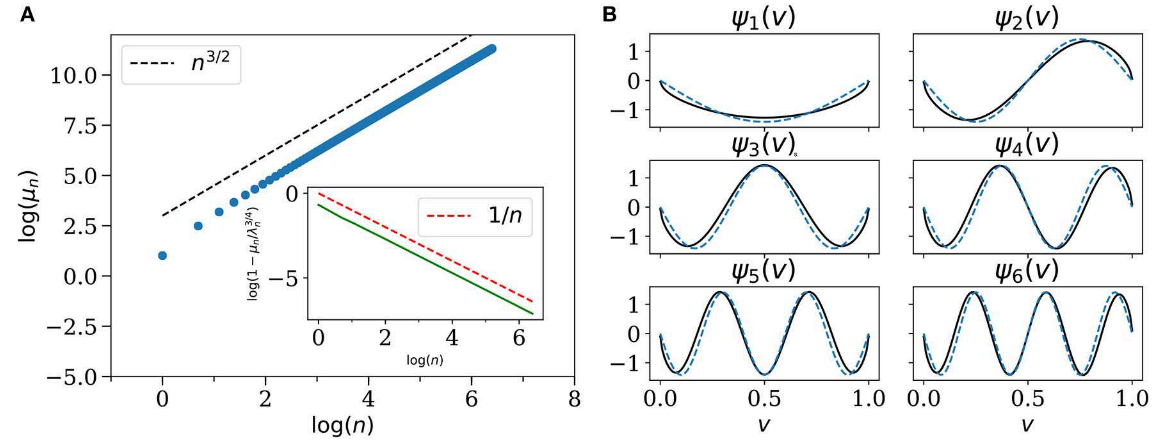

FIGURE 13 | (A) Eigenvalues of the fractional operator in Equation (90) corresponding to Dirichlet boundary conditions. For large n, the slope is seen to approach that of $n^{3/2}$ (black dashed line). For small n there is a systematic difference between the Dirichlet and Neumann eigenvalue and the inset plots the difference between the two. For large n the difference between the two decreases inversely with n. **(B)** The first six eigenvectors, $\psi_n(v)$ (black lines), are compared to the corresponding Dirichlet eigenfunctions of Laplacian, i.e., sin-functions (blue dashed lines). The eigenstates are different from sin-functions, especially near the boundaries, even for large n (adapted from Kundu et al. with permission from [37] Copyright SISSA Medialab Srl, IOP Publishing).

which gives the spectrum directly as roots of a transcendental equation and explicit series form expressions for the wave functions in the ϕ_n basis. The numerical values of the computed eigenvalues are plotted in **Figure 13A**, where we see that for large n the eigenvalues scale as $\mu_n \approx (n\pi)^{3/2}$. At smaller values n there is a systematic deviation from the Neumann spectrum, λ_n, for example the first three eigenvalues (μ_n) are given by $\mu_1 \approx 2.75, \mu_2 \approx 12.02, \mu_3 \approx 24.22$. As shown in the inset of **Figure 13A** the relative difference between μ_n and λ_n decreases as $1/n$. The first few numerically computed eigenvectors are shown in **Figure 13B** where they are compared with the basis functions α_n which are the Dirichlet eigenfunctions of the usual Laplacian. We observe that they are different and in particular show a non-analytic behavior at the boundaries. For example near the boundaries one finds $\psi_n(\delta v) \sim \sqrt{\delta v}$, where δv is the distance from the boundaries. The eigenspectrum of fractional operator in a bounded domain, with different boundary conditions, has been discussed earlier in the literature, using somewhat heuristic approaches [75, 80–82]. However, their connection to the spectrum of $\mathbb{L}^{\not{f}}$ defined here is unclear.

Using these Dirichlet eigenvalues and eigenfunctions, we follow the steps leading to Equation (71) and obtain the following for the time evolution of an arbitrary initial profile:

$$\mathcal{T}_r(v,\tau) = \int_0^1 dv' \left[\sum_{l=1}^{\infty} \psi_l(v)\psi_l(v')e^{-\bar{\kappa}\mu_l\tau}\right] \mathcal{T}(v',0)\,. \tag{93}$$

In **Figure 12B**, a numerical verification of the above time evolution is shown. We note that Equation (91) can be cast in the form of a continuity equation $\partial_\tau \mathcal{T}_r(v,\tau) = -\partial_v j(v,\tau)$ with j in the form [37]

$$j(v,\tau) = -\bar{\kappa}\int_0^1 dv' \mathcal{K}(v,v')\partial_{v'}\mathcal{T}(v',\tau)\,, \tag{94}$$

where the kernel $\mathcal{K}$ is defined through it's action on a test function $g(v) = \sum_{n=1}^{\infty} g_n\alpha_n(v)$

$$\int_0^1 dv' \mathcal{K}(v,v')g(v') = \sum_{n=1}^{\infty} \frac{1}{\sqrt{n\pi}} g_n\alpha_n(v)\,. \tag{95}$$

The operator $\mathbb{L}^{\not{f}}$ can be expressed in terms of $\mathcal{K}$ as

$$\langle v|\mathbb{L}^{\not{f}}|v'\rangle = \partial_v \mathcal{K}(v,v')\partial_{v'}\,. \tag{96}$$

4.2.2. Characterization of Fluctuations

The discussions till now describe only the average or typical behavior of the conserved density fields and the associated current fields. The equation (91) describes the evolution of the average temperature profile as well as the evolution of a localized energy pulse in a thermally equilibrated system. However, other interesting aspects that characterize the NESS are the distributions of density and current fluctuations, long range correlations and the large deviations. To study these aspects, one requires to have a stochastic description of the evolution at the macroscopic length and time scales.

In the context of diffusive transport, a general framework called the macroscopic fluctuation theory has been developed in the last decade which allows to provide such a description for fluctuations [83–85]. Starting from the microscopic description of the system one can show that in the diffusive scaling limit, the fluctuating energy density field $e(x,t)$ and the corresponding fluctuating current $J_e(x,t)$ still satisfy the continuity equation but now, in addition to the regular diffusive part of the current, there is a fluctuating part $J_e(x,t) = -D(e)\frac{\partial e(x,t)}{\partial x} + \sqrt{\chi(e)}\,\eta(x,t)$, where $\chi(e(x,t))$ is the mobility of the system which is related to the diffusivity $D(e(x,t))$ through the fluctuation dissipation relation and $\eta(x,t)$ is a mean zero white Gaussian noise with the properties $\langle \eta(x,t)\rangle = 0$ and $\langle \eta(x,t)\eta(x',t')\rangle = \delta(x-x')\delta(t-t')$. The evolution equation for the energy density is given by

$$\frac{\partial e(x,t)}{\partial t} = \frac{\partial}{\partial x}\left[D(e)\frac{\partial}{\partial x}e(x,t) - \sqrt{\chi(e)}\,\eta(x,t)\right]. \qquad (97)$$

Starting from this stochastic equation one can compute various moments, fluctuations and correlations of $e(x,t)$ and $j(x,t)$ both in stationary and non-stationary regime. This description also allows one to compute the probabilities of observing atypical density and current profiles which are characterized by large deviation functions. The whole program has been established and applied in several microscopic systems which show diffusive behavior at macroscopic scales. We ask if a similar procedure works for our system, displaying anomalous transport, and described by the fractional diffusion equation. Recently such an extension has been proposed in [37] which we now describe. The approach in [37] is to include a noise part in the current expression in such a way that the fluctuation-dissipation theorem is satisfied. For a system in equilibrium at temperature T this leads to the unique choice

$$\begin{aligned} \partial_\tau e(v,\tau) &= -\partial_v j(v,\tau), \\ \text{with } j(v,\tau) &= -\bar{\kappa}\int_0^1 dv'\mathcal{K}(v,v')\partial_{v'}e(v',\tau) \\ &\quad -\sqrt{2\bar{\kappa}}\,T\int_0^1 dv' B(v,v')\eta(v',\tau), \end{aligned} \qquad (98)$$

where $\eta(v,\tau)$ is white Gaussian noise with $\langle \eta(v,\tau)\rangle = 0$, $\langle \eta(v,\tau)\eta(v',\tau')\rangle = \delta(v-v')\delta(\tau-\tau')$ and the fluctuation-dissipation theorem implies the relation

$$\mathcal{K}(v,v') = BB^\dagger(v,v')\,, \qquad (99)$$

with $B^\dagger$ defined as the adjoint of B. It was verified in Kundu et al. [37] that Equation (98) reproduces correctly results on energy correlations and current fluctuations in equilibrium. Extending this approach to the non-equilibrium situation was also attempted in [37] and a conjecture for long-range correlations in the NESS was proposed.

4.2.3. Role of Boundary Conditions: Hydrodynamic Theory

In the previous section we have mainly discussed the fixed boundary condition, in which case we have learned that the transport behavior in HCME model is anomalous with exponent $\alpha = 1/2$ and the Fourier's law gets modified to a non-local linear response relation as in the form of Equation (94) with an explicit form for the kernel $\mathcal{K}(v,v')$ given in Equation (95). Also in this case the evolution of the temperature profile is given by a non-local equation (91) with $\mathbb{L}^p$ defined through Equations (95) and (96). In this section we would like to understand the dependence of these results on the choice of boundary conditions. In particular we focus on the case of free boundary conditions, i.e., for $\zeta = 1$ in Equation (73).

Energy transport in HCME with free boundary condition was studied numerically in [28] where it was observed that the system size scaling of the current j in the steady state is again proportional to $1/\sqrt{N}$, as for fixed BC. However, in contrast to the fixed BC case, the proportionality constant depends on the friction coefficient λ. It was also observed that the temperature profile in this case is non-linear but the associated meniscus exponent μ depends strongly on the relative values of λ and ω. For this case finding the appropriate boundary conditions for Equations (74, 75, 76) is a difficult problem [28] and has so far not been possible. A different approach, based on linear response theory and NFH was proposed in [36] and we present some details here.

This approach starts with the following non-local linear response result

$$j(x) = -\int_0^N dy\, K_N(x,y)\,\frac{dT(y)}{dy}, \qquad (100)$$

which is based on a linear response calculation as done in [67] but around a local equilibrium state characterized by a temperature profile. According to this calculation the Kernel is related to the equilibrium current-current correlation [36]

$$K_N(x,y) = \frac{1}{\bar{T}^2}\int_0^{aN} dt\,\langle j(x,t)j(y,0)\rangle_{eq}, \qquad (101)$$

where $j(x,t)$ is the local current and a is a constant. For systems with AHT we expect $N\langle j(x,t)j(y,0)\rangle_{eq} \sim t^{1-\alpha}$ which means that $K_N(x,y)$ should scale as $N^{\alpha-1}$. Hence we expect that the limit

$$\mathcal{K}(v,v') = \lim_{N\to\infty} N^{1-\alpha}K_N(vN,v'N), \qquad (102)$$

exists, which implies also that $j = J/N^{1-\alpha}$ with J given by

$$J = -\Delta T\int_0^1 dv'\,\mathcal{K}(v,v')\,\partial_{v'}\Theta(v'). \qquad (103)$$

where the temperature profile $T(x)$ is assumed to have the scaling form $T(x) = \bar{T} + \Delta T\,\Theta(x/N)$. This equation can then be used to compute the NESS temperature profile and also the current. The remaining task now is to compute the kernel $\mathcal{K}(v,v')$.

For HCME, the kernel $\mathcal{K}(u,v)$ has recently been computed in [36] using the techniques of NFH as introduced in section 3.2. Following this procedure for the HCME model, one finds that on hydrodynamic length and time scales, a random fluctuation created inside the system decomposes into two ballistically moving but diffusively spreading sound modes $\phi_\pm$ and a stationary heat mode ϕ_0. In terms of the local stretch $r_i = q_{i+1} - q_i$ and energy $e_i = p_i^2/2 + \omega^2 r_i^2/2$, the sound modes and the heat mode are expressed as $\phi_\pm = \omega r \mp p$ and $\phi_0 = e$, respectively. The evolution of these modes are given by [4]

$$\begin{aligned} \partial_t\phi_\pm &= -\partial_x[\pm c_s\phi_\pm - D\partial_x\phi_\pm - \sqrt{2D}\eta_\pm], \\ \partial_t\phi_0 &= -\partial_x[G(\phi_+^2 - \phi_-^2) - D_0\partial_x\phi_0 - \sqrt{2D_0}\eta_0], \end{aligned} \qquad (104)$$

where $c_s = \omega$ is the speed of sound, η_+, η_0 and η_- are uncorrelated Gaussian white noises, $G = \frac{\omega}{4}$ and D and D_0 are phenomenological diffusion coefficients.

The instantaneous energy current can be read from (104),

$$j(x,t) = G[\phi_+^2(x,t) - \phi_-^2(x,t)], \tag{105}$$

neglecting the sub-dominant terms arising from the momentum exchange and the noises $\eta_\pm$ [62]. The stochastic momentum exchange process generate a diffusive contribution (see Equation 104) which becomes sub-leading at large N and the noises $\eta_\pm$ also do not contribute since their time averages vanish.

In order to compute the kernel in (101) using the form of $j(x,t)$ in (105), one needs to solve the equations of $\phi_\pm$ in (104) inside a finite domain with suitable BCs. At this point we would like to mention that originally the NFH theory was formulated for an infinite domain [62]. The work in [36] provides an extension to incorporate boundary conditions for a finite domain, in the context of the HCME model. As the equations for ϕ_+ and ϕ_- are independent of ϕ_0, it is straightforward to write the solution in terms of the appropriate Green's function, as shown later.

We now discuss how to get the boundary conditions of fields $\phi_\pm$. The strategy that has been followed in [36] is to introduce extra stretch and momentum variables in such a way that the equations at the boundary points ($i = 1, N$) are also included into the structure of the bulk equations. This can be achieved by introducing additional conditions, which after appropriate coarse-graining become the hydrodynamic BCs. To explain the procedure let us consider the free BC case as an example. We first introduce an extra dynamical variable r_0 in such a way that the form of the equation satisfied by p_1 becomes same as that of the bulk evolution equations with the condition

$$\omega^2 r_0 = \lambda p_1, \tag{106}$$

where we have neglected the noise terms in (73). This provides one BC. We need another BC as the Equation (104) is of second order in space. As before, introducing p_0 in such a way that one can make r_0 to satisfy a regular equation of motion in the bulk at the cost of an extra condition, provides the second BC. Taking single derivative with respect to time on both sides of the first condition yields

$$p_1 - p_0 = \lambda(r_1 - r_0). \tag{107}$$

One can get two other boundary conditions by applying similar procedure to the equations of the last (Nth) particle. Finally, coarse-graining over space and expressing the stretch r and momenta p in terms of the sound modes $\phi_\pm$, we obtain the following BCs for free boundaries:

$$\begin{aligned} (\partial_x\phi_+ + w\,\partial_x\phi_-)|_{x=0} = (\phi_+ - w\,\phi_-)|_{x=0} &= 0, \\ (\partial_x\phi_- + w\,\partial_x\phi_+)|_{x=N} = (\phi_- - w\,\phi_+)|_{x=N} &= 0 \end{aligned} \tag{108}$$

where

$$w = \frac{\lambda - \omega}{\lambda + \omega}. \tag{109}$$

These BCs can be interpreted physically as some sort of partially "reflecting" boundaries. The BCs on the first (second) line of Equation (108) mean that when a ϕ_+ (resp. ϕ_-) Gaussian peak hits the right (resp. left) boundary, it gets reflected as a ϕ_- (resp. ϕ_+) Gaussian peak with area under the peak reduced by a factor w. This feature has been observed in numerical simulations and the validity of (108) has been confirmed [36]. There are two interesting cases $w = 0$ and $w \to 1$. In case of *resonance* (also called impedance matching) $\lambda = \omega$, i.e., $w = 0$ [66], once a $\phi_\pm$ peak hits the boundary nothing gets reflected because everything gets absorbed at the boundary reservoirs. On the other hand, $w \to 1$ corresponds to almost perfectly reflecting case. This situation arises for the fixed BCs in the microscopic dynamics. Following a similar procedure as done for free BCs, it is possible to show that one arrives at the same hydrodynamic BCs Equation (108) except now $w = 1$. From Equation (109), one can easily see that the $w \to 1$ limit is achieved for $\lambda \to \infty$. In this limit, the 1st and the Nth particles hardly move, i.e., their positions q_1 and q_N stay very close to 0 for all times due to infinite dissipation and therefore mimic the fixed BCs for the microscopic dynamics. So for fixed BCs we have the hydrodynamic BCs Equation (108) with $w = 1$.

Since the hydrodynamic equations (104) for ϕ_+ and ϕ_- along with the BCs (108) are linear, it is easy to solve them for arbitrary initial condition. The solutions are best expressed in terms of the four Green's functions $f_{\sigma,\tau}(x,y,t)$ for $\sigma, \tau = \pm$, as

$$\begin{aligned} \phi_\sigma(x,t) = \sum_{\tau=\pm} \Bigg[&\int_{y=0}^{N} \mathrm{d}y f_{\sigma,\tau}(x,y,t)\phi_\tau(y,0) \\ &+ \sqrt{2D}\int_{y=0}^{N}\mathrm{d}y \int_{t'=0}^{t} \mathrm{d}t' f_{\sigma,\tau}(x,y,t-t')\partial_y \eta_\tau(y,t') \Bigg], \end{aligned} \tag{110}$$

$$\text{where,}\quad f_{\sigma,\tau}(x,y,t) = \sum_{n=-\infty}^{\infty} w^{2n+\frac{\sigma-\tau}{2}} \frac{\exp\left(-\frac{(x-\sigma\tau y+2\sigma nN-\sigma c_s t)^2}{4Dt}\right)}{\sqrt{4\pi Dt}}, \tag{111}$$

with $w = 1$ for fixed BCs and $w = \frac{\lambda-\omega}{\lambda+\omega}$ for free BCs.

Using this expression in Equation (105) one finally gets from Equations (101, 102) the following expression for the kernel:

$$\begin{aligned} \mathcal{K}(v,v') &= A\,\mathcal{K}_R, \quad \text{where } \mathcal{K}_R \\ &= \frac{1}{\sqrt{2\pi}} \sum_{n=-\infty}^{\infty} \left[\frac{R^{|2n|}}{\sqrt{|2n+v-v'|}} - \frac{R^{|2n+1|}}{\sqrt{|2n+v+v'|}} \right], \end{aligned} \tag{112}$$

where the constant $A = \frac{G^2 S^2}{\bar{T}^2\sqrt{Dc_s}}$ with $S = \langle\phi_+(x,0)^2\rangle_{\text{eq}} = \langle\phi_-(x,0)^2\rangle_{\text{eq}} = 2\bar{T}$ and $R = w^2$. The diffusion constant D appearing in the equation for $\phi_\pm$ arises from the exchange mechanism and it can be shown from a microscopic calculation that $D = \gamma/2$. This then gives $A = \omega^{3/2}/(2\sqrt{2\gamma})$ which we note coincides with the expression for $\bar{\kappa}$ in Equation (72), and so we identify $A = \bar{\kappa}$. One can use this kernel in Equation (103) to compute the current and the temperature profile $\Theta(v)$.

Let us define the Greens function, $\mathcal{G}_R$, corresponding to the kernel $\mathcal{K}_R$ through the equation

$$\int_0^1 d\nu'' \mathcal{K}_R(\nu, \nu'') \mathcal{G}_R(\nu'', \nu') = \delta(\nu - \nu'). \tag{113}$$

Then Equation(103) can be inverted to give

$$\partial_\nu \Theta(\nu) = -\frac{J}{\bar{\kappa}\Delta T} \int_0^1 d\nu' \mathcal{G}_R(\nu, \nu') \tag{114}$$

Solving this equation with the boundary conditions $\Theta(0) = 1/2, \Theta(1) = -1/2$ gives us the expressions for the current and temperature profile

$$J = \bar{\kappa}\Delta T \left[\int_0^1 \int_0^1 d\nu' d\nu'' \mathcal{G}_R(\nu', \nu'') \right]^{-1}, \tag{115}$$

$$\Theta(\nu) = \frac{1}{2} - \frac{\int_0^\nu \int_0^1 d\nu' d\nu'' \mathcal{G}_R(\nu', \nu'')}{\int_0^1 \int_0^1 d\nu' d\nu'' \mathcal{G}_R(\nu', \nu'')}. \tag{116}$$

One uses this in Equation (103) to solve for the temperature profile $\Theta(\nu)$. The above analysis, based on linear response calculation, assumes $|\Delta T| << \overline{T}$. However, for HCME, one observes that the quadratic correlations satisfy a closed set of linear equations with a source term proportional to ΔT [26]. Hence the temperature profile $\Theta(\nu)$ in (116) is also valid for any ΔT.

It turns out the Equation (114) can be solved analytically and exact expressions of the temperature profile $\Theta(\nu)$ can be obtained in the following two limiting cases—

(i) Free resonant case $R = 0$: In this case the kernel is simply given $\mathcal{K}_0 = 1/\sqrt{2\pi\,|\nu - \nu'|}$ which is same as that of an infinite system. For this kernel, the solution of Equation (103) can be directly written using standard results on solution of integral equations [86] as

$$\partial_\nu \Theta(\nu) = -\frac{J}{\bar{\kappa}\Delta T} \frac{1}{\sqrt{\pi}\nu^{1/4}(1 - \nu)^{1/4}}. \tag{117}$$

This can be solved with the boundary conditions to give the temperature profile

$$\Theta_{R=0}(\nu) = \frac{1}{2} - \frac{\sqrt{\pi}\nu^{3/4}{}_2F_1\left(\frac{1}{4}, \frac{3}{4}; \frac{7}{4}; \nu\right)}{2\Gamma\left(\frac{3}{4}\right)\Gamma\left(\frac{7}{4}\right)}, \tag{118}$$

where ${}_2F_1$ is hypergeometric function, and the current

$$J = \bar{\kappa}\Delta T \frac{\pi}{2\Gamma^2(3/4)} \tag{119}$$

This profile is verified numerically in **Figure 14** (left panel), where we observe diverging derivatives at the boundaries. From the above expression it is possible to show that the meniscus exponent is $\mu = 3/4$.

(ii) Perfectly reflecting case $R \to 1$: As mentioned above this is equivalent to fixed BC for which the temperature profile, given in Equation (83), was computed from microscopic calculation in the previous section. In this case it is known [37] that the eigenfunctions of the operator $\mathcal{K}_R$ are precisely the sine-functions $\alpha_n(\nu)$, i.e.,

$$\int_0^1 d\nu' \mathcal{K}_R(\nu, \nu')\alpha_n(\nu') = (n\pi)^{-1/2}\alpha_n(\nu), \tag{120}$$

which is consistent with Equation (95). This then gives us the corresponding Green's function

$$\mathcal{G}_R(\nu, \nu') = \sum_{n=1}^{\infty} (n\pi)^{1/2} \alpha_n(\nu)\alpha_n(\nu'). \tag{121}$$

Using this and Equations (114, 115) we recover the exact expressions for the temperature profile and current given in Equations (83, 85) [37].

For free BCs with $\lambda \neq \omega$ we have $0 < R < 1$. In this case it is difficult to solve Equations (103, 112) analytically but numerical solutions have been obtained. In **Figure 14** (right panel) a comparison of the temperature profile obtained from the numerical solution and from direct microscopic simulations for $R = 1/2$ and one can observe excellent agreement. Note again that the temperature profile is singular at the boundaries. It turns out that the exponent μ characterizing this singularity depends on not only on α but also on R [66]. To determine this dependence we take a derivative with respect to ν of Equation (103) and get $\int_0^1 d\nu' \; \partial_\nu \mathcal{K}_R \; \partial_{\nu'} \Theta(\nu') = 0$. Although the integral is identically zero for all ν, the individual terms in the integrand have divergences. For example, the kernel diverges as $\mathcal{K}_R \sim |\nu - \nu'|^{-1/2}$ while $\partial_{\nu'}\Theta(\nu')$ diverges as $|\delta\nu|^{\mu-1}$. Requiring that all divergent integrals cancel each other, leads to the following relation between R and μ:

$$R = \frac{\int_0^1 \frac{q^{\mu-1} - q^{1/2-\mu}}{(1-q)^{3/2}} \mathrm{d}q}{\int_0^1 \frac{q^{\mu-1} + q^{1/2-\mu}}{(1+q)^{3/2}} \mathrm{d}q}. \tag{122}$$

The integrals can be performed explicitly to give

$$\mu = 1 - \frac{1}{\pi} \arctan\left(\frac{\sqrt{2 - \mathrm{R}^2} + \mathrm{R}}{\sqrt{2 - \mathrm{R}^2} - \mathrm{R}} \right), \tag{123}$$

which is plotted in **Figure 15** along with results extracted from the temperature profile obtained from direct numerical solution of Equation (103). We note that this result differs from the one conjectured in [66] though rather interestingly, the values of μ at $R = 0$ and $R = 1$ obtained from the two expressions agree. A generalization of the above result for arbitrary α is possible using the Lévy walk approach with the general kernel in Equation (42) which leads to an expression similar to Equation (122), now with the right hand depending explicitly on α.

5. SUMMARY AND OPEN QUESTIONS

Heat transport in a large class of one-dimensional systems with Hamiltonian or conservative stochastic dynamics is known

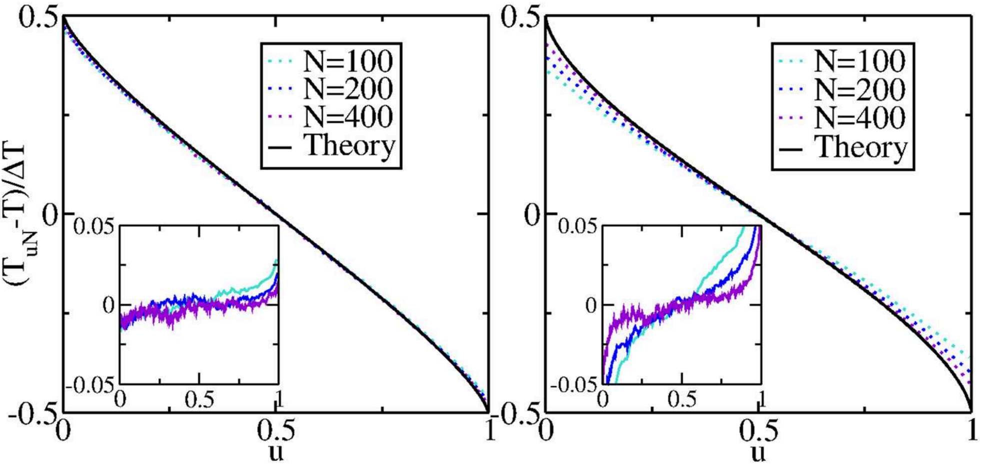

FIGURE 14 | Rescaled temperature profile for resonant BCs $R = 0$ (left) and free BCs with $R = \frac{1}{2}$ (right). In the main plots results of Monte-Carlo simulations for increasing system sizes $N = 100$, 200, and 400 are compared to the theoretical predictions given by Equation (118) for the $R = 0$ case (left panel) and the numerical solution of Equations (103, 112) with $R = \frac{1}{2}$ for the plots in the right panel. In the insets the differences between measurements and theory are shown. The other parameter values are $T_+ = 1.5$, $T_- = 0.5$, and $\omega = \gamma = 1$ (adapted from Cividini et al. with permission from [36] Copyright SISSA Medialab Srl, IOP Publishing).

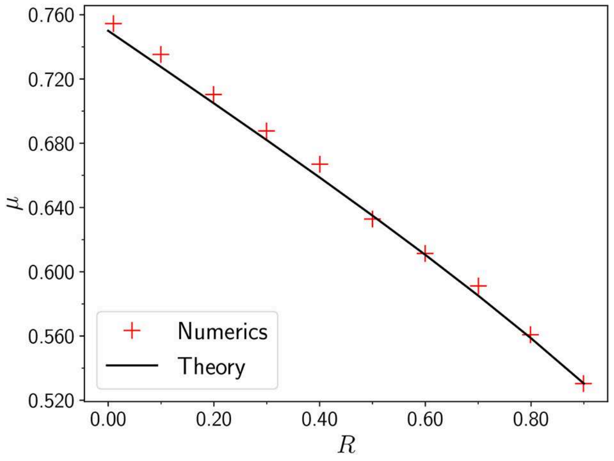

FIGURE 15 | The meniscus exponent μ as a function of R for $\alpha = 1/2$. The prediction from Equation (123) is plotted against the values obtained from the numerical solution of the integral Equation (103) with the kernel in Equation (112).

to be anomalous. Some typical signatures of anomalous transport include NESS studies which find that the thermal conductivity κ, diverges with system size N as $\kappa \sim N^{\alpha}$, and the temperature profile $T(x)$ is typically non-linear, with a singular dependence $T(\delta x) \sim (\delta x)^{\mu}$ for small distance δx from the boundary. In the closed system one finds that heat pulses and correlation functions spread super-diffusively and are associated to propagators that have the scaling form $t^{-\gamma}\mathcal{G}(t^{-\gamma}x)$. The scaling form is valid for times $|x| < ct$, where c is the sound speed in the system, beyond which time the correlations decay exponentially. The scaling function is given by the Lévy-stable distribution in the bulk and the finite cut-off leads to the width of the pulse scaling as $\sigma(t) \sim t^{\beta/2}$.

In this review we discussed these signatures of anomalous transport and showed how they can be understood within three different but related frameworks—(a) a phenomenological model where the heat carriers are taken to be Lévy walkers, (b) a microscopic phenomenological approach based on non-linear fluctuating hydrodynamics and (c) exact results obtained for certain stochastic models. The main picture that emerges is that anomalous heat transport can be understood by replacing Fourier's law in Equation (1) by a non-local fractional-type diffusion equation given in Equation (3), where the precise form of the kernel $K_R(x,y)$ depends on the specific set-up and boundary conditions. For the stochastic models the form of the kernel is known explicitly both for the closed system (infinite line) and the open system. In the Lévy walk picture, where the distribution of flight times has a power-law dependence $\sim 1/t^{\nu+1}$, the kernel has the asymptotic form $K_R(x,y) \sim 1/|x-y|^{\nu-1}$. We saw from the various approaches, that all the different exponents mentioned above are related to each other and in fact can be expressed in terms of the Lévy walk exponent as

$$\alpha = 2-\nu, \quad \beta = 3-\nu, \quad \gamma = 1/\nu. \tag{124}$$

For the Hamiltonian models that we discussed, namely the alternate mass hard-particle gas and the FPUT model, the various exponents are given by $\alpha = 1/3, \beta = 4/3, \gamma = 3/5$ and correspond to a Lévy-walk exponent $\nu = 5/3$. For the stochastic momentum exchange model we have $\alpha = 1/2, \beta = 3/2, \gamma = 2/3$ which corresponds to $\nu = 3/2$. The meniscus exponent μ is non-universal and depends on ν and on boundary conditions through a single dimensionless number R, which can be interpreted as the reflection coefficient of the Lévy walkers at the boundaries. In the context of the exactly solvable stochastic models, we discussed the spectrum of the fractional-type Laplacian operator [specified by the kernel $K_R(x,y)$] in the open set-up, and pointed out important differences with the spectrum of the usual Laplacian for diffusive processes.

We conclude by mentioning some outstanding open questions in the field.

- Hamiltonian systems—The Lévy walk behavior has been clearly observed in large number of simulations. The formalism of NFH gives a microscopic justification of the Lévy walk model and the fractional-diffusion type description of the heat mode. Some open questions include:
    1. A more rigorous microscopic derivation of the evolution equation of a localized heat pulse in an equilibrium system, to show that the central peak satisfies a fractional-diffusion type equation of a form similar to that in Equation (3).
    2. Extension of the NFH formalism to the non-equilibrium case to study transport in finite open system and understand the role of BCs. Detailed simulations are also required to understand the effect of BCs.
    3. Establishing the Lévy walk picture from a microscopic viewpoint?
- Stochastic systems—For the HCME model, the non-local version of Fourier's law has been established and the response kernel K_R computed so far using two methods: (i) exact microscopic method for the BC corresponding to $R = 1$ and (ii) using NFH for arbitrary R. Is it possible to extend the exact microscopic approach to find the non-local kernel K_R for general boundary conditions. Similarly for the HCVE it would be interesting to explore the role of BCs.
- For the HCME model, it has been possible to find the eigenspectrum of the non-local kernel K_R for the case $R = 1$ and it was observed that the eigenvalues for Dirichlet and Neumann boundary conditions differ (unlike for the usual Laplacian). Finding the spectrum of the non-local kernel K_R for general R, for Dirichlet and Neumann boundary conditions, is an interesting mathematical problem. The knowledge of the spectrum, namely eigenvectors and eigenvalues, enables one to study the time-evolution.
- For the HCME model we showed that it is possible to write a stochastic non-local equation (Equation 98) to describe equilibrium fluctuations. An open problem is to write such an equation in the non-equilibrium set-up. For diffusive systems this is given by Equation (97) and this equation enables one to compute long-range correlations in the NESS and large deviation functions.

AUTHOR CONTRIBUTIONS

All authors listed have made a substantial, direct and intellectual contribution to the work, and approved it for publication.

ACKNOWLEDGMENTS

AnK would like to acknowledge the support from DST grant under project No. ECR/2017/000634. AD would like to acknowledge support of the project EDNHS ANR-14-CE25-0011 of the French National Research Agency (ANR). AnK and AD would like to acknowledge the support from the project 5604-2 of the Indo-French Centre for the Promotion of Advanced Research (IFCPAR).

REFERENCES

1. Bonetto F, Lebowitz JL, Rey-Bellet L. Fourier's law: a challenge to theorists. In: A. Fokas, A. Grigoryan, T. Kibble, B. Zegarlinski, editors. *Mathematical Physics 2000*. Imperial College London; World Scientific (2000). p. 128–50. doi: 10.1142/9781848160224_0008
2. Lepri S, Livi R, Politi A. Thermal conduction in classical low-dimensional lattices. *Phys Rep.* (2003) **377**:1–80. doi: 10.1016/S0370-1573(02)00558-6
3. Dhar A. Heat transport in low-dimensional systems. *Adv Phys.* (2008) **57**:457–537. doi: 10.1080/00018730802538522
4. Lepri S, editor. *Thermal Transport in Low Dimensions: From Statistical Physics to Nanoscale Heat Transfer*. Vol. 921. Heidelberg: Springer (2016).
5. Lepri S, Livi R, Politi A. Heat conduction in chains of nonlinear oscillators. *Phys Rev Lett.* (1997) **78**:1896.
6. Dhar A. Heat conduction in a one-dimensional gas of elastically colliding particles of unequal masses. *Phys Rev Lett.* (2001) **86**:3554–7. doi: 10.1103/PhysRevLett.86.3554
7. Grassberger P, Nadler W, Yang L. Heat conduction and entropy production in a one-dimensional hard-particle gas. *Phys Rev Lett.* (2002) **89**:180601. doi: 10.1103/PhysRevLett.89.180601
8. Cipriani P, Denisov S, Politi A. From anomalous energy diffusion to Levy walks and heat conductivity in one-dimensional systems. *Phys Rev Lett.* (2005) **94**:244301. doi: 10.1103/PhysRevLett.94.244301
9. Basile G, Bernardin C, Olla S. Momentum conserving model with anomalous thermal conductivity in low dimensional systems. *Phys Rev Lett.* (2006) **96**:1–4. doi: 10.1103/PhysRevLett.96.204303
10. Mai T, Dhar A, Narayan O. Equilibration and universal heat conduction in fermi-pasta-ulam chains. *Phys Rev Lett.* (2007) **98**:184301. doi: 10.1103/PhysRevLett.98.184301
11. Dhar A, Saito K. Heat conduction in the disordered Fermi-Pasta-Ulam chain. *Phys Rev E.* (2008) **78**:061136. doi: 10.1103/PhysRevE.78.061136
12. Chen S, Wang J, Casati G, Benenti G. Nonintegrability and the Fourier heat conduction law. *Phys Rev E.* (2014) **90**:032134. doi: 10.1103/PhysRevE.90.032134
13. Chang CW, Okawa D, Garcia H, Majumdar A, Zettl A. Breakdown of Fourier's law in nanotube thermal conductors. *Phys Rev Lett.* (2008) **101**:075903. doi: 10.1103/PhysRevLett.101.075903
14. Xu X, Pereira LF, Wang Y, Wu J, Zhang K, Zhao X, et al. Length-dependent thermal conductivity in suspended single-layer graphene. *Nat Commun.* (2014) **5**:3689. doi: 10.1038/ncomms4689
15. Lee V, Wu CH, Lou ZX, Lee WL, Chang CW. Divergent and ultrahigh thermal conductivity in millimeter-long nanotubes. *Phys Rev Lett.* (2017) **118**:135901. doi: 10.1103/PhysRevLett.118.135901
16. Majee AK, Aksamija Z. Length divergence of the lattice thermal conductivity in suspended graphene nanoribbons. *Phys Rev B.* (2016) **93**:235423. doi: 10.1103/PhysRevB.93.235423
17. Pereira LFC, Donadio D. Divergence of the thermal conductivity in uniaxially strained graphene. *Phys Rev B.* (2013) **87**:125424. doi: 10.1103/PhysRevB.87.125424
18. Nika DL, Askerov AS, Balandin AA. Anomalous size dependence of the thermal conductivity of graphene ribbons. *Nano Lett.* (2012) **12**:3238–44. doi: 10.1021/nl301230g

19. Xu Z. Heat transport in low-dimensional materials: a review and perspective. *Theor Appl Mech Lett.* (2016) **6**:113–21. doi: 10.1016/j.taml.2016.04.002
20. Meier T, Menges F, Nirmalraj P, Hölscher H, Riel H, Gotsmann B. Length-dependent thermal transport along molecular chains. *Phys Rev Lett.* (2014) **113**:060801. doi: 10.1103/PhysRevLett.113.060801
21. Zhao H. Identifying diffusion processes in one-dimensional lattices in thermal equilibrium. *Phys Rev Lett.* (2006) **96**:140602. doi: 10.1103/PhysRevLett.96.140602
22. Mendl CB, Spohn H. Dynamic correlators of fermi-pasta-ulam chains and nonlinear fluctuating hydrodynamics. *Phys Rev Lett.* (2013) **111**:230601. doi: 10.1103/PhysRevLett.111.230601
23. Green MS. Markoff random processes and the statistical mechanics of time-dependent phenomena. II. Irreversible processes in fluids. *J Chem Phys.* (1954) **22**:398–413.
24. Kubo R. Statistical-mechanical theory of irreversible processes. I. General theory and simple applications to magnetic and conduction problems. *J Phys Soc Jpn.* (1957) **12**:570–86.
25. Jara M, Komorowski T, Olla S. Limit theorems for additive functionals of a Markov chain. *Ann Appl Probab.* (2009) **19**:2270–300. doi: 10.1214/09-AAP610
26. Lepri S, Mejía-Monasterio C, Politi A. A stochastic model of anomalous heat transport: analytical solution of the steady state. *J Phys A Math Theor.* (2009) **42**:025001. doi: 10.1088/1751-8113/42/2/025001
27. Lepri S, Mejia Monasterio C, Politi A. Nonequilibrium dynamics of a stochastic model of anomalous heat transport. *J Phys A Math Theor.* (2010) **43**:065002.
28. Delfini L, Lepri S, Livi R, Mejía-Monasterio C, Politi A. Nonequilibrium dynamics of a stochastic model of anomalous heat transport: numerical analysis. *J Phys A Math Theor.* (2010) **43**:145001. doi: 10.1088/1751-8113/43/14/145001
29. Jara M, Komorowski T, Olla S. Superdiffusion of energy in a chain of harmonic oscillators with noise. *Commun Math Phys.* (2015) **339**:407–53. doi: 10.1007/s00220-015-2417-6
30. Bernardin C, Stoltz G. Anomalous diffusion for a class of systems with two conserved quantities. *Nonlinearity.* (2012) **25**:1099–133. doi: 10.1088/0951-7715/25/4/1099
31. Bernardin C, Gonçalves P, Jara M. 3/4-Fractional superdiffusion in a system of harmonic oscillators perturbed by a conservative noise. *Arch Rational Mech Anal.* (2016) **220**:505–42. doi: 10.1007/s00205-015-0936-0
32. Mellet A, Mischler S, Mouhot C. Fractional diffusion limit for collisional kinetic equations. *Arch Rational Mech Anal.* (2011) **199**:493–525. doi: 10.1007/s00205-010-0354-2
33. Basile G, Bernardin C, Olla S. Thermal conductivity for a momentum conservative model. *Commun Math Phys.* (2009) **287**:67–98. doi: 10.1007/s00220-008-0662-7
34. Priyanka, Kundu A, Dhar A, Kundu A. Anomalous heat equation in a system connected to thermal reservoirs. *Phys Rev E.* (2018) **98**:042105. doi: 10.1103/PhysRevE.98.042105
35. Miron A, Cividini J, Kundu A, Mukamel D. Derivation of fluctuating hydrodynamics and crossover from diffusive to anomalous transport in a hard-particle gas. *Phys Rev E.* (2019) **99**:012124. doi: 10.1103/PhysRevE.99.012124
36. Cividini J, Kundu A, Miron A, Mukamel D. Temperature profile and boundary conditions in an anomalous heat transport model. *J Stat Mech Theory Exp.* (2017) 013203. doi: 10.1088/1742-5468/aa5337
37. Kundu A, Bernardin C, Saito K, Kundu A, Dhar A. Fractional equation description of an open anomalous heat conduction set-up. *J Stat Mech Theory Exp.* (2019) **2019**:013205. doi: 10.1088/1742-5468/aaf630
38. Lepri S, Livi R, Politi A. On the anomalous thermal conductivity of one-dimensional lattices. *Europhys Lett.* (1998) **43**:271.
39. Delfini L, Lepri S, Livi R, Politi A. Anomalous kinetics and transport from 1D self-consistent mode-coupling theory. *J Stat Mech Theory Exp.* (2007) **2007**:P02007. doi: 10.1088/1742-5468/2007/02/P02007
40. Lepri S. Relaxation of classical many-body Hamiltonians in one dimension. *Phys Rev E.* (1998) **58**:7165–71. doi: 10.1103/PhysRevE.58.7165
41. Lepri S, Livi R, Politi A. Universality of anomalous one-dimensional heat conductivity. *Phys Rev E.* (2003) **68**:067102. doi: 10.1103/PhysRevE.68.067102
42. Delfini L, Lepri S, Livi R, Politi A. Self-consistent mode-coupling approach to one-dimensional heat transport. *Phys Rev E.* (2006) **73**:060201. doi: 10.1103/PhysRevE.73.060201
43. Wang JS, Li B. Intriguing heat conduction of a chain with transverse motions. *Phys Rev Lett.* (2004) **92**:074302. doi: 10.1103/PhysRevLett.92.074302
44. Wang JS, Li B. Mode-coupling theory and molecular dynamics simulation for heat conduction in a chain with transverse motions. *Phys Rev E.* (2004) **70**:021204. doi: 10.1103/PhysRevE.70.021204
45. Pereverzev A. Fermi-Pasta-Ulam β lattice: Peierls equation and anomalous heat conductivity. *Phys Rev E.* (2003) **68**:056124. doi: 10.1103/PhysRevE.68.056124
46. Lukkarinen J, Spohn H. Anomalous energy transport in the FPU-β chain. *Commun Pure Appl Math.* (2008) **61**:1753–86. doi: 10.1002/cpa.20243
47. van Beijeren H. Exact results for anomalous transport in one-dimensional Hamiltonian systems. *Phys Rev Lett.* (2012) **108**:180601. doi: 10.1103/PhysRevLett.108.180601
48. Casati G, Prosen T. Anomalous heat conduction in a one-dimensional ideal gas. *Phys Rev E.* (2003) **67**:015203. doi: 10.1103/PhysRevE.67.015203
49. Prosen T, Campbell DK. Normal and anomalous heat transport in one-dimensional classical lattices. *Chaos.* (2005) **15**:015117. doi: 10.1063/1.1868532
50. Li B, Wang L, Casati G. Thermal diode: rectification of heat flux. *Phys Rev Lett.* (2004) **93**:184301. doi: 10.1103/PhysRevLett.93.184301
51. Wang L, Wang T. Power-law divergent heat conductivity in one-dimensional momentum-conserving nonlinear lattices. *Europhys Lett.* (2011) **93**:54002. doi: 10.1209/0295-5075/93/54002
52. Tamaki S, Sasada M, Saito K. Heat transport via low-dimensional systems with broken time-reversal symmetry. *Phys Rev Lett.* (2017) **119**:110602. doi: 10.1103/PhysRevLett.119.110602
53. Saito K, Sasada M. Thermal conductivity for coupled charged harmonic oscillators with noise in a magnetic field. *Commun Math Phys.* (2018) **361**:951–95. doi: 10.1007/s00220-018-3198-5
54. Li B, Wang J. Anomalous heat conduction and anomalous diffusion in one-dimensional systems. *Phys Rev Lett.* (2003) **91**:044301. doi: 10.1103/PhysRevLett.91.044301
55. Chen S, Zhang Y, Wang J, Zhao H. Connection between heat diffusion and heat conduction in one-dimensional systems. *Sci China Phys Mech Astron.* (2013) **56**:1466–71. doi: 10.1007/s11433-013-5163-9
56. Wang L, Wu Z, Xu L. Super heat diffusion in one-dimensional momentum-conserving nonlinear lattices. *Phys Rev E.* (2015) **91**:062130. doi: 10.1103/PhysRevE.91.062130
57. Zaburdaev V, Denisov S, Hänggi P. Perturbation spreading in many-particle systems: a random walk approach. *Phys Rev Lett.* (2011) **106**:180601. doi: 10.1103/PhysRevLett.106.180601
58. Li Y, Liu S, Li N, Hanggi P, Li B. 1D momentum-conserving systems: the conundrum of anomalous versus normal heat transport. *New J Phys.* (2015) **17**:043064. doi: 10.1088/1367-2630/17/4/043064
59. Liu S, Hänggi P, Li N, Ren J, Li B. Anomalous heat diffusion. *Phys Rev Lett.* (2014) **112**:040601. doi: 10.1103/PhysRevLett.112.040601
60. Narayan O, Ramaswamy S. Anomalous heat conduction in one-dimensional momentum-conserving systems. *Phys Rev Lett.* (2002) **89**:200601. doi: 10.1103/PhysRevLett.89.200601
61. Spohn H. Nonlinear fluctuating hydrodynamics for anharmonic chains. *J Stat Phys.* (2014) **154**:1191–227. doi: 10.1007/s10955-014-0933-y
62. Spohn H, Stoltz G. Nonlinear fluctuating hydrodynamics in one dimension: the case of two conserved fields. *J Stat Phys.* (2015) **160**:861–84. doi: 10.1007/s10955-015-1214-0
63. Das SG, Dhar A, Saito K, Mendl CB, Spohn H. Numerical test of hydrodynamic fluctuation theory in the Fermi-Pasta-Ulam chain. *Phys Rev E.* (2014) **90**:012124. doi: 10.1103/PhysRevE.90.012124
64. Deutsch J, Narayan O. One-dimensional heat conductivity exponent from a random collision model. *Phys Rev E.* (2003) **68**:010201. doi: 10.1103/PhysRevE.68.010201
65. Roy D. Crossover from Fermi-Pasta-Ulam to normal diffusive behavior in heat conduction through open anharmonic lattices. *Phys Rev E.* (2012) **86**:041102. doi: 10.1103/PhysRevE.86.041102
66. Lepri S, Politi A. Density profiles in open superdiffusive systems. *Phys Rev E.* (2011) **83**:030107. doi: 10.1103/PhysRevE.83.030107

67. Kundu A, Dhar A, Narayan O. The Green-Kubo formula for heat conduction in open systems. *J Stat Mech Theory Exp.* (2009) **03**:L03001. doi: 10.1088/1742-5468/2009/03/L03001
68. Denisov S, Klafter J, Urbakh M. Dynamical heat channels. *Phys Rev Lett.* (2003) **91**:194301. doi: 10.1103/PhysRevLett.91.194301
69. Dhar A, Saito K, Derrida B. Exact solution of a Lévy walk model for anomalous heat transport. *Phys Rev E.* (2013) **87**:010103. doi: 10.1103/PhysRevE.87.010103
70. Dhar A, Saito K. Anomalous transport and current fluctuations in a model of diffusing Levy walkers. *arXiv* (2013) arXiv:13085476.
71. Dhar A, Saito K, Roy A. Energy current cumulants in one-dimensional systems in equilibrium. *Phys Rev Lett.* (2018) **120**:220603. doi: 10.1103/PhysRevLett.120.220603
72. Klafter J, Zumofen G. Dynamically generated enhanced diffusion: the stationary state case. *Phys A.* (1993) **196**:102–15.
73. Zumofen G, Klafter J. Scale-invariant motion in intermittent chaotic systems. *Phys Rev E.* (1993) **47**:851–63.
74. Metzler R, Compte A. Stochastic foundation of normal and anomalous Cattaneo-type transport. *Phys A.* (1999) **268**:454–68.
75. Buldyrev SV, Havlin S, Kazakov AY, da Luz MGE, Raposo EP, Stanley HE, et al. Average time spent by Lévy flights and walks on an interval with absorbing boundaries. *Phys Rev E.* (2001) **64**:041108. doi: 10.1103/PhysRevE.64.041108
76. Miron A. Levy walks on finite intervals: a step beyond asymptotics. *arXiv* (2019) arXiv:190208974.
77. Prähofer M, Spohn H. Exact scaling functions for one-dimensional stationary KPZ growth. *J Stat Phys.* (2004) **115**:255–79. doi: 10.1023/B:JOSS.0000019810.21828.fc
78. Prahofer. Available online at: https://www-m5.ma.tum.de/KPZ
79. Mellet A, Merino-Aceituno S. Anomalous energy transport in FPU-β chain. *J Stat Phys.* (2015) **160**:583–621. doi: 10.1007/s10955-015-1273-2
80. Zoia A, Rosso A, Kardar M. Fractional Laplacian in bounded domains. *Phys Rev E.* (2007) **76**:021116. doi: 10.1103/PhysRevE.76.021116
81. Buldyrev SV, Gitterman M, Havlin S, Kazakov AY, Da Luz MGE, Raposo EP, et al. Properties of Lévy flights on an interval with absorbing boundaries. *Phys A.* (2001) **302**:148–61. doi: 10.1016/S0378-4371(01)00461-7
82. Chen W, Holm S. Fractional Laplacian time-space models for linear and nonlinear lossy media exhibiting arbitrary frequency power-law dependency. *J Acoust Soc Am.* (2004) **115**:1424–30. doi: 10.1121/1.1646399
83. Derrida B. Non-equilibrium steady states: fluctuations and large deviations of the density and of the current. *J Stat Mech.* (2007) **2007**:P07023. doi: 10.1088/1742-5468/2007/07/P07023
84. Bertini L, De Sole A, Gabrielli D, Jona-Lasinio G, Landim C. Macroscopic fluctuation theory. *Rev Mod Phys.* (2015) **87**:593–636. doi: 10.1103/RevModPhys.87.593
85. Bertini L, De Sole A, Gabrielli D, Jona-Lasinio G, Landim C. Macroscopic fluctuation theory for stationary non-equilibrium states. *J Stat Phys.* (2002) **107**:635–75. doi: 10.1023/A:1014525911391
86. Polyanin AD, Manzhirov AV. *Handbook of Integral Equations*, 2nd ed. New York, NY: Chapman and Hall/CRC (2008).

Conflict of Interest: The authors declare that the research was conducted in the absence of any commercial or financial relationships that could be construed as a potential conflict of interest.

frontiers in Physics

ORIGINAL RESEARCH
published: 12 November 2019
doi: 10.3389/fphy.2019.00180

$O(N)$ Fluctuations and Lattice Distortions in 1-Dimensional Systems

Claudio Giberti[1]*, **Lamberto Rondoni**[2,3,4†‡] **and Cecilia Vernia**[5]

[1] Dipartimento di Scienze e Metodi dell'Ingegneria, Università di Modena e Reggio Emilia, Modena, Italy, [2] Dipartimento di Scienze Matematiche, Politecnico di Torino, Turin, Italy, [3] Istituto Nazionale di Fisica Nucleare, Sezione di Torino, Turin, Italy, [4] Malaysia-Italy Centre of Excellence for Mathematical Sciences, Universiti Putra Malaysia, Seri Kembangan, Malaysia, [5] Dipartimento di Scienze Fisiche, Informatiche e Matematiche, Università di Modena e Reggio Emilia, Modena, Italy

Statistical mechanics harmonizes mechanical and thermodynamical quantities, via the notion of local thermodynamic equilibrium (LTE). In absence of external drivings, LTE becomes equilibrium tout court, and states are characterized by several thermodynamic quantities, each of which is associated with negligibly fluctuating microscopic properties. Under small driving and LTE, locally conserved quantities are transported as prescribed by linear hydrodynamic laws, in which the local material properties of the system are represented by the transport coefficients. In 1-dimensional systems, on the other hand, various anomalies are reported, such as the dependence of the heat conductivity on the global state, rather than on the local state. Such deductions, that rely on the existence of thermodynamic quantities like temperature and heat, are here interpreted within the framework of boundary driven 1-dimensional Lennard-Jones chains of N oscillators. It is found that these chains experience non-negligible $O(N)$ lattice distortions, resulting in strongly inhomogeneous systems, and $O(N)$ position fluctuations, that are in contrast with the requirements of LTE.

Keywords: chains of oscillators, local thermodynamic equilibrium, lattice distortion, macroscopic fluctuations, Lennard-Jones potential

Edited by:
Ralf Metzler,
University of Potsdam, Germany

Reviewed by:
Punyabrata Pradhan,
S. N. Bose National Centre for Basic Sciences, India
Herbert Spohn,
Technical University of Munich, Germany

***Correspondence:**
Claudio Giberti
claudio.giberti@unimore.it

†Present address:
Lamberto Rondoni,
Civil and Environmental Engineering Department, Princeton Environmental Institute, Princeton University, Princeton, NJ, United States

‡ORCID:
Lamberto Rondoni
orcid.org/0000-0002-4223-6279

Specialty section:
This article was submitted to Interdisciplinary Physics, a section of the journal Frontiers in Physics

Received: 26 July 2019
Accepted: 23 October 2019
Published: 12 November 2019

Citation:
Giberti C, Rondoni L and Vernia C (2019) O(N) Fluctuations and Lattice Distortions in 1-Dimensional Systems. Front. Phys. 7:180. doi: 10.3389/fphy.2019.00180

1. INTRODUCTION

In a seminal paper, Rieder, Lebowitz, and Lieb investigated the properties of chains of N harmonic oscillators, interacting at their ends with stochastic heat baths [1]. These authors proved that while energy flows from hot to cold baths, the kinetic temperature profile decreases exponentially in the direction of the hotter bath, rather than increasing, and in the bulk its slope vanishes as N grows. Thus, in case the kinetic temperature equals the thermodynamic temperature, heat flows against the direction of energy, in the bulk of such 1D systems. Were this a real fact, no steady state would be reached, because at the boundaries heat would flow in opposite directions and indefinitely accumulate. On the contrary, Rieder et al. [1] proves the existence of and explicitly expresses the steady state. Taken in Rieder et al. [1] as a paradox without explanation, this fact is now understood as related to the absence of phononic interactions in harmonic chains [2], and it reveals that, in harmonic chains, the kinetic temperature does not correspond to the thermodynamic temperature, or the energy flux does not represent a heat flux, or both.

Thermodynamically peculiar behaviors are realized in anharmonic chains as well. In particular, 1D chains of N oscillators without on-site potentials, and conserving momentum, generically enjoy anomalous transport, i.e., the divergence with N of the thermal conductivity, $\kappa_N = \frac{\langle J \rangle N}{T_R - T_L}$, where T_R and T_L are the temperatures at the two ends of a chain and $\langle J \rangle$ is the average heat flux [2–5]. On the other hand, evidence of normal transport in chains with asymmetric interactions, such as Lennard-Jones potentials, is reported in Zhong et al. [6] and Chen et al. [7]. Unexpected phenomena that seem to contradict the hydrodynanmic laws of transport, e.g., currents going against the density gradient, a phenomenon called "uphill diffusion," can be observed in several experimental settings. In e.g., Colangeli et al. [8], the readers my find further references and a non-equilibrium model with phase transition exhibiting uphill diffusion, whose thermodynamic relevance is still under investigation.

The fact is that temperature and heat pertain to macroscopic objects with microscopic states corresponding to Local Thermodynamic Equilibrium (LTE); they cannot be directly identified with mechanical quantities such as kinetic energy and energy flux, Landau and Lifshitz [9], section 9 and Chibbaro et al. [10] chapters 3, 4, and 5. LTE is the essence of Thermodynamics: it can be viewed at once as the precondition for the existence of the thermodynamic fields, such as temperature and heat, and as the natural state of objects obeying the thermodynamic laws. The microscopic conditions under which LTE is expected to hold are extensively discussed in the literature, e.g., [11] section 15.1, [12] section 2.3, [13] section 3.3, [14] chapter 1. In short, LTE requires the existence of three well-separated time and space scales, so that: (1) a macroscopic object can be subdivided in mesoscopic cells that look like a point to macroscopic observers, while containing a large number of molecules; (2) boundary effects are negligible compared to bulk effects, so that the contributions of neighboring cells to the mass and energy of a given cell are inappreciable within a cell; (3) particle interactions allow the cells to thermalize (positions and velocities become respectively uniformly and Maxwell-Boltzmann distributed) within times that are mere instants on the macroscopic scale.

That macroscopic observables are not affected by microscopic fluctuations, despite the exceedingly disordered and energetic microscopic motions, is essential for mesoscopic quantities to be sufficiently stable that thermodynamic laws apply, e.g., Landau and Lifshitz [9], section 1 and 2. This is the case for a quantity that is spatially weakly inhomogeneous, when the number N of particles in a cell is large, and the molecular interactions randomize positions and momenta so that, for instance, the fluctuations of a quantity ϕ of size $O(N)$ are order $O(\sqrt{N})$. The bulk of the cell then dominates in- and out-fluxes, and variations of ϕ are sufficiently slow on the mesoscopic scale.

Quantitatively, the space and time scales for which this description holds depend on the properties of the microscopic components of the systems of interest, [11–16]. However, the general rule is that fluctuations be negligible compared to the signal of interest; were e.g., position fluctuations large, two solids could kick each other, when placed at a short distance from each other. This, of course, is impossible in the thermodynamic realm (see also Exercise 4.5 in [17]).

Under the LTE condition, matter can be considered a continuum, obeying hydrodynamic laws, i.e., balance equations for locally conserved quantities, such as mass, momentum and energy [12, 18–20]. For small to moderate driving, they take a linear form, in which the local material properties are expressed by the linear transport coefficients. Locality implies that such coefficients do not depend on the conditions of the system far away from the considered region. The thermal conductivity of an iron bar at a given temperature at a given point in space does not depend on the conditions of the bar far from that region; cutting the bar in two, or joining it to another bar, without changing the local state, leaves unchanged its local properties.

Fluctuations remain of course present in systems made of particles; they are larger for larger systems, they may be observed [21, 22], and they play a major role in many circumstances (see e.g., [23, 24]). This motivates a considerable fraction of research in statistical physics, e.g., [25, 26], concerning scales much smaller than the macroscopic ones, or occurring in low dimensional (1D and 2D) systems [4, 27–30]. In these phenomena, the linear transport coefficients do not always seem to exist [4], the robustness of the thermodynamic laws appear to be violated, and the behaviors appear to be strongly affected by boundary conditions and by all parameters that characterize a given object [7, 31–37]. It is also well-known that chains of oscillators behave more like some kind of (non-standard) fluids than like solids, because of the loss of crystalline structure, caused by cumulative position fluctuations [38]. Consequently, a fluid-like (possibly fluctuating) description has been adopted in a number of papers, cf. [39, 40].

In driven systems, the situation is problematic also because equipartition may be violated [41–43], the state of the system is model dependent, and the ergodic properties are partially understood [44, 45]. Hence, there is no universal agreement on the microscopic notion of temperature in non-equilibrium conditions [43, 46–51]. Further, a microscopic definition of heat flux requires a clear distinction between convection, i.e., energy transport due to macroscopic motions, and conduction, that is transport without macroscopic motions, cf. Chapter 4 of Zemansky and Dittman [52], and section III.2 and Chapter XI of De Groot et al. [18]. In 1D systems, this may not always be possible [53].

One interpretation of these facts is that LTE is violated in some situations, hence that thermodynamic concepts, such as heat and temperature, may be inappropriate [33, 34]. Another interpretation is that thermodynamic notions should be modified to treat small and strongly non-equilibrium systems (see e.g., [46–49]). It is therefore interesting to investigate the validity and universality of the mechanical counterparts of thermodynamic quantities, in situations in which LTE is not expected to hold, and "anomalous" phenomena have been reported.

We address such questions considering chains of N Lennard-Jones oscillators interacting with deterministic baths at their ends, and without on-site potentials. We mainly focus on two quantities: the distortion of the equilibrium lattice and the fluctuations of the particles, whose position will be denoted by x_i's. The former is the displacement of the average of x_i with respect to its mechanical equilibrium value, while the latter is the standard deviation of x_i. Our central findings are that:

- thermostats at different temperatures induce $O(N)$ distortions of the equilibrium lattice, resulting in highly in-homogeneous chains;

- thermostats induce collective order $O(N)$ fluctuations, i.e., "macroscopic" motions. Negligible incoherent $O(\sqrt{N})$ vibrations typical of 3D equilibrium systems are thus replaced by kind of convective motions, even in chains bounded by still walls.

Note that these are two well distinct effects; the latter is crucial in our investigation, since it hinders thermodynamic properties, cf. section 3. Combined with the results of Rieder et al. [1] and further literature, e.g., [41, 46–50], this suggests that microscopic definitions appropriate for 3-dimensional equilibrium thermodynamic quantities, need extra scrutiny in 1D. As an example of the effects on observables of both $O(N)$ lattice distortions and position fluctuations, we consider the notion of heat flux, J say, given by Equation (23) of Lepri et al. [2]. This confirms from a different standpoint conclusions reached in previous studies on the inapplicability of standard hydrodynamics [54, 55]. Note that Equation (23) of Lepri et al. [2] has been criticized as an incorrect expression for the "heat flow." In fact, it would only reduce to the correct expression, e.g., Equation (3.8) of Spohn [12], (a) apart from a dimensional constant, (b) if the position in space could be identified with the position of one particle, and (c) if position fluctuations about the equilibrium lattice positions would be totally negligible. Such negligible fluctuations would at once satisfy one of the conditions for the validity of LTE, allow the particle position to play the role of a position in space, and make valid the periodic lattice assumption of Lepri et al. [2]. Therefore, this quantity suits us, in order to illustrate the effect of non-negligible fluctuations and of lattice distortions. We find that:

- J is not spatially uniform in steady states. Variations of J decrease if the baths temperature difference is reduced at constant N, but they do not if the mean temperature gradient is reduced increasing N at constant baths temperatures.
- Dividing J by the local mass density partially balances the lattice inhomogeneity and yields an approximately uniform quantity. This suggests that, although relevant, the lattice deformation is not the only reason for J to fail.

These observations should be combined with those of Giberti et al. [53] and Lepri et al. [55], according to which collective and molecular motions are correlated, making hard to disentangle convection from conduction. Whatever their motion, single particles push their neighbors, producing kinds of convective cascades. That difficulties do not ease when N grows, because of $O(N)$ fluctuations and lattice distortions, explains why LTE, hence thermodynamic quantities, cannot be established in our 1D systems.

2. CHAINS OF LENNARD-JONES OSCILLATORS

Consider a 1D chain of N identical moving particles of equal mass m, and positions x_i, $i = 1, ..., N$. Add two particles with fixed positions, $x_0 = 0$ and $x_{N+1} = (N+1)a$, where a is the lattice spacing. Let nearest neighbors interact via the Lennard-Jones potential (LJ):

$$V_1(r) = \epsilon\left[\left(\frac{a}{r}\right)^{12} - 2\left(\frac{a}{r}\right)^{6}\right], \tag{1}$$

where r is the distance between nearest neighbors: $r = |x_i - x_{i-1}|$ and $\epsilon > 0$ is the depth of the potential well. Thus, $x_i = ai$, with $i = 0, \ldots, N+1$, is a configuration of stable mechanical equilibrium for the system. We also consider interactions involving first and second nearest neighbors, with second potential given by [56, 57]:

$$V_2(s) = \epsilon\left[\left(\frac{2a}{s}\right)^{12} - 2\left(\frac{2a}{s}\right)^{6}\right], \tag{2}$$

where $s = |x_i - x_{i-2}|$. Further, we add two particles with fixed positions $x_{-1} = -a$ and $x_{N+2} = (N+2)a$. With potential $V = V_1 + V_2$, the system has the usual stable mechanical equilibrium configuration $x_i = ai$, $i = -1, \ldots, N+2$. The first and last moving particles are in contact with two Nosé-Hoover thermostats, at kinetic temperatures T_L (on the left) and T_R (on the right) and with relaxation times θ_L and θ_R. Introducing the forces

$$F_1(r) = \frac{\partial V_1}{\partial r}(r), \quad F_2(s) = \frac{\partial V_2}{\partial s}(s)\,, \tag{3}$$

the equations of motion are given by:

$$m\ddot{x}_1 = F_1(x_1) - F_1(x_2 - x_1) - \xi_1\dot{x}_1, \tag{4}$$

$$m\ddot{x}_i = F_1(x_i - x_{i-1}) - F_1(x_{i+1} - x_i),\ i = 2, ..., N-1, \tag{5}$$

$$m\ddot{x}_N = F_1(x_N - x_{N-1}) - F_1(x_{N+1} - x_N) - \xi_N\dot{x}_N, \tag{6}$$

with

$$\dot{\xi}_1 = \frac{1}{\theta_L^2}\left(\frac{m\dot{x}_1^2}{T_L} - 1\right), \quad \dot{\xi}_N = \frac{1}{\theta_R^2}\left(\frac{m\dot{x}_N^2}{T_R} - 1\right), \tag{7}$$

in the case of nearest neighbors interaction. For first and second neighbors interactions, we have:

$$\begin{aligned}
m\ddot{x}_1 &= F_1(x_1) - F_1(x_2 - x_1) + F_2(x_1 + a) - F_2(x_3 - x_1)\\
&\quad -\xi_1\dot{x}_1,\\
m\ddot{x}_2 &= F_1(x_2 - x_1) - F_1(x_3 - x_2) + F_2(x_2) - F_2(x_4 - x_2)\\
&\quad -\xi_2\dot{x}_2,\\
m\ddot{x}_i &= F_1(x_i - x_{i-1}) - F_1(x_{i+1} - x_i) + F_2(x_i - x_{i-2})\\
&\quad -F_2(x_{i+2} - x_i), \qquad i = 3, \ldots, N-2, \qquad\qquad (8)\\
m\ddot{x}_{N-1} &= F_1(x_{N-1} - x_{N-2}) - F_1(x_N - x_{N-1})\\
&\quad +F_2(x_{N-1} - x_{N-3}) - F_2(x_{N+1} - x_{N-1}) - \xi_{N-1}\dot{x}_{N-1},\\
m\ddot{x}_N &= F_1(x_N - x_{N-1}) - F_1(x_{N+1} - x_N) + F_2(x_N - x_{N-2})\\
&\quad -F_2(x_{N+2} - x_N) - \xi_N\dot{x}_N,
\end{aligned}$$

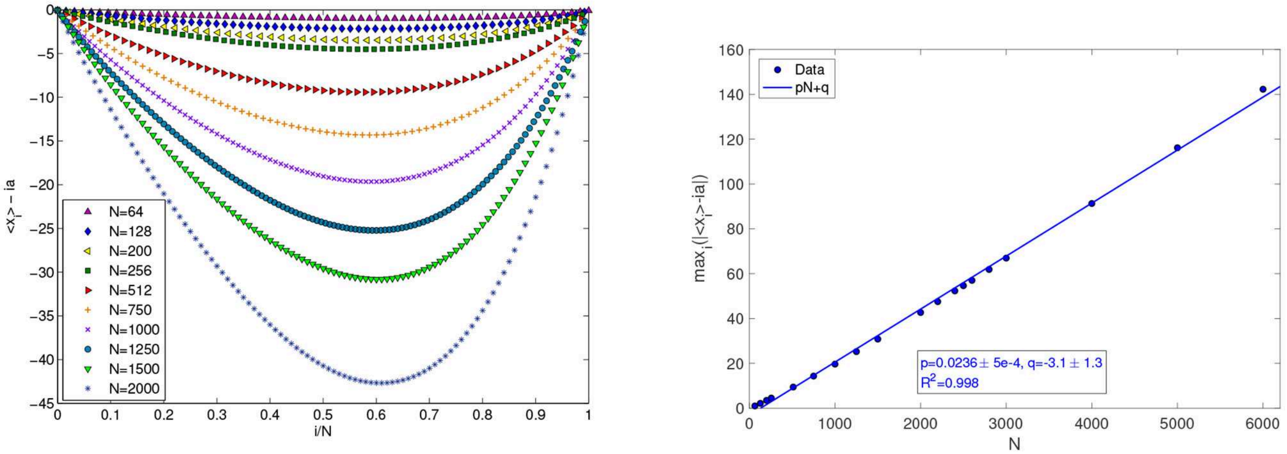

FIGURE 1 | (Left) Plot of the displacement of the mean position of particle *i* from its mechanical equilibrium position, $(\langle x_i \rangle - ia)$, for different values of *N*, for first and second neighbors interaction, when $T_L = 1$ and $T_R = 10$. The lattice is strongly distorted in presence of temperature differences. **(Right)** Linear fit of $\max_i(\langle x_i \rangle - ia)$ as a function of *N* ranging from 64 to 6000, for $N > 400$. The label of the particle corresponding to the maximum lattice distortion is fitted by $i_{\text{mld}} = 0.6063N - 6.804$ with $R^2 = 0.9997$.

with

$$\dot{\xi}_l = \frac{1}{\theta_L^2}\left(\frac{m\dot{x}_l^2}{T_L} - 1\right), \; l = 1, 2,$$
$$\dot{\xi}_l = \frac{1}{\theta_R^2}\left(\frac{m\dot{x}_l^2}{T_R} - 1\right), \; l = N-1, N. \tag{9}$$

The hard-core nature of the LJ potentials preserves the order of particles: $0 < x_1 < x_2 < \cdots < x_N < (N+1)a$ holds at all times, if it does at the initial time[1].

For such systems, a form of single particle virial relation is often found to hold[2]. That fact is usually mentioned to identify the average kinetic energy of a given particle with the temperature T_i in position x_i [2]:

$$T_i = \left\langle \frac{p_i{}^2}{m} \right\rangle, \qquad i = 1, ..., N. \tag{10}$$

Here, p_i is the momentum of particle *i*, the angular brackets $\langle \cdot \rangle$ denote time average, and T_i is called *single particle kinetic temperature*.

However, the validity of Equation (10) does not imply a Maxwell-Boltzmann distribution of velocities, corresponding to a thermodynamic temperature [53]. Indeed, for $T_L \neq T_R$, the single particle kinetic temperature profile may take rather peculiar forms, compared to the linear thermodynamic temperature profiles in homogeneous solids when Fourier law holds. This is illustrated in great detail in the specialized literature, cf. [2–4, 34, 59–63] just to cite a few. Also, numerically simulated profiles of various kinds of 1D systems, appear to be sensitive to parameters such as the relaxation constants of the thermostats, the interaction parameters, the form of the boundaries *etc.* cf. e.g., [34]. This is not surprising, since many correlations persist in space and time in low dimensional systems, hindering the realization of LTE and leading to anomalous behaviors [33, 54, 55, 64–70]. As a further testimony of the complex behavior of 1D chains, we mention that heat conductivity may depend on details of the interaction potential such as its asymmetry; see [6, 7] in which evidence is given for normal conductivity in chains with LJ potential.

In the following sections, we report our results about systems with various numbers of particles *N*. The parameters defining the Lennard-Jones potentials are $\epsilon = 1$ and $a = 1$, while the mass of the particles is $m = 1$. The relaxation times of the thermostats θ_L and θ_R are set to 1. The numerical integrator used is the fourth-order Runge-Kutta method with step size 10^{-3}. The time averages are typically taken over $O(10^8) - O(10^9)$ time steps in the stationary state.

3. LARGE LATTICE DEFORMATIONS AND FLUCTUATIONS

The distinction between the different states of aggregation of matter is not strictly possible in 1D systems with short range interactions; one nevertheless realizes that our oscillators chains are more similar to (a kind of) compressible fluids than to solids [34, 54]. In particular, Lepri et al. [55] shows persistent correlations, $O(N)$ dependence of relaxation times, and the failure of standard hydrodynamics, in non-driven LJ systems. Along similar lines of inquiry, we investigated two different effects in non-equilibrium conditions: the distortion of the equilibrium lattice and the size of the fluctuations of the particles.

---

[1] In some cases, we extended the Lennard-Jones interaction to the third nearest neighbors, preserving the equilibrium configuration $x_i = ia$. The corresponding equations of motion and thermostats are the natural modification of the previous ones, hence are not reported here.

[2] In Falasco et al. [58] a nonequilibrium mesoscopic version of the virial relation in given.

For the first, we find that temperature differences at the boundaries of the chains induce "macroscopic" deformations of the periodic structure of the lattice; cf. Zhong et al. [6] for the influence of the asymmetry of the potential on such phenomenon. For all i, we obtain $(\langle x_i\rangle - ia) \sim O(N)$, as shown in **Figure 1**, whose right panel plots the quantity $\max_i(|\langle x_i\rangle - ia|)$ as a function of N. Consequently, for sufficiently large N the system cannot be treated as a spatially homogeneous object.

Our second observation, which concerns fluctuations, is that the presence of thermostats at different temperatures enhances the size of the vibrations, given by $\sqrt{\langle x_i^2\rangle - \langle x_i\rangle^2}$, of each particle i about its average position $\langle x_i\rangle$. Such vibrations are order $O(i^{1/2})$ in chains without thermostats with origin in $i = 0$ [38], which means that, for sufficiently large i, position fluctuations are incompatible with a crystal structure. In our framework, the length of chains is bounded, therefore the size of particle vibrations cannot indefinitely grow with particle index i: the vibrations are larger for particles in the bulk than for particles near the boundaries of the chains, see the left panel of **Figure 2** More precisely, we find that for every particle i, the size of vibrations can be called "macroscopic": $\sqrt{\langle x_i^2\rangle - \langle x_i\rangle^2} \sim O(N)$. In the right panel of **Figure 2** and in **Figure 3**, square root fits and linear fits are compared for N ranging from 64 to 6000. The square root fits are appropriate for small N, while at large N the linear fit takes over. The size of these vibrations appears even more striking observing that displacing by a large amount one of them, a whole collection of particles must be correspondingly displaced. Indeed, the repulsive part of the LJ potential does not allow particles' order to be modified, as noted also in Lepri et al. [55]. As observed e.g., in Giberti and Rondoni [34],

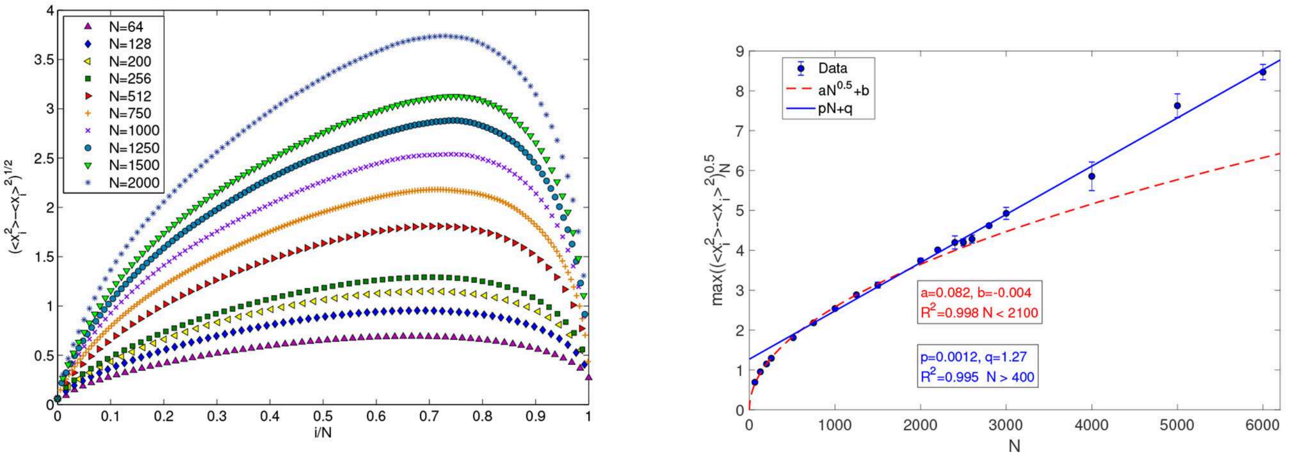

FIGURE 2 | (Left) Standard deviations of the particles vibrations about their average position, in lattice vectors units, for the case of **Figure 1**. **(Right)** Dependence on N (ranging from 64 to 6000) of the maximum standard deviation together with a linear fit for $N > 400$ (continuous blue line) and one square root fit for lattices with $N < 2100$ (dashed red line). Growing linearly with N, collective vibrations look like convective motions. The label of the particle corresponding to the maximum fluctuation amplitude is fitted by $i_{\text{mfa}} = 0.7398N - 6.75$ with $R^2 = 0.9993$.

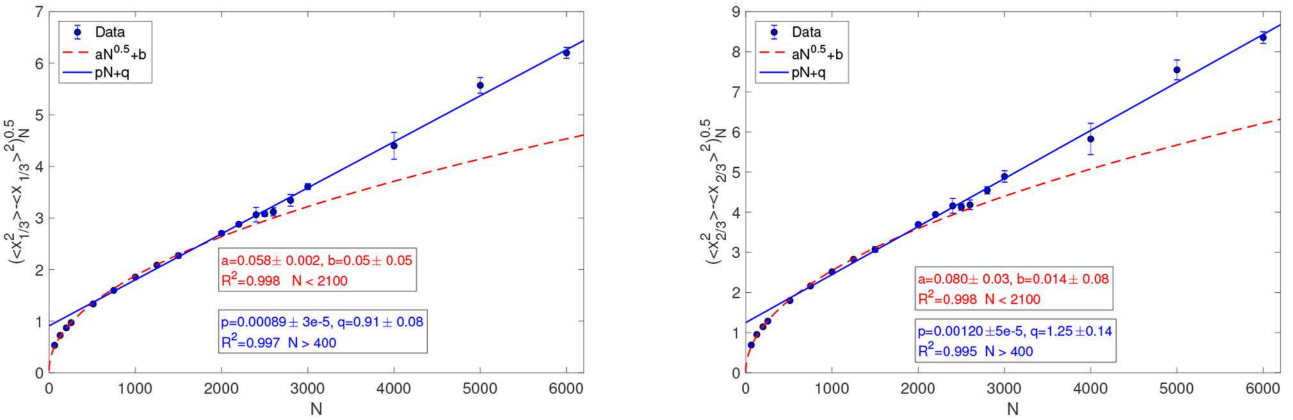

FIGURE 3 | (Left) Dependence on N of the standard deviations of the vibrations of particles at 1/3 of the chain. **(Right)** Dependence on N of the standard deviations of the vibrations at 2/3 of the chain. In both cases, a square root and a linear fit are drawn. The square root fit holds at small N. At large N the linear fit takes over. In both panels N ranges from 64 to 6000. Particles motions look more like some kind of convection rather than like microscopic lattice vibrations.

this kind of constraint leads to long-range correlations, that necessarily develop while the $O(N)$ fluctuations observed here take place. Concerning thermodynamics, they are in fact like the two sides of a coin: both long range correlations and large spatial fluctuations break locality, connecting mesoscopic cells over long distances. This violates the conditions for the validity of LTE, which require mesoscopic cells to be small independent equilibrium systems [14]. Absence of LTE in our systems was already noted e.g., Giberti et al. [53], in which non-Maxwellian velocities distributions were portrayed.

As a result, the motion of particles about their average positions is not an irregular motion about fixed positions. In accord with the observations on persistent correlations, this motion looks like a kind of convection, although LTE and standard hydrodynamics do not hold [34, 39, 40, 54, 55]. It follows that, in these cases, energy transport cannot be directly related to "heat" flows.

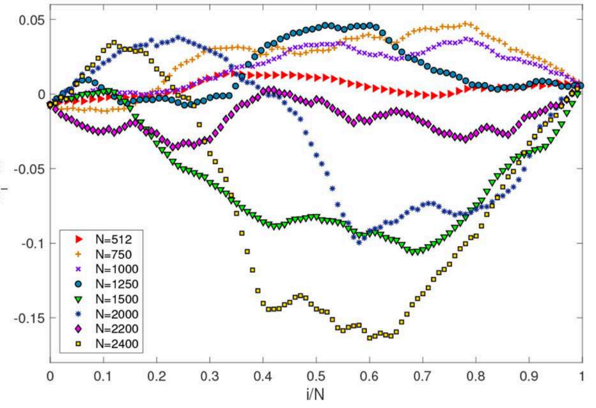

FIGURE 4 | Equilibrium simulations. Plot of the displacement of the mean position of particle *i* from its mechanical equilibrium position, $\langle x_i \rangle - ia$, for various values of *N*, for first and second neighbors interactions when $T_L = T_R = 5$. The deviations from the mechanical equilibrium are negligible.

The situation is different for $T_L = T_R$. **Figure 4** shows that the lattice deformations are much smaller than the lattice spacing *a*, and can be neglected. The computed values of $(\langle x_i \rangle - ia)$ practically vanish and do not depend on *N*. The standard deviation of the vibrations about the mean position is represented in the left panel of **Figure 5** and it appears to be closer to $O(\sqrt{N})$ than to $O(N)$ as can be seen in the right panel of **Figure 5**. In this case, in which there is no net energy transport, the system also behaves more like a fluid than like a solid in sense closer to that of Peierls [38], although our results refers to a different situation.

4. ENERGY BALANCE

In order to understand the effect of $O(N)$ fluctuations and lattice distortions on LTE, we now consider, as an example, the "heat flux" J_i given by Equation (23) of Lepri et al. [2]. Note, exact expressions for the energy balance about single particles exist, e.g., Equation (17) of Lepri et al. [2]. Nevertheless, J_i, which had been presented as more accurate than Equation (17) of Lepri et al. [2], is here interesting because, in presence of LTE, it does correspond to a heat flux, apart from a dimensional constant, which is irrelevant for our investigation. Then, as the energy current flowing between neighboring particles labeled by *i* and $i+1$ should not depend on *i*, the same should happen to the time average $\langle J_i \rangle$. In this section, we investigate whether this holds or not. A critical analysis of Equation (23) of Lepri et al. [2] as a heat flux is provided in Mejía-Monasterio et al. [71].

For the case of first and second nearest neighbors interactions, the expression given by Equation (23) of Lepri et al. [2] must be modified as follows:

$$\begin{aligned} J_i = &\frac{1}{2}(x_{i+1} - x_i)F_1(x_{i+1} - x_i)(\dot{x}_{i+1} + \dot{x}_i) \\ &+ (x_{i+2} - x_i)F_2(x_{i+2} - x_i)(\dot{x}_{i+2} + \dot{x}_i) + \dot{x}_i h_i \,, \end{aligned} \tag{11}$$

where F_1 and F_2 are defined by Equation (3) and h_i is the energy of the *i*-th particle.

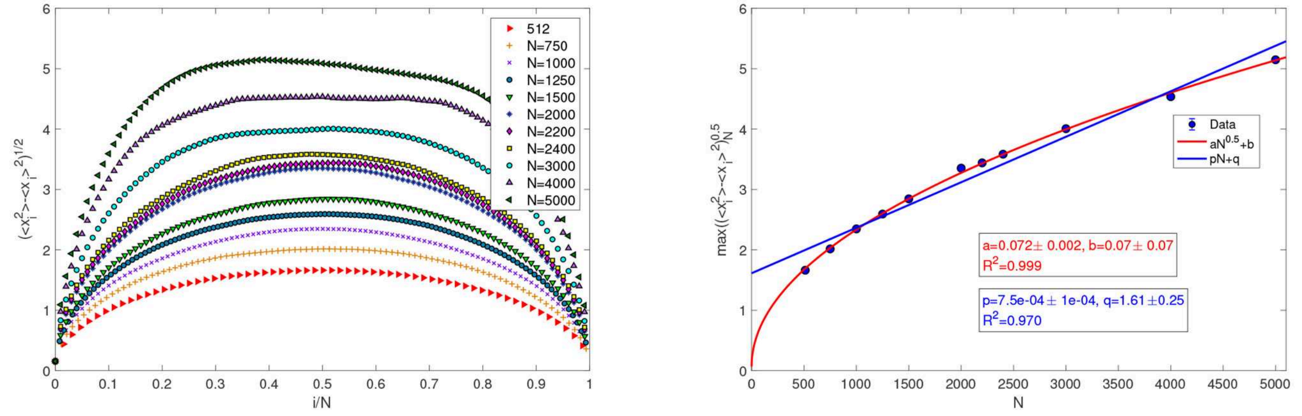

FIGURE 5 | Equilibrium simulations ($T_L = T_R = 5$) for *N* ranging from 512 to 5000. **(Left)** Standard deviations of the particles vibrations about their average position $(x_i - \langle x_i \rangle)$, in lattice vectors units. **(Right)** Dependence on *N* of the maximum standard deviation, together with linear and square root fits. This dependence on *N* should not be confused with the $O(\sqrt{i})$ dependence on *i* of Peierls [38].

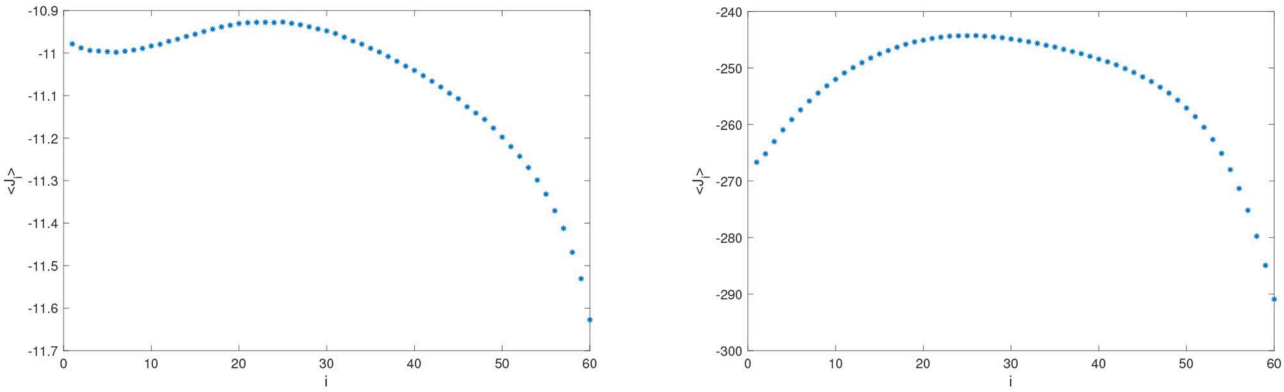

FIGURE 6 | Chains with nearest neighbors Lennard-Jones interactions. **(Left)** Flux $\langle J_i \rangle$ computed according to Equation (11), for $N = 64$, $T_L = 1$, $T_R = 4$. **(Right)** $\langle J_i \rangle$ for $N = 64$, $T_L = 1$, $T_R = 64$.

The quantity J_i is only apparently "local" because it quantifies a flow through the position of particle i, and not through a fixed position in space. Moreover, it implicitly requires small position fluctuations and small lattice deformations, because Equation (11) is obtained through Fourier analysis for spatially homogeneous systems, in the limit of small wave vectors, [2, 28]. For instance, denoting by k the wave-vector, Equation (23) of Lepri et al. [2] follows from Equation (21) only if $k(x_{n+1} - x_n)$ is small. On the contrary, in our cases, this quantity strongly varies in space and time, and average lattice distortions are of order $O(N)$, cf. section 3. Therefore, one expects J_i to fail, and it is interesting to investigate how that is realized, varying the relevant model parameters.

For chains with nearest neighbors Lennard-Jones interactions [$F_2 \equiv 0$ in Equation (11)], we find that while the steady state heat flow should not depend on position, the time average of J_i substantially changes with i, cf. **Figure 6**. To quantify this phenomenon, we introduce the relative variation of $\langle J_i \rangle$,

$$\delta = \left| \frac{\max_i \langle J_i \rangle - \min_i \langle J_i \rangle}{\bar{J}} \right| \; , \quad \text{where } \bar{J} = \frac{1}{N} \sum_i \langle J_i \rangle \; ,$$

In **Tables 1**, **2**, for average temperature gradients similar to those commonly found in the literature [62, 63, 72], we observe that δ tends to grow with the temperature gradient, at fixed N. In general, however, reducing the average gradient by increasing the system size, does not lead to smaller δ [3].

TABLE 1 | Relative variation δ of the flux J_i for $N = 64$ particles with first and second nearest neighbors interactions.

T_R	δ_1	δ_2
1.1	0.0240	0.0199
1.5	0.0091	0.0077
2	0.0142	0.0145
4	0.0480	0.0481
8	0.0831	0.0829
16	0.1060	0.1062
32	0.1199	0.1201
64	0.1229	0.1232

$T_L = 1$ while T_R takes eight different values. δ_1 is computed averaging over $2 \cdot 10^9$ time steps, δ_2 over $4 \cdot 10^9$ time steps.

TABLE 2 | Relative variation δ of the average fluxes $\langle J_i \rangle$ defined by Equation (11).

T_R	$N = 64$	$N = 128$	$N = 256$
1.1	0.0240	0.0117	0.0110656
1.5	0.0091	0.0297	0.0317283
2	0.0142	0.0534	0.0555437
4	0.0480	0.0817	0.104345
8	0.0831	0.0659	0.0907829
16	0.1060	0.0683	0.0485491
32	0.1199	0.1560	0.0643797
64	0.1229	0.2306	0.195046

Chains with $N = 64$, $N = 128$, and with $N = 256$ particles, with nearest neighbors interactions are considered. Averages are computed over $2 \cdot 10^9$ time steps. $T_L = 1$, while T_R takes eight different values.

We conclude that under our conditions the quantity J_i represents neither a heat nor an energy flow, and that this is not a consequence of the size of temperature gradients, but of the size of fluctuations. These increase with growing N, thus preventing LTE and standard hydrodynamics in the large N limit [34, 54, 55]. One may nevertheless ask whether the observed features of J_i are merely due to the deformation of the lattice, which invalidates the Fourier expansion of Lepri et al. [2]. One may thus take into account the lattice deformations and restore the correct units, normalizing J_i by the average distance between particles, as follows:

$$J_i^n = \frac{J_i}{\langle x_{i+1} - x_i \rangle} \; , \qquad i = 2, ..., N - 2. \qquad (12)$$

---

[3] Actually, for mere energy flows, there is no reason to be bounded by small temperature gradients.

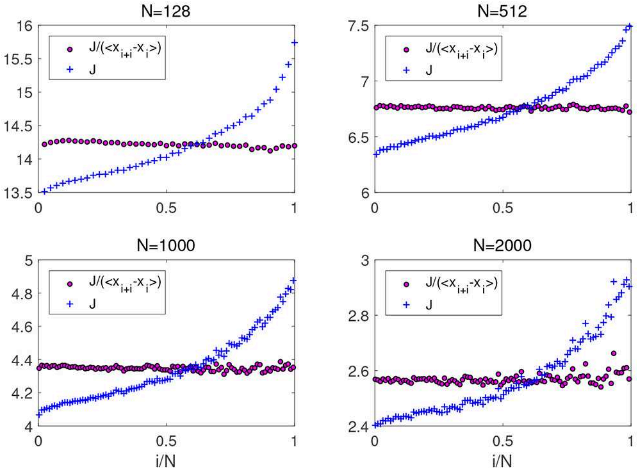

FIGURE 7 | Normalized energy flux J^n (o) and the flux J (+) defined by Equation (11) for chains of different lengths ($N = 128$, 512, 1,000, 2,000) and with $T_L = 1$ and $T_R = 10$. Although J^n is not exactly constant, at large N it enjoys small fluctuations about a given average value.

This quantity, that should not be taken as a correct alternative to the definition of heat flux, is indeed approximately constant as a function of i. This is shown in **Figure 7**, where J_i^n results more stable than J_i as a function of i, thus indicating that the lattice inhomogeneity is one cause of error in J_i. However, the spurious fluctuations visible in **Figure 7**, reveal that lattice deformations are only one of the difficulties affecting J_i as a definition of heat flux.

5. CONCLUDING REMARKS

In this work we have presented numerical results on one 1D chains of Lennard-Jones oscillators, in contact with two Nosé-Hoover thermostats. Scrutinizing the behavior of mechanical quantities that are commonly considered in the specialized literature, we have investigated the fluctuations and lattice distortions, which are expected to prevent the onset of "thermodynamic" regimes [33, 34, 50, 55].

The thermodynamic behavior emerges from the collective behavior of very large assemblies of interacting particles, provided that two conditions are met: rapid (compared to observation time scales) decay of correlation and negligible boundary effects. These conditions often take place for 3D mesoscopic cells containing large numbers of properly interacting particles, but it is not obvious in 1D systems. Indeed, quoting Spohn: *"The propagation of local equilibrium in time, if true, is a deep and highly non-obvious property of a system of many particles governed by Newton's equations of motion"*, see [12] section 3.1.

In particular, we have observed that temperature differences at the boundaries produce $O(N)$ deformations of the lattice, that result in strongly inhomogeneous systems, and $O(N)$ position fluctuations that hinder LTE. In turn, we have observed that such $O(N)$ effects imply that increasing N, and correspondingly decreasing "temperature gradient," does not lead our systems any closer to thermodynamic systems. Consequently, as observed also elsewhere, standard hydrodynamics does not apply [34, 54, 55]. This must be taken into account when defining e.g., the heat conductivity, because its anomalies are necessarily related to the absence of LTE.

DATA AVAILABILITY STATEMENT

The datasets generated for this study are available on request to the corresponding author.

AUTHOR CONTRIBUTIONS

All authors listed have made a substantial, direct and intellectual contribution to the work, and approved it for publication.

FUNDING

This work is partially supported by Gruppo Nazionale per la Fisica Matematica (GNFM-INdAM). CG and CV acknowledge financial supports from Fondo di Ateneo per la Ricerca 2016 and Fondo di Ateneo per la Ricerca 2017- Università di Modena e Reggio Emilia. LR has been partially supported by Ministero dell'Istruzione dell'Università e della Ricerca (MIUR) grant Dipartimenti di Eccellenza 2018–2022.

ACKNOWLEDGMENTS

The authors are grateful to Carlos Mejia-Monasterio for extensive discussions and enlightening remarks. The authors are grateful to Antonio Politi for very useful suggestions. Antonio Politi, in particular has suggested the normalization of the energy flux.

REFERENCES

1. Rieder Z, Lebowitz JL, Lieb E. Properties of a harmonic crystal in a stationary nonequilibrium state. *J Math Phys.* (1967) **8**:1073. doi: 10.1063/1.1705319
2. Lepri S, Livi R, Politi A. Thermal conduction in classical low-dimensional lattices. *Phys Rep.* (2003) **377**:1–80. doi: 10.1016/S0370-1573(02)00558-6
3. Dhar A. Heat Transport in low-dimensional systems. *Adv Phys.* (2008) **57**:457–537. doi: 10.1080/00018730802538522
4. Lepri S, editor. Thermal transport in low dimensions - From Statistical Physics to Nanoscale Heat Transfer. In: *Lecture Notes in Physics, Vol. 921*. Heidelberg: Springer (2016). p. 1–411.
5. Lepri S, Livi R, Politi A. Heat transport in low dimensions: introduction and phenomenology. In: Lepri S, editor. *Thermal Transport in Low Dimensions - From Statistical Physics to Nanoscale Heat Transfer. Lecture Notes in Physics Vol. 921*. Heidelberg: Springer (2016).
6. Zhong V, Zhang Y, Wang J, Zhao H. Normal heat conduction in one-dimensional momentum conserving lattices with asymmetric interactions. *Phys Rev E.* (2012) **85**:060102(R). doi: 10.1103/PhysRevE.85.060102
7. Chen S, Zhang Y, Wang J, Zhao H. Key role of asymmetric interactions in low-dimensional heat transport. *J Stat Mech.* (2016) **2016**:033205. doi: 10.1088/1742-5468/2016/03/033205

8. Colangeli M, Giardinà C, Giberti C, Vernia C. Nonequilibrium two-dimensional Ising model with stationary uphill diffusion. *Phys Rev E*. (2018) **97**:030103(R). doi: 10.1103/PhysRevE.97.030103
9. Landau LD, Lifshitz EM. *Statistical Physics. Volume 5 of Course of Theoretical Physics, Part 1*. Oxford: Pergamon Press (1980). p. 544.
10. Chibbaro S, Rondoni L, Vulpiani A. *Reductionism, Emergence and Levels of Reality*. New York, NY: Springer Verlag (2014). p. 154.
11. Kondepudi D, Prigogine I. *Modern Thermodynamics: From Heat Engines to Dissipative Structures*. Chichester: John Wiley & Sons Ltd (1998). p. 486.
12. Spohn H. *Large Scale Dynamics of Interacting Particles, Texts and Monographs in Physics*. Heidelberg: Springer-Verlag (1991). p. 342.
13. Bellissard J. Coherent and dissipative transport in aperiodic solids: an overview. In: Garbaczewski P, Olkiewicz R, editors. *Dynamics of Dissipation*. Berlin: Springer Verlag (2002). p. 413–85.
14. Kreuzer HJ. *Nonequilibrium Thermodynamics and Its Statistical Foundations*. Oxford: Claredon Press (1981). p. 458.
15. Falcioni M, Palatella L, Pigolotti S, Rondoni L, Vulpiani A. Initial growth of Boltzmann entropy and chaos in a large assembly of weakly interacting systems. *Physica A*. (2007) **385**:170–84. doi: 10.1016/j.physa.2007.06.036
16. Rondoni L, Pigolotti S. On $\Gamma-$ and $\mu-$space descriptions: Gibbs and Boltzmann entropies of symplectic coupled maps. *Phys Scr*. (2012) **86**:058513. doi: 10.1088/0031-8949/86/05/058513
17. Huang K. *Statistical Mechanics*. New York, NY: John Wiley & Sons (1987). p. 493.
18. De Groot SR, Mazur, P. *Non-equilibrium Thermodynamics*. New York, NY: Dover Publication (1984). p. 528.
19. Cohen EGD, Rondoni L. Note on phase space contraction and entropy production in thermostatted hamiltonian systems. *Chaos*. (1998) **8**:357. doi: 10.1063/1.166317
20. Rondoni L, Cohen EGD. On some derivations of irreversible thermodynamics from dynamical systems theory. *Physica D*. (2002) **168–9**:341–55. doi: 10.1016/S0167-2789(02)00522-5
21. Bonaldi M, Conti L, De Gregorio P, Rondoni L, Vedovato G, Vinante A, et al. Nonequilibrium steady-state fluctuations in actively cooled resonators. *Phys Rev Lett*. (2009) **103**:010601. doi: 10.1103/PhysRevLett.103.010601
22. Conti L, Bonaldi M, Rondoni L. RareNoise: non-equilibrium effects in detectors of gravitational waves. *Class Quantum Grav*. (2010) **27**:084032. doi: 10.1088/0264-9381/27/8/084032
23. Mishin Y. Thermodynamic theory of equilibrium fluctuations. *Ann Phys*. (2015) **363**:48–97. doi: 10.1016/j.aop.2015.09.015
24. Hickman J, Mishin Y. Temperature fluctuations in canonical systems: insights from molecular dynamics simulations. *Phys Rev B*. (2016) **94**:184311. doi: 10.1103/PhysRevB.94.184311
25. Seifert U. Stochastic thermodynamics, fluctuation theorems and molecular machines. *Rep Prog Phys*. (2012) **75**:126001. doi: 10.1088/0034-4885/75/12/126001
26. Benenti G, Casati G, Saito K, Whitney RS. Fundamental aspects of steady-state conversion of heat to work at the nanoscale. *Phys Rep*. (2017) **694**:1–124. doi: 10.1016/j.physrep.2017.05.008
27. Gao Z, Li N, Li B. Heat conduction and energy diffusion in momentum-conserving one-dimensional full-lattice ding-a-ling model. *Phys Rev E*. (2016) **93**:022102. doi: 10.1103/PhysRevE.93.022102
28. Das SG, Dhar A, Narayan O. Heat conduction in the α - β Fermi-Pasta-Ulam chain. *J Stat Phys*. (2014) **154**:204–13. doi: 10.1007/s10955-013-0871-0
29. Liu S, Hänggi P, Li N, Ren J, Li B. Anomalous heat diffusion. *Phys Rev Lett*. (2014) **112**:040601. doi: 10.1103/PhysRevLett.112.040601
30. Wang J, Casati G. One dimensional self-organization and nonequilibrium phase transition in a Hamiltonian system. *Phys Rev Lett*. (2017) **118**:040601. doi: 10.1103/PhysRevLett.118.040601
31. Chang CW, Okawa D, Garcia H, Majumdar A, Zettl A. Breakdown of Fourier's law in nanotube thermal conductors. *Phys Rev Lett*. (2008) **101**:075903. doi: 10.1103/PhysRevLett.101.075903
32. Xu X, Pereira LF, Wang Y, Wu J, Zhang K, Zhao X, et al. Length-dependent thermal conductivity in suspended single-layer graphene. *Nat Commun*. (2014) **5**:3689. doi: 10.1038/ncomms4689
33. Jepps OG, Rondoni L. Thermodynamics and complexity of simple transport phenomena. *J Phys A*. (2006) **39**:1311–38. doi: 10.1088/0305-4470/39/6/007
34. Giberti C, Rondoni L. Anomalies and absence of local equilibrium, and universality, in one-dimensional particles systems. *Phys Rev E*. (2011) **83**:041115. doi: 10.1103/PhysRevE.83.041115
35. Chen S, Zhang Y, Wang J, Zhao H. Diffusion of heat, energy, momentum and mass in one-dimensional systems. *Phys Rev E*. (2013) **87**:032153. doi: 10.1103/PhysRevE.87.032153
36. Onorato M, Vozella L, Proment D, Lvov YV. Route to thermalization in the α-Fermi–Pasta–Ulam system. *Proc Natl Acad Sci USA*. (2015) **112**:4208–13. doi: 10.1073/pnas.1404397112
37. Dhar A, Saito K. Heat conduction in the disordered Fermi-Pasta-Ulam chain. *Phys Rev E*. (2008) **78**:061136. doi: 10.1103/PhysRevE.78.061136
38. Peierls R. Chapter 4: Melting in one, two and three dimensions. In: *Surprises in Theoretical Physics, Princeton Series in Physics*. Princeton, NJ: Princeton University Press (1979). p. 176.
39. Narayan O, Ramaswamy S. Anomalous heat conduction in one-dimensional momentum-conserving systems. *Phys Rev Lett*. (2002) **89**:200601. doi: 10.1103/PhysRevLett.89.200601
40. Mai T, Narayan O. Universality of one-dimensional heat conductivity. *Phys Rev E*. (2006) **73**:061202. doi: 10.1103/PhysRevE.73.061202
41. Conti L, De Gregorio P, Karapetyan G, Lazzaro C, Pegoraro M, Bonaldi M, et al. Effects of breaking vibrational energy equipartition on measurements of temperature in macroscopic oscillators subject to heat flux. *J Stat Mech*. (2013) **12**:P12003. doi: 10.1088/1742-5468/2013/12/P12003
42. Ortiz de Zárate JM, Sengers JV. *Hydrodynamic Fluctuations in Fluids and Fluid Mixtures*. Amsterdam: Elsevier (2006). p. 320.
43. Puglisi A, Sarracino A, Vulpiani A. Temperature in and out of equilibrium: a review of concepts, tools and attempts. *Phys Rep*. (2017) **709–10**:1–60. doi: 10.1016/j.physrep.2017.09.001
44. Gallavotti G. *Nonequilibrium and Irreversibility*. New York, NY: Springer (2014). p. 248.
45. Evans DJ, Williams SR, Searles DJ, Rondoni L. On Typicality in Nonequilibrium Steady States. *J Stat Phys*. (2016) **164**:842–57. doi: 10.1007/s10955-016-1563-3
46. Morriss GP, Rondoni L. Definition of temperature in equilibrium and nonequilibrium systems. *Phys Rev E*. (1999) **59**:R5. doi: 10.1103/PhysRevE.59.R5
47. Casas-Vázquez J, Jou D. Temperature in non-equilibrium states: a review of open problems and current proposals. *Rep Prog Phys*. (2003) **66**:1937–2023. doi: 10.1088/0034-4885/66/11/R03
48. Jou D, Restuccia L. Caloric and entropic temperatures in non-equilibrium steady states. *Physica A*. (2016) **460**:246–53. doi: 10.1016/j.physa.2016.04.034
49. Cao X, He D. Interfacial thermal conduction and negative temperature jump in one-dimensional lattices. *Phys Rev E*. (2015) **92**:032135. doi: 10.1103/PhysRevE.92.032135
50. Jou DJ, Casas-Vàzquez J, Lebon G. *Extended Irreversible Thermodynamics*. New York, NY: Springer-Verlag (2010). p. 463.
51. Criado-Sancho M, Jou D, Casas-Vázquez J. Nonequilibrium kinetic temperatures in flowing gases. *Phys Lett A*. (2006) **350**:339–41. doi: 10.1016/j.physleta.2005.10.043
52. Zemansky MW, Dittman RH. *Heat and Thermodynamics*. New York, NY: McGraw-Hill (1997). p. 487.
53. Giberti C, Rondoni L, Vernia C. Temperature and correlations in 1-dimensional systems. *Eur Phys J Spec Top*. (2019) **228**:129. doi: 10.1140/epjst/e2019-800138-8
54. Hurtado PI. Breakdown of hydrodynamics in a simple one-dimensional fluid. *Phys Rev Lett*. (2006) **96**:010601. doi: 10.1103/PhysRevLett.96.010601
55. Lepri S, Sandri P, Politi A. The one-dimensional Lennard-Jones system: collective fluctuations and breakdown of hydrodynamics. *Eur Phys J B*. (2005) **47**:549–55. doi: 10.1140/epjb/e2005-00360-7
56. De Gregorio P, Rondoni L, Bonaldi M Conti L. One-dimensional models and thermomechanical properties of solids. *Phys Rev B*. (2011) **84**:224103. doi: 10.1103/PhysRevB.84.224103
57. Conti L, De Gregorio P, Bonaldi M, Borrielli A, Crivellari M, Karapetyan G, et al. Elasticity of mechanical oscillators in nonequilibrium steady states: experimental, numerical, and theoretical

results. *Phys Rev E*. (2012) **85**:066605. doi: 10.1103/PhysRevE.85.066605
58. Falasco G, Baldovin F, Kroy K, Baiesi M. Mesoscopic virial equation for nonequilibrium statistical mechanics. *New J Phys*. (2016) **18**:093043. doi: 10.1088/1367-2630/18/9/093043
59. Delfini L, Lepri S, Livi R, Politi A. Self-consistent mode-coupling approach to one-dimensional heat transport. *Phys Rev E*. (2006) **73**:060201(R). doi: 10.1103/PhysRevE.73.060201
60. Lepri S, Mejía-Monasterio C, Politi A. Nonequilibrium dynamics of a stochastic model of anomalous heat transport. *J Phys A*. (2010) **43**:065002. doi: 10.1088/1751-8113/43/6/065002
61. Delfini L, Lepri S, Livi R, Mejía-Monasterio C, Politi A. Nonequilibrium dynamics of a stochastic model of anomalous heat transport: numerical analysis. *J Phys A*. (2010) **43**:145001. doi: 10.1088/1751-8113/43/14/145001
62. Lepri S, Livi R, Politi A. Heat conduction in chains of nonlinear oscillators. *Phys Rev Lett*. (1997) **78**:1896–9. doi: 10.1103/PhysRevLett.78.1896
63. Lepri S, Livi R, Politi A. Energy transport in anharmonic lattices close to and far from equilibrium. *Physica D*. (1998) **119**:140–7. doi: 10.1016/S0167-2789(98)00076-1
64. Davie SJ, Jepps OG, Rondoni L, Reid JC, Searles DJ. Applicability of optimal protocols and the Jarzynski equality. *Phys Scr*. (2014) **89**:048002. doi: 10.1088/0031-8949/89/04/048002
65. Jepps O, Bianca C, Rondoni L. Onset of diffusive behaviour in confined transport systems. *Chaos*. (2008) **18**:013127. doi: 10.1063/1.2888759
66. Bianca C, Rondoni L. The nonequilibrium Ehrenfest gas: a chaotic model with flat obstacles? *Chaos*. (2009) **19**:013121. doi: 10.1063/1.3085954
67. Salari L, Rondoni L, Giberti C, Klages R. A simple non-chaotic map generating subdiffusive, diffusive and superdiffusive dynamics. *Chaos*. (2015) **25**:073113. doi: 10.1063/1.4926621
68. Spohn H. Nonlinear fluctuating hydrodynamics for anharmonic chains. *J Stat Phys*. (2014) **154**:1191–227. doi: 10.1007/s10955-014-0933-y
69. Mendl CB, Spohn H. Dynamic correlators of Fermi-Pasta-Ulam chains and nonlinear fluctuating hydrodynamics. *Phys Rev Lett*. (2013) **111**:230601. doi: 10.1103/PhysRevLett.111.230601
70. van Beijeren H. Exact results for anomalous transport in one-dimensional hamiltonian systems. *Phys Rev Lett*. (2012) **108**:180801. doi: 10.1103/PhysRevLett.108.180601
71. Mejía-Monasterio C, Politi A. Rondoni L. Heat flux in one-dimesional systems. *arXiv [preprint]*. arXiv:1905.03326.
72. Kaburaki H, Machida M. Thermal conductivity in one-dimensional lattices of Fermi-Pasta-Ulam type. *Phys Lett A*. (1993) **181**:85–90. doi: 10.1016/0375-9601(93)91129-S

Conflict of Interest: The authors declare that the research was conducted in the absence of any commercial or financial relationships that could be construed as a potential conflict of interest.

frontiers in Physics

ORIGINAL RESEARCH
published: 20 November 2019
doi: 10.3389/fphy.2019.00182

Manifestations of Projection-Induced Memory: General Theory and the Tilted Single File

*Alessio Lapolla and Aljaž Godec**

Mathematical Biophysics Group, Max Planck Institute for Biophysical Chemistry, Göttingen, Germany

Over the years the field of non-Markovian stochastic processes and anomalous diffusion evolved from a specialized topic to mainstream theory, which transgressed the realms of physics to chemistry, biology and ecology. Numerous phenomenological approaches emerged, which can more or less successfully reproduce or account for experimental observations in condensed matter, biological and/or single-particle systems. However, as far as their predictions are concerned these approaches are not unique, often build on conceptually orthogonal ideas, and are typically employed on an *ad-hoc* basis. It therefore seems timely and desirable to establish a systematic, mathematically unifying and clean approach starting from more fine-grained principles. Here we analyze projection-induced ergodic non-Markovian dynamics, both reversible as well as irreversible, using spectral theory. We investigate dynamical correlations between histories of projected and latent observables that give rise to memory in projected dynamics, and rigorously establish conditions under which projected dynamics is Markovian or renewal. A systematic metric is proposed for quantifying the degree of non-Markovianity. As a simple, illustrative but non-trivial example we study single file diffusion in a tilted box, which, for the first time, we solve exactly using the coordinate Bethe ansatz. Our results provide a solid foundation for a deeper and more systematic analysis of projection-induced non-Markovian dynamics and anomalous diffusion.

Keywords: Fokker-Planck equation, spectral theory, projection operator method, occupation time, single file diffusion, Bethe ansatz, free energy landscape

Edited by:
Carlos Mejía-Monasterio, Polytechnic University of Madrid, Spain

Reviewed by:
Ludvig Lizana, Umeå University, Sweden
Luciano Calheiros Lapas, Universidade Federal da Integração Latino-Americana, Brazil

***Correspondence:**
Aljaž Godec
agodec@mpibpc.mpg.de

Specialty section:
This article was submitted to Interdisciplinary Physics, a section of the journal Frontiers in Physics

Received: *26 August 2019*
Accepted: *28 October 2019*
Published: *20 November 2019*

Citation:
Lapolla A and Godec A (2019) Manifestations of Projection-Induced Memory: General Theory and the Tilted Single File. Front. Phys. 7:182. doi: 10.3389/fphy.2019.00182

1. INTRODUCTION

Over the past decades the field of anomalous diffusion and non-Markovian dynamics grew to a mainstream physical topic [1–10] backed up by a surge of experimental observations [11–16] (the list of works is anything but exhaustive). From a theoretical point of view the description of anomalous and non-Markovian phenomena is not universal [1] and can be roughly (and judiciously) classified according to the underlying phenomenology: (i) renewal continuous-time random walk and fractional Fokker-Planck approaches [1–3, 17, 18], (ii) diffusion in disordered media [19–27], (iii) generalized Langevin equation descriptions [28–36], (iv) spatially heterogeneous diffusion [37–43], and more recently also (v) the so-called diffusing diffusivity models [44–50].

From a more general first-principles perspective non-Markovian dynamics in physical systems are always a result of the projection of nominally deterministic and/or Markovian high-dimensional dynamics to a lower-dimensional subspace [51–60]. The projection in general induces a dependence of the dynamics on the initial conditions of the latent degrees of freedom, i.e., those being integrated out, thereby leading to memory [51, 54–56] and possibly (depending on the system) also to anomalous diffusion [61–68].

Hallmarks of broken Markovianity are the non-validity of the Chapman–Kolmogorov equation, and, on the level of individual trajectories, correlations between histories of projected observables and latent degrees of freedom [67]. The advantage of a first principles approach is that it allows for a deeper understanding and complete control over the origin and nature of memory effects. It might, however, be difficult to integrate out exactly degrees of freedom in a given microscopic model, and in practice this seems to be only possible for simple models, e.g., harmonic systems (e.g., [69]), comb-models (e.g., [70–72]) or simple obstruction models [61–67], to name but a few.

Here, instead of deriving effective evolution operators for projected dynamics [51, 54–56] we use a spectral-theoretic approach and focus on the consequences of the projection directly on the level of probability density functions of projected variables—both in a general setting as well as by means of a simplistic yet non-trivial model of single file diffusion in a tilted box. Using spectral theory we first present a rigorous and quite general analysis of the problem and establish conditions, under which the projection in fact leads to Markovian or renewal-type dynamics. We then apply these general results to the analysis of tagged particle diffusion in a single file confined in a tilted box. We obtain an exact solution of the full many-body and projected tagged particle propagators using the coordinate Bethe ansatz, and provide exact results for tagged particle local time statistics and correlations between tagged particle histories. Finally, to asses the degree of non-Markovianity induced by the projection, we compute the Kullback–Leibler divergence between the exact tagged particle propagator and the propagator of Markovian diffusion in the respective free energy landscape, i.e., in the so-called free energy landscape perspective. Our results provide a deeper understanding of projection-induced memory and anomalous diffusion and highlight important pitfalls in applications of free energy landscape-ideas in absence of a time-scale separation.

2. THEORY

2.1. Notation and Mathematical Preliminaries

Although all presented result hold identically for discrete-state jump dynamics governed by a Markovian master equation we will here throughout be interested in projections of strongly Markovian diffusion in continuous time and in a continuous domain $\Omega \in \mathbb{R}^d$ in a vector field $\mathbf{F}(\mathbf{x}):\mathbb{R}^d \rightarrow \mathbb{R}^d$ (not necessarily a potential field), which is either nominally confining (in this case Ω is open) or is accompanied by corresponding reflecting boundary conditions at $\partial\Omega$ (in this case Ω is closed) thus guaranteeing the existence of an invariant measure and hence ergodicity. The dynamics are governed by the (forward) Fokker-Planck operator $\hat{\mathcal{L}}: V \rightarrow V$ or its adjoint (or backward) operator $\hat{\mathcal{L}}^\dagger: W \rightarrow W$, where V is a complete normed linear vector space with elements $f \in C^2(\mathbb{R}^d)$, and W is the space dual to V. In particular,

$$\hat{\mathcal{L}} = \nabla\cdot\mathbf{D}\nabla - \nabla\cdot\mathbf{F}(\mathbf{x}), \qquad \hat{\mathcal{L}}^\dagger = \nabla\cdot\mathbf{D}\nabla + \mathbf{F}(\mathbf{x})\cdot\nabla, \tag{1}$$

where $\mathbf{D}$ is the symmetric positive-definite diffusion matrix. $\hat{\mathcal{L}}$ propagates probability measures $\mu_t(\mathbf{x})$ in time, which will throughout be assumed to posses well-behaved probability density functions $P(\mathbf{x},t)$, i.e., $d\mu_t(\mathbf{x}) = P(\mathbf{x},t)d\mathbf{x}$ [thereby posing some restrictions on $\mathbf{F}(\mathbf{x})$]. On the level of individual trajectories Equation (1) corresponds to the Itô equation $d\mathbf{x}_t = \mathbf{F}(\mathbf{x}_t)dt + \boldsymbol{\sigma}d\mathbf{W}_t$ with $\mathbf{W}_t$ being a d-dimensional vector of independent Wiener processes whose increments have a Gaussian distribution with zero mean and variance dt, i.e., $\langle dW_{t,i}dW_{t',j}\rangle = \delta_{ij}\delta(t-t')dt$, and where $\boldsymbol{\sigma}$ is a $d\times d$ symmetric noise matrix such that $\mathbf{D} = \boldsymbol{\sigma}\boldsymbol{\sigma}^T/2$. Moreover, we assume that $\mathbf{F}(\mathbf{x})$ admits the following decomposition into a potential (irrotational) field $-\mathbf{D}\nabla\varphi(\mathbf{x})$ and a non-conservative component $\boldsymbol{\vartheta}(\mathbf{x})$, $\mathbf{F}(\mathbf{x}) = -\mathbf{D}\nabla\varphi(\mathbf{x}) + \boldsymbol{\vartheta}(\mathbf{x})$ with the two fields being mutually orthogonal $\nabla\varphi(\mathbf{x})\cdot\boldsymbol{\vartheta}(\mathbf{x}) = 0$ [73]. By insertion into Equation (1) one can now easily check that $\hat{\mathcal{L}}\mathrm{e}^{-\varphi(\mathbf{x})} = 0$, such that the stationary solution of the Fokker-Planck equation (also referred to as the steady state [74, 75], which is the terminology we adopt here) by construction does not depend on the non-conservative part $\boldsymbol{\vartheta}(\mathbf{x})$. Before proceeding we first establish the decomposition of the drift field $\mathbf{F}(\mathbf{x})$ of the full dynamics, which with the knowledge of $\varphi(\mathbf{x})$ can be shown to have the form

$$\mathbf{F}(\mathbf{x}) = -\mathbf{D}\nabla\varphi(\mathbf{x}) + \mathrm{e}^{\varphi(\mathbf{x})}\mathbf{j}_{\mathrm{ss}}(\mathbf{x}), \tag{2}$$

$\mathbf{j}_{\mathrm{ss}}(\mathbf{x})$ denoting the steady-state probability current and $\boldsymbol{\vartheta}(\mathbf{x}) \equiv \mathrm{e}^{\varphi(\mathbf{x})}\mathbf{j}_{\mathrm{ss}}(\mathbf{x})$ being incompressible. The proof follows straightforwardly. We take $\boldsymbol{\vartheta}(\mathbf{x}) = \mathbf{F}(\mathbf{x}) + \mathbf{D}\nabla\varphi(\mathbf{x})$ and use $\varphi(\mathbf{x})$ to determine the steady-state current $\mathbf{j}_{\mathrm{ss}}(\mathbf{x}) = (\boldsymbol{\vartheta}(\mathbf{x}) - \mathbf{D}\nabla\varphi(\mathbf{x}))\mathrm{e}^{-\varphi(\mathbf{x})} + \mathbf{D}\nabla\mathrm{e}^{-\varphi(\mathbf{x})}$, such that immediately $\boldsymbol{\vartheta}(\mathbf{x}) = \mathrm{e}^{\varphi(\mathbf{x})}\mathbf{j}_{\mathrm{ss}}(\mathbf{x})$ and in turn follows $\mathbf{F}(\mathbf{x})$ in Equation (2). To check for incompressibility we note that $\mathbf{j}_{\mathrm{ss}}(\mathbf{x})$ is by definition divergence free and so $\nabla\cdot\boldsymbol{\vartheta}(\mathbf{x}) = \mathrm{e}^{\varphi(\mathbf{x})}(\mathbf{j}_{\mathrm{ss}}(\mathbf{x})\cdot\nabla\varphi(\mathbf{x})) \equiv \boldsymbol{\vartheta}(\mathbf{x})\cdot\nabla\varphi(\mathbf{x}) = 0$, i.e., $\mathrm{e}^{\varphi(\mathbf{x})}\mathbf{j}_{\mathrm{ss}}(\mathbf{x})$ is divergence-free, as claimed.

We define the forward and backward propagators by $\hat{U}(t) = \mathrm{e}^{\hat{\mathcal{L}}t}$ and $\hat{U}^\dagger(t) = \mathrm{e}^{\hat{\mathcal{L}}^\dagger t}$ such that $\hat{\mathcal{L}}$ and $\hat{\mathcal{L}}^\dagger$ are generators of a semi-group $\hat{U}(t+t') = \hat{U}(t)\hat{U}(t')$ and $\hat{U}^\dagger(t+t') = \hat{U}^\dagger(t)\hat{U}^\dagger(t')$, respectively. $\hat{\mathcal{L}}$ propagates probability measures $\mu_t(\mathbf{x})$ in time, whereas $\hat{\mathcal{L}}^\dagger$ propagates observables $\mathcal{A}(\mathbf{x}_t)$ in time, which is best seen from the definition of the expectation

$$\langle\mathcal{A}(\mathbf{x}_t)\rangle \equiv \int\mathcal{A}(\mathbf{x})d\mu_t(\mathbf{x}) = \int\mathcal{A}(\mathbf{x})\mathrm{e}^{\hat{\mathcal{L}}t}P(\mathbf{x},0)d\mathbf{x} = \int P(\mathbf{x},0)\mathrm{e}^{\hat{\mathcal{L}}^\dagger t}\mathcal{A}(\mathbf{x})d\mathbf{x} \equiv \int d\mu_0(\mathbf{x}_0)\langle\mathcal{A}(\mathbf{x}_0,t)\rangle, \tag{3}$$

where $\langle\mathcal{A}(\mathbf{x}_0,t)\rangle$ was defined to give a correct behavior after averaging over the realizations of the Itô process but before averaging over the initial conditions $P(\mathbf{x},0)$ for the forward in time process (or end-point conditions for the adjoint, backward in time process). The propagation of measures by $\hat{\mathcal{L}}$ corresponds to the "Schrödinger" picture of quantum mechanics, whereas the propagation of observables resembles the "Heisenberg" picture.

For convenience we introduce the bra-ket notation with the "ket" $|f\rangle$ representing a vector in V (or W, respectively) written in position basis as $f(\mathbf{x}) \equiv \langle\mathbf{x}|f\rangle$, and the "bra" $\langle g|$ as the integral $\int d\mathbf{x}g^\dagger$. The scalar product is defined as $\langle g|f\rangle = \int d\mathbf{x}g^\dagger(\mathbf{x})f(\mathbf{x})$. Therefore we have, in operator notation, the following evolution equation for the conditional probability density function starting from an initial condition $|p_0\rangle$: $|p_t\rangle = \mathrm{e}^{\hat{\mathcal{L}}t}|p_0\rangle$. Since the process is ergodic we have $\lim_{t\to\infty}\mathrm{e}^{\hat{\mathcal{L}}t}|p_0\rangle = |\mathrm{ss}\rangle$, where we have defined the equilibrium or non-equilibrium steady state, $\hat{\mathcal{L}}|\mathrm{ss}\rangle = 0$ and $\langle\mathrm{ss}|\hat{\mathcal{L}}^\dagger = 0$, as a result of the duality. The steady state refers to a probability density function $\langle\mathbf{x}|\mathrm{ss}\rangle$ of the invariant measure, which might carry a time-independent non-vanishing probability current $\mathbf{j}_{\mathrm{ss}}(\mathbf{x})$. We also define the (typically non-normalizable) "flat" state $|-\rangle$, such that $\langle\mathbf{x}|-\rangle = 1$ and $\langle-|p_t\rangle = 1$. Hence, $\partial_t\langle-|p_t\rangle = 0$ and $\langle-|\hat{\mathcal{L}} = 0$ and $\hat{\mathcal{L}}^\dagger|-\rangle = 0$. We define the Green's function of the process as the conditional probability density function for a localized initial condition $\langle\mathbf{x}|p_0\rangle = \delta(\mathbf{x}-\mathbf{x}_0)$ as

$$G(\mathbf{x},t|\mathbf{x}_0,0) = \langle\mathbf{x}|\hat{U}(t)|\mathbf{x}_0\rangle \equiv \langle\mathbf{x}_0|\hat{U}^\dagger(t)|\mathbf{x}\rangle, \tag{4}$$

such that the conditional probability density starting from a general initial condition $|p_0\rangle$ becomes $P(\mathbf{x},t|p_0,0) = \langle\mathbf{x}|\hat{U}(t)|p_0\rangle \equiv \int d\mathbf{x}_0 p_0(\mathbf{x}_0)G(\mathbf{x},t|\mathbf{x}_0,0)$. Moreover, as $\mathbf{F}(\mathbf{x})$ is assumed to be sufficiently confining (i.e., $\lim_{\mathbf{x}\to\infty}P(\mathbf{x},t) = 0, \forall t$ sufficiently fast), such that $\hat{\mathcal{L}}$ corresponds to a coercive and densely defined operator on V (and $\hat{\mathcal{L}}^\dagger$ on W, respectively) [76–78]. Finally, $\hat{\mathcal{L}}$ is throughout assumed to be *normal*, i.e., $\hat{\mathcal{L}}^\dagger\hat{\mathcal{L}} - \hat{\mathcal{L}}\hat{\mathcal{L}}^\dagger = 0$ and thus henceforth $V = W$, where for reversible system (i.e., those obeying detailed balance) we have $\hat{\mathcal{L}} \Leftrightarrow \hat{\mathcal{L}}^\dagger$. Because any normal compact operator is diagonalizable [79], we can expand $\hat{\mathcal{L}}$ (and $\hat{\mathcal{L}}^\dagger$) in a complete bi-orthonormal set of left $\langle\psi_k^L|$ and right $|\psi_k^R\rangle$ ($\langle\psi_k^R|$ and $|\psi_k^L\rangle$, respectively) eigenstates

$$\hat{\mathcal{L}}|\psi_k^R\rangle = -\lambda_k|\psi_k^R\rangle, \qquad \hat{\mathcal{L}}^\dagger|\psi_k^L\rangle = -\alpha_k|\psi_k^L\rangle, \tag{5}$$

with $\mathrm{Re}(\lambda_k) \geq 0$, and according to our definition of the scalar product we have

$$\langle\psi_k^L|\hat{\mathcal{L}}|\psi_k^R\rangle = -\lambda_k\langle\psi_k^L|\psi_k^R\rangle = \left(\langle\psi_k^R|\hat{\mathcal{L}}^\dagger|\psi_k^L\rangle\right)^\dagger = -\alpha_k^\dagger\langle\psi_k^R|\psi_k^L\rangle \tag{6}$$

and hence the spectra of $\hat{\mathcal{L}}$ and $\hat{\mathcal{L}}^\dagger$ are complex conjugates, $\alpha_k = \lambda_k^\dagger$. Moreover, $\lambda_0 = 0$, $|\psi_0^R\rangle = |\mathrm{ss}\rangle$, $\langle\psi_0^L| = \langle-|$, and $\langle\psi_k^L|\psi_l^R\rangle = \delta_{kl}$. Finally, we also have the resolution of identity $\mathbf{1} = \sum_k|\psi_k^R\rangle\langle\psi_k^L|$ and the propagator $\hat{U}(t) = \sum_k|\psi_k^R\rangle\langle\psi_k^L|\mathrm{e}^{-\lambda_k t}$. It follows that the spectral expansion of the Green's function reads

$$G(\mathbf{x},t|\mathbf{x}_0,0) = \sum_k \psi_k^R(\mathbf{x})\psi_k^{L\dagger}(\mathbf{x}_0)\mathrm{e}^{-\lambda_k t} \equiv \sum_k \psi_k^L(\mathbf{x}_0)\psi_k^{R\dagger}(\mathbf{x})\mathrm{e}^{-\lambda_k^\dagger t}, \tag{7}$$

We now define, $\hat{\mathcal{P}}_{\mathbf{x}}(\mathbf{\Gamma};\mathbf{q})$, a (potentially oblique) projection operator into a subspace of random variables – a mapping $\mathbf{q} = \mathbf{\Gamma}(\mathbf{x}):\mathbb{R}^d \to \mathbb{R}^a$ to a subset of coordinates $\mathbf{q}$ lying in some orthogonal system in Euclidean space, $\mathbf{q} \in \Xi(\mathbb{R}^a) \subset \Omega(\mathbb{R}^d)$ with $a < d$. For example, the projection operator applied to some function $R(\mathbf{x}) \in V$ gives

$$\hat{\mathcal{P}}_{\mathbf{x}}(\mathbf{\Gamma};\mathbf{q})R(\mathbf{x}) = \int_\Omega d\mathbf{x}\delta(\mathbf{\Gamma}(\mathbf{x})-\mathbf{q})R(\mathbf{x}). \tag{8}$$

The spectral expansion of $\hat{\mathcal{L}}$ (and $\hat{\mathcal{L}}^\dagger$) in the bi-orthogonal Hilbert space alongside the projection operator $\hat{\mathcal{P}}_{\mathbf{x}}(\mathbf{\Gamma};\mathbf{q})$ will now allow us to define and analyze projection-induced non-Markovian dynamics.

2.2. General Results

2.2.1. Non-Markovian Dynamics and (Non)Existence of a Semigroup

Using the projection operator $\hat{\mathcal{P}}_{\mathbf{x}}(\mathbf{\Gamma};\mathbf{q})$ defined in Equation (8) we can define the (in general) non-Markovian Green's function of the projected dynamics as the conditional probability density of projected dynamics starting from a localized initial condition $\mathbf{q}_0$

$$\begin{aligned} Q_{p_0}(\mathbf{q},t|\mathbf{q}_0,0) &= \frac{Q_{p_0}(\mathbf{q},t,\mathbf{q}_0,0)_{p_0}}{Q^0_{p_0}(\mathbf{q}_0)} \\ &\equiv \frac{\hat{\mathcal{P}}_{\mathbf{x}}(\Gamma;\mathbf{q})\hat{\mathcal{P}}_{\mathbf{x}_0}(\Gamma;\mathbf{q}_0)G(\mathbf{x},t|\mathbf{x}_0,0)p_0(\mathbf{x}_0)}{\hat{\mathcal{P}}_{\mathbf{x}_0}(\Gamma;\mathbf{q}_0)p_0(\mathbf{x}_0)}, \end{aligned} \tag{9}$$

which demonstrates that the time evolution of projected dynamics starting from a fixed condition $\mathbf{q}_0$ depends on the initial preparation of the full system $p_0(\mathbf{x}_0)$ as denoted by the subscript. This is a first signature of the non-Markovian and non-stationary nature of projected dynamics and was noted upon also in [55]. Obviously, $\int_\Xi d\mathbf{q}Q_{p_0}(\mathbf{q},t|\mathbf{q}_0,0) = 1$ for any initial condition $\mathbf{q}_0$. We will refer to $\mathbf{q}$ as the projected degrees of freedom, whereas those integrated out will be called latent. For the sake of simplicity we will here mostly limit our discussion to a stationary preparation of the system, i.e., $p_0(\mathbf{x}_0) = p_{\mathrm{ss}}(\mathbf{x}_0) = \langle\mathbf{x}_0|\mathrm{ss}\rangle$. In order to avoid duplicating results we will explicitly carry out the calculation with the spectral expansion of $\hat{\mathcal{L}}$ but note that equivalent results are obtained using $\hat{\mathcal{L}}^\dagger$. Using the spectral expansion Equation (7) and introducing $\Psi_{kl}(\mathbf{q})$, the elements of an infinite-dimensional matrix

$$\Psi_{kl}(\mathbf{q}) = \langle\psi_k^L|\delta(\mathbf{\Gamma}(\mathbf{x})-\mathbf{q})|\psi_l^R\rangle \tag{10}$$

we find from Equation (9)

$$Q_{p_{\mathrm{ss}}}(\mathbf{q},t|\mathbf{q}_0,0) = \sum_k \Psi_{0k}(\mathbf{q})(\Psi_{k0}(\mathbf{q}_0)/\Psi_{00}(\mathbf{q}_0))\mathrm{e}^{-\lambda_k t} \tag{11}$$

with $\Psi_{00}(\mathbf{q}_0) = Q^0_{p_{\mathrm{ss}}}(\mathbf{q}_0)$. If one would to identify $\Psi_{0k}(\mathbf{q}) = \Psi^R_{0k}(\mathbf{q})$ and $\Psi_{00}(\mathbf{q}_0)^{-1}\Psi_{0k}(\mathbf{q}) = \Psi^L_{0k}(\mathbf{q})$, Equation (11) at first sight looks deceivingly similar to the Markovian Green's function in Equation (7). Moreover, a hallmark of Markovian dynamics is that it obeys the Chapman–Kolmogorov equation and indeed, since $\langle\psi_k^L|\psi_l^R\rangle = \delta_{kl}$, we find from the spectral expansion Equation (7) directly for any $0 < t' < t$ that

$$\begin{aligned}\int_\Omega d\mathbf{x}' G(\mathbf{x},t|\mathbf{x}',t')G(\mathbf{x}',t'|\mathbf{x}_0,0)\\ =\sum_{k,l}\psi_k^R(\mathbf{x})\langle\psi_k^L|\psi_l^R\rangle\psi_l^{L\dagger}(\mathbf{x}_0)\mathrm{e}^{-\lambda_k(t-t')-\lambda_l t'}\\ \equiv G(\mathbf{x},t|\mathbf{x}_0,0).\end{aligned} \tag{12}$$

For non-Markovian dynamics with a stationary $p_0(\mathbf{x})$ we here prove the following

Proposition 2.2.1.1. *Let the full system be prepared in a steady state, $p_0(\mathbf{x}) = p_{\mathrm{ss}}(\mathbf{x})$, and let non-Markovian Green's function be defined by Equation (9). We take $\Psi_{kl}(\mathbf{q})$ as defined in Equation (10) and define a scalar product with respect to a Lebesgue measure w as $\langle f|g\rangle_w \equiv \int d\mathbf{x}w(\mathbf{x})f^\dagger(\mathbf{x})g(\mathbf{x})$. Then the Green's function of the projected process will obey the Chapman–Kolmogorov equation if and only if $\langle\Psi_{l0}|\Psi_{k0}\rangle_{\Psi_{00}^{-1}} = 0, \forall k,l$.*

We need to prove if and under which conditions

$$\int_\Xi d\mathbf{q}' Q_{p_{\mathrm{ss}}}(\mathbf{q},t|\mathbf{q}',t')Q_{p_{\mathrm{ss}}}(\mathbf{q}',t'|\mathbf{q}_0,0) \tag{13}$$

can be equal to $Q_{p_{\mathrm{ss}}}(\mathbf{q},t|\mathbf{q}_0,0)$. As this will generally not be the case this essentially means that the projected dynamics is in general non-Markovian. The proof is established by noticing that $\Psi_{kl}(\mathbf{q}') = \Psi_{lk}^\dagger(\mathbf{q}')$ such that $\langle\Psi_{l0}|\Psi_{k0}\rangle_{\Psi_{00}^{-1}} \equiv \int_\Xi d\mathbf{q}'\Psi_{00}(\mathbf{q}')^{-1}\Psi_{0l}(\mathbf{q}')\Psi_{k0}(\mathbf{q}')$. As a result Equation (13) can be written analogously to the first equality in Equation (12) as

$$\sum_{k,l}\Psi_{0k}(\mathbf{q})\langle\Psi_{l0}|\Psi_{k0}\rangle_{\Psi_{00}^{-1}}(\Psi_{0l}^\dagger(\mathbf{q}_0)/\Psi_{00}(\mathbf{q}_0))\mathrm{e}^{-\lambda_k(t-t')-\lambda_l t'}. \tag{14}$$

But since the projection mixes all excited eigenstates with $k > 0$ (to a k-dependent extent) with the left and right ground states [see Equation (10)], the orthogonality between $\Psi_{00}(\mathbf{q})^{-1/2}\Psi_{0l}(\mathbf{q})$ and $\Psi_{00}(\mathbf{q})^{-1/2}\Psi_{k0}(\mathbf{q})$ is in general lost, and $\langle\Psi_{l0}|\Psi_{k0}\rangle_{\Psi_{00}^{-1}} \neq 0$ for $k \neq l$ as claimed above. The Chapman–Kolmogorov equation can hence be satisfied if and only if $\langle\Psi_{l0}|\Psi_{k0}\rangle_{\Psi_{00}^{-1}} = 0$ for all $k \neq l$.

The possibility that the Chapman–Kolmogorov equation remains valid for non-Markovian process has been demonstrated previously on the hand of specific models (see e.g., [80, 81]). Here we establish the necessary and sufficient conditions for this to be the case in a quite general setting. In turn, even if $\langle\Psi_{l0}|\Psi_{k0}\rangle_{\Psi_{00}^{-1}} = 0, \forall k \neq l$ that this does not guarantee that the projected process is actually Markovian. The computation of higher-order probability densities is necessary in order to check for Markovianity.

2.2.2. When Is the Projected Dynamics Markovian or Renewal?

A) Projected Dynamics is Markovian

A particularly useful aspect of the present spectral-theoretic approach is its ability to establish rigorous conditions for the emergence of (exactly) Markovian and (exactly) renewal-type dynamics from a microscopic, first principles point of view. Note that in this section we assume a general, non-stationary preparation of the system [i.e., $p_0(\mathbf{x}_0) \neq p_{\mathrm{ss}}(\mathbf{x}_0)$]. By inspection of Equations (10) and (11) one can establish that:

Theorem 2.2.2.1. *The necessary and sufficient condition for the projected dynamics to be Markovian if is that the projection $\hat{\mathcal{P}}_{\mathbf{x}}(\mathbf{\Gamma};\mathbf{q})$ (whatever its form) nominally projects into the nullspace of latent dynamics. In other words, the latent and projected dynamics remain decoupled and orthogonal for all times. This means that (i) there exists a bijective map $\mathbf{y} = f(\mathbf{x})$ to a decomposable coordinate system $\mathbf{y} = (\mathbf{q},\mathbf{q}'')$, in which the forward generator decomposes to $\hat{\mathcal{L}} = \hat{\mathcal{L}}_p + \hat{\mathcal{L}}_l$, where $\hat{\mathcal{L}}_p$ only acts and depends on the projected degrees of freedom $\mathbf{q} \in \Xi(\mathbb{R}^a) \subset \Omega(\mathbb{R}^d)$ with $a < d$ and $\hat{\mathcal{L}}_l$ only acts and depends on the latent coordinates $\mathbf{q}'' \in \Xi^c(\mathbb{R}^d) \subset \Omega(\mathbb{R}^d)$ (with, $\Xi \cap \Xi'' = \emptyset$, $\Omega = \Xi \cup \Xi''$), (ii) the boundary conditions on $\partial\Xi$ and $\partial\Xi^c$ are decoupled, and (iii) the projection operator $\hat{\mathcal{P}}_{\mathbf{y}}(\cdot;\mathbf{q}) = \int d\mathbf{q}''$ onto the subset of coordinates $\mathbf{q} \in \Xi(\mathbb{R}^a) \subset \Omega$ corresponds to an integral over the subset of latent coordinates $\mathbf{q}'' \in \Xi^c(\mathbb{R}^{d-a}) \subset \Omega$, which does not mix projected and latent degrees of freedom, or alternatively $\hat{\mathcal{L}}_l p_0(\mathbf{q}_0,\mathbf{q}_0'') = 0$.*

The statement of the theorem is intuitive and has most likely already been presented elsewhere in the existing literature, although we were not able to find it in the present form. The proof is rather straightforward and follows from the fact that if (and only if) the projected dynamics is Markovian it must be governed as well by a formal (Markovian) Fokker-Planck generator $\hat{\mathcal{L}}_p$ as in Equation (1), in which the projected and latent degrees of freedom are separable $\hat{\mathcal{L}} = \hat{\mathcal{L}}_p + \hat{\mathcal{L}}_l$, and that the full Hilbert space is a direct sum of Hilbert spaces of the $V = V_p \oplus V_l$, that is $\hat{\mathcal{L}}: V \to V$, $\hat{\mathcal{L}}_p: V_p \to V_p$ and $\hat{\mathcal{L}}_l: V_l \to V_l$ and $V_p \cap V_l = \emptyset$. This also requires that there is no boundary condition coupling vectors from V_p and V_l. In turn this implies assertion (i) above. If $\hat{\mathcal{P}}_{\mathbf{y}}(\cdot;\mathbf{q})$ is such that it does not mix eigenfunctions in V_p and V_l (i.e., it only involves vectors from V_p) then ecause of bi-orthonormality and the fact that $\langle -|\hat{\mathcal{L}} = 0$ the projected Green's function in full space $Q(\mathbf{q},t|\mathbf{q}_0)$ for $\mathbf{q} \in \Xi(\mathbb{R}^a)$ will be identical to the full Green's function in the isolated domain $G(\mathbf{x},t|\mathbf{x}_0)$ for $\mathbf{x} \in \Xi(\mathbb{R}^a)$ and the non-mixing condition is satisfied. The effect is the same if the latent degrees of freedom already start in a steady state, $\hat{\mathcal{L}}_l p_0(\mathbf{q}_0,\mathbf{q}_0'') = 0$. This establishes sufficiency. However, as soon as the projection mixes the two Hilbert spaces V_p and V_l, the generator of projected dynamics will pick up contributions from $\hat{\mathcal{L}}_l$ and will, upon integrating out the latent degrees of freedom, not be Markovian. This completes the proof.

B) Projected Dynamics is Renewal

We can also rigorously establish sufficient conditions for the projected dynamics to poses the renewal property. Namely, the physical notion of a waiting time or a random change of time-scale (see e.g., [2, 3]) can as well be attributed a microscopic origin. The idea of a random waiting time (or a random change of time scale) nominally implies a period of time and thereby the existence of some subdomain, during which and within the latent degrees evolve while the projected dynamics does not change. For this to be the case the latent degrees of freedom must be perfectly orthogonal to the projected degrees of freedom, both in the two domains as well as on their boundaries (a prominent simple example is the so-called comb model [70–72]). Moreover, the projected degrees of freedom evolve only when the latent degrees of freedom reside in some subdomain $\Upsilon \subset \Xi^c(\mathbb{R}^{d-a})$. In turn, this means that the dynamics until a time t ideally partitions between projected and latent degrees of freedom, which are coupled solely by the fact that the total time spent in each must add to t, which effects the waiting time. In a comb-setting the motion along the backbone occurs only when the particle is in the center of the orthogonal plane. In the context of a low-dimensional projection of ergodic Markovian dynamics, we can in fact prove the following general theorem:

Theorem 2.2.2.2. *Let there exists a bijective map* $\mathbf{y} = f(\mathbf{x})$ *to a decomposable coordinate system* $\mathbf{y} = (\mathbf{q}, \mathbf{q}'')$ *as in A) with the projected* $\mathbf{q} \in \Xi(\mathbb{R}^a)$ *and latent degrees of freedom* $\mathbf{q}'' \in \Xi^c(\mathbb{R}^{d-a}) \equiv \Omega(\mathbb{R}^d) \setminus \Xi(\mathbb{R}^a)$. *Furthermore, let* $\Upsilon \subset \Xi^c(\mathbb{R}^{d-a})$ *and let* $\mathbb{1}_\Upsilon(\mathbf{q}'')$ *denote the indicator function of the region* Υ *(i.e.,* $\mathbb{1}_\Upsilon(\mathbf{q}'') = 1$ *if* $\mathbf{q}'' \in \Upsilon$ *and zero otherwise). Moreover, let the full system be prepared in an initial condition* $p_0(\mathbf{q}, \mathbf{q}'')$. *Then a sufficient condition for renewal-type dynamics is (i) that the forward generator in* $(\mathbf{q}, \mathbf{q}'')$ *decomposes* $\hat{\mathcal{L}} = \mathbb{1}_\Upsilon(\mathbf{q}'')\hat{\mathcal{L}}_p + \hat{\mathcal{L}}_l$, *and where* $\hat{\mathcal{L}}_p$ *only acts and depends on* $\mathbf{q}$ *and* $\hat{\mathcal{L}}_l$ *only acts and depends on* $\mathbf{q}''$, *and (ii) the boundary conditions do not cause a coupling of latent and projected degrees of freedom (as in the Markov case above).*

Theorem 2.2.2.2 and lemma 2.2.2.2.1 below appear to be new, and the proof can be established by an explicit construction of the exact evolution equation for the projected variables. Let $G_l(\mathbf{q}'', t|\mathbf{q}_0'')$ denote the Green's functions of the Markovian problem for the latent degrees of freedom, $G_l(\mathbf{q}'', t|\mathbf{q}_0'') = \langle \mathbf{q}''|\mathrm{e}^{\hat{\mathcal{L}}_l t}|\mathbf{q}_0''\rangle = \sum_k \langle \mathbf{q}''|\psi_k^{l,R}\rangle\langle\psi_k^{l,L}|\mathbf{q}_0''\rangle \mathrm{e}^{-\lambda_k^l t}$ and let $\tilde{g}(s) = \int_0^\infty \mathrm{e}^{-st} g(t)dt$ denoted the Laplace transform of a function $g(t)$. The projection operator in this case corresponds to $\hat{\mathcal{P}}_{\mathbf{q}''}(\cdot; \mathbf{q}) = \int_{\Xi^c} d\mathbf{q}''$. We introduce the shorthand notation $\overline{p}_0(\mathbf{q}) = \int_{\Xi^c} d\mathbf{q}_0'' p_0(\mathbf{q}_0, \mathbf{q}_0'')$ and define the conditional initial probability density $p_0(\mathbf{q}_0''|\mathbf{q}_0) = p_0(\mathbf{q}_0, \mathbf{q}_0'')/\overline{p}_0(\mathbf{q}_0)$. The Green's function of projected dynamics becomes $Q_{p_0}(\mathbf{q}, t|\mathbf{q}_0) = \int_{\Xi^c} d\mathbf{q}'' \int_{\Xi^c} d\mathbf{q}_0'' G(\mathbf{q}, \mathbf{q}'', t|\mathbf{q}_0, \mathbf{q}_0'') p_0(\mathbf{q}_0, \mathbf{q}_0'')/\overline{p}_0(\mathbf{q}_0)$. We then have the following

Lemma 2.2.2.2.1. *Under the specified assumptions* $Q(\mathbf{q}, t|\mathbf{q}_0)$ *exactly obeys the renewal-type non-Markovian Fokker-Planck equation*

$$\partial_t Q_{p_0}(\mathbf{q}, t|\mathbf{q}_0) = \int_0^t d\tau K_{p_0}(t-\tau)\hat{\mathcal{L}}_p Q_{p_0}(\mathbf{q}, \tau|\mathbf{q}_0), \tag{15}$$

with the memory kernel

$$\begin{aligned} K_{p_0}(t) &= (\delta(t) + \partial_t)\int_\Upsilon d\mathbf{q}'' \int_{\Xi^c} d\mathbf{q}_0'' p_0(\mathbf{q}_0''|\mathbf{q}_0)\langle \mathbf{q}''|\mathrm{e}^{\hat{\mathcal{L}}_l t}|\mathbf{q}_0''\rangle \\ &= \sum_k \left(\int_{\Xi^c} d\mathbf{q}_0'' \psi_k^{l,L\dagger}(\mathbf{q}_0'') p_0(\mathbf{q}_0''|\mathbf{q}_0)\right) \\ &\quad \left(\int_\Upsilon d\mathbf{q}'' \psi_k^{l,R}(\mathbf{q}'')\right)(\delta(t) - \lambda_k^l \mathrm{e}^{-\lambda_k^l t}) \end{aligned} \tag{16}$$

that is independent of $\mathbf{q}$. *Moreover,* $Q(\mathbf{q}, t|\mathbf{q}_0) > 0$ *for all* $t > 0$ *and for all* $\mathbf{q}, \mathbf{q}_0 \in \Xi$.

To prove the lemma we Laplace transform equation ($t \to u$) $\partial_t G(\mathbf{q}, \mathbf{q}'', t|\mathbf{q}_0, \mathbf{q}_0'') = \hat{\mathcal{L}} G(\mathbf{q}, \mathbf{q}'', t|\mathbf{q}_0, \mathbf{q}_0'')$ and realize that the structure of $\hat{\mathcal{L}}$ implies that its solution with initial condition $\delta(\mathbf{q} - \mathbf{q}_0)\delta(\mathbf{q}'' - \mathbf{q}_0'')$ in Laplace space factorizes $\tilde{G}(\mathbf{q}, \mathbf{q}'', u|\mathbf{q}_0, \mathbf{q}_0'') = f_u(\mathbf{q}|\mathbf{q}_0) g_u(\mathbf{q}''|\mathbf{q}_0'')$ with g_u and f_u to be determined. Note that $\int_\Xi d\mathbf{q} \int_{\Xi^c} d\mathbf{q}'' \tilde{G}(\mathbf{q}, \mathbf{q}'', u|\mathbf{q}_0, \mathbf{q}_0'') = \int_\Xi d\mathbf{q} f_u(\mathbf{q}|\mathbf{q}_0) \int_{\Xi^c} d\mathbf{q}'' g_u(\mathbf{q}''|\mathbf{q}_0'') = u^{-1}$ and we can chose, without any loss of generality that $\int_\Xi d\mathbf{q} f_u(\mathbf{q}|\mathbf{q}_0) = 1$. Plugging in the factorized ansatz and rearranging leads to

$$\begin{aligned} &g_u(\mathbf{q}''|\mathbf{q}_0'')\left(u f_u(\mathbf{q}|\mathbf{q}_0) - \mathbb{1}_\Upsilon(\mathbf{q}'')\hat{\mathcal{L}}_p f_u(\mathbf{q}|\mathbf{q}_0)\right) \\ &-f_u(\mathbf{q}|\mathbf{q}_0)\hat{\mathcal{L}}_l g_u(\mathbf{q}''|\mathbf{q}_0'') - \delta(\mathbf{q} - \mathbf{q}_0)\delta(\mathbf{q}'' - \mathbf{q}_0'') = 0. \end{aligned} \tag{17}$$

Noticing that $\int_\Xi d\mathbf{q} \hat{\mathcal{L}}_p f(\mathbf{q}|\mathbf{q}_0) = 0$ as a result of the divergence theorem (as we assumed that $\mathbf{F}(\mathbf{x})$ is strongly confining implying that the current vanishes at the boundaries) we obtain, upon integrating Equation (17) over $\mathbf{q}$

$$u g_u(\mathbf{q}''|\mathbf{q}_0'') - \delta(\mathbf{q}'' - \mathbf{q}_0'') - \hat{\mathcal{L}}_l g_u(\mathbf{q}''|\mathbf{q}_0'') = 0, \tag{18}$$

implying that $g_u(\mathbf{q}''|\mathbf{q}_0'') = \tilde{G}_l(\mathbf{q}'', u|\mathbf{q}_0'')$. As $\tilde{G}_l(\mathbf{q}'', u|\mathbf{q}_0'')$ is the Laplace image of a Markovian Green's function we use $\int_{\Xi^c} d\mathbf{q}'' \tilde{G}_l(\mathbf{q}'', u|\mathbf{q}_0'') = u^{-1}$ in order to deduce that $\tilde{Q}_{p_0}(\mathbf{q}, u|\mathbf{q}_0) = f_u(\mathbf{q}|\mathbf{q}_0)/u$. The final step involves using the identified functions f_u and g_u in Equation (17), multiplying with $p_0(\mathbf{q}_0''|\mathbf{q}_0)$, integrating over $\mathbf{q}''$ and $\mathbf{q}_0''$ while using the divergence theorem implying $\int_{\Xi^c} d\mathbf{q}'' \hat{\mathcal{L}}_l \tilde{G}_l(\mathbf{q}'', u|\mathbf{q}_0'') = 0$ (as before) to obtain

$$\begin{aligned} &u\tilde{Q}_{p_0}(\mathbf{q}, u|\mathbf{q}_0) - \delta(\mathbf{q} - \mathbf{q}_0) \\ &= \left(u \int_\Upsilon d\mathbf{q}'' \int_{\Xi^c} d\mathbf{q}_0'' \tilde{G}_l(\mathbf{q}'', u|\mathbf{q}_0'') p_0(\mathbf{q}_0''|\mathbf{q}_0)\right) \hat{\mathcal{L}}_p \tilde{Q}_{p_0}(\mathbf{q}, u|\mathbf{q}_0). \end{aligned} \tag{19}$$

Finally, since the Laplace transform of $\partial_t g(t) + \delta(t)g(0)$ corresponds to $u\tilde{g}(u)$, taking the inverse Laplace transform of Equation (19) finally leads to Equations (15) and (16) and completes the proof of the lemma, since now we can take $Q_{p_0}(\mathbf{q}, t|\mathbf{q}_0) > 0$ by definition because Equation (15) is an identity of Equation (1) integrated over $\mathbf{q}''$. Moreover, the rate of change of the Green's function $Q_{p_0}(\mathbf{q}, t|\mathbf{q}_0)$ in Equation (15) depends, at any instance t, position $\mathbf{q}$ and for any initial condition $\mathbf{q}_0$ only on the current position $\mathbf{q}$ and a waiting time (or random time-change) encoded in the memory kernel $K(t)$; $Q_{p_0}(\mathbf{q}, t|\mathbf{q}_0)$ is the Green's function of a renewal process. This completes the proof of sufficiency.

Furthermore, for the situation where the full system is prepared in a stationary state, i.e., $p_0(\mathbf{x}) = p_s(\mathbf{x})$, we have the following

Corollary 2.2.2.2.1. *Let the system and projection be defined as in Theorem 2.2.2.2. If the full system is prepared such that the latent degrees of freedom are in a stationary state* $p_0(\mathbf{q}_0, \mathbf{q}_0'')$, *such that*

$\hat{\mathcal{L}}_l p_0(\mathbf{q}_0''|\mathbf{q}_0) = 0, \forall \mathbf{q}_0 \in \Xi$ and hence also $\overline{p}_0(\mathbf{q}_0'') = \overline{p}_{\mathrm{ss}}(\mathbf{q}_0'')$, then $p_0(\mathbf{q}_0''|\mathbf{q}_0) = \psi_0^{l,R}(\mathbf{q}_0'')$ and consequently $K_{p_0} = \delta(t) \int_\Upsilon d\mathbf{q}_0''\overline{p}_{\mathrm{ss}}(\mathbf{q}_0'')$, and therefore the projected dynamics is Markovian. Moreover, if the system is prepared such that the latent degrees of freedom are not in a stationary state, i.e., $p_0(\mathbf{q}_0|\mathbf{q}_0'') \neq \overline{p}_{\mathrm{ss}}(\mathbf{q}_0''), \forall \mathbf{q}_0$, there exists a finite time $t_M > 0$ after which the dynamics will be arbitrarily close to being Markovian.

The statement of this corollary is again intuitive. The proof of the first part follows from the bi-orthogonality of eigenfunctions of latent dynamics $\langle \psi_k^{l,R} | \psi_0^{l,R} \rangle = \delta_{k,0}$, rendering all terms in Equation (16) in Lemma 2.2.2.2.1 identically zero except for $k = 0$ with $\lambda_k^l = 0$. The second part is established by the fact that for times $t_M \gg 1/\lambda_1^l$, with $-\lambda_1^l$ being the largest (i.e., least negative) non-zero eigenvalue, all terms but the $k = 0$ term in Equation (16) in Lemma 2.2.2.2.1 become arbitrarily small.

Having established sufficiency, we now also comment on necessity of the conditions (i) and (ii) above for renewal dynamics. It is clear that the splitting of $\hat{\mathcal{L}}$ into $\hat{\mathcal{L}}_p$ and $\hat{\mathcal{L}}_l$, where $\hat{\mathcal{L}}_l$ does not act nor depend on projected variables, is also necessary condition for renewal. This can be established by contradiction as loosening these assumptions leads to dynamics that is not renewal. This can be understood intuitively, because it must hold that the latent degrees of freedom remain entirely decoupled from the projected ones (but not vice versa) and that the motion along both is mutually orthogonal. To illustrate this think of the paradigmatic comb model (see schematic in **Figure 1**) [70–72] and realize that renewal will be violated as soon as we tilt the side-branches for some angle from being orthogonal to the backbone.

However, since it is difficult to establish the most general class of admissible functions $h(\mathbf{q}'')$ used in $\hat{\mathcal{L}} = h(\mathbf{q}'')\hat{\mathcal{L}}_p + \hat{\mathcal{L}}_l$, we are not able to prove necessity. Based on the present analysis it seems somewhat difficult to systematically relax the assumptions for projected dynamics to be renewal without assuming, in addition, some sort of spatial discretization. We therefore hypothesize that the sufficient conditions stated in Theorem 2.2.2.2, potentially with some additional assumptions on $h(\mathbf{q}'')$ are also necessary conditions. Notably, however, that microscopic derivations of non-Markovian master equations of the form given in Equation (15) often start in discretized space or *ad-hoc* introduce a random change in time scale (see e.g., [2, 17, 82]). We end this section with the following final

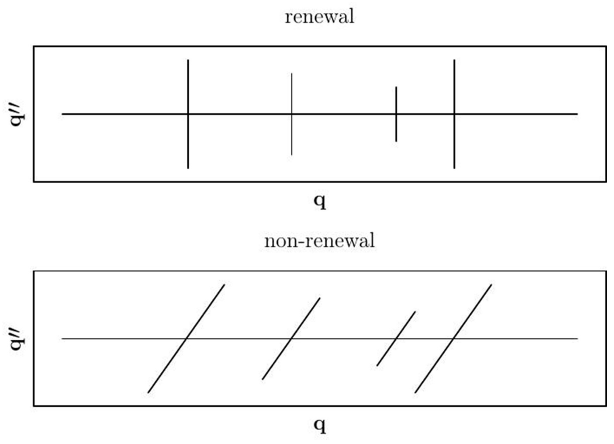

FIGURE 1 | Schematics of a generalized comb model. For the sake of clarity only a couple of side-branches are shown, whereas the model is to be understood in the sense of densely populated side-branches. (top) As long as the projected q and latent q'' degree of freedom remain orthogonal, the projected dynamics will be of renewal-type. However, as soon as this ceases to be the case the projected dynamics will not be renewal.

Remark 2.2.2.1. *An arbitrary projection $\hat{\mathcal{P}}_{\mathbf{x}}(\mathbf{\Gamma}; \mathbf{q})$ defined in Equation (8) will most likely lead to dynamics that is neither Markovian nor renewal.*

This follows from the strong assumptions required for Markovian and renewal dynamics, respectively. The properties of the corresponding general evolution operator will be described in a separate publication.

2.2.3. Markovian Approximation and the Degree of Non-Markovianity

In order to quantify the degree of non-Markovianity induced by the projection we propose to compare the full non-Markovian dynamics with projected dynamics evolving under a complete time-scale separation, i.e., under the assumption of all latent degrees of freedom being in the stationary state. To do so we proceed as follows. The projected coordinates $\mathbf{q}$ are now assumed to represent a subset of another d-dimensional orthogonal system in Euclidean space $\mathbf{q}' \in \mathbb{R}^d$, and we assume the map $\mathbf{q}'(\mathbf{x})$ is bijective. We denote the conditional probability density in this system by $G'(\mathbf{q}', t|\mathbf{q}_0', 0)$. The underlying physical idea is that an observer can only see the projected dynamics, which since it is non-Markovian stems from a projection but not necessarily onto Cartesian coordinates. Therefore, from a physical perspective not too much generality seems to be lost with this assumption.

As a concrete example one can consider the non-spherically symmetric Fokker-Planck process in a sphere, corresponding to the full Markovian parent system projected onto angular variables (either one or both). This way one first transforms from $\mathbf{x} \in \mathbb{R}^3$ to spherical coordinates $\mathbf{q}' = (r, \phi, \theta)$ and then, e.g., projects on the the lines $\mathbf{q} = \phi \in [0, 2\pi)$.

Since the transformation of the Fokker-Planck equation under a general change of coordinates is well-known [83] the task is actually simple. Under the complete map $\mathbf{q}' = \mathbf{\Gamma}(\mathbf{x})$ with $\mathbf{\Gamma} : \mathbb{R}^d \to \mathbb{R}^d$ the forward Fokker-Planck operator in Equation (1) transforms as $\hat{\mathcal{L}}' = \nabla_{\mathbf{q}'} \otimes \nabla_{\mathbf{q}'} : \tilde{D}(\mathbf{q}') - \nabla_{\mathbf{q}'} \cdot \tilde{\mathbf{F}}(\mathbf{q}')$, where $\otimes$ and $:$ denote, respectively, the tensor and double-dot product, and the transformed drift field and diffusion tensor can be written as

$$(\tilde{\mathbf{F}}(\mathbf{q}'))_k = \sum_{i=1}^{d} \frac{\partial q_k'}{\partial x_i} \mathbf{F}_i + \sum_{i,j=1}^{d} D_{ij} \frac{\partial^2 q_k}{\partial x_i \partial x_j},$$

$$(\tilde{D}(\mathbf{q}'))_{kl} = \sum_{i,j=1}^{d} D_{ij} \frac{\partial q_k'}{\partial x_i} \frac{\partial q_l'}{\partial x_j}. \qquad (20)$$

We note that unless the mapping is linear, the old diffusion matrix affects the new drift vector and the diffusion matrix picks up a spatial dependence. For an excellent account of the transformation properties in the more general case of a position dependent diffusion matrix [i.e., $\mathbf{D} \to \mathbf{D}(\mathbf{x})$] we refer the reader to [84]. We now want to marginalize over the remaining (i.e., non-projected) coordinates $\mathbf{q}'' \in \Omega \setminus \Xi$ but beforehand make the Markovian approximation $G'(\mathbf{q}', t|\mathbf{q}_0, 0) \approx Q_M(\mathbf{q}, t|\mathbf{q}_0)p_{\mathrm{ss}}(\mathbf{q}'')$. Then we have $\hat{\mathcal{L}}' G'(\mathbf{q}', t|\mathbf{q}_0, 0) \approx p_{\mathrm{ss}}(\mathbf{q}'')\hat{\mathcal{L}}' Q_M(\mathbf{q}, t|\mathbf{q}_0)$, implying that the operator $\hat{\mathcal{L}}'$ approximately splits into one part operating on the projected coordinates alone, $\hat{\mathcal{L}}'_M$, and one operating only on the latent stationary coordinates, $\hat{\mathcal{L}}''$, for which $\hat{\mathcal{L}}'' p_{\mathrm{ss}}(\mathbf{q}'') = 0$. The physical idea behind the Markovian approximation is that the latent degrees of freedom relax infinitely fast compared to the projected ones. Therefore, we can straightforwardly average the Fokker-Planck operator over the stationary latent coordinates $\mathbf{q}''$, $\langle \hat{\mathcal{L}}'_M \rangle_{\mathbf{q}''}$, where we have defined the latent averaging operation $\langle \cdot \rangle_{\mathbf{q}''} \equiv \int d\mathbf{q}'' p_{\mathrm{ss}}(\mathbf{q}'') \cdot$. Note that the remaining dependence of $\hat{\mathcal{L}}'$ on the latent stationary coordinates $\mathbf{q}''$ is only due to $\tilde{\mathbf{F}}(\mathbf{q}')$ and $\tilde{D}(\mathbf{q}')$. The averaged drift field and diffusion matrix now become

$$\langle \tilde{\mathbf{F}}(\mathbf{q}) \rangle_k = \sum_{i=1}^{d} \left\langle \frac{\partial q'_k}{\partial x_i} \mathbf{F}_i \right\rangle_{\mathbf{q}''} + \sum_{i,j=1}^{d} D_{ij} \left\langle \frac{\partial^2 q_k}{\partial x_i \partial x_j} \right\rangle_{\mathbf{q}''},$$
$$\langle \tilde{D}(\mathbf{q}) \rangle_{kl} = \sum_{i,j=1}^{d} D_{ij} \left\langle \frac{\partial q'_k}{\partial x_i} \frac{\partial q'_l}{\partial x_j} \right\rangle_{\mathbf{q}''}. \tag{21}$$

We can further decompose the effective drift field into a conservative and a non-conservative part

$$\left\langle \frac{\partial q'_k}{\partial x_i} \mathbf{F}_i \right\rangle_{\mathbf{q}''} = -\left\langle \frac{\partial q'_k}{\partial x_i} (\mathbf{D}\nabla\varphi)_i \right\rangle_{\mathbf{q}''} + \left\langle \mathrm{e}^{\varphi} \frac{\partial q'_k}{\partial x_i} (\mathbf{j}_{\mathrm{ss}})_i \right\rangle_{\mathbf{q}''}, \tag{22}$$

which establishes the Markovian approximation also for a broad class of irreversible systems. The approximate effective Fokker-Planck operator for the projected dynamics in turn reads

$$\langle \hat{\mathcal{L}}' \rangle_{\mathbf{q}''} = \nabla_{\mathbf{q}} \otimes \nabla_{\mathbf{q}} : \langle \tilde{D}(\mathbf{q}) \rangle_{\mathbf{q}''} - \nabla_{\mathbf{q}} \cdot \langle \tilde{\mathbf{F}}(\mathbf{q}) \rangle_{\mathbf{q}''}. \tag{23}$$

By design the kernel of $\langle \hat{\mathcal{L}}' \rangle_{\mathbf{q}''}$ is equal to $p_{\mathrm{ss}}(\mathbf{q}) \equiv \hat{\mathcal{P}}_{\mathbf{x}}(\mathbf{\Gamma}; \mathbf{q}) p_{\mathrm{ss}}(\mathbf{x})$, hence $\langle \hat{\mathcal{L}}' \rangle_{\mathbf{q}''}$ governs the relaxation toward the steady-state density (not necessarily equilibrium) evolving from some initial state $\mathbf{q}_0$ in the Markovian approximation with the corresponding Green's function $Q_M(\mathbf{q}, t|\mathbf{q}_0, 0) \equiv \langle \mathbf{q}| \mathrm{e}^{\langle \hat{\mathcal{L}}' \rangle_{\mathbf{q}''} t} |\mathbf{q}_0\rangle$.

In order to quantify the departure of the exact dynamics from the corresponding Markovian behavior we propose to evaluate the Kullback–Leibler divergence between the Green's functions of the exact and Markovian propagator as a function of time

$$\mathcal{D}_t(Q||Q_M) = \int_{\Xi} d\mathbf{q} Q(\mathbf{q}, t|\mathbf{q}_0, 0) \ln\left(\frac{Q(\mathbf{q}, t|\mathbf{q}_0, 0)}{Q_M(\mathbf{q}, t|\mathbf{q}_0, 0)}\right). \tag{24}$$

By definition $\mathcal{D}_t(Q||Q_M) \geq 0$ and since the non-Markovian behavior of the exact projected dynamics is transient with a lifetime λ_1^{-1}, we have that $\lim_{t\to\infty} \mathcal{D}_t(Q||Q_M) = 0$. Our choice of quantifying the departure of the exact dynamics from the corresponding Markovian behavior is not unique. The Kullback–Leibler divergence introduced here can hence be used to quantify how fast the correlation of the latent degrees of freedom with the projected degrees of freedom dies out. Notably, in a related manner the Kullback–Leibler divergence was also used in the context of stochastic thermodynamics in order to disprove the hypothesis about the monotonicity of the entropy production as a general time evolution principle [85].

2.2.4. Functionals of Projected Dynamics

In order to gain deeper insight into the origin and manifestation of non-Markovian behavior it is instructive to focus on the statistics of time-average observables, that is functionals of projected dynamics. As in the previous sections we assume that the full system was prepared in a (potentially non-equilibrium current-carrying) steady state. To that end we have, using Feynman-Kac theory, recently proven a theorem connecting any bounded additive functional $\Phi_t[\mathbf{q}(\tau)] = t^{-1}\int_0^t Z(\mathbf{q}(\tau))d\tau$ (with a function $Z : \Xi(\mathbb{R}^a) \to \mathbb{R}$ locally strictly bounded in Ξ) of projected dynamics $\mathbf{q}(\tau)$ of a parent Markovian diffusion $\mathbf{x}(t)$ to the eigenspectrum of the Markov generator of the full dynamics $\hat{\mathcal{L}}$ or $\hat{\mathcal{L}}^{\dagger}$ [67]. The central quantity of the theory is $\theta_t(\mathbf{s})$, the so-called local time fraction spent by a trajectory $\mathbf{q}(\tau)$ in a infinitesimal volume element $d\mathbf{s}$ centered at $\mathbf{s}$ up until a time t enabling

$$\theta_t(\mathbf{s}) = t^{-1}\int_0^t d\tau \mathbb{1}_{\mathbf{s}}(\mathbf{q}(\tau)) \quad \to \quad \Phi_t[\mathbf{q}(\tau)] = \int_{\Xi} d\mathbf{s} Z(\mathbf{s})\theta_t(\mathbf{s}), \tag{25}$$

where the indicator function $\mathbb{1}_{\mathbf{s}}(\mathbf{q}) = 1$ if $\mathbf{q} = \mathbf{s}$ and zero otherwise. We are here interested in the fluctuations of $\theta_t(\mathbf{s})$ and correlation functions between the local time fraction of a projected observable $\mathbf{q}(t)$ at a point $\mathbf{s}$ and $\theta''(\mathbf{s}')$, the local time some latent (hidden) observable $\mathbf{q}''(t)$ a the point $\mathbf{s}'$:

$$\sigma_t^2(\mathbf{s}) = \langle \theta_t^2(\mathbf{s}) \rangle - \langle \theta_t(\mathbf{s}) \rangle^2, \quad \mathcal{C}_t(\mathbf{s}; \mathbf{s}')$$
$$= \langle \theta_t(\mathbf{s})\theta''_t(\mathbf{s}') \rangle - \langle \theta_t(\mathbf{s}) \rangle \langle \theta''_t(\mathbf{s}') \rangle, \tag{26}$$

where $\langle \cdot \rangle$ now denotes the average over all forward paths starting from the steady state $|\mathbf{q}_0\rangle = |\mathrm{ss}\rangle$ (and ending anywhere, i.e., $\langle \mathbf{q}| = \langle - |$), or, using the backward approach, all paths starting in the flat state $|\mathbf{q}\rangle = |-\rangle$ and propagating backward in time toward the steady state $\langle \mathbf{q}_0| = \langle \mathrm{ss}|$. We note that any correlation function of a general additive bounded functional $\Phi_t^i[\mathbf{q}(\tau)]$ of the form $\langle \Phi_t^i[\mathbf{q}(\tau)] \Phi_t^j[\mathbf{q}''(\tau)] \rangle$ (as well as the second moment of $\Phi_t^i[\mathbf{q}(\tau)]$) follows directly from the local time fraction, namely, $\langle \Phi_t^i[\mathbf{q}(\tau)] \Phi_t^j[\mathbf{q}''(\tau)] \rangle = \int_{\Xi}\int_{\Xi} d\mathbf{s}d\mathbf{s}' Z_i(\mathbf{s}) Z_j(\mathbf{s}') \langle \theta_t(\mathbf{s}) \theta''_t(\mathbf{s}') \rangle$. For details of the theory and corresponding proofs please see [67], here we will simply state the main result:

Theorem 2.2.4.1. *Let the Green's function of the full parent dynamics* $\mathbf{x}(t)$ *be given by Equation (7) and the local time fraction* $\theta_t(\mathbf{s})$ *by Equation (25), then the variance and correlation function* *defined in Equation (26) is given exactly as*

$$\sigma_t^2(\mathbf{s}) = 2\sum_{k>0} \frac{\langle -|\mathbb{1}_\mathbf{s}|\psi_k^R\rangle\langle\psi_k^L|\mathbb{1}_\mathbf{s}|\mathrm{ss}\rangle}{\lambda_k t}\left(1-\frac{1-\mathrm{e}^{-\lambda_k t}}{\lambda_k t}\right)$$

$$\mathcal{C}_t(\mathbf{s};\mathbf{s}') = \sum_{k>0} \frac{\langle -|\mathbb{1}_\mathbf{s}|\psi_k^R\rangle\langle\psi_k^L|\mathbb{1}''_{\mathbf{s}'}|\mathrm{ss}\rangle + \langle -|\mathbb{1}''_{\mathbf{s}'}|\psi_k^R\rangle\langle\psi_k^L|\mathbb{1}_\mathbf{s}|\mathrm{ss}\rangle}{\lambda_k t} \left(1-\frac{1-\mathrm{e}^{-\lambda_k t}}{\lambda_k t}\right), \tag{27}$$

and analogous equations are obtained using the backward approach [67].

The usefulness of Equation (27) can be understood as follows. By varying $\mathbf{s}$ and $\mathbf{s}'$ one can establish *directly* the regions in space responsible for the build-up (and subsequent decay) of memory in projected dynamics and simultaneously monitor the fluctuations of the time spent of a projected trajectory in said regions. Note that because the full process is assumed to be ergodic, the statistics of $\theta_t(\mathbf{s})$ will be asymptotically Gaussian obeying the large deviation principle. This concludes our general results. In the following section we apply the theoretical framework to the analysis of projected dynamics in a strongly-correlated stochastic many-body system, namely to tagged particle dynamics in a single file confined to a tilted box.

3. SINGLE FILE DIFFUSION IN A TILTED BOX

We now apply the theory developed in the previous section (here we use the backward approach) to the paradigmatic single file diffusion in a unit interval but here with a twist, namely, the diffusing particles experience a constant force. In particular, the full state-space is spanned by the positions of all N-particles defining the state vector $\mathbf{x}_0 = (x_{0,1},\dots,x_{0,N})^T \in [0,1]^N$ and diffusion coefficients of all particles are assumed to be equal and the thermal (white) fluctuations due to the bath are assumed to be independent, i.e., $\mathbf{D} = D\mathbf{1}$. In addition to being confined in a unit interval, all particles experience the same constant force $\mathbf{F}(\mathbf{x}_0) = -\beta DF$ with $\beta = (k_BT)^{-1}$ is the inverse thermal energy. The evolution of the Green's function is governed by the Fokker-Planck equation Equation (1) equipped with the external and internal (i.e., non-crossing) reflecting boundary conditions for the backward generator $\hat{\mathcal{L}}^\dagger = \sum_{i=1}^N D(\partial^2_{x_{0,i}} - \beta\, F\partial_{x_{0,i}})$:

$$\partial_{x_{0,1}} G(\mathbf{x},t|\mathbf{x}_0)|_{x_{0,1}=0} = \partial_{x_{0,N}} G(\mathbf{x},t|\mathbf{x}_0)|_{x_{0,N}=1} = 0, \qquad \lim_{x_{0,i}\to x_{0,j}} (\partial_{x_{0,i+1}} - \partial_{x_{0,i}}) G(\mathbf{x},t|\mathbf{x}_0) = 0, \tag{28}$$

where we adopted the notation in Equation (7). The boundary conditions in Equation (28) restrict the domain to a hypercone $\mathbf{x}_0 \in \Xi$ such that $x_{0,i} \le x_{0,i+1}$ for $i = 1,\dots,N-1$. The dynamics is reversible, hence the steady state current vanishes and all eigenvalues and eigenfunctions are real. Moreover, for systems obeying detailed balance $\varphi(\mathbf{x})$ corresponds to the density of the Boltzmann-Gibbs measure and it is known that $|\psi_k^L\rangle \equiv \mathrm{e}^{-\varphi(\mathbf{x})}|\psi_k^R\rangle$. The single file backward generator already has a separated form $\hat{\mathcal{L}}^\dagger = \sum_{i=1}^N \mathcal{L}_i^\dagger$ and the coupling between particles enters solely through the non-crossing boundary condition Equation (28) and is hence Bethe-integrable [86]. However, because the projected and latent degrees of freedom are coupled through the boundary conditions Equation (28) the tagged particle dynamics is not of renewal type.

3.1. Diagonalization of the Generator With the Coordinate Bethe Ansatz

Specifically, the backward generator $\hat{\mathcal{L}}^\dagger$ can be diagonalized exactly using the coordinate Bethe ansatz (see e.g., [67]). To that end we first require the solution of the separated (i.e., single particle) eigenvalue problem $\mathcal{L}_i^\dagger|\psi_{k_i}^L\rangle = -\lambda_{k_i}|\psi_{k_i}^L\rangle$ under the imposed external boundary conditions. Since $\varphi(x_{0,i}) = Fx_{0,i} + const$ we find that $p_{\mathrm{ss}}(x_{0,i}) = \beta F\mathrm{e}^{-\beta Fx_{0,i}}(1-\mathrm{e}^{-\beta F})^{-1}$ and because of the confinement we also have $\lambda_{0,i} = 0$ as well as $\psi_{0_i}^L(x_{0,i}) \equiv \langle x_{0,i}|\psi_{0_i}^L\rangle = 1$ and $\psi_{0_i}^R(x_{0,i}) \equiv \langle\psi_{0_i}^R|x_{0,i}\rangle = p_{\mathrm{ss}}(x_{0,i})$. We are here interested in the role of particle number N and not of the magnitude of the force F, therefore we will henceforth set, for the sake of simplicity, $\beta F = D = 1$. The excited separated eigenvalues and eigenfunctions then read

$$\lambda_{k_i} = \pi^2k_i^2 + \frac{1}{4}, \qquad \psi_{k_i}^L(x_{0,i}) = \frac{\mathrm{e}^{x_{0,i}/2}}{(2\pi^2k_i^2+1/2)^{1/2}}\left(\sin(k_i\pi x_{0,i}) - 2k_i\pi\,\cos(k_i\pi x_{0,i})\right), \quad \forall k_i \in \mathbb{Z}^+, \tag{29}$$

with $\psi_{k_i}^R(x_{0,i}) = \mathrm{e}^{-x_{0,i}}\psi_{k_i}^L(x_{0,i})$. It is straightforward to check that $\langle\psi_{k_i}^R|\psi_{l_i}^L\rangle = \delta_{k_i,l_i}$. Denoting by $\mathbf{k} = (k_i, k_2,\dots,k_N)$ the N-tuple of all single-state indices k_i one can show by direct substitution that the many-body eigenvalues are given by $\lambda_\mathbf{k} = \sum_{i=1}^N \lambda_{k_i}$ and the corresponding orthonormal many-body eigenfunctions that obey the non-crossing internal boundary conditions Equation (28) have the form

$$\boldsymbol{\psi}_\mathbf{0}^L(\mathbf{x}_0) = 1, \quad \boldsymbol{\psi}_\mathbf{0}^R(\mathbf{x}_0) = N!\prod_{i=1}^N \frac{\mathrm{e}^{-x_{0,i}}}{1-\mathrm{e}^{-1}}$$

$$\boldsymbol{\psi}_\mathbf{k}^L(\mathbf{x}_0) = \sum_{\{k_i\}}\prod_{i=1}^N \psi_{k_i}^L(x_{0,i}), \boldsymbol{\psi}_\mathbf{k}^R(\mathbf{x}_0) = \mathbf{m}_\mathbf{k}!\sum_{\{k_i\}}\prod_{i=1}^N \psi_{k_i}^R(x_{0,i}), \tag{30}$$

where $\sum_{\{k_i\}}$ denotes the sum over all permutations of the elements of the N-tuple $\mathbf{k}$ and $\mathbf{m}_\mathbf{k}! = \prod_i m_{k_i}!$ is the respective multiplicity of the eigenstate with m_{k_i} corresponding to the number of times a particular value of k_i appears in the tuple. It can be checked by explicit computation that the eigenfunctions defined in Equation (30) form a complete bi-orthonormal set, that is $\langle\psi_\mathbf{k}^R|\psi_\mathbf{l}^L\rangle = \delta_{\mathbf{k},\mathbf{l}}$ and $\sum_\mathbf{k}\boldsymbol{\psi}_\mathbf{k}^L(\mathbf{x}_0)\boldsymbol{\psi}_\mathbf{k}^R(\mathbf{x}) = \delta(\mathbf{x}-\mathbf{x}_0)$.

3.2. Projection-Induced Non-Markovian Tagged Particle Dynamics

In the case of single file dynamics the physically motivated projection corresponds to the dynamics of a tagged particle upon integrating out the dynamics of the remaining particles. As before, we assume that the full system is prepared in a steady state. The projection operator for the dynamics of the j-th particle is therefore defined as

$$\hat{\mathcal{P}}_{\mathbf{x}}(\delta; q_j) = \int_{\Xi} d\mathbf{x}\delta(x_j - q_j) = \left[\hat{O}\prod_{i=1}^{N}\int_0^1 dx_i\right]\delta(x_j - q_j), \quad (31)$$

where the operator $\hat{O}$ orders the integration limits $\int_0^1 dx_N \int_0^{x_N} dx_{N-1}\cdots\int_0^{x_2} dx_1$ since the domain Ξ is a hypercone. Here, the projection is from $\mathbb{R}^N$ to $\mathbb{R}$. Integrals of this kind are easily solvable with the so-called 'extended phase-space integration' [62, 87]. The non-Markovian Green's function is defined as

$$Q(q_j, t|q_{0,j}) = \frac{\hat{\mathcal{P}}_{\mathbf{x}}(\delta; q_j)\hat{\mathcal{P}}_{\mathbf{x}_0}(\delta; q_{0,j})G(\mathbf{x}, t|\mathbf{x}_0)p_{\rm ss}(\mathbf{x}_0)}{\hat{\mathcal{P}}_{\mathbf{x}_0}(\delta; q_{0,j})p_{\rm ss}(\mathbf{x}_0)} \quad (32)$$

and can be computed exactly according to Equation (10) to give

$$Q(q_j, t|q_{0,j}) = \Psi_{\mathbf{00}}(q_{0,j})^{-1}\sum_{\mathbf{k}}\Psi_{\mathbf{0k}}(q_j)\Psi_{\mathbf{k0}}(q_{0,j})\mathrm{e}^{-\lambda_{\mathbf{k}}t}, \quad (33)$$

where the sum is over all Bethe eigenstates. If we denote the number of left and right neighbors by $N_L = (N - j + 1)$ and $N_R = j - 1$, respectively, all terms in Equation (33) read explicitly

$$\begin{aligned}\Psi_{\mathbf{00}}(q_j) &= \frac{N!}{N_L!N_R!(1-\mathrm{e}^{-1})^N}\mathrm{e}^{-q_j}(1-\mathrm{e}^{-q_j})^{N_L}(\mathrm{e}^{-q_j}-\mathrm{e}^{-1})^{N_R}\\ \Psi_{\mathbf{k0}}(q_j) &= \frac{N!}{N_L!N_R!(1-\mathrm{e}^{-1})^N}\sum_{\{k_i\}}T(q_j)\prod_{i=1}^{j-1}L(q_j)\prod_{i=j+1}^{N}R(q_j)\end{aligned} \quad (34)$$

and $\Psi_{\mathbf{0k}}(q_j) \equiv \Psi^{\dagger}_{\mathbf{k0}}(q_j) = \frac{\mathbf{m_k}!(1-\mathrm{e}^{-1})^N}{N!}\Psi_{\mathbf{k0}}(q_j)$. In Equation (34) we have introduced the auxiliary functions

$$\begin{aligned}T(q_j) &= \delta_{\lambda_j,0}\mathrm{e}^{-q_j} + (1-\delta_{\lambda_j,0})\frac{\mathrm{e}^{-q_j/2}}{\sqrt{1/2+2\pi^2\lambda_j^2}}\\ &\quad\left(\sin(\lambda_j\pi q_j) - 2\lambda_j\pi\cos(\lambda_j\pi q_j)\right)\\ L(q_j) &= \delta_{\lambda_j,0}(1-\mathrm{e}^{-q_j}) - 2(1-\delta_{\lambda_j,0})\frac{\mathrm{e}^{-q_j/2}\sin(\lambda_j\pi q_j)}{\sqrt{1/2+2\pi^2\lambda_j^2}}\\ R(q_j) &= \delta_{\lambda_j,0}(\mathrm{e}^{-q_j}-\mathrm{e}^{-1}) + 2(1-\delta_{\lambda_j,0})\frac{\mathrm{e}^{-q_j/2}\sin(\lambda_j\pi q_j)}{\sqrt{1/2+2\pi^2\lambda_j^2}}\end{aligned} \quad (35)$$

To the best of our knowledge, Equations (33) to (35) delivering the exact non-Markovian Green's function for the dynamics of the j-th particle in a tilted single file of N particles, have not yet been derived before. Note that one can also show that $\int_0^1 dq_j\Psi_{\mathbf{0k}}(q_j)\Psi_{\mathbf{l0}}(q_j) \neq 0$ and hence the Chapman–Kolmogorov equation is violated in agreement with Equation (13) confirming that the tagged particle diffusion is indeed non-Markovian on time-scales $t \lesssim \lambda_{\mathbf{1}}^{-1}$.

3.3. Markovian Approximation and Degree of Broken Markovianity

Since the projection leaves the coordinates untransformed the effective Markovian approximation in Equation (23) is particularly simple and corresponds to diffusion in the presence of an effective force deriving from the free energy of the tagged particle upon integrating out all the remaining particles assumed to be in equilibrium $\langle F(q_j)\rangle_{\mathbf{x}''} = -\langle\beta DF\delta(x_j - q_j)\rangle_{\mathbf{x}''}$ or, since $-\beta DFp_{\rm ss}(\mathbf{x}) = \partial_{x_j}p_{\rm ss}(\mathbf{x})$, explicitly defined as

$$\langle F(q_j)\rangle_{\mathbf{x}''} = \frac{\int_{\Xi} d\mathbf{x}\delta(x_j - q_j)\partial_{x_j}p_{\rm ss}(\mathbf{x})}{\int_{\Xi} d\mathbf{x}\delta(x_j - q_j)p_{\rm ss}(\mathbf{x})} \equiv \frac{\partial_{q_j}\int_{\Xi} d\mathbf{x}\delta(x_j - q_j)p_{\rm ss}(\mathbf{x})}{\int_{\Xi} d\mathbf{x}\delta(x_j - q_j)p_{\rm ss}(\mathbf{x})}. \quad (36)$$

Upon taking as before $D = \beta F = 1$, and noticing that $\Psi_{\mathbf{00}}(q_j) = \int_{\Xi} d\mathbf{x}\delta(x_j - q_j)p_{\rm ss}(\mathbf{x})$ we find

$$\begin{aligned}\langle\hat{\mathcal{L}}\rangle_{\mathbf{q}''} &= \partial_{q_j}^2 + \partial_{q_j}\left\{\partial_{q_j}\ln\Psi_{\mathbf{00}}(q_j)\right\},\\ \langle\hat{\mathcal{L}}^{\dagger}\rangle_{\mathbf{q}''} &= \partial_{q_j}^2 - \left\{\partial_{q_j}\ln\Psi_{\mathbf{00}}(q_j)\right\}\partial_{q_j}\end{aligned} \quad (37)$$

where the curly bracket $\{\cdot\}$ denotes that the operator inside the bracket only acts within the bracket. The Markovian approximation of the Green's function thus becomes $Q_M(q_j, t|q_{0,j}) = \langle q_{0,j}|\mathrm{e}^{\langle\hat{\mathcal{L}}^{\dagger}\rangle_{\mathbf{x}''}t}|q_j\rangle$ and is to be compared to the exact non-Markovian Green's function (33) via the Kullback–Leibler divergence in Equation (24).

Our focus here is to asses how the "degree" of the projection, i.e., $d = N$, $a = 1$ and thus $d - a = N - 1$ – the number of latent degrees of freedom (here positions of non-tagged particles) being integrated out affects the time-dependence of the Kullback–Leibler divergence. Since the Markovian generator cannot be diagonalized analytically we used a finite element numerical method cross-checked with Brownian dynamics simulations to calculate $Q_M(q_j, t|q_{0,j})$. The corresponding Kullback–Leibler divergence (24) was in turn calculated by means of a numerical integration. We present results for the time dependence $\mathcal{D}_t(Q||Q_M)$ in two different representations, the absolute (dimensionless) time t and in units of the average number of collisions $\tilde{t} = t/N^2$, tagging the third particle ($j = 3$). The reason to adopt this second choice as the natural physical time-scale is that collisions in fact establish the effective dynamics and hence a typical collision time sets the natural time-scale.

Before going into details we comment on the following. Because we start from the same initial condition for projected coordinate (i.e., tagged particle) in both, the non-Markovian and Markovian setting, it follows trivially that $\lim_{t\to 0}\mathcal{D}_t(Q||Q_M) = 0$. A zero $\mathcal{D}_t(Q||Q_M)$ would persist until the typical time of occurrence of the first collision event. This collision time is, however, much shorter than t/N^2 because we start from equilibrium initial conditions on the full, many-body level implying a continuous (Boltzmann-weighted) distribution of initial distances of the tagged particle to its nearest neighbors. Using a spectral expansion, however, such vanishingly short time-scales are very difficult to capture, i.e., it would require an astronomically large number of eigenstates, which is computationally not feasible. Conversely, because the tagged-particle invariant measures are by definition the same for the single file and its Markovian approximation [i.e., $\Psi_{\mathbf{00}}(q_j)$ is equal for both; the first of Equation (34) enters Equation (37)], it also follows that $\lim_{t\to\infty}\mathcal{D}_t(Q||Q_M) = 0$. The relaxation time $\lambda_{\mathbf{1}}^{-1}$ in the many-body problem corresponds to the exploration of the entire system of length L (here set to unity); for further details see [67]. For a finite single file deviations from Markovianity are therefore transient, starting at zero, passing through a maximum, and decaying back to zero at times longer than the relaxation time $\lambda_{\mathbf{1}}^{-1}$ of the full, many-body model.

The results for $\mathcal{D}_t(Q||Q_M)$ for intermediate and long times are shown in **Figure 2**. From **Figure 2**, we confirm that the Markovianity is broken transiently (on time-scales $t \lesssim \lambda_{\mathbf{1}}^{-1}$, which holds for any ergodic dynamics in the sense of generating an invariant measure. Notably, the relaxation time $\lambda_{\mathbf{1}}$ does *not* depend on N and is hence equal for all cases considered here. Moreover, as expected, the magnitude of broken Markovianity increases with the "degree" of the projection (here with the particle number N), as is best seen on a natural time-scale (see **Figure 2B**). Conversely, on the absolute time-scale the relaxation rate of the Markovian approximation, describing diffusion on a free energy landscape $f(q_3) = -\beta \ln \Psi_{\mathbf{00}}(q_3)$, which can be defined as

$$\lambda_1^M = -\lim_{t\to\infty} t^{-1} \ln(Q_M(q_j, t|q_{0,j}) - \Psi_{\mathbf{00}}(q_j)) \qquad (38)$$

increases with increasing N (see inset in **Figure 2B**). Therefore, while both have by construction the same invariant measure, the Markovian approximation overestimates the rate of relaxation. This highlights the pitfall in using free energy landscape ideas in absence of a time-scale separation.

3.4. Tagged Particle Local Times Probing the Origin of Broken Markovianity

In order to gain deeper insight into the origin and physical meaning of memory emerging from integrating out latent degrees of freedom we inspect how a given tagged particle explores the configuration space starting from a stationary (equilibrium) initial condition. To that end we first compute the variance of local time of a tagged particle, $\theta_t(q_j)$ in Equation (25), given in the general form in Equation (26), which applied to tagged particle diffusion in a tilted single file reads:

$$\sigma_t^2(q_j) = 2\sum_{\mathbf{k}} \frac{\Psi_{\mathbf{0k}}(q_j)\Psi_{\mathbf{k0}}(q_j)}{\lambda_{\mathbf{k}} t}\left(1 - \frac{1 - e^{-\lambda_{\mathbf{k}} t}}{\lambda_{\mathbf{k}} t}\right) \qquad (39)$$

where $\Psi_{\mathbf{k0}}(q_j)$ is given by Equation (34) and $\Psi_{\mathbf{0k}}(q_j) = \frac{\mathbf{m_k}!}{N!}\Psi_{\mathbf{k0}}(q_j)$. Note that since the process in ergodic we have $\langle\theta_t(q_j)\rangle = \Psi_{\mathbf{00}}(q_j)$, and because the projected dynamics becomes asymptotically Gaussian (i.e., the correlations between $\theta_t(q_j)$ at different t gradually decorrelate) we also have the large deviation $\lim_{t\to\infty} t\sigma_t^2(q_j) = 2\sum_{\mathbf{k}} \lambda_{\mathbf{k}}^{-1}\Psi_{\mathbf{0k}}(q_j)\Psi_{\mathbf{k0}}(q_j) \neq f(t)$. Moreover, because of detailed balance the large deviation principle represents an upper bound to fluctuations of time-average observables $\sigma_t^2(q_j) \leq 2\sum_{\mathbf{k}} \frac{\Psi_{\mathbf{0k}}(q_j)\Psi_{\mathbf{k0}}(q_j)}{\lambda_{\mathbf{k}} t}, \forall\, t$.

In order to gain more intuition we inspect the statistics of $\theta_t(q_j)$ for a single file of four particles (see **Figure 3**) at different lengths of trajectory t (plotted here on the absolute time-scale). In **Figure 3**, we show $\langle\theta_t(q_j)\rangle$ with full lines, and the region bounded by the standard deviation $\pm\sigma_t(q_j)$ with the shaded area.

The scatter of $\theta_t(q_j)$ is largest near the respective free energy minima.

To understand further how this coupling to non-relaxed latent degrees of freedom arises we inspect the correlations between

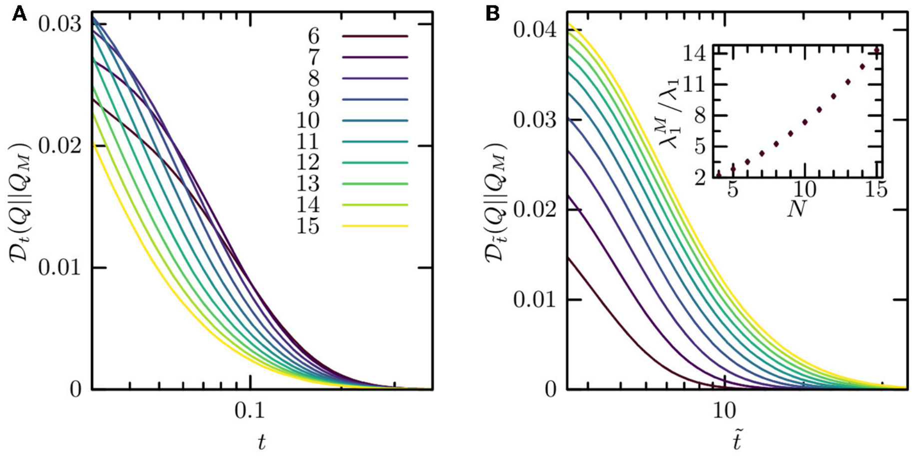

FIGURE 2 | The Kullback–Leibler divergence between the exact non-Markovian Green's function $Q(q_3, t|q_{0,3})$ and the Markovian approximation $Q_M(q_3, t|q_{0,3})$ as a function of time (measured in units of collision time) for increasing values of particle numbers N: **(A)** results shown on the absolute (dimensionless) time-scale and **(B)** on the natural time-scale, that is, expressed in units of collision time $\tilde{t}$. Inset: λ_1^M, the slowest relaxation rate of $Q_M(q_3, t|q_{0,3})$ compared to the corresponding eigenvalue λ_1 of the exact $Q(q_3, t|q_{0,3})$.

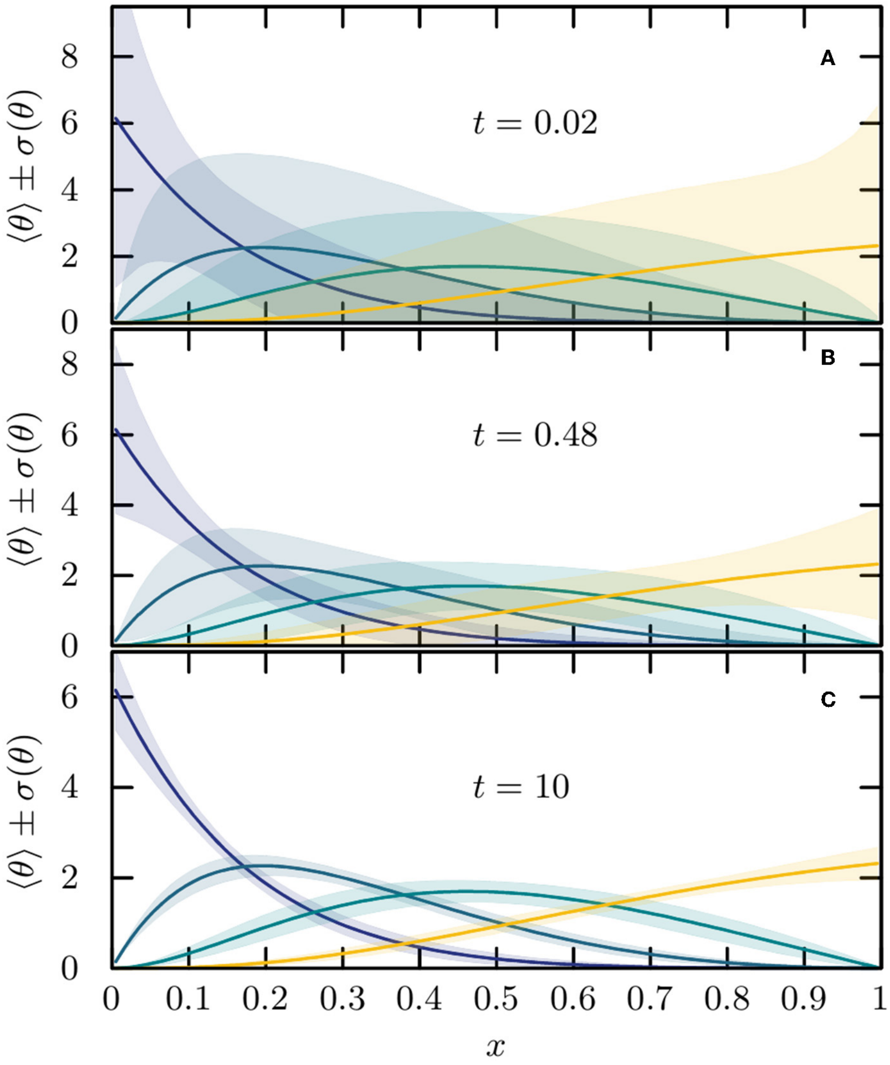

FIGURE 3 | Statistics of tagged particle local time for all members of a single file of four particles starting from stationary initial conditions; $\langle\theta_t(q_j)\rangle$ is represented by full lines and the region bounded by the standard deviation $\pm\sigma_t(q_j)$ with the corresponding shaded area. The color code is: $j = 1$ violet, $j = 2$ blue, $j = 3$, green and $j = 4$ yellow. The relaxation time corresponds to $\lambda_1^{-1} \simeq 0.1$. Therefore, panel **(A)** depicts fluctuations on a time scale much shorter that λ_1^{-1}, whereas **(B,C)** already belong deeply into the ergodic large deviation regime.

tagged particle histories

$$\mathcal{C}_t(q_i; q_j) = \sum_{\mathbf{k}} \frac{\Psi_{\mathbf{0k}}(q_i)\Psi_{\mathbf{k0}}(q_j) + \Psi_{\mathbf{0k}}(q_j)\Psi_{\mathbf{k0}}(q_i)}{\lambda_k t}\left(1 - \frac{1-\mathrm{e}^{-\lambda_k t}}{\lambda_k t}\right), \tag{40}$$

where as before $\lim_{t\to\infty} t\mathcal{C}_t(q_i; q_j) \equiv \overline{\mathcal{C}}_t(q_i; q_j) = \sum_{\mathbf{k}} \lambda_{\mathbf{k}}^{-1}(\Psi_{\mathbf{0k}}(q_i)\Psi_{\mathbf{k0}}(q_j) + \Psi_{\mathbf{0k}}(q_j)\Psi_{\mathbf{k0}}(q_i)) \neq f(t)$ as a manifestation of the central limit theorem, since $\theta_t(q_i)$ and $\theta_t(q_j)$ asymptotically decorrelate. In other words, taking $\mathcal{C}_t(q_i; q_i) \equiv \sigma_t^2(q_i)$, the complete large deviation statistics of $\theta_t(q_i)$ (i.e., on ergodically long time-scales) is a N-dimensional Gaussian with covariance matrix $t^{-1}\overline{\mathcal{C}}_t(q_i; q_j)$.

To visualize these results we present in **Figures 4**, **5** two-tag nearest neighbor and next-nearest correlations, $\mathcal{C}_t(q_1; q_3)$ and as $\mathcal{C}_t(q_2; q_3)$ respectively, for a single file of $N = 4$ and $N = 7$ particles at two different trajectory lengths. We find that, alongside the fact that correlations intuitively increase with the N, both the magnitude and the sign of $\mathcal{C}_t$ depend on which particles we tag and even more so, where we tag these particles. Along the (upward shifted) diagonal $\mathcal{C}_t$ is positive, implying the two tagged particles along a stochastic many-body trajectory effectively (in the sense of the local time) move together, such that if one particle spends more time in a given region, so will the other. At fixed F (here assumed to be equal to 1) the magnitude of the upward shift depends on which particles we tag as well as on N. This

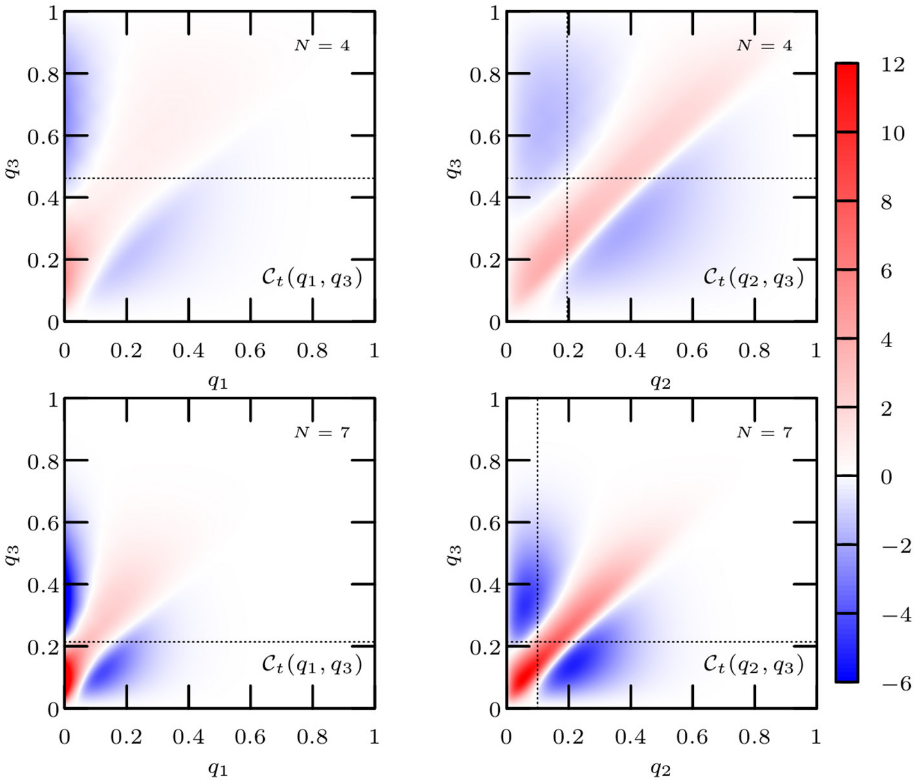

FIGURE 4 | Two-tag local time correlations $\mathcal{C}_t(q_1; q_3)$ **(left)** and $\mathcal{C}_t(q_2; q_3)$ **(right)** for a single file of $N = 4$ **(top)** and $N = 7$ **(bottom)** particles for a (very short) trajectory length $t = 0.01$. The relaxation time corresponds to $\lambda_1^{-1} \simeq 0.1$. The dashed lines denote the positions of the two free energy minima.

intuitive idea is backed up mathematically by realizing that the lowest excited Bethe-eigenfunctions correspond to collective ("in phase") motion (see Equations 29, 30). Furthermore, defining the free energy minima of the tagged particles with $q_i^{\min}$ and $q_i^{\min}$ (see dashed lines in **Figures 4**, **5**) we would expect, if the particles were to explore their respective free energy minima, a peak localized at $(q_i^{\min}, q_i^{\min})$ (i.e., at the crossing of dashed line in **Figures 4**, **5**). We find, however, that this is not the case, all together implying that the *tagged particles do not, along a many-body trajectory, explore their respective free energy minima*. Instead, as mentioned above, they move collectively close to each other. The collective dynamics is therefore non-trivial and the tagged particle dynamics cannot be, at least for $t \lesssim \lambda_1^{-1}$ coarse grained to a Markovian diffusion on $-\beta \ln \Psi_{\mathbf{00}}(q_j)$, the free energy landscape of the tagged particle j. Conversely, the fact that all correlations (positive and negative) die our as $q_{i,j} \to 1$ is a straightforward consequence of the tilting of the confining box.

Focusing now on the dependence on the length of the trajectory we see at very short time (much shorter than the relaxation time) the correlations are stronger, and that positive correlations peak further away from the two respective tagged particle free energy minima (compare **Figure 4** and **Figure 5**). In addition, the maximum of $\mathcal{C}_t(q_i; q_j)$ appears to be somewhat more localized at longer (nearly ergodic) times (see **Figure 5**). In addition, the tagged particle dynamics seem to be localized more strongly near the free energy minimum if we tag the first particle and if N is larger, presumably because of a faster relaxation due to the presence of the wall effecting more frequent collisions with the wall, during which the particle eventually loses memory.

4. SUMMARY AND OUTLOOK

Non-Markovian dynamics and anomalous diffusion are particularly ubiquitous and important in biophysical systems [1–16]. There, however, it appears that the quite many non-Markovian observations are described theoretically by phenomenological approaches with *ad-hoc* memory kernels, which in specific cases can lead to mathematically unsound or even unphysical behavior [82]. It therefore seems timely and useful to provide a theoretical perspective of non-Markovian dynamics starting from more fine-grained principles and considering a projection to some effective lower-dimensional configuration space.

The ideas presented here are neither new nor completely general. Projection-operator concepts date back to the original works by Zwanzig, Mori, Nakajima, van Kampen, Hänggi and other pioneers. However, these seminal contributions focused mostly on the derivation and analysis of effective non-Markovian evolution operators, whereas here we provide a thorough analysis of the manifestations of the projection on the level of Green's functions with the aim to somewhat relieve the need for choosing a particular model based solely on physical intuition.

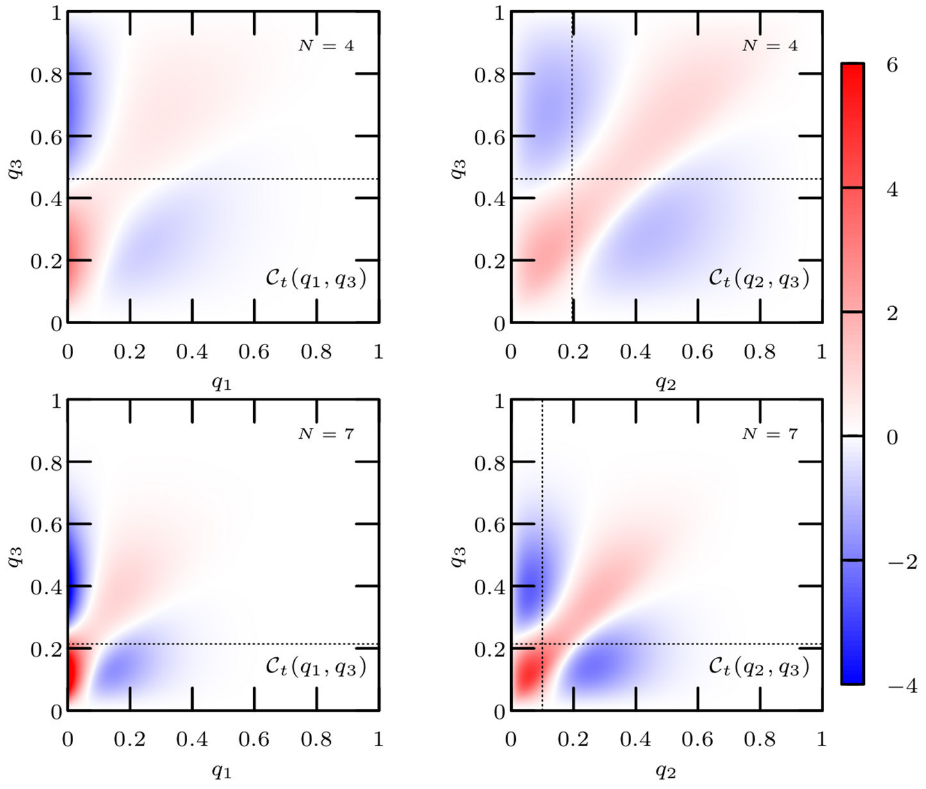

FIGURE 5 | Two-tag local time correlations $\mathcal{C}_t(q_1; q_3)$ **(left)** and $\mathcal{C}_t(q_2; q_3)$ **(right)** for a single file of $N = 4$ **(top)** and $N = 7$ **(bottom)** particles for a trajectory length comparable to the relaxation time $t = 0.12 \simeq \lambda_1^{-1}$. The relaxation time corresponds to $\lambda_1^{-1} \simeq 0.1$. The dashed lines denote the positions of the two free energy minima.

Furthermore, we rigorously establish conditions under which the projected dynamics become Markovian and renewal-type, and derive Markovian approximations to projected generators. As a diagnostic tool we propose a novel framework for the assessment of the degree of broken Markovianity as well as for the elucidation of the origins of non-Markovian behavior.

An important remark concerns the transience of broken Markovianity, which is a consequence of the fact that we assumed that the complete dynamics is ergodic. First we note that (i) for any finite observation of length t it is *de facto* not possible to discern whether the observation (and the dynamics in general) will be ergodic or not on a time scale $\tau > t$. (ii) All physical observations are (trivially) finite. (iii) In a nominally ergodic dynamics on any finite time scale t, where the dynamics starting from some non-stationary initial condition $\mathbf{x}_0$ has not yet reached the steady state (in the language of this work $t < \lambda_1^{-1}$), it is not possible to observe the effect of a sufficiently distant confining boundary $\partial\Omega(\mathbf{x})$ (potentially located at infinity if the drift field $\mathbf{F}(\mathbf{x})$ is sufficiently confining) that would assure ergodicity (in the language of this work $\forall t \ll \lambda_1^{-1}$ such that $G(\boldsymbol{l}_{\min}, t|\mathbf{x}_0, 0) \simeq 0$ where $|\boldsymbol{l}_{\min}| \equiv \min_{\mathbf{x}}|\mathbf{x}_0 - \partial\Omega(\mathbf{x})|$). Therefore *no generality is lost in our work by assuming that the complete dynamics is nominally ergodic*, even in a rigorous treatment of so-called weakly non-ergodic dynamics with diverging mean waiting times (see e.g., [1, 6]) or generalized Langevin dynamics with diverging correlation times (see e.g., [29–34]) on finite time-scales. As a corollary, in the description of such dynamics on any finite time-scale it is *a priori* by no means necessary to assume that the dynamics is non-ergodic or has a diverging correlation time. This does not imply, however, that the assumption of diverging mean waiting times or diverging correlation times cannot render the analysis of specific models simpler.

Notably, our work considers parent dynamics with a potentially broken time-reversal symmetry and hence includes the description of projection-induced non-Markovian dynamics in non-equilibrium (i.e., irreversible) systems. In the latter case the relaxation process of the parent microscopic process might not be monotonic (i.e., may oscillate), and it will be very interesting to explore the manifestations and importance of these oscillations in projected non-Markovian dynamics.

In the context of renewal dynamics our work builds on firm mathematical foundations of Markov processes and therefore provides mathematically and physically consistent explicit (but notably not necessarily the most general) memory kernels derived from microscopic (or fine-grained) principles, which can serve for the development, assessment and fine-tuning of empirical memory kernels that are used frequently in the theoretical modeling of non-Markovian phenomena (e.g., power-law, exponential, stretched exponential etc; [2, 82]). In particular, power-law kernels are expected to emerge as transients in cases, where the latent degrees of freedom relax over multiple time-scales with a nearly continuous and self-similar spectrum. Conversely, the quite strongly restrictive conditions imposed on the microscopic (parent) dynamics that lead to renewal dynamics, which we reveal here, suggest that renewal type transport in continuous space (e.g., continuous-time random walks [1, 2]) might not be the most abundant processes underlying projection-induced non-Markovian dynamics in physical systems, but are more likely to arise due to some disorder averaging. In general, it seems natural that coarse graining involving some degree of spatial discretization should underly renewal type ideas.

From a more general perspective beyond the theory of anomalous diffusion our results are relevant for the description and understanding of experimental observables $a(\mathbf{q})$ coupled to projected dynamics $\mathbf{q}(t)$ in presence of slow latent degrees of freedom (e.g., a FRET experiment measuring the distance within a protein or a DNA molecule [88]), as well as for exploring stochastic thermodynamic properties of projected dynamics with slow hidden degrees of freedom [89–91]. An important field of applications of the spectral-theoretic ideas developed here is the field of statistical kinetics in the context of first passage concepts (e.g., [92–94]), where general results for non-Markovian dynamics are quite sparse [46, 49, 95–100] and will be the subject of our future studies.

DATA AVAILABILITY STATEMENT

All datasets generated for this study are included in the article/supplementary material.

AUTHOR CONTRIBUTIONS

AL and AG conceived the research, performed the research, and wrote and reviewed the paper.

FUNDING

The financial support from the German Research Foundation (DFG) through the Emmy Noether Program GO 2762/1-1 (to AG), and an IMPRS fellowship of the Max Planck Society (to AL) are gratefully acknowledged.

ACKNOWLEDGMENTS

We thank David Hartich for fruitful discussions and critical reading of the manuscript. AG in addition thanks Ralf Metzler for introducing him to the field on anomalous and non-Markovian dynamics and for years of inspiring and encouraging discussions.

REFERENCES

1. Metzler R, Klafter J. The random walk's guide to anomalous diffusion: a fractional dynamics approach. *Phys Rep.* (2000) **339**:1–77. doi: 10.1016/S0370-1573(00)00070-3
2. Metzler R, Klafter J. The restaurant at the end of the random walk: recent developments in the description of anomalous transport by fractional dynamics. *J Phys A Math Gen.* (2004) **37**:R161–208. doi: 10.1088/0305-4470/37/31/R01
3. Sokolov IM, Klafter J. From diffusion to anomalous diffusion: a century after Einstein's Brownian motion. *Chaos.* (2005) **15**:026103. doi: 10.1063/1.1860472
4. Klages R, Radons G, Sokolov IM. *Anomalous Transport: Foundations and Applications.* Weinheim: Wiley-VCH Verlag GmbH and Co. (2008).
5. Godec A, Bauer M, Metzler R. Collective dynamics effect transient subdiffusion of inert tracers in flexible gel networks. *N J Phys.* (2014) **16**:092002. doi: 10.1088/1367-2630/16/9/092002
6. Metzler R, Jepn JH, Cherstvy AG, Barkai E. Anomalous diffusion models and their properties: non-stationarity, non-ergodicity, and ageing at the centenary of single particle tracking. *Phys Chem Chem Phys.* (2014) **16**:24128–64. doi: 10.1039/C4CP03465A
7. Höfling F, Franosch T. Anomalous transport in the crowded world of biological cells. *Rep Prog Phys.* (2013) **76**:046602. doi: 10.1088/0034-4885/76/4/046602
8. Sokolov IM. Models of anomalous diffusion in crowded environments. *Soft Matter.* (2012) **8**:9043–52. doi: 10.1039/c2sm25701g
9. Metzler R, Jeon JH, Cherstvy AG. Non-Brownian diffusion in lipid membranes: experiments and simulations. *Biochim Biophys Acta Biomemb.* (2016) **1858**:2451–67. doi: 10.1016/j.bbamem.2016.01.022
10. Oliveira FA, Ferreira RMS, Lapas LC, Vainstein MH. Anomalous diffusion: a basic mechanism for the evolution of inhomogeneous systems. *Front Phys.* (2019) **7**:18. doi: 10.3389/fphy.2019.00018
11. Woringer M, Darzacq X. *Protein Motion in the Nucleus: From Anomalous Diffusion to Weak Interactions.* Biochemical Society Transactions (2018). Available online at: http://www.biochemsoctrans.org/content/early/2018/07/29/BST20170310
12. Dix JA, Verkman AS. Crowding effects on diffusion in solutions and cells. *Annu Rev Biophys.* (2008) **37**:247–63. doi: 10.1146/annurev.biophys.37.032807.125824
13. Krapf D. Chapter 5: Mechanisms underlying anomalous diffusion in the plasma membrane. In: Kenworthy AK, editor. *Lipid Domains. Vol. 75 of Current Topics in Membranes.* Academic Press (2015). p. 167–207.
14. Golding I, Cox EC. Physical nature of bacterial cytoplasm. *Phys Rev Lett.* (2006) **96**:098102. doi: 10.1103/PhysRevLett.96.098102
15. Jeon JH, Javanainen M, Martinez-Seara H, Metzler R, Vattulainen I. Protein crowding in lipid bilayers gives rise to non-Gaussian anomalous lateral diffusion of phospholipids and proteins. *Phys Rev X.* (2016) **6**:021006. doi: 10.1103/PhysRevX.6.021006
16. Rienzo CD, Piazza V, Gratton E, Beltram F, Cardarelli F. Probing short-range protein Brownian motion in the cytoplasm of living cells. *Nat Commun.* (2014) **5**:5891. doi: 10.1038/ncomms6891
17. Metzler R, Klafter J. Anomalous stochastic processes in the fractional dynamics framework: fokker:planck equation, dispersive transport, and non?exponential relaxation. In: Prigogine I and Rice SA editors. *Advances in Chemical Physics*, Vol 116. JohnWiley and Sons, Ltd (2007). doi: 10.1002/9780470141762.ch3
18. Lomholt MA, Lizana L, Metzler R, Ambjörnsson T. Microscopic origin of the logarithmic time evolution of aging processes in complex systems. *Phys Rev Lett.* (2013) **110**:208301. doi: 10.1103/PhysRevLett.110.208301
19. Bouchaud JP, Georges A. Anomalous diffusion in disordered media: statistical mechanisms, models and physical applications. *Phys Rep.* (1990) **195**:127–93.
20. Bouchaud JP, Comtet A, Georges A, Doussal PL. Classical diffusion of a particle in a one-dimensional random force field. *Ann Phys.* (1990) **201**:285–341.
21. Sinai YG. The limiting behavior of a one-dimensional random walk in a random medium. *Theory Prob Appl.* (1982) **27**:285–341.

22. Oshanin G, Rosso A, Schehr G. Anomalous fluctuations of currents in sinai-type random chains with strongly correlated disorder. *Phys Rev Lett.* (2013) **110**:100602. doi: 10.1103/PhysRevLett.110.100602
23. Dean DS, Gupta S, Oshanin G, Rosso A, Schehr G. Diffusion in periodic, correlated random forcing landscapes. *J Phys A Math Theor.* (2014) **47**:372001. doi: 10.1088/1751-8113/47/37/372001
24. Radons G. Anomalous transport in disordered dynamical systems. *Phys D Nonlinear Phenomena.* (2004) **187**:3–19. doi: 10.1016/j.physd.2003.09.001
25. Godec A, Chechkin AV, Barkai E, Kantz H, Metzler R. Localisation and universal fluctuations in ultraslow diffusion processes. *J Phys A Math Theor.* (2014) **47**:492002. doi: 10.1088/1751-8113/47/49/492002
26. Krüsemann H, Godec A, Metzler R. First-passage statistics for aging diffusion in systems with annealed and quenched disorder. *Phys Rev E.* (2014) **89**:040101. doi: 10.1103/PhysRevE.89.040101
27. Krsemann H, Godec A, Metzler R. Ageing first passage time density in continuous time random walks and quenched energy landscapes. *J Phys A Math Theor.* (2015) **48**:285001. doi: 10.1088/1751-8113/48/28/285001
28. Coffey WT, Kalmykov YP, Waldron JT. *The Langevin Equation.* World Scientific (1996). Available online at: https://www.worldscientific.com/doi/abs/10.1142/2256
29. Jeon JH, Metzler R. Fractional Brownian motion and motion governed by the fractional Langevin equation in confined geometries. *Phys Rev E.* (2010) **81**:021103. doi: 10.1103/PhysRevE.81.021103
30. Lutz E. Fractional Langevin equation. *Phys Rev E.* (2001) **64**:051106. doi: 10.1103/PhysRevE.64.051106
31. Deng W, Barkai E. Ergodic properties of fractional Brownian-Langevin motion. *Phys Rev E.* (2009) **79**:011112. doi: 10.1103/PhysRevE.79.011112
32. Metzler R, Klafter J. Subdiffusive transport close to thermal equilibrium: From the Langevin equation to fractional diffusion. *Phys Rev E.* (2000) **61**:6308–11. doi: 10.1103/PhysRevE.61.6308
33. Kou SC, Xie XS. Generalized Langevin equation with fractional Gaussian noise: subdiffusion within a single protein molecule. *Phys Rev Lett.* (2004) **93**:180603. doi: 10.1103/PhysRevLett.93.180603
34. Burov S, Barkai E. Critical exponent of the fractional Langevin equation. *Phys Rev Lett.* (2008) **100**:070601. doi: 10.1103/PhysRevLett.100.070601
35. Goychuk I. Viscoelastic subdiffusion: generalized langevin equation approach. In: Rice SA, Dinner AR editors. *Advances in Chemical Physics*, Vol 150. JohnWiley and Sons, Ltd (2012). doi: 10.1002/9781118197714.ch5
36. Dubkov AA, Hänggi P, Goychuk I. Non-linear Brownian motion: the problem of obtaining the thermal Langevin equation for a non-Gaussian bath. *J Stat Mech Theory Exp.* (2009) (2009) 2009:P01034. doi: 10.1088/1742-5468/2009/01/P01034
37. Cherstvy AG, Chechkin AV, Metzler R. Anomalous diffusion and ergodicity breaking in heterogeneous diffusion processes. *N J Phys.* (2013) **15**:083039. doi: 10.1088/1367-2630/15/8/083039
38. Cherstvy AG, Metzler R. Nonergodicity, fluctuations, and criticality in heterogeneous diffusion processes. *Phys Rev E.* (2014) **90**:012134. doi: 10.1103/PhysRevE.90.012134
39. Massignan P, Manzo C, Torreno-Pina JA, García-Parajo MF, Lewenstein M, Lapeyre GJ. Nonergodic subdiffusion from Brownian motion in an inhomogeneous medium. *Phys Rev Lett.* (2014) **112**:150603. doi: 10.1103/PhysRevLett.112.150603
40. Guérin T, Dean DS. Force-induced dispersion in heterogeneous media. *Phys Rev Lett.* (2015) **115**:020601. doi: 10.1103/PhysRevLett.115.020601
41. Godec A, Metzler R. Optimization and universality of Brownian search in a basic model of quenched heterogeneous media. *Phys Rev E.* (2015) **91**:052134. doi: 10.1103/PhysRevE.91.052134
42. Vaccario G, Antoine C, Talbot J. First-passage times in *d*-dimensional heterogeneous media. *Phys Rev Lett.* (2015) **115**:240601. doi: 10.1103/PhysRevLett.115.240601
43. Godec A, Metzler R. First passage time distribution in heterogeneity controlled kinetics: going beyond the mean first passage time. *Sci Rep.* (2016) **6**:20349. doi: 10.1038/srep20349
44. Chubynsky MV, Slater GW. Diffusing diffusivity: a model for anomalous, yet Brownian, diffusion. *Phys Rev Lett.* (2014) **113**:098302. doi: 10.1103/PhysRevLett.113.098302
45. Chechkin AV, Seno F, Metzler R, Sokolov IM. Brownian yet non-Gaussian diffusion: from superstatistics to subordination of diffusing diffusivities. *Phys Rev X.* (2017) **7**:021002. doi: 10.1103/PhysRevX.7.021002
46. Godec A, Metzler R. First passage time statistics for two-channel diffusion. *J Phys A Math Theor.* (2017) **50**:084001. doi: 10.1088/1751-8121/aa5204
47. Sposini V, Chechkin AV, Seno F, Pagnini G, Metzler R. Random diffusivity from stochastic equations: comparison of two models for Brownian yet non-Gaussian diffusion. *N J Physics.* (2018) **20**:043044. doi: 10.1088/1367-2630/aab696
48. Lanoiselée Y, Grebenkov DS. A model of non-Gaussian diffusion in heterogeneous media. *J Phys A Math Theor.* (2018) **51**:145602. doi: 10.1088/1751-8121/aab15f
49. Grebenkov DS. A unifying approach to first-passage time distributions in diffusing diffusivity and switching diffusion models. *J Phys A Math Theor.* (2019) **52**:174001. doi: 10.1088/1751-8121/ab0dae
50. Lanoiselee Y, Moutal N, Grebenkov DS. Diffusion-limited reactions in dynamic heterogeneous media. *Nat Commun.* (2018) **9**:4398. doi: 10.1038/s41467-018-06610-6
51. Zwanzig R. Ensemble method in the theory of irreversibility. *J Chem Phys.* (1960) **33**:1338–41. doi: 10.1063/1.1731409
52. Nordholm S, Zwanzig R. A systematic derivation of exact generalized Brownian motion theory. *J Stat Phys.* (1975) **13**:347–71. doi: 10.1007/BF01012013
53. Mori H. Transport, collective motion, and Brownian motion*). *Prog Theor Phys.* (1965) **33**:423–55. doi: 10.1143/PTP.33.423
54. Grabert H, Talkner P, Hänggi P. Microdynamics and time-evolution of macroscopic non-Markovian systems. *Z B Condensed Matter.* (1977) **26**:389–95. doi: 10.1007/BF01570749
55. Hänggi P, Thomas H. Time evolution, correlations, and linear response of non-Markov processes. *Z Condensed Matter.* (1977) **26**:85–92. doi: 10.1007/BF01313376
56. Grabert H, Talkner P, Hänggi P, Thomas H. Microdynamics and time-evolution of macroscopic non-Markovian systems. II. *Z B Condensed Matter.* (1978) **29**:273–80. doi: 10.1007/BF01321192
57. Hynes JT, Kapral R, Weinberg M. Microscopic theory of Brownian motion: mori friction kernel and Langevin-equation derivation. *Phys A Stat Mech Appl.* (1975) **80**:105–27.
58. Haken H. Cooperative phenomena in systems far from thermal equilibrium and in nonphysical systems. *Rev Mod Phys.* (1975) **47**:67–121. doi: 10.1103/RevModPhys.47.67
59. Ferrario M, Grigolini P. The non-Markovian relaxation process as a "contraction" of a multidimensional one of Markovian type. *J Math Phys.* (1979) **20**:2567–72. doi: 10.1063/1.524019
60. Grigolini P. A Fokker-Planck equation for canonical non-Markovian systems: a local linearization approach. *J Chem Phys.* (1988) **89**:4300–8. doi: 10.1063/1.454812
61. Harris TE. Diffusion with "collisions" between particles. *J Appl Probab.* (1965) **2**:323–38.
62. Lizana L, Ambjörnsson T. Single-file diffusion in a box. *Phys Rev Lett.* (2008) **100**:200601. doi: 10.1103/PhysRevLett.100.200601
63. Barkai E, Silbey R. Theory of single file diffusion in a force field. *Phys Rev Lett.* (2009) **102**:050602. doi: 10.1103/PhysRevLett.102.050602
64. Sanders LP, Lomholt MA, Lizana L, Fogelmark K, Metzler R, Ambjrnsson T. Severe slowing-down and universality of the dynamics in disordered interacting many-body systems: ageing and ultraslow diffusion. *N J Phys.* (2014) **16**:113050. doi: 10.1088/1367-2630/16/11/113050
65. Illien P, Bénichou O, Mejía-Monasterio C, Oshanin G, Voituriez R. Active transport in dense diffusive single-file systems. *Phys Rev Lett.* (2013) **111**:038102. doi: 10.1103/PhysRevLett.111.038102
66. Bertrand T, Illien P, Bénichou O, Voituriez R. Dynamics of run-and-tumble particles in dense single-file systems. *N J Phys.* (2018) **20**:113045. doi: 10.1088/1367-2630/aaef6f
67. Lapolla A, Godec A. Unfolding tagged particle histories in single-file diffusion: exact single- and two-tag local times beyond large deviation theory. *N J Phys.* (2018) **20**:113021. doi: 10.1088/1367-2630/aaea1b
68. Godec A, Metzler R. Signal focusing through active transport. *Phys Rev E.* (2015) **92**:010701. doi: 10.1103/PhysRevE.92.010701

69. Deutch JM, Silbey R. Exact generalized Langevin equation for a particle in a harmonic lattice. *Phys Rev A.* (1971) **3**:2049–52. doi: 10.1103/PhysRevA.3.2049
70. Havlin S, Kiefer JE, Weiss GH. Anomalous diffusion on a random comblike structure. *Phys Rev A.* (1987) **36**:1403–8. doi: 10.1103/PhysRevA.36.1403
71. Pottier N. Analytic study of a model of diffusion on random comb-like structures. *Il Nuovo Cimento D.* (1994) **16**:1223–30. doi: 10.1007/BF02458804
72. Berezhkovskii AM, Dagdug L, Bezrukov SM. From normal to anomalous diffusion in comb-like structures in three dimensions. *J Chem Phys.* (2014) **141**:054907. doi: 10.1063/1.4891566
73. Qian H. A decomposition of irreversible diffusion processes without detailed balance. *J Math Phys.* (2013) **54**:053302. doi: 10.1063/1.4803847
74. Gray AH. Uniqueness of steady-state solutions to the Fokker-Planck equation. *J Math Phys.* (1965) **6**:644–7. doi: 10.1063/1.1704316
75. Huang W, Ji M, Liu Z, Yi Y. Steady states of Fokker–Planck equations: I. existence. *J Dyn Diff Equ.* (2015) **27**:721–42. doi: 10.1007/s10884-015-9454-x
76. Helffer B, Nier F. *Hypoelliptic Estimates and Spectral Theory for Fokker-Planck Operators and Witten Laplacians.* Berlin; Heidelberg: Springer (2005).
77. Chupin L. Fokker-Planck equation in bounded domain. *Ann Inst Fourier.* (2010) **60**:217. doi: 10.5802/aif.2521
78. Reed M, Simon B. *Methods of Modern Mathematical Physics I: Functional Analysis.* New York, NY: Academic Press (1972).
79. Conway JB. *A Course in Functional Analysis.* New York, NY: Springer-Verlag (1985).
80. Feller W. Non-Markovian processes with the semigroup property. *Ann Math Statist.* (1959) **30**:1252–3. doi: 10.1214/aoms/1177706110
81. Hanggi P, Thomas H, Grabert H, Talkner P. Note on time evolution of non-Markov processes. *J Stat Phys.* (1978) **18**:155–9. doi: 10.1007/BF01014306
82. Sokolov IM. Solutions of a class of non-Markovian Fokker-Planck equations. *Phys Rev E.* (2002) **66**:041101. doi: 10.1103/PhysRevE.66.041101
83. Risken H, Haken H. *The Fokker-Planck Equation: Methods of Solution and Applications.* 2nd ed. Springer (1989).
84. Polettini M. Generally covariant state-dependent diffusion. *J Stat Mech Theory Exp.* (2013) **2013**:P07005. doi: 10.1088/1742-5468/2013/07/P07005
85. Polettini M, Esposito M. Nonconvexity of the relative entropy for Markov dynamics: a Fisher information approach. *Phys Rev E.* (2013) **88**:012112. doi: 10.1103/PhysRevE.88.012112
86. Korepin VE, Bogoliubov NM, Izergin AG. *Quantum Inverse Scattering Method and Correlation Functions.* Cambridge University Press (1993). doi: 10.1017/CBO9780511628832
87. Lizana L, Ambjörnsson T. Diffusion of finite-sized hard-core interacting particles in a one-dimensional box: tagged particle dynamics. *Phys Rev E.* (2009) **80**:051103. doi: 10.1103/PhysRevE.80.051103
88. Gopich IV, Szabo A. Theory of the energy transfer efficiency and fluorescence lifetime distribution in single-molecule FRET. *Proc Natl Acad Sci USA.* (2012) **109**:7747–52. doi: 10.1073/pnas.1205120109
89. Seifert U. Stochastic thermodynamics, fluctuation theorems and molecular machines. *Rep Prog Phys.* (2012) **75**:126001. doi: 10.1088/0034-4885/75/12/126001
90. Mehl J, Lander B, Bechinger C, Blickle V, Seifert U. Role of hidden slow degrees of freedom in the fluctuation theorem. *Phys Rev Lett.* (2012) **108**:220601. doi: 10.1103/PhysRevLett.108.220601
91. Uhl M, Pietzonka P, Seifert U. Fluctuations of apparent entropy production in networks with hidden slow degrees of freedom. *J Stat Mech Theory Exp.* (2018) **2018**:023203. doi: 10.1088/1742-5468/aaa78b
92. Hartich D, Godec A. Duality between relaxation and first passage in reversible Markov dynamics: rugged energy landscapes disentangled. *N J Phys.* (2018) **20**:112002. doi: 10.1088/1367-2630/aaf038
93. Hartich D, Godec A. Interlacing relaxation and first-passage phenomena in reversible discrete and continuous space Markovian dynamics. *J Stat Mech Theory Exp.* (2019) **2019**:024002. doi: 10.1088/1742-5468/ab00df
94. Hartich D, Godec A. Extreme value statistics of ergodic Markov processes from first passage times in the large deviation limit. *J Phys A Math Theor.* (2019) **52**:244001. doi: 10.1088/1751-8121/ab1eca
95. Hänggi P, Talkner P. Non-Markov processes: the problem of the mean first passage time. *Z B Condensed Matter.* (1981) **45**:79–83. doi: 10.1007/BF01294279
96. Balakrishnan V, Van den Broeck C, Hänggi P. First-passage times of non-Markovian processes: the case of a reflecting boundary. *Phys Rev A.* (1988) **38**:4213–22. doi: 10.1103/PhysRevA.38.4213
97. McKane AJ, Luckock HC, Bray AJ. Path integrals and non-Markov processes. I. General formalism. *Phys Rev A.* (1990) **41**:644–56. doi: 10.1103/PhysRevA.41.644
98. Reimann P, Schmid GJ, Hänggi P. Universal equivalence of mean first-passage time and Kramers rate. *Phys Rev E.* (1999) **60**:R1–4. doi: 10.1103/PhysRevE.60.R1
99. Bray AJ, Majumdar SN, Schehr G. Persistence and first-passage properties in nonequilibrium systems. *Adv Phys.* (2013) **62**:225–361. doi: 10.1080/00018732.2013.803819
100. Guerin T, Levernier N, Benichou O, Voituriez R. Mean first-passage times of non-Markovian random walkers in confinement. *Nature.* (2016) **534**:356–9. doi: 10.1038/nature18272

Conflict of Interest: The authors declare that the research was conducted in the absence of any commercial or financial relationships that could be construed as a potential conflict of interest.

frontiers in Physics

CORRECTION
published: 31 January 2020
doi: 10.3389/fphy.2020.00007

Corrigendum: Manifestations of Projection-Induced Memory: General Theory and the Tilted Single File

*Alessio Lapolla and Aljaž Godec**

Mathematical Biophysics Group, Max Planck Institute for Biophysical Chemistry, Göttingen, Germany

Keywords: Fokker-Planck equation, spectral theory, projection operator method, occupation time, single file diffusion, Bethe ansatz, free energy landscape

Edited and reviewed by:
Carlos Mejía-Monasterio,
Polytechnic University of Madrid,
Spain

****Correspondence:***
Aljaž Godec
agodec@mpibpc.mpg.de

Specialty section:
This article was submitted to
Interdisciplinary Physics,
a section of the journal
Frontiers in Physics

Received: *12 December 2019*
Accepted: *08 January 2020*
Published: *31 January 2020*

Citation:
Lapolla A and Godec A (2020)
Corrigendum: Manifestations of
Projection-Induced Memory: General
Theory and the Tilted Single File.
Front. Phys. 8:7.
doi: 10.3389/fphy.2020.00007

A Corrigendum on

Manifestations of Projection-Induced Memory: General Theory and the Tilted Single File
by Lapolla, A., and Godec, A. (2019). Front. Phys. 7:182. doi: 10.3389/fphy.2019.00182

In the original article, there was an error. In section 2.1 the diffusion matrix $\mathbf{D}$ the in-line equation was defined with a factor of 2 instead of $1/2$, i.e., $\mathbf{D} = 2\boldsymbol{\sigma}\boldsymbol{\sigma}^T$ instead of $\mathbf{D} = \boldsymbol{\sigma}\boldsymbol{\sigma}^T/2$.

In section 2.1 in the paragraph following Equation (4), a copy-paste error occurred in the sentence "... where for reversible system (i.e., those obeying detailed balance) we have $\hat{\mathcal{L}}\hat{\mathcal{L}}^\dagger = \hat{\mathcal{L}}^\dagger\hat{\mathcal{L}} = 0$."

In section 2.2. in the paragraph following Equation (13) there is an obvious redundant additional factor $\Psi_{00}^{-1}(\mathbf{q})d\mathbf{q}$ present immediately after the in-line equation: $\langle\Psi_{l0}|\Psi_{k0}\rangle_{\Psi_{00}^{-1}} \equiv \int_\Xi d\mathbf{q}'\Psi_{00}(\mathbf{q}')^{-1}\Psi_{0l}(\mathbf{q}')\Psi_{k0}(\mathbf{q}')$.

A correction has been made to section 2.1 [paragraph following Equation (1)]. The paragraph now reads:

"where $\mathbf{D}$ is the symmetric positive-definite diffusion matrix. $\hat{\mathcal{L}}$ propagates probability measures $\mu_t(\mathbf{x})$ in time, which will throughout be assumed to posses well-behaved probability density functions $P(\mathbf{x}, t)$, i.e., $d\mu_t(\mathbf{x}) = P(\mathbf{x}, t)d\mathbf{x}$ [thereby posing some restrictions on $\mathbf{F}(\mathbf{x})$]. On the level of individual trajectories Equation (1) corresponds to the Itô equation $d\mathbf{x}_t = \mathbf{F}(\mathbf{x}_t)dt + \boldsymbol{\sigma}\, d\mathbf{W}_t$ with $\mathbf{W}_t$ being a d-dimensional vector of independent Wiener processes whose increments have a Gaussian distribution with zero mean and variance dt, i.e., $\langle dW_{t,i}dW_{t',j}\rangle = \delta_{ij}\delta(t-t')dt$, and where $\boldsymbol{\sigma}$ is a $d\times d$ symmetric noise matrix such that $\mathbf{D} = \boldsymbol{\sigma}\boldsymbol{\sigma}^T/2$. Moreover, we assume that $\mathbf{F}(\mathbf{x})$ admits the following decomposition into a potential (irrotational) field $-\mathbf{D}\nabla\varphi(\mathbf{x})$ and a non-conservative component $\boldsymbol{\vartheta}(\mathbf{x})$, $\mathbf{F}(\mathbf{x}) = -\mathbf{D}\nabla\varphi(\mathbf{x}) + \boldsymbol{\vartheta}(\mathbf{x})$ with the two fields being mutually orthogonal $\nabla\varphi(\mathbf{x})\cdot\boldsymbol{\vartheta}(\mathbf{x}) = 0$ [73]. By insertion into Equation (1) one can now easily check that $\hat{\mathcal{L}}\mathrm{e}^{-\varphi(\mathbf{x})} = 0$, such that the stationary solution of the Fokker-Planck equation (also referred to as the steady state [74, 75], which is the terminology we adopt here) by construction does not depend on the non-conservative part $\boldsymbol{\vartheta}(\mathbf{x})$."

A correction has been made to the aforementioned sentence in section 2.1, in the paragraph following Equation (4), which now reads:

"such that the conditional probability density starting from a general initial condition $|p_0\rangle$ becomes $P(\mathbf{x}, t|p_0, 0) = \langle\mathbf{x}|\hat{U}(t)|p_0\rangle \equiv \int d\mathbf{x}_0 p_0(\mathbf{x}_0)G(\mathbf{x}, t|\mathbf{x}_0, 0)$. Moreover, as $\mathbf{F}(\mathbf{x})$ is assumed to be sufficiently confining (i.e., $\lim_{\mathbf{x}\to\infty} P(\mathbf{x}, t) = 0, \forall t$ sufficiently fast), such that $\hat{\mathcal{L}}$ corresponds to a coercive and densely defined operator on V (and $\hat{\mathcal{L}}^\dagger$ on W, respectively) [76–78]. Finally, $\hat{\mathcal{L}}$ is throughout assumed to be *normal*, i.e., $\hat{\mathcal{L}}^\dagger\hat{\mathcal{L}} - \hat{\mathcal{L}}\hat{\mathcal{L}}^\dagger = 0$ and thus henceforth $V = W$, where for reversible system (i.e., those obeying detailed balance) we have $\hat{\mathcal{L}} \Leftrightarrow \hat{\mathcal{L}}^\dagger$".

Finally, the redundant factor $\Psi_{00}^{-1}(\mathbf{q})d\mathbf{q}$ has been deleted in section 2.2 in the paragraph following Equation (13).

“can be equal to $Q_{p_{\mathrm{ss}}}(\mathbf{q}, t|\mathbf{q}_0, 0)$. As this will generally not be the case this essentially means that the projected dynamics is in general non-Markovian. The proof is established by noticing that $\Psi_{kl}(\mathbf{q}') = \Psi^{\dagger}_{lk}(\mathbf{q}')$ such that $\langle\Psi_{l0}|\Psi_{k0}\rangle_{\Psi_{00}^{-1}} \equiv \int_{\Xi} d\mathbf{q}'\Psi_{00}(\mathbf{q}')^{-1}\Psi_{0l}(\mathbf{q}')\Psi_{k0}(\mathbf{q}')$.”

The authors apologize for this error and state that this does not change the scientific conclusions of the article in any way. The original article has been updated.

frontiers in Physics

ORIGINAL RESEARCH
published: 10 January 2020
doi: 10.3389/fphy.2019.00224

Diffusion of Anisotropic Particles in Random Energy Landscapes—An Experimental Study

Juan Pablo Segovia-Gutiérrez[1], *Manuel A. Escobedo-Sánchez*[1], *Erick Sarmiento-Gómez*[1,2] *and Stefan U. Egelhaaf*[1]*

[1] *Condensed Matter Physics Laboratory, Heinrich Heine University, Düsseldorf, Germany,* [2] *División de Ciencias e Ingenierías, Departamento de Ingeniería Física, Universidad de Guanajuato, León, Mexico*

If a colloidal particle is exposed to an external field, its Brownian motion is modified. In the case of an anisotropic particle, the external potential might not only affect its translation but also its rotation. We experimentally investigate the dynamics of a trimer, which consists of three spherical particles, within a random potential energy landscape. This energy landscape has energy values drawn from a Gamma distribution, a spatial correlation length similar to the particle size and is realized by a random light field, that is a laser speckle pattern. The particle translation and rotation are quantified by the mean squared (angular) displacement, the van Hove function and other observable quantities. The translation shows an intermediate subdiffusive regime and a long-time diffusion that slows down upon increasing the modulation of the potential. In contrast, the mean squared angular displacement exhibits only small deviations from a linear time dependence but a more detailed analysis reveals discrete angular jumps reflecting the symmetry of the trimer. A coupling between the translation and rotation is observed and found to depend on the length scale.

Keywords: random walk, anomalous diffusion, translational motion, rotational motion, potential energy landscape, colloidal molecules, video microscopy

Edited by:
Ralf Metzler,
University of Potsdam, Germany

Reviewed by:
Heiko Rieger,
Saarland University, Germany
Andrew James Spakowitz,
Stanford University, United States

Correspondence:
Stefan U. Egelhaaf
stefan.egelhaaf@uni-duesseldorf.de

Specialty section:
This article was submitted to Interdisciplinary Physics, a section of the journal Frontiers in Physics

Received: *08 August 2019*
Accepted: *02 December 2019*
Published: *10 January 2020*

Citation:
Segovia-Gutiérrez JP, Escobedo-Sánchez MA, Sarmiento-Gómez E and Egelhaaf SU (2020) Diffusion of Anisotropic Particles in Random Energy Landscapes—An Experimental Study. Front. Phys. 7:224. doi: 10.3389/fphy.2019.00224

1. INTRODUCTION

Colloidal particles undergo random thermal motion. Free diffusion is characterized by a mean squared displacement which increases linearly with time. The slope is determined by the diffusion coefficient that depends on the temperature, the particle size, and the viscosity of the medium. However, colloidal particles in more complex situations, for example in the presence of interparticle interactions or external potentials, can show different behavior such as subdiffusion or superdiffusion. These imply mean squared displacements with time dependencies that are less than or greater than linear, respectively [1]. Such dynamics are frequently encountered in systems with biological or industrial relevance. For example, they are observed in living cells [2–5], biological membranes [6–8], porous media [9], and glassy systems [10–14]. Due to the analogy between the behaviors of colloidal particles and many different complex and experimentally less accessible systems, colloidal suspensions are frequently used as model systems to systematically and quantitatively study particle dynamics.

Although spherical colloidal particles are usually investigated, most molecular, biological or industrial systems contain non-spherical objects. The behavior of these objects can be modeled using anisotropic colloidal particles, which can be made using different synthesis routes [15–18]. Anisotropy introduces additional degrees of freedom but also, for instance, more complex interparticle interactions and particle dynamics. Anisotropic particles are, therefore, also interesting in their own right. For example, elongated particles, such as ellipsoidal particles and dumbbells made of two spherical particles, show free diffusion that, up to intermediate times, shows a directional dependence [19, 20]. In addition, experiments on dumbbells and planar clusters of colloidal particles have shown a decoupling between translational and rotational motion at high concentrations [21, 22]. A more complex system, tetrahedral colloidal clusters immersed in a supercooled colloidal fluid, was investigated [23]. Also in this system a decoupling between translational and rotational diffusion was observed when the volume fraction approached the glass transition. Furthermore, molecular dynamics simulations revealed that dumbbells in a porous medium show dynamical heterogeneities [24]. This illustrates that an anisotropic shape as well as external constraints can significantly change the particle dynamics.

Colloidal particles can be manipulated using optical trapping, a phenomenon exploited in optical tweezers [25, 26]. Optical trapping relies on the momentum transfer between the photons to the colloidal particles during refraction and scattering. The magnitude of the effect depends on the intensity and intensity gradient of the light, the refractive index mismatch between the medium and the particle, the wavelength of the light and the particle size and shape [27–29]. In addition to optical tweezers, extended light fields can be used to expose particles to external potential energy landscapes [30]. Different light fields can be created to produce random, periodic or other potential energy landscapes [31–36]. Typically, energy modulations of the order of the thermal energy, $k_B T$, are applied. Subjecting colloids to these energy landscapes will affect their dynamics [30, 37–41]. Therefore, colloids exposed to light fields can serve as a model system to investigate the effect of external potentials on the particle dynamics.

Recently light fields have also been imposed on anisotropic particles [36, 42, 43]. Dilute suspensions of ellipsoids or multimers consisting of spherical particles, particularly dimers and trimers, have been subjected to a periodic light field. In the case of multimers, this results in a small number of preferred states, which reflects the limited number of spatial and orientational configurations the multimers attain due to their confinement in the periodic energy minima. The actual number of configurations depends on the ratio between the particle size and the periodicity of the potential. This suggests that the translational and rotational motions are coupled.

In this work, we study the translational and rotational dynamics of trimers. Trimers are anisotropic particles consisting of three spherical colloidal particles bonded together. They are exposed to a random light field, which imposes a random potential energy landscape. Due to the convolution of the light field with the particle volume, the distribution of energy values follows a Gamma distribution and the spatial correlation length of the potential is about the size of an individual sphere [34]. We characterize the dynamics by several parameters, such as the mean squared (angular) displacement and the van Hove function. The random potential energy landscape leads to an intermediate subdiffusive regime in the translational motion and the long-time translational diffusion is found to be reduced upon increasing the modulation of the potential, which is controlled by the laser intensity. The mean squared angular displacement, however, is hardly affected by the external potential. Nevertheless, a detailed quantitative analysis of the rotational motion uncovers characteristic angular jumps of approximately 120° that reflect the three-fold symmetry of the trimers. Furthermore, it reveals a complex coupling between the translational motion and the rotational motion.

2. MATERIALS AND METHODS

2.1. Synthesis of Trimers and Sample Preparation

Cross-linked poly(methyl methacrylate) (PMMA) spheres with a diameter $\sigma \approx 2.1$ μm were synthesized based on previously established methods [44–46]. After the synthesis, the solvent was exchanged by centrifugation in a two-step washing process: first, the suspension was washed three times with n-hexane (Sigma-Aldrich, Ref. Num. 1043671000) to remove leftovers from the reaction, then seven times with decahydronaphthalene (mixture of cis and trans isomers, 98%, Alfa Aesar, Ref. Num. A13883) to change the solvent to decahydronaphthalene. The particle suspension at 30 vol% was then used as stock to prepare trimers [18]. First, decahydronaphthalene was replaced with toluene (anhydrous, 99.8%, Sigma-Aldrich, Ref. Num. 244511) by washing three times. After the last washing step a suspension with a volume fraction of 3.66 vol% was obtained. 3 ml of this suspension was mixed with 15 ml of ultra pure water (resistivity 18 MΩ/cm) containing 0.5 wt% sodium dodecyl sulfate (SDS, Sigma-Aldirch, Ref. Num. L4509) to yield the precursor emulsion. To narrow down the size distribution of the emulsion droplets, the emulsion was homogenized by applying a T25 ULTRA-TURRAX® (IKA, Ref. Num. IK0003725000) for 60 s at 8,000 rpm followed by 25 s at 9,600 rpm. The emulsion was poured into a round-bottomed reaction flask with a capacity of 100 ml and subsequently placed in a constant temperature bath at 80 °C. The sample was slowly stirred for 2 h while the toluene evaporated.

The obtained suspension contained different multimers. It was, therefore, fractionated using a density gradient from a water-saccharose-surfactant solution. The density gradient was prepared from two solutions. The denser solution (density $\rho \approx$ 1.17 g/ml) contained 40 wt% D(+)-Saccharose (99.5%, Sigma-Aldrich, Ref. Num. 4661.1) and 0.1 wt% SDS. The less dense solution ($\rho \approx 1.08$ g/ml) was prepared by diluting the denser solution by a factor of two with ultra pure water; typically 5 ml of the denser solution was diluted with 5 ml of water. Equal volumes of the two solutions were mixed using a density gradient maker with two chambers where each chamber was filled with one of the solutions. The mixed solution was transferred into a round-bottomed glass centrifuge tube. Then, the suspension containing the clusters was carefully loaded on top of the gradient column yielding a thin layer with a height of about 0.5 cm. The tube subsequently was placed in a centrifuge (Hermle Z323, rotor 221.12V01) and subjected to 2,000 rpm centrifugation for

4 min with the brake set to 0. This procedure was repeated many times to obtain a sufficient amount of trimer suspension. Finally, the collected suspension was washed a few times with ultra pure water to remove the surfactant and saccharose. The suspension contained trimers and a very small number of tetramers. The monomers obtained during the fractionation were used to calibrate the energy landscape as described below. An image of the trimers is shown in **Figure 1A**.

For the experiments, a dilute suspension of trimers was transferred into a quasi-two-dimensional cell consisting of a microscope slide and a cover slip [47], which were first carefully cleaned. The few pyramid-like tetramers present in the suspension served as spacers between the microscope slide and the cover slip. The confinement to quasi-two-dimensions reduces the degrees of freedom of each trimer to a center-of-mass translation and a rotation around one axis. Experiments were performed at a temperature of $\sim 20\,^{\circ}$C.

2.2. Random Light Field

The random light field is a speckle pattern (**Figure 1B**). It was generated as described previously [34]. The central optical element is a diffuser (RPC Photonics Inc., Engineered Diffuser$^{\text{TM}}$ EDC-1-A-1r), which is illuminated with a planar wave with a Gaussian intensity distribution from a laser (Laser Quantum, Opus 532, wavelength $\lambda = 532$ nm). The diffuser creates a top-hat beam including a speckle pattern, which is directed to the sample plane of an inverted microscope. The average speckle size, which determines the correlation length of the light field, matches approximately the monomer size. The magnitude of the modulations is controlled via the laser power P_{L}. Four different laser intensities were applied: $P_{\text{L}} = 0$, 1.15, 1.60, and 2.10 W. The magnitude of the modulations also depends on the refractive index difference between the medium, in this case water with a refractive index of 1.330, and the PMMA particles with a refractive index of about 1.494 for the present wavelength.

2.3. Image Acquisition and Particle Tracking

The quasi-two-dimensional geometry allows us to use conventional optical microscopy. An inverted bright field microscope (Nikon, Eclipse Ti-U) with a 60× objective (Nikon, S Plan Fluor ELWD, NA 0.7) equipped with a CMOS camera (Allied Vision, Mako U-130B, $1{,}280 \times 1{,}024$ px^2) was used. The effective pixel pitch was 0.08 μm/px and the observation area was $\sim 100 \times 82\,\mu\text{m}^2$. This area typically contained about 6 trimers.

Before each individual measurement, the diffuser was rotated in order to probe different realizations of the random potential. Then the sample was left to equilibrate for 30 min while it was exposed to the random light field. Subsequently, a series of 36,000 images was recorded at 10 fps resulting in an individual measurement time of 1 h. For each laser intensity, at least 15 individual measurements were performed, which resulted in a minimum of 90 trajectories. The measurements were controlled with a custom-written LabView programme. The positions and trajectories of individual spheres were extracted from the recorded images using a custom-written Matlab programme based on standard algorithms [48]. Based on these trajectories, the center-of-mass trajectories and the orientations of the trimers were determined.

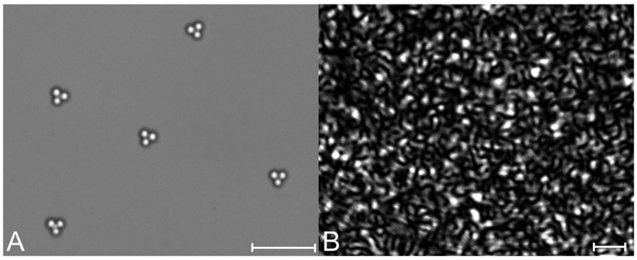

FIGURE 1 | (A) Optical microscopy image of trimers. **(B)** Random light field (speckle pattern) created by a diffuser illuminated with a laser beam. Particles exposed to such a light field experience a random potential energy landscape. Scale bars are 10 μm.

3. RESULTS AND DISCUSSION

We investigated trimers consisting of three joined spherical particles (**Figure 1A**). They were confined between two glass plates resulting in a quasi-two-dimensional system. Thus, their thermal motion contains two contributions: center-of-mass translation and rotation around the symmetry axis. The motion was modified by a random potential energy landscape whose values are drawn from a Gamma distribution with standard deviation ϵ and whose spatial correlation length is about the size of a spherical particle [34]. The magnitude of the modulations, quantified by ϵ, was varied with the maximum reaching a few times the thermal energy. This potential was imposed on the particles by applying a random light field and the magnitude of the modulations was controlled through the laser intensity P_{L} (**Figure 1B**). A convolution with the particle volume results in the potential energy landscape [34, 43, 49].

Examples of center-of-mass trajectories of trimers are shown in **Figure 2**. It illustrates the effect of the potential energy landscape on the translation of the trimers. Within the same time, trimers not exposed to a random potential explore a much larger region than trimers exposed to a random potential. The effect of the random potential on the translational motion will be quantified and compared to the effect on the rotational motion below. However, first the calibration of the random potential energy landscape will be explained.

3.1. Calibration of the Random Potential Energy Landscape—Translation of Spherical Particles

The magnitude of the modulations of the potential is estimated using the dynamics of spherical particles for which a theoretical prediction is available [50]. The dynamics of spherical particles, the building blocks of the trimers, are followed in the same random potential and characterized by the mean squared

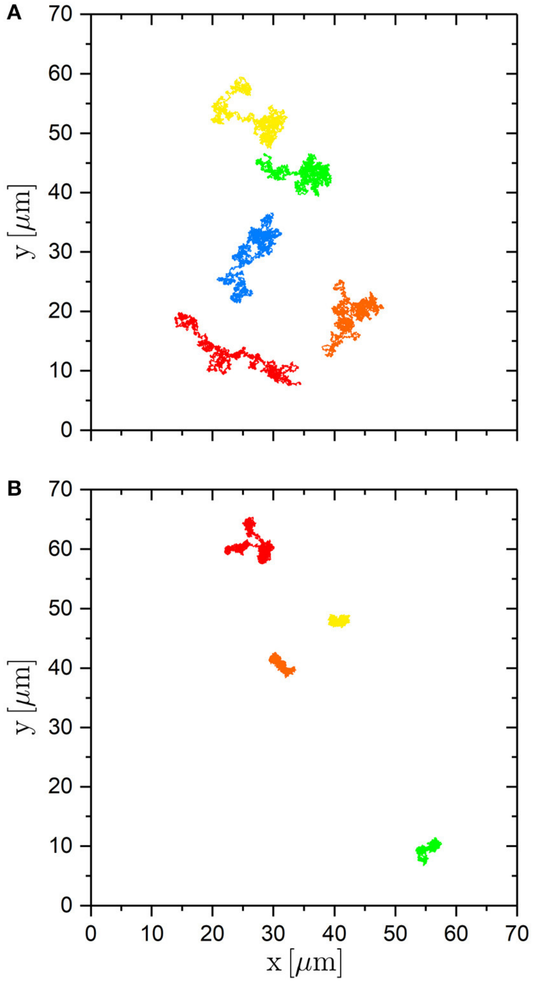

FIGURE 2 | Trajectories of the center-of-mass of trimers **(A)** in the absence of an external potential and **(B)** in the presence of an external potential created with the maximum laser intensity $P_L = 2.10$ W. The trajectories are followed for 60 min.

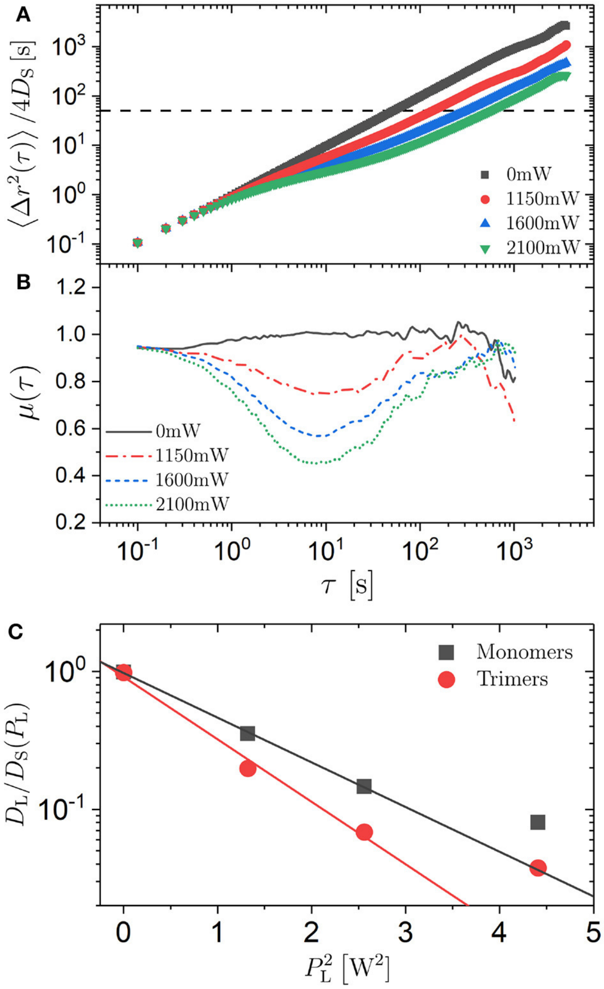

FIGURE 3 | (A) Mean squared displacement (MSD) $\langle \Delta r(\tau)^2 \rangle$ normalized by the short-time diffusion coefficient D_S and **(B)** exponent $\mu = \partial \log(\langle \Delta r(\tau)^2 \rangle)/\partial \log(\tau)$ as a function of delay time τ for spherical particles ("monomers") exposed to different laser intensities P_L (as indicated). The horizontal line in **(A)** indicates $\sigma^2/4D_S$. **(C)** Ratio of the long-time (D_L) to the short-time (D_S) diffusion coefficient as a function of the square of the laser intensity, P_L^2, of spherical particles (squares) and trimers (circles). The lines are linear fits to the data except at the highest P_L where D_L cannot be determined reliably.

displacement (MSD) [51]

$$\langle \Delta \mathbf{r}^2(\tau) \rangle = \langle [\mathbf{r}_i(t_0+\tau) - \mathbf{r}_i(t_0)]^2 \rangle_{i,t_0} \, , \tag{1}$$

where $\mathbf{r}_i(t)$ is the position of particle i at time t and the average is taken over all particles i and all start times t_0. This means that we consider the ensemble and time average. Without an external potential, the MSD increases linearly with delay time τ as expected (**Figure 3A**). In contrast, in the presence of an external potential, the MSD indicates different dynamic regimes: at short times diffusion, at intermediate times subdiffusion and at long times again diffusion but with a considerably reduced diffusion coefficient D_L. Whereas the diffusion at short times is not significantly affected by the external potential, the subdiffusion becomes more pronounced and the long-time diffusion increasingly slower with increasing laser intensity P_L. This can be quantified by calculating the exponent $\mu(\tau)$ in the relation $\langle \Delta \mathbf{r}^2(\tau) \rangle \sim \tau^{\mu(\tau)}$ from the slope of the MSD in double-logartihmic representation

$$\mu(\tau) = \frac{\partial \log \left\{ \langle \Delta \mathbf{r}^2(\tau) \rangle \right\}}{\partial \log \{\tau\}} . \tag{2}$$

The values of this parameter indicate initial diffusion ($\mu \approx 1$), intermediate subdiffusion with μ reaching values as small as about 0.5 and the re-establishment of diffusion at long times τ (**Figure 3B**). These observations agree with previous results [30, 39].

For a quantitative analysis, the confinement of the particles between two plates with only a small gap has to be considered.

Furthermore, radiation pressure pushes the particles in the direction of the laser beam and hence affects the distance between the particles and the two plates [27–29]. The resulting hydrodynamic interactions slow down diffusion regardless of whether there is an external potential [52, 53]. This results in a diffusion coefficient which is reduced compared to the bulk diffusion coefficient $D_0 = k_B T/(3\pi \eta \sigma)$, where η is the viscosity of the medium. Thus, the short-time diffusion coefficient D_S, which is affected by the hydrodynamic interactions with the plates but not by the external potential, was used to normalize the MSD and other dynamic parameters to account for the hydrodynamic interactions with the plates (**Figure 3A**). The short-time diffusion coefficient D_S was determined from the slope of the MSD at short times by

$$D_\mathrm{S} = \frac{1}{4} \lim_{\tau \to 0} \left\{ \frac{\partial \langle \Delta \mathbf{r}^2(\tau) \rangle}{\partial \tau} \right\}. \tag{3}$$

It was found to increase by ∼12 % within the range of investigated laser intensities P_L (**Table 1**).

For the case of a random potential energy landscape with the energy values drawn from a Gaussian distribution with standard deviation ϵ, the long-time diffusion coefficient D_L is related to the short-time diffusion coefficient D_S by [50]

$$\frac{D_\mathrm{L}}{D_\mathrm{S}} = \exp\left[-\frac{1}{2} \left(\frac{\epsilon}{k_B T} \right)^2 \right]. \tag{4}$$

In our experiments, the energy values are Gamma distributed with a shape parameter $M \approx 1.7$ [34]. Assuming that the deviations from a Gaussian distribution are negligible, the experimentally determined ratio $D_\mathrm{L}/D_\mathrm{S}$ can be used to relate the laser intensity P_L to the standard deviation of the energy distribution, ϵ. The long-time diffusion coefficient D_L was determined from the slope of the MSD at long times, analogous to the short-time diffusion coefficient D_S (Equation 3), if diffusion is re-established within the experimental time window. If this was not the case, D_L was determined based on the last data point at τ_max, $D_\mathrm{L} = \langle \Delta \mathbf{r}^2(\tau_\mathrm{max}) \rangle / 4\tau_\mathrm{max}$ (or an average of the values from the last few data points), which is likely to overestimate D_L. Within the range of investigated laser intensities P_L, the ratio $D_\mathrm{L}/D_\mathrm{S}$ decreases by slightly more than an order of magnitude (**Table 1**, **Figure 3C**) and using Equation (4) one obtains $\epsilon = 0.00$, 1.44, 1.92, and $2.25\, k_B T$, respectively. Thus, the magnitude of the modulations of the potential, ϵ, to which individual spherical particles and hence also each sphere forming a trimer is exposed, is linearly proportional to the laser intensity P_L at least for small P_L. This is indicated by the linear dependence of $\log(D_\mathrm{L}/D_\mathrm{S})$ on P_L^2 (**Figure 3C**). The deviation from linearity at the largest $P_\mathrm{L} = 2.10\,\mathrm{W}$ could be due to a non-linearity between ϵ and P_L or the fact that diffusion is not re-established in the experimental window and hence D_L is overestimated and ϵ underestimated. The latter is more likely to be the reason. Due to this and the assumption concerning the distribution of energy values, in the following we will refer to the applied laser intensity P_L as a measure for the magnitude of the modulations of the random potential. Nevertheless, this analysis provides an estimate of the magnitude of the modulations which can reach a few times the thermal energy.

3.2. Translation of Trimers

3.2.1. Mean Squared Displacement

The MSD of the trimers was calculated following Equation (1) with $\mathbf{r}_i(t)$ now representing the trajectory of the center-of-mass of trimer i. As in the case of the spherical particles, the MSD was normalized by the short-time diffusion coefficient D_S to account for the hydrodynamic interactions with the glass plates. The hydrodynamic interactions depend on the separation of the trimers from the two plates which is affected by the radiation pressure and hence the laser intensity P_L. Within the range of investigated laser intensities P_L, the short-time diffusion coefficient D_S was found to increase by ∼25 % (**Table 1**). This increase is larger than for the spherical particles but still rather modest.

In the absence of a random potential, the MSD increases linearly with delay time τ over the whole investigated time window (**Figure 4A**) reflecting the expected free diffusion. In the presence of an external potential, however, different regimes are observed. At short delay times, a linear increase is observed which does not depend on laser intensity P_L because the time

TABLE 1 | Diffusion coefficients for particles exposed to different laser intensities P_L: short-time diffusion coefficient D_S for spherical particles, ratio of the long-time to the short-time diffusion coefficient ($D_\mathrm{L}/D_\mathrm{S}$) for spherical particles, short-time translational diffusion coefficient D_S for the center-of-mass motion of trimers, ratio of the long-time to the short-time translational diffusion coefficient ($D_\mathrm{L}/D_\mathrm{S}$) for the center-of-mass motion of trimers, short-time rotational diffusion coefficient $D_\mathrm{S}^\mathrm{rot}$ for trimers, ratio of the long-time to the short-time rotational diffusion coefficient ($D_\mathrm{L}^\mathrm{rot}/D_\mathrm{S}^\mathrm{rot}$) for trimers, mean residence time $\langle \Delta t \rangle$ (where the ranges indicate the uncertainties of the fits), mean residence time estimated from the ratio of the total measurement time T_m to the total number of jumps N_m, ratio of the long-time to the short-time rotational diffusion coefficient ($D_\mathrm{L}^\mathrm{rot}/D_\mathrm{S}^\mathrm{rot}$) for trimers calculated based on the mean residence time $\langle \Delta t \rangle$.

	Monomer		**Trimer**						
	Translation		**Translation**		**Rotation**		**Rotation (calculated)**		
P_L [W]	**D_S [μm^2/s]**	**$D_\mathrm{L}/D_\mathrm{S}$**	**D_S [μm^2/s]**	**$D_\mathrm{L}/D_\mathrm{S}$**	**$D_\mathrm{S}^\mathrm{rot}$ [rad^2/s]**	**$D_\mathrm{L}^\mathrm{rot}/D_\mathrm{S}^\mathrm{rot}$**	**$\langle \Delta t \rangle$ [s]**	**$T_\mathrm{m}/N_\mathrm{m}$ [s]**	**$D_\mathrm{L}^\mathrm{rot}/D_\mathrm{S}^\mathrm{rot}$**
0	0.022	0.99	0.0089	0.98	0.013	1.03	159 ± 3	178	1.07
1.15	0.024	0.35	0.0092	0.20	0.013	0.81	185 ± 2	215	0.90
1.60	0.023	0.15	0.0096	0.07	0.014	0.77	214 ± 6	254	0.76
2.10	0.024	0.08	0.0112	0.04	0.015	0.60	230 ± 5	275	0.62

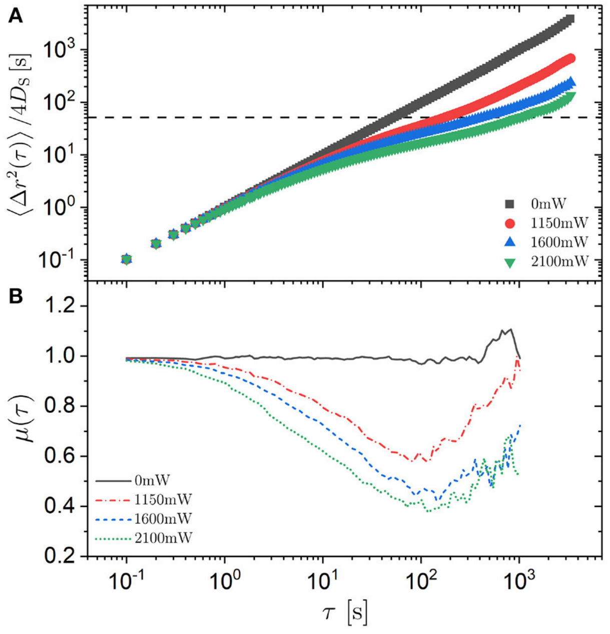

FIGURE 4 | (A) Mean squared displacement (MSD) $\langle \Delta r(\tau)^2 \rangle$ normalized by the short-time diffusion coefficient D_S and **(B)** exponent $\mu = \partial \log(\langle \Delta r(\tau)^2 \rangle)/\partial \log(\tau)$ as a function of delay time τ for the center-of-mass of trimers exposed to different laser intensities P_L (as indicated). The horizontal line in **(A)** indicates $\sigma^2/4D_S$.

and distances traveled during this time are too short for the trimer to experience significant changes of the external potential. Subsequently, subdiffusion is indicated by a slope μ smaller than 1 with the slope decreasing upon increasing the laser intensity P_L (**Figure 4B**). This is due to the confinement of the trimer to a potential minimum or the confinement of the constituent three spheres to neighboring potential minima. The trimers wiggle within the minima but they do not leave the minima within this time scale. The potential minima correspond to the randomly distributed bright speckles in the light pattern that have an average size of about 2 μm (**Figure 1B**) similar to the sphere diameter $\sigma \approx 2.1$ μm (**Figure 4A**, dashed horizontal line). The relatively small values of $\langle \mathbf{r}^2(\tau) \rangle$ in the intermediate regime indicate that the trimers only explore the central part of the minima. A slope $\mu \approx 1$ is again reached and hence diffusion is re-established at very long times. This time scale is long enough for the trimers to leave the minima and move from minimum to minimum in a random fashion. The ratio of the long-time to the short-time diffusion coefficient (D_L/D_S) shows a major decrease by about one and a half order of magnitude within the range of investigated laser intensities P_L (**Table 1**, **Figure 3C**). Thus it is significantly more pronounced than for spherical particles. The dependence of $\log(D_L/D_S)$ on P_L^2 is linear except for the largest laser intensity $P_L = 2.10$ W, which again is attributed to the difficulty in reliably determining the long-time diffusion coefficient D_L in this case because the long-time diffusive regime is not reached within the experimental time window (**Figure 4B**). The linear dependence is consistent with Equation (4). Moreover, the MSDs of the trimers and of the spherical particles, the "monomers," show similar behavior over the whole experimental time window (**Figures 3A**, **4A**). The dependences of the long-time diffusion coefficient D_L on the laser intensity P_L also show comparable trends but the D_L of the trimers is significantly smaller (**Figure 3C**), which is due to the stronger effect of the light field on the three spheres forming the trimers than on an individual sphere. Nevertheless, there are quantitative differences. In the case of trimers, the subdiffusive regime starts at larger delay times and extends to longer times (**Figures 3B**, **4B**).

3.2.2. Self Part of the van Hove Function

While the mean squared displacement characterizes the width of the distribution of displacements, more detailed information on the dynamics can be obtained by examining the distribution of displacements itself. The probability to find a particle at position $\mathbf{r} + \Delta\mathbf{r}$ at time $t_0 + \tau$ given that there was a particle at position $\mathbf{r}$ at time t_0 is given by the van Hove function

$$G(\Delta\mathbf{r}, \tau) = \frac{1}{N} \left\langle \sum_{i=1}^{N} \sum_{j=1}^{N} \delta\{\Delta\mathbf{r} - [\mathbf{r}_i(t_0+\tau) - \mathbf{r}_j(t_0)]\} \right\rangle_{t_0}, \qquad (5)$$

where the average is taken over the start time t_0. The van Hove function can be separated in a self ($i = j$) and distinct ($i \neq j$) part. Here we focus on the motion of individual particles and hence are interested in the self part of the van Hove function

$$G_s(\Delta\mathbf{r}, \tau) = \frac{1}{N} \left\langle \sum_{i=1}^{N} \delta\{\Delta\mathbf{r} - [\mathbf{r}_i(t_0+\tau) - \mathbf{r}_i(t_0)]\} \right\rangle_{t_0}. \qquad (6)$$

For an isotropic particle undergoing free diffusion, the self part of the van Hove functions is a Gaussian distribution with mean zero and the square of the standard deviation represented by the MSD.

Based on the trajectories, the self part of the van Hove function $G_s(\Delta\mathbf{r}, \tau)$ can be calculated for the different laser intensities P_L. We consider the individual components of the displacement vector $\Delta\mathbf{r}$, namely Δx and Δy, as well as its magnitude, Δr (**Figure 5**). In the absence of the random potential, in other words in the case of free diffusion, the self part of the van Hove function $G_s(\Delta x, \tau)$ shows the expected Gaussian shape with the width increasing with delay time τ. If the random potential is present, at intermediate delay times the distribution is narrower. This corresponds to the sublinear increase of the MSD with delay time τ and is due to the fact that the trimers remain in the central part of the potential minima for some time. At longer delay times, the self part of the van Hove function develops shoulders on both sides of the central maximum and minor maxima at $\Delta x \approx -4$ μm and $\Delta x \approx 4$ μm. These shoulders become more pronounced for longer delay times τ and larger laser intensities P_L. They reflect the random motion between minima that are randomly distributed and separated by a few μm (**Figure 1B**). Furthermore, the shape of $G_s(\Delta x, \tau)$ increasingly deviates from

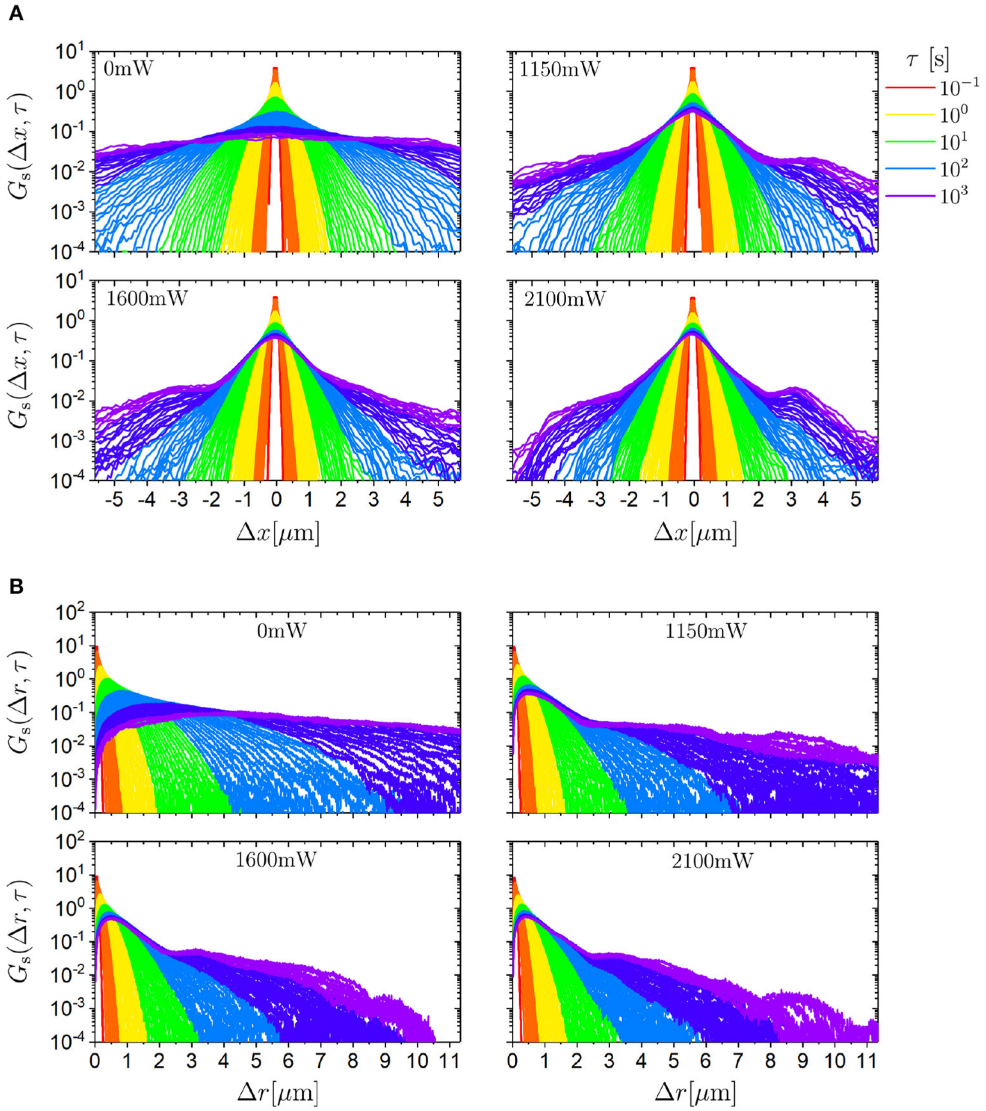

FIGURE 5 | Self part of the van Hove function G_s for **(A)** displacements in *x* direction (Δx) and **(B)** modulus of the displacement vector (Δr) for different delay times τ (indicated by the color) for trimers exposed to different laser intensities P_L (as indicated).

a Gaussian shape and, at long times, can better be described by a Laplacian shape.

The distribution of the magnitude of the displacement, $G_s(\Delta r, \tau)$ (**Figure 5B**), resembles the expected Rayleigh distribution in the absence of the random potential. In the presence of the random potential, the evolution with delay time τ and laser intensity P_L corresponds to the dependence observed in $G_s(\Delta x, \tau)$. These are a limited broadening of the main peak and the development of shoulders and minor maxima at intermediate and long times.

3.2.3. Non-gaussian Parameter

Since the self part of the van Hove function $G_s(\Delta x, \tau)$ is not Gaussian in the presence of the random potential (**Figure 5A**), it cannot be fully characterized by only the MSD (**Figure 4A**) but further moments are required. Thus, the fourth moment is considered, which usually is normalized to yield the non-Gaussian parameter $\alpha_2(\tau)$ [54]. We focus on the distributions of one-dimensional displacements, $G_s(\Delta x, \tau)$, and hence use the corresponding non-Gaussian parameter defined for one dimension [55]

$$\alpha_2(\tau) = \frac{\langle \Delta x^4(\tau) \rangle}{3\langle \Delta x^2(\tau) \rangle^2} - 1 \qquad (7)$$

and similarly for the *y* direction. Other definitions of the non-Gaussian parameter have been proposed, for example [56], which only differ by a constant factor. Since $\alpha_2(\tau)$ contains a higher order moment than the MSD, it is more prone to noise and hence has to be based on more data pairs for comparable statistics implying a more restricted range of delay times τ.

The non-Gaussian parameter $\alpha_2(\tau)$ was determined for Δx and Δy, which, not surprisingly, show similar behavior (**Figure 6**). As expected, in the absence of an external potential the non-Gaussian parameter $\alpha_2(\tau) \approx 0$. In the presence of an external potential, $\alpha_2(\tau) \approx 0$ at short times and hence small traveled distances, during which no significant changes of the external potential are experienced. However, at intermediate times $\alpha_2(\tau)$ increases, reaches a maximum and decreases again. The maximum reaches values as large as $\alpha_2 \approx 2.5$. This large value reflects the pronounced tails and minor maxima in the self part of the van Hove function $G_s(\Delta x, \tau)$ (**Figure 5**). The maximum is located at the transition from the intermediate subdiffusion to the long-time diffusion (**Figure 4**) because, at this time, many trimers still reside in their initial minima while a similarly large number of trimers have already moved to other minima and thus the ensemble of trimers exhibits very heterogeneous dynamics. Once most of the trimers have moved to other minima and diffusion is re-established, the non-Gaussian parameter $\alpha_2(\tau)$ returns to zero.

3.3. Rotation of Trimers

The rotation of a trimer can be deduced from the position of its three constituent spheres. One of the three spheres is chosen arbitrarily. The line connecting the center-of-mass of the trimer with the center of this sphere is considered to be the direction of the trimer (**Figure 7A**, arrow in inset). The angle between this line and an arbitrary but fixed direction (here the x direction) is taken to quantify the orientation of the trimer. This angle $\theta_i(t)$ is followed as a function of time t for each trimer i. Based on $\theta_i(t)$ the rotational dynamics can be investigated.

3.3.1. Mean Squared Angular Displacement

In analogy to Equation (1), the mean squared angular displacement (MSAD) is defined as

$$\langle \Delta\theta^2(\tau)\rangle = \langle [\theta_i(t_0+\tau) - \theta_i(t_0)]^2 \rangle_{i,t_0} \,. \tag{8}$$

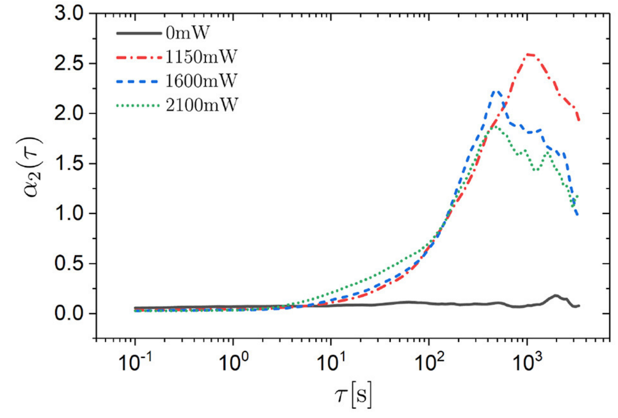

FIGURE 6 | Non-Gaussian parameter $\alpha_2(\tau)$ for displacements in the x direction as a function of the delay time τ for trimers exposed to different laser intensities P_L (as indicated).

The MSAD was determined based on the experimentally observed $\theta_i(t)$. Similar to the analysis of the translational motion, the MSAD was normalized by the short-time rotational diffusion coefficient D_S^{rot} to account for the effects of hydrodynamic interactions. Similar to the short-time diffusion coefficient D_S, the short-time rotational diffusion coefficient D_S^{rot} is affected by the hydrodynamic interactions but hardly affected by the external potential. It was determined from the slope of the MSAD at short times, analogous to the determination of D_S (Equation 3). The frame rate was chosen to be fast enough (10 fps) for a reliable determination of the initial slope. The short-time rotational diffusion coefficient D_S^{rot} increases within the investigated range of laser intensities P_L by $\sim 20\,\%$ (**Table 1**) which is similar to

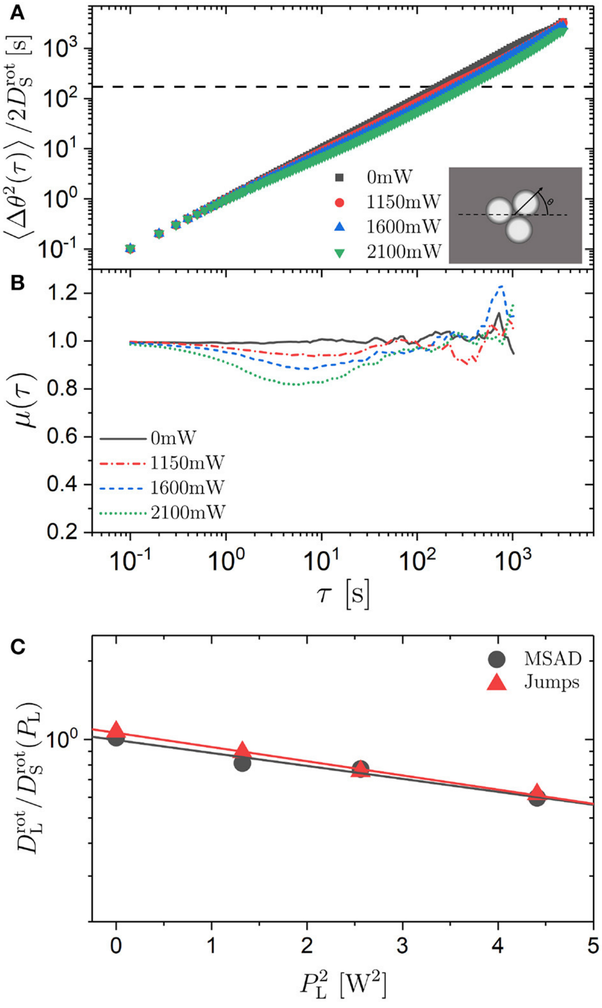

FIGURE 7 | (A) Mean squared angular displacement (MSAD) $\langle\Delta\theta(\tau)^2\rangle$ normalized by the short-time rotational diffusion coefficient D_S^{rot} and **(B)** exponent $\mu = \partial \log(\langle\Delta\theta(\tau)^2\rangle)/\partial \log(\tau)$ as a function of delay time τ for trimers exposed to different laser intensities P_L (as indicated). The horizontal line in (A) indicates $(120°)^2/2D_S^{rot}$. **(C)** Ratio of the long-time (D_L^{rot}) to the short-time (D_S^{rot}) rotational diffusion coefficient as a function of the square of the laser intensity, P_L^2, for trimers as determined from the MSAD (circles) and calculated based on the jump statistics (triangles). The lines are linear fits.

the increase of the short-time diffusion coefficient D_S of the center-of-mass diffusion of trimers.

The normalized MSAD was calculated for all laser intensities P_L (**Figure 7A**). The effect of the external potential on the MSAD is modest. At intermediate times the slope is only slightly smaller than unity ($\mu > 0.8$ for all P_L, **Figure 7B**) and the reduction of the long-time diffusion coefficient D_L^{rot} is very limited (**Figure 7C**). The ratio of the long-time to the short-time rotational diffusion coefficient (D_L^{rot}/D_S^{rot}) decreases by less than a factor of 2 within the range of investigated laser intensities P_L. The modest decrease of the long-time rotational diffusion coefficient D_L^{rot} is in strong contrast to the pronounced effect of the external potential on the long-time translational diffusion coefficient D_L (**Figure 3C**). However, $\log(D_L^{rot}/D_S^{rot})$ decreases linearly with the square of the laser intensity, P_L^2 similar to D_L (**Figure 7C**, Equation 4). Moreover, the intermediate subdiffusion of the rotational motion is not only much less pronounced than the one for the translational motion, it also occurs significantly earlier than the one for the translational motion: at times about an order of magnitude smaller (**Figure 4B**). This time window is comparable to the one during which the intermediate subdiffusion of individual spheres is observed (**Figure 3B**).

3.3.2. Self Part of the van Hove Function and Non-gaussian Parameter

Despite the innocuous-looking MSAD, we determined the self part of the van Hove function for angular displacements, $G_s(\Delta\theta, \tau)$ (defined analogous to Equation 6). Overall, $G_s(\Delta\theta, \tau)$ has a Gaussian shape with the width increasing with delay time τ (**Figures 8A–D**). Nevertheless, with increasing delay time τ and especially with increasing laser intensity P_L oscillations emerge which are separated by about 120°. The effect of increasing P_L, which increases the magnitude of the modulations of the potential, while keeping the delay time constant (data are averaged over the interval 35 min $< \tau <$ 60 min) is illustrated

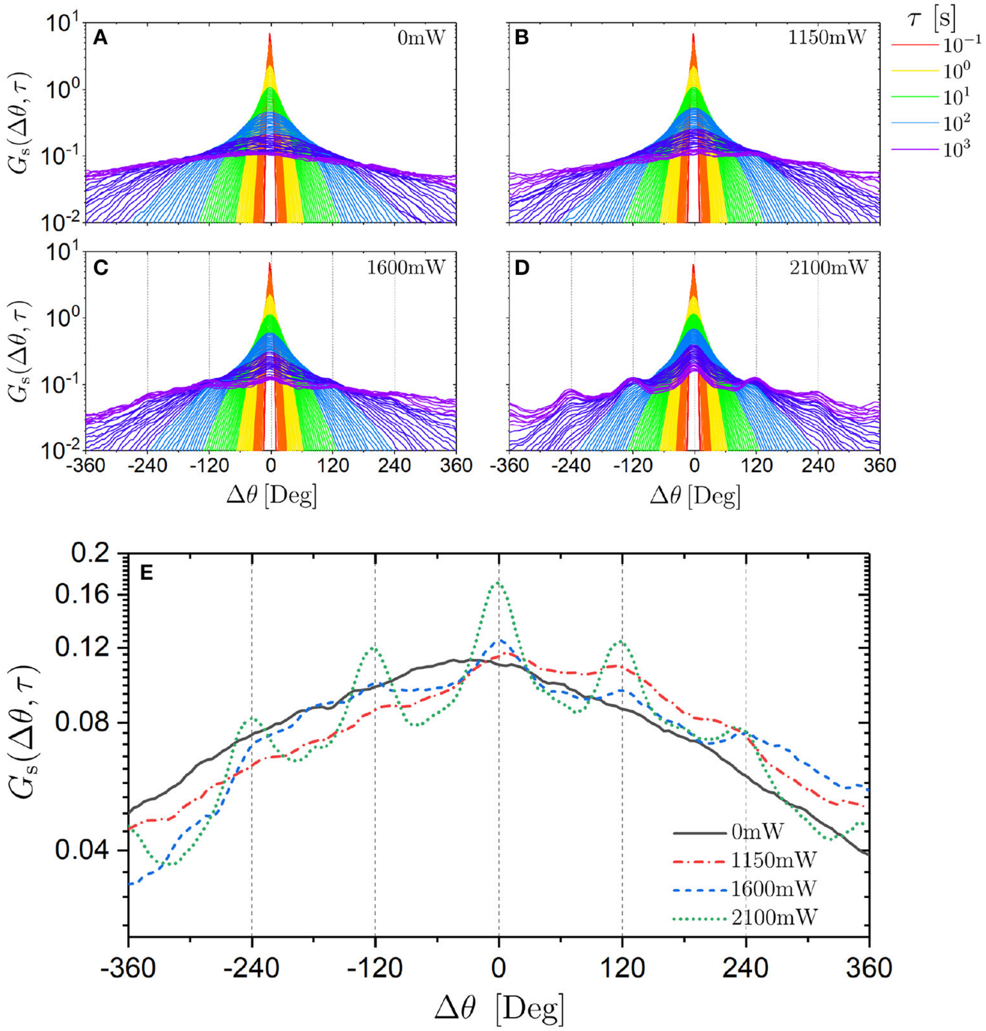

FIGURE 8 | Self part of the van Hove function $G_s(\Delta\theta, \tau)$ for angular displacements $\Delta\theta$ for trimers exposed to different laser intensities P_L (as indicated) **(A–D)** for different delay times τ (indicated by the color) and **(E)** for a long delay time (averaged over delay times 35 min $< \tau <$ 60 min) for different P_L (as indicated).

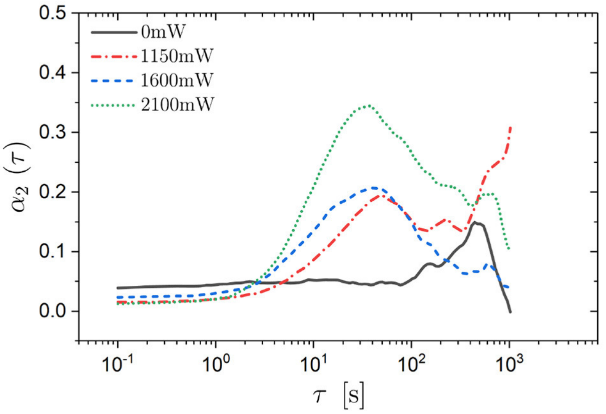

FIGURE 9 | Non-Gaussian parameter $\alpha_2(\tau)$ for rotational displacements $\Delta\theta$ as a function of delay time τ for trimers exposed to different laser intensities P_L (as indicated).

in **Figure 8E**. The data suggest that the trimers perform discrete rotational jumps of about 120° which become increasingly important as the magnitude of the modulations of the potential is increased. (Note that, although there are characteristic rotational jumps with $\Delta\theta \approx 120°$, the orientations of the trimers, $\theta_i(t)$, remain random). Whereas the oscillations become significantly more pronounced, in particular at the highest laser intensity, the overall Gaussian shape is hardly affected by the external potential. This is consistent with the non-Gaussian parameter $\alpha_2(\tau)$ (**Figure 9**). It only shows a moderate maximum ($\alpha_2 \approx 0.3$) which is approximately an order of magnitude smaller than the maximum observed in the $\alpha_2(\tau)$ of the translational motion (**Figure 6**). Furthermore, the time window during which the non-Gaussian parameter is significantly different from zero occurs much earlier for rotational motion than the corresponding time window of the translational motion (**Figure 6**): again by approximately an order of magnitude.

3.3.3. Angular Jumps

A typical trajectory $\mathbf{r}_i(t)$ of a particle exposed to a high laser intensity $P_L = 2.10$ W lasting 1 h is shown in **Figure 10A**. The trajectory indicates that the trimer remains in a limited area for some time before moving on. The size of these areas is about 2 μm, which is similar to the speckle size (**Figure 1B**). This suggests that the trajectories reflect the wiggling in minima as well as the motion between minima as is also indicated by the MSD (**Figure 4A**). The corresponding time evolutions of the center-of-mass, $r_i(t)$, and of the orientation, $\theta_i(t)$, are shown in **Figure 10B**. They show many small displacements and a few larger displacements of the center-of-mass, $r_i(t)$, as well as of the orientation, $\theta_i(t)$. To analyse the discrete angular jumps suggested by the self part of the van Hove function, $G_s(\Delta\theta, \tau)$ (**Figure 8**), a previously proposed algorithm based on the so-called hop identifier function $p_{\text{hop}}(t)$ [57, 58] was adapted. It detects major changes of the orientation occurring during a time interval T centered around the time t. The evolution of the orientation during the two neighboring time periods $[t-T/2, t]$, and $[t, t+T/2]$ (labeled A and B, respectively), is considered. The average orientations during the two periods $\langle\theta_i(t)\rangle_{t\in A}$ and $\langle\theta_i(t)\rangle_{t\in B}$ are determined. Then the hop identifier function $p_{\text{hop}}(t)$ is calculated which compares the values in one of the periods with the average during the other period. It is defined as

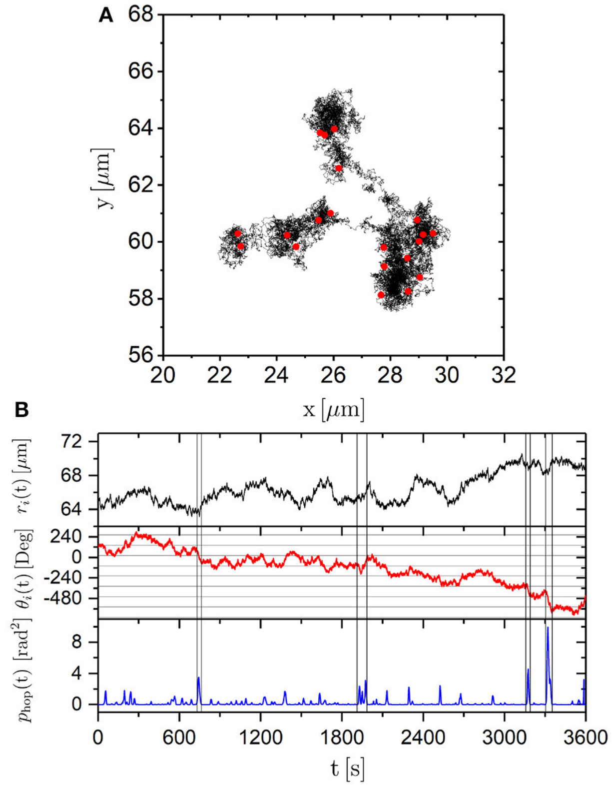

FIGURE 10 | (A) Trajectory of a trimer exposed to a laser intensity $P_L = 2.10$ W lasting 1 h. Red points indicate angular jumps defined by $p_{\text{hop}} > 0.75$ rad^2. **(B)** Corresponding time-dependence of the center-of mass $r_i(t)$ (top), orientation $\theta_i(t)$ (middle) and angular hop identifier $p_{\text{hop}}(t)$ (bottom). The vertical lines indicate regions of large values of $p_{\text{hop}}(t)$.

$$p_{\text{hop}}(t) = \sqrt{\left\langle[\theta_i(t') - \langle\theta_i(t'')\rangle_{t''\in B}]^2\right\rangle_{t'\in A} \left\langle[\theta_i(t'') - \langle\theta_i(t')\rangle_{t'\in A}]^2\right\rangle_{t''\in B}}. \tag{9}$$

Here we consider a time interval $T = 15$ s, which corresponds to 150 points in the trajectory and sweeps over the experimentally observed angular traces $\theta_i(t)$. With the help of p_{hop} major changes in $\theta_i(t)$ were identified with the value of p_{hop} characterizing the magnitude and temporal extent of the change. A large value of p_{hop} indicates large changes in the orientation during a short time (**Figure 10B**). The magnitude of the angular change $\Delta\Theta_i(t_j)$ of trimer i at time t_j is defined as

$$\Delta\Theta_i(t_j) = |\langle\theta_i(t')\rangle_{t'\in\mathbb{A}} - \left\langle\theta_i(t')\right\rangle_{t'\in\mathbb{B}}|, \tag{10}$$

where the averages are taken over the time intervals before and after the jump at time t_j, i.e., $\mathbb{A} = [t_{j-1} + T/2, t_j - T/2]$ and

$\mathbb{B} = [t_j + T/2, t_{j+1} - T/2]$, respectively. (Note that, in contrast, $\Delta\theta_i(\tau, t) = \theta_i(t+\tau) - \theta_i(t)$ represents the difference between two instantaneous angles).

We consider changes in the angular trace corresponding to $p_{\text{hop}}(t_j) > 0.75\ \text{rad}^2$ as significant changes ("jumps") occurring at time t_j. Smaller threshold values were found to be too close to the noise level and hence to yield unreliable results. In **Figure 10A** red dots indicate where angular jumps occurred along the trajectory. Several angular jumps occur while the trimer remains in an individual minima. Therefore, the angular jumps are not related to escapes from minima. This can also be seen from a comparison of $r_i(t)$ and $p_{\text{hop}}(t)$. At times t_j where $p_{\text{hop}}(t_j)$ shows a peak and hence indicates a jump in $\theta_i(t)$, the translational motion $r_i(t)$ does not show significant changes or jumps. Thus, based on $p_{\text{hop}}(t)$, angular jumps can be identified but they seem uncorrelated with the translational motion. Angular jumps have previously been observed for the motion of dimers exposed to a periodic potential energy landscape created by a fringe pattern [43]. In this study, rotations within the one-dimensional potential minima have been experimentally observed and theoretically predicted to occur through discrete rotational jumps. These rotational jumps were found to be coupled to the translational motion.

Having identified the angular jumps, the occurrences of clockwise and counter-clockwise jumps were compared. They are equally likely and independent of the previous jump direction. The ratios of the probabilities for clockwise and counter-clockwise jumps were found to be between 0.989 and 1.011 for the different laser intensities P_{L} and do not show a dependence on the laser intensities P_{L} (taking into account a total of 6,615 jumps during a total measurement time of $\sim$ 235 h). Thus, memory effects are absent for all investigated laser intensities P_{L}.

The probability distribution of the magnitude of angular jumps, $p(\Delta\Theta)$, was investigated. Again, $p_{\text{hop}}(t_j) > 0.75\ \text{rad}^2$ is taken to indicate jumps. This criterion suppresses small $\Delta\Theta$ and hence the resulting distribution will not represent the true distribution reliably at small $\Delta\Theta$ ($\Delta\Theta < \sqrt{0.75}$ rad $\approx 50°$) and, depending on the temporal extent of the jumps, at larger values of $\Delta\Theta$. Despite these shortcomings, we will continue with this analysis. In addition to the anticipated suppression of small values of $\Delta\Theta$, $p(\Delta\Theta)$ decreases for increasingly large jumps (**Figure 11A**). In the absence of an external potential, the decrease of $p(\Delta\Theta)$ follows a Gaussian distribution as expected. With increasing laser intensity P_{L}, $p(\Delta\Theta)$ keeps its overall shape but shows a high probability for jumps with $\Delta\Theta \approx 120°$. This is in agreement with the increasingly more pronounced oscillations in $G_{\text{s}}(\Delta\theta, \tau)$ (**Figure 8**) and supports the idea of discrete angular jumps with $\Delta\Theta \approx 120°$.

Based on $p_{\text{hop}}(t)$, the residence time between two jumps, $\Delta t = t_j - t_{j-1}$, can be extracted as the time elapsed between two consecutive occurrences of $p_{\text{hop}}(t_j) > 0.75\ \text{rad}^2$ and the distribution of residence times, $p(\Delta t)$, determined. The times are found to be exponentially distributed for all laser intensities P_{L} (**Figure 11B**) as expected for a Poisson process. An exponential fit provides the mean residence time $\langle\Delta t\rangle$. It ranges from $\sim$ 160 to 230 s with increasing laser intensity P_{L} (**Table 1**). These values can be compared to the mean residence times estimated from the ratio of the total measurement time T_{m} and the total number of jumps during this time, N_{m}, where $T_{\text{m}} \approx 100$ h and $N_{\text{m}} \approx 1{,}700$ for each laser intensity (**Table 1**). The values are in reasonable agreement given the different weightings involved in the two approaches.

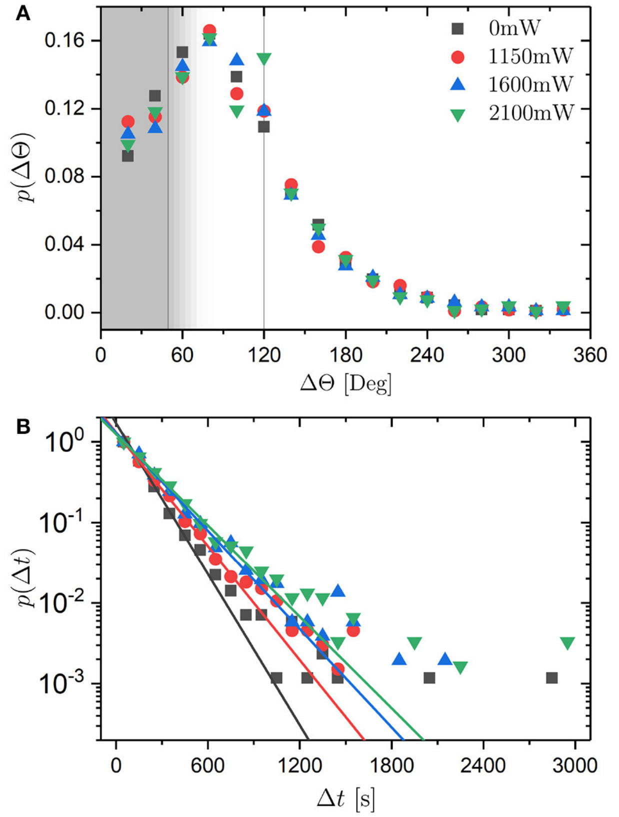

FIGURE 11 | (A) Probability distribution $p(\Delta\Theta)$ of angular jumps $\Delta\Theta$ for different laser intensities P_{L} (as indicated). Angular jumps are identified by $p_{\text{hop}}(t) > 0.75\ \text{rad}^2$ which implies that small jumps with $\Delta\Theta < \sqrt{0.75}$ rad $\approx 50°$ are suppressed (vertical line in gray area) and, depending on the temporal extent of the jumps, jumps with larger values of $\Delta\Theta$ (gray area). **(B)** Probability distribution $p(\Delta t)$ of residence times Δt for different laser intensities P_{L} (as indicated). Straight lines represent exponential fits to $p(\Delta t)$ at small Δt.

Based on the second moment of $p(\Delta\Theta)$ and the mean of $p(\Delta t)$, the long-time rotational diffusion coefficient $D_{\text{L}}^{\text{rot}}$ can be calculated assuming that the jumps dominate the long-time rotational diffusion:

$$D_{\text{L}}^{\text{rot}} = \frac{\langle\Delta\Theta^2\rangle}{2\langle\Delta t\rangle}\,, \tag{11}$$

where we take $\langle\Delta\Theta^2\rangle = (120°)^2 = (2.09\ \text{rad})^2$. With the values of $\langle\Delta t\rangle$ given above, $D_{\text{L}}^{\text{rot}}$ can be calculated for the different P_{L} (**Table 1**). The calculated values are in very good agreement with the experimentally determined values (**Figure 7C**).

3.3.4. Link Between Rotation and Translation

Above we considered the self part of the van Hove function for angular displacements $G_{\text{s}}(\Delta\theta, \tau)$ as a function of delay time τ (**Figure 8**). To investigate the correlation between rotation (angular displacements $\Delta\theta$) and translation (spatial displacements Δr), the self part of the van Hove function for angular displacements $G_s(\Delta\theta, \Delta r)$ as a function of displacements Δr is considered [**Figures 12A–D** which for clarity shows $G_s(|\Delta\theta|, \Delta r)$ instead of the symmetrical $G_s(\Delta\theta, \Delta r)$]. Without an external potential, $G_s(\Delta\theta, \Delta r)$ broadens with increasing Δr. As the translational displacement Δr increases, larger angular displacements $\Delta\theta$ also become more likely. In the presence of an external potential, $G_s(\Delta\theta, \Delta r)$ also broadens and in addition develops characteristic maxima. This indicates that the particles have preferences for specific angular displacements $\Delta\theta$. With increasing laser intensity P_L, the maxima become more pronounced but the general behavior remains similar. For small $\Delta r \lesssim 0.8\,\mu$m, large values of $G_s(\Delta\theta, \Delta r)$ are observed at multiples of 120°. This is consistent with the jumps of 120° discussed above and demonstrated, for example, by maxima in $G_s(\Delta\theta, \tau)$ separated by $\sim$ 120° (**Figure 8**) or by the high probability for jumps with $\Delta\Theta \approx 120°$ in $p(\Delta\Theta)$ (**Figure 11A**). Since the displacements of the center-of-mass are quite small, these observations reflect rotations of the trimers with the spheres swapping their locations but the center-of-mass of the trimer essentially remaining in the same position (**Figure 13A**). This explains why no significant translational displacements are observed when angular jumps are identified (**Figure 10B**) and hence why the rotation and translation appear uncorrelated based on $p_{\mathrm{hop}}(t)$. Upon increasing the translational displacements to $0.8\,\mu\mathrm{m} \leq \Delta r \leq 1.4\,\mu$m, the maxima at multiples of 120° vanish and instead maxima at 60° and much smaller maxima at 180° and 300° emerge. This is consistent with two minima remaining occupied while one neighboring minimum is newly occupied (**Figure 13B**) because, in an idealized situation, this involves a rotation by 60° and possible further rotations by multiples of 120° in addition to a translational motion by $\sigma/\sqrt{3} \approx 1.2\,\mu$m. Therefore, in this case, a rotation of 60° is coupled to a translation of about $\sigma/\sqrt{3}$. This coupling of translation and rotation could not be detected with the hop identifier because it cannot reliably identify a jump of 60° with the criterion $p_{\mathrm{hop}}(t_j) > 0.75$ rad^2. Larger translational motions ($\Delta r > 1.4\,\mu$m) imply that at most one minimum remains occupied whereas two neighboring minima are newly occupied. If one minimum remains occupied, this involves in the idealized case shown in **Figure 13C** a rotation between 120° and 180° and possibly further rotations by multiples of 120° as well as a displacement $\sigma \leq \Delta r \leq 2\sigma/\sqrt{3}$. Moreover, a motion to new minima can involve any rotation and any displacement with $\Delta r \gtrsim \sigma$. This is reflected in the broad distribution of angular displacements and the lack of a preference for a specific angular displacement for large translational displacements $\Delta r \gtrsim 1.6\,\mu$m. This is qualitatively different from the van Hove function for angular displacements as a function of delay time τ, $G_s(\Delta\theta, \tau)$, which also shows maxima at specific angular displacements at long delay times τ (**Figure 8**). This preference of $G_s(\Delta\theta, \tau)$ for specific angular displacements can be maintained during long time periods because a long time period does not necessarily imply significant translational motion during which any angular displacement can occur but does allow for negligible translational motion while a swap of the positions of the spheres results in a rotation by a multiple of 120° (**Figure 13A**). Thus, the coupling between translation and rotation depends on the distance the

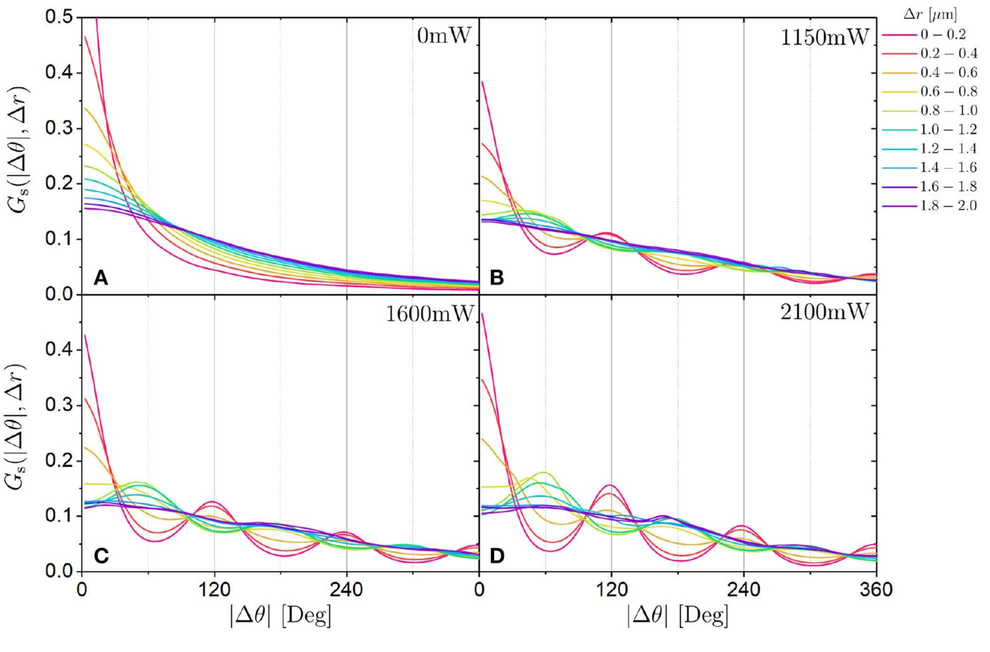

FIGURE 12 | Self part of the van Hove function $G_s(|\Delta\theta|, \Delta r)$ for angular displacements $|\Delta\theta|$ for different translational displacements Δr (indicated by the color) for trimers exposed to different laser intensities P_L (as indicated, **A–D**). Note that $G_s(\Delta\theta, \Delta r)$ is symmetrical and hence $G_s(|\Delta\theta|, \Delta r)$ is shown for clarity.

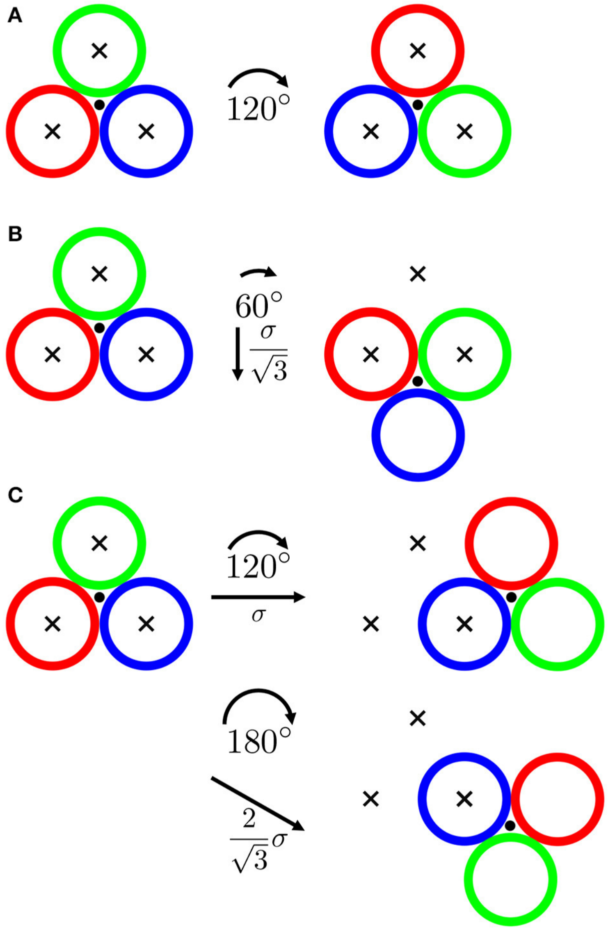

FIGURE 13 | Schematic representation of a trimer (differently colored open circles) undergoing rearrangements involving **(A)** three, **(B)** two and **(C)** one initial minima remaining occupied as well as the corresponding angular ($\Delta\theta$, arcs) and translational (Δr, arrows), displacements. The center-of-mass is indicated by a filled circle and the initially occupied minima are indicated by crosses. The particle size and the speckle size are assumed to be equal. Idealized situations with all three spheres initially perfectly placed in minima are represented here. This does not fully reflect the random nature of the potential but may reasonably approximate the actually occupied locations with low potential energies for the whole trimer.

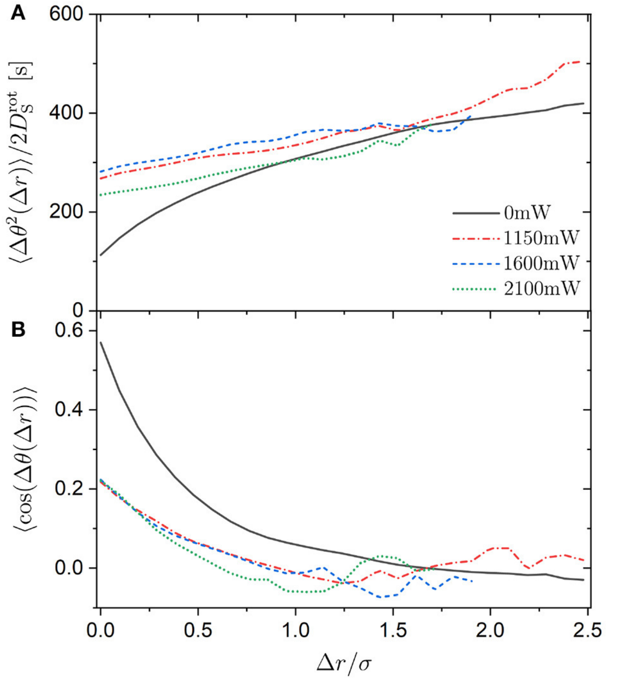

FIGURE 14 | (A) Mean squared angular displacement (MSAD) $\langle\Delta\theta(\Delta r)^2\rangle$ normalized by the short-time rotational diffusion coefficient D_s^{rot} and **(B)** orientation correlation function $\langle\cos(\Delta\theta(\Delta r))\rangle$ as a function of displacement Δr normalized by the sphere diameter σ for trimers exposed to different laser intensities P_L (as indicated).

particle traveled. At very small distances and hence without significant translation, rotations can occur. In contrast, rotations are coupled to translations at intermediate distances ($0.8\,\mu\mathrm{m} \leq \Delta r \leq 1.4\,\mu\mathrm{m}$). At larger distances translations and rotations are again decoupled.

In addition to the maxima of the van Hove function $G_s(\Delta\theta, \Delta r)$, the general broadening of $G_s(\Delta\theta, \Delta r)$ is characterized by the mean squared angular displacement (MSAD) $\langle\Delta\theta^2(\Delta r)\rangle$ as a function of the translational displacement Δr (**Figure 14A**). Without an external potential, $\langle\Delta\theta^2(\Delta r)\rangle$ increases with increasing translational displacement Δr. In contrast to $\langle\Delta\theta^2(\tau)\rangle$ (**Figure 7A**), $\langle\Delta\theta^2(\Delta r)\rangle$ starts at $\Delta r = 0$ with a finite value since the trimer can rotate without translating, whereas it cannot rotate in no time ($\langle\Delta\theta^2(\tau{=}0)\rangle = 0$). In the presence of an external potential, translation is restricted and hence even larger angular displacements are possible during small translational displacements. With increasing translational displacements, $\langle\Delta\theta^2(\Delta r)\rangle$ increases further.

The experimental uncertainties at large displacements are quite considerable in the presence of a random potential. This is due to the long time required for large displacements resulting in only a small number of large displacements being observed. This is particularly true for large laser intensities P_L. The data shown in **Figure 14** are based on at least 150 displacements. This number of displacements is easily observed without an external potential. However, with increasing laser intensity P_L, this number of displacements is only detected for progressively smaller displacements Δr. Nevertheless, within the experimental uncertainties, the data suggest that $\langle\Delta\theta^2(\Delta r)\rangle$ does not depend on the laser intensity P_L. This implies that the random potential slows down the translation and rotation of the trimers equally. This seems reasonable because the spheres have to move in the same random potential for both, a translation and a rotation of the trimer. Translation and rotation are considered separately only to simplify the analysis and data interpretation and thus for our convenience. Moreover, although at large distances Δr the uncertainties do not allow for unambiguous conclusions, the data seem to indicate that $\langle\Delta\theta^2(\Delta r)\rangle$ might not depend on the presence of an external potential at distances beyond

$\Delta r \approx 2\,\mu$m. This is about the spatial correlation length of the random potential [34]. This suggests that, at distances larger than the spatial heterogeneity of the random potential, the random potential has no specific effect on the translation and rotation except to generally slow down the motion. In contrast, at distances smaller than the spatial heterogeneity, the random potential leads to specific movements resulting in all or some of the occupied minima remaining occupied (**Figure 13**).

The coupling between rotation and translation is also characterized by the orientation correlation function $\langle \cos(\Delta\theta(\Delta r)) \rangle$ (**Figure 14B**). Essentially independent of the laser intensity P_{L}, the orientation correlation function $\langle \cos(\Delta\theta(\Delta r)) \rangle$ decays within $\Delta r \approx 2\,\mu$m and hence on a length scale very similar to the one found above and to the spatial correlation length of the random potential [34]. Additionally, $\langle \cos(\Delta\theta(\Delta r)) \rangle$ for trimers not exposed to a random potential decays on a comparable length scale. This could be a coincidence since the spatial correlation length of the random potential and the size of an individual sphere are similar. Future experiments with different particle sizes and different spatial correlation lengths, which can be varied as previously described [34], will be devoted to this issue.

4. CONCLUSIONS

The translational and rotational dynamics of trimers subjected to a random potential energy landscape have been investigated. The translational center-of-mass motion is characterized by subdiffusion at intermediate times due to the confinement to the minima and diffusion at long times reflecting the random motion between minima. The dynamics hence resemble the dynamics of spheres, which are the building blocks of the trimers, but the trimers are more strongly affected by the potential. The rotational mean squared angular displacements (MSAD) are only slightly affected by the potential. However, a more detailed analysis based on the van Hove distribution function and the hop identifier indicates discrete jumps of 120° that are particularly pronounced at long times and large magnitudes of the modulations of the random potential. These jumps are found to dominate the long-time rotational diffusion.

The rotational motion is correlated with the translational motion due to the symmetry of the trimers. During the angular jumps of about 120°, the spheres forming the trimer swap their positions without any significant translational motion. If only two out of the three initial minima remain occupied, a jump of 60° is coupled to a translational motion between $\sim$ 0.8 and $1.4\,\mu$m. This is in agreement with an idealized model (**Figure 13**). Upon a larger translational motion, beyond the spatial correlation length of the random potential, any angular displacement becomes possible and hence the correlation between translation and rotation is lost. In this regime, the random potential slows down the translational and rotational dynamics equally.

The work presented here can be extended in future projects. For example, different particle or speckle sizes could be investigated to study the effect of their size ratio. Depending on the size ratio, the rotational dynamics could be favored or disfavoured compared to the translational dynamics. The coupling between translation and rotation might also be affected by the symmetry of the particles and hence other multimers, such as dumbbells, or other anisotropic particles, such as elliptical or platelike particles, could be studied. In addition, in concentrated samples the interplay between the external random potential and the particle–particle interactions can be explored. The random potential could also be replaced by a periodic potential which would also have a very significant effect on the correlation between translation and rotation.

DATA AVAILABILITY STATEMENT

The datasets generated for this study are available on request to the corresponding author.

AUTHOR CONTRIBUTIONS

JS-G, ME-S, and SE designed the experiments. JS-G and ME-S prepared the particles. JS-G performed the experiments. JS-G, ME-S, ES-G, and SE analyzed the data. JS-G, ES-G, and SE wrote the manuscript.

FUNDING

This work was supported by the Deutsche Forschungsgemeinschaft (DFG), Project No. EG269/6-1.

ACKNOWLEDGMENTS

We thank Daniela Pérez-Guerrero, Milana Popara, and Alejandro Villada-Balbuena for useful discussions and for early contributions to the project and Katherine Macmillan for very helpful comments on the manuscript as well as the referees for very helpful and inspiring comments.

REFERENCES

1. Metzler R, Jeon JH, Cherstvy AG, Barkai E. Anomalous diffusion models and their properties: non-stationarity, non-ergodicity, and ageing at the centenary of single particle tracking. *Phys Chem Chem Phys.* (2014) **16**:24128–64. doi: 10.1039/C4CP03465A
2. Weiss M, Elsner M, Kartberg F, Nilsson T. Anomalous subdiffusion is a measure for cytoplasmic crowding in living cells. *Biophys J.* (2004) **87**:3518–24. doi: 10.1529/biophysj.104.044263
3. Seisenberger G, Ried MU, Endress T, Büning H, Hallek M, Bräuchle C. Real-time single-molecule imaging of the infection pathway of an adeno-associated virus. *Science.* (2001) **294**:1929–32. doi: 10.1126/science.1064103
4. Reverey JF, Jeon JH, Bao H, Leippe M, Metzler R, Selhuber-Unkel C. Superdiffusion dominates intracellular particle motion in the supercrowded cytoplasm of pathogenic *Acanthamoeba castellanii*. *Sci Rep.* (2015) **5**:11690. doi: 10.1038/srep11690
5. Thapa S, Lukat N, Selhuber-Unke C, Cherstvy AG, Metzler R. Transient superdiffusion of polydisperse vacuoles in highly motile

amoeboid cells. *J Chem Phys.* (2019) **150**:144901. doi: 10.1063/1.5086269

6. Nicolau DV, Hancock JF, Burrage K. Sources of anomalous diffusion on cell membranes: a Monte Carlo study. *Biophys J.* (2007) **92**:1975–87. doi: 10.1529/biophysj.105.076869
7. Metzler R, Jeon JH, Cherstvy AG. Non-Brownian diffusion in lipid membranes: Experiments and simulations. *Biochim Biophys Acta.* (2016) **1858**:2451–67. doi: 10.1016/j.bbamem.2016.01.022
8. Daddi-Moussa-Ider A, Goh S, Liebchen B, Hoell C, Mathijssen AJTM, Guzmán-Lastra F, et al. Membrane penetration and trappingof an active particle. *J Chem Phys.* (2019) **150**:064906. doi: 10.1063/1.5080807
9. Dickson RM, Norris DJ, Tzeng Y, Moerner WE. Three-dimensional imaging of single molecules solvated in pores of poly(acrylamide) gels. *Science.* (1996) **274**:966–8. doi: 10.1126/science.274.5289.966
10. Gibbs JH, DiMarzio EA. Nature of the glass transition and the glassy state. *J Chem Phys.* (1958) **28**:373–83. doi: 10.1063/1.1744141
11. Adam G, Gibbs JH. On the temperature dependence of cooperative relaxation properties in glass-forming liquids. *J Chem Phys.* (1965) **43**:139–46. doi: 10.1063/1.1696442
12. Heuer A. Exploring the potential energy landscape of glass-forming systems: from inherent structures via metabasins to macroscopic transport. *J Phys Condens Matter.* (2008) **20**:373101. doi: 10.1088/0953-8984/20/37/373101
13. Hunter GL, Weeks ER. The physics of the colloidal glass transition. *Rep Prog Phys.* (2012) **75**:066501. doi: 10.1088/0034-4885/75/6/066501
14. Stillinger FH, Debenedetti PG. Glass transition thermodynamics and kinetics. *Annu Rev Condens Matter Phys.* (2013) **4**:263–85. doi: 10.1146/annurev-conmatphys-030212-184329
15. Ho CC, Keller A, Odell JA, Ottewill RH. Preparation of monodisperse ellipsoidal polystyrene particles. *Coll Polym Sci.* (1993) **271**:469–79. doi: 10.1007/BF00657391
16. Wolters JR, Avvisati G, Hagemans F, Vissers T, Kraft DJ, Dijkstra M, et al. Self-assembly of "Mickey Mouse" shaped colloids into tube-like structures: experiments and simulations. *Soft Matter.* (2015) **11**:1067–77. doi: 10.1039/C4SM02375G
17. Peng B, van der Wee E, Imhof A, van Blaaderen A. Synthesis of monodisperse, highly Cross-Linked, fluorescent PMMA particles by dispersion polymerization. *Langmuir.* (2012) **28**:6776–85. doi: 10.1021/la301288r
18. Manoharan VN, Elsesser MT, Pine DJ. Dense packing and symmetry in small clusters of microspheres. *Science.* (2003) **301**:483. doi: 10.1126/science.1086189
19. Han Y, Alsayed AM, Nobili M, Zhang J, Lubensky TC, Yodh AG. Brownian motion of an ellipsoid. *Science.* (2006) **314**:626–30. doi: 10.1126/science.1130146
20. Villanueva-Valencia JR, Santana-Solano J, Sarmiento-Gómez E, Herrera-Velarde S, Arauz-Lara JL, Castaneda-Priego R. Long-time dynamics and hydrodynamic correlations in quasi-two-dimensional anisotropic colloidal mixtures. *Phys Rev E.* (2018) **98**:062605. doi: 10.1103/PhysRevE.98.062605
21. Vivek S, Weeks ER. Decoupling of translational and rotational diffusion in quasi-2D colloidal fluids. *J Chem Phys.* (2017) **147**:134502. doi: 10.1063/1.4996733
22. Anthony SM, Kim M, Granick S. Translation-rotation decoupling of colloidal clusters of various symmetries. *J Chem Phys.* (2008) **129**:244701. doi: 10.1063/1.3043443
23. Edmond KV, Elsesser MT, Hunter GL, Pine DJ, Weeks ER. Decoupling of rotational and translational diffusion in supercooled colloidal fluids. *Proc Natl Acad Sci USA.* (2012) **109**:17891–6. doi: 10.1073/pnas.1203328109
24. Jeon H, Cho HW, Kim J, Sung BJ. Non-Gaussian rotational diffusion in heterogeneous media. *Phys Rev E.* (2014) **90**:042105. doi: 10.1103/PhysRevE.90.042105
25. Ashkin A. Acceleration and trapping of particles by radiation pressure. *Phys Rev Lett.* (1970) **24**:156–9. doi: 10.1103/PhysRevLett.24.156
26. Ashkin A, Dziedzic JM, Bjorkholm JE, Chu S. Observation of a single-beam gradient force optical trap for dielectric particles. *Opt Lett.* (1986) **11**:288–90. doi: 10.1364/OL.11.000288
27. Molloy JE, Padgett MJ. Lights, action: optical tweezers. *Contemp Phys.* (2002) **43**:241–58. doi: 10.1080/00107510110116051
28. Neuman KC, Block SM. Optical trapping. *Rev Sci Instrum.* (2004) **75**:2787–809. doi: 10.1063/1.1785844
29. Dienerowitz M, Mazilu M, Dholakia K. Optical manipulation of nanoparticles: a reivew. *J Nanophoton.* (2008) **2**:021875. doi: 10.1117/1.2992045
30. Evers F, Hanes RDL, Zunke C, Capellmann RF, Bewerunge J, Dalle-Ferrier C, et al. Colloids in light fields: Particle dynamics in random and periodic energy landscapes. *Eur Phys J Special Topics.* (2013) **222**:2995–3009. doi: 10.1140/epjst/e2013-02071-2
31. Jenkins MC, Egelhaaf SU. Colloidal suspensions in modulated light fields. *J Phys Condens Matter.* (2008) **20**:404220. doi: 10.1088/0953-8984/20/40/404220
32. Capellmann RF, Bewerunge J, Platten F, Egelhaaf SU. Note: using a Kösters prism to create a fringe pattern. *Rev Sci Instrum.* (2017) **88**:056102. doi: 10.1063/1.4982587
33. Juniper MPN, Besseling R, Aarts DGAL, Dullens RPA. Acousto-optically generated potential energy landscapes: Potential mapping using colloids under flow. *Opt Express.* (2012) **20**:28707–16. doi: 10.1364/OE.20.028707
34. Bewerunge J, Egelhaaf SU. Experimental creation and characterization of random potential-energy landscapes exploiting speckle patterns. *Phys Rev A.* (2016) **93**:013806. doi: 10.1103/PhysRevA.93.013806
35. Hanes RDL, Jenkins MC, Egelhaaf SU. Combined holographic-mechanical optical tweezers: construction, optimization, and calibration. *Rev Sci Instrum.* (2009) **80**:083703. doi: 10.1063/1.3196181
36. Abbott JL, Spiers JA, Gao Y, Aarts DGA, Dullens RPA. Colloidal rods in optical potential energy landscapes. *J Phys D Appl Phys.* (2019) **52**:024002. doi: 10.1088/1361-6463/aae5d0
37. Dalle-Ferrier C, Krüger M, Hanes RDL, Walta S, Jenkins MC, Egelhaaf SU. Dynamics of dilute colloidal suspensions in modulated potentials. *Soft Matter.* (2011) **7**:2064–75. doi: 10.1039/C0SM01051K
38. Hanes RDL, Dalle-Ferrier C, Schmiedeberg M, Jenkins MC, Egelhaaf SU. Colloids in one dimensional random energy landscapes. *Soft Matter.* (2012) **8**:2714–23. doi: 10.1039/c2sm07102a
39. Evers F, Zunke C, Hanes RDL, Bewerunge J, Ladadwa I, Heuer A, et al. Particle dynamics in two-dimensional random-energy landscapes: Experiments and simulations. *Phys Rev E.* (2013) **88**:022125. doi: 10.1103/PhysRevE.88.022125
40. Bianchi S, Pruner R, Vizsnyiczai G, Maggi C, Leonardo RD. Active dynamics of colloidal particles in time-varying laser speckle patterns. *Sci Rep.* (2016) **6**:27681. doi: 10.1038/srep27681
41. Volpe G, Volpe G, Gigan S. Brownian motion in a speckle light field: tunable anomalous diffusion and selective optical manipulation. *Sci Rep.* (2014) **4**:3936. doi: 10.1038/srep03936
42. Sarmiento-Gómez E, Rivera-Moráña JA, Arauz-Lara JL. Single particle states of colloidal particles in 2D periodic potentials. *Soft Matter.* (2018) **14**:3684–8. doi: 10.1039/C8SM00326B
43. Sarmiento-Gómez E, Rivera-Moráña JA, Arauz-Lara JL. Energy landscape of colloidal dumbbells in a periodic distribution of light. *Soft Matter.* (2019) **15**:3573–9. doi: 10.1039/C9SM00472F
44. Dullens RPA, Claesson EM, Kegel WK. Preparation and properties of cross-linked fluorescent poly(methyl methacrylate) latex colloids. *Langmuir.* (2004) **20**:658–64. doi: 10.1021/la035729a
45. Elsesser MT, Hollingsworth AD, Edmond KV, Pine DJ. Large core-shell poly(methyl methacrylate) colloidal clusters: synthesis, characterization, and tracking. *Langmuir.* (2010) **27**:917–27. doi: 10.1021/la1034905
46. Antl L, Goodwin JW, Hill RD, Ottewill RH, Owens SM, Papworth S. The preparation of poly(methyl methacrylate) lattices in non-aqueous media. *Coll Surf.* (1986) **17**:67–78. doi: 10.1016/0166-6622(86)80187-1
47. Carbajal-Tinoco MD, de Léon GC, Arauz-Lara JL. Brownian motion in quasibidimensional colloidal suspensions. *Phys Rev E.* (1997) **56**:6962. doi: 10.1103/PhysRevE.56.6962
48. Crocker JC, Grier DG. Methods of digital video microscopy for colloidal studies. *J Coll Interf Sci.* (1996) **179**:298–310. doi: 10.1006/jcis.1996.0217
49. Landau LD, Lifshitz EM. *The Cassical Theory of Fields.* London: Pergamon Press (1971).
50. Dean DS, Drummond IT, Horgan RR. Effective transport properties for diffusion in random media. *J Stat Mech.* (2007) **2007**:P07013. doi: 10.1088/1742-5468/2007/07/P07013
51. Bewerunge J, Ladadwa I, Platten F, Zunke C, Heuer A, Egelhaaf SU. Time- and ensemble-averages in evolving systems: the case of Brownian particles in random potentials. *Phys Chem Chem Phys.* (2016) **18**:18887–95. doi: 10.1039/C6CP02559E

52. Pagac ES, Tilton RD, Prieve DC. Hindered mobility of a rigid sphere near a wall. *Chem Eng Comm.* (1996) **148–50**:105–22. doi: 10.1080/00986449608936511
53. Sharma P, Ghosh S, Bhattacharya S. A high-precision study of hindered diffusion near a wall. *Appl Phys Lett.* (2010) **97**:104101. doi: 10.1063/1.3486123
54. Rahman A. Correlations in the motion of atoms in liquid argon. *Phys Rev.* (1964) **136**:A405. doi: 10.1103/PhysRev.136.A405
55. Shell MS, Debenedetti PG, Stillinger FH. Dynamic heterogeneity and non-Gaussian behaviour in a model supercooled liquid. *J Phys Condens Matter.* (2005) **17**:S4035–46. doi: 10.1088/0953-8984/17/49/002
56. Vorselaars B, Lyulin AV, Karatasos K, Michels MAJ. Non-Gaussian nature of glassy dynamics by cage to cage motion. *Soft Matter.* (2007) **75**:011504. doi: 10.1103/PhysRevE.75.011504
57. Candelier R, Widmer-Cooper A, Kummerfeld JK, Dauchot O, Biroli G, Harrowell P, et al. Spatiotemporal hierarchy of relaxation events, dynamical heterogeneities, and structural reorganization in a supercooled liquid. *Phys Rev Lett.* (2010) **105**:135702. doi: 10.1103/PhysRevLett.105.135702
58. Smessaert A, Rottler J. Distribution of local relaxation events in an aging three-dimensional glass: spatiotemporal correlation and dynamical heterogeneity. *Phys Rev E.* (2013) **88**:022314. doi: 10.1103/PhysRevE.88.022314

Conflict of Interest: The authors declare that the research was conducted in the absence of any commercial or financial relationships that could be construed as a potential conflict of interest.

frontiers in Physics

PERSPECTIVE
published: 14 May 2020
doi: 10.3389/fphy.2020.00134

Anomalous Subdiffusion in Living Cells: Bridging the Gap Between Experiments and Realistic Models Through Collaborative Challenges

Maxime Woringer[1,2,3,4], *Ignacio Izeddin*[4,5], *Cyril Favard*[4,6]* and *Hugues Berry*[4,7,8]*

[1] Unité Imagerie et Modélisation, CNRS UMR 3691, and C3BI (Center of Bioinformatics, Biostatistics and Integrative Biology), CNRS USR 3756, Institut Pasteur, Paris, France, [2] Sorbonne Universités, CNRS, Paris, France, [3] Department of Molecular and Cell Biology, Li Ka Shing Center for Biomedical and Health Sciences, and CIRM Center of Excellence in Stem Cell Genomics, University of California, Berkeley, Berkeley, CA, United States, [4] GDR Imabio, CNRS, Lille, France, [5] Institut Langevin, ESPCI Paris, PSL University, CNRS, Paris, France, [6] Membrane Domains and Viral Assembly, Institut de Recherche en Infectiologie de Montpellier, CNRS UMR 9004, Montpellier, France, [7] Inria, Lyon, Villeurbanne, France, [8] Université de Lyon, LIRIS UMR5205, Villeurbanne, France

The life of a cell is governed by highly dynamical microscopic processes. Two notable examples are the diffusion of membrane receptors and the kinetics of transcription factors governing the rates of gene expression. Different fluorescence imaging techniques have emerged to study molecular dynamics. Among them, fluorescence correlation spectroscopy (FCS) and single-particle tracking (SPT) have proven to be instrumental to our understanding of cell dynamics and function. The analysis of SPT and FCS is an ongoing effort, and despite decades of work, much progress remains to be done. In this paper, we give a quick overview of the existing techniques used to analyze anomalous diffusion in cells and propose a collaborative challenge to foster the development of state-of-the-art analysis algorithms. We propose to provide labeled (training) and unlabeled (evaluation) simulated data to competitors all over the world in an open and fair challenge. The goal is to offer unified data benchmarks based on biologically-relevant metrics in order to compare the diffusion analysis software available for the community.

Keywords: diffusion in cells, continuous-time random walks, fractional Brownian motion, fluorescence correlation spectroscopy, single-particle tracking

Edited by:
Ralf Metzler,
University of Potsdam, Germany

Reviewed by:
Haroldo Valentin Ribeiro,
State University of Maringá, Brazil
Jae-Hyung Jeon,
Pohang University of Science and Technology, South Korea

Correspondence:
Cyril Favard
cyril.favard@irim.cnrs.fr
Hugues Berry
hugues.berry@inria.fr

Specialty section:
This article was submitted to Interdisciplinary Physics, a section of the journal Frontiers in Physics

Received: *23 September 2019*
Accepted: *06 April 2020*
Published: *14 May 2020*

Citation:
Woringer M, Izeddin I, Favard C and Berry H (2020) Anomalous Subdiffusion in Living Cells: Bridging the Gap Between Experiments and Realistic Models Through Collaborative Challenges. Front. Phys. 8:134. doi: 10.3389/fphy.2020.00134

1. INTRODUCTION

The life of a cell is governed by highly dynamical microscopic processes occurring at different space and time scales from single macromolecules up to organelles. Optical microscopy provided four decades ago the first measurements of biomolecule motion in cells. First by fluorescence recovery after photobleaching (FRAP) [1] and fluorescence correlation spectroscopy (FCS) [2], and more recently with the help of single particle tracking (SPT) [3, 4]. Several factors have colluded to popularize these techniques in many biophysics and biology labs: (i) the development of highly sensitive detectors, (ii) the emergence of genetically encoded fluorescent protein labeling in the late 90s [5–7], and (iii) the advent in the years 2000–2010 of far-field super-resolution microscopy [8–12]. All these technological efforts have granted us access to the monitoring of molecular motion in cells with unprecedented spatial (down to single molecule) and temporal resolution [13, 14]. The adoption of these techniques has been paramount in the advancement of the understanding of cell organization and dynamics [15–17].

While acquiring sufficient experimental data sets used to be a limiting factor, these technological advances combined with data acquisition parallelization provide nowadays huge amounts of data available for analysis of molecular motion inside the cell. In turn, the richness of this data has unraveled an unforeseen complexity and diversity of mechanisms for biomolecule motion in cells. Therefore, many efforts are devoted to analyze data provided by FCS or SPT with direct or inference approaches.

However, choosing the appropriate algorithms to analyse the complexity of the observed phenomena is still an important challenge. Indeed, the richness of experimental data often makes it difficult to determine which are the physical models to be considered and which are the relevant biophysical parameters to be estimated from them. We review and address this issue in this perspective.

We will first briefly review key anomalous diffusion models relevant to cell biology and summarily describe some of the existing techniques to either infer model parameters or to perform model selection. We will discuss the relevance of numerical simulations and the importance of designing realistic data sets closely mimicking the results obtained in experiments on biological samples. We will also highlight the often overlooked limitations in current acquisition methods and emphasize the role of experimental noise and biases of the aforementioned techniques. Finally, we will present and advocate in favor of the development of comprehensive sets of simulated data and metrics, allowing the community to objectively evaluate existing and new analysis tools. Our hope is that this work will instigate an open discussion about the limitations and challenges of analysing and modeling diffusion of molecules in the complex environment of the cell.

2. BROWNIAN VS. ANOMALOUS DIFFUSION

Maybe one of the best-known result of the theory of Brownian diffusion is that the mean squared displacement (MSD) of a random walker scales linearly with time, and is proportional to the diffusion coefficient of the fluid in which diffusion takes place. With $x(t)$ being the position of the random walker at time t (in one dimension), this means that the MSD $\left\langle x(t)^2 \right\rangle = 2Dt$, where $\langle \cdot \rangle$ denotes ensemble averaging and $x(0) = 0$. However, Brownian diffusion does not explain the physics of disordered systems. Interestingly, an ubiquitous observation in cell biology is that the diffusive motion of macromolecules and organelles is anomalous, i.e., the MSD change with time is typically characterized by a sublinear increase. In most instances, this sublinear increase of the MSD with time can be fitted to a power-law relation $\left\langle x(t)^2 \right\rangle \propto t^\alpha$ with exponent $\alpha < 1$, which justifies the vocable of "subdiffusion." Subdiffusion is usually attributed to cellular crowding, spatial heterogeneity or molecular interactions. Another possibility of anomalous diffusion is superdiffusion, with $1 < \alpha < 2$. Indeed a lot of processes in biology exhibit active transport or combinations of active and random motions.

Anomalous diffusion in cells is therefore a very active area of research involving biophysics, cell biology, statistical physics and mathematical modeling.

When confronted to a set of data retrieved from FCS or SPT experiments, the first question that one needs to answer is whether the measured subdiffusion is indeed a manifestation of an anomalous process. Often, a combination of several normal diffusion mechanisms or experimental artifacts gives rise to an apparent diffusion. If an anomalous subdiffusion—characterized by a power law scaling of the MSD with time—can be identified, establishing the physical model behind the diffusion process can shed light on the molecular mechanisms driving the motion of the molecule of interest.

Below, we will first focus on three classical models for anomalous subdiffusion and their common biological interpretation, namely the continuous-time random walk (CTRW) model, the fractional Brownian motion (fBm) model, and random walks on fractal and disordered systems (for a review, see e.g., [18]), then we will briefly describe different models covering super-diffusion processes that can be encountered in cells, such as run and tumble model, Lévy flights and super-diffusive fBm.

The **continuous-time random walk** model is a generalization of a random walk in which the diffusing particle waits for a random time between jumps. More generally, when the distribution $\phi(\tau)$ of waiting times τ is long-tailed and cannot be averaged (with e.g., $\phi(\tau) \propto \tau^{-(1+\alpha)}$ and $0 < \alpha < 1$), the ensemble-averaged MSD shows anomalous scaling with a power law. A straightforward interpretation of a CTRW in the context of molecular biology is assimilating the waiting times to interactions of the molecule with an immobile substrate (at the relevant temporal and spatial scales). It is important to note that an interaction with a characteristic residence time does not fulfill the conditions of the model. Interestingly, however, the waiting-time distribution of non-specific interactions, abundant in the cell, might be non-averageable and thus CTRW a good microscopic model for one type of anomalous subdiffusion in the cell. It has been proposed to govern the cytosolic diffusion of nanosized objects in mammalian cells [19] and it has also been used to explain the lateral motion of potassium channels in the plasma membrane of cells [20].

The **fractional Brownian motion** model is a different generalization of Brownian diffusion in which the jumps between lag times follow a normal distribution but respect a correlation function given by $\left\langle x(t)x(s) \right\rangle = 1/2(t^{2H} + s^{2H} - (t-s)^{2H})$ for $t > s > 0$. A fBm process is thus characterized by the Hurst index H, ranging between 0 and 1. The value of H determines the type of jump dependence in the fBm process, such that $H > 1/2$ indicates a positive correlation between the increments, Brownian motion is achieved for $H = 1/2$, and the increments are negatively correlated when $H < 1/2$. The MSD of a fBm is given by $\left\langle x(t)^2 \right\rangle \propto t^{2H}$, which, again, encompasses Brownian diffusion for $H = 1/2$ and yields subdiffusion for $H < 1/2$ or superdiffusion for $H > 1/2$ (see below). The fBm model describes faithfully the diffusion of particles in a viscoelastic fluid [21], and it has been often argued that molecular crowding in the cell gives rise to microviscosity and therefore to anomalous diffusion. It was proposed as the model of telomere diffusion in nucleus [22, 23].

Another possible model for anomalous diffusion in the cell is that of **random walks in fractal media and disordered systems**. Fractals are self-similar mathematical objects built upon the repetition of simple rules and characterized by a non-integer number: the *fractal dimension*. Although still under debate, some authors have proposed that chromatin organization follows, as a first order approximation, a fractal structure, and estimates of its fractal dimension have been proposed [24]. Random walks on fractals are subdiffusive due to the spatial correlation of displacements, and the power law scaling factor of the MSD with time is given by $2/d_w$, where d_w is the *dimension of the walk* that is specific to the fractal. Although the pertinence of a fractal network model to describe molecular diffusion is still up to debate, it is justified to attempt to integrate the multiscale characteristics of the cell organization to such fractal model.

Amongst the existing superdiffusive motion in cells is the run-and-tumble process, which consists of alternating phases of fast active and slow passive motion leading to transient anomalous diffusion [25]. Initially observed for bacteria motion it has recently been used to describe molecular motions in cells, such as the motion of motors along cytoskeletal filaments. Motor proteins perform a number of steps (run) until they randomly unbind from the filaments and diffuse in the crowded cytoplasm (tumble) before rebinding [26]. The same could also stand for transcription factors in the nucleus searching for their initiation codon, alternating successively diffusion and 1D sliding along the DNA. Superdiffusive fBm which is characterized by an Hurst index $H > 1/2$ has been described as the intracellular motion of particles in the super-crowded cytoplasm of a amibae [27]. Finally, Lévy flights, has previously been proposed for intracellular actin-based transport mediated by molecular motors [28] and recently in the case of a membrane targeting C2 protein [29].

Note that by no means the above described models exhaustively cover the range of models that are known to exhibit anomalous diffusion (see e.g., [30–32]). However, the CTRW, fBM, and random walks in a fractal models have been extensively studied; more importantly, they have the potential to map parameters of the model to relevant biological and biophysical features. Therefore, we will limit our discussion to the aforementioned cases, and how they can be used to analyse and interpret experimental data obtained by FCS and SPT.

3. WHICH METHODS TO CORRECTLY ANALYSE DIFFUSIVE PROCESS?

3.1. Fluorescence Correlation Spectroscopy

The principle of FCS consists in measuring the temporal variations of molecular concentration at a given position within the volume of a biological sample. This is achieved by monitoring the temporal fluctuations of fluorescence signal emitted by the molecules present in the observation volume, which is excited with a focused laser. The underlying assumption of FCS is that the system is in a dynamic equilibrium and therefore the signal fluctuation can be correlated to the diffusion of molecules within the observation volume. While the amplitude of the fluctuations relates to the number of molecules in the observation volume, the decay of their autocorrelation in time depends on their mobility.

A typical FCS set-up consists of an illumination laser and a confocal microscope with a fast single-channel single-photon detector. The laser beam illuminates the detection volume with, usually, a Gaussian intensity profile and excites the fluorophores in the focal volume. The emitted fluorescent light is collected by the detector and it depends on the fluctuations of the local concentration of the labeled molecules.

Parameters, such as the average number of molecules (N) and their mean residence time (τ_d) in the confocal volume (surface) can be obtained either directly from this fluorescence intensity fluctuation measurement or indirectly by a temporal auto-correlation of this fluctuation. The second method is the most popular approach for FCS data analysis (see **Figure 1**). The main drawback of standard FCS is the lack in directly monitoring possible spatial and/or temporal heterogeneities that will give rise to deviation from pure Brownian motion. Several approaches have been proposed to overcome this issue including spot variation FCS (sv-FCS) [14, 33], line scanning FCS and STED-FCS [34, 35], as well as imaging approaches, such as (spatio)-temporal imaging correlation spectroscopy [(S)TICS], raster imaging correlation spectroscopy (RICS) [36] or more recently whole plane Imaging FCS (Im-FCS) [37]. With the development of commercial microscopes coupled to FCS capabilities, this technique and its derivatives are now becoming more and more popular in biology labs.

A large range of dynamic processes leading to concentration fluctuations (i.e., diffusion, flow, chemical reactions and different combinations of these) has been investigated to generate corresponding analytical expressions of the temporal autocorrelation curve $G(t)$ in the case of Gaussian (laser confocal) illumination/detection geometry (for a review, see [38] and references therein). For instance, in the case of a Brownian motion in 2D, $G(t) = 1/\{\bar{N}(1 + 4Dt/w^2)\}$ where w is the size of the beam waist and $\bar{N}$ is the average number of molecules in the observation volume. The main approach to diffusive process identification and quantification in FCS consists in non linear least square fitting of experimental autocorrelation curves using above described analytical expressions and discriminate amongst these models which suits the best using various statistical test. Although it can deliver quantitative values of the parameters of the statistically chosen model of motion, it could be strongly biased, in particular for complex motions. A Bayesian approach to single spot FCS correlogram analysis has been proposed to discriminate between different models without bias [39, 40].

Another way to discriminate between different types of motion is to explore space and time with FCS using svFCS for example. svFCS offers the opportunity to generate so-called "diffusion-laws" by plotting changes in the residence time (τ_d) as a function of the surface (i.e., laser waist) explored w^2. This has enabled to directly identify deviations from pure Brownian motion in the plasma membrane of cells [41] or

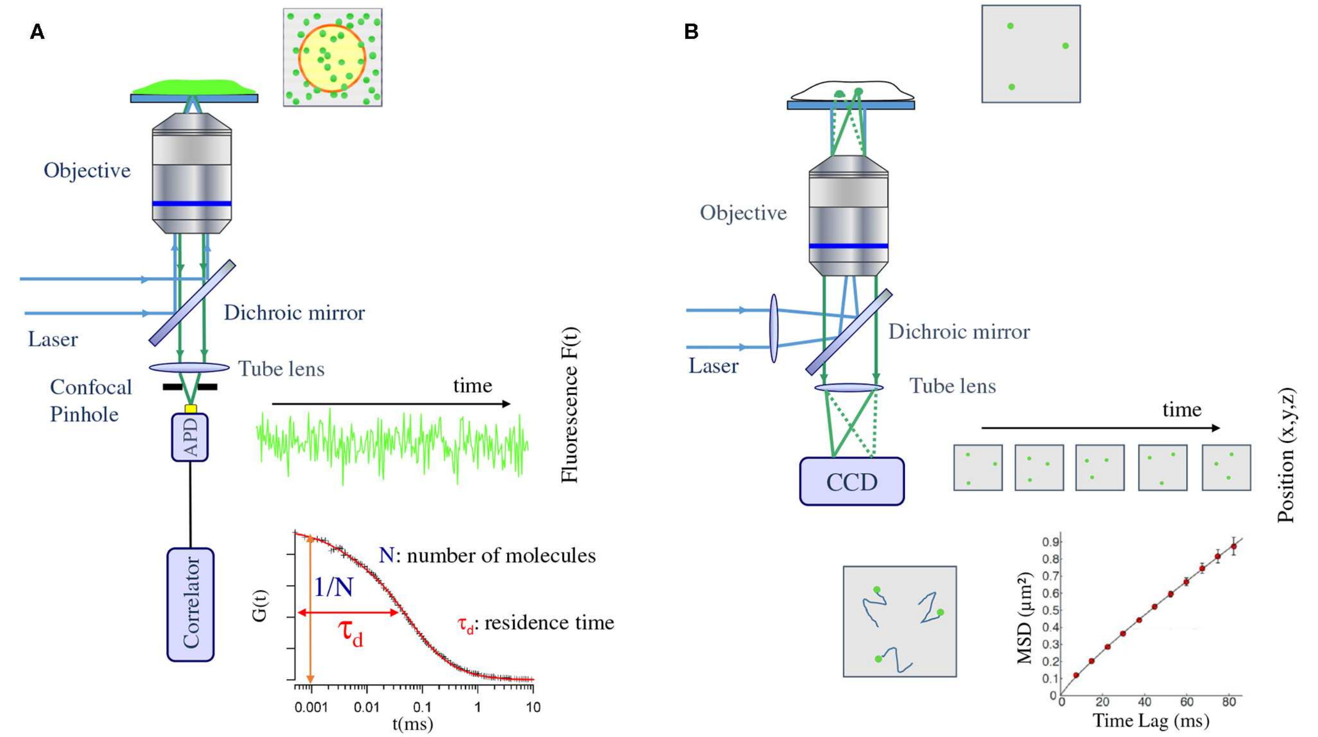

FIGURE 1 | Schematic view of the typical setup used in fluorescence correlation spectroscopy **(A)** and single/multiple particle tracking **(B)** experiments. **(A)** A laser is focused on the fluorescently labeled sample by the objective of a microscope. The fluorescence is then collected by the objective and focused in a confocal way (using a pinhole) on a single photon counting detector (avalanche photodiode, APD). This detector records the fluctuation of fluorescence emission within the confocal volume of the sample. A direct link to an electronic correlator authorize on line generation of the autocorrelogram. **(B)** A laser is focused at the back focal plane of a microscope objective in order to obtain a full field illumination of the sample. The fluorescence emitted by each single particle present in the illumination field is then directly imaged on a sensitive camera (Charge Coupled Device, CCD). A movie is obtained and the post processing of this movie allow tracking of the individual emitter and latter on, generation of Mean Square Displacement (MSD) as a function of lag time curves.

anomalous diffusion occurring, either during first order lipid phase transition [42] or in non-homogeneous fluids, gels and crowded solutions [43, 44]. It has been recently extended to the line-scanning STED-FCS [45] and to Im-FCS [46].

3.2. Single/Multiple Particle(s) Tracking

While the concentration of the subset of fluorescent molecules within a confocal volume in FCS experiments is close to the single-molecule regime, the measurement gauges the average motion of the ensemble of molecules diffusing in and out the observation spot. Conversely, SPT is by construction a single-molecule approach, monitoring thus the motion of individual molecules. One of the strengths of SPT is the potential to capture rare events or behaviors that would otherwise be buried within an average.

The principle of SPT experiments is simple, it consists in retrieving the changes in position of individual molecules within the sample of interest, i.e., the time series of two-dimensional or three-dimensional coordinates of the molecule location. This is achieved in two stages: firstly by estimating the centroid of the measured point spread function (PSF) of each detected individual emitter, and secondly by linking the trajectory of the same molecule between consecutive images. Importantly, the accuracy at which one is able to pinpoint the molecule position depends only on the signal-to-noise ratio of the measured PSF, obtaining sub-wavelength accuracy typically in the order of ∼10 nm.

The basic SPT experimental setup consists of an excitation laser, a high NA objective, a set of dichroic and filters to separate the excitation and emission wavelengths, a tube lens, and a highly sensitive camera capable of detecting single fluorophores (see **Figure 1**). The laser is focused on the back focal plane of the objective to obtain a wide-field illumination configuration, which can be adjusted to total internal reflection (TIRF) or highly inclined illumination (HILO) [47] to increase the SNR when studying molecular dynamics in cellular membranes or at the interior of cells, respectively. The fluorescence light is collected by the same objective, and an image of the single emitters is formed on the camera plane via the tube lens [13, 48].

The amount of retrieved information about the biological system from an SPT assay depends on the nature of the experiment. The study of a slowly diffusing transmembrane protein will yield much longer traces than a fast diffusing transcription factor in the nucleus. In the latter case, the traces will be limited to the number of images in which the tracked particle remains within the depth of focus around the image plane, unlike the former case where photobleaching is the limiting factor.

The classical analysis of a set of trajectories consists in computing the dependence of the MSD (time-average or ensemble-average) over time from the distribution of jumps at increasing lag times defined by the camera acquisition, typically in the order of tens of ms. However, as we will see in the following section, different approaches and estimators have been proposed in order to analyze and interpret SPT data to its full extent. In comparison to FCS, the analysis of SPT has been intensively investigated, and one can distinguish several families of techniques (see also for reviews: [24, 49, 50]). In the field of stochastic processes, the inference of a diffusion coefficient from a sampled process is a common problem (see for instance [51, 52]). However, this theory cannot be applied when moving to experimental trajectories, and other approaches have been proposed.

3.2.1. MSD-Based Techniques

A first family of SPT analysis algorithms tries to perform robust MSD inference. The use of MSD to study diffusion was introduced by Einstein in 1906, and was revived in biology by [53]. MSD analysis can either be performed by inferring a diffusion coefficient from a single trajectory (a setting studied in [54]) or by pooling various trajectories [55], and many refinements and estimators based on the MSD have been proposed [56, 57].

When inferring kinetic parameters from a series of single trajectories, one faces the issue that for common trajectory lengths obtained in nuclear SPT (length of $<<$ 20 points per track) and common localization error, inaccuracy might reach 100% [54, 58]. As such, any approach that uses MSD on short trajectories should be evaluated with great care. For longer trajectories (such as diffusion in a membrane), approaches have been proposed that can segment trajectories based on the type of motion [59].

3.2.2. Hidden Markov Models (HMMs)

A second family of SPT analysis algorithms derives from Markov models and Hidden Markov Models. Most of them were derived to perform trajectory segment classification, the hidden variable inferred being the state of diffusion, or the current diffusion coefficient. For instance, Monnier et al. [60] introduces the HMM-Bayes technique to infer whether a trajectory segment is in one (or several) diffusive or active transport states. Moreover, Slator et al. [61] implemented the inference of localization noise to infer switches in diffusion coefficient within one trajectory. A similar approach was used to detect confinement [62].

These methods often rely on a fixed number of states, which comes from significant mathematical limitations. Some of these limitations were overcome using so-called variational Bayesian inference [63]. The prototypical algorithm performing variational Bayesian inference on a HMM is vbSPT [64]. This algorithm can estimate the number of diffusive states and progressively consolidate increasing information about these states as trajectories are analyzed. The algorithm was further refined to incorporate the estimate of localization error [65].

3.2.3. Inferring Maps of Diffusion Coefficients

A third family of SPT analysis algorithms not only infers the diffusion coefficient over the population of diffusing molecules, but also a spatial map of diffusivity [66, 67]. This approach has been pioneered in membranes, where a high density of tracks can easily be obtained. An extension of this approach using an overdamped Langevin equation of the single molecule motion has shed new lights on HIV-1 assembly within living cells [68]. These promising techniques have not been tested beyond membrane molecules, but the high diffusion coefficients of freely diffusing cellular proteins might render such a map difficult to establish. Moreover, unlike in membranes, proteins can reside at the same location with different diffusion coefficients, depending on whether they are interacting with a given structure or not.

3.2.4. Inferring Anomalous Diffusion

Many approaches have been proposed to infer anomalous diffusion in cells; some of them are reviewed in Guigas and Weiss [69]. A direct technique can be used by fitting the MSD with a power law to estimate the anomalous diffusion coefficient α. However, alternative techniques have been proposed, many of them focused on the inference of model-specific parameters, or on techniques to distinguish between types of anomalous diffusion.

Several methods have been proposed to infer diffusion parameters for several anomalous diffusion models. For the case of diffusion in disordered (fractal) media, Shkilev [70] proposes estimators that can be applied to SPT, FCS and FRAP. For the case of fractional Brownian motion, techniques to infer both the anomalous diffusion coefficient (α) and the generalized diffusion coefficient (D_α) have been proposed. The former approach [71] takes into account noise (localization error) and drift, and uses Bayesian inference. The latter [72] relies on squared displacements and uses least squares to estimate D_α.

Conversely, instead of trying to estimate the parameters of a known model, a key question is to distinguish between various anomalous diffusion models. A prototypical approach [73] used Bayesian inference to distinguish between Brownian, anomalous, confined and directed diffusion, and uses the propagators associated with each different diffusion model. However, Hellmann et al. [74] found using simulations that it is very hard to distinguish between fBm and diffusion on a fractal when localization noise is present, both in SPT and FCS. The authors used a combination of techniques for the inference, including MSD and p-variation techniques. In Burnecki et al. [23], the authors propose a series of tests to "unambiguously" identify fBm, by progressively proving that several other models are wrong. Other tests were proposed to distinguish fBm from a CTRW using a test based on p-variations [75]. The p-variations are the finite sum of the p-th powers of the increments of the trajectory. Finally, approaches inferring the mean first passage time of a particle were used to distinguish between CTRW and diffusion in fractals [76, 77].

Many other families of techniques to identify types of diffusion have been proposed. Some relied on maximum likelihood estimates [78], auto-correlation functions [79] or on more exotic estimators [80]. Another line of progress was made in the type of models being simulated. For instance, Amitai [81] introduced a model in which TFs can bind and rebind in a dense chromatin mesh. This model was successively fitted to explain anomalous diffusion of CTCF dynamics [82].

Finally, we note that many models were developed to infer trapping potential in membranes ([83, 84] for instance). We do not review them here since their application seems limited to membranes.

3.3. Strengths and Limitations of the Two Techniques

A strong limitation is that the experimental context, either in FCS or in SPT, may lead to spurious determination of anomalous diffusion. In other words, specific experimental parameters (low statistics, location noise, spatial confinement, etc.) and/or inappropriate analysis of the data can lead to incorrectly conclude that the diffusion exponent $\alpha \neq 1$. Those artifacts concern both SPT [85] and FCS [43]. This is for instance the case if α is determined by a fit of the MSD or the autocorrelation with time and the statistical power is low (low sampling of the time points or short trajectories in SPT, low signal/noise at small or large times in FCS). To avoid such caveats, model selection must use more elaborate approaches to unambiguously demonstrate and characterize an underlying complex diffusion process.

So far, most of the inference tools available in the literature only partially account for the biases detailed above, and are usually limited in terms of the anomalous diffusion models they consider. For instance, in Hansen et al. [58], the authors showed that an algorithm not taking into account localization error was likely to improperly estimate diffusion coefficients. Similarly, the fact that the observed proteins diffuse in a confined volume leads to a sublinear MSD, a phenomenon that has been widely documented and that needs to be taken into account to properly distinguish between genuine anomalous diffusion and mere confinement effect. Similarly, tracking errors (misconnections between tracks) can also look like anomalous diffusion.

Some of these biases can be minimized at the acquisition step (for instance by using fast frame rates and low labeling density [58]), other need to be explicitly taken into account in the model. As of today, most inference algorithms available have not been benchmarked against realistic imaging conditions. Furthermore, a general realistic inference algorithm is still missing.

4. CONCLUSION: THE NEED FOR CONTROLLED BENCHMARKS

Confronted with the variety of approaches described above, one would like to know the performance of each approach on typical representative datasets. For the comparison to be fair, this demands two main ingredients: (i) the existence of a reference dataset, or benchmark—possibly one reference dataset for each main classes of experimental methods and (ii) a fair, objective, transparent and open comparison process, with datasets, comparison procedures and performance results that are clearly stated and publicly available. Several fields in computer science have been using open community competitions to organize the process and produce open benchmarks for the community. Computer vision, applied machine learning or time series forecasting, among many others, have a long tradition of leveraging these competitions. The strategy has been widely successful because it parallelizes research along a vast community of high-skilled researchers. Internet platforms or services are even available to that purpose, including, among many others, Kaggle (www.kaggle.com) or DrivenData (www.drivendata.org). This increases further the size of the competing community, and the richness of the proposals. In fact, in addition to providing reference datasets and benchmarks, open competitive challenges can also foster the emergence of radically new approaches to the open problem at hand. Many of these competitive challenges are concerned with biomedical applications (for instance, http://dreamchallenges.org or https://grand-challenge.org), including several revolving around microscopy (see e.g., https://cremi.org). Recently, a series of consecutive community competitions for single-molecule imaging have involved dozens of labs and focused on tracking algorithms [86], and 2D and 3D localization for super-resolution [87]. Finally, another challenge has also been set up recently to infer the anomalous diffusion exponent from particle trajectories (http://www.andi-challenge.org/) [88].

In practice, an important feature of competitive challenges is to provide labeled data examples that the participants will be able to use as a training set. Indeed according to standard machine learning practice, this training dataset must be distinct from the test set, that includes the data used to estimate the performance of the algorithm. The organizers therefore usually publish two datasets (training dataset and test), of which only the training dataset comes with the label of each examples—only the organizers know the true label of the test dataset. After training, the results of the challenge is based on some quantification of the performance of the participant tools on the test set, although performance on the learning set can also be communicated as a way to judge overtraining/generalization capacities. In many cases however, it is not possible to provide the "true" label of experimental data, because such a gold standard does not exist. In this case, computer simulations can be used to generate synthetic data, as long as these simulations are realistic enough that the performance of the algorithms is not different than their performance on real experimental measurements. In the recent challenges on super-resolution, training and test data were a combination of computer-generated data and experimental data. Computer-generated data gives a clear access to ground truth whereas experimental data incorporate uncharacterized biases that can affect the inference process.

Here we propose to organize an international open collaborative challenge for the quantification and analysis of molecule movements in living cells via SPT and FCS. To date, the generation of realistic computer-simulated data has been hampered by the number of experimental biases to be taken into account, and by the diversity of the diffusion models, in particular for anomalous diffusion. For the challenge, we will generate both SPT and FCS data from the same set of simulated trajectories and in different modalities (2D in membranes and 3D in the nucleus) using a dedicated open source simulation software, simSPT (https://gitlab.com/tjian-darzacq-lab/simSPT), that is freely available to the participants to generate their own additional training sets if needed.

The challenge will be organized around various sub-challenges that represent the main classes of experimental situations (high-density short trajectories in membranes, less dense long trajectories in membranes, very short trajectories in the nucleus) and the main types of Brownian and anomalous diffusion (Brownian motion, fractional Brownian motion, continuous-time random walks and diffusion on fractals), and mixtures thereof. In the long run, we will also propose sub-challenges where the molecule dynamics depends on the location, to emulate localized spatial heterogeneity in the dynamics (local potentials, position-dependent diffusion coefficients). Moreover, we will progressively propose two challenge categories. In parameter inference challenges, the models used to generate the trajectories (Brownian motion, anomalous diffusion, …) will be given and the task will be to infer as precisely as possible the value of the parameters used for the generation. In model selection challenges, the goal will be to infer what model was used to generate the data given a known limited list of models.

Finally, we are aware that it may well be that no generic tool is able to solve all the sub-challenges evoked above. We are also aware that the difficulty of each sub-challenges can be quite variable. We therefore propose to start with the simple challenges and work in collaboration with the community involved in the analysis of molecular dynamics in living cells, to progressively climb the steps toward the more difficult sub-challenges. In this strategy, maintaining an open communication channel between the organizers and the participants is paramount. To this aim, we propose to start with a mailing list that will be used to support this communication. Every interested individual is therefore welcome to subscribe to the mailing list of the challenge by visiting https://listes.services.cnrs.fr/wws/info/diffusion.challenge. Once registered in the mailing list through this website, participants will be able to exchange with themselves and the organizers and they will receive the instructions to access the datasets of the challenge.

AUTHOR CONTRIBUTIONS

MW, II, CF, and HB developed these perspectives and wrote the manuscript.

FUNDING

This work was partly funded by the CNRS-supported GDR ImaBio, http://imabio-cnrs.fr.

REFERENCES

1. Axelrod D, Koppel DE, Schlessinger J, Elson E, Webb WW. Mobility measurement by analysis of fluorescence photobleaching recovery kinetics. *Biophys J*. (1976) **16**:1055–69. doi: 10.1016/S0006-3495(76)85755-4
2. Magde D, Webb W, Elson E. Thermodynamic fluctuations in a reacting system–measurement by fluorescence correlation spectroscopy. *Phys Rev Lett*. (1972) **29**:705. doi: 10.1103/PhysRevLett.29.705
3. Geerts H, De Brabander M, Nuydens R, Geuens S, Moeremans M, De Mey J, et al. Nanovid tracking: a new automatic method for the study of mobility in living cells based on colloidal gold and video microscopy. *Biophys J*. (1987) **52**:775–82. doi: 10.1016/S0006-3495(87)83271-X
4. Geerts H, de Brabander M, Nuydens R. Nanovid microscopy. *Nature*. (1991) **351**:765–6. doi: 10.1038/351765a0
5. Heim R, Prasher DC, Tsien RY. Wavelength mutations and posttranslational autoxidation of green fluorescent protein. *Proc Natl Acad Sci USA*. (1994) **91**:12501–4. doi: 10.1073/pnas.91.26.12501
6. Heim R, Tsien RY. Engineering green fluorescent protein for improved brightness, longer wavelengths and fluorescence resonance energy transfer. *Curr Biol*. (1996) **6**:178–82. doi: 10.1016/S0960-9822(02)00450-5
7. Matz MV, Fradkov AF, Labas YA, Savitsky AP, Zaraisky AG, Markelov ML, et al. Fluorescent proteins from nonbioluminescent Anthozoa species. *Nat Biotechnol*. (1999) **17**:969–73. doi: 10.1038/13657
8. Hell SW, Wichmann J. Breaking the diffraction resolution limit by stimulated emission: stimulated-emission-depletion fluorescence microscopy. *Opt Lett*. (1994) **19**:780–2. doi: 10.1364/OL.19.000780
9. Betzig E, Patterson GH, Sougrat R, Lindwasser OW, Olenych S, Bonifacino JS, et al. Imaging intracellular fluorescent proteins at nanometer resolution. *Science*. (2006) **313**:1642–5. doi: 10.1126/science.1127344
10. Hess ST, Girirajan TP, Mason MD. Ultra-high resolution imaging by fluorescence photoactivation localization microscopy. *Biophys J*. (2006) **91**:02222. doi: 10.1529/biophysj.106.091116
11. Klar TA, Jakobs S, Dyba M, Egner A, Hell SW. Fluorescence microscopy with diffraction resolution barrier broken by stimulated emission. *Proc Natl Acad Sci USA*. (2000) **97**:8206–10. doi: 10.1073/pnas.97.15.8206
12. Rust MJ, Bates M, Zhuang X. Sub-diffraction-limit imaging by stochastic optical reconstruction microscopy (STORM). *Nat Methods*. (2006) **3**:793–5. doi: 10.1038/nmeth929
13. Manley S, Gillette JM, Patterson GH, Shroff H, Hess HF, Betzig E, et al. High-density mapping of single-molecule trajectories with photoactivated localization microscopy. *Nat Methods*. (2008) **5**:155–7. doi: 10.1038/nmeth.1176
14. Eggeling C, Ringemann C, Medda R, Schwarzmann G, Sandhoff K, Polyakova S, et al. Direct observation of the nanoscale dynamics of membrane lipids in a living cell. *Nature*. (2009) **457**:1159–62. doi: 10.1038/nature07596
15. Sarkar P, Chattopadhyay A. Exploring membrane organization at varying spatiotemporal resolutions utilizing fluorescence-based approaches: implications in membrane biology. *Phys Chem Chem Phys*. (2019) **21**:11554–63. doi: 10.1039/C9CP02087J
16. Liu H, Ye Z, Wang X, Wei L, Xiao L. Molecular and living cell dynamic assays with optical microscopy imaging techniques. *Analyst*. (2019) **144**:859–71. doi: 10.1039/C8AN01420E
17. Priest DG, Solano A, Lou J, Hinde E. Fluorescence fluctuation spectroscopy: an invaluable microscopy tool for uncovering the biophysical rules for navigating the nuclear landscape. *Biochem Soc Trans*. (2019) **47**:1117–29. doi: 10.1042/BST20180604
18. Hoefling F, Franosch T. Anomalous transport in the crowded world of biological cells. *Rep Prog Phys*. (2013) **76**:046602. doi: 10.1088/0034-4885/76/4/046602
19. Etoc F, Balloul E, Vicario C, Normanno D, Lie D, Sittner A, et al. Non-specific interactions govern cytosolic diffusion of nanosized objects in mammalian cells. *Nat Mater*. (2018) **17**:740–6. doi: 10.1038/s41563-018-0120-7
20. Weigel AV, Simon B, Tamkun MM, Krapf D. Ergodic and nonergodic processes coexist in the plasma membrane as observed by single-molecule tracking. *Proc Natl Acad Sci USA*. (2011) **108**:6438–43. doi: 10.1073/pnas.1016325108
21. Ernst D, Hellmann M, Köhler J, Weiss M. Fractional brownian motion in crowded fluids. *Soft Matter*. (2012) **8**:4886–9. doi: 10.1039/c2sm25220a

22. Kepten E, Bronshtein I, Garini Y. Ergodicity convergence test suggests telomere motion obeys fractional dynamics. *Phys Rev E*. (2011) **83**:041919. doi: 10.1103/PhysRevE.83.041919
23. Burnecki K, Kepten E, Janczura J, Bronshtein I, Garini Y, Weron A. Universal algorithm for identification of fractional brownian motion. A case of telomere subdiffusion. *Biophys J*. (2012) **103**:1839–47. doi: 10.1016/j.bpj.2012.09.040
24. Rcamier V, Izeddin I, Bosanac L, Dahan M, Proux F, Darzacq X. Single cell correlation fractal dimension of chromatin: a framework to interpret 3D single molecule super-resolution. *Nucleus*. (2014) **5**:75–84. doi: 10.4161/nucl.28227
25. Shaebani MR, Rieger H. Transient anomalous diffusion in run-and-tumble dynamics. *Front Phys*. (2019) **7**:120. doi: 10.3389/fphy.2019.00120
26. Hafner AE, Santen L, Rieger H, Shaebani MR. Run-and-pause dynamics of cytoskeletal motor proteins. *Sci Rep*. (2016) **6**:37162. doi: 10.1038/srep37162
27. Reverey JF, Jeon JH, Bao H, Leippe M, Metzler R, Selhuber-Unkel C. Superdiffusion dominates intracellular particle motion in the supercrowded cytoplasm of pathogenic *Acanthamoeba castellanii. Sci Rep*. (2015) **5**:11690. doi: 10.1038/srep11690
28. Bruno L, Levi V, Brunstein M, Despósito MA. Transition to superdiffusive behavior in intracellular actin-based transport mediated by molecular motors. *Phys Rev E*. (2009) **80**:011912. doi: 10.1103/PhysRevE.80.011912
29. Campagnola G, Nepal K, Schroder BW, Peersen OB, Krapf D. Superdiffusive motion of membrane-targeting C2 domains. *Sci Rep*. (2015) **5**:17721. doi: 10.1038/srep17721
30. Metzler R, Jeon JH, Cherstvy AG, Barkai E. Anomalous diffusion models and their properties: non-stationarity, non-ergodicity, and ageing at the centenary of single particle tracking. *Phys Chem Chem Phys*. (2014) **16**:24128–64. doi: 10.1039/C4CP03465A
31. Pavlos GP, Karakatsanis LP, Xenakis MN, Pavlos EG, Iliopoulos AC, Sarafopoulos DV. Universality of non-extensive Tsallis statistics and time series analysis: theory and applications. *Phys A Stat Mech Appl*. (2014) **395**:58–95. doi: 10.1016/j.physa.2013.08.026
32. Lenzi EK, Ribeiro HV, Tateishi AA, Zola RS, Evangelista LR. Anomalous diffusion and transport in heterogeneous systems separated by a membrane. *Proc R Soc A Math Phys Eng Sci*. (2016) **472**:20160502. doi: 10.1098/rspa.2016.0502
33. Wawrezinieck L, Rigneault H, Marguet D, Lenne PF. Fluorescence correlation spectroscopy diffusion laws to probe the submicron cell membrane organization. *Biophys J*. (2005) **89**:4029–42. doi: 10.1529/biophysj.105.067959
34. Petrek Z, Schwille P. Precise measurement of diffusion coefficients using scanning fluorescence correlation spectroscopy. *Biophys J*. (2008) **94**:1437–48. doi: 10.1529/biophysj.107.108811
35. Honigmann A, Mueller V, Ta H, Schoenle A, Sezgin E, Hell SW, et al. Scanning STED-FCS reveals spatiotemporal heterogeneity of lipid interaction in the plasma membrane of living cells. *Nat Commun*. (2014) **5**:5412. doi: 10.1038/ncomms6412
36. Digman MA, Brown CM, Sengupta P, Wiseman PW, Horwitz AR, Gratton E. Measuring fast dynamics in solutions and cells with a laser scanning microscope. *Biophys J*. (2005) **89**:1317–27. doi: 10.1529/biophysj.105.062836
37. Kannan B, Har JY, Liu P, Maruyama I, Ding JL, Wohland T. Electron multiplying charge-coupled device camera based fluorescence correlation spectroscopy. *Anal Chem*. (2006) **78**:3444–51. doi: 10.1021/ac0600959
38. Elson E. Fluorescence correlation spectroscopy: past, present, future. *Biophys J*. (2011) **101**:2855–70. doi: 10.1016/j.bpj.2011.11.012
39. He J, Guo SM, Bathe M. Bayesian approach to the analysis of fluorescence correlation spectroscopy data I: theory. *Anal Chem*. (2012) **84**:3871–9. doi: 10.1021/ac2034369
40. Guo SM, He J, Monnier N, Sun G, Wohland T, Bathe M. Bayesian approach to the analysis of fluorescence correlation spectroscopy data II: application to simulated and *in vitro* data. *Anal Chem*. (2012) **84**:3880–8. doi: 10.1021/ac2034375
41. Lenne PF, Wawrezinieck L, Conchonaud F, Wurtz O, Boned A, Guo XJ, et al. Dynamic molecular confinement in the plasma membrane by microdomains and the cytoskeleton meshwork. *EMBO J*. (2006) **25**:3245–56. doi: 10.1038/sj.emboj.7601214
42. Favard C, Wenger J, Lenne PF, Rigneault H. FCS diffusion laws in two-phase lipid membranes: determination of domain mean size by experiments and Monte Carlo simulations. *Biophys J*. (2011) **100**:1242–51. doi: 10.1016/j.bpj.2010.12.3738
43. Banks DS, Tressler C, Peters RD, Hfling F, Fradin C. Characterizing anomalous diffusion in crowded polymer solutions and gels over five decades in time with variable-lengthscale fluorescence correlation spectroscopy. *Soft Matter*. (2016) **12**:4190–203. doi: 10.1039/C5SM01213A
44. Masuda A, Ushida K, Okamoto T. Direct observation of spatiotemporal dependence of anomalous diffusion in inhomogeneous fluid by sampling-volume-controlled fluorescence correlation spectroscopy. *Phys Rev E*. (2005) **72**:060101. doi: 10.1103/PhysRevE.72.060101
45. Schneider F, Waithe D, Galiani S, Bernardino de la Serna J, Sezgin E, Eggeling C. Nanoscale spatiotemporal diffusion modes measured by simultaneous confocal and stimulated emission depletion nanoscopy imaging. *Nano Lett*. (2018) **18**:4233–40. doi: 10.1021/acs.nanolett.8b01190
46. Veerapathiran S, Wohland T. The imaging FCS diffusion law in the presence of multiple diffusive modes. *Methods*. (2018) 140–141:140–50. doi: 10.1016/j.ymeth.2017.11.016
47. Tokunaga M, Imamoto N, Sakata-Sogawa K. Highly inclined thin illumination enables clear single-molecule imaging in cells. *Nat Methods*. (2008) **5**:159–61. doi: 10.1038/nmeth1171
48. Izeddin I, Récamier V, Bosanac L, CisséII, Boudarene L, Dugast-Darzacq C, et al. Single-molecule tracking in live cells reveals distinct target-search strategies of transcription factors in the nucleus. *eLife*. (2014) **3**:e02230. doi: 10.7554/eLife.02230
49. Metzler R, Tejedor V, Jeon JH, He Y, Deng WH, Burov S, et al. Analysis of single particle trajectories: from normal to anomalous diffusion. *Acta Phys Pol B*. (2009) **40**:1315. Available online at: https://www.actaphys.uj.edu.pl/R/40/5/1315/pdf
50. Ernst D, Köhler J, Weiss M. Probing the type of anomalous diffusion with single-particle tracking. *Phys Chem Chem Phys*. (2014) **16**:7686–91. doi: 10.1039/C4CP00292J
51. Florens-Zmirou D. On estimating the diffusion coefficient from discrete observations. *J Appl Probab*. (1993) **30**:790. doi: 10.1017/S0021900200044570
52. Hoffmann M. On estimating the diffusion coefficient: parametric versus nonparametric. *Ann l'IHP Probab Stat*. (2001) **37**:339–72. doi: 10.1016/S0246-0203(00)01070-0
53. Qian H, Sheetz MP, Elson EL. Single particle tracking. Analysis of diffusion and flow in two-dimensional systems. *Biophys J*. (1991) **60**:910–21. doi: 10.1016/S0006-3495(91)82125-7
54. Michalet X, Berglund AJ. Optimal diffusion coefficient estimation in single-particle tracking. *Phys Rev E*. (2012) **85**:061916. doi: 10.1103/PhysRevE.85.061916
55. Liu Z, Legant WR, Chen BC, Li L, Grimm JB, Lavis LD, et al. 3D imaging of Sox2 enhancer clusters in embryonic stem cells. *eLife*. (2014) **3**:e04236. doi: 10.7554/eLife.04236
56. Michalet X. Mean square displacement analysis of single-particle trajectories with localization error: Brownian motion in an isotropic medium. *Phys Rev E*. (2010) **82**:041914. doi: 10.1103/PhysRevE.82.041914
57. Boyer D, Dean DS, Mejía-Monasterio C, Oshanin G. Optimal estimates of the diffusion coefficient of a single brownian trajectory. *Phys Rev E*. (2012) **85**:031136. doi: 10.1103/PhysRevE.85.031136
58. Hansen AS, Woringer M, Grimm JB, Lavis LD, Tjian R, Darzacq X. Robust model-based analysis of single-particle tracking experiments with spot-on. *eLife*. (2018) **7**:e33125. doi: 10.7554/eLife.33125
59. Monnier N, Guo SM, Mori M, He J, Lénárt P, Bathe M. Bayesian approach to MSD-based analysis of particle motion in live cells. *Biophys J*. (2012) **103**:616–26. doi: 10.1016/j.bpj.2012.06.029
60. Monnier N, Barry Z, Park HY, Su KC, Katz Z, English BP, et al. Inferring transient particle transport dynamics in live cells. *Nat Methods*. (2015) **12**:838–40. doi: 10.1038/nmeth.3483
61. Slator PJ, Cairo CW, Burroughs NJ. Detection of diffusion heterogeneity in single particle tracking trajectories using a hidden Markov model with measurement noise propagation. *PLoS ONE*. (2015) **10**:e0140759. doi: 10.1371/journal.pone.0140759
62. Slator PJ, Burroughs N. A hidden Markov model for detecting confinement in single particle tracking trajectories. *bioRXiv*. (2018) 275107. doi: 10.1101/275107

63. Blei DM, Kucukelbir A, McAuliffe JD. Variational inference: a review for statisticians. *arXiv*. (2016) **112**:859–77. doi: 10.1080/01621459.2017.1285773
64. Persson F, Lindn M, Unoson C, Elf J. Extracting intracellular diffusive states and transition rates from single-molecule tracking data. *Nat Methods*. (2013) **10**:265–9. doi: 10.1038/nmeth.2367
65. Lindén M, Elf J. Variational algorithms for analyzing noisy multistate diffusion trajectories. *Biophys J*. (2018) **115**:276–82. doi: 10.1016/j.bpj.2018.05.027
66. Masson JB, Casanova D, Türkcan S, Voisinne G, Popoff MR, Vergassola M, et al. Inferring maps of forces inside cell membrane microdomains. *Phys Rev Lett*. (2009) **102**:048103. doi: 10.1103/PhysRevLett.102.048103
67. El Beheiry M, Dahan M, Masson JB. InferenceMAP: mapping of single-molecule dynamics with Bayesian inference. *Nat Methods*. (2015) **12**:594–5. doi: 10.1038/nmeth.3441
68. Floderer C, Masson JB, Boilley E, Georgeault S, Merida P, El Beheiry M, et al. Single molecule localisation microscopy reveals how HIV-1 Gag proteins sense membrane virus assembly sites in living host CD4 T cells. *Sci Rep*. (2018) **8**:16283. doi: 10.1038/s41598-018-34536-y
69. Guigas G, Weiss M. Sampling the cell with anomalous diffusion—the discovery of slowness. *Biophys J*. (2008) **94**:90–4. doi: 10.1529/biophysj.107.117044
70. Shkilev VP. A kinetic model for fluorescence microscopy experiments in disordered media that contains binding sites and obstacles. *Phys Rev E*. (2018) **98**:032140. doi: 10.1103/PhysRevE.98.032140
71. Krog J, Jacobsen LH, Lund FW, Wstner D, Lomholt MA. Bayesian model selection with fractional Brownian motion. *J Stat Mech Theory Exp*. (2018) **2018**:093501. doi: 10.1088/1742-5468/aadb0e
72. Boyer D, Dean DS, Mejia-Monasterio C, Oshanin G. On ergodic least-squares estimators of the generalized diffusion coefficient for fractional Brownian motion. *Biophys J*. (2013) **87**:030103. doi: 10.1103/PhysRevE.87.030103
73. Robson A, Burrage K, Leake MC. Inferring diffusion in single live cells at the single-molecule level. *Philos Trans R Soc B Biol Sci*. (2012) **368**:20120029. doi: 10.1098/rstb.2012.0029
74. Hellmann M, Klafter J, Heermann DW, Weiss M. Challenges in determining anomalous diffusion in crowded fluids. *J Phys Condens Matter*. (2011) **23**:234113. doi: 10.1088/0953-8984/23/23/234113
75. Magdziarz M, Weron A, Burnecki K, Klafter J. Fractional Brownian motion versus the continuous-time random walk: a simple test for subdiffusive dynamics. *Phys Rev Lett*. (2009) **103**:180602. doi: 10.1103/PhysRevLett.103.180602
76. Condamin S, Bénichou O, Tejedor V, Voituriez R, Klafter J. First-passage times in complex scale-invariant media. *Nature*. (2007) **450**:77–80. doi: 10.1038/nature06201
77. Condamin S, Tejedor V, Voituriez R, Benichou O, Klafter J. Probing microscopic origins of confined subdiffusion by first-passage observables. *Proc Natl Acad Sci USA*. (2008) **105**:5675–80. doi: 10.1073/pnas.0712158105
78. Thapa S, Lomholt MA, Krog J, Cherstvy AG, Metzler R. Bayesian analysis of single-particle tracking data using the nested-sampling algorithm: maximum-likelihood model selection applied to stochastic-diffusivity data. *Phys Chem Chem Phys*. (2018) **20**:29018–37. doi: 10.1039/C8CP04043E
79. Weber SC, Thompson MA, Moerner WE, Spakowitz AJ, Theriot JA. Analytical tools to distinguish the effects of localization error, confinement, and medium elasticity on the velocity autocorrelation function. *Biophys J*. (2012) **102**:2443–50. doi: 10.1016/j.bpj.2012.03.062
80. Vestergaard CL, Blainey PC, Flyvbjerg H. Optimal estimation of diffusion coefficients from single-particle trajectories. *Phys Rev E*. (2014) **89**:022726. doi: 10.1103/PhysRevE.89.022726
81. Amitai A. Chromatin configuration affects the dynamics and distribution of a transiently interacting protein. *Biophys J*. (2019) **114**:766–71. doi: 10.1016/j.bpj.2017.12.037
82. Hansen AS, Amitai A, Cattoglio C, Tjian R, Darzacq X. Guided nuclear exploration increases CTCF target search efficiency. *bioRXiv*. (2018) 495457. doi: 10.1101/495457
83. Türkcan S, Alexandrou A, Masson JB. A Bayesian inference scheme to extract diffusivity and potential fields from confined single-molecule trajectories. *Biophys J*. (2012) **102**:2288–98. doi: 10.1016/j.bpj.2012.01.063
84. Masson JB, Dionne P, Salvatico C, Renner M, Specht CG, Triller A, et al. Mapping the energy and diffusion landscapes of membrane proteins at the cell surface using high-density single-molecule imaging and Bayesian inference: application to the multiscale dynamics of glycine receptors in the neuronal membrane. *Biophys J*. (2014) **106**:74–83. doi: 10.1016/j.bpj.2013.10.027
85. Martin DS, Forstner MB, Ks JA. Apparent subdiffusion inherent to single particle tracking. *Biophys J*. (2002) **83**:2109–17. doi: 10.1016/S0006-3495(02)73971-4
86. Chenouard N, Smal I, de Chaumont F, Maka M, Sbalzarini IF, Gong Y, et al. Objective comparison of particle tracking methods. *Nat Methods*. (2014) **11**:281–9. doi: 10.1038/nmeth.2808
87. Sage D, Pham Ta, Babcock H, Lukes T, Pengo T, Chao J, et al. Super-resolution fight club: assessment of 2D & 3D single-molecule localization microscopy software. *Nat Methods*. (2019) **16**:387–95. doi: 10.1101/362517
88. Muñoz-Gil G, Volpe G, Garcia-March MA, Metzler R, Lewenstein M, Manzo C. AnDi: the anomalous diffusion challenge. *arXiv*. (2020) *ArXiv:2003.12036*.

Conflict of Interest: The authors declare that the research was conducted in the absence of any commercial or financial relationships that could be construed as a potential conflict of interest.

frontiers
in Applied Mathematics and Statistics

ORIGINAL RESEARCH
published: 26 May 2020
doi: 10.3389/fams.2020.00014

Identifying Arguments of Space-Time Fractional Diffusion: Data-Driven Approach

Mohamed Ridha Znaidi†, **Gaurav Gupta**†, **Kamiar Asgari** and **Paul Bogdan***

Ming Hsieh Department of Electrical and Computer Engineering, Viterbi School of Engineering, University of Southern California, Los Angeles, CA, United States

A plethora of complex dynamical systems from disordered media to biological systems exhibit mathematical characteristics (e.g., long-range dependence, self-similar and power law magnitude increments) that are well-fitted by fractional partial differential equations (PDEs). For instance, some biological systems displaying an anomalous diffusion behavior, which is characterized by a non-linear mean-square displacement relation, can be mathematically described by fractional PDEs. In general, the PDEs represent various physical laws or rules governing complex dynamical systems. Since prior knowledge about the mathematical equations describing complex dynamical systems in biology, healthcare, disaster mitigation, transportation, or environmental sciences may not be available, we aim to provide algorithmic strategies to discover the integer or fractional PDEs and their parameters from system's evolution data. Toward deciphering non-trivial mechanisms driving a complex system, we propose a data-driven approach that estimates the parameters of a fractional PDE model. We study the space-time fractional diffusion model that describes a complex stochastic process, where the magnitude and the time increments are stable processes. Starting from limited time-series data recorded while the system is evolving, we develop a fractional-order moments-based approach to determine the parameters of a generalized fractional PDE. We formulate two optimization problems to allow us to estimate the arguments of the fractional PDE. Employing extensive simulation studies, we show that the proposed approach is effective at retrieving the relevant parameters of the space-time fractional PDE. The presented mathematical approach can be further enhanced and generalized to include additional operators that may help to identify the dominant rule governing the measurements or to determine the degree to which multiple physical laws contribute to the observed dynamics.

Keywords: anomalous diffusion, fractional derivative, Fourier transform, Laplace transform, regression

Edited by:
Ralf Metzler,
University of Potsdam, Germany

Reviewed by:
Aljaz Godec,
Max Planck Institute for Biophysical Chemistry, Germany
Rainer Klages,
Queen Mary University of London, United Kingdom

***Correspondence:**
Paul Bogdan
pbogdan@usc.edu

†These authors have contributed equally to this work

Specialty section:
This article was submitted to Mathematics of Computation and Data Science, a section of the journal Frontiers in Applied Mathematics and Statistics

Received: *09 August 2019*
Accepted: *17 April 2020*
Published: *26 May 2020*

Citation:
Znaidi MR, Gupta G, Asgari K and Bogdan P (2020) Identifying Arguments of Space-Time Fractional Diffusion: Data-Driven Approach. Front. Appl. Math. Stat. 6:14. doi: 10.3389/fams.2020.00014

1. INTRODUCTION

Technological advances ranging from an impressive improvement in the sensing and computational resources to the enhancement in data storage play a prominent role in offering researchers' new directions to investigate unknown or poorly understood phenomena and boost numerous scientific areas (e.g., neuroscience, synthetic and system biology, finance, anthropology, and political sciences). This impact on all sciences is likely to persist with the booming advances in data science (DS), machine learning (ML), and artificial intelligence (AI) [1–4]. Apart from the impressive contribution of AI in pattern recognition (e.g., images) and language processing, nowadays AI and data science are contributing to several developing scientific fields (e.g., the discovery of unwanted effects of drugs and drug repositioning [5, 6]). For example, one can consider the problem of "Lamisil" drug used for the treatment of skin infections, which caused deaths and other liver reactions after being on the market for years. Although it was found that the drug is behind the TBF-A generation, which has toxicological effects, it was not possible to explain how the drug boosts the TBF-A formation. In 2018, a deep learning-based investigation identified the pathways leading to TBF-A formation [5]. The process of TBF-A formation could not be identified before launching the product on the market due to its complicated mechanism and limited information on its manifestations. Such a discovery can have a primordial role in drug discovery and development by pharmaceutical industries and startups working in drug discovery (e.g., Kebotix, Deep Genomics).

Furthermore, AI has been recently considered as a useful analysis and discovery tool in medicine and healthcare. For instance, computer scientists and radiologists incorporated ML and AI techniques into the radiological examination in order to provide better results in medical imaging [7] and to detect early signs of diseases. Indeed, convolutional neural networks based approaches enabled the analysis of three dimensional MRI images and the identification of symptoms of Alzheimer's disease [8]. Similarly, AI-based investigation provided new approaches for quantifying the risk of autism [9]. It is also worth mentioning that AI has also been introduced in ophthalmology [10]. Beyond the medical field, reinforcement learning has been recently used in meteorology in order to study the climate [11, 12]. Consequently, we are witnessing a paradigm shift in mining and understanding real-world problems, as a variety of late innovations are based on applying ML algorithms to analyze and characterize high-dimensional experimental data.

Despite the tremendous boost that is provided by the ML and AI for the analysis of static data through identifying the statistical interdependence between components of a system of interest, there is little to say about analyzing dynamical processes from big data and uncertainty quantification for large-scale complex systems. Specifically, ML has a limiting ability in deciphering the physical driving laws and governing equations from multi-modal heterogeneous, scarce, and/or noisy time-series data associated with complex systems exhibiting multi-scale and multi-physics spatiotemporal evolution. These multi-scale and multi-physics spatiotemporal characteristics that occur in physics, biology, chemistry, neuroscience, and even geology, are usually encoded through (fractional or integer order) partial differential equations (PDEs) with possibly uncertain parameters. These PDEs are derived from conservation laws on energy, momentum, or electric charge (e.g., diffusion equation, Maxwell's equations, Navier-Stokes equations, Schrodinger equations). However, a plethora of complex systems from biology, neuroscience, or finance have numerous hidden interaction mechanisms, and the derivation of the PDEs describing their evolution is unknown. In the big data era, we witness new opportunities for data-driven discoveries of potentially new physical phenomena and new physics laws (or rules). Consequently, one may ask the following fundamental question: Can we learn a PDE model from a given set of time-series measurements and perform accurate, efficient, and robust predictions using this learned model? This question has motivated researchers to develop methods for estimating PDE parameters using numerical solutions of PDEs [13, 14] (which requires careful parameterizations and high computational cost), Bayesian approaches [15], and a two-state approach [16–19] where the parameters of the PDEs are estimated via least squares. However, exploiting the higher-order statistics of the measurements, which can characterize the rare events for a robust understanding of complex systems, and determining whether fractional or integer order PDEs together with their corresponding parameters govern the observations, has not been addressed.

Diffusion is one of the fundamental mechanisms used for analyzing the transport of particles, and a common example of a diffusion process is the Brownian motion. Chaotic motion of a particle characterizes the latter process, and it can be modeled by a random walk such that the mean square displacement follows the diffusing scaling $<(\Delta X)^2> \sim t$ (where $<.>$ designates the mean). Furthermore, diffusion is a principal concept that explains many natural and scientific/technological phenomena (e.g., particles motion [20], DNA and cellular processing [21–24], microbial communities [25], brain activity [26], physiological complexity and cyber-physical systems modeling [27–29]), neuron spikes [30]. The focus on analyzing complex systems led to studying anomalous diffusion [31–43] to decipher complex system properties (e.g., long-range memory, higher-order correlations, ergodicity breaking measured as a discrepancy between the long time-averaged mean squared displacement and the ensemble-averaged mean squared displacement). The anomalous diffusion has been shown to be able to describe complex fluid dynamics [44, 45], biological systems [46–48], transport [49], dynamics in fractal structures [50–52], and economics [53]. Contrary to random walks processes describing classical diffusion (e.g., Brownian motion), the particle possesses an internal memory that leads to a non-stationary motion, where the mean square displacement is heavy-tailed $<(\Delta X)^2> \sim t^{\beta}$ (β is a parameter that is related to the memory of a particle).

The principal purpose for studying anomalous diffusion is to take into account complex/non-trivial behavior of the motion of particles usually found in transport processes in disordered and complex systems. From a phenomenological perspective, the anomalous diffusion can be better understood by recalling the assumptions made by Einstein [20] on defining the normal diffusion: the motion of the Brownian particles are independent (valid for small concentrations), there exist a small time scale during which the particle displacements are statistically independent (i.e., a Markovian behavior), and the particle displacements at these time scales correspond to a mean free path distributed symmetrically in positive or negative directions (i.e., a symmetric Gaussian statistical behavior). In contrast, anomalous diffusion generalizes the normal diffusion framework by removing one or more of such requirements on either Markovian or Gaussian behavior [42, 43]. In the literature, there are many methods used to analyze anomalous diffusion, mainly generalized Langevin equation [54, 55], thermodynamics [56, 57] and in this article, we concentrate our analysis on the discussion of incorporating fractional derivatives into PDEs to model anomalous diffusion. In fact, the mathematical description of anomalous diffusion involves a power law expression of the mean square displacement as a function of time. It often relies on fractional-order derivatives acting on either space or time components of a PDE [29, 42, 43]. Indeed, modeling anomalous diffusion via fractional diffusion equation (i.e., PDE) can be provided by the master equation for continuous time random walk, and the solutions of the fractional diffusion equation can be interpreted as spatial probability densities evolving in time, related to self-similar stochastic process encoding the long-range memory property [58]. For instance, the anomalous diffusion of a particle subject to an external non-linear force and a thermal bath is described in Metzler et al. [59] through a fractional Fokker-Planck equation. Here, the time-fractional Riemann-Liouville derivative models the long-range memory effects characteristic to anomalous diffusion in random environments and chaotic Hamiltonian systems [59]. More generally, the anomalous diffusion has been successfully modeled by a space-time fractional diffusion equation that assumes that the process has memory (i.e., time-fractional derivative) as well as being non-local (space-fractional derivative). More recently, a comprehensive analysis of the higher-order moments associated with the amplitude fluctuations of the time-averaged mean square displacement for an anomalous diffusion model demonstrated that the skewness and kurtosis can improve the estimation of the anomalous diffusion exponent and can help at classifying the anomalous stochastic processes [60].

Despite the significant body of work on anomalous diffusion models, finding the exact parameters of the corresponding governing PDE is not a trivial task. In this context, given a spatiotemporal dataset, we aim to develop an efficient algorithm for estimating the parameters of the generalized fractional-order PDE that models the dynamics of the process under investigation. Consequently, by identifying these parameters, one can also investigate the physical rules modeled by the PDE. In the results section, we analyze two types of PDEs and discuss algorithmic approaches to determine their parameters from the time-series data. We also provide a simulation study where we verify the correctness and effectiveness of the proposed algorithmic approaches on deriving the exact parameters using synthetic trajectories generated from the PDE model.

2. DATA-DRIVEN APPROACH FOR ANALYZING ANOMALOUS DIFFUSION

2.1. Space-Time Fractional Diffusion Equation

The space-time fractional diffusion equation has been proposed in previous works as a mathematical model to analyze anomalous diffusion [34, 61–65]. In a nutshell, the space-time fractional diffusion equation in (1) consists of a fractional Riesz-Feller derivative of the order $\alpha > 0$ (space-derivative) that encodes the space variations and a fractional Caputo derivative of the order $\beta > 0$ (time-derivative) that measures the time variations. To better generalize, we also consider the skewness factor in the space derivative of the diffusion equation. Hence, the space-time fractional diffusion equation is defined as

$$ {}_t\mathcal{D}^{\beta}_{*} u(x,t) = D \times {}_x\mathcal{D}^{\alpha}_{\theta} u(x,t), \qquad \forall x \in \mathbb{R}, \forall t \in \mathbb{R}^{+}, \tag{1} $$

where the operators ${}_x\mathcal{D}^{\alpha}_{\theta}$ and ${}_t\mathcal{D}^{\beta}_{*}$ designate the fractional Riesz-Feller derivative of order α and skewness θ [66], and the Caputo time-fractional derivative of order β [67], respectively[1]. The parameter D denotes the generalized diffusion coefficient. The parameters α, β and θ satisfy the following constraints, $0 < \alpha \leq 2$, $0 < \beta \leq 1$ and $|\theta| \leq \min\{\alpha, 2-\alpha\}$.

Given a set of time-series trajectories that record the evolution of particles or agents that exhibits anomalous diffusion modeled by Equation (1), without prior knowledge about the parameters of the space-time fractional diffusion equation, our goal is to use the dataset available to retrieve the exact fractional PDE that generates the given time-series. Toward this end, we develop a mathematical framework where the parameter and mathematical (operator) expression identification task is defined as a regression problem (**Figure 1**). Indeed, the regression is formulated as a least squares problem, where the minimization involves the theoretical and the empirical statistical (higher order) moments (i.e., specifically the absolute moments). The choice of the statistical moments for performing the regression is convenient because we could derive its closed form expressions just from the generalized fractional PDE given in Equation (1). For the given time-series data, $X_n(t), 1 \leq n \leq N$, where N denotes the total number of trajectories, the time empirical moments are defined as follows

$$ M_t^{\delta} = \frac{1}{N}\sum_{n=1}^{N} |X_n(t)|^{\delta}, \qquad S_t^{\delta} = \frac{1}{N}\sum_{n=1}^{N} X_n(t)^{\langle\delta\rangle}, \tag{2} $$

where $x^{\langle\delta\rangle}$ denotes the signed absolute δ-th power of x and $x^{\langle\delta\rangle} = |x|^{\delta}\text{sign}(x)$. The time-dependent absolute moment of the data generated according to the fractional PDE in (1) is given by the following result.

Proposition 1. *The time-dependent absolute moment of the order* δ *with* $0 < \delta < \alpha$ *is written as follows*

$$ \mathbb{E}[|X(t)|^{\delta}] = t^{\delta\frac{\beta}{\alpha}} D^{\frac{\delta}{\alpha}} \times \frac{\Gamma(1-\frac{\delta}{\alpha})\Gamma(1+\frac{\delta}{\alpha})\cos(\frac{\delta\pi\theta}{2\alpha})}{\Gamma(1-\delta)\Gamma(1+\delta\frac{\beta}{\alpha})\cos(\frac{\delta\pi}{2})}, \tag{3} $$

where $\Gamma(\cdot)$ *designates the gamma function.*

To find the parameters of the fractional PDE in (1), we rely on analyzing the higher order moments and minimize the quadratic error between the theoretical and the empirical absolute higher order moments. However, due to the non-linear non-convex expression stated in the Equation (3), such a regression problem is non-trivial and it is non-trivial to provide

---

[1] The two operators are clearly defined in the **Supplementary Material**.

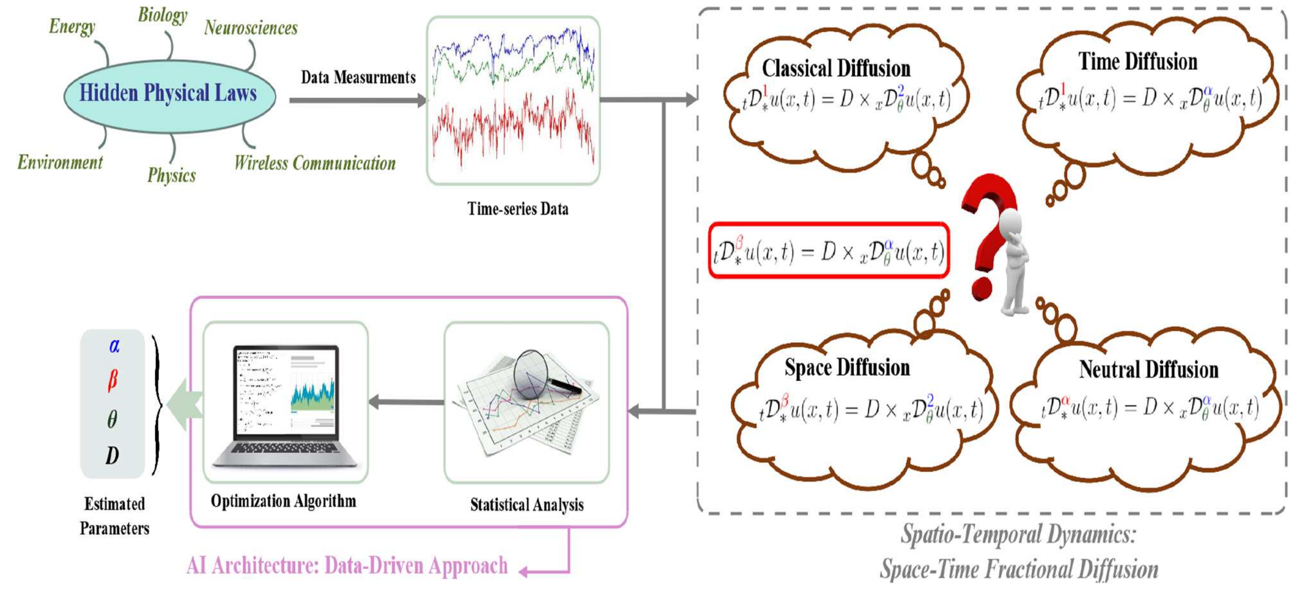

FIGURE 1 | Flowchart showing an AI architecture used to uncover hidden patterns governing complex phenomena: a data-driven based approach to estimate the parameters of the space-time fractional diffusion equation from spatiotemporal dynamics.

the theoretical guarantees about the convergence of a multi-dimensional optimization algorithm used to solve the problem in one-shot. To tackle the non-convexity, we aim to approach the parameters estimation via multi-step optimization. For obtaining additional information from the data, we also derive the signed absolute as in the following result.

Proposition 2. *The time-dependent signed absolute moment of the order* δ *with* $0 < \delta < \alpha$ *is written as follows*

$$\mathbb{E}[X(t)^{\langle\delta\rangle}] = -t^{\delta\frac{\beta}{\alpha}} D^{\frac{\delta}{\alpha}} \times \frac{\Gamma(1-\frac{\delta}{\alpha})\Gamma(1+\frac{\delta}{\alpha})\sin(\frac{\delta\pi\theta}{2\alpha})}{\Gamma(1+\delta\frac{\beta}{\alpha})\Gamma(1-\delta)\sin(\frac{\delta\pi}{2})}. \qquad (4)$$

We refer the reader to the **Supplementary Materials** for the proofs of the above Propositions. Using the above results, the estimation of parameters is detailed in the following section.

2.2. Parameter Estimation

Absolute Moments Approach: Starting from a dataset containing N independent trajectories (realizations of the Equation (1) with unknown parameters) sampled uniformly at times $\{t_1, t_2, \cdots, t_L\}$, we aim at estimating the actual parameters of the Equation (1) via a moments-based approach, i.e., determining the parameters using empirical moments and the theoretical expressions. Thus, the proposed scheme to find the parameters is mainly a two-step approach, regression over time on one hand and over space on the other hand. The method is summarized as follows.

For a given order δ, the log of absolute moments in Equation (3) varies as

$$\log(\mathbb{E}[|X(t)|^\delta]) = \delta\frac{\beta}{\alpha}\log(t) + C_1, \qquad (5)$$

where C_1 does not depend on t. Using the estimated empirical moments from Equation (2), we replace the theoretical moments with the empirical values in the Equation (5). The parameter ratio β/α can then be estimated by performing linear regression of $\log(t_l)$ vs. $\log(M^\delta_{t_l})$ using a total of L points (i.e., $l = 1, 2, \cdots, L$). It is worthwhile to note that the precision in estimation of β/α can be improved upon using multiple values of moment exponent δ for increasing the total diverse points in linear regression. For example, a set $\Delta = \{\delta_1, \delta_2, \ldots, \delta_K\}$ can be used for having $K \times L$ diverse points for linear regression by repeating the Equation (5) with different δ_k. Hence, we can make a trade-off between space and time, i.e., enlarging the cardinality of Δ when the available time-series are short, in other words when L is small.

Next, we use the results of Proposition 1 and 2 to get the ratio of $\mathbb{E}[|X(t)|^\delta]$ and $\mathbb{E}[X(t)^{\langle\delta\rangle}]$ as the following ratio r

$$r = \frac{\mathbb{E}[X(t)^{\langle\delta\rangle}]}{\mathbb{E}[|X(t)|^\delta]} = -\frac{\tan(\frac{\pi\delta\theta}{2\alpha})}{\tan(\frac{\pi\delta}{2})}.$$

Upon replacing the theoretical moments with the ones derived in Equation (2) we can invert the tangent function to have the ratio θ/α. In addition, although the ratio r is independent of time t, the empirical ratio of the data will possibly not be a constant across time. We therefore, replace r with time average of the ratio of $S^\delta_{t_l}$ and $M^\delta_{t_l}$ as $\overline{S^\delta_{t_l}/M^\delta_{t_l}}$. From section 2.1, we know that the parameter θ is constrained as $|\theta| \leq \min(\alpha, 2-\alpha)$, therefore, we have $|\theta/\alpha| \leq 1$. Next, we define the following function

$$w_L(x) = \begin{cases} -1 & x < -1 \\ x & -1 \leq x \leq 1 \\ 1 & x > 1 \end{cases}.$$

Finally, the ratio of parameters θ and α can now be written as

$$\frac{\theta}{\alpha} = w_L\left(-\frac{2}{\pi\delta}\arctan\left(\tan\left(\frac{\pi\delta}{2}\right)\overline{\left(\frac{S^{\delta}_{t_l}}{M^{\delta}_{t_l}}\right)}\right)\right). \tag{6}$$

As argued before, to improve the precision of the estimation, we can add diversity by having a set of moment exponents $\Delta = \{\delta_1, \delta_2, \ldots, \delta_K\}$. For each $\delta_k \in \Delta$ (where $k = 1, 2, \cdots, K$), we use the Equation (6) to obtain $\widehat{(\theta/\alpha)}_k$, and finally obtain the estimated ratio of parameters as $\widehat{(\theta/\alpha)} = \frac{1}{K}\sum_{k=1}^{K}\widehat{(\theta/\alpha)}_k$.

The absolute moments of order δ from Proposition 1 can be re-written as follows

$$\begin{aligned}\frac{\mathbb{E}[|X(t)|^{\delta}]}{t^{\delta\frac{\beta}{\alpha}}} &= D^{\frac{\delta}{\alpha}} \times \frac{\Gamma(1-\frac{\delta}{\alpha})\Gamma(1+\frac{\delta}{\alpha})\cos(\frac{\delta\pi\theta}{2\alpha})}{\Gamma(1-\delta)\Gamma(1+\delta\frac{\beta}{\alpha})\cos(\frac{\delta\pi}{2})}\\ &= D^{\frac{\delta}{\alpha}} \times \frac{\frac{\pi\delta}{\alpha}}{\sin(\frac{\pi\delta}{\alpha})} \times \frac{\cos(\frac{\pi\delta\theta}{2\alpha})}{\Gamma(1-\delta)\Gamma(1+\frac{\delta\beta}{\alpha})\cos(\frac{\pi\delta}{2})}.\end{aligned}$$

Therefore, for the given value of the order $\delta = \delta_k$, the estimation of α and diffusion coefficient D can be written as the following non-linear equation

$$\begin{aligned}C_k &= \frac{\Gamma(1-\delta_k)\Gamma(1+\frac{\delta_k\beta}{\alpha})\cos(\frac{\pi\delta_k}{2})}{\cos(\frac{\pi\delta_k\theta}{2\alpha})} \times \frac{\mathbb{E}[|X(t)|^{\delta_k}]}{t^{\delta_k\frac{\beta}{\alpha}}}\\ &= D^{\frac{\delta_k}{\alpha}} \times \frac{\frac{\pi\delta_k}{\alpha}}{\sin(\frac{\pi\delta_k}{\alpha})}.\end{aligned} \tag{7}$$

To solve the non-linear equation in (7) for α and D, we use non-linear least squares method (trust region reflective method). The input variables to the non-linear optimization are the values of order $\delta \in \Delta$, where $\Delta = \{\delta_1, \delta_2, \ldots, \delta_K\}$. Formally, the optimization problem is written as follows.

$$\{\hat{D}, \hat{\alpha}\} = \underset{\alpha, D}{\operatorname{argmin}} \sum_{k=1}^{K}\left|D^{\frac{\delta_k}{\alpha}} \times \frac{\frac{\delta_k\pi}{\alpha}}{\sin(\frac{\delta_k\pi}{\alpha})} - C_k\right|^2. \tag{8}$$

We note that the values of C_k can be efficiently estimated by first performing the linear regression of $t^{\delta\frac{\beta}{\alpha}}$ vs $\mathbb{E}[|X(t)|^{\delta}]$ with the condition of zero intercept, and then substituting the ratio (slope of the linear regression) in Equation (7). The optimization problem in (8) is non-convex, therefore, the global optimum solution is not guaranteed by the solvers. Note that, in some scenarios, we may have a prior knowledge about boundaries of the parameter α (i.e., $\alpha_{\min} \le \alpha \le \alpha_{\max}$). Thus, we solve the constrained optimization problem.

Finally, the values of β and θ can be estimated upon estimating α, as we already have the ratios β/α and θ/α from Equation (5) and Equation (6), respectively. The approach described is summarized as Algorithm 1.

Remark: Note that for $\alpha \neq 2$, when the order δ is close to the boundary values, the theoretical absolute moment goes to $+\infty$. However, the empirical one is finite, so in order to have a small error associated to the estimated parameters, we choose the order δ to be far enough from the end points of allowed region. Notice that, the value of α is unknown while the condition $-\min\{\alpha, 1\} < \Re(\delta) < \alpha$ is dependent of it, so assuming an $\alpha_{\min}$ as lower bound for α is rational. We note that the Algorithm 1 is dependent upon the solution of non-linear non-convex optimization problem in (8), and therefore, convergence to the global solution is not guaranteed. Also, we need to provide an input set Δ such that the absolute and signed moments are computable for unknown α. The choice of Δ has to be made by having some idea about lower bound of the α parameter. To take care of these two issues together, we next present an alternative approach in which we do not require non-linear optimization as well as do not require to have the knowledge of Δ set.

Log Absolute Moments Approach: In this subsection, we rely on the moments of log absolute values of the trajectories. Similar to absolute moments with order δ, the log absolute moments can be computed as we present in the following results.

Proposition 3. *The time-dependent expected log absolute value of $X(t)$ is written as follows*

$$\mathbb{E}[\log|X(t)|] = \frac{\beta}{\alpha}\log(t) + \frac{\log(D)}{\alpha} + \gamma\left(\frac{\beta}{\alpha} - 1\right), \tag{9}$$

where γ is the Euler-Mascheroni constant.

Next, the variance of the log absolute values of the trajectories can be written as the following results.

Proposition 4. *The variance of log absolute value of $X(t)$ is written as follows*

$$var(\log|X(t)|) = \frac{\pi^2}{6}\left(\frac{1}{\alpha^2} + \frac{1}{2}\right) - \left(\frac{\pi\theta}{2\alpha}\right)^2. \tag{10}$$

It is interesting to note that the variance is independent of time as well as a function of α and θ/α. We exploit this feature of the variance to obtain an estimate of the α with the ratio θ/α known. Hence, the need for performing non-linear optimization in Algorithm 1 is omitted. We also write the second moment of the log absolute values in the following result.

Proposition 5. *The time-dependent expected square of log absolute value of $X(t)$ is written as follows*

$$\mathbb{E}[(\log|X(t)|)^2] = \frac{\beta^2}{\alpha^2}\log^2(t) + 2\frac{\beta\gamma}{\alpha}\left(\frac{\beta}{\alpha} - 1\right)\log(t) + c, \tag{11}$$

where $c = \frac{\pi^2}{6}\left(\frac{1}{\alpha^2} + \frac{1}{2}\right) - \left(\frac{\pi\theta}{2\alpha}\right)^2 + \left(\frac{\log(D)}{\alpha} + \gamma\left(\frac{\beta}{\alpha} - 1\right)\right)^2 + \frac{\pi^2}{6\alpha^2}(1 - \beta^2)$, and γ is the Euler-Mascheroni constant.

The proof of the Propositions 3, 4, and 5 are provided in the **Supplementary Materials**. Using the above results for log absolute values, we now present the second approach to estimate the parameters of the space-time fractional PDE in (1).

We proceed similarly to the first approach of the δ order absolute moments, however, now equating the theoretical and

Algorithm 1: | Space-Time Fractional Diffusion: Parameters Estimation

```
Input: Time-series data $\{X_n(t_l); 1 \leq n \leq N, 1 \leq l \leq L\}$, order $\delta$, $\Delta = \{\delta_1, \delta_2, \cdots, \delta_K\}$
Output: Parameters: $\alpha, \beta, \theta$ and $D$
for $l = 1, 2, \cdots, L$ do
    Calculate the empirical absolute and signed moments $M_{t_l}^{\delta}$ and $S_{t_l}^{\delta}$    ▷ Eq.2
end for
$\widehat{\left(\frac{\beta}{\alpha}\right)} \leftarrow \frac{m_1}{\delta}$, $m_1$ being slope of linear regression $\log(t)$ vs $\log(M_t^{\delta})$
Get the estimate $\widehat{\left(\frac{\theta}{\alpha}\right)}$    ▷ Eq.6
for $k = 1, 2, \cdots, K$ do
    Calculate the empirical absolute moments $M_{t_l}^{\delta_k}$,   $\forall l$ ▷ Eq.2
    $m_2 \leftarrow$ slope of linear regression $t^{\delta_k \widehat{\left(\frac{\beta}{\alpha}\right)}}$ vs $M_t^{\delta_k}$ with zero intercept
    $C_k \leftarrow m_2 . \frac{\Gamma\left(1+\delta_k \widehat{\left(\frac{\beta}{\alpha}\right)}\right)\Gamma(1-\delta_k)\cos\left(\frac{\pi\delta_k}{2}\right)}{\cos\left(\frac{\pi\delta_k}{2}\widehat{\left(\frac{\theta}{\alpha}\right)}\right)}$    ▷ Eq. 3
end for
Find $\hat{\alpha}, \widehat{D} \leftarrow \underset{\alpha,D}{\operatorname{argmin}} \sum_{k=1}^{K} \left| D^{\frac{\delta_k}{\alpha}} \times \frac{\frac{\delta_k \pi}{\alpha}}{\sin(\frac{\delta_k \pi}{\alpha})} - C_k \right|^2$: non-linear regression over space (sinc inversion)
Calculate $\hat{\beta}, \hat{\theta}$.
```

empirical expressions of the log absolute moments. The empirical log absolute moments are written as

$$
\begin{aligned}
L_t^{(1)} &= \frac{1}{N}\sum_{n=1}^{N} \log|X_n(t)|, \\
L_t^{(2)} &= \frac{1}{N}\sum_{n=1}^{N} \log|X_n(t)|^2, \\
\overline{\operatorname{var}(\log|X(t)|)} &= \frac{1}{N-1}\sum_{n=1}^{N}\left(\log|X_n(t)| - L_t^{(1)}\right)^2. \qquad (12)
\end{aligned}
$$

The parameter ratio β/α is estimated by performing the linear regression of $\log(t)$ vs $L_t^{(1)}$. The slope of the regression output is the estimated ratio $\widehat{(\beta/\alpha)}$. Next, the ratio of the parameters θ and α is estimated using the same approach as described previously in Equation (6).

We note that upon having an estimate of the parameter ratio $\widehat{\theta/\alpha}$, the variance is one-to-one function of α since $\alpha \geq 0$. Therefore, on substituting the value of $\widehat{\theta/\alpha}$ in Equation (10) we compute the value of $\widehat{\alpha}$. Finally, with $\widehat{\alpha}$ and $\widehat{\beta/\alpha}$ known, the value of diffusion coefficient is estimated from the intercept of the linear regression of $\log(t)$ vs $L_t^{(1)}$ as $\widehat{D}$. The above described approach is summarized as an algorithmic strategy in Algorithm 2.

Algorithm 2: | Space-Time Fractional Diffusion: Parameters Estimation

```
Input: Time-series data $\{X_n(t_l); 1 \leq n \leq N, 1 \leq l \leq L\}$, order $\delta$
Output: Parameters: $\alpha, \beta, \theta$ and $D$
for $l = 1, 2, \cdots, L$ do
    Calculate the empirical absolute and signed moment $M_{t_l}^{\delta}$ and $S_{t_l}^{\delta}$    ▷ Eq.2
    Calculate log absolute moments $L_t^{(1)}$    ▷ Eq.12
end for
$\widehat{\left(\frac{\beta}{\alpha}\right)} \leftarrow m$, $(m, c)$ being (slope, intercept) of linear regression $L_t^{(1)}$ vs $\log(t)$
Get the estimate $\widehat{\left(\frac{\theta}{\alpha}\right)}$    ▷ Eq.6
Calculate empirical variance of log absolute values $\overline{\operatorname{var}(\log(|X(t)|))}$ as $\sigma^2$    ▷ Eq.12
$\hat{\alpha} \leftarrow \left(\sigma^2 \frac{6}{\pi^2} - \frac{1}{2}\right)^{-\frac{1}{2}}$
$\hat{D} \leftarrow \exp\left\{\hat{\alpha}\left(c - \gamma\left(\widehat{\left(\frac{\beta}{\alpha}\right)} - 1\right)\right)\right\}$    ▷ Eq.3
Calculate $\hat{\beta}, \hat{\theta}$.
```

It should be noted that the approach utilizing log absolute moments does not require a predefined set of order values Δ. In addition, this does not suffer from the convergence issues as there is no non-linear non-convex optimization involved.

Note: The estimated parameters in both algorithms are not guaranteed to be optimal. For example, it is not straightforward to guarantee maximum likelihood sense as solving maximum likelihood involves solution to non-convex problem. We evaluate the efficiency of the both algorithms in the following section.

3. EXPERIMENTAL RESULTS

As we described previously, both algorithms depend mainly on the statistical absolute moments, statistical signed absolute moments and the expected log absolute value of the process $X(t)$. For this reason, we first start by validating the theoretical expressions derived in Equations (3), (4) and (9). We consider different scenarios (normal diffusion equation, neutral diffusion equation [68–71], space diffusion equation [71], and time diffusion equation [71]). In these experiments, we generate synthetic data corresponding to $N = 100$ trajectories simulated according to the diffusion model under study with a generalized diffusion coefficient $D = 1$. Note that the data generation procedure is presented in details in the **Supplementary Material**. In **Figure 2**, we present panel of 4 × 3 plots where we refer by a row the scenario considered (normal, time, space, neutral diffusion) and we plot the statistical absolute moments, statistical signed absolute moments and the expected log absolute value of the process $X(t)$ for an order $\delta = 0.001$ vs. time in the columns. The signed moment deviates a little from the theoretical expression for some scenarios, due to lack of sufficient samples. For the particular case of **Figure 2E**, we observe that there is nearly perfect match with the theoretical

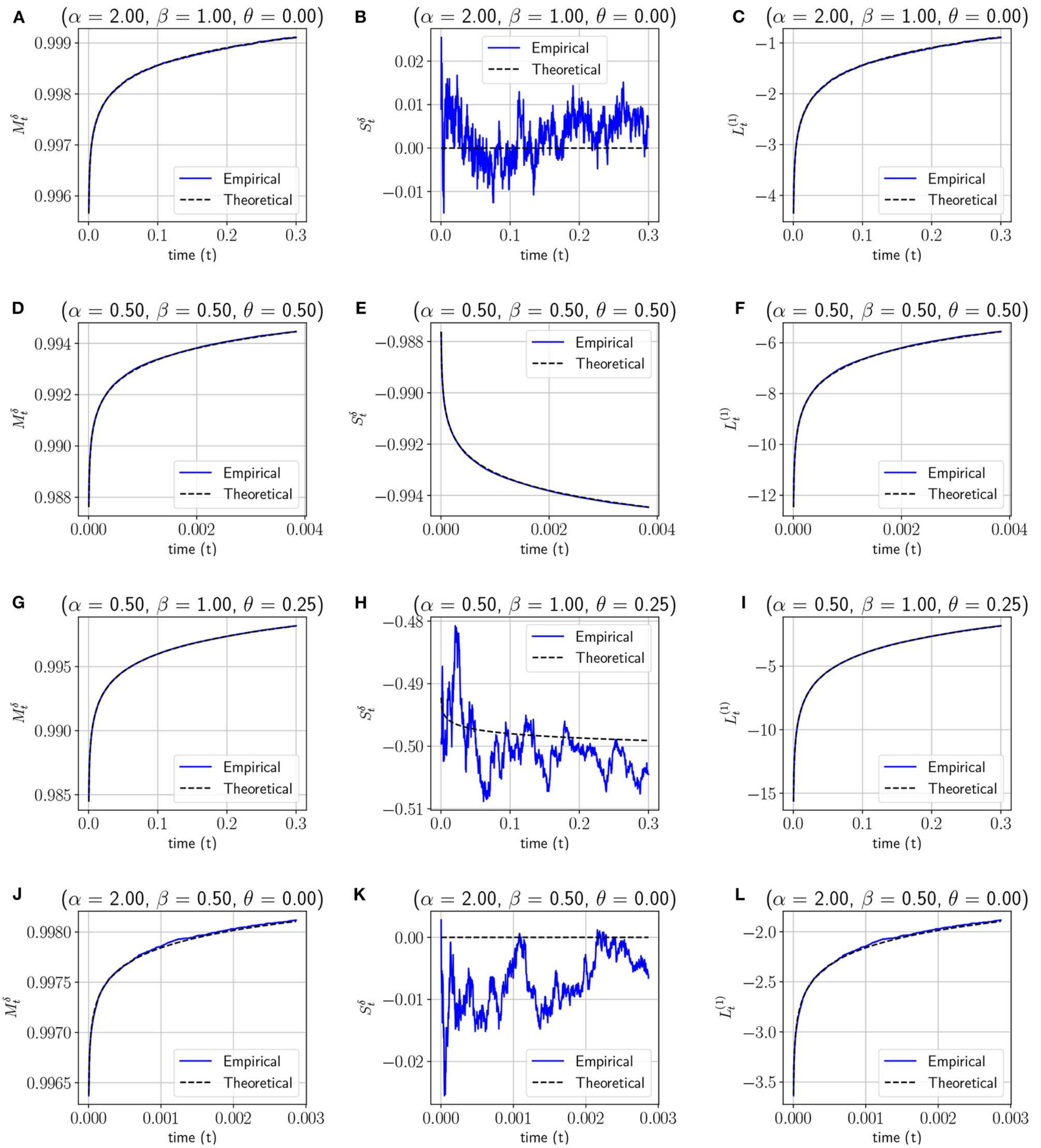

FIGURE 2 | The time-dependent theoretical and empirical absolute moments and signed absolute moments of order $\delta = 0.001$, the time-dependent theoretical and empirical expected log absolute for the following four types of diffusion models: **(A–C)** Normal diffusion equation, **(D–F)** Neutral diffusion equation, **(G–I)** Space fractional diffusion equation, **(J–L)** Time fractional diffusion equation.

expression. The reason being, in this case, the parameters $\alpha = \theta$, hence the trajectories are generated from a negatively skewed alpha-stable distribution, therefore $X(t) \leq 0\ \forall t$. We note that a similar situation happens when we have the parameters $\alpha = -\theta$. In this case, we have a positive skewed alpha distribution, and therefore, $X(t) \geq 0\, \forall t$. In all scenarios, we can observe that the empirical statistical moments match perfectly the theoretical ones in all scenarios. This result confirms our

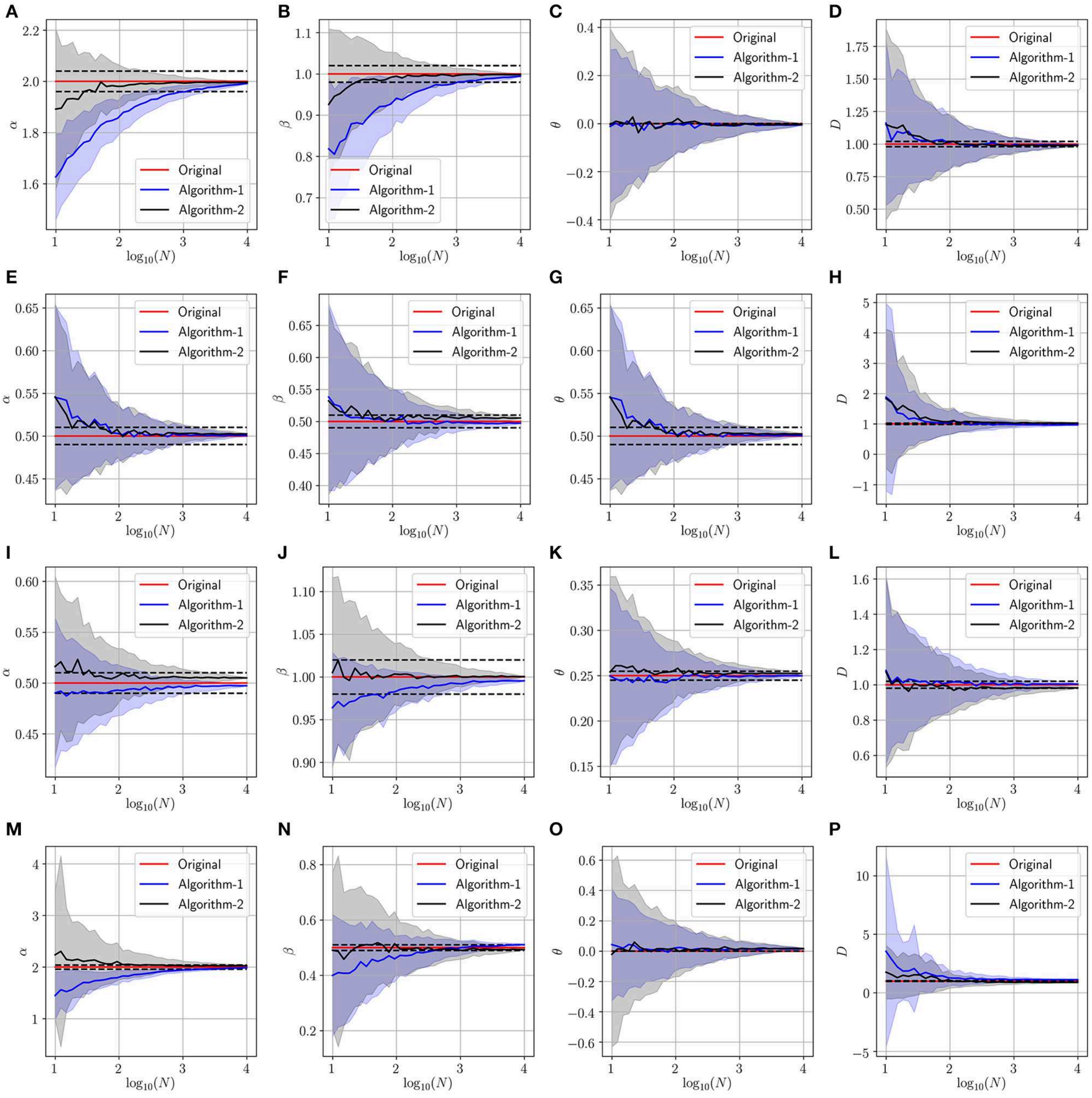

FIGURE 3 | Determining the parameters of the space-time fractional diffusion via the two proposed algorithms while varying the number of trajectories and the generalized diffusion coefficient $D = 1$. The dotted line indicate 2% error tube around the original parameter value in the red: **(A–D)** Normal diffusion equation ($\alpha = 2, \beta = 1, \theta = 0$), **(E–H)** Neutral diffusion equation ($\alpha = 0.5, \beta = 0.5, \theta = 0.5$), **(I–L)** Space fractional diffusion equation ($\alpha = 0.5, \beta = 1, \theta = 0.25$), **(M–P)** Time fractional diffusion equation ($\alpha = 2, \beta = 0.5, \theta = 0$).

theoretical derivations and motivates us to move forward with this approach.

3.1. Parameters Estimation of Synthetic Data

In this experiment, we validate the proposed approach using artificially generated spatiotemporal data according to the PDE model presented in Equation (1). More precisely, we use the above-mentioned schemes (Algorithm 1 and Algorithm 2) to retrieve the parameters (α, β, θ and D) used during the data generation step. **Figures 3–5** summarize several experiments done for different diffusion models (classical, neutral, space, and time diffusion), where we assume a set of combination of α, β and θ parameters for a generalized diffusion coefficient $D = 1, 2$ and $D = 5$, respectively. In each figure we present a panel of 4×4 different plots where a row represents the

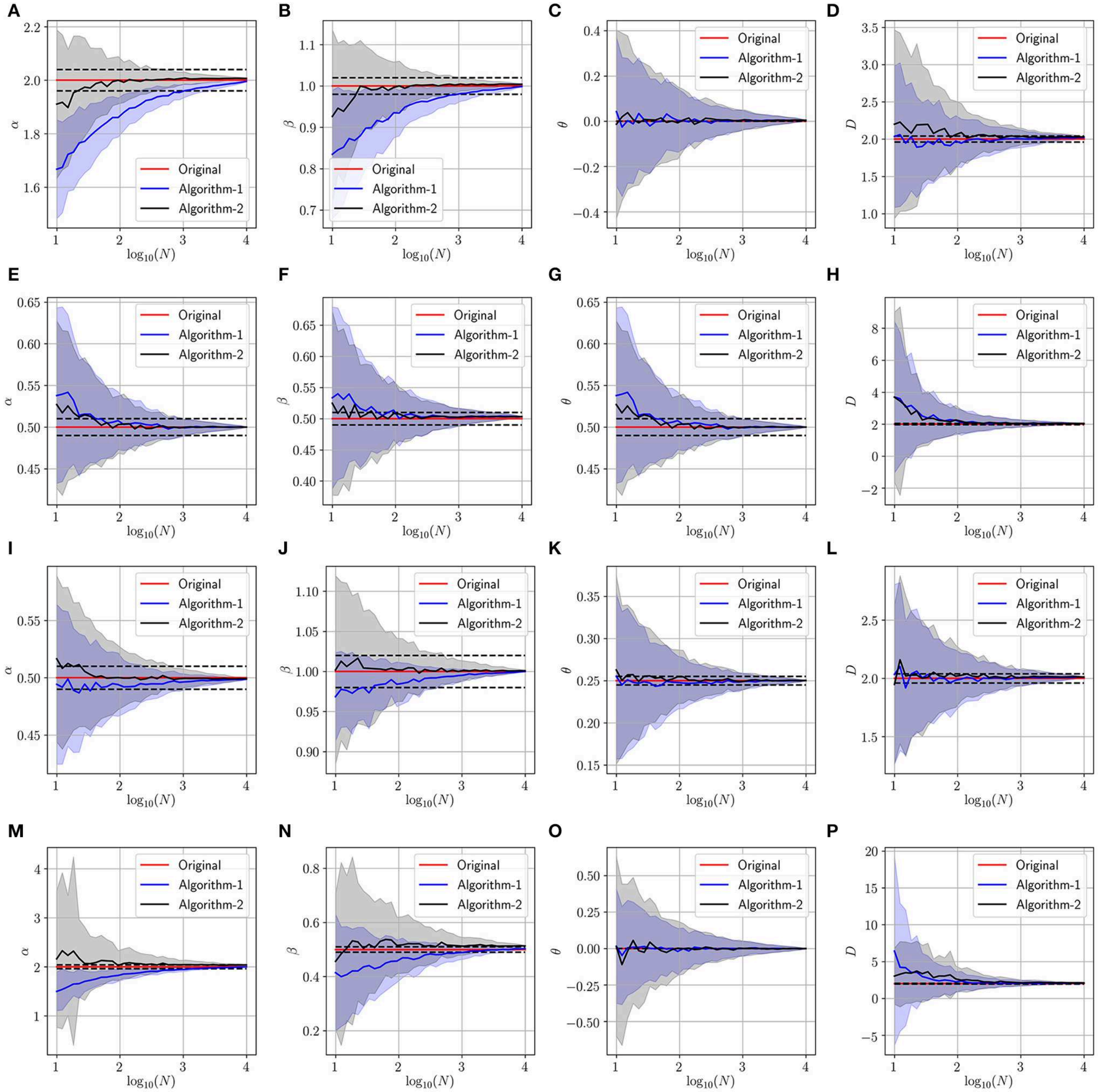

FIGURE 4 | Determining the parameters of the space-time fractional diffusion via the two proposed algorithms while varying the number of trajectories and the generalized diffusion coefficient $D = 2$. The dotted line indicate 2% error tube around the original parameter value in the red: **(A–D)** Normal diffusion equation ($\alpha = 2, \beta = 1, \theta = 0$), **(E–H)** Neutral diffusion equation ($\alpha = 0.5, \beta = 0.5, \theta = 0.5$), **(I–L)** Space fractional diffusion equation ($\alpha = 0.5, \beta = 1, \theta = 0.25$), **(M–P)** Time fractional diffusion equation ($\alpha = 2, \beta = 0.5, \theta = 0$).

type of diffusion considered and columns 1, 2, 3 and 4 designate the parameters α, β, θ and D, respectively. In each of the sub-figure, we plot the estimated parameter using both algorithms (blue line for Algorithm 1 and the black line for Algorithm 2) vs. the number of trajectories considered during the estimation process. We also plot the true value as a red line, and a narrow interval around the true value using black dashed lines. The presented blue and gray shaded regions represent the standard deviation for the estimated parameters associated to Algorithm 1 and Algorithm 2, respectively. All sub-figures in **Figures 3–5** show that the proposed schemes are doing well in all scenarios where we are able to retrieve the exact set of parameters α, β, θ

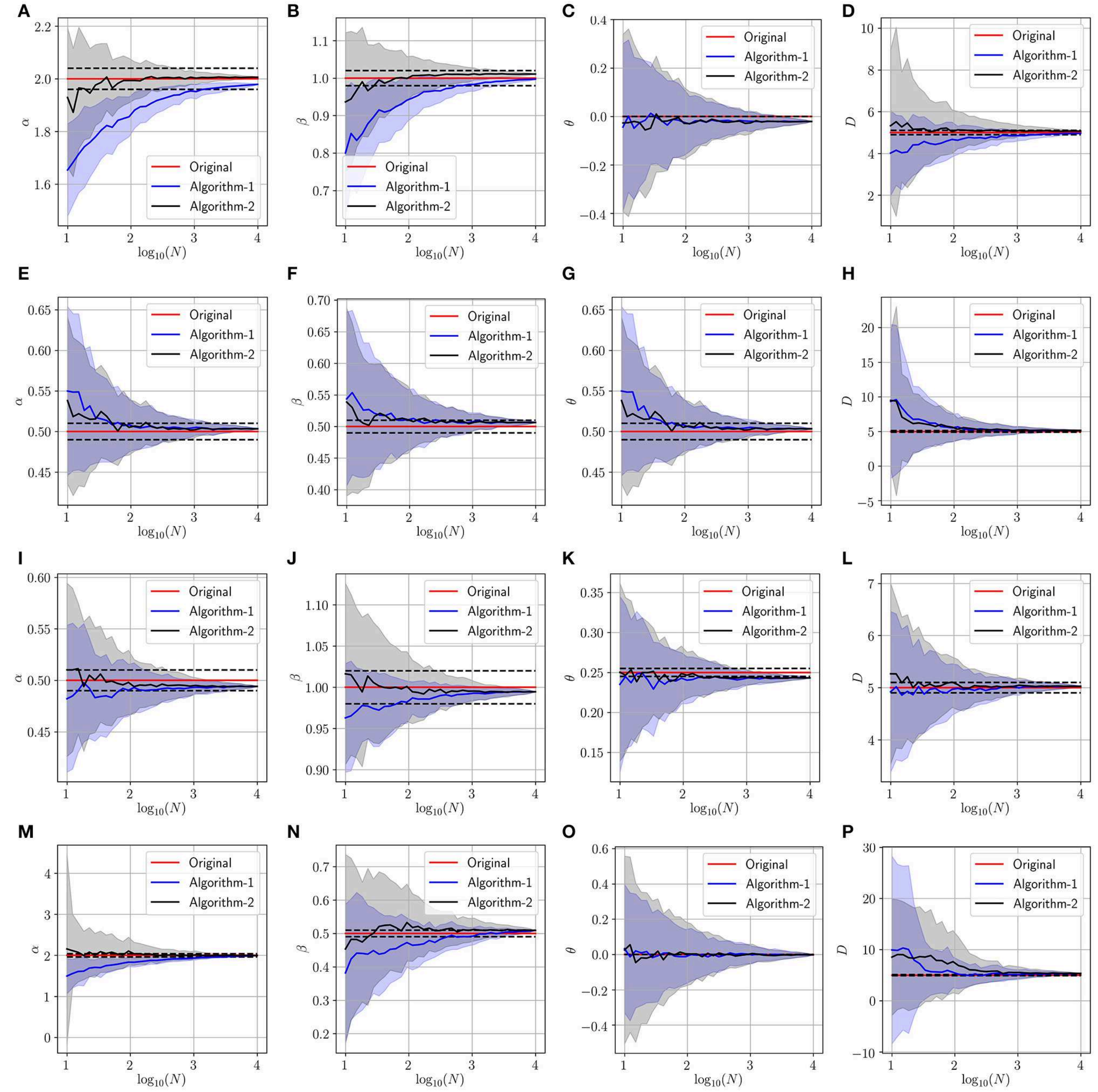

FIGURE 5 | Determining the parameters of the space-time fractional diffusion via the two proposed algorithms while varying the number of trajectories and the generalized diffusion coefficient $D = 5$. The dotted line indicate 2% error tube around the original parameter value in the red: **(A–D)** Normal diffusion equation ($\alpha = 2, \beta = 1, \theta = 0$), **(E–H)** Neutral diffusion equation ($\alpha = 0.5, \beta = 0.5, \theta = 0.5$), **(I–L)** Space fractional diffusion equation ($\alpha = 0.5, \beta = 1, \theta = 0.25$), **(M–P)** Time fractional diffusion equation ($\alpha = 2, \beta = 0.5, \theta = 0$).

and D with a small/negligible error[2]. Also, we can see how the standard deviation of the estimated parameters decreases as the number of trajectories increases. Furthermore, we can remark that Algorithm 2 is performing slightly better than Algorithm 1 in terms of rate of convergence. Although the variance is quite high when fewer trajectories are considered, we remark that in some scenarios we can get good estimates of the parameters even with reduced number of trajectories.

In **Tables 1–3**, we provide further details about the results we have described in **Figures 3–5**, respectively. Indeed, for both algorithms, we report the estimated value of each parameter, in

---

[2] Additional simulations for other scenarios are presented in the **Supplementary Material**.

TABLE 1 | Numerical results for fractional diffusion parameter estimation with $D = 1$.

Parameters	Algorithm-1			Algorithm-2		
	$N_{90}^{(1)}$	Final value	Final relative error	$N_{90}^{(2)}$	Final value	Final relative error
			$\alpha = 2.0, \beta = 1.0, \theta = 0.0$			
α	41	1.992	0.400%	10	1.996	**0.200%**
β	50	0.994	0.600%	10	0.998	**0.200%**
θ	−−	−0.006	−−	−−	−0.004	−−
D	12	0.992	**0.800%**	22	0.989	1.100%
			$\alpha = 0.5, \beta = 0.5, \theta = 0.5$			
α	10	0.501	**0.200%**	10	0.502	0.400%
β	10	0.497	**0.600%**	10	0.505	1.000%
θ	10	0.501	**0.200%**	10	0.502	0.400%
D	41	0.968	3.200%	140	1.027	**2.700%**
			$\alpha = 0.5, \beta = 1.0, \theta = 0.25$			
α	10	0.497	**0.600%**	10	0.505	1.000%
β	10	0.995	0.500%	10	1.000	**0.000%**
θ	10	0.250	**0.000%**	10	0.253	1.200%
D	10	1.004	**0.400%**	10	0.982	1.800%
			$\alpha = 2.0, \beta = 0.5, \theta = 0.0$			
α	114	1.985	0.750%	15	2.000	**0.000%**
β	41	0.511	2.200%	10	0.493	**1.400%**
θ	−−	0.015	−−	−−	0.017	−−
D	−−	1.119	11.900%	−−	0.890	**11.000%**

The bold values are used to highlight the best performance for each case across the 2 algorithms.

TABLE 2 | Numerical results for fractional diffusion parameter estimation with $D = 2$.

Parameters	Algorithm-1			Algorithm-2		
	$N_{90}^{(1)}$	Final value	Final relative error	$N_{90}^{(2)}$	Final value	Final relative error
			$\alpha = 2.0, \beta = 1.0, \theta = 0.0$			
α	41	1.995	0.250%	10	2.000	**0.000%**
β	50	0.999	0.100%	10	1.000	**0.000%**
θ	−−	0.004	−−	−−	0.004	−−
D	10	2.022	**1.100%**	15	2.030	1.500%
			$\alpha = 0.5, \beta = 0.5, \theta = 0.5$			
α	10	0.500	0.000%	10	0.500	**0.000%**
β	10	0.503	0.600%	10	0.503	**0.600%**
θ	10	0.500	0.000%	10	0.500	**0.000%**
D	114	2.039	1.950%	114	2.039	**1.950%**
			$\alpha = 0.5, \beta = 1.0, \theta = 0.25$			
α	10	0.499	0.200%	10	0.499	**0.200%**
β	10	1.000	0.000%	10	1.000	**0.000%**
θ	10	0.250	0.000%	10	0.250	**0.000%**
D	10	2.011	**0.550%**	10	2.012	0.600%
			$\alpha = 2.0, \beta = 0.5, \theta = 0.0$			
α	76	1.999	0.050%	22	2.000	**0.000%**
β	62	0.504	**0.800%**	10	0.513	2.600%
θ	−−	−0.001	−−	−−	−0.001	−−
D	140	2.082	**4.100%**	712	2.111	5.550%

The bold values are used to highlight the best performance for each case across the 2 algorithms.

the column entitled the final value, of the space-time fractional diffusion equation (i.e., α, β, θ and D) and the final relative error, which is defined as the percentage of the discrepancy between the exact value and the estimated one, or $\varepsilon_\xi = \frac{|\hat{\xi}-\xi|}{|\xi|} \times 100$, where $\hat{\xi}$ and ξ are any estimated and original parameters, respectively. We also report the parameter $N_{90}^{(i)}$, which we define as the minimum number of trajectories beyond which the accuracy using algorithm i is at least 90% and formally can be written as

$$N_{90}^{(i)}(\xi) = \inf\{N \mid \varepsilon_\xi \leq 10,\ \forall N > N_{90}, \xi \leftarrow \mathcal{A}_i(\{X_n(t_l)\}_{n=1}^{N})\},$$

where $\xi \in \{\alpha, \beta, \theta, D\}$ and $\mathcal{A}_i(\{X_n(t_l)\}_{n=1}^{N})$ denotes the output of the i-th Algorithm ($i \in \{1, 2\}$). By looking at the values reported in the column $N_{90}^{(i)}$, we can analyze the performance of both algorithms. For instance, we can remark that a dozen of trajectories is sufficient for both algorithms to achieve at least 90% accuracy in most of the settings. We note that a missing value for $N_{90}^{(i)}$ could be an indicator of either a bias in the Algorithm i which is greater than 10%, or the situation that the maximum considered trajectories ($N = 10^4$) in our experiments are not sufficient enough for achieving accuracy more than 90%. Lastly, it is worth to note that increasing the number of trajectories will lead to a smaller final relative error.

3.2. Parameters Estimation of Fractional Brownian Motion

In this experiment, we present a study of fractional Brownian motion (fBm) process. More precisely, we consider a dataset of trajectories generated using the fBm model, then we parameterize the data according to the fractional diffusion equation under study in order to estimate the parameters of the fBm process generating the data (i.e., the Hurst exponent H and the diffusion constant D_0). From the Langevin equation associated with the fBm, we can remark that the fBm exhibits a long-time correlation which makes the process non-Markovian. The effective Fokker-Planck equation is given as

$$\frac{\partial p(x,t)}{\partial t} = D_0 2Ht^{2H-1} \frac{\partial^2 p(x,t)}{\partial x^2}. \tag{13}$$

The solution for the aforementioned equation is provided in Wang and Lung [72]

TABLE 3 | Numerical results for fractional diffusion parameter estimation with $D = 5$.

Parameters	**Algorithm-1**			**Algorithm-2**		
	$N_{90}^{(1)}$	**Final value**	**Final relative Error**	$N_{90}^{(2)}$	**Final value**	**Final relative error**
			$\alpha = 2.0, \beta = 1.0, \theta = 0.0$			
α	33	1.979	1.050%	10	2.000	**0.000%**
β	33	0.997	0.300%	10	1.000	**0.000%**
θ	−−	−0.021	−−	−−	−0.021	−−
D	76	4.960	**0.800%**	15	5.069	1.380%
			$\alpha = 0.5, \beta = 0.5, \theta = 0.5$			
α	10	0.503	0.600%	10	0.503	**0.600%**
β	15	0.507	1.400%	10	0.506	**1.200%**
θ	10	0.503	0.600%	10	0.503	**0.600%**
D	140	5.145	2.900%	171	5.142	**2.840%**
			$\alpha = 0.5, \beta = 1.0, \theta = 0.25$			
α	10	0.494	1.200%	10	0.494	**1.200%**
β	10	0.995	0.500%	10	0.995	**0.500%**
θ	10	0.243	2.800%	10	0.243	**2.800%**
D	10	5.027	0.540%	10	5.027	**0.540%**
			$\alpha = 2.0, \beta = 0.5, \theta = 0.0$			
α	76	1.994	0.300%	10	1.994	**0.300%**
β	50	0.509	1.800%	10	0.509	**1.800%**
θ	−−	−0.002	−−	−−	−0.002	−−
D	114	5.338	6.760%	1311	5.335	**6.700%**

The bold values are used to highlight the best performance for each case across the 2 algorithms.

$$p(x,t) = \frac{1}{\sqrt{4\pi D_0 t^{2H}}} \exp\left(\frac{-x^2}{4D_0 t^{2H}}\right). \tag{14}$$

Thus, the fractional absolute moment of a fBm process with a parameter $0 < H < 0.5$ is given as

$$\mathbb{E}[|X(t)|^{\delta}] = (2D_0 t^{2H})^{\delta/2} \frac{\Gamma(\frac{1+\delta}{2})}{\sqrt{\pi}}. \tag{15}$$

Based on the expressions (3) and (15), we can use the space-time fractional diffusion equation under study to parameterize an fBm process. Indeed, by mapping the two expressions, we get $\alpha = 2$, $\beta = 2H$, $\theta = 0$ and $D = \frac{D_0}{2}$. In this experiment, we assume that the given trajectories are following an fBm model and the task is to apply the proposed algorithms to identify the parameters associated with the fBm (H and D_0).

Last, in **Figure 6**, we present the simulation results associated with this experiment. The figure represents a panel of 4 × 4 plots where a row is associated with a set of parameters H and D_0 associated to a fBm process, and columns $1, 2, 3$ and 4 are associated with the estimation of the parameters α, β, θ and D, respectively. Hence the estimation of the parameters H and D_0. In these simulations, we generate N trajectories following four different fBm models using the built-in function `wfbm` in Matlab (i.e., in **Figure 6**, rows $1, 2, 3$ and 4 are associated to fBm with Hurst exponents $H = 0.25$, $H = 0.3$, $H = 0.35$ and $H = 0.4$, respectively). As we can observe, Algorithm 2 (plotted using black line) can efficiently provide accurate estimates of the Hurst exponent and the diffusion constant and it performs better than Algorithm 1. The reason behind this is that Algorithm 1 requires solving a non-linear non-convex optimization problem which is not the case for the second algorithm. Also, we remark that finding the parameters of the fBm using Algorithm 2 does not require very large number of trajectories. In fact, we can determine an accurate estimates of the parameters (α, β) with an error close to 2% by performing Algorithm 2 on dataset of few trajectories obeying the fBm model (i.e., $N \leq 10$).

From the simulation results related to fBm in **Figure 6**, we can see that Algorithm 2 is capable to accurately estimate the parameters α and $\beta = 2H$ hence H. However, the estimation of the parameter D_0 is not accurate because of the non-conformity of the equation under study with the fBm model for all parameters values. Indeed, both models coincide, in terms of moments, only when $\alpha = 2$, $\theta = 0$ and $\beta = 2H$. Interestingly, in the current experiment, we focus more on determining an accurate estimate of the parameter H that is related to the long-time memory of an fBm process. Therefore, the proposed algorithms can be used as a tool to quantify the memory of an unknown process that follows the fBm model from given trajectories.

In **Table 4**, we report further elaboration of the results in **Figure 6**. In fact, we can remark that all the bold marked minimum relative errors are in the column associated with Algorithm 2, which endorse our previous claim about the effectiveness of the second algorithm. Related to the discussion of the estimation of α and β, we can see that the column $N_{90}^{(1)}$ has a lot of missing values, and this indicates that using Algorithm 1 for these experiments lead to a final relative error that is greater than 10%. More interestingly, we can remark that with just around 10 trajectories, Algorithm 2 can provide an estimate of either α or β that is within the 10% error margin.

4. DISCUSSION

Understanding complex dynamics remains a challenging task when their generative model is unknown. This task is more complicated when it comes to analyze spatiotemporal kinetics and infer the model that dictate their evolution. Although, the physics that drive the dynamics are unknowns, data-driven based approaches are prominent tools to discover the physical laws/rules governing complex observed dynamics (from heterogeneous, sparse, scarce or even noisy data). Indeed, such a discovery plays a crucial role in diverse fields ranging from system biology, neuroscience, econophysics to social studies. Toward addressing this goal, in this manuscript, we have considered a generalized space-time fractional PDE and have developed an effective, rigorous and robust algorithmic strategies to estimate the parameters and so identify the main mathematical operators appearing in the PDE.

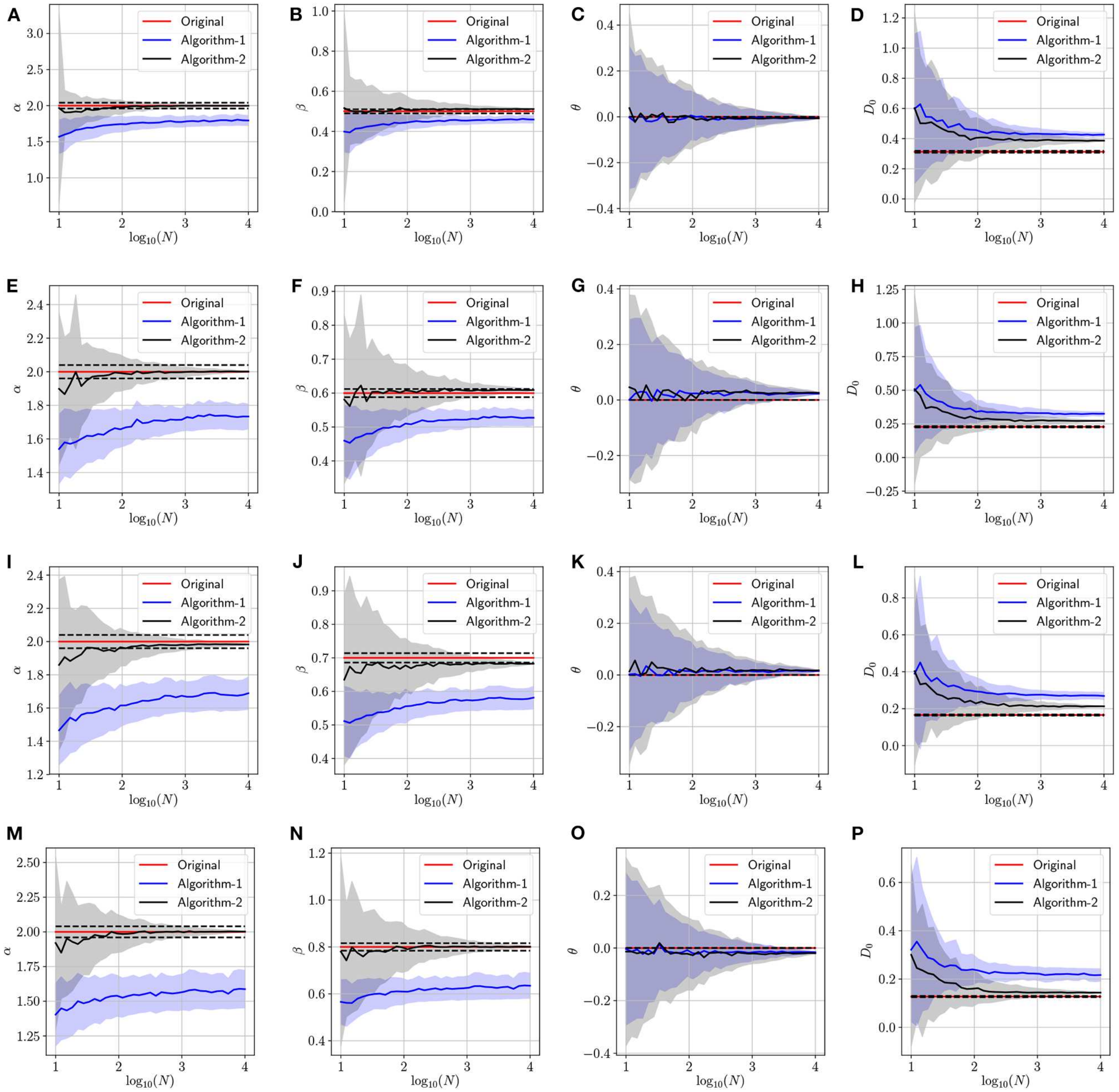

FIGURE 6 | Determining the parameters of the fractional Brownian motion via the two proposed algorithms while varying the number of trajectories. The dotted line indicate 2% error tube around the original parameter value in the red: **(A–D)** with $H = 0.25$ and ($\alpha = 2, \beta = 2H, \theta = 0, D_0 = 0.31$), **(E–H)** with $H = 0.3$ and ($\alpha = 2, \beta = 2H, \theta = 0, D_0 = 0.22$), **(I–L)** with $H = 0.35$ and ($\alpha = 2, \beta = 2H, \theta = 0, D_0 = 0.16$), **(M–P)** with $H = 0.4$ and ($\alpha = 2, \beta = 2H, \theta = 0, D_0 = 0.12$).

In contrast to prior work, we investigated the effectiveness and robustness of the proposed algorithmic approach for estimating the correct parameters as a function of the available number of trajectories. From our simulation results, we observe that for all considered types of diffusion models except the classical one (i.e., all combination of the parameters α, β, θ, and D), a few number of recorded time-series (less than 100 trajectories) is required to attain the correct estimation of the PDE parameters with less then 2% confidence interval. For the case of the normal diffusion (i.e., except for the case $\alpha = 2$ and $\beta = 1$), we may need more trajectories to achieve similar accuracy. Therefore, we hope that the proposed algorithms will help the community to better analyze complex spatiotemporal data, in order to unravel new physical laws in different applications (social networks, neuroscience, etc.) and decipher the causal interdependence between different processes.

Furthermore, we performed a study on the properties of fBm processes. We can remark from the Fokker Planck equation

TABLE 4 | Numerical results for fBm parameter estimation.

Parameters	Algorithm-1			Algorithm-2		
	$N_{90}^{(1)}$	Final value	Final relative error	$N_{90}^{(2)}$	Final value	Final relative error
			$H = 0.25$			
α	−−	1.794	10.300%	10	1.998	**0.100%**
β	210	0.459	8.200%	10	0.511	**2.200%**
θ	−−	−0.006	−−	−−	−0.006	−−
D	−−	0.426	36.132%	−−	0.386	**23.350%**
			$H = 0.30$			
α	−−	1.733	13.350%	10	2.000	**0.000%**
β	−−	0.527	12.167%	10	0.609	**1.500%**
θ	−−	0.023	−−	−−	0.026	−−
D	−−	0.325	42.284%	−−	0.273	**19.518%**
			$H = 0.35$			
α	−−	1.689	15.550%	10	1.983	**0.850%**
β	−−	0.581	17.000%	10	0.683	**2.429%**
θ	−−	0.015	−−	−−	0.018	−−
D	−−	0.269	62.570%	−−	0.213	**28.727%**
			$H = 0.40$			
α	−−	1.587	20.650%	10	2.000	**0.000%**
β	−−	0.635	20.625%	10	0.801	**0.125%**
θ	−−	−0.016	−−	−−	−0.020	−−
D	−−	0.217	70.179%	−−	0.144	**12.930%**

The bold values are used to highlight the best performance for each case across the 2 algorithms.

associated with the fBm process, mentioned in the manuscript, that the effective diffusion coefficient is time-dependent. Even though, this type of equation does not perfectly match the class of fractional diffusion equation that we are dealing with in this work, we applied the proposed algorithms to a dataset of trajectories generated according to the fBm model to retrieve the Hurst exponent and the diffusion constant. Indeed, we were able to identify these parameters since the absolute and signed absolute moments present similar structure as the ones calculated for a process that is generated according to the fractional diffusion equation under study. Therefore, we provide a new/alternative approach to quantify the memory of a fBm process. Note that without knowing the model that governs the dynamics of the process and using this framework, we can estimate the parameters α and θ to be equal to 2 and 0, respectively, but in the current stage we are not able to confirm that the data is generated either from a space-time fractional diffusion equation with a constant generalized diffusion coefficient or from a fBm process with time varying diffusion coefficient. In future work, we will push forward the analysis to identify whether the diffusion coefficient is time-dependent or it is a constant, and thus to differentiate between the space-time fractional diffusion equation and the Fokker Planck equation associated with the fBm process.

This mathematical formalism can be further developed and generalized to include additional operators and take into account advection phenomena as well as combined with other advanced statistics and information theory inspired methods to discriminate among various mathematical expressions (operators) in order to either identify the dominant physical phenomenon (or rule) governing the measurements or to determine the degree to which multiple physical laws contribute to the observed dynamics. Also, analyzing noisy data originated from real world applications will be taken into account in order to cope with complex scenario. We plan to build on these grounds, enrich the mathematical formalism and contribute to a significant paradigm shift in the context of data-driven discovery architectures of physical phenomena as well as enabling accurate predictions concerning complex evolving systems without requiring to know the regimes of variation for parameters, the types of mathematical operators or the fact that the data should be sampled at a particular level.

DATA AVAILABILITY STATEMENT

The raw data supporting the conclusions of this article will be made available by the authors, without undue reservation, to any qualified researcher.

AUTHOR CONTRIBUTIONS

MZ and GG have equal contribution to the manuscript. MZ, GG, and PB contributed to formulating the problem, setup the experimental case studies, and wrote the manuscript. MZ and GG collaborated on the design of the simulations, run comprehensive case studies, processed the simulation data, prepared the plots and modified the supplementary material. KA contributed to the design of some of the simulations and wrote some parts of the supplementary material.

FUNDING

The authors gratefully acknowledge the support by the National Science Foundation under the Career Award CPS/CNS-1453860, the NSF award under Grant numbers CCF-1837131, MCB-1936775, and CNS-1932620, the U.S. Army Research Office (ARO) under Grant No. W911NF-17-1-0076 and the DARPA Young Faculty Award and DARPA Director Award, under grant number N66001-17-1-4044, and a Northrop Grumman grant. The views, opinions, and/or findings contained in this article are those of the authors and should not be interpreted as representing the official views or policies, either expressed or implied by the Defense Advanced Research Projects Agency, the Department of Defense or the National Science Foundation.

SUPPLEMENTARY MATERIAL

The Supplementary Material for this article can be found online at: https://www.frontiersin.org/articles/10.3389/fams.2020.00014/full#supplementary-material

The code to reproduce the results is available at: https://github.com/gaurav71531/fractDiffusion.

REFERENCES

1. Alber M, Tepole AB, Cannon WR, De S, Dura-Bernal S, Garikipati K, et al. Integrating machine learning and multiscale modeling–perspectives, challenges, and opportunities in the biological, biomedical, and behavioral sciences. *NPJ Digital Med*. (2019) **2**:115. doi: 10.1038/s41746-019-0193-y
2. Gruson D, Helleputte T, Rousseau P, Gruson D. Data science, artificial intelligence, and machine learning: Opportunities for laboratory medicine and the value of positive regulation. *Clin Biochem*. (2019) **69**:1–7. doi: 10.1016/j.clinbiochem.2019.04.013
3. Bergen KJ, Johnson PA, de Hoop MV, Beroza GC. Machine learning for data-driven discovery in solid Earth geoscience. *Science*. (2019) **363**:eaau0323. doi: 10.1126/science.aau0323
4. He J, Baxter SL, Xu J, Xu J, Zhou X, Zhang K. The practical implementation of artificial intelligence technologies in medicine. *Nat Med*. (2019) **25**:30–36. doi: 10.1038/s41591-018-0307-0
5. Barnette DA, Davis MA, Dang NL, Pidugu AS, Hughes T, Swamidass SJ, et al. Lamisil (terbinafine) toxicity: determining pathways to bioactivation through computational and experimental approaches. *Biochem Pharmacol*. (2018) **156**:10–21. doi: 10.1016/j.bcp.2018.07.043
6. Udrescu L, Sbarcea L, Topirceanu A, Iovanovici A, Kurunczi L, Bogdan P, et al. Clustering drug-drug interaction networks with energy model layouts: community analysis and drug repurposing. *Sci Rep*. (2016) **6**:32745. doi: 10.1038/srep32745
7. Marinelli B, Kang M, Martini M, Zech JR, Titano J, Cho S, et al. Combination of active transfer learning and natural language processing to improve liver volumetry using surrogate metrics with deep learning. *Radiol Artif Intell*. (2019) **1**:e180019. doi: 10.1148/ryai.2019180019
8. Yang J, Feng X, Laine A, Angelini E. Characterizing Alzheimer's disease with image and genetic biomarkers using supervised topic models. *IEEE J Biomed Health Inform*. (2019) **24**:1180–7. doi: 10.1109/JBHI.2019.2928831
9. Hazlett HC, Gu H, Munsell BC, Kim SH, Styner M, Wolff JJ, et al. Early brain development in infants at high risk for autism spectrum disorder. *Nature*. (2017) **542**:348. doi: 10.1038/nature21369
10. Ting DSW, Pasquale LR, Peng L, Campbell JP, Lee AY, Raman R, et al. Artificial intelligence and deep learning in ophthalmology. *Brit J Ophthalmol*. (2019) **103**:167–75. doi: 10.1136/bjophthalmol-2018-313173
11. Furquim G, Pessin G, Faiçal BS, Mendiondo EM, Ueyama J. Improving the accuracy of a flood forecasting model by means of machine learning and chaos theory. *Neural Comput Appl*. (2016) **27**:1129–41. doi: 10.1007/s00521-015-1930-z
12. Mojaddadi H, Pradhan B, Nampak H, Ahmad N, bin Ghazali AH. Ensemble machine-learning-based geospatial approach for flood risk assessment using multi-sensor remote-sensing data and GIS. *Geomat Nat Hazards Risk*. (2017) **8**:1080–102. doi: 10.1080/19475705.2017.1294113
13. Fox C, Nicholls G. Statistical estimation of the parameters of a PDE. *Can appl Math Quater*. (2001) 10:277–306.
14. Müller TG, Timmer J. Fitting parameters in partial differential equations from partially observed noisy data. *Phys D Nonlinear Phenomena*. (2002) **171**:1–7. doi: 10.1016/S0167-2789(02)00546-8
15. Xun X, Cao J, Mallick B, Maity A, Carroll RJ. Parameter estimation of partial differential equation models. *J Am Stat Assoc*. (2013) **108**:1009–20. doi: 10.1080/01621459.2013.794730
16. Liang H, Wu H. Parameter estimation for differential equation models using a framework of measurement error in regression models. *J Am Stat Assoc*. (2008) **103**:1570–83. doi: 10.1198/016214508000000797
17. Bär M, Hegger R, Kantz H. Fitting partial differential equations to space-time dynamics. *Phys Rev E*. (1999) **59**:337. doi: 10.1103/PhysRevE.59.337
18. Müller T, Timmer J. Parameter identification techniques for partial differential equations. *Int J Bifurcat Chaos*. (2004) **14**:2053–60. doi: 10.1142/S0218127404010424
19. Voss HU, Kolodner P, Abel M, Kurths J. Amplitude equations from spatiotemporal binary-fluid convection data. *Phys Rev Lett*. (1999) **83**:3422. doi: 10.1103/PhysRevLett.83.3422
20. Einstein A. Über die von der molekularkinetischen Theorie der Wärme geforderte Bewegung von in ruhenden Flüssigkeiten suspendierten Teilchen. *Annalen der Physik*. (1905). 322:549–60. doi: 10.1002/andp.19053220806
21. Barkai E, Garini Y, Metzler R. Strange kinetics of single molecules in living cells. *Phys Tdy*. (2012) **65**:29–5. doi: 10.1063/PT.3.1677
22. Tolić-Nørrelykke IM, Munteanu EL, Thon G, Oddershede L, Berg-Sorensen K. Anomalous diffusion in living yeast cells. *Phys Rev Lett*. (2004) **93**:078102. doi: 10.1103/PhysRevLett.93.078102
23. Jeon JH, Tejedor V, Burov S, Barkai E, Selhuber-Unkel C, Berg-Sørensen K, et al. *In vivo* anomalous diffusion and weak ergodicity breaking of lipid granules. *Phys Rev Lett*. (2011) **106**:048103. doi: 10.1103/PhysRevLett.106.048103
24. Goychuk I. Anomalous transport of subdiffusing cargos by single kinesin motors: the role of mechano-chemical coupling and anharmonicity of tether. *Phys Biol*. (2015) **12**:016013. doi: 10.1088/1478-3975/12/1/016013
25. Koorehdavoudi H, Bogdan P, Wei G, Marculescu R, Zhuang J, Carlsen RW, et al. Multi-fractal characterization of bacterial swimming dynamics: a case study on real and simulated serratia marcescens. *Proc R Soc A Math Phys Eng Sci*. (2017) **473**:20170154. doi: 10.1098/rspa.2017.0154
26. Papo D. Functional significance of complex fluctuations in brain activity: from resting state to cognitive neuroscience. *Front Syst Neurosci*. (2014) **8**:112. doi: 10.3389/fnsys.2014.00112
27. Gupta G, Pequito S, Bogdan P. Dealing with unknown unknowns: Identification and selection of minimal sensing for fractional dynamics with unknown inputs. In: *2018 Annual American Control Conference (ACC)*. Milwaukee, WI: IEEE (2018). p. 2814–20. doi: 10.23919/ACC.2018.8430866
28. Gupta G, Pequito S, Bogdan P. Learning latent fractional dynamics with unknown unknowns. In: *2019 American Control Conference (ACC)*. Philadelphia, PA (2019). p. 217–22. doi: 10.23919/ACC.2019.8815074
29. Xue Y, Bogdan P. Constructing compact causal mathematical models for complex dynamics. In: *Proceedings of the 8th International Conference on Cyber-Physical Systems. ICCPS '17*. Pittsburgh, PA: ACM (2017). p. 97–107. doi: 10.1145/3055004.3055017
30. Yang R, Gupta G, Bogdan P. Data-driven perception of neuron point process with unknown unknowns. In: *Proceedings of the 10th ACM/IEEE International Conference on Cyber-Physical Systems. ICCPS '19*. Montreal, QC (2019). p. 259–69. doi: 10.1145/3302509.3311056
31. Gefen Y, Aharony A, Alexander S. Anomalous diffusion on percolating clusters. *Phys Rev Lett*. (1983) **50**:77–80. doi: 10.1103/PhysRevLett.50.77
32. Klafter J, Blumen A, Shlesinger MF. Stochastic pathway to anomalous diffusion. Phys Rev A. (1987) **35**:3081–5. doi: 10.1103/PhysRevA.35.3081
33. Bouchaud JP, Georges A. Anomalous diffusion in disordered media: Statistical mechanisms, models and physical applications. *Phys Rep*. (1990) **195**:127–293. doi: 10.1016/0370-1573(90)90099-N
34. Metzler R, Klafter J. The random walk's guide to anomalous diffusion: a fractional dynamics approach. *Phys Rep*. (2000) **339**:1–77. doi: 10.1016/S0370-1573(00)00070-3
35. Metzler R, Glockle WG, Nonnenmacher TF. Fractional model equation for anomalous diffusion. *Phys A Stat Mech Appl*. (1994) **211**:13–24. doi: 10.1016/0378-4371(94)90064-7
36. Metzler R, Klafter J. The restaurant at the end of the random walk: recent developments in the description of anomalous transport by fractional dynamics. *J Phys A Math Gen*. (2004) **37**:R161. doi: 10.1088/0305-4470/37/31/R01
37. Klafter J, Sokolov IM. Anomalous diffusion spreads its wings. *Phys World*. (2005) **18**:29–32. doi: 10.1088/2058-7058/18/8/33
38. Thiel F, Flegel F, Sokolov IM. Disentangling sources of anomalous diffusion. *Phys Rev Lett*. (2013) **111**:010601. doi: 10.1103/PhysRevLett.111.010601
39. McKinley SA, Nguyen HD. Anomalous diffusion and the generalized Langevin equation. *SIAM J Math Anal*. (2018) **50**:5119–60. doi: 10.1137/17M115517X
40. Oliveira FA, Ferreira RMS, Lapas LC, Vainstein MH. Anomalous diffusion: a basic mechanism for the evolution of inhomogeneous systems. *Front Phys*. (2019) **7**:18. doi: 10.3389/fphy.2019.00018
41. Morgado R, Oliveira FA, Batrouni GG, Hansen A. Relation between anomalous and normal diffusion in systems with memory. *Phys Rev Lett*. (2002) **89**:100601. doi: 10.1103/PhysRevLett.89.100601
42. Metzler R, Jeon JH, Cherstvy AG, Barkai E. Anomalous diffusion models and their properties: non-stationarity, non-ergodicity, and ageing at the centenary

of single particle tracking. *Phys Chem Chem Phys*. (2014) **16**:24128–64. doi: 10.1039/C4CP03465A

43. Sokolov IM. Models of anomalous diffusion in crowded environments. *Soft Matter*. (2012) **8**:9043–52. doi: 10.1039/c2sm25701g
44. Grmela M, Öttinger HC. Dynamics and thermodynamics of complex fluids. I. Development of a general formalism. *Phys Rev E*. (1997) **56**:6620. doi: 10.1103/PhysRevE.56.6620
45. Cabreira RG, da Silva Ferreira A, Kouyaté M, Demouchy G, Mériguet G, Aquino R, et al. Thermodiffusion of repulsive charged nanoparticles-the interplay between single-particle and thermoelectric contributions. *Phys Chem Chem Phys*. (2018) **20**:16402–13. doi: 10.1039/C8CP02558D
46. Brangwynne CP, Koenderink GH, MacKintosh FC, Weitz DA. Intracellular transport by active diffusion. *Trends Cell Biol*. (2009) **19**:423–7. doi: 10.1016/j.tcb.2009.04.004
47. Palmieri B, Bresler Y, Wirtz D, Grant M. Multiple scale model for cell migration in monolayers: elastic mismatch between cells enhances motility. *Sci Rep*. (2015) **5**:11745. doi: 10.1038/srep11745
48. Lomholt MA, Ambjörnsson T, Metzler R. Optimal target search on a fast-folding polymer chain with volume exchange. *Phys Rev Lett*. (2005) **95**:260603. doi: 10.1103/PhysRevLett.95.260603
49. Klages R, Radons, G, Sokolov IM. *Anomalous Transport: Foundations and Applications.* Weinheim: John Wiley & Sons, Ltd. (2008). doi: 10.1002/9783527622979
50. Mandelbrot BB. *The Fractal Geometry of Nature. Einaudi Paperbacks*. 3rd edn. San Francisco, CA: W. H. Freeman and Company (1983). Available online at: https://books.google.com/books?id=SWcPAQAAMAAJ
51. Balankin AS. Mapping physical problems on fractals onto boundary value problems within continuum framework. *Phys Lett A*. (2018) **382**:141–46. doi: 10.1016/j.physleta.2017.11.005
52. Bogdan P, Marculescu R. A fractional calculus approach to modeling fractal dynamic games. In: *2011 50th IEEE Conference on Decision and Control and European Control Conference*. Orlando, FL: IEEE (2011). p. 255–60. doi: 10.1109/CDC.2011.6161323
53. Scalas E. The application of continuous-time random walks in finance and economics. *Phys A Stat Mech Appl*. (2006) **362**:225–39. doi: 10.1016/j.physa.2005.11.024
54. Morgado R, Cieśla M, Longa L, Oliveira FA. Synchronization in the presence of memory. *Europhys Lett*. (2007) **79**:10002. doi: 10.1209/0295-5075/79/10002
55. Lapas L, Costa I, Vainstein M, Oliveira F. Entropy, non-ergodicity and non-Gaussian behaviour in ballistic transport. *Europhys Lett*. (2007) **77**:37004. doi: 10.1209/0295-5075/77/37004
56. Kusmierz L, Dybiec B, Gudowska-Nowak E. Thermodynamics of superdiffusion generated by Lévy-Wiener fluctuating forces. *Entropy*. (2018) **20**:658. doi: 10.3390/e20090658
57. Pérez-Madrid A. Gibbs entropy and irreversibility. *Phys A Stat Mech Appl*. (2004) **339**:339–46. doi: 10.1016/j.physa.2004.04.106
58. Gorenflo R, Mainardi F. Fractional diffusion processes: probability distributions and continuous time random walk. In: Rangarajan G, Ding M, editors. *Processes with Long-Range Correlations: Theory and Applications*. Berlin; Heidelberg: Springer (2003). p. 148–66. doi: 10.1007/3-540-44832-2_8
59. Metzler R, Barkai E, Klafter J. Anomalous diffusion and relaxation close to thermal equilibrium: a fractional Fokker-Planck equation approach. *Phys Rev Lett*. (1999) **82**:3563–7. doi: 10.1103/PhysRevLett.82.3563
60. Schwarzl M, Godec A, Metzler R. Quantifying non-ergodicity of anomalous diffusion with higher order moments. *Sci Rep*. (2017) **7**:3878. doi: 10.1038/s41598-017-03712-x
61. Gorenflo R, Mainardi F. Parametric subordination in fractional diffusion processes. *arXiv preprint arXiv:12108414* (2012). doi: 10.1142/9789814340595_0010
62. Mainardi F, Luchko Y, Pagnini G. The fundamental solution of the space-time fractional diffusion equation. *arXiv preprint arXiv:cond-mat/0702419* (2007).
63. Saichev AI, Zaslavsky GM. Fractional kinetic equations: solutions and applications. *Chaos*. (1997) **7**:753–64. doi: 10.1063/1.166272
64. Gorenflo R, Iskenderov A, Luchko Y. Mapping between solutions of fractional diffusion-wave equations. *Fract Calculus Appl Anal*. (2000) **3**:75–86.
65. Scalas E, Gorenflo R, Mainardi F. Fractional calculus and continuous-time finance. *Phys A Stat Mech Appl*. (2000) **284**:376–84. doi: 10.1016/S0378-4371(00)00255-7
66. Feller W. *On a Generalization of Marcel Riesz' Potentials and the Semi-groups Generated by Them*. Gleerup. (1962) Available online at: https://books.google.com/books?id=UZTqjwEACAAJ
67. Caputo M. Linear models of dissipation whose Q is almost frequency independent-II. *Geophys J Int*. (1967) **13**:529–39. doi: 10.1111/j.1365-246X.1967.tb02303.x
68. Gorenflo R, Mainardi F, Moretti D, Pagnini G, Paradisi P. Discrete random walk models for space-time fractional diffusion. *Chem Phys*. (2002) **284**:521–41. doi: 10.1016/S0301-0104(02)00714-0
69. Metzler R, Nonnenmacher TF. Space- and time-fractional diffusion and wave equations, fractional Fokke-Planck equations, and physical motivation. *Chem Phys*. (2002) **284**:67–90. doi: 10.1016/S0301-0104(02)00537-2
70. Luchko Y. Models of the neutral-fractional anomalous diffusion and their analysis. *AIP Conf Proc*. (2012) **1493**:626–32. doi: 10.1063/1.4765552
71. Tarasov VE. *Handbook of Fractional Calculus with Applications: Applications in Physics (Part 2)*. Berlin; Boston, MA: De Gruyter (2019).
72. Wang K, Lung C. Long-time correlation effects and fractal Brownian motion. *Phys Lett A*. (1990) **151**:119–21. doi: 10.1016/0375-9601(90)90175-N

Conflict of Interest: The authors declare that the research was conducted in the absence of any commercial or financial relationships that could be construed as a potential conflict of interest.

frontiers in Physics

REVIEW
published: 17 September 2020
doi: 10.3389/fphy.2020.00292

Anomalous Heat Transport in Classical Many-Body Systems: Overview and Perspectives

Giuliano Benenti[1,2,3], *Stefano Lepri*[4,5*] *and Roberto Livi*[4,5,6]

[1] *Dipartimento di Scienza e Alta Tecnologia, Center for Nonlinear and Complex Systems, Università degli Studi dell'Insubria, Como, Italy,* [2] *Istituto Nazionale di Fisica Nucleare, Sezione di Milano, Milan, Italy,* [3] *NEST, Istituto Nanoscienze-Consiglio Nazionale delle Ricerche, Pisa, Italy,* [4] *Consiglio Nazionale delle Ricerche, Istituto dei Sistemi Complessi, Florence, Italy,* [5] *Istituto Nazionale di Fisica Nucleare, Sezione di Firenze, Florence, Italy,* [6] *Dipartimento di Fisica e Astronomia and CSDC, Universitá di Firenze, Sesto Fiorentino, Italy*

In this review paper we survey recent achievements in anomalous heat diffusion, while highlighting open problems and research perspectives. First, we briefly recall the main features of the phenomenon in low-dimensional classical anharmonic chains and outline some recent developments in the study of perturbed integrable systems and the effect of long-range forces and magnetic fields. Selected applications to heat transfer in material science at the nanoscale are described. In the second part, we discuss of the role of anomalous conduction in coupled transport and describe how systems with anomalous (thermal) diffusion allow a much better power-efficiency trade-off for the conversion of thermal to particle current.

Keywords: anomalous transport and diffusion, non-linear chains, Kardar Parisi Zhang equation, thermoelectricity, efficiency, multi-particle-collision

Edited by:
Carlos Mejía-Monasterio,
Polytechnic University of Madrid,
Spain

Reviewed by:
Hernán Larralde,
National Autonomous University of Mexico, Mexico
Cédric Bernardin,
Université Côte d'Azur, France

***Correspondence:**
Stefano Lepri
stefano.lepri@isc.cnr.it

Specialty section:
This article was submitted to Interdisciplinary Physics, a section of the journal Frontiers in Physics

Received: *12 February 2020*
Accepted: *26 June 2020*
Published: *17 September 2020*

Citation:
Benenti G, Lepri S and Livi R (2020) Anomalous Heat Transport in Classical Many-Body Systems: Overview and Perspectives. Front. Phys. 8:292. doi: 10.3389/fphy.2020.00292

1. INTRODUCTION

Anomalous diffusion is a well-established concept in statistical physics and has been used to describe many diverse kinetic phenomena. Detailed insights have been gained by generalizing the motion of Brownian particles, as done for the continuous-time random walk and for Lèvy flights and walks. A formidable body of literature on the topic exists; we refer to, for example, Klages et al. [1] as well as the present issue for an overview.

The above particle models are based on a single-particle description, whereby a single walker performs a non-standard diffusive motion. How do the features of anomalous diffusion emerge when dealing with a many-body problem? What are the conditions for a statistical system composed of many interacting particles to yield effectively anomalous diffusion of particles or quasi-particles? Another question concerns how such anomalies in diffusion are related to transport and whether they can somehow be exploited to achieve some design principle, such as efficiency of energy conversion. In fact, although thermoelectric phenomena have been known for centuries, it is only recently that a novel point of view on the problem has emerged [2]. Generally speaking, the renewed research activity is motivated also by the possibility of applying the thermodynamics and statistical mechanics to nano- and micro-sized systems, with applications in molecular biology, micro-mechanics, nano-phononics, etc. This involves dealing with systems far from the thermodynamic limit, where fluctuations and interactions with the environment are critically relevant and need to be understood in detail.

In this article, we first review how anomalous energy diffusion arises in lattices of classical oscillators as a joint effect of non-linear forces and reduced dimensionality (and in this respect we will mostly discuss one-dimensional chains). This amounts to saying that the anomalous dynamics of energy carriers is an emergent feature stemming from correlations of the full many-body dynamics. As a consequence, Fourier's law breaks down: the motion of energy carriers is so correlated that they are able to propagate faster than diffusively. In the second part of the paper, we discuss how this feature influences coupled transport and how it can be used to enhance the efficiency of thermodiffusive processes.

We conclude our review of the multifaceted problem of heat transport in classical systems with a short summary of possible extensions to the quantum domain, with reference to related open problems that merit attention in the near future.

2. ANOMALOUS HEAT TRANSPORT IN CLASSICAL ANHARMONIC LATTICES

The presence of a heat conductivity that diverges with the system size in a chain of coupled non-linear oscillators was first pointed out in Lepri et al. [3, 4]. This marked the beginning of a research endeavor that, over more than two decades, has been devoted to understanding the mechanisms giving rise to anomalous transport in low-dimensional systems. Far from being a purely academic exercise, this research has unveiled the possibility of observing such peculiar effects in nanomaterials, such as nanotubes, nanowires, or graphene [5, 6]. Extended review articles on this problem have existed for many years [7, 8], while a collection of works about more recent achievements can be found in Lepri [9] and a review article [10] in the present issue. Here it is useful to first provide a short summary of the state of the art in the field, while the main part of the paper will focus on recent achievements that point to promising and challenging directions for future investigations.

In any model where anomalous transport has been observed, it emerges as a hydrodynamic effect due to a combination of reduced space dimensionality and conservation laws, yielding non-standard relaxation properties even in a linear response regime. As a reference we consider the basic class of models represented by a Hamiltonian of the following form:

$$H = \sum_{n=1}^{L} \left[\frac{p_n^2}{2m} + V(q_{n+1} - q_n) \right]. \tag{1}$$

Typical choices for the interaction include the famous Fermi-Pasta-Ulam-Tsingou (FPUT) potential, where $V(x) = V_{\mathrm{FPUT}}(x) \equiv \frac{1}{2}x^2 + \frac{\alpha}{3}x^3 + \frac{\beta}{4}x^4$, and the rotor (or Hamiltonian XY) model, where $V(x) = V_{XY}(x) \equiv 1 - \cos x$. With regard to conservation laws, in $d = 1$ anomalous transport has been generically observed in Hamiltonian models of type (1), where energy, momentum, and the "stretch" variable $\sum_n (q_{n+1} - q_n)$ are conserved. It is worth recalling that any approach aiming to describe out-of-equilibrium conditions, such as stationary transport processes, has to be based on the hydrodynamic equations associated with such locally conserved quantities. One-dimensional oscillator models with only one conserved quantity, such as the Frenkel-Kontorova or ϕ^4 models [11], or two conserved quantities, such as the rotor model [12, 13] or the discrete non-linear Schrödinger lattice [14, 15], instead show standard diffusive transport. Intuitively, this is due to the presence of scattering sources for acoustic waves propagating through the lattice induced by the presence of a local non-linear potential, which breaks translation invariance (i.e., momentum conservation). This argument does not apply to the rotor model, where only the stretch variable is not conserved, owing to the angular nature of the q_n variables; in any case standard diffusion is allowed because of the boundedness of the cosine potential. Concerning dimensionality, in $d = 3$ normal diffusion regimes are expected to characterize heat transport in non-linear lattices. Only in $d = 2$ can one find evidence of a diverging heat conductivity that exhibits a logarithmic dependence on the system size L [16–18].

The main distinctive feature of anomalous heat transport in one-dimensional Hamiltonian models of anharmonic lattices is that the finite-size heat conductivity $\kappa(L)$ diverges in the limit $L \to \infty$ of a large system size [3] as

$$\kappa(L) \propto L^{\gamma},$$

with $0 < \gamma \leq 1$ (the $\gamma = 1$ case corresponds to integrable models, such as the Toda lattice discussed in section 2.2). This implies that this transport coefficient is, in the thermodynamic limit, not well-defined. In the linear response regime, this is equivalent to finding that the equilibrium correlator of the energy current $J(t)$ displays, for long times t, a non-integrable power-law decay of the form

$$\langle J(t)J(0)\rangle \propto t^{-(1-\delta)}, \tag{2}$$

with $0 \leq \delta < 1$. Accordingly, the Green-Kubo formula yields an infinite value of the heat conductivity and allows one to establish the equivalence of the exponents, i.e., $\gamma = \delta$, provided that the sound velocity is finite [4]. In **Figure 1** we show two typical simulations of the FPUT model demonstrating the results above.

The most basic issue of the anomalous feature relates to anomalous dynamical scaling of the equilibrium correlation of the hydrodynamic modes. A simple way to state this is that fluctuations of the conserved quantities with small wavenumber k evolve on time scales of order $\tau(k) \sim |k|^{-z}$. For standard diffusion one has $z = 2$. Within the non-linear fluctuating hydrodynamics approach it has been shown [19, 20] that models like (1) belong generically to the universality class of the famous Kardar-Parisi-Zhang (KPZ) equation, originally formulated in the context of growing interfaces. It is well-known that this equation in $d = 1$ is characterized by the dynamical exponent $z = 3/2$. The origin of this non-trivial dynamical exponent can be traced back to the non-linear interaction of long-wavelength modes. This leads to the prediction $\gamma = (2 - z)/z = 1/3$ (at least in the linear response regime), a value that should be largely universal, as confirmed by many numerical experiments.

The above consideration applies generically to anharmonic chains with three conservation laws [20]. There is, however, the possibility of having a different universality class depending on the number of conserved quantities [21] or on the non-linear

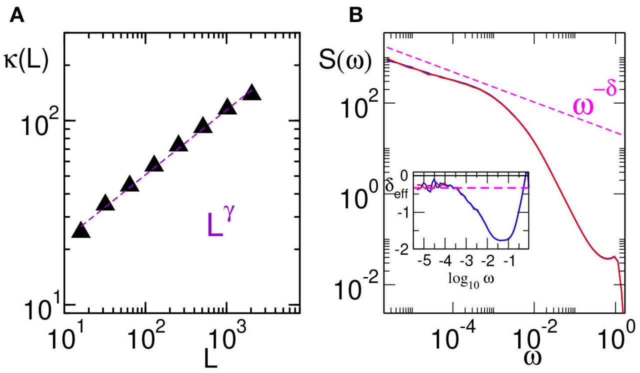

FIGURE 1 | Anomalous thermal conductivity for the FPUT model with cubic and quartic potential terms ($\alpha = 0.25$, $\beta = 1$): **(A)** finite-size conductivity measured in the non-equilibrium steady state; **(B)** power spectrum $S(\omega)$ of heat current fluctuations [i.e., the Fourier transform of $\langle J(t)J(0)\rangle$]. The long-time tail in (2) corresponds to a divergence $\omega^{-\delta}$ at small frequencies. The inset of **(B)** displays the logarithmic derivative $\delta_{\mathrm{eff}} = d\log_{10} S/d\log_{10}\omega$. The data are compatible with $\delta = \gamma = 1/3$ (dashed lines). Microcanonical simulations are performed at energy density 0.5.

coupling between the hydrodynamic modes [20]. For instance, model (1) with an even potential $V(x) = V(-x)$ should belong to a different universality class having a different exponent γ. In fact, the precise value of γ is still somewhat controversial: the theoretical prediction from the mode-coupling approximation of the hydrodynamic theory yields $\gamma = 1/2$ [20, 22, 23], while kinetic theory yields $\gamma = 2/5$ [24], a value closer to that measured numerically [25, 26] (see also [27, 28] for related results on exactly solvable models). The existence of the two classes can be demonstrated either by direct measurement of the exponents [25] or via suitable changes of the thermodynamic parameters. For instance, a non-linear chain with a symmetric potential subject to a suitable pressure acting at its boundaries may exhibit a change from exponent $\gamma = 1/2$ to $\gamma = 1/3$ [29]. This observation is relevant to possible experimental verification of anomalous heat transport, as it indicates that the pressure or torque applied to any one-dimensional material should be taken into account for a correct comparison with theoretical predictions.

A physically intuitive way to describe anomalous heat transport is to think in terms of a Lévy walk, namely an ensemble of random walkers performing free ballistic steps with finite velocity for times that are power-law distributed [30]. This simple description accounts very well for many features of anharmonic lattices and fluids in various non-equilibrium settings [31–33]. For instance, energy perturbations propagate superdiffusively [31, 34, 35]: an initially localized perturbation of the energy broadens, and its variance grows in time as $\sigma^2 \propto t^\eta$ with $\eta > 1$. These empirical observations have a theoretical justification within the framework of non-linear fluctuating hydrodynamics. Indeed, the theory predicts a hydrodynamic "heat mode" that has the characteristic shape given by a Lévy-stable distribution [see [20, 36] for details]. Further support comes from mathematical results: superdiffusive behavior has been proven for one-dimensional infinite chains of harmonic oscillators undergoing stochastic collisions that conserve energy and momentum [37, 38]. In the same spirit, the more difficult case of non-linear oscillators with conservative noise has been discussed [39]. For exponential interactions (the Kac-van Moerbecke model), superdiffusion of energy has again been demonstrated, and a lower bound on the decay of the current correlation function has been obtained [40]. In reference [20] it is argued that such models should also belong to the KPZ class.

A related distinctive feature of anomalous transport is that the temperature profiles in non-equilibrium steady states are non-linear, even for vanishing applied temperature gradients [32, 41]. There is indeed a close connection with the fractional heat equation, which has been demonstrated and discussed in recent literature [10, 42].

2.1. The Importance of Being Small

As mentioned above, theoretical results on the problem of heat transport in anharmonic chains are based on the fundamental assumption that one should compute any relevant quantity in the limits $L \to \infty$ and $t \to \infty$, performed in that specific order. On the other hand, in any numerical simulation or for real low-dimensional heat conductors, such as nanowires, carbon nanotubes, polymers, or even thin fibers, one has to deal with finite size and finite time corrections. These can be controlled in a linear response regime if the mean free path of propagating excitations, λ, and their mean interaction time, τ, are such that $\lambda \ll L$ and $\tau \ll t$. It is a fact that when dealing with models of anharmonic chains, such control is often not guaranteed, mainly because of non-linear effects. This is a very relevant problem also for interpreting possible experimental verifications of anomalous transport in real systems as well as for designing nanomaterials that exhibit deviations from the standard diffusive conductivity.

In fact, severe finite size effects invariably arise when one tries to check predictions numerically. Very often, estimates of the relevant exponents γ and δ systematically deviate from the expected values and sometimes even seem to depend on parameters [43–46]. If universality were to hold (as we believe), these effects should be due to subleading corrective terms to the asymptotics that are still relevant on the scales accessible in simulations. Besides these issues, other unexpected effects arise. For instance, for the FPUT [47], Toda [43], and Kac-van Moerbecke [38] chains perturbed by conservative noise, the exponent γ increases with the noise strength. Apart from the problem of evaluating the precise exponents, this observation is quite surprising since it suggests that greater stochasticity in the model makes the system more diffusive, at least for finite systems.

Another example of finite size corrections being "amplified" by non-linear effects is the case of anharmonic chains with asymmetric potential, i.e., where $V(x) \neq V(-x)$ as in the FPUT model with $\alpha \neq 0$. As shown in **Figure 1**, both equilibrium and out-of-equilibrium measurements of the heat conductivity in the presence of an applied thermal gradient are usually consistent with KPZ scaling. However, in other temperature regimes Fourier's law appears to hold, i.e., thermal conductivity is constant over a large range of sizes [48]. This has been traced back to the relatively long relaxation time of mass inhomogeneities induced by the asymmetry of the interaction potential and acting as scatterers of phonons [48]. Actually, it was later shown in Wang et al. [49], Das et al. [50], and Chen et al. [51] that this is a strong finite size effect, as it persists for relatively large values of L and t. Yet, the expected theoretical prediction of a diverging heat conductivity can be recovered in simulations performed for sufficiently large values of L and t. It should be pointed out that all of these speculations are based on numerical results, and a theoretical approach capable of providing estimates for the combination of non-linear and finite size corrections to the hydrodynamics would be useful. Indeed, fluctuating hydrodynamics can provide some kind of prediction: subleading corrections to the leading asymptotic decay in (2) can be very large and decay very slowly [20].

There are other aspects to finite size effects. A remarkable example is the discrete non-linear Schrödinger equation, a well-known model for atomic condensates in periodic optical lattices. The model has two conserved quantities (energy and number density) and exhibits normal diffusive transport [14]. However, at very low temperatures another almost-conserved quantity (the phase difference between oscillators) appears, and for a finite chain and long times the dynamics is the same as that of a generic anharmonic model, leading to KPZ scaling of correlations and anomalous transport [52, 53]. Further unexpected features have been reported also in Xiong and Zhang [54], where the authors study this problem for the FPUT-β model (i.e., Equation 1) with $V = V_{\mathrm{FPUT}}$ and $\alpha = 0$) with an additional local, also called "pinning," potential of the form

$$U(q) = \frac{1}{2}\sum_{n=1}^{L} q_n^2 . \tag{3}$$

This term breaks translational invariance, making energy the sole conserved quantity. By varying the non-linear coupling β, one observes a crossover from ballistic transport, typical of an integrable model, to an anomalous diffusive regime governed by an exponent of the time correlation function, which corresponds to a value of $\gamma \sim 0.2$. The crossover occurs in the parameter region $0.1 < \beta < 1$. Numerical simulations performed for a chain of a few thousands of oscillators show that further increasing β seems to yield an increasing γ. The overall outcome challenges the basic theoretical argument, which predicts that an anharmonic chain equipped with a local potential should exhibit normal diffusion. For the sake of completeness it is worth mentioning that in this paper the model under scrutiny is compared with the so-called ϕ^4 model, where the non-linear term in Hamiltonian (1), i.e., $\beta(q_{n+1}-q_n)^4$, is replaced with βq_n^4. For this model one also observes, in the same parameter region, a crossover from a ballistic regime to an anomalous diffusive regime, but for $\beta > 1$ one eventually obtains numerical estimates yielding $\gamma \sim 0$, i.e., the expected diffusive behavior is recovered.

All of these results have a logical interpretation only if we take into account, once again, the role of finite size corrections combined with non-linearity. Actually, for the ϕ^4 model there is no way to argue that a ballistic regime should be observed for any finite, even if small, value of β. The ballistic behavior observed in both models for $\beta < 0.1$ seems to suggest that for small non-linearities one needs to explore considerably larger chains and integrate the dynamics over much longer times than in Xiong and Zhang [54], before phonon-like waves in both chains may experience the scattering effects due to the local potential. Moreover, the weaker quadratic pinning potential of the original model seems to still be affected by finite size corrections, even in the region $\beta > 1$. A problem that should be investigated systematically is the dependence on β of the chain length and of the integration time necessary to recover standard diffusive transport, at least in the crossover region $0.1 < \beta < 1$, where one can expect to perform proper numerical analysis in reasonable computational time.

2.2. Chimeras of Ballistic Regimes

In the light of the discussion in the previous subsection, one should not be surprised to encounter further non-linear chain models equipped with a pinning potential that exhibit a regime of ballistic transport of energy, compatible with a linearly divergent heat conductivity, $\kappa(L) \sim L$. Again, one might conjecture that this is due to the puzzling combination of non-linearity and finite size effects, although, as we shall see, the scenario that emerges is more intricate and interesting than the former statement indicates.

As a preliminary remark we recall that ballistic transport is the typical situation of an integrable Hamiltonian chain, the prototypical example of which is the harmonic lattice, with $V(x) = \frac{1}{2}x^2$ in Hamiltonian (1). It is worth pointing out that the addition of the harmonic pinning term (3) again keeps the harmonic chain integrable. With this in mind, it seems reasonable that for sufficiently small non-linearities both the FPUT-β and the ϕ^4 chains, as discussed in the previous subsection, would exhibit a seemingly ballistic regime for $\beta < 0.1$ also in the presence of the pinning potential. Recovering the expected diffusive transport regime is a matter of simulating exceedingly large chains over extremely long times.

The special role played by the quadratic pinning potential (3) has been revealed also by a recent study of heat transport in the Toda chain [55]. It is worth recalling that the unpinned Toda chain is an integrable Hamiltonian model of the form (1) with $V(x) = e^{-x} + x - 1$; in this model heat transport is ballistic due to the finite-speed propagation of solitons (rather than phonons, as in the harmonic chain). Toda solitons are localized non-linear excitations which are known to interact with each other by a non-dissipative diffusion mechanism; a soliton experiences a random sequence of spatial shifts as it moves through the lattice and interacts with other excitations without exchanging momentum [56]. In fact, the calculation of the transport coefficients by the Green-Kubo formula indicates the presence of a finite Onsager coefficient, which corresponds to a diffusive process on top of the dominant ballistic one [57, 58].

When the pinning term (3) is included, the Toda chain becomes chaotic, as one can easily see by measuring the spectrum of Lyapunov exponents [55]. Despite this, not only the energy but also the "center of mass"

$$h_c = \frac{1}{2}\left(\sum_{n=1}^{L} q_n\right)^2 + \frac{1}{2}\left(\sum_{n=1}^{L} p_n\right)^2$$

are conserved quantities. The special role of the quadratic pinning potential (3) is evidenced by the fact that if one turns it into a quartic one, i.e., $U(q_i) = \frac{1}{4}\sum_{n=1}^{L} q_n^4$, the quantity h_c is no longer conserved. Non-equilibrium simulations of the Toda chain with the addition of (3), with heat reservoirs at different temperatures $T_1 > T_2$ acting at its boundaries, yield a "flat" temperature profile at $T = (T_1 + T_2)/2$ in the bulk of the chain. This scenario would be expected for the pure Toda chain, but it is inconsistent with the basic consideration that the presence of (3) breaks translation invariance and total momentum is no longer conserved. This notwithstanding, in order to observe a temperature profile in the form of a linear interpolation between T_1 and T_2 (i.e., Fourier's law), one has to simulate the dynamics of very large chains over very long times, typically $L \sim \mathcal{O}(10^4)$ and $t \sim \mathcal{O}(10^6)$, when all the parameters of the model are set to unity.

Equilibrium measurements based on the Green-Kubo relation, i.e., based on the behavior of the energy current correlator (2), lead to further interesting findings in this scenario. By comparing the Toda chain with quadratic and quartic pinning potentials, one observes in the latter case clear indications of a diffusive regime, i.e., a finite heat conductivity, and a practically negligible influence of finite size corrections, whereas in the former case the power spectrum [i.e., the Fourier transform of (2)] is found to exhibit a peculiar scaling regime (with power $-5/3$) before eventually reaching a plateau that indicates a standard diffusion. In the same region of the spectrum, the FPUT model (where the parameters α and β have been chosen in such a way to correspond to a Taylor series expansion of the Toda chain) with the addition of (3) is found to converge to a plateau, in the absence of any precursor of a power-law scaling.

Further details about the unexpected transport regimes encountered in the Toda chain equipped with the quadratic pinning can be found in Dhar et al. [59]. We point out that many of the observations still await a convincing theoretical interpretation.

2.3. Anomalous Transport in the Presence of a Magnetic Field

Recent contributions [60, 61] have dealt with the important problem of heat transport in chains of charged oscillators in the presence of a magnetic field $\mathbf{B}$. The model is a one-dimensional polymer that allows transverse motion of the oscillators interacting via a harmonic potential. For $\mathbf{B} = 0$ the exponent of the energy current correlator is $\delta = \frac{1}{2}$, indicating the presence of anomalous transport and a divergent heat conductivity $\kappa(L) \sim L^{\frac{1}{2}}$. Upon switching on $\mathbf{B}$, the first basic consequence is the breaking of translation invariance, so that the total momentum is no longer conserved. This notwithstanding, the total pseudo-momentum is conserved, but the hydrodynamics of the model is definitely modified. In fact, numerical and analytical estimates indicate that the exponent δ may change to a value different from $\frac{1}{2}$. In particular, in Tamaki et al. [60] two different cases were considered: one where oscillators have the same charge and one where oscillators have alternate charges of sign $(-1)^n$, n being the integer index numbering oscillators along the chain. It can easily be shown that in the former case the sound velocity is null and the energy correlator exhibits a thermal peak centered at the origin and spreading in time. By contrast, in the latter case the sound velocity has a finite, $\mathbf{B}$-dependent value and the thermal peak of the energy correlator is coupled to sound modes propagating through the chain. In the case of finite sound velocity (alternate charges), the exponent governing the divergence of the heat conductivity with the system size is found to remain the same as that for $\mathbf{B} = 0$, i.e., $\gamma = \frac{1}{2}$. This is not surprising, since for $\mathbf{B} = 0$ the sound velocity in the model is also finite. In the case of equally charged oscillators, on the other hand, a new exponent $\gamma = \frac{3}{8}$ appears, which corresponds to a universality class different from all the others encountered in anomalous transport in non-linear chains of oscillators. An important remark about this new exponent is that in the absence of a finite sound velocity, the identification of the exponents δ and γ, introduced in section 2, is no longer correct. In fact, in this case the value of the exponent δ is found to be very close to $\frac{3}{4}$. Rigorous estimates of all of these exponents, also for the $d = 2$ and $d = 3$ versions of the charged polymer model, have been obtained through the asymptotics of the corresponding Green-Kubo integrals, where the deterministic dynamics has been replaced with a stochastic version that conserves the same quantities [61]. For the different one-dimensional cases, these rigorous estimates agree with the previous findings, while in $d = 2$ and $d = 3$ dimensions the expected logarithmic divergence and finite heat conductivity have been singled out, respectively.

2.4. The Case of Long-Range Interactions

Long-range forces that slowly decay with the relative distance between particles are well-studied in statistical mechanics. They characterize a wide range of physical situations, such as self-gravitating systems, plasmas, interacting vortices in fluids, capillary effects of colloids at an interface, chemo-attractant dynamics, cold atoms in optical lattices, and colloidal active particles. Several unusual features are known: ensemble inequivalence, long-lived metastable states and anomalous energy diffusion [62, 63], inhomogeneous stationary states [64], lack of thermalization on interaction with a single external bath [65], etc. Moreover, perturbations can spread with infinite velocities, leading to qualitative differences from their short-range counterparts [66, 67].

Heat transport in chains with long-range interactions has been studied only recently [68–72]. The main question is to what extent the anomalous properties change as the spatial range of interactions between oscillators increases. In two recent papers [73, 74] this problem was investigated for Hamiltonian chains with a long-range potential of the form

$$V = \frac{1}{2N_0(\alpha)} \sum_{i=1}^{N} \sum_{i \neq j}^{N} \frac{v(q_i - q_j)}{|i - j|^{\alpha}}, \tag{4}$$

where the generalized Kac factor

$$N_0(\alpha) = \frac{1}{N} \sum_{i=1}^{N} \sum_{j \neq i}^{N} \frac{1}{|i-j|^{\alpha}} \tag{5}$$

guarantees the extensivity of the Hamiltonian [62, 63]. In particular, the long-range versions of both the rotor chain, with $v(x) = V_{XY}(x)$, and the FPUT-β model, with $v(x) = \frac{1}{2}x^2 + \frac{1}{4}x^4$, have been investigated. The reason for studying these two choices is that the nearest-neighbor version (i.e., $\alpha \to +\infty$) of the former model exhibits standard diffusion of energy while that of the latter is characterized by anomalous diffusion.

For the rotor chain, non-equilibrium measurements with thermal reservoirs at different temperatures, $T_1 > T_2$, acting at the chain ends show that when $\alpha > 1$, the resulting temperature profile interpolates linearly between T_1 and T_2. Despite the long-range nature of the interaction, this is a strong indication that a standard diffusive process still governs energy transport through the rotor chain, as in the limit $\alpha \to +\infty$. In contrast, when $\alpha < 1$ the temperature profile progressively flattens until it reaches a constant bulk temperature $T = (T_1 + T_2)/2$ in the "mean-field" limit $\alpha \to 0^+$. It is important to note that, in contrast to the situation of chimeras of integrable models discussed in section 2.2, such flat temperature profiles have nothing to do with integrability, but rather are driven by the dominance of a "parallel" energy transport mechanism, which connects the heat baths at the chain boundaries with each other directly through the individual rotors in the bulk of the chain. Energy transport along the chain is practically immaterial, and the overall process is mediated by the rotors, which have to compromise between the two different temperatures imposed by the reservoirs. A sketch of this mechanism is presented in **Figure 2**. For small α, each lattice site in the bulk is directly coupled to both thermal baths, and its temperature tends to the average $(T_1+T_2)/2$ independently of the system size. Moreover, the average heat current exchanged with any other site is negligibly small.

At least for $\alpha < 1$, a similar scenario seems to characterize the FPUT model: flat temperature profiles are observed also in this case, and one can verify that the same parallel transport mechanism as described for rotors is at work. On the other hand, the behavior is definitely more complicated for $\alpha > 1$. Careful numerical studies exploring finite size effects give an overall picture in which an anomalous diffusion mechanism sets in, characterized by an exponent γ that is expected to increase up to that of the quartic FPUT model in the limit $\alpha \to +\infty$. But one is faced with a first surprise at $\alpha = 2$, where a flat temperature profile is restored, although, as the numerics clearly indicates, the mechanism of transport along the chain certainly dominates the parallel transport process. In the light of what was discussed in section 2.2, this would appear to be a possible manifestation of a chimera ballistic regime, although there is no simple argument allowing us to invoke a relation of this special case with an integrable approximation, if any. That the $\alpha = 2$ case is characterized by a somewhat "weaker non-integrability" has been confirmed also for a related model [70, 72]. This can be traced back to the fact that in this case the lattice supports a special type of free-tail localized excitations (traveling discrete breathers) that enhance energy transfer [72].

A complementary approach is the analysis of space-time scaling of equilibrium correlations, which in the short-range case yields useful information via the dynamical exponent z [20]. A numerical study of the structure factors of the FPUT model [74] shows that for $\alpha > 1$ the dynamical exponent z certainly depends on α in a different way from that expected from the theory of Lévy processes. Moreover, upon adding the cubic term $\frac{1}{3}(q_i - q_j)^3$ to the potential, one recovers the same dependence of z on α, up to $\alpha = 5$. This is again a surprise, because in the limit $\alpha \to +\infty$ the cubic and quartic versions of the FPUT model should converge to different values of z. At present, no theoretical explanation exists for this challenging scenario; in particular, to the best of our knowledge, no hydrodynamic description is available.

2.5. Anomalous Transport via the Multi-Particle Collision Method

So far we have discussed the case of lattice models. To test the universality of the results, it is important to consider more general low-dimensional many-body systems, such as interacting fluids or even plasmas. Although molecular dynamics would be the natural choice, it is computationally convenient to consider effective stochastic processes capable of mimicking particle interactions through random collisions. A prominent example is the multi-particle collision (MPC) simulation scheme [75], proposed to simulate the mesoscopic dynamics of polymers in solution, as well as colloidal and complex fluids. Another

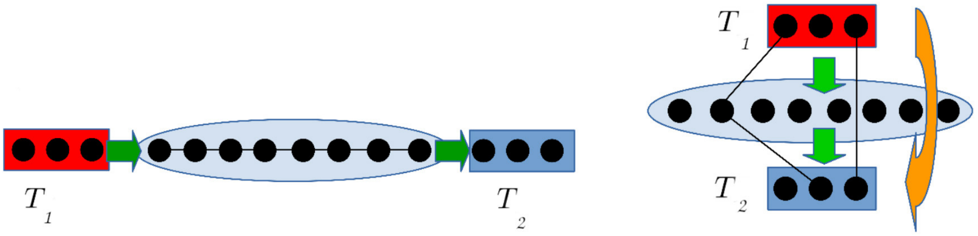

FIGURE 2 | Pictorial representations of heat transfer processes for long-range interacting chains, in the limiting cases of $\alpha = \infty$ (left) and $\alpha = 0$ (right). Oscillators in contact with thermal reservoirs are enclosed in rectangular boxes while ones in the bulk are enclosed in the ellipse. The relevant transport channels are represented by black lines. Adapted with permission from Di Cintio et al. [74]. Copyright © 2019 American Physical Society.

application is the modeling of parallel heat transport in edge tokamak plasma [76]. Indeed, in the regimes of interest for magnetic fusion devices, large temperature gradients will build up along the field line joining the hot plasma region (hot source) and the colder one close to the wall (which acts as a sink). Besides this motivation, we mention some results that are pertinent to the problem of anomalous transport.

In brief, the MPC method consists in partitioning the set of N_p point particles into N_c disjoint cells. Within each cell, the coordinates of the local center of mass and the velocity are computed, and a rotation of the particle velocities about a random axis in the cell's center-of-mass frame is performed. The rotation angles are fixed by requiring that the conserved quantities (energy, momentum) be locally preserved. All particles are then propagated freely. Physical details of the interaction can easily be included phenomenologically, for instance by introducing energy-dependent collision rates [18]. Interaction with external reservoirs can be also included by imposing Maxwellian distributions of velocity and chemical potentials on the thermostatted cells [77].

For a one-dimensional MPC fluid, since the conservation laws are the same as in, say, the FPUT model, we expect it to belong to the same KPZ universality class of anomalous transport. Indeed, numerical measurements of dynamical scaling fully confirm this prediction [78], and the result is quite robust. The same type of anomalies have been shown to occur also for quasi-one-dimensional MPC dynamics, namely in the case of a fluid confined in a box with a sufficiently large aspect ratio [18].

2.6. Anomalous Heat Transport in Material Science

The discovery of anomalous heat transport in anharmonic chains has triggered a search for this important physical effect in real low-dimensional materials. There is now a vast literature in which this kind of phenomenon has been predicted and experimentally observed; an overview of part of this growing research field is given in Lepri [9]. Here we just illustrate two recent contributions which will help the reader to appreciate the relevance of this phenomenon for nanowires and polymers. We point out that a review of the recent literature in both fields is contained in the bibliographies of these two contributions.

In Upadhyaya and Aksamija [79] the problem of lattice thermal conductivity in Si-Ge nanowires was tackled by solving the Boltzmann transport equation. More precisely, the authors used a Monte Carlo algorithm to sample the phonon mean free path, and combined this with phenomenological results concerning a suitable representation of realistic boundary conditions. It is quite remarkable that they found evidence of a heat transport mechanism ruled by a Lévy walk dynamics of phonon flights through the lattice structure. In particular, the phonon mean free paths are found to be characterized by a heavy-tailed distribution, which is associated with an anomalous diffusive behavior characterized by a size-divergent heat conductivity $\kappa(L) \sim L^{0.33}$. This behavior has been checked for system sizes in the range of $10\,\text{nm} < L < 10\,\mu\text{m}$. Notice that the phonon mean free path is orders of magnitude smaller than this size range. It is important to note that this scenario is robust across different alloy compositions, where the Ge component varies in the range $[6, 86\%]$. All of these results fully agree with the theoretical expectation that anharmonic chains with leading cubic non-linearity should exhibit a divergent heat conductivity with an exponent $\gamma = \frac{1}{3}$.

In Crnjar et al. [80] atomistic simulations were performed for poly(3,4-ethylenedioxythiophene), abbreviated PEDOT, a conjugated polymer that is of interest in view of its tunable and large electrical conductivity, transparency, and air stability [81]. The authors simulated this polymer model in $d = 1$ and $d = 3$, in both equilibrium and non-equilibrium settings. More precisely, equilibrium measurements were performed by estimating the dependence of the heat conductivity κ on the system size L via the Green-Kubo formula, where one has to estimate the asymptotic decay in time of the correlator of the total energy current (2). The outcome of this analysis was compared with the numerics obtained in non-equilibrium conditions. The setup used in this case is based on a transient measurement of the effective heat diffusivity $\bar{\kappa}$. The two halves of the system were initially prepared in two thermalized states at different temperatures T_1 and T_2. By running a molecular dynamics simulation, one can measure $\bar{\kappa}$ as a function of L during the transient evolution to the thermal equilibrium state at temperature $(T_1 + T_2)/2$. More precisely, the estimate of $\bar{\kappa}$ relies on the fit of the time-dependent temperature difference in the two regions (for details see Equation 9 in [80]). Finally, the thermal conductivity is obtained from the formula $\kappa = \bar{\kappa}\,\rho\, c_V$, where ρ is the polymer mass density and c_V its specific heat. The authors obtained consistent results showing that for the polymer chain anomalous diffusion, $\kappa(L) \sim L^{\gamma}$ with $\gamma \simeq \frac{1}{2}$, is observed, whereas for the polymer crystal standard diffusion, i.e., a size-independent finite thermal conductivity κ, is recovered. These results are quite remarkable because they provide very clear confirmation of the role played by the space dimension in determining anomalous transport effects. On the other hand, the authors point out that the exponent $\gamma \simeq \frac{1}{2}$ does not agree with the expected theoretical value $\frac{1}{3}$, since the phenomenological AMBER non-linear potential adopted for the PEDOT model is certainly asymmetric, dominated by a leading cubic non-linearity. Simulations of the polymer chain have been performed for quite large system sizes, namely $0.376\,\mu\text{m} < L < 7.526\,\mu\text{m}$. This notwithstanding, we cannot exclude the possibility that, as discussed in the previous section, the combination of finite size effects and non-linearity might also be at work in this case, yielding a power-law divergence of $\kappa(L)$ that should be compatible with a symmetric phenomenological potential.

These findings should be compared with those obtained for simpler models. For instance, in the case mentioned in section 2.3, the exponent $\gamma = \frac{1}{2}$ was found in a chain model with a quadratic interaction potential between the beads [60] (notice that the possibility of displacements in both the horizontal and the vertical directions make this model non-integrable, in contrast to the harmonic chain). On the other hand, a three-dimensional anharmonic chain with cubic and quartic interactions has been shown to belong instead to the

KPZ class with $\gamma = 1/3$ [82]. One could speculate that in any polymer model the basic scaling associated with anomalous transport is determined only by the quadratic term, and this is a conjecture that certainly merits further theoretical and numerical investigation.

To conclude this section, we briefly mention some experimental studies. Thermal properties of nanosized objects are of intrinsic technological interest for nanoscale thermal management. In this general context, nanowires and single-walled nanotubes have been analyzed to look for deviation from the standard Fourier's law [5]. Some experimental evidence of anomalous transport in very long carbon nanotubes has been reported [83], although the results are controversial [84]. Experiments demonstrating a non-trivial length dependence of thermal conductance for molecular chains have also been reported [85]. Admittedly, such experimental evidence of anomalous transport is rather limited and not exempt from criticism. Heat transfer measurements on nanosized objects are notoriously difficult but may be undertaken in the future, possibly guided by the theoretical insights summarized here.

3. COUPLED TRANSPORT

In this section we discuss the relevance of anomalous diffusion in coupled transport. In particular, we focus on steady-state transport and for concreteness use the language of thermoelectricity [2, 86], in which the coupled flows are charge and heat flow (other examples where the flow coupled to heat is particle or magnetization flow could be treated similarly). Moreover, we shall limit our discussion to power production, even though many of the results and open problems highlighted below can be readily extended to refrigeration. Thermoelectricity is a steady-state heat engine. Relevant quantities for characterizing the performance of a generic heat engine, which operates between a hot reservoir at temperature T_h and a cold one at T_c, are the following:

- The efficiency $\eta = W/Q_h$, where W is the output work and Q_h the heat extracted from the hot reservoir. For cyclic as well as for steady-state heat engines, the Carnot efficiency $\eta_C = 1 - T_c/T_h$ is an upper bound for the efficiency η.
- The output power P. It is a common belief that an engine attaining the Carnot efficiency would require a quasi-static transformation, i.e., an infinite cycle-time, implying vanishing power. For steady-state engines this argument is replaced by one saying that finite currents would imply dissipation, thus precluding Carnot efficiency for non-zero power. Hence, it is important to consider the power-efficiency trade-off. This is a key problem in the field of finite-time thermodynamics [87], in relation to the fundamental thermodynamic bounds on the performance of heat engines, as well as the practical purpose of designing engines that, for a given output power, work at the maximum possible efficiency. For classical cyclic heat engines, whose interactions with a heat bath can be described by a Markov process, it was proved [88] that the mean power P has an upper bound
$$P \leq \frac{A}{T_c}\,\eta(\eta_c - \eta), \tag{6}$$
where A is a system-specific pre-factor (see also [89] for an analogous linear response result within the framework of stochastic thermodynamics [90]). While at first sight this bound implies that $P \to 0$ as $\eta \to \eta_c$ (and of course when $\eta \to 0$), so that an engine of this kind with finite power never attains the Carnot efficiency, one cannot exclude the possibility that the amplitude A diverges as the efficiency approaches the Carnot value [91].
- The fluctuations in the power output about its mean value P. Indeed, large fluctuations render heat engines unreliable. Especially for heat engines at the nanoscale, one expects power fluctuations due to, e.g., thermal noise, which are not negligible in comparison with the mean output power. In general, one would like to obtain high efficiency (as close as possible to the Carnot efficiency), large power, and small fluctuations. However, a trade-off between these three quantities has been proved [92] for a broad class of steady-state heat engines (including machines described by suitable rate equations or modeled by overdamped Langevin dynamics):
$$P\,\frac{\eta}{\eta_C - \eta}\,\frac{k_B T_c}{\Delta_P} \leq \frac{1}{2}, \tag{7}$$
where the (steady-state) power fluctuations are given by
$$\Delta_P \equiv \lim_{t\to\infty} [P(t) - P]^2\, t, \tag{8}$$
with $P(t)$ being the mean power delivered up to time t. For $t \to \infty$, since $P(t)$ converges to P as $1/\sqrt{t}$, an additional factor of t in (8) is needed to obtain a finite limit for Δ_P. Equation (7) tells us that efficiency close to the Carnot value and high power entail large fluctuations. We note that the bound (8) has recently been generalized to periodically driven systems [93].

3.1. Linear Response

In the linear response setting, the relationship between currents and generalized forces is linear [94, 95]. In particular, for thermoelectric transport we have
$$\begin{cases} j_e = L_{ee}\mathcal{F}_e + L_{eu}\mathcal{F}_h, \\ j_u = L_{ue}\mathcal{F}_e + L_{uu}\mathcal{F}_h, \end{cases} \tag{9}$$
where j_e is the electric current density, j_u is the energy current density, and the conjugated generalized forces are $\mathcal{F}_e = -\nabla(\mu/eT)$ and $\mathcal{F}_h = \nabla(1/T)$, with μ being the electrochemical potential and e the electron charge. The coefficients L_{ab} $(a, b = e, u)$ are known as kinetic or Onsager coefficients; we will denote by $\boldsymbol{L}$ the Onsager matrix with matrix elements L_{ab}. Note that the (total) energy current $j_u = j_h + (\mu/e)j_e$ is the sum of the heat current j_h and the electrochemical potential energy current $(\mu/e)j_e$.

The Onsager coefficients must satisfy two fundamental constraints. First, the second law of thermodynamics, i.e., the positivity of the entropy production rate, $\dot{s} = \mathcal{F}_e j_e + \mathcal{F}_u j_u \geq 0$, implies

$$L_{ee}, L_{uu} \geq 0, \quad L_{ee}L_{uu} - \frac{1}{4}(L_{eu} + L_{ue})^2 \geq 0. \tag{10}$$

Second, for systems with time-reversal symmetry, Onsager derived fundamental relations, $L_{eu} = L_{ue}$, known as Onsager reciprocal relations.

The kinetic coefficients L_{ab} are related to the familiar thermoelectric transport coefficients, namely the electrical conductivity σ, the thermal conductivity κ, the thermopower (or Seebeck coefficient) S, and the Peltier coefficient Π:

$$\sigma = -e\left(\frac{j_e}{\nabla\mu}\right)_{\nabla T=0} = \frac{L_{ee}}{T}, \tag{11}$$

$$\kappa = -\left(\frac{j_h}{\nabla T}\right)_{j_e=0} = \frac{1}{T^2}\frac{\det \boldsymbol{L}}{L_{ee}}, \tag{12}$$

$$S = -\frac{1}{e}\left(\frac{\nabla\mu}{\nabla T}\right)_{j_e=0} = \frac{1}{T}\left(\frac{L_{eu}}{L_{ee}} - \frac{\mu}{e}\right), \tag{13}$$

$$\Pi = \left(\frac{j_h}{j_e}\right)_{\nabla T=0} = \frac{L_{ue}}{L_{ee}} - \frac{\mu}{e}. \tag{14}$$

For systems with time-reversal symmetry, the Onsager reciprocal relations give $\Pi = TS$.

The thermoelectric performance is governed by the thermoelectric figure of merit

$$ZT = \frac{\sigma S^2}{\kappa}. \tag{15}$$

Thermodynamics imposes a lower bound on the figure of merit: $ZT \geq 0$. Moreover, the thermoelectric conversion efficiency is a monotonically increasing function of ZT, with $\eta = 0$ at $ZT = 0$ and $\eta \to \eta_C$ in the limit $ZT \to \infty$. Nowadays, most efficient thermoelectric devices operate at around $ZT \approx 1$. On the other hand, it is generally accepted that $ZT > 3$–5 is the target value for efficient, commercially competitive thermoelectric technology. It is a great challenge to increase the thermoelectric efficiency, since the transport coefficients S, σ, and κ are generally interdependent. For instance, in metals σ and κ are proportional according to the Wiedemann-Franz law, and the thermopower is small; these properties make metals poor thermoelectric materials. It is therefore of great importance to understand the physical mechanisms that might allow us to independently control the above transport coefficients.

3.2. Anomalous Transport and Efficiency

The theoretical discussion of the role of anomalous (thermal) diffusion in thermoelectric transport is based on the Green-Kubo formula. expresses the Onsager coefficients in terms of dynamic correlation functions of the corresponding currents, computed at thermodynamic equilibrium. If the current-current correlations $\langle j_a(0)j_b(t)\rangle$ (where $\langle\cdot\rangle$ denotes the canonical average at a given temperature T) do not decay after time-averaging, then by definition the corresponding Drude weight

$$D_{ab} = \lim_{t\to\infty}\lim_{\Lambda\to\infty}\frac{1}{2\Omega(\Lambda)t}\int_0^t dt\,\langle j_a(0)j_b(t)\rangle \tag{16}$$

is different from zero. Here Ω is the system's volume and Λ is the system's size along the direction of the currents. It has been shown [96–99] that a non-zero Drude weight D_{ab} is a signature of ballistic transport, i.e., in the thermodynamic limit the corresponding kinetic coefficient L_{ab} diverges linearly with the system size. Non-zero Drude weights can be related to the existence of relevant conserved quantities, which determine a lower bound on D_{ab} [100, 101]. By definition, a constant of motion Q is relevant if it is not orthogonal to the currents under consideration; in thermoelectricity this means $\langle j_e Q\rangle \neq 0$ and $\langle j_u Q\rangle \neq 0$.

With regard to thermoelectric efficiency, a theoretical argument [102] predicts that for systems with a single relevant conserved quantity, as is the case for non-integrable systems with elastic collisions (momentum-conserving systems), the figure of merit ZT diverges at the thermodynamic limit, so that the Carnot efficiency is attained in that limit. Indeed, for systems in which the total momentum along the direction of the currents is the only relevant constant of motion, as a consequence of ballistic transport the Onsager coefficients L_{ab} are proportional to Λ. Therefore, the electrical current is ballistic, $\sigma \sim L_{ee} \sim \Lambda$, while the thermopower is asymptotically size-independent, $S \sim L_{eu}/L_{ee} \sim \Lambda^0$. On the other hand, for such systems the ballistic contribution to $\det \boldsymbol{L}$ is expected to vanish [102]. Hence the thermal conductivity $\kappa \sim \det \boldsymbol{L}/L_{ee}$ grows sub-ballistically, $\kappa \sim \Lambda^\gamma$ with $\gamma < 1$. Since $\sigma \sim \Lambda$ and $S \sim \Lambda^0$, we can conclude that $ZT \sim \Lambda^{1-\gamma}$; that is, ZT diverges in the thermodynamic limit $\Lambda \to \infty$.

This result has been demonstrated in several models: in a diatomic chain of hard-point colliding particles [102] (see **Figure 3**), in a two-dimensional system [77] with dynamics simulated by the MPC method discussed in section 2.5 [75], and in a one-dimensional gas of particles with screened (nearest-neighbor) Coulomb interactions [104]. In all these (classical) models, the collisions are elastic and the only relevant constant of motion is the component of momentum in the direction of the charge and heat flows. In the numerical simulations, openings connect the system with two electrochemical reservoirs. The left (L) and right (R) reservoirs are modeled as ideal gases, at temperature T_γ and electrochemical potential μ_γ ($\gamma = L, R$). A stochastic model of the reservoirs [105, 106] is used: whenever a particle of the system crosses the opening that separates the system from the left or right reservoir, it is removed. Particles are injected into the system through the openings, with rates and energy distribution determined by the temperature and electrochemical potential (see e.g., [2]).

We now show that systems with anomalous (thermal) diffusion allow a much better power-efficiency trade-off than is achievable by non-interacting systems or, more generally, by any system that can be described by the scattering theory.

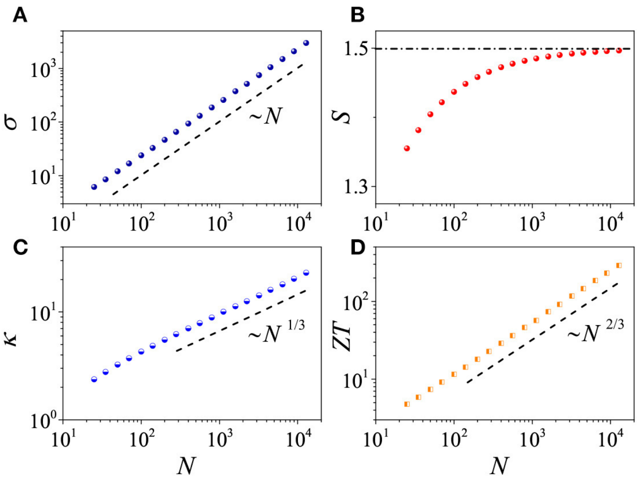

FIGURE 3 | (A) Electrical conductivity σ, **(B)** Seebeck coefficient S, **(C)** thermal conductivity κ, and **(D)** thermoelectric figure of merit ZT plotted as functions of the mean number N of particles in the system, for a one-dimensional diatomic hard-point gas. Parameter values are $m = 1$ and $M = 3$ for the masses, $T = 1$, $\mu = 0$, and $k_B = e = 1$, with the system length Λ set equal to the number of particles. Adapted with permission from Luo et al. [103]. Copyright © 2018 American Physical Society.

We first briefly discuss non-interacting systems. In this case, we can express the charge current according to the Landauer-Büttiker scattering theory [107], adapted to classical physics:

$$j_e = \frac{e}{h}\int_0^\infty d\epsilon\, [f_L(\epsilon) - f_R(\epsilon)]\mathcal{T}(\epsilon), \tag{17}$$

where $f_\gamma(\epsilon) = e^{-\beta_\gamma(\epsilon-\mu_\gamma)}$ is the Maxwell-Boltzmann distribution function for reservoir γ and $\mathcal{T}(\epsilon)$ is the transmission probability of a particle with energy ϵ going from one reservoir to the other, so that $0 \leq \mathcal{T}(\epsilon) \leq 1$. Similarly, we obtain the heat current from reservoir γ as

$$J_{h,\gamma} = \frac{1}{h}\int_0^\infty d\epsilon\, (\epsilon - \mu_\gamma)[f_L(\epsilon) - f_R(\epsilon)]\mathcal{T}(\epsilon). \tag{18}$$

For a given output power $P = (\Delta\mu/e)J_e$ (where $\Delta\mu = \mu_R - \mu_L > 0$ and we set $\mu_L = 0$ for simplicity), the transmission function that maximizes the efficiency of the heat engine, $\eta(P) = P/J_{h,L}$ (with $P, J_{h,L} > 0$ and $T_L > T_R$) was determined in Luo et al. [103] by closely following the method developed for the quantum case in Whitney [108, 109]. The optimal transmission function is a boxcar function, $\mathcal{T}(\epsilon) = 1$ for $\epsilon_0 < \epsilon < \epsilon_1$ and $\mathcal{T}(\epsilon) = 0$ otherwise. Here $\epsilon_0 = \Delta\mu/\eta_C$ is obtained from the condition $f_L(\epsilon_0) = f_R(\epsilon_0)$ and corresponds to the special value of energy for which the flow of particles from left to right is the same as the flow from right to left. Thus, if particles only flow at energy ϵ_0, the flow can be considered "reversible" in a thermodynamic sense. The energy ϵ_1 and $\Delta\mu$ are determined numerically in the optimization procedure [103, 108, 109]. The maximum achievable power is obtained when $\epsilon_1 \to \infty$:

$$P^{(\mathrm{st})}_{\max} = A\,\frac{\pi^2}{h}\,k_B^2\,(\Delta T)^2, \tag{19}$$

where $\Delta T = T_L - T_R$, $A \approx 0.0373$, and the superscript "(st)" reminds us that the results are obtained within the scattering theory framework. At small output power, $P/P^{(\mathrm{st})}_{\max} \ll 1$, we have

$$\eta(P) \leq \eta^{(\mathrm{st})}_{\max}(P) = \eta_C\left(1 - B\sqrt{\frac{T_R}{T_L}\frac{P}{P^{(\mathrm{st})}_{\max}}}\right), \tag{20}$$

where $B \approx 0.493$. Note that in the limit $P \to 0$ the upper bound on efficiency achieves the Carnot value and the energy window for transmission, $\delta = \epsilon_1 - \epsilon_0$, tends to 0. That is, we recover the celebrated delta-energy filtering mechanism for Carnot efficiency [110–112]. Hence, the Carnot limit corresponds to the aforementioned reversible, zero-power flow of particles.

It is clear that selecting transmission over a small energy window reduces power production. We would thus expect a different mechanism for reaching Carnot efficiency to be more favorable for power production. Such an expectation is supported by numerical data for the interacting momentum-conserving systems described above. For these systems, the Carnot efficiency can be reached without delta-energy filtering [113], and the power-efficiency trade-off can be improved. **Figure 4** shows, for a given ΔT and different system sizes, η/η_C as a function of $P/P_{\max}$. The curves have two branches. Indeed, they are obtained by increasing $\Delta\mu$ from zero, where trivially $P = 0$, up to the stopping value, where again $P = 0$. In the latter case, the power vanishes because the electrochemical potential difference becomes too great to be overcome by the temperature difference. The power first increases with $\Delta\mu$, up to its maximum value $P = P_{\max}$, and then decreases, leading to a two-branch curve. Note that, despite the relatively high value of $\Delta T/T = 0.2$, the numerical results are in rather good agreement with the universal linear curves, which depend only on the figure of merit ZT [103]. Not surprisingly, the agreement improves with increasing system size, since $|\nabla T| = \Delta T/N$ decreases as N increases. In **Figure 4** we also plot the limiting curve corresponding to $ZT = \infty$, obtained in momentum-conserving models in the thermodynamic limit $N \to \infty$. The upper branch of this curve is the universal linear response upper bound on efficiency for a given power P. For $P/P_{\max} \ll 1$, this bound reads

$$\eta_{\mathrm{lr}}(P) = \eta_C\left(1 - \frac{1}{4}\frac{P}{P_{\max}}\right), \tag{21}$$

which is much less restrictive than the bound (20) obtained from scattering theory. Note that, by using the linear response result $P_{\max} \propto (\Delta T)^2$, from (21) we obtain $P \propto \Delta T\,(\eta_C - \eta)$. Accordingly, when $\eta \approx \eta_C \propto \Delta T$, we find the same dependence as in bound (6), which was obtained in a rather different context.

3.3. Open Problems

Several open questions about the role of anomalous transport in coupled transport remain, notably the following:

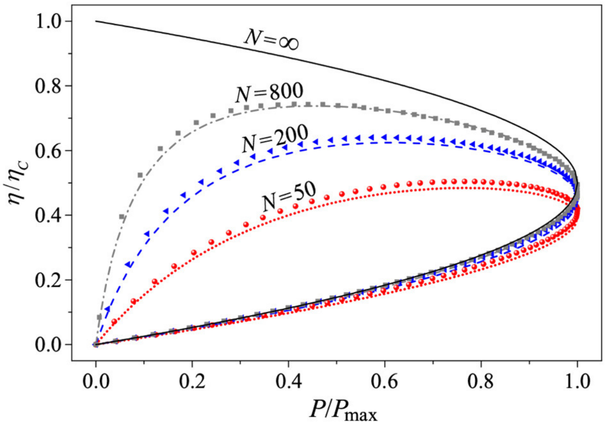

FIGURE 4 | Relative efficiency η/η_C vs. normalized power $P/P_{\max}$ at different system sizes. The dotted, dashed, and dot-dashed curves represent the linear response predictions at the $ZT(N)$ value corresponding to the given system size $\Lambda = N$. The solid line is the linear response curve for $ZT = \infty$ (i.e., $N = \infty$). The model parameter values are as in **Figure 3**, with $\Delta T = 0.2$ ($T_L = 1.1$ and $T_R = 0.9$). Adapted with permission from Luo et al. [103]. Copyright © 2019 American Physical Society.

- As discussed in section 2.4, heat transport in the presence of long-range interactions has been investigated recently. However, the effect of the range of interactions on coupled transport, and in particular on the power-efficiency trade-off, is unknown.
- While momentum-conserving systems greatly improve the power-efficiency trade-off relative to the non-interacting case, it is not known how they would behave with respect to the bound (7), which simultaneously involves the efficiency, power, and fluctuations. That bound was obtained within the framework of stochastic thermodynamics [90], with the transition rates between the system's states obeying the local detailed balance principle, and without precise modeling of the underlying particle-particle interactions. On the other hand, in the models described in the present paper, stochasticity is confined to the baths and the internal system dynamics plays a crucial role. This has allowed us to assess the impact of constants of motion and anomalous transport on the efficiency of heat-to-work conversion and could also be relevant to the bound (7).
- Although the results reviewed in this section have been corroborated by numerical simulations of several classical one- and two-dimensional systems, their extension to the quantum case remains a challenging problem for future investigation.
- The discussion in this section has neglected phonons. Nevertheless, besides being of fundamental interest, the results presented here could be of practical relevance to very clean systems where the elastic mean free path of the conducting particles is much longer than the length scale associated with elastic particle-particle collisions, for instance in high-mobility two-dimensional electron gases at very low temperatures. Phonon-free thermoelectricity (or, more precisely, thermodiffusion) has been experimentally realized in the context of cold atoms, first for weakly interacting particles [114] and more recently in a regime with strong interactions [115]. In the latter case, a strong violation of the Wiedemann-Franz law has been observed. Such violations cannot be explained by the Landauer-Büttiker scattering theory. It would be interesting to investigate whether in such systems where a high thermoelectric efficiency has been observed, the non-interacting bound on efficiency for a given power could be outperformed.

4. OVERVIEW

In spite of the significant progress made over the past few decades, the study of anomalous heat transport in non-linear systems remains a challenging research field. While this review has focused on some promising directions in regard to classical systems, a main avenue for future investigations should undoubtedly be sought in the quantum domain. At the quantum level, anomalous heat transport is considerably less well-understood than in the classical case, due to both conceptual and practical difficulties. The definitions of thermodynamic observables, such as temperature, heat, and work, and of the concept of local equilibrium, become problematic in nanoscale systems. For instance, in solid-state nanodevices we can have structures smaller than the length scale over which electrons relax to a local equilibrium due to electron-electron or electron-phonon interactions. Consequently, quantum interference effects, quantum correlations, and quantum fluctuation effects should be taken into account [2]. In particular, many-body localization provides a mechanism by which thermalization can fail in strongly disordered systems, with anomalous transport in the vicinity of the transition between many-body localized and ergodic phases [116, 117].

From a practical viewpoint, one faces challenges arising from the computational complexity of simulating many-body open quantum systems, with the size of the Hilbert space growing exponentially with the number of particles. Notwithstanding these difficulties, a time-dependent density matrix renormalization group method allows the computation of transport properties of integrable and non-integrable quantum spin chains driven by local (Lindblad) operators acting close to their boundaries [118]. Sizes up to $n \sim 100$ spins can be simulated, much larger than the $n \sim 20$ spins achievable with other methods, such as Monte Carlo wavefunction approaches [119]. The results obtained confirm the relevance of constants of motion to transport properties, with integrable systems that exhibit ballistic heat transport, whereas for quantum chaotic systems heat transport is normal (according to Fourier's law; see [120, 121]). In passing, we note that for magnetization transport in some integrable models like XXZ, one can obtain diffusive behavior (Fick's law; see [118]).

From a thermodynamic perspective, the use of local Lindblad operators is problematic. Except in quantum chaotic systems, such operators do not drive the system to a grand-canonical state [122]. Furthermore, the use of local Lindblad baths may result in apparent violations of the second law of thermodynamics [123]. Global Lindblad dissipators are free from such problems and can be used to simulate heat transport (see e.g., [124]), but are not practical in that they are limited to very small system sizes. Furthermore, for the description of quantum heat engines in the extreme case where the working medium may even consist of a single two-level quantum system, it is crucial to take into account medium-reservoir quantum correlations as well as non-Markovian effects, which are not included in the standard, weak-coupling Lindblad description of quantum open systems. For first steps in this challenging direction, see Carrega et al. [125], Tamascelli et al. [126], and Wiedmann et al. [127]. The investigation of anomalous heat transport in such regimes is *terra incognita*.

AUTHOR CONTRIBUTIONS

All authors listed have made a substantial, direct and intellectual contribution to the work, and approved it for publication.

ACKNOWLEDGMENTS

SL and RL acknowledge partial support from project MIUR-PRIN2017 Coarse-grained description for non-equilibrium systems and transport phenomena (CO-NEST) N. 201798CZL. They thank P. Di Cintio and S. Iubini for invaluable help.

REFERENCES

1. Klages R, Radons G, Sokolov IM. *Anomalous Transport: Foundations and Applications*. Weinheim: John Wiley & Sons (2008).
2. Benenti G, Casati G, Saito K, Whitney RS. Fundamental aspects of steady-state conversion of heat to work at the nanoscale. *Phys Rep.* (2017) **694**:1–124. doi: 10.1016/j.physrep.2017.05.008
3. Lepri S, Livi R, Politi A. Heat conduction in chains of nonlinear oscillators. *Phys Rev Lett.* (1997) **78**:1896–9. doi: 10.1103/PhysRevLett.78.1896
4. Lepri S, Livi R, Politi A. On the anomalous thermal conductivity of one-dimensional lattices. *Europhys Lett.* (1998) **43**:271–6. doi: 10.1209/epl/i1998-00352-3
5. Chang CW. Experimental probing of non-fourier thermal conductors. In: Lepri S, editor. *Thermal Transport in Low Dimensions: From Statistical Physics to Nanoscale Heat Transfer*. Berlin; Heidelberg: Springer-Verlag (2016). p. 305–38. doi: 10.1007/978-3-319-29261-8_8
6. Balandin AA. Thermal properties of graphene and nanostructured carbon materials. *Nat Mater.* (2011) **10**:569–81. doi: 10.1038/nmat3064
7. Lepri S, Livi R, Politi A. Thermal conduction in classical low-dimensional lattices. *Phys Rep.* (2003) **377**:1. doi: 10.1016/S0370-1573(02)00558-6
8. Dhar A. Heat Transport in low-dimensional systems. *Adv Phys.* (2008) **57**:457–537. doi: 10.1080/00018730802538522
9. Lepri S, editor. *Thermal Transport in Low Dimensions: From Statistical Physics to Nanoscale Heat Transfer. Vol. 921 of Lecture Notes in Physics*. Berlin; Heidelberg: Springer-Verlag (2016) 1–407. doi: 10.1007/978-3-319-29261-8
10. Dhar A, Kundu A, Kundu A. Anomalous heat transport in one dimensional systems: a description using non-local fractional-type diffusion equation. *Front Phys.* (2019) **7**:159. doi: 10.3389/fphy.2019.00159
11. Aoki K, Kusnezov D. Bulk properties of anharmonic chains in strong thermal gradients: non-equilibrium ϕ^4 theory. *Phys Lett A.* (2000) **265**:250. doi: 10.1016/S0375-9601(99)00899-3
12. Giardiná C, Livi R, Politi A, Vassalli M. Finite thermal conductivity in 1D lattices. *Phys Rev Lett.* (2000) **84**:2144–7. doi: 10.1103/PhysRevLett.84.2144
13. Gendelman OV, Savin AV. Normal heat conductivity of the one-dimensional lattice with periodic potential of nearest-neighbor interaction. *Phys Rev Lett.* (2000) **84**:2381–4. doi: 10.1103/PhysRevLett.84.2381
14. Iubini S, Lepri S, Politi A. Nonequilibrium discrete nonlinear Schrödinger equation. *Phys Rev E.* (2012) **86**:011108. doi: 10.1103/PhysRevE.86.011108
15. Mendl CB, Spohn H. Low temperature dynamics of the one-dimensional discrete nonlinear Schroedinger equation. *J Stat Mech: Theory Exp.* (2015) **2015**:P08028. doi: 10.1088/1742-5468/2015/08/P08028
16. Lippi A, Livi R. Heat conduction in two-dimensional nonlinear lattices. *J Stat Phys.* (2000) **100**:1147–72. doi: 10.1023/A:1018721525900
17. Wang L, Hu B, Li B. Logarithmic divergent thermal conductivity in two-dimensional nonlinear lattices. *Phys Rev E.* (2012) **86**:040101. doi: 10.1103/PhysRevE.86.040101
18. Di Cintio P, Livi R, Lepri S, Ciraolo G. Multiparticle collision simulations of two-dimensional one-component plasmas: anomalous transport and dimensional crossovers. *Phys Rev E.* (2017) **95**:043203. doi: 10.1103/PhysRevE.95.043203
19. van Beijeren H. Exact results for anomalous transport in one-dimensional Hamiltonian systems. *Phys Rev Lett.* (2012) **108**:180601. doi: 10.1103/PhysRevLett.108.180601
20. Spohn H. Nonlinear fluctuating hydrodynamics for anharmonic chains. *J Stat Phys.* (2014) **154**:1191–227. doi: 10.1007/s10955-014-0933-y
21. Popkov V, Schadschneider A, Schmidt J, Schütz GM. Fibonacci family of dynamical universality classes. *Proc Natl Acad Sci USA.* (2015) **112**:12645–50. doi: 10.1073/pnas.1512261112
22. Lee-Dadswell GR, Nickel BG, Gray CG. Thermal conductivity and bulk viscosity in quartic oscillator chains. *Phys Rev E.* (2005) **72**:031202. doi: 10.1103/PhysRevE.72.031202
23. Delfini L, Lepri S, Livi R, Politi A. Anomalous kinetics and transport from 1D self-consistent mode-coupling theory. *J Stat Mech Theory Exp.* (2007) **2007**:P02007. doi: 10.1088/1742-5468/2007/02/P02007
24. Lukkarinen J, Spohn H. Anomalous energy transport in the FPU-β chain. *Commun Pure Appl Math.* (2008) **61**:1753–86. doi: 10.1002/cpa.20243
25. Lepri S, Livi R, Politi A. Universality of anomalous one-dimensional heat conductivity. *Phys Rev E.* (2003) **68**:067102. doi: 10.1103/PhysRevE.68.067102
26. Wang L, Wang T. Power-law divergent heat conductivity in one-dimensional momentum-conserving nonlinear lattices. *Europhys Lett.* (2011) **93**:54002. doi: 10.1209/0295-5075/93/54002
27. Basile G, Bernardin C, Olla S. Momentum conserving model with anomalous thermal conductivity in low dimensional systems. *Phys Rev Lett.* (2006) **96**:204303. doi: 10.1103/PhysRevLett.96.204303
28. Lepri S, Mejía-Monasterio C, Politi A. Stochastic model of anomalous heat transport. *J Phys A Math Theor.* (2009) **42**:025001. doi: 10.1088/1751-8113/42/2/025001
29. Lee-Dadswell G. Universality classes for thermal transport in one-dimensional oscillator systems. *Phys Rev E.* (2015) **91**:032102. doi: 10.1103/PhysRevE.91.032102
30. Zaburdaev V, Denisov S, Klafter J. Lévy walks. *Rev Mod Phys.* (2015) **87**:483. doi: 10.1103/RevModPhys.87.483
31. Cipriani P, Denisov S, Politi A. From anomalous energy diffusion to Lévy Walks and heat conductivity in one-dimensional systems. *Phys Rev Lett.* (2005) **94**:244301. doi: 10.1103/PhysRevLett.94.244301
32. Lepri S, Politi A. Density profiles in open superdiffusive systems. *Phys Rev E.* (2011) **83**:030107. doi: 10.1103/PhysRevE.83.030107
33. Dhar A, Saito K, Derrida B. Exact solution of a Lévy walk model for anomalous heat transport. *Phys Rev E.* (2013) **87**:010103. doi: 10.1103/PhysRevE.87.010103
34. Denisov S, Klafter J, Urbakh M. Dynamical heat channels. *Phys Rev Lett.* (2003) **91**:194301. doi: 10.1103/PhysRevLett.91.194301

35. Liu S, Haenggi P, Li N, Ren J, Li B. Anomalous heat diffusion. *Phys Rev Lett.* (2014) **112**:040601. doi: 10.1103/PhysRevLett.112.040601
36. Mendl CB, Spohn H. Equilibrium time-correlation functions for one-dimensional hard-point systems. *Phys Rev E.* (2014) **90**:012147. doi: 10.1103/PhysRevE.90.012147
37. Jara M, Komorowski T, Olla S. Superdiffusion of energy in a chain of harmonic oscillators with noise. *Commun Math Phys.* (2015) **339**:407–53. doi: 10.1007/s00220-015-2417-6
38. Bernardin C, Gonçalves P, Jara M. 3/4-fractional superdiffusion in a system of harmonic oscillators perturbed by a conservative noise. *Archiv Ration Mech Anal.* (2016) **220**:505–42. doi: 10.1007/s00205-015-0936-0
39. Bernardin C, Stoltz G. Anomalous diffusion for a class of systems with two conserved quantities. *Nonlinearity.* (2012) **25**:1099. doi: 10.1088/0951-7715/25/4/1099
40. Bernardin C, Gonçalves P. Anomalous fluctuations for a perturbed Hamiltonian system with exponential interactions. *Commun Math Phys.* (2014) **325**:291–332. doi: 10.1007/s00220-013-1860-5
41. Delfini L, Lepri S, Livi R, Mejia-Monasterio C, Politi A. Nonequilibrium dynamics of a stochastic model of anomalous heat transport: numerical analysis. *J Phys A Math Theor.* (2010) **43**:145001. doi: 10.1088/1751-8113/43/14/145001
42. Kundu A, Bernardin C, Saito K, Kundu A, Dhar A. Fractional equation description of an open anomalous heat conduction set-up. *J Stat Mech Theory Exp.* (2019) **2019**:013205. doi: 10.1088/1742-5468/aaf630
43. Iacobucci A, Legoll F, Olla S, Stoltz G. Thermal conductivity of the Toda lattice with conservative noise. *J Stat Phys.* (2010) **140**:336–48. doi: 10.1007/s10955-010-9996-6
44. Hurtado PI, Garrido PL. A violation of universality in anomalous Fourier's law. *Sci Rep.* (2016) **6**:38823. doi: 10.1038/srep38823
45. Xiong D. Underlying mechanisms for normal heat transport in one-dimensional anharmonic oscillator systems with a double-well interparticle interaction. *J Stat Mech Theory Exp.* (2016) **2016**:043208. doi: 10.1088/1742-5468/2016/04/043208
46. Archana GR, Barik D. Temperature-dependent divergence of thermal conductivity in momentum-conserving one-dimensional lattices with asymmetric potential. *Phys Rev E.* (2019) **99**:022103. doi: 10.1103/PhysRevE.99.022103
47. Basile G, Delfini L, Lepri S, Livi R, Olla S, Politi A. Anomalous transport and relaxation in classical one-dimensional models. *Eur Phys J Spec Top.* (2007) **151**:85–93. doi: 10.1140/epjst/e2007-00364-7
48. Zhong Y, Zhang Y, Wang J, Zhao H. Normal heat conduction in one-dimensional momentum conserving lattices with asymmetric interactions. *Phys Rev E.* (2012) **85**:060102. doi: 10.1103/PhysRevE.85.060102
49. Wang L, Hu B, Li B. Validity of Fourier's law in one-dimensional momentum-conserving lattices with asymmetric interparticle interactions. *Phys Rev E.* (2013) **88**:052112. doi: 10.1103/PhysRevE.88.052112
50. Das S, Dhar A, Narayan O. Heat conduction in the α-β Fermi-Pasta-Ulam chain. *J Stat Phys.* (2014) **154**:204–13. doi: 10.1007/s10955-013-0871-0
51. Chen S, Wang J, Casati G, Benenti G. Nonintegrability and the Fourier heat conduction law. *Phys Rev E.* (2014) **90**:032134. doi: 10.1103/PhysRevE.90.032134
52. Spohn H. Fluctuating hydrodynamics for a chain of nonlinearly coupled rotators. (2014). *arXiv[Preprint].arXiv:14113907.*
53. Kulkarni M, Huse DA, Spohn H. Fluctuating hydrodynamics for a discrete Gross-Pitaevskii equation: mapping onto the Kardar-Parisi-Zhang universality class. *Phys Rev A.* (2015) **92**:043612. doi: 10.1103/PhysRevA.92.043612
54. Xiong D, Zhang Y. One-dimensional superdiffusive heat propagation induced by optical phonon-phonon interactions. *Phys Rev E.* (2018) **98**:012130. doi: 10.1103/PhysRevE.98.012130
55. Di Cintio P, Iubini S, Lepri S, Livi R. Transport in perturbed classical integrable systems: the pinned Toda chain. *Chaos Solit Fract.* (2018) **117**:249–54. doi: 10.1016/j.chaos.2018.11.003
56. Theodorakopoulos N, Peyrard M. Solitons and nondissipative diffusion. *Phys Rev Lett.* (1999) **83**:2293. doi: 10.1103/PhysRevLett.83.2293
57. Spohn H. Interacting and noninteracting integrable systems. *J Math Phys.* (2018) **59**:091402. doi: 10.1063/1.5018624
58. Kundu A, Dhar A. Equilibrium dynamical correlations in the Toda chain and other integrable models. *Phys Rev E.* (2016) **94**:062130. doi: 10.1103/PhysRevE.94.062130
59. Dhar A, Kundu A, Lebowitz JL, Scaramazza JA. Transport properties of the classical Toda chain: effect of a pinning potential. *J Stat Phys.* (2019) **175**:1298–310. doi: 10.1007/s10955-019-02284-6
60. Tamaki S, Sasada M, Saito K. Heat transport via low-dimensional systems with broken time-reversal symmetry. *Phys Rev Lett.* (2017) **119**:110602. doi: 10.1103/PhysRevLett.119.110602
61. Saito K, Sasada M. Thermal conductivity for coupled charged harmonic oscillators with noise in a magnetic field. *Commun Math Phys.* (2018) **361**:951–95. doi: 10.1007/s00220-018-3198-5
62. Bouchet F, Gupta S, Mukamel D. Thermodynamics and dynamics of systems with long-range interactions. *Phys A Stat Mech Appl.* (2010) **389**:4389–405. doi: 10.1016/j.physa.2010.02.024
63. Campa A, Dauxois T, Ruffo S. Statistical mechanics and dynamics of solvable models with long-range interactions. *Phys Rep.* (2009) **480**:57–159. doi: 10.1016/j.physrep.2009.07.001
64. Gupta S, Casetti L. Surprises from quenches in long-range-interacting systems: temperature inversion and cooling. *New J Phys.* (2016) **18**:103051. doi: 10.1088/1367-2630/18/10/103051
65. de Buyl P, De Ninno G, Fanelli D, Nardini C, Patelli A, Piazza F, et al. Absence of thermalization for systems with long-range interactions coupled to a thermal bath. *Phys Rev E.* (2013) **87**:042110. doi: 10.1103/PhysRevE.87.042110
66. Torcini A, Lepri S. Disturbance propagation in chaotic extended systems with long-range coupling. *Phys Rev E.* (1997) **55**:R3805. doi: 10.1103/PhysRevE.55.R3805
67. Métivier D, Bachelard R, Kastner M. Spreading of perturbations in long-range interacting classical lattice models. *Phys Rev Lett.* (2014) **112**:210601. doi: 10.1103/PhysRevLett.112.210601
68. Ávila RR, Pereira E, Teixeira DL. Length dependence of heat conduction in (an) harmonic chains with asymmetries or long range interparticle interactions. *Phys A Stat Mech Appl.* (2015) **423**:51–60. doi: 10.1016/j.physa.2014.12.018
69. Olivares C, Anteneodo C. Role of the range of the interactions in thermal conduction. *Phys Rev E.* (2016) **94**:042117. doi: 10.1103/PhysRevE.94.042117
70. Bagchi D. Thermal transport in the Fermi-Pasta-Ulam model with long-range interactions. *Phys Rev E.* (2017) **95**:032102. doi: 10.1103/PhysRevE.95.032102
71. Tamaki S, Saito K. Energy current correlation in solvable long-range interacting systems. (2019). *arXiv[Preprint].arXiv:190608457.* doi: 10.1103/PhysRevE.101.042118
72. Wang J, Dmitriev SV, Xiong D. Extremely high length-divergent thermal conductivity in long-range interacting Fermi-Pasta-Ulam Chains. (2019). *arXiv[Preprint].arXiv:190611086.* doi: 10.1103/PhysRevResearch.2.013179
73. Iubini S, Di Cintio P, Lepri S, Livi R, Casetti L. Heat transport in oscillator chains with long-range interactions coupled to thermal reservoirs. *Phys Rev E.* (2018) **97**:032102. doi: 10.1103/PhysRevE.97.032102
74. Di Cintio P, Iubini S, Lepri S, Livi R. Equilibrium time-correlation functions of the long-range interacting Fermi-Pasta-Ulam model. *J Phys A Math Theor.* (2019) **52**:274001. doi: 10.1088/1751-8121/ab22f7
75. Malevanets A, Kapral R. Mesoscopic model for solvent dynamics. *J Chem Phys.* (1999) **110**:8605. doi: 10.1063/1.478857
76. Ciraolo G, Bufferand H, Di Cintio P, Ghendrih P, Lepri S, Livi R, et al. Fluid and kinetic modelling for non-local heat transport in magnetic fusion devices. *Contrib Plasma Phys.* (2018) **58**:457–64. doi: 10.1002/ctpp.201700222
77. Benenti G, Casati G, Mejía-Monasterio C. Thermoelectric efficiency in momentum-conserving systems. *New J Phys.* (2014) **16**:015014. doi: 10.1088/1367-2630/16/1/015014

78. Di Cintio P, Livi R, Bufferand H, Ciraolo G, Lepri S, Straka MJ. Anomalous dynamical scaling in anharmonic chains and plasma models with multiparticle collisions. *Phys Rev E.* (2015) **92**:062108. doi: 10.1103/PhysRevE.92.062108
79. Upadhyaya M, Aksamija Z. Nondiffusive lattice thermal transport in Si-Ge alloy nanowires. *Phys Rev B.* (2016) **94**:174303. doi: 10.1103/PhysRevB.94.174303
80. Crnjar A, Melis C, Colombo L. Assessing the anomalous superdiffusive heat transport in a single one-dimensional PEDOT chain. *Phys Rev Mater.* (2018) **2**:015603. doi: 10.1103/PhysRevMaterials.2.015603
81. Sun K, Zhang S, Li P, Xia Y, Zhang X, Du D, et al. Review on application of PEDOTs and PEDOT:PSS in energy conversion and storage devices. *J Mater Sci Mater Electron.* (2015) **26**:4438–62. doi: 10.1007/s10854-015-2895-5
82. Barreto R, Carusela M, Monastra A. Nonlinear fluctuating hydrodynamics with many conserved fields: the case of a three-dimensional anharmonic chain. *Phys Rev E.* (2019) **100**:022118. doi: 10.1103/PhysRevE.100.022118
83. Lee V, Wu CH, Lou ZX, Lee WL, Chang CW. Divergent and ultrahigh thermal conductivity in millimeter-long nanotubes. *Phys Rev Lett.* (2017) **118**:135901. doi: 10.1103/PhysRevLett.118.135901
84. Li QY, Takahashi K, Zhang X. Comment on "Divergent and ultrahigh thermal conductivity in millimeter-long nanotubes". *Phys Rev Lett.* (2017) **119**:179601. doi: 10.1103/PhysRevLett.119.179601
85. Meier T, Menges F, Nirmalraj P, Hölscher H, Riel H, Gotsmann B. Length-dependent thermal transport along molecular chains. *Phys Rev Lett.* (2014) **113**:060801. doi: 10.1103/PhysRevLett.113.060801
86. Benenti G, Casati G, Mejía-Monasterio C, Peyrard M. From thermal rectifiers to thermoelectric devices. In: Lepri S, editor. *Thermal Transport in Low Dimensions. Lecture Notes in Physics*. Cham: Springer (2016) 365–407. doi: 10.1007/978-3-319-29261-8_10
87. Andresen B. Current trends in finite-time thermodynamics. *Angew Chem Int Ed.* (2011) **50**:2690–704. doi: 10.1002/chin.201123258
88. Shiraishi N, Saito K, Tasaki H. Universal trade-off relation between power and efficiency for heat engines. *Phys Rev Lett.* (2016) **117**:190601. doi: 10.1103/PhysRevLett.117.190601
89. Brandner K, Saito K, Seifert U. Thermodynamics of micro- and nano-systems driven by periodic temperature variations. *Phys Rev X.* (2015) **5**:031019. doi: 10.1103/PhysRevX.5.031019
90. Seifert U. Stochastic thermodynamics, fluctuation theorems and molecular machines. *Rep Prog Phys.* (2012) **75**:126001. doi: 10.1088/0034-4885/75/12/126001
91. Campisi M, Fazio R. The power of a critical heat engine. *Nat Commun.* (2016) **7**:11895. doi: 10.1038/ncomms11895
92. Pietzonka P, Seifert U. Universal trade-off between power, efficiency, and constancy in steady-state heat engines. *Phys Rev Lett.* (2018) **120**:190602. doi: 10.1103/PhysRevLett.120.190602
93. Koyuk T, Seifert U. Operationally accessible bounds on fluctuations and entropy production in periodically driven systems. *Phys Rev Lett.* (2019) **122**:230601. doi: 10.1103/PhysRevLett.122.230601
94. Callen HB. *Thermodynamics and An Introduction to Thermostatics*. New York, NY: John Wiley & Sons (1985).
95. de Groot SR, Mazur P. *Non-equilibrium Thermodynamics*. New York, NY: Dover (1984).
96. Zotos X, Naef FP, Prelovšek P. Transport and conservation laws. *Phys Rev E.* (1997) **55**:11029. doi: 10.1103/PhysRevB.55.11029
97. Zotos X, Prelovšek P. Transport in one dimensional quantum systems. In: Baeriswyl D, Degiorgi L, editors. *Strong Interactions in Low Dimensions. Physics and Chemistry of Materials With Low-Dimens*. Dordrecht: Kluwer Academic Piublishers (2004).
98. Garst M, Rosch A. Transport in a classical model of a one-dimensional Mott insulator: Influence of conservation laws. *Europhys Lett.* (2001) **55**:66. doi: 10.1209/epl/i2001-00382-3
99. Heidrich-Meisner F, Hoenecker A, Brenig W. Thermal transport of the *XXZ* chain in a magnetic field. *Phys Rev B.* (2005) **71**:184415. doi: 10.1103/PhysRevB.71.184415
100. Mazur P. Non-ergodicity of phase functions in certain systems. *Physica.* (1969) **43**:533–45. doi: 10.1016/0031-8914(69)90185-2
101. Suzuki M. Ergodicity, constants of motion, and bounds for susceptibilities. *Physica.* (1971) **51**:277. doi: 10.1016/0031-8914(71)90226-6
102. Benenti G, Casati G, Wang J. Conservation laws and thermodynamic efficiencies. *Phys Rev Lett.* (2013) **110**:70604. doi: 10.1103/PhysRevLett.110.070604
103. Luo R, Benenti G, Casati G, Wang J. Thermodynamic bound on heat-to-power conversion. *Phys Rev Lett.* (2018) **121**:080602. doi: 10.1103/PhysRevLett.121.080602
104. Chen S, Wang J, Casati G, Benenti G. Thermoelectricity of interacting particles: a numerical approach. *Phys Rev E.* (2015) **92**:032139. doi: 10.1103/PhysRevE.92.032139
105. Mejía-Monasterio C, Larralde H, Leyvraz F. Coupled normal heat and matter transport in a simple model system. *Phys Rev Lett.* (2001) **86**:5417–20. doi: 10.1103/PhysRevLett.86.5417
106. Larralde H, Leyvraz F, Mejía-Monasterio C. Transport properties of a modified Lorentz gas. *J Stat Phys.* (2003) **113**:197–231. doi: 10.1023/A:1025726905782
107. Datta S. *Electronic Transport in Mesoscopic Systems*. Cambridge: Cambridge University Press (1995).
108. Whitney RS. Most efficient quantum thermoelectric at finite power output. *Phys Rev Lett.* (2014) **112**:130601. doi: 10.1103/PhysRevLett.112.130601
109. Whitney RS. Finding the quantum thermoelectric with maximal efficiency and minimal entropy production at given power output. *Phys Rev B.* (2015) **91**:115425. doi: 10.1103/PhysRevB.91.115425
110. Mahan GD, Sofo JO. The best thermoelectric. *Proc Natl Acad Sci USA.* (1996) **93**:7436. doi: 10.1073/pnas.93.15.7436
111. Humphrey TE, Newbury R, Taylor RP, Linke H. Reversible quantum Brownian heat engines for electrons. *Phys Rev Lett.* (2002) **89**:116801. doi: 10.1103/PhysRevLett.89.116801
112. Humphrey TE, Linke H. Reversible thermoelectric nanomaterials. *Phys Rev Lett.* (2005) **94**:096601. doi: 10.1103/PhysRevLett.94.096601
113. Saito K, Benenti G, Casati G. A microscopic mechanism for increasing thermoelectric efficiency. *Chem Phys.* (2010) **375**:508–13. doi: 10.1016/j.chemphys.2010.06.009
114. Brantut JP, Grenier C, Meineke J, Stadler D, Krinner S, Kollath C, et al. A thermoelectric heat engine with ultracold atoms. *Science.* (2013) **342**:713. doi: 10.1126/science.1242308
115. Husmann D, Lebrat M, Häusler S, Brantut JP, Corman L, Esslinger T. Breakdown of the Wiedemann-Franz law in a unitary Fermi gas. *Proc Natl Acad Sci USA.* (2018) **115**:8563–68. doi: 10.1073/pnas.1803336115
116. Vasseur R, Moore JE. Nonequilibrium quantum dynamics and transport: from integrability to many-body localization. *J Stat Mech.* (2016) **2016**:064010. doi: 10.1088/1742-5468/2016/06/064010
117. Abanin DA, Altman E, Bloch I, Serbyn M. Many-body localization, thermalization, and entanglement. *Rev Mod Phys.* (2019) **91**:021001. doi: 10.1103/RevModPhys.91.021001
118. Prosen T, Žnidarič M. Matrix product simulations of non-equilibrium steady states of quantum spin chains. *J Stat Mech.* (2009) **2009**:P02035. doi: 10.1088/1742-5468/2009/02/P02035
119. Mejia-Monasterio C, Wichterich H. Heat transport in quantum spin chains. *Eur Phys J Spec Top.* (2007) **151**:113–25. doi: 10.1140/epjst/e2007-00367-4
120. Saito K. Strong evidence of normal heat conduction in a one-dimensional quantum system. *Europhys Lett.* (2003) **61**:34. doi: 10.1209/epl/i2003-00241-3
121. Mejía-Monasterio C, Casati G, Prosen T. Fourier's law in a quantum spin chain and the onset of quantum chaos. *Europhys Lett.* (2005) **72**:520. doi: 10.1209/epl/i2005-10267-y
122. Znidarič M, Prosen T, Benenti G, Casati G, Rossini D. Thermalization and ergodicity in one-dimensional many-body open quantum systems. *Phys Rev E.* (2010) **81**:051135. doi: 10.1103/PhysRevE.81.051135
123. Levy A, Kosloff R. The local approach to quantum transport may violate the second law of thermodynamics. *Europhys Lett.* (2014) **107**:2004. doi: 10.1209/0295-5075/107/20004
124. Balachandran V, Benenti G, Pereira E, Casati G, Poletti D. Heat current rectification in segmented XXZ chains. *Phys Rev E.* (2019) **99**:032136. doi: 10.1103/PhysRevE.99.032136

125. Carrega M, Solinas P, Braggio A, Sassetti M, Weiss U. Functional integral approach to time-dependent heat exchange in open quantum systems: general method and applications. *New J Phys.* (2015) **17**:045030. doi: 10.1088/1367-2630/17/4/045030
126. Tamascelli D, Smirne A, Lim J, Huelga SF, Plenio MB. Efficient simulation of finite-temperature open quantum systems. *Phys Rev Lett.* (2019) **123**:090402. doi: 10.1103/PhysRevLett.123.090402
127. Wiedmann M, Stockburger TJ, Ankerjold J. Out-of-equilibrium operation of a quantum heat engine: the cost of thermal coupling control. (2019) *arXiv[Preprint].arXiv:190311368*.

Conflict of Interest: The authors declare that the research was conducted in the absence of any commercial or financial relationships that could be construed as a potential conflict of interest.

Advantages of publishing in Frontiers

OPEN ACCESS
Articles are free to read
for greatest visibility
and readership

FAST PUBLICATION
Around 90 days
from submission
to decision

HIGH QUALITY PEER-REVIEW
Rigorous, collaborative,
and constructive
peer-review

TRANSPARENT PEER-REVIEW
Editors and reviewers
acknowledged by name
on published articles

Frontiers
Avenue du Tribunal-Fédéral 34
1005 Lausanne | Switzerland

Visit us: www.frontiersin.org
Contact us: info@frontiersin.org | +41 21 510 17 00

REPRODUCIBILITY OF RESEARCH
Support open data
and methods to enhance
research reproducibility

DIGITAL PUBLISHING
Articles designed
for optimal readership
across devices

FOLLOW US
@frontiersin

IMPACT METRICS
Advanced article metrics
track visibility across
digital media

EXTENSIVE PROMOTION
Marketing
and promotion
of impactful research

LOOP RESEARCH NETWORK
Our network
increases your
article's readership